Framework for Seismic Vulnerability Assessment of RC High-rise Wall Buildings

A thesis submitted for the degree of Doctor of Philosophy
in the Faculty of Engineering of the University of Sheffield

By

Wael Alwaeli

(B.Sc. Civil Engineering, M.Sc. Structural Engineering)

Earthquake Engineering Group (EEG)
Department of Civil & Structural Engineering
The University of Sheffield

June 2019

This page is intentionally left in blank

ABSTRACT

With population growth and urbanization, the number of high-rise buildings is rapidly growing worldwide resulting in increased exposure to multiple-scenario earthquakes and associated risks. The wide range in the frequency content of expected ground motions impacts the seismic response and vulnerability of this class of structures. While the seismic vulnerability of some high-rise building classes has been evaluated, the vulnerability of these structures under multiple earthquake scenarios is not fully understood, highlighting the pressing need for the development of a framework to address this complex issue.

This study aims to establish a refined framework to assess the seismic vulnerability of RC high-rise wall buildings in multiple-scenario earthquake-prone regions. A deeper understanding of the responsive nature of these structures under different seismic scenarios is developed as a tool to build the framework. The framework is concluded with analytically-driven sets of Seismic Scenario-Structure-Based (SSSB) fragility relations.

Different nonlinear modelling approaches, software, and key parameters contributing to the nonlinear analytical models of RC high-rise wall structures are investigated and verified against full-scale shake table tests through a multi-level nonlinear modelling verification scheme. The study reveals the superior performance of 4-noded fibre-based wall/shell element modelling approach in accounting for the 3D effects and deformation compatibility. A fundamental mode damping value in the range of 0.5% is found sufficient to capture the inelastic response when initial stiffness-based damping matrix is employed.

A 30-storey reference wall building located in the multiple-scenario earthquake-prone city of Dubai (UAE) is fully designed and numerically modelled as a case study to illustrate the proposed framework. A total of 40 real earthquake records, representing severe distant and moderate near-field seismic scenarios, are used in the Multi-Record Incremental Dynamic Analyses (MRIDAs) along with a new scalar intensity measure.

A methodology is proposed to obtain reliable SSSB definitions of limit state criteria for RC high-rise wall buildings. The local response of the reference building is mapped using Net Inter-Storey Drift (NISD) as a global damage measure. The study reveals that for this class of structures, higher modes shift the shear wall response from flexure-controlled under severe distant earthquakes to shear-controlled under moderate near-field events. A numerical parametric study employing seven RC high-rise wall buildings with varying height is conducted to investigate the effect of total height on the local damage-drift relation. The study reveals that, for buildings with varying heights and similar structural system, NISD is better linked to the building response and well correlated to structural member damage, which indicates that only one set of SSSB limit state criteria is necessary for a range of buildings.

The study concludes with finalising the layout of the proposed refined framework to assess the seismic vulnerability of RC high-rise wall buildings under multiple earthquake scenarios. A methodology to develop refined fragility relations is presented where the derived fragility curves are analysed, compared, and correlated to varying states of damage.

Finally, a methodology to develop Cheaper (simplified) Fragility Curves (CFC) using the defined limit state criteria with a lower number of records is proposed along with a new record selection criterion and fragility curve acceptance procedure. It is concluded that fairly reliable CFCs can be achieved with 5 to 6 earthquake records only.

ACKNOWLEDGEMENTS

This work would not have been possible nor achievable without the guidance and support of several people. People, who in many ways, did not hesitate to generously extend their valuable assistance both physically and mentally with the preparation and completion of this thesis.

Firstly, I must express my genuine gratitude and sincere regards to my supervisors and dear friends, **Prof. Kypros Pilakoutas** and **Associate Prof. Aman Mwafy**. Your guidance, profound intellect, keen eye and continuous encouragement have all made this thesis possible. I am deeply and wholeheartedly thankful to **Dr. Maurizio Guadagnini** for his co-supervision, advice, and invaluable friendship.

Thank you to all my colleagues in rooms E110 and E110a, substantially to **Dr. Kamaran Ismail, Dr. Reyes Garcia, and Dr. Bestun**. It was the utmost pleasure to work with you.

Notable thanks to **Archt. Yousuf Al Muhaideb** (chairman of AREX Consultant, Dubai, UAE), my dearest **Eng. Huda al Mashhadani**, the late **Dr. Hameed Al Roba'I**, my close friend and brother Eng. **Ahmed K. Alsharbati** for their absolute and distinct support and understanding during my research years.

My heart goes out to my late father, **Qahtan Alwaeli**, for planting the seed of belief and determination in me. To my mother, **Salwa Almusawi**, for assuring this grand dream of mine came true with constant prayers and insurmountable love. To my brother **Samar**, my brother-in-law **Ali**, and my sisters, **Awael**, **Sana'**, and **Rosul** for their endless support and devotion throughout this journey.

To my beloved family; my wife **Yusra**, who has been my confidant and shoulder to rest on in times of need. My children, **Tiba**, **Awael**, **Hassan** and **Ahmed**, for their never-ending adoration and encouragement. They have been there for me when I was not able to be there for myself. Without them, I would have never amounted to where I am today.

I would like to sincerely thank **Prof. Andreas Kappos** and **Dr. Iman Hajirasouliha** (the examiners) for their time and effort spent in reviewing the thesis. Their comments and suggestions during and post the Viva have notably enhanced the thesis material both on the technical and writing levels.

Thanks to Allah swt, for helping the little wounded ant summit this mighty mountain.

LIST OF PUBLICATIONS

Published:

Alwaeli, W., Mwafy, A., Pilakoutas, K., & Guadagnini, M. (2017). **A methodology for defining seismic scenario-structure-based limit state criteria for RC high-rise wall buildings using net drift**. *Earthquake Engineering & Structural Dynamics*, *46*(8), 1325-1344.

Alwaeli, W., Mwafy, A., Pilakoutas, K., & Guadagnini, M. (2017). **Multi-level nonlinear modelling verification scheme of RC high-rise wall buildings**. *Bulletin of Earthquake Engineering*, *15*(5), 2035-2053.

Alwaeli, W., Mwafy, A., Pilakoutas, K., & Guadagnini, M. (2016) **Performance criteria for RC high-rise wall buildings exposed to varied seismic scenarios**. *16th World Conference on Earthquake Engineering (16WCEE), Santiago, Chile.*

Alwaeli, W., Mwafy, A., Pilakoutas, K., & Guadagnini, M. (2015). **Seismic scenario-structure-based performance criteria for RC high-rise wall buildings**. *Third EAGE International Conference on Engineering Geophysics, Al Ain, UAE.*

Alwaeli, W., Mwafy, A., Pilakoutas, K., & Guadagnini, M. (2014). **Framework for developing fragility relations of high-rise RC wall buildings based on verified modelling approach**. *Second European Conference on Earthquake Engineering and Seismology (2ECEES), Istanbul, Turkey.*

Alwaeli, W., Mwafy, A., Pilakoutas, K., & Guadagnini, M. (2013). **Seismic loss assessment framework for RC high-rise wall buildings: Dubai case study**. *Second EAGE International Conference on Engineering Geophysics, Al Ain, UAE*.

Submitted (under the first round of review):

Alwaeli, W., Mwafy, A., Pilakoutas, K., & Guadagnini, M. (October 2019). **Rigorous versus less-demanding fragility relations for RC high-rise buildings**, *Bulletin of Earthquake Engineering.*

Under preparation:

Alwaeli, W., Mwafy, A., Pilakoutas, K., & Guadagnini, M. (2020). **Seismic vulnerability of high-rise wall buildings: Problem definition and framework.**

LIST OF NOTATIONS

A_g	cross-sectional gross area
cov	coefficient of variation for the MRIDAs
D	dead load
Dis_V	vertical displacement at the wall segment node
D_{rms}	variable to verify the spectral compatibility of a selected record with the target spectrum
E	modulus of elasticity
E_c	concrete modulus of elasticity
f_c'	cylindrical compressive strength of concrete
f_i	frequency of the i-th mode
f_y	yield strength of reinforcing steel bars
f_1	frequency of the first mode
h_i	height of the i^{th} storey
h_w	wall height
i	mode of vibration number
I_g	cross-sectional gross moment of inertia
L	live load
L_{cb}	length of the coupling beam
L_w (l_w)	wall length
MPR_i	mass participation ratio corresponded to the i^{th} mode of vibration
M_u	ultimate moment
N	number of periods at which the spectral shape is specified
n	number of sample data demand points; cycle number
$NISD_i$	net inter-storey drift of the i^{th} storey
NOR	number of records used to develop the fragility curve
$NVDisp_i$	net vertical inter-story displacement of the i^{th} storey
P	axial load
PGA_s	zero-period anchor point of the target spectrum
PGA_0	peak ground acceleration of the selected record
P_{lower}	lower end point of the confidence interval for the mean of a log-normal distribution
PLS_i	i^{th} performance limit state
$POE(PLS_i\|IM)$	probability of exceeding the i^{th} performance limit state given the IM value
P_{upper}	upper end point of the confidence interval for the mean of a log-normal distribution

S_a	spectral acceleration
S_{ai}	spectral acceleration ordinate corresponded to the time period of the i^{th} mode
$S_a(T_1)$	spectral acceleration at the fundamental period of the structure
$S_{a(wa)}$	spectral acceleration at weighted-average period
$(S_a)_{NOR}^{NOR+1}$	absolute of the difference ratio between S_a^{NOR+1}@50%POE and S_a^{NOR}@50%POE
S_a^R	spectral acceleration value of the record at the specified time period
S_a^{UHS}	spectral acceleration value of the UHS at the specified time period
$S_{a(0.2s)}$	spectral acceleration at 0.2 second time period
$S_{a(1s)}$	spectral acceleration at 1 second time period
s^2	standard error of the demand DM data
$S\alpha_s(T_i)$	target spectral acceleration at period T_i
$S\alpha_0(T_i)$	spectral acceleration of the selected record at period T_i
$T_{average(mi,j)}$	arithmetic mean of the ith and jth mode periods
TDP	difference in the damage probability
TFC	fragility curve tolerance factor
THDispi	total lateral (horizontal) inter-storey displacement of the ith storey
T_{mi}	building equivalent inelastic time period of the ith mode
TR	record tolerance factor
T_{wa}	weighted-average period
$T_{wa(mi,j)}$	building weighted-average period of the i^{th} and j^{th} modes
v_n	wall nominal shear strength from ACI code
V_u	ultimate shear force
W	confidence interval relative width
Y_k	observed median DM given the IM value
Y_p	power law estimated median DM given the IM value
α	angle of the diagonal reinforcement in the coupling beam
$\alpha_{(DM\|IM)}$	natural logarithm of the calculated median demand DM given the IM value
$\alpha_{(DM\|PLS_i)}$	natural logarithm of the median DM capacity for the i^{th} performance limit state
$\beta_{(DM\|IM)}$	demand uncertainty given the IM value
$\beta_{(DM\|PLS_i)}$	capacity uncertainty for the i^{th} performance limit state
β_m	modelling uncertainty
γ	constant, equals 1.2 for RC buildings
δ_θ	equivalent displacement in the coupling beam at rotation θ
ε	axial strain in walls

θ	coupling beam rotation in radians
θ_i	tangent angle at the bottom end of the i^{th} storey
ξ_i	damping ratio of the i-th mode
ξ_1	damping ratio at the first mode
σ	standard deviation of the sample mean
σ^{NOR}	standard deviation of the $S_{a(wa)}$ values at the (NOR) fragility curve corresponding to POE levels of 16%, 50%, and 84%
σ^{NOR+1}	standard deviation of the $S_{a(wa)}$ values at the (NOR+1) fragility curve corresponding to POE levels of 16%, 50%, and 84%
σ_{NOR}^{NOR+1}	absolute of the difference ratio between σ^{NOR+1} and σ^{NOR}
φ	wall curvature; standard normal distribution function
φ_y	wall yield curvature

LIST OF ABBREVIATIONS

a/v	acceleration to velocity ratio
C/D	capacity to demand ratio
CFC	cheaper fragility curve
CP	collapse prevention
CQC	complete quadratic combination
DBE	designed-based earthquake
DI	damage index
DM	damage measure
DPO	dynamic pushover
DSHA	deterministic seismic hazard assessment
EDP	engineering demand parameter
ELFP	equivalent lateral force procedure
ERA	earthquake risk assessment
FC	fragility curve
F-D	force-deformation relation
FFM	free-field motion
FFT	fast fourier transform
FIM	foundation input motion
GIS	geographic information system
GMPE	ground motion prediction equation
HDSIs	high definition satellite images
IDA	incremental dynamic analysis
IM	intensity measure
IO	immediate occupancy
IOC	impaired occupancy
IPO	input-process-output
ISD	inter-storey drift
LS	life safety
M	earthquake magnitude
MCE	maximum considered earthquake
MDOF	multidegree-of-freedom
MLNMVS	multi-level nonlinear modelling verification scheme
MPR	mass participation ratio
MRIDA	multi-record incremental dynamic analysis
MRSA	modal response spectrum analysis

M/V	moment to shear ratio
MVLE	multi vertical line element
NISD	net inter-storey drift
NRHA	nonlinear response history analysis
PGA	peak ground acceleration
PLS	performance limit state
POE	probability of exceedance
PSHA	probabilistic seismic hazard assessment
R	earthquake site-to-source distance
RBM	rigid body motion
RBMISD	rigid body motion inter-storey drift component
RPLSC	reference performance limit state criteria
RSC	record selection criterion
S	soil profile
SC	structural collapse
SD	structural damage
SDC	seismic design category
SDOF	single-degree-of-freedom
SF	scale factor
SLE	serviceability level earthquake
SPLSC	specified performance limit state criteria
SRIDA	single-record incremental dynamic analysis
SSI	soil-structure interaction
SSSB	seismic scenario-structure-based
TISD	total inter-storey drift
UHS	uniform hazard spectrum (spectra)
UOC	unimpaired occupancy

TABLE OF CONTENTS

LIST OF FIGURES

CHAPTER 2

CHAPTER 3

CHAPTER 4

CHAPTER 5

CHAPTER 6

LIST OF TABLES

CHAPTER 3

CHAPTER 4

CHAPTER 5

CHAPTER 6

APPENDIX A

CHAPTER 1. Introduction

1.1 Problem definition and significance

With changing socioeconomic conditions, rapid population growth and urbanization, many cities all over the world have expanded rapidly in recent years. This expansion has led to a massive increase in high-rise buildings and to the spread of cities to multiple-scenario earthquake-prone regions. This increases the exposure to seismic risk and consequently, the concern for the seismic performance of this class of structures, especially following the extensive damages caused by strong earthquakes that occurred in the last three decades (e.g. Kobe 1995; Kocaeli, 1999; Chi-Chi, 1999; Tohoku, 2011). The quantification and mitigation of seismic risk require a deep understanding of the hazard and vulnerability (e.g. Pilakoutas, 1990, Kappos et al., 2010, Hajirasouliha and Pilakoutas, 2012, Mwafy, 2012a).

High-rise buildings are at most risk from earthquake events since they represent a high level of financial investment and population densities. The majority of high-rise buildings in most countries employ RC walls and cores as the primary lateral-force-

resisting system due to their effectiveness in providing the strength, stiffness, and deformation capacity needed to meet the seismic demand. The trend to increasingly use RC in high-rise buildings is expected to continue due to the development of commercial high-strength concrete and new advances in construction technologies (Ali and Moon, 2007). The broad range of frequency content in real strong ground motions, representative of different seismic scenarios such as distant and near-field earthquakes, can impose different levels of excitation on both fundamental and higher modes in RC high-rise wall structures. This will result in more complex, seismic scenario-based inelastic response.

Earthquake-resistant buildings are designed and detailed to respond inelastically under the Design and Maximum Considered Earthquakes (DBE and MCE). In RC high-rise buildings, well designed and proportioned RC slender shear walls ensure the adequate performance of the building in the "service", "ultimate", and "collapse prevention" limit states. Various aspects of nonlinear modelling, such as element discretisation, material force-deformation relationships, and assumptions on the modelling of damping are essential in defining the level of model accuracy for predicting the global and local seismic response of a structure. Despite the ability of sophisticated wall micro-scale models (i.e. continuum FE models) to provide a refined and detailed definition of the local response with a high level of flexibility and accuracy, the associated computational effort and time demands render these models forbiddingly expensive especially when Multi-Record Incremental Dynamic Analysis (MRIDA) techniques are adopted. Alternatively, the meso-scale fibre-based element modelling approach is commonly used for RC shear walls (Wallace, 2007, Wallace, 2012). Given the limitation in experimental data for RC structural wall systems subjected to cycling loading as most tests conducted are on isolated wall elements, limited (shake table test results-based) analytical verification attempts have been previously conducted with an extended verification scheme that covers and compare different nonlinear modelling aspects in the same verification attempt. These modelling aspects are namely: (i) wall modelling approaches, i.e. frame (2-noded) and shell (4-noded) fibre-based elements; (ii) different approaches in modelling of key parameters such as material and damping; and (iii) three-dimensional interaction effects. Hence, there is still a need for an extended verification scheme of building response for such structures which is essential for assessing their seismic vulnerability and risk. (Ji et al., 2007a, Martinelli and Filippou, 2009, PEER/ATC, 2010).

Quantitative definitions of limit state criteria form the spine of seismic vulnerability assessment. These definitions require mathematical representations of local damage indices, such as deformations, forces, or energy based on designated structural response levels. Therefore, suitable damage measures need to be adapted to sufficiently correlate local damage (events) in the building to its global response. There are several factors affecting failure modes in this class of structures including building height, axial force levels, supplementary regulations introduced by local authorities, as well as local trends in design and construction. When the building response is dominated by the fundamental mode, the taller the building, the larger is the expected Total Inter-Storey Drift (TISD) due to the rigid body motion phenomenon. This is not necessarily associated with seismic demand and level of damage at the lower floors in the building. Hence, reliable definitions of limit state criteria corresponding to predefined performance levels for RC high-rise wall buildings is another significant research issue.

For RC high-rise building inventory, even small errors in the derived sets of fragility relations may have a significant impact on the estimated regional losses and associated cost (in the fold of hundreds of millions or even billions of dollars). Hence, the key parameters that control the resultant fragility curves need to be accurately decided and calculated, including:

i. Uncertainties in input ground motions, controlled by the record selection criteria.
ii. Building seismic response, characterised by the two main measures that are shaping the MRIDAs, namely the Intensity Measure (IM) and the Damage Measure (DM).
iii. Building seismic performance capacity, represented by the seismic scenario-based limit state criteria.

In MRIDA using real input ground motions, the seismic scenario-based record selection criteria mainly include magnitude, distance, and site conditions without an explicit reflection of structural characteristics of the building(s) under investigation (Iervolino and Cornell, 2005, Mwafy et al., 2006, Mwafy, 2012a). This way of record selection requires the calculation of seismic response for all ground motion records representative of an earthquake scenario. It would, therefore, be useful to add another criterion to the record selection in such a way that the selected records are the best representatives for the prediction of the seismic response of the investigated structures. By adding this element to the framework for deriving fragility relations of high-rise buildings, a

significant decrease in the number of ground motion records needed for the sufficiently accurate prediction of seismic response and fragility relations with a predefined acceptance level may be achieved.

1.2 Research aims and objectives

This study aims to establish a refined framework to assess the seismic vulnerability of RC high-rise wall buildings in multiple-scenario earthquake-prone regions. The framework is to be concluded with analytically-driven sets of seismic scenario-structure-based (SSSB) fragility relations that can be developed using either a refined or a simplified methodology.

The specific objectives of this research are:

(A) Establish a literature review-based problem definition.

A.1. Define the research problem through an Input-Process-Output (IPO) model that presents the general framework to assess the seismic vulnerability of RC high-rise wall building(s).

A.2. Critical review of the relevant literature on the key parameters and variables that control each component in the framework.

(B) Investigate nonlinear modelling approaches, nonlinear modelling tools, and modelling key parameters.

B.1. Investigate different nonlinear modelling approaches, tools, and modelling key parameters to verify their effectiveness in simulating the seismic response of RC high-rise wall structures.

B.2. Conduct a multi-level nonlinear modelling verification scheme (MLNMVS) to verify the nonlinear modelling approach, tool, and modelling key parameters to be adopted in the present study. The MLNMVS involves the simulation of the shake table seismic response of a full-scale multi-storey RC wall building.

(C) Build a case study to implement and verify the presented framework.

C.1. Select a study region, represented by the multiple-scenario earthquake-prone Emirate of Dubai (United Arab Emirates). Dubai is worldwide

known for its escalating number of modern RC high-rise buildings and skyscrapers.

C.2. Study the seismic hazard of the selected region to identify the seismic scenarios, Uniform Hazard Spectrum (UHS) and site classification.

C.3. Utilise the available earthquake databases to assemble seismic scenario-based real input ground motions to represent the seismic hazard of the study region. For this purpose, a record selection criterion is to be set.

C.4. Choose, fully design, and idealise a reference (sample) building for the case study.

(D) Set a methodology to derive new sets of SSSB limit state criteria for RC high-rise wall buildings.

D.1. Investigate and propose new IM that best represents the seismic response of the class of structures under investigation.

D.2. Investigate and propose new DM that best correlate local to global damage of the class of structures under investigation.

D.3. Investigate the behaviour of the reference building under different seismic scenarios to identify the modes of failure that control the seismic response and the building performance.

(E) Set a methodology to derive refined SSSB analytically-driven fragility relations for RC high-rise wall buildings.

E.1. Derive new sets of refined fragility relations for the reference building to demonstrate the efficiency of the refined methodology.

E.2. Assess and compare the derived fragility relations to give insight into the differences in the vulnerability of RC high-rise wall buildings under multiple earthquake scenarios.

(F) Set a simplified methodology to derive less demanding (Cheaper) Fragility Curves (CFC) for RC high-rise wall buildings.

F.1. Propose a new criterion for the record selection process to better link the selected records to the structural characteristics of the investigated

building(s) and consequently reduce the total number of input ground motions to be used in MRIDA.

F.2. Propose a new acceptance tolerance factor to set the desired accuracy level of the developed CFCs.

F.3. Verify the proposed record selection criterion and the acceptance tolerance factor used to derive the CFCs. The verification is through applying the simplified methodology on the reference building (and three other buildings with varying total height) and comparing the derived CFCs with the refined ones.

1.3 Thesis layout

This thesis is organised into seven chapters and one appendix, written following the "traditional" thesis format. A brief overview of each chapter is given below.

CHAPTER 2 presents the problem definition. In Section 2.1, a list of defined terms is established, to be used throughout this thesis. In Section 2.2, an IPO model is presented to best define the problem of assessing the seismic vulnerability of a building or building stock. In this section, the relevant literature on the key parameters and variables shaping the problem are critically reviewed.

CHAPTER 3 discusses the verification of nonlinear modelling of RC high-rise wall structures. The chapter is divided into six sections. Following the chapter introduction in Section 3.1, Section 3.2 presents the key features of the utilised analytical tools, including cross-sections, element formulation, material models and numerical strategy. A brief description of the University of California San Diego (USCD) shake table test program and the test structure are given in Section 3.3. Section 3.4 discusses the four input ground motions used in the tests. The analytical models created in the current study along with the comparison of their results with experimental data are detailed in Section 3.5. The chapter concludes with a summary of the work, findings, and modelling recommendations (Section 3.6).

CHAPTER 4 presents the case study utilised in the current work. It consists of five main sections. Section 4.1 presents the seismicity of the study region (Dubai). Hazard studies on the region are critically reviewed and appropriate seismic characteristics are selected for the subsequent seismic vulnerability assessment. Section 4.2 discusses the

criteria for the selection of input ground motions, where forty real records are selected to represent two seismic scenarios. Section 4.3 discusses the selection, analysis, and design of a 30-storey RC building that is utilised as the reference structure for the current study. Section 4.4 details the nonlinear modelling of the 30-storey reference building using the modelling approach and key parameters presented in CHAPTER 3. The chapter concludes with a summary of the work (Section 4.5).

CHAPTER 5, dealing with the SSSB limit state criteria of RC high-rise buildings, is divided into seven sections. Following the chapter introduction in Section 5.1, Section 5.2 presents the results of the MRIDAs conducted on the reference building using the two sets of seismic scenario-based records (20 records in each set). In this section, a new scalar IM is proposed. In Section 5.3, the local response of the reference building is mapped using a total of seven local Damage Indices (DIs) and two representative records. Furthermore, the adopted DIs are discussed in detail. In Section 5.4, the seismic scenario-based local response of the reference building is mapped against and correlated to the acceleration, velocity and displacement time histories of the two records used in Section 5.25.3. In Section 5.5, a new global DM is proposed to be used in defining seismic scenario-based limit state criteria for the reference building. In this section, a numerical parametric study is conducted, utilising seven RC high-rise buildings with varying height, to investigate the effect of building total height on the relationship between local damage events and drifts. In Section 5.6, new sets of seismic scenario-based limit state criteria are defined for the three adopted performance levels (Immediate Occupancy “IO”, Life Safety “LS”, and Collapse Prevention “CP”). Furthermore, the reference building response and thus the defined limit state criteria are discussed in detail for each of the two investigated seismic scenarios. Section 5.7 presents the summary and concluding remarks of the chapter.

CHAPTER 6 deals with the development of fragility relations for RC high-rise wall buildings. It contains five sections. Section 6.1 comprises the development of the seismic scenario-based refined fragility relations for the reference building. This represents the concluding step in the proposed framework for the seismic vulnerability assessment of RC high-rise wall buildings. In Section 6.2, the refined fragility relations are examined at selected earthquake intensity levels to assess their accuracy. Furthermore, the characteristics of the developed fragility relations under the two investigated seismic scenarios are analysed and compared. This section is concluded

with correlating the refined fragility relations with four states of damage in the reference building, that are unimpaired occupancy “UOC”, impaired occupancy “IOC”, structural damage “SD”, and structural collapse “SC”. In Section 6.3, a simplified methodology towards developing fragility relations with less computational effort is proposed. By utilising this methodology, the fragility curves of reinforced concrete high-rise buildings related to a certain seismic scenario can be generated with a much lower number of input ground motions compared to those needed to derive the refined fragility curves in Section 6.1. Section 6.4 presents the developed fragility curves for three out of the six additional buildings employed in the parametric study that was presented in CHAPTER 5. Section 6.46.5 presents the summary and concluding remarks of the chapter.

CHAPTER 7 summarises the research work, draws general conclusions and gives recommendations for future work.

Appendix A discusses the different structural systems in RC high-rise buildings.

CHAPTER 2. Problem definition

The seismic vulnerability assessment of multiple-scenario earthquake-prone RC high-rise wall buildings is a challenging and ongoing task for researchers. Considering this task as an engineering problem, addressing it involves several components. The objective of the first section of this chapter (Section 2.1) is to establish a list of key terms that will be used throughout this document with a clear definition to each of them. The terms will be listed in alphabetical order. In Section 2.2, an IPO model is presented to best define the problem of assessing the seismic vulnerability of a building or a building stock. In this section, the relevant literature on the key parameters and variables shaping the problem are critically reviewed.

2.1 Term definitions

A list of key term definitions is constructed hereafter in alphabetical order.

Building Inventory: Is a class of buildings often defined by structural material, height range, lateral force-resisting system, occupancy, period of construction, and physical condition for a specific region or country.

Seismic Damage Measure (DM): Is a structural state variable represented by a non-negative scalar that signifies the additional response of the structural model as a result of a predefined seismic loading.

Engineering Demand Parameter (EDP): Is the structural response variable of interest. This can be either a global response such as peak inter-storey drift of any given storey and peak floor acceleration, or a local response such as structural member force, deformation, or energy dissipation.

Fragility (Vulnerability): Fragility is a probability-valued function of an Engineering Demand Parameter (EDP) or an IM. Component fragility can be defined as the cumulative distribution function of the EDP capacity of a building structural or non-structural component to resist a specific damage state. Despite being varied by component, the damage states are generally defined in terms of objective physical damage linked to a particular repair cost. Fundamentally, the component fragility is a function that outputs the probability of exceeding a predefined damage state of a component for input values of a specified EDP. In structural component fragility functions, different EDPs could be used as the argument such as member deformation, force, and or hysteretic energy dissipation.

In the field of Earthquake Risk Assessment (ERA), researchers are commonly implementing the fragility function approach in defining damage states for a whole storey in a building (storey fragility function) or even for an entire building (building fragility function). Storey or building fragility is defined exactly the same way as for the component fragility; except for using IM as the argument and the damage state is being for the entire storey or building. In developing building-based fragility relations, it is essential to use a proper DM that is able to well correlate the building global response to the local damage at the component level.

The term “fragility” is commonly used interchangeably with the term “vulnerability”, considering the two offer an exact same meaning. It can be defined as the probabilistic vulnerability function (e.g. Kappos and Panagopoulos, 2010, Stefanidou et al., 2017). What is common between fragility and vulnerability though is that they are both functions whose only argument is a single scalar value of seismic intensity or structural response. The seismic intensity is generally described by the IM while the structural response variable of interest is referred to as the EDP. The main difference between the two terms, on the other hand, is at their output value. Vulnerability is a loss-valued function for an entire storey or a building. The vulnerability function establishes the relation between the IM and the Mean Damage Ratio (MDR), which is the repair/reconstruction cost. In the present study though, the term “vulnerability” refers to the fragility of the entire structure.

Incremental Dynamic Analysis (IDA) curve: Is a plot of a predefined DM recorded in an IDA study of a given structural model versus one IM or more that parameterized the applied scaled ground motion accelerogram.

Intensity Measure (IM): Is a non-negative scalar (or vector) that constitutes a function of the scaled accelerogram. It refers to the unscaled accelerogram and is increasing or decreasing *monotonically* with a predefined scaling algorithm.

Multi-Record Incremental Dynamic Analysis (MRIDA): Is an assembly of SRIDA studies for a specific structural model under multiple accelerograms. As a result of such a study, a set of IDA curves is produced, which by sharing the same DM and a common selection of IM variables, can be plotted on one graph.

Scaled Accelerogram: Is an accelerogram scaled with a non-negative scale factor (SF). The SF establishes a one-to-one mapping from the unscaled (original) accelerogram to all its scaled images. A value of SF = 1 indicates the natural accelerogram, SF > 1 is a scaled-up accelerogram, while SF < 1 corresponds to a scaled-down one. A scaling algorithm is used to estimate the intervals of the SF.

Scaling Algorithm: Is an algorithm intended to select an optimum grid of distinct intensity measure values that will deliver the desired coverage of building seismic response with the objectives of achieving a minimum number of runs, high demand resolution, and high capacity resolution.

Seismic Hazard: Is the probability of reaching or exceeding certain ground shaking intensity (e.g. magnitude, acceleration, velocity, or displacement) for a given area and a reference time period.

Single-Record Incremental Dynamic Analysis (SRIDA): Also known as Incremental Dynamic Analysis (IDA) or simply a Dynamic Pushover (DPO). It is a dynamic analysis study of specific structural model characterised by the SF of a given single ground motion accelerogram.

The IDA involves a series of nonlinear dynamic runs performed using an accelerogram with multiple scaled images, whereby the IMs are selected to cover the whole response range from elastic to nonlinear all the way to the collapse state of the studied structure. The intention is to monitor and record the DMs of the structural model at each IM level of the scaled accelerogram. The results, DM response values against IM levels, are often plotted as a continuous IDA curve.

Soil-Structure Interaction (SSI) analysis: Is the analysis that evaluates the collective seismic response of the structure, foundation, and the surrounding/underlying soil, to given free-field ground motion.

2.2 IPO model

Similar to any other engineering problem, the seismic vulnerability assessment of a building (or a building inventory) can be presented using the Input-Process-Output (IPO) model. Figure 2.1 illustrates the IPO model of the seismic vulnerability assessment problem using the aforementioned concept. In the succeeding sub-sections, each of the components in the three main blocks of the IPO model is further broken down into its sub-components, whose critical literature reviewing is presented.

2.2.1 Structure

A building (or a building inventory) forms the input in this problem, in which all other components of the IPO model are applied to, processed off, or resulted from. Figure 2.2 shows the collapsing chart for the “Structure” component of the IPO model. In the last few decades, the developments of RC tall buildings have been rapidly increasing worldwide. Varies factors drive these developments including but not limited to

economics, politics, aesthetics, advancing in construction and material technology, and municipal regulations. As a result of the pressing demand, sometimes desire, for taller and taller buildings, combined with the revolution in architectural styles, the development of the structural systems utilised in high-rise RC buildings has been a continuously evolving process. The next subsections provide a brief discussion on high-rise building definitions, the topic of building inventory, structural systems used in RC high-rise buildings, and special provisions for the seismic design and performance of this class of structures.

2.2.1.1 High-rise building definition

To the author's knowledge, there is no consensus on the definition of a "Tall building", equivalent to a "High-rise building" used herein, where a clear height cutoff between high-rise and low-to-mid-rise buildings is established. The Council of Tall Buildings and Urban Habitat (CTBUH) describe a high-rise building as "A building whose height creates different conditions in the design, construction, and use than those that exists in common buildings of a certain region and period".(CTBUH, 2008). Moehle (2007) defined high-rise buildings as those with a height of 73 m (240 feet) or taller. Other studies defined the cutoff height as approximately 49m (160feet), where the height is measured from the building ground level (e.g. PEER/ATC, 2010, LATBSDC, 2011). In the Pacific Earthquake Engineering Research Centre (PEER) guidelines for performance-based seismic design of tall buildings (PEER, 2010), the definition of high-rise buildings is those with unique seismic response characteristics in terms of the fundamental translational period of vibration, mass participation in higher modes, and the predominance of axial deformation of the vertical structural members (walls and/or columns) in the lateral drift of the building.

For the current work, the reference structure utilised to illustrate the proposed methodology of assessing the seismic vulnerability of RC high-rise buildings satisfies all the aforementioned definitions. It is a 30-storey bearing wall RC building with an above ground level-height of 89.6m. The total height of the building including the two subterranean levels is 97.3m.

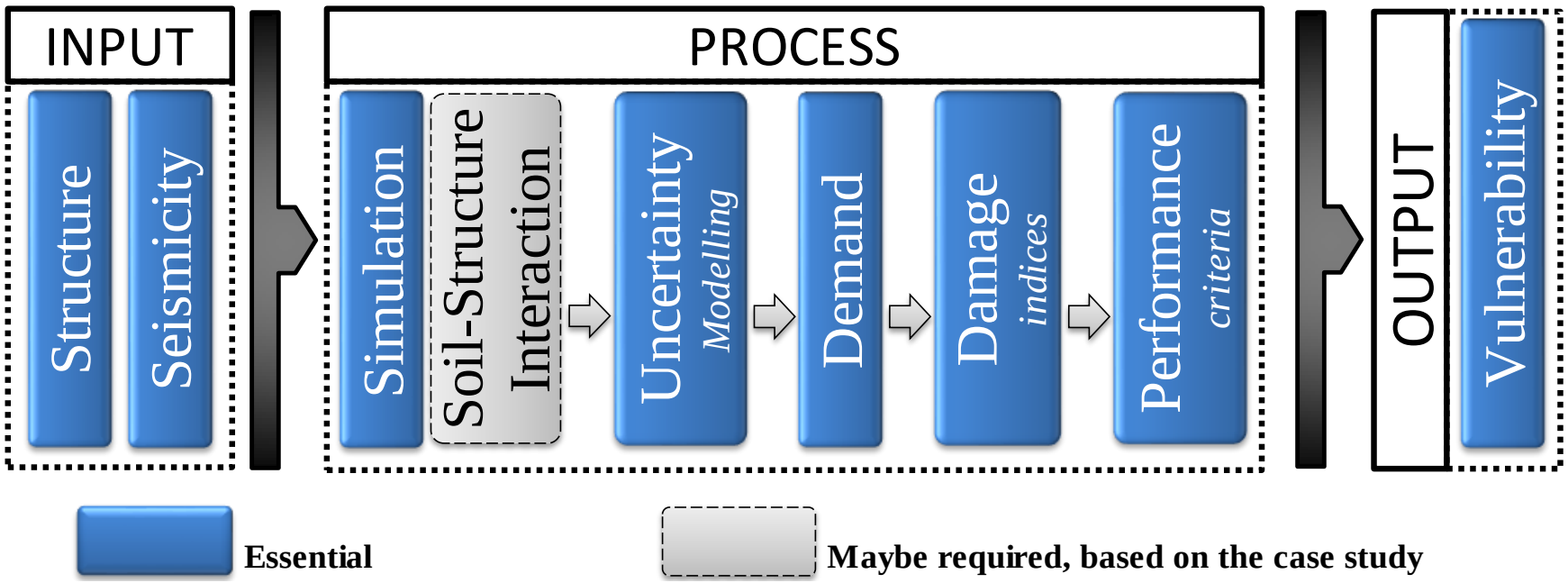

Figure 2.1. Input-Process-Output (IPO) model to the engineering problem of seismic vulnerability assessment of high-rise buildings

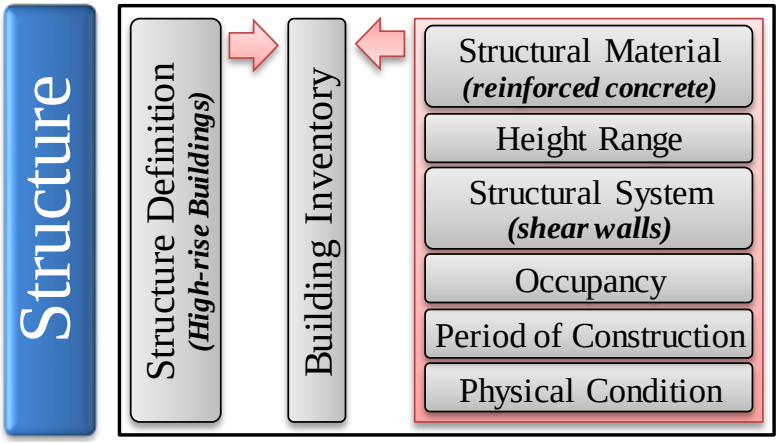

Figure 2.2. Collapsing chart for the "Structure" component in the IPO model

2.2.1.2 Building inventory

Recalling the definition in Section 2.1, building inventory (stock) is a class of buildings often defined by structural material, height range, lateral force-resisting system, occupancy, period of construction, and physical condition for a specific region or country. Since vulnerable building stocks remain the main cause of concern among the factors that contribute to heavy casualties from significant earthquakes (e.g. Coburn and Spence, 2003, Yepes-Estrada et al., 2017), limitations in inventory data significantly impact the outcomes of earthquake loss and risk estimation studies (e.g. Rojahn and Sharpe, 1985a, Coburn et al., 1992, Shakhramanian et al., 2000, Bommer et al., 2002, FEMA, 2019). Different sources can be utilised to obtain building inventory in a country or a region, among these are population census, field inspection, and technical documentation. With the advancements in satellite technology, researchers have developed other approaches to estimate building inventories. Some characteristics of the building stock such as the height and the structural system estimation through the geometries of building footprints may be obtained from satellite imageries (e.g. French and Muthukumar, 2006, Rafi et al., 2016, Moya et al., 2018). Although the field inventory data are the most accurate compared to data from other sources, the relatively high cost and long period associated with field inspections render inventories for earthquake loss studies mostly based on data from the other above-stated sources.

Hereafter, each of the classification criteria forming the building inventory definition is briefly discussed, followed by literature on building inventory and data sources.

- **Structural material:** Buildings are to be grouped according to their construction material, mainly as: reinforced concrete (RC), masonry, steel, wood, and composite.

- **Height range:** Building height is one of the most significant parameters to be considered when creating a building inventory. It reflects the dynamic characteristics and seismic response of the buildings under study. Previous studies on past earthquakes have shown that, depending on other factors such as site classification and ground motion characteristics, damage can be concentrated in buildings with a specific height range (Sucuoglu and Yazgan, 2003, Sucuoglu et al., 2007). With the continuous advancement in reinforced concrete material and construction technologies, high-rise RC buildings are getting higher and higher. This presses for a more detailed height classification for building inventory.

- **Structural system:** The lateral force-resisting structural system (or systems) in a high-rise building identifies its seismic response and consequently the vulnerability and loss due to earthquakes. With the wide range of structural systems that can be employed in RC high-rise buildings, the lateral force-resisting structural system stands as an important building classification parameter for the establishment of building inventory for this class of structures. Upon the availability of more detailed data, buildings may further be classified according to some structural system-related aspects such as the presence of soft and or weak storeys, short columns, long-span cantilevers, and pounding (Inel et al., 2008). More details with regards to the classification of structural systems used in RC high-rise buildings are given in Section 2.2.1.2.1 and Appendix A.

- **Occupancy:** The occupancy type of a building or a building stock is a crucial classification parameter for the estimation of casualties in earthquake risk and mitigation studies. It also dictates the performance level assigned to the structure for the purpose of vulnerability assessments. ASCE/SEI 7-16 (2017) classifies buildings into four categories based on their use or occupancy: Category I: Buildings that represent a low risk to human life in the event of failure; Category II: All buildings except those listed in Categories I, III, and IV; Category III: Buildings of which the failure could pose a substantial risk to human life, a substantial economic impact, and industrial buildings containing

toxic/explosive substances sufficient to pose a threat to the public if released; and Category IV: Buildings designated as essential facilities, buildings of which the failure could pose a substantial hazard to the community, industrial buildings containing toxic/explosive substances sufficient to be dangerous to the public if released, and buildings required to maintain the functionality after an earthquake event. For high-rise buildings, the occupancy classification can be subdivided to residential, commercial, and mixed-use buildings. Such sub-classification is essential in estimating the potential level of casualties caused by an earthquake event at different timing (day or night).

- **Period of construction:** Building age is a key factor in determining the design code in practice, the quality of construction material, and the detailing/ construction quality control level. Different regions in the world have different dates that distinguish between the so-called pre-code and seismically-designed buildings (Inel et al., 2008, Mwafy, 2012b). Furthermore, the construction era implicitly defines the strength of the material utilised in the construction as well as the construction techniques available at the time. All of which, contribute to the response and consequently the seismic vulnerability of the building stock under study.

- **Physical condition:** the physical appearance of a building often reflects the level of care given to its maintenance. Again, this may have an impact on the performance of the building during an earthquake event. Structures that are well-maintained against corrosion, rust, and other environmental and time-dependent factors are expected to perform better in general and specifically under cyclic loading such that from an earthquake. Classification of building inventory using the physical condition parameter often involves a scale, say 1-10, where a scale value is assigned to the building.

There have been various loss estimation methodologies developed in the past at both national and regional levels. Inventory data used in those methodologies were prepared with a primary focus on the economic impact assessment of an earthquake. It is worth noting that the development of building inventory at a country or regional level involves extensive efforts both in terms of identification and data assembling. In many countries over the world, the basic inventory material requisite for completion of an earthquake loss database either does not exist or is inaccessible.

In 1983, Petrovski used a questionnaire-based technique to estimate the building type classification in several Middle Eastern regions in an attempt to assess the associated vulnerability in the studied countries (Petrovski, 1983). The information gathered through questionnaires was very limited as no corresponding data were practically available on the building structural systems.

In the ATC-13 project (1985b), the inventory model developed by the Applied Technology Council (ATC) and incorporated by the Federal Emergency Management Agency (FEMA) in the database of HAZUS loss assessment software (FEMA, 2019) uses a consensus-based approach. In this model, the building stock is classified based on the structural system and occupancy with three-level data entry.

The Early Post-Earthquake Damage Assessment Tool (EPEDAT) developed in 1997 to estimate the casualties and regional damage for southern California used inventory data from housing census, employment data, and county assessors' records for buildings (Eguchi et al., 1997). The inventory database of EPEDAT includes building age, location, height, structural system, and occupancy. However, the methods used for the building type classification, determination of day and night time population distribution, and building occupancy have not been discussed in detail by the authors.

In the EXTREMUM computer tool developed by Shakhramanian et al. (2000), the earthquake consequence forecasting model uses inventory data extracted from population and building documentation in 89 regions in the Russian Federation. Neither the procedure used in developing the inventory data nor whether the data have been field validated were discussed in detail by the authors. QUAKELOSS, a newer version of EXTREMUM, is created by the staff of the Extreme Situations Research Centre in Moscow. QUAKELOSS is currently used by the World Agency of Planetary Monitoring and Earthquake Risk Reduction (WAPMEER) to provide a near-real-time assessment of injuries and death due to earthquakes anywhere in the world. The building inventory incorporated in QUAKELOSS is reportedly covering two million territories throughout the world.

In 2002, KOERILOSS, a scenario-based building loss and casualty estimation tool for four cities in Turkey (Istanbul, Izmir, Bishkek, and Tashkent) was developed by Bogazici University (Erdik and Aydinoglu, 2002, Erdik et al., 2003, Erdik and Fahjan, 2006). The building inventory for this program, utilising information from the State

Statistical Institute, categorizes the building stock data mainly based on the number of storeys (height), structural system, and period of construction. As for the estimation of day and night time population, the Istanbul Transportation Master Plan is utilised.

In 2006, Geoscience Australia developed an event-based tool called EQRM "EarthQuake Risk Management" for scenario-loss, probabilistic seismic hazard, and risk modelling (Robinson et al., 2006). The EQRM tool is created based on a two-phase project for the development of national building exposure database carried by the same government body (Nadimpalli et al., 2002).

Ongoing inventory development projects for earthquake estimation at the regional level in Europe include LESSLOSS and NERIES. LESSLOSS, developed by the European Centres of Excellence in earthquake and geotechnical engineering, focuses on risk mitigation for earthquake and landslides in European countries. NERIES (Network of Research Infrastructures for European Seismology), in addition to focusing on the development of new generation of hazard and risk estimation tools, is designed to combine transnational access and joint research activities to support improved access to standardized procedures, common protocols and distributed databases for long-term archiving and distribution of seismological data.

In 2010, a project funded by the United Arab Emirates University (UAEU) was launched to develop, among other tasks, a building inventory for the region of Dubai, United Arab Emirates (UAE), (Mwafy, 2012b). The building data is assembled using High Definition Satellite Images (HDSIs), field inspection, and the Geographic Information System (GIS) database of the Dubai Municipality. The studied region was divided into seven zones each of which was further sub-sectored. The 29279 counted buildings in the studied region were classified based on building height, occupancy, period of construction, and the population intensity. Due to the limited information that can be extracted from the HDSIs and GIS, along with access restriction to most of the buildings, the structural system criterion was implicitly included in the developed inventory based on the building height. This stands as a drawback in this promising project, especially when real high-rise building inventory is of concern (Ashri and Mwafy, 2014).

2.2.1.2.1 Structural systems of RC high-rise buildings

One of the earliest efforts to classify structural systems of high-rise buildings according to building height and system efficiency was that of Fazlur Khan in 1969 for steel structures (Khan, 1969). This classification manifested the beginning of a new era of tall buildings revolution utilising multiple structural systems. A few years later, Khan upgraded his classifications by developing schemes for both steel and concrete (Khan, 1972, Khan, 1973) as shown in Figure 2.3, taken after Ali and Moon (2007).

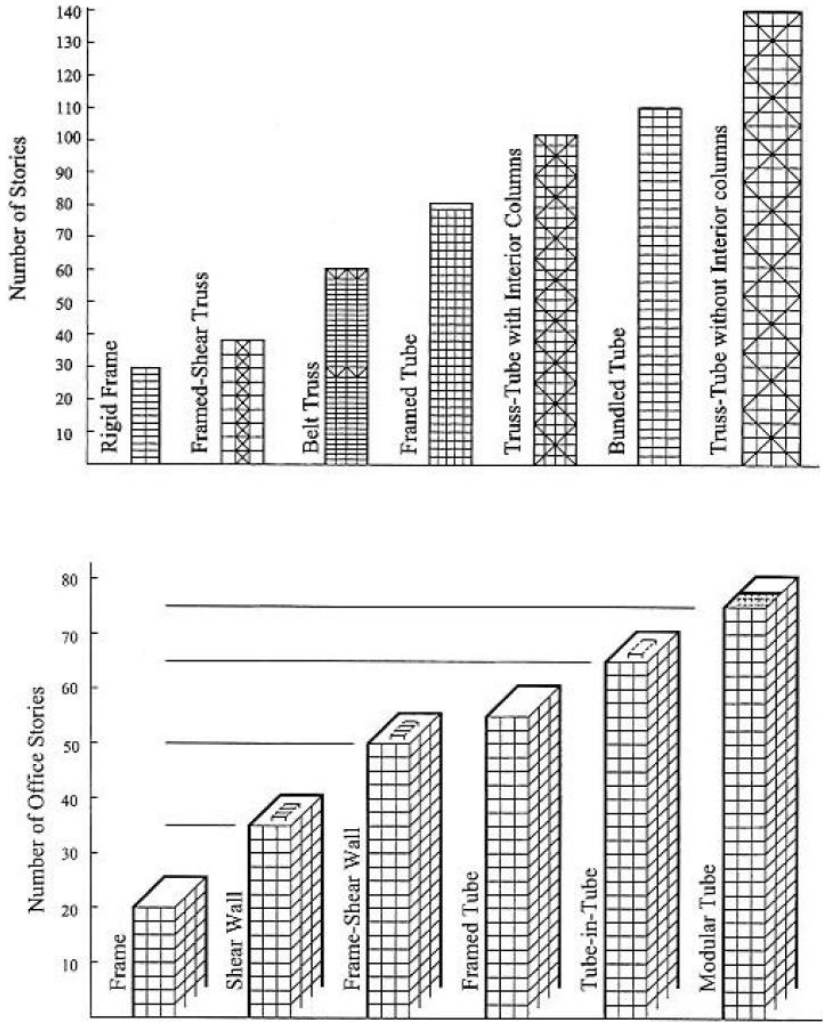

Figure 2.3. Structural systems classification for high-rise buildings by Fazlur Khan: above for steel; below for concrete (*after* Ali and Moon, 2007)

The shear wall-rigid frame interaction design approach first introduced by Khan and Sbarounis (1964) has played a significant role in shaping the structural systems of modern high-rise structures. The combination of the two structural forms leads to a

highly efficient system, allowing a highly competitive design of 20- to 40-storey buildings constructed either fully of reinforced concrete or composite with steel. In 1980, Khan and Rankine proposed yet another significant innovation in high-rises (Khan and Rankine, 1980). They proposed, as it is called now, the exterior perforated or framed tube system, where the exterior perimeter of the building is made of a system of deep spandrels and closely-spaced columns forming a hollow thin-walled tube with punched holes. For the sake of brevity, the classification and examples of the structural systems in RC high-rise buildings are given in Appendix A.

2.2.1.2.2 Performance of seismic-resistant RC high-rise buildings

During earthquake events, the structural characteristics of the previously-described structural systems determine the performance and stability of RC high-rise buildings. For many decades now, internationally-recognised building codes have been developed and maintained for seismic design of buildings. Among these codes are the late Uniform Building Code (UBC) and the International Building Code (IBC) with their incorporated national reference standards including the ACI 318 and the ASCE/SEI 7-16 (UBC, 1997, ACI, 2014, IBC, 2015, ASCE/SEI-7, 2017). In these codes, however, the seismic design provisions are based primarily on an understanding of the expected behaviour of low- to mid-rise buildings. In order to extrapolate the design and detailing provisions for use in high-rise structures, height limits were set for each of the identified structural systems with some systems not permitted under certain seismic design categories.

The recent developments in high-rise buildings, including innovative structural systems, advanced material, and high-tech construction methods, have raised questions regarding the applicability of prescriptive code provisions to the structural systems used in tall buildings. As a result, performance-based, as well as consequence-based design approaches using nonlinear analyses, have emerged as alternatives to the code-adopted traditional strength-based design (e.g. PEER, 2010, PEER/ATC, 2010, LATBSDC, 2011). Hereafter, the major engineering, scientific, and regulatory issues specific to the seismic design of high-rise buildings are addressed.

- **Structural systems and materials:** Revolutionary developments in the architectural and functional requirements for high-rise buildings have resulted in

new structural systems and building materials that do not necessarily satisfy the prescriptive provisions and requirements of currently-enforced building codes.

- **Hazard and performance objectives:** As a result of the increasing demand for high occupancy along with the interest in continued occupancy following the earthquake event, the performance objectives and ground shaking levels for the seismic design of high-rise buildings are to be reconsidered. Hence, new initiatives in the analysis, design, and performance of high-rise buildings start to emerge to the surface (e.g. PEER, 2010). Tall buildings, as a minimum, must be collapse-prevented under long-return period earthquakes and significant aftershocks, while serviceability criteria are to be met in more frequent events.

- **Input ground motions:** The results of the nonlinear response history analysis of high-rise buildings are significantly influenced by the selection, scaling, and spectral alteration of input ground motions. Proper seismological methods are to be implemented in the assembly of the seismic record sets to correctly represent the duration and energy content required in the seismic design of high-rise buildings.

- **Simulation, analysis, and acceptance criteria:** In current codes, the seismic design provisions do not specify appropriate simulation (modelling), analysis methods, and acceptance criteria explicitly for high-rise buildings. Safety, reliability, functionality, and re-occupancy criteria are therefore needed for this class of buildings. Recently, there has been some effort to overcome these shortcomings via pre-standards that are focusing on high-rise structures (e.g. PEER, 2010, PEER/ATC, 2010, LATBSDC, 2011)

- **SSI for high-rise buildings with subterranean levels:** High-rise buildings are commonly constructed with several underground levels. Interaction between soil, foundation, and structure can significantly alter the characteristics of the input ground motion and consequently the response of the structure.

- **Local supplementary regulations in design and construction practices:** Peer reviewers and building authorities around the world often have their own design and construction regulations specific to high-rise buildings as supplementary to the seismic provisions. These regulations may have an impact on the

performance of these structures during an earthquake event, therefore, need to be carefully considered during the design stage.

2.2.2 Seismicity

Seismic hazard, as defined in Section 2.1, is the probability of reaching or exceeding certain ground shaking intensity (e.g. magnitude, acceleration, velocity, or displacement) for a given area and a reference time period. It relates to all earthquake-induced phenomena (e.g. strong ground shaking, tsunamis, liquefaction, landslides, and fire) that may have direct and/or indirect effects on building inventories and infrastructure. Seismic hazard assessment can be performed on national (country), regional, urban, or site-specific scales (Figure 2.4). There are also some recent initiatives at the global scale (GEM, 2019). As Figure 2.1 shows, the seismic hazard assessment, referred to as "seismicity", is a major component in the evaluation of seismic vulnerability and risk of high-rise buildings. Figure 2.5 shows the collapsing chart for the "Seismicity" component in the IPO model, while a brief discussion on the involved steps is presented in the succeeding subsections

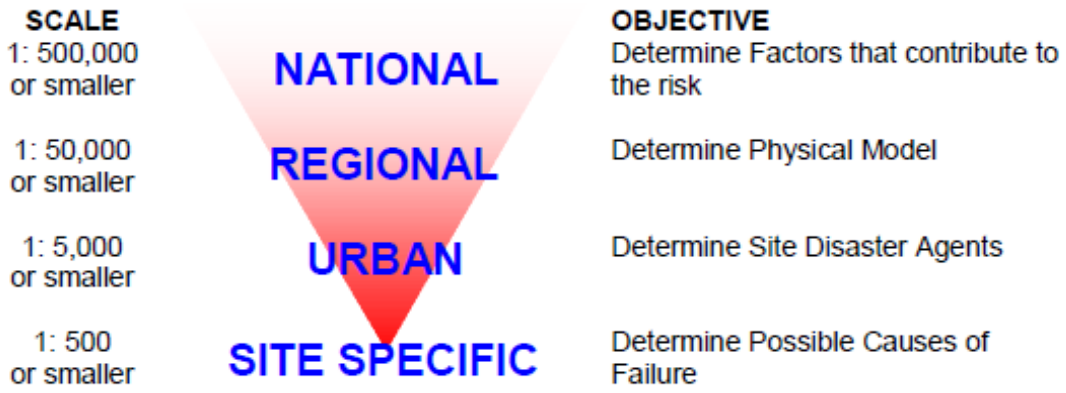

Figure 2.4. Study scales for the seismic hazard assessment (*after* Hays, 1994)

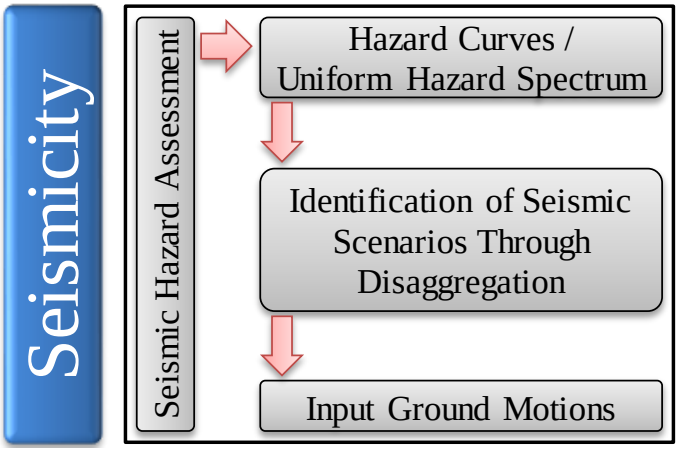

Figure 2.5. Collapsing chart for the "Seismicity" component in the IPO model

2.2.2.1 Seismic hazard assessment

There are five different methods available for the use in seismic hazard assessments. Namely: (1) Observational; (2) Statistical; (3) Deterministic; (4) Probabilistic; and (5) Time-dependent. Depending on the intended use of the results, one or more of these methods can be used by engineers, insurance companies, and or governmental bodies. The outcomes of a seismic hazard study can be used either to obtain the ground shaking intensities for seismic design, calculate the appropriate insurance premium rates, or to estimate the probable maximum incurred loss in the event of an earthquake.

2.2.2.2 Hazard curves and UHS

A common approach for developing design response spectra based on a Probabilistic Seismic Hazard Assessment (PSHA) is to employ the UHS, which is developed by first generating hazard curves for a set of spectral periods using the PSHA output. Next, for a given return period, the ground shaking spectral parameter is measured for each spectral period from the hazard curves. The final step is to plot these measured spectral parameter values in pairing with their respective spectral periods. The process of developing UHS is illustrated in Figure 2.6.

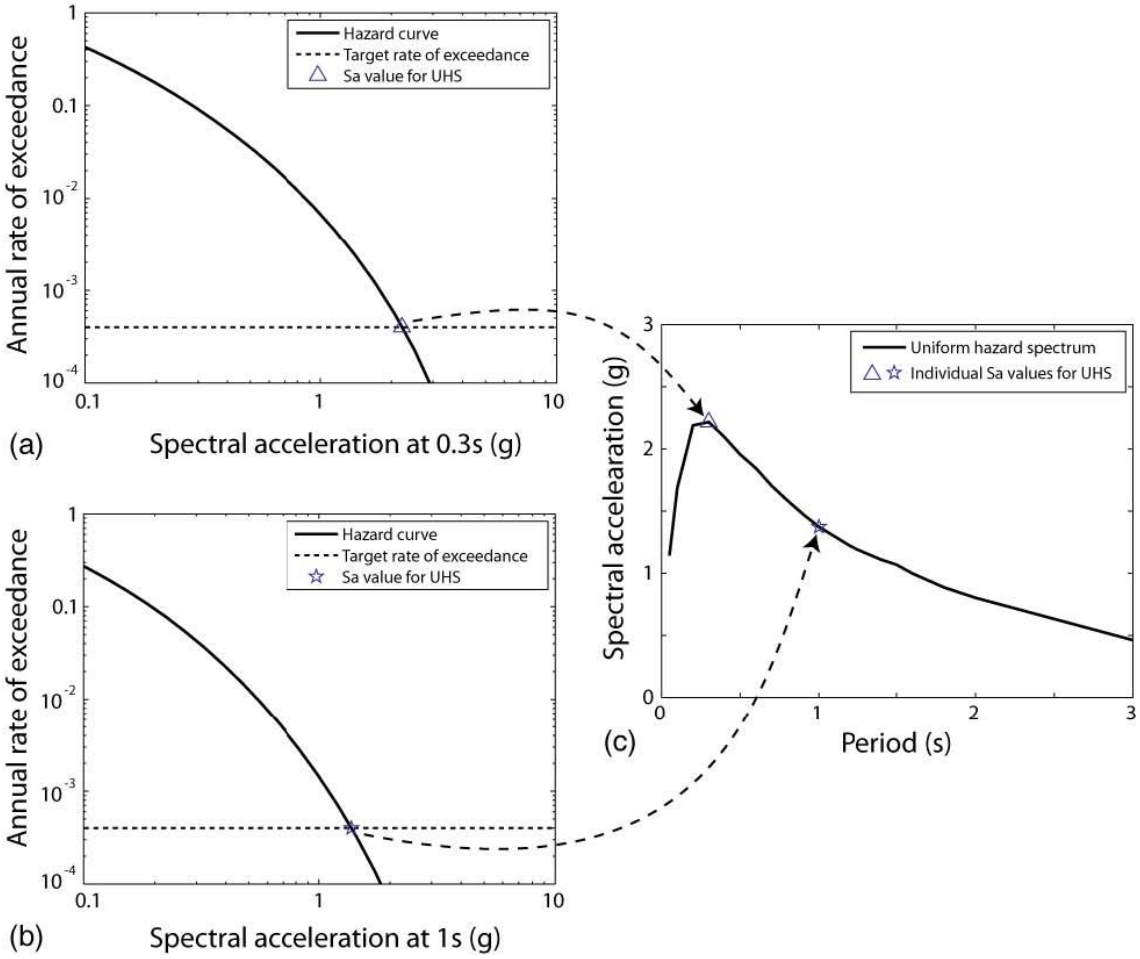

Figure 2.6. An example of combining hazard curves from individual periods to develop a UHS for a site in Los Angeles (*after* Baker, 2013): (a) Hazed curve for $S_{A(0.3s)}$; (b) Hazard curve for $S_{A(1s)}$; and (c) UHS for a set of spectral periods like those in (a) and (b)

The term "uniform hazard spectrum" came from the fact that every ordinate in the UHS has an equal probability of being exceeded. It should be clear that since the hazard curves are independently computed for each spectral period in the set, the UHS does not represent the spectrum of any single earthquake. It is common in a UHS to find that the spectral acceleration values in the high-frequency zone (T < 0.2s) are controlled by near-field moderate earthquakes, whereas, the values in the long period zone (T > 1s) are controlled by distant strong events. The UHS is the only step in the PSHA that combines the ground shaking parameters from multiple earthquakes.

The mixing of events in the UHS is sometimes cited for criticising the entire PSHA approach. It is essential to recognize though that the UHS is merely a way to present the output of a PSHA. No step in the PSHA requires the use of a UHS. Therefore, it is totally possible to conduct a PSHA and productively use its results without ever developing a UHS. This can be achieved by employing the disaggregation concept to

the PSHA results. The design response spectra and or input ground motions can then be generated based on the identified scenario-based earthquakes. This concept is further discussed hereafter.

2.2.2.3 Seismic scenarios through disaggregation of PSHA results

In a PSHA, the hazard curve presents the combined effect of all magnitudes and distances on the probability of exceeding a specified level of a ground-shaking parameter. Accounting for all potential earthquake sources in the concerned region when estimating the seismic hazard, being the strength of PSHA methods, is also a disadvantage. Once the PSHA is completed, a logical question to ask is: Which earthquake scenario is most likely to cause Peak Ground Acceleration (PGA) of a certain value? Since all of the sources, distances, and magnitudes are integrated into it, it is difficult to recognize what controls the hazard from the hazard curve by itself. The solution to this problem is to break down the hazard at a given ground shaking level to its contributions from different earthquake scenarios. This process is called "Disaggregation", also referred to as deaggregation, (e.g. McGuire, 1995, Bazzurro and Cornell, 1999, Fox et al., 2016, Sousa et al., 2017, Şeşetyan et al., 2018). In this process, the fractional contribution of different scenario sets to the total hazard is calculated. The most common form of the disaggregation approach is the two-dimensional magnitude-distance bins where the dominate earthquake scenarios, categorised by their magnitude-distance pair, can be identified.

To determine the dominate scenarios, either the mean or the mode of the disaggregation is usually employed. The advantage of using the mean is that it is unambiguously defined with no dependency to the bin size. The drawback, however, is that if there is more than one source with significant contribution to the hazard, the mean may correspond to an unrealistic scenario. The mode corresponds to the scenario set that has the largest disaggregation value. It has the advantage of being always corresponding to a realistic source. The disadvantage of using the mode is that it is a bin size-dependent. For example, if we use broader distance bins at larger distances and finer distance bins at shorter distances in a disaggregation process, the mode would shift to the large distant earthquake. In standard practice, the mode of the disaggregation is used to define the seismic scenarios. Therefore, the distance and magnitude bins are to be carefully selected. Appropriate bin size is subjected to the end use of the disaggregation. One of the common usages, as in the current study, is to identify seismic scenarios for selecting

time histories to be used in nonlinear analysis. Here, the change in the characteristics of the time histories (e.g. duration, pulses, and spectral shape), and consequently the seismic response of the building under study, alongside the magnitude and distance will control the appropriate bin size. As an alternative, the mean magnitude and mean distance for each controlling scenario is calculated. This is a robust approach in that it is insensitive to the bin size, however, can be quite complicated if the controlling scenarios overlap. In conclusion, there is not a unique optimum bin size for all projects thus the hazard analyst needs to consider the end use of the disaggregation results when deciding the bin sizes.

Figure 2.7 shows a sample of the disaggregation results for the Dubai region based on the PSHA conducted by Aldama-Bustos et al. (2009). The results in the figure are for a 500-year return period, presented in terms of PGA and spectral accelerations.

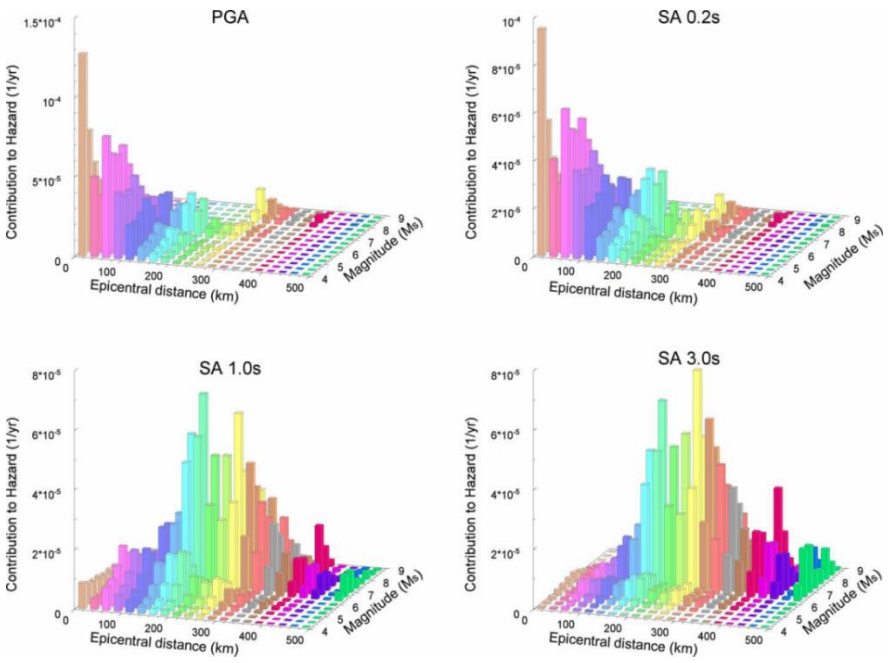

Figure 2.7. Disaggregation results for the PSHA of Dubai, UAE (500-year return period) presented in PGA and spectral accelerations of 0.2, 1, and 3s (*after* Aldama-Bustos et al., 2009)

2.2.2.4 Input ground motions

Due to the rapidly increasing computational power and the evolution of engineering software during the last two decades, time-history analysis has been made feasible to complex structures. As a result, time-domain analysis is prescribed for high-rise structures in modern seismic codes. On the other hand, previous studies have shown that among all uncertainty sources, input ground motions are the most unpredictable and

carry a significant impact on the variability in the predicted structural response (e.g. Elnashai and Izzuddin, 1993b, Padgett and DesRoches, 2007, Kappos, 2014, Mangalathu et al., 2017, Kowsari et al., 2019). Ground motions appear random in time and space due to the complex path that seismic waves follow from the source through bedrock (Papageorgiou and Aki, 1983) and then through soil layers to reach the structure foundation level (Manolis, 2002). Despite the above-discussed uncertainty, ground motion record selection provisions in current codes are considered rather simplified compared to the potential impact of the selection procedure on the analysis results.

Selected input ground motions should represent the seismicity of the region under study and must comply with design-based (or expected) earthquakes. In other words, the selected records have to fulfil the earthquake scenarios that are identified through the disaggregation process of PSHA results discussed in the previous section. In terms of obtaining acceleration time-series, among the available approaches are (i) artificial spectrum-matched accelerograms; (ii) synthetic accelerograms based on seismological source models; and (iii) real earthquake accelerograms using scenario-based magnitude and distance bins. These approaches are further discussed hereafter.

2.2.2.4.1 Artificial spectrum-matched accelerograms

Specialised software packages are employed to generate artificial spectrum-compatible accelerograms for the use in the time-history analysis. This approach starts with generating power spectral density function out of the smoothed response spectrum, followed by deriving sinusoidal signals of random amplitudes and phase angles. These signals are then summed to generate the accelerograms where an iterative procedure is used to improve the match with the target response spectrum.

This approach is obviously attractive in such that one can generate as many acceleration time-series as desired, all of which almost completely compatible with the target spectrum. Nevertheless, it is now broadly not recommended to use artificial records because they generally have an excessive number of strong-motion cycles and as a result carry unreasonably high energy content (e.g. Seifried and Baker, 2016, Bani-Hani and Malkawi, 2017). Gascot and Montejo (2016) evaluated three different methodologies for the generation of spectrum compatible records: (i) wavelet-based modification of real records; (ii) real record adjustment based on the Continuous

Wavelet Transform; and (iii) synthetic record generation in the frequency domain. The study concluded that even though the three methodologies are capable of generating compatible records with an acceptable level of match, the records generated using the frequency domain approach exhibit unrealistic strong motion characteristics. In the case of methodologies based on the modification of real earthquake records, it was found that when the real records are selected based on their initial compatibility with the target spectrum, the resultant compatible records not only retain better the original characteristic of the records but also reducing the variability in the structural response.

Matching artificial records to the entire target response spectrum, which is usually either a UHS obtained from the PSHA or a UHS-based design spectrum, is neither reasonable nor realistic (Naeim and Lew, 1995). This is certainly the case when the UHS is an envelope of more than one earthquake scenario as for the study region in the current work, where spectrum-matched artificial records will tend to be effectively unrealistic.

2.2.2.4.2 Synthetic accelerograms based on seismological source models

Synthetic acceleration time-series that account for path and site effect can be generated from seismological source models. These models range from point sources, finite sources, all the way to fully dynamic models of stress release. Software packages for generating such synthetic records are freely available (e.g. Boore, 2003). Their application, however, in terms of the definition of the parameters required to describe the earthquake source generally requires the engagement of a seismologist. There is a high degree of invariably- carried uncertainty in the determination of the source parameters for past earthquakes. As for future earthquakes, the definition of these parameters, to which the resulting synthetic records can be highly sensitive, normally involves a substantial degree of expert judgment (e.g. Bommer and Acevedo, 2004, Tang et al., 2016, Fahjan et al., 2017, Ghosh and Chakraborty, 2017).

2.2.2.4.3 Scenario-based real accelerograms

The third approach for obtaining time-series to be used in the time-history analysis is real accelerograms recorded during past earthquakes. By definition, real records are free of the issues associated with artificial spectrum-matched records. Among the selection criteria, the earthquake magnitude (M) and source-to-site distance (R) bins that

characterise the dominate earthquake scenarios in the area of interest are the most common parameters used in the selection of real records.

Along this line, Shome et al. (1998) formed a bin of records using four different M-R pairs to assess the seismic response of a five-storey building. Furthermore, Youngs and his group (2006) and established the Design Ground Motion Library; an electronic library of recorded accelerograms suitable for use in the time-history analysis of structures. The total number of the record sets in the developed library was 26. In the study of Wang et al. (Wang et al., 2015), a Design Ground Motion Library (DGML) is presented for selecting earthquake ground motion time histories based on contemporary knowledge and engineering practice. The library was created from a ground motion database that consists of 3,182 records from shallow crustal earthquakes in active tectonic regions rotated to fault-normal and fault-parallel directions. The DGML enables users to construct design response spectra based on Next-Generation Attenuation (NGA) relationships, including conditional mean spectra, code spectra, and user specified spectra. Several studies (e.g. Stewart et al., 2002, Bommer and Acevedo, 2004, Ha and Han, 2016, Baker and Lee, 2018) also considered magnitude as an important parameter in the selection of real records, arguing that when the magnitude search window is kept as narrow as possible, the range for the source-to-site distance can be widened.

Other studies, on the other hand, have examined the dependency of the inelastic seismic response of structures on the M-R parameter pair used in the record selection (e.g. Bazzurro and Cornell, 1994a, Bazzurro and Cornell, 1994b, Shome and Cornell, 1998, Carballo and Cornel, 2000, Luco et al., 2002, Jalayer, 2003, Medina and Krawinkler, 2004, Baker and Cornell, 2005, Iervolino and Cornell, 2005, Vlachos et al., 2018). In sum, these studies have concluded that deformation-based response has less dependency on the M-R parameter pair when compared with the cumulative energy-based response. They also verified the general independency of inelastic structural displacements to the source-to-distance parameter R. Nevertheless, the conclusions drawn from these studies may not be valid in the case of high-rise buildings. In this class of structures, the duration of the selected records, which is a seismic scenario -dependent, plays an essential role in the influence and contribution level of higher modes to the building nonlinear response (e.g. Samanta and Pandey, 2018).

Following the initial selection of real accelerograms based on the M-R parameter pair, spectral matching is usually considered as a second-level selection criterion. In this exercise, the response spectra of the selected records are to be modified in order to be compatible with the corresponding target spectrum (UHS or design response spectrum). It must be clarified here that spectral matching of real records is not to be confused with the generation of spectral-matched artificial accelerograms discussed in Section 2.2.2.4.1. Through the European strong-motion databank, Ambraseys et al. (2004) proposed an Eqn. (2.1) to verify the spectral compatibility of a selected record with the target spectrum.

$$D_{rms} = \frac{1}{N}\sqrt{\sum_{i=1}^{N}\left[\frac{S\alpha_0(T_i)}{PGA_0} - \frac{S\alpha_s(T_i)}{PGA_s}\right]^2} \tag{2.1}$$

Where N is the number of periods at which the spectral shape is specified, $S\alpha_0(T_i)$ is the spectral acceleration of the selected record at period T_i, $S\alpha_s(T_i)$ is the target spectral acceleration at the same period, PGA_0 is the peak ground acceleration of the selected record, and PGA_s is the zero-period anchor point of the target spectrum. Closer matching between the shapes of the selected record and target spectra is indicated by a small value of D_{rms}.

It is important to recall that different M-R-based developed records are corresponding to different earthquake scenarios, and that target spectrum is an envelope of all dominate earthquake scenarios. Hence, the shapes of the record spectra in each record set are only to be compatible with the part of the target spectrum that relates to the seismic scenario employed in the developing of that set. Furthermore, when the seismic vulnerability assessment of existing and new structures is the target of the study, obtaining a very small value of D_{rms} would not be that important. This is so because the selected real records in each set will be subjected to a scaling scheme to cover the entire range of the building response from elastic all the way to collapse. More insight on this matter is given in CHAPTER 5.

Along with the discussed M-R pair and spectral-match selection criteria, there are three additional complementary criteria that can be used in the real records selection process, namely: (i) soil profile; (ii) strong motion duration; and (iii) acceleration to velocity ratio (a/v). A brief discussion of each is bulleted hereafter.

- ***Soil profile:*** The actual soil profile (S) at the site of interest can be added to both the earthquake magnitude and distance in the search window, leading to (M-R-S) record bins (e.g. Kurama and Farrow, 2003, Youngs et al., 2006, Mwafy, 2012a, Mwafy et al., 2015b). The soil profile is known to influence ground motions by altering both their amplitude and the calculated response spectra (e.g. Bommer and Acevedo, 2004, Pandey et al., 2016, Trifunac, 2016, Barani and Spallarossa, 2017). In general, the shear-wave velocity at the top 30m layer of soil ($V_{S,30}$) is a suitable measure to be used for site classification. Alternatively, the site can be classified according to the well-established soil categorization schemes included in seismic codes. Previous studies have concluded that (M-R-S) selection approach may significantly reduce the number of qualified records compared to the simpler (M-R) approach (e.g. Bommer and Scott, 2000). Notwithstanding the restrictions implied to the selection process, consideration of soil profile remains an important selection criterion.

- ***Duration of ground motion:*** The duration of ground motion constitutes another complementary parameter for the selection of real accelerograms. The ground-shaking duration is typically controlled by the duration of the fault rupture, which in turn is a function of the earthquake magnitude. Different types of structural DIs are affected by ground motion duration in different ways. To be specific, peak response-type DIs are independent of duration, while energy-based DIs such as fatigue and absorbed hysteretic energy are interrelated to this parameter (e.g. Shome et al., 1998, Iervolino et al., 2006, Chandramohan et al., 2016a, Chandramohan et al., 2016b, Barbosa et al., 2017). In a study by Hankock and Bommer (2006), the dependency of the abovementioned phenomenon on the structural model itself is highlighted. Indeed, structures modelled to exhibit stiffness and/or strength degradation under cyclic loading are more sensitive to the number of cycles in the earthquake record and hence to the shaking duration.

- ***Acceleration to velocity ratio (a/v):*** As a complementary criterion for the record selection process, the ground motion a/v forms an important measure of the magnitude, frequency content and site-to-source distance of the earthquake event (e.g. Tso et al., 1992, Carlton and Tokimatsu, 2016, Kohrangi et al., 2017, Macedo and Castro, 2017). High a/v ratios (>1.2g/m/s) signify events with high

dominant frequencies, medium-to-small magnitudes, short site-to-source distances and short duration periods. Low a/v ratios (<0.8g/m/s), on the other hand, represent earthquakes with low dominant frequencies, high-to-medium magnitudes, long site-to-source distances and long duration periods. Examples of studies that have considered the a/v criterion in the real records selection process are the ones by Mwafy (2012a) and Ilyas et al. (2018).

2.2.3 Simulation

Based on modern seismic codes, earthquake-resistant RC buildings are designed and detailed to respond well beyond the elastic range under DBE level ground motions. Hence, verified nonlinear simulation, referred to hereafter as modelling, for building response is essential in assessing the vulnerability of such structures. It is always easy to forget that when a structure is analysed, the analysis is actually conducted on the model of the structure and not the structure itself. In other words, the analytical model is an approximation of the actual structure.

For RC high-rise wall buildings, Nonlinear Response History Analysis (NRHA) stands as the most realistic tool currently available for predicting building response at different levels of ground motion intensity. In NRHA, the accuracy of the nonlinear model is measured by its sufficiency in capturing significant modes of deformation and deterioration in the analysed structure from the onset of damage all the way to collapse.

Various aspects of nonlinear modelling such as element discretisation, material force-deformation (also referred to as stress-strain) relations, and assumptions on modelling of viscous damping and structural mass are essential in defining the level of accuracy a model can have in predicting the seismic global and local response of the structure. Figure 2.8 illustrates the collapsing chart for the “Simulation” component in the IPO model, while the aforementioned modelling aspects are briefly discussed in the succeeding subsections.

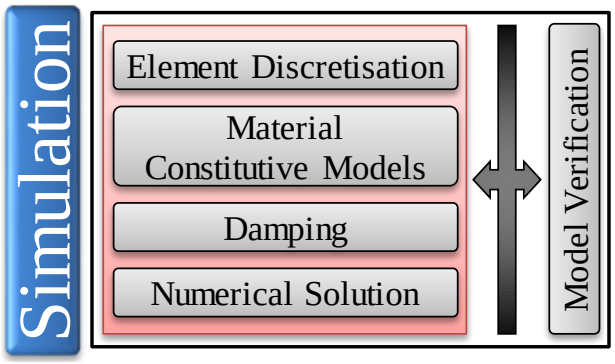

Figure 2.8. Collapsing chart for the "Simulation" component in the IPO model

2.2.3.1 Element discretisation

Inelastic structural component models can generally be differentiated by the degree of idealization in the model. In other words, the way plasticity is distributed through the structural member cross-sections and along its length (Powell, 2010). Several model types are available with the most detailed continuum finite element model at one extreme and the lumped plasticity (concentrated hinge) model at the other. These modelling types can also be used in modelling other types of structural members such as slabs, braces and flexural walls.

In RC high-rise wall buildings, the fibre-based element is the most common modelling approach used to model the structural walls which are expected to undergo inelastic behaviour during the analysis (Wallace, 2007). This approach supports a proper description of the wall geometry and the detailing of steel reinforcing bars and material behaviour. It accounts for key response features including (i) relocation (shifting) of the neutral axis along the cross-section of the wall during loading and unloading phases; (ii) interaction with the other components connecting the walls/cores in the structure both in and out of the wall's plane such as the gravity frames and coupling beams; and (iii) the impact of variation of axial load on wall flexural strength and stiffness.

Giving the above, fibre-based modelling approach will be adopted in the current study for the RC walls as well as for the flooring system (flat plate) of the reference structure. Coupling beams, on the other hand, will be modelled using a combination of elastic elements and nonlinear hinges. Literature, key parameters, and modelling issues for the said structural members are discussed in the following subsections.

2.2.3.1.1 RC Walls

As a result of recent earthquakes (e.g. 2010 Chile M 8.8, 2011 New Zealand M 6.2, and 2011 Japan M 9.0), a wealth of new data on the performance of modern RC buildings utilising structural walls in their primary lateral force-resisting system have become available. For instance, the 2010 Chile earthquake caused significant damage to many slender RC wall buildings, including spalling/crushing of concrete and buckling of vertical reinforcement largely extended over the wall length (Figure 2.9). Apparently, the bulking of vertical bars renders the damage to be concentrated over a short height (around one to three times the wall thickness). The boundary zones in these walls were found with a relatively large spacing of horizontal web reinforcement and hoops (Figure 2.9d). This was consistent with the seismic provisions of the Chilean Building Code NCh 433 (1996) adopted in the design of the damaged buildings (Wallace, 2012). In some cases, lateral buckling of the walls was detected (Figure 2.10).

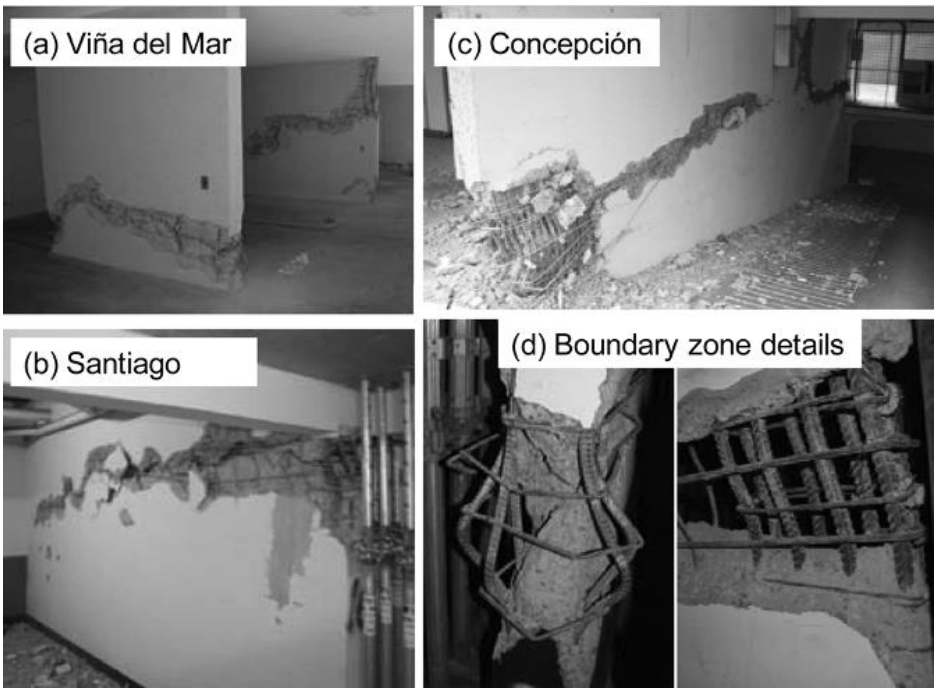

Figure 2.9. 2010 Chile M_W 8.8 Earthquake: Typical wall damage (after Wallace, 2012)

Figure 2.10. 2010 Chile M_W 8.8 Earthquake: Wall lateral buckling (after Wallace, 2012)

Similar wall failures were observed following the 2011 Christchurch, New Zealand earthquake (Comerio et al., 2011, NZRC, 2012), signifying that the deficiencies deducted in the 2010 Chile earthquake are not isolated (Figure 2.11). Wall boundary regions are observed to be susceptible to out-of-plane buckling following spalling of concrete cover. The Christchurch earthquake observations also included diaphragm-to-wall connection failures. This mode of failure believed to have potentially contributed to the collapse of several buildings (EERI, 2011). However, this was not observed in Chile. This can be attributed to the well-distributed, in-plane large number of walls that Chilean typical buildings had.

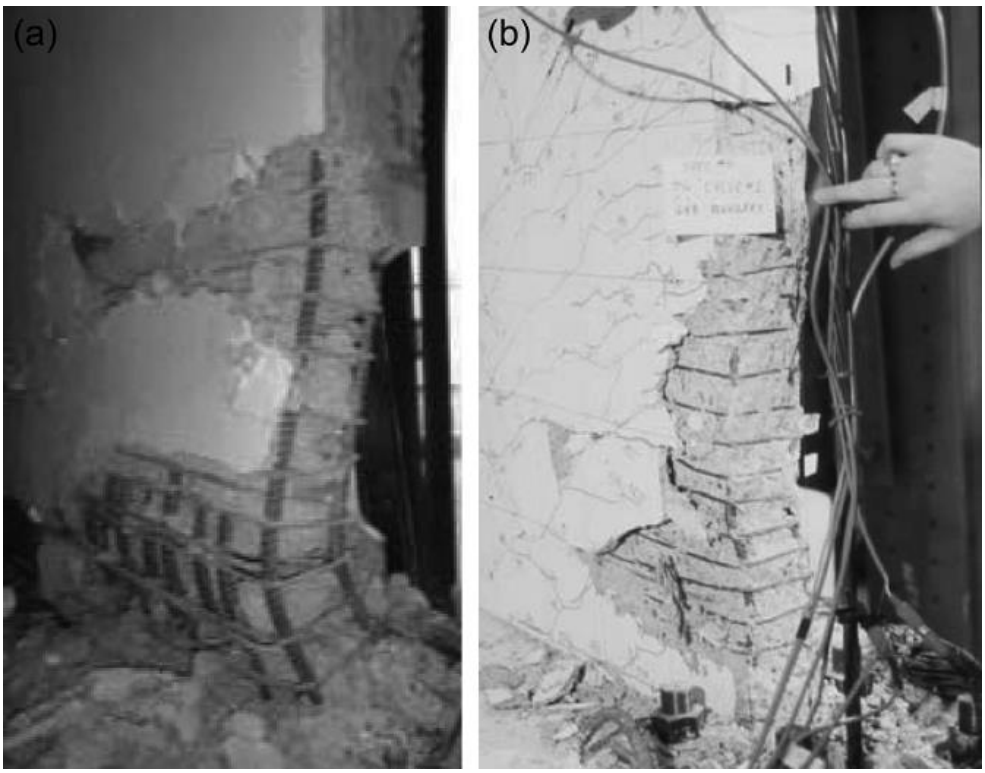

Figure 2.11. 2011 Christchurch, New Zealand M_L 6.3 Earthquake: Typical wall damage (after Wallace, 2012)

In the last ten years, there have been several laboratory-based tests of isolated and coupled RC walls or walls as part of a structure. These testing programs focused on studying the performance of rectangular and T-shaped walls under uniaxial/biaxial loading (e.g. Waugh et al., 2008, Brueggen, 2009, Waugh, 2009, Brueggen and French, 2010), walls with high shear demand (e.g. Birely et al., 2008, Birely et al., 2010, Sriram and Sritharan, 2010), walls with splices and couples in the plastic hinge region (e.g. Birely et al., 2010), and walls with coupling beams (e.g. Naish, 2010, Naish and Wallace, 2010, Parra-Montesinos et al., 2012). All these tests involved quasi-static loading. Shake table testing programs, on the other hand, have been quite limited with the exception of few (e.g. Panagiotou and Restrepo, 2007, Ghorbanirenani et al., 2011, Nagae et al., 2011). More details on the aforementioned studies can be found in the study of Wallace (2012).

In terms of RC wall modelling, a comprehensive study is presented by Orakcal and Wallace (2006) on the ability of available modelling approaches to capture the cycling response of slender RC walls under combined bending and axial load. In this study, a Multi Vertical Line Element (MVLE) model was employed for walls under cyclic uniaxial loading. The MVLE is similar in concept to the fibre-based modelling approach

embedded in some computer packages such as PERFORM-3D (CSI, 2011). The overall modelling process presented in Orakcal and Wallace study (2006) includes: (i) subdividing the wall cross-section into reinforcement fibres, confined concrete fibres, and unconfined concrete fibres; (ii) employing suitable material constitutive relations; (iii) dividing the wall height into a specified number of elements (components); (iv) defining boundary conditions; and (v) applying a predefined load/displacement history. The test walls were around one-fourth scale models, proportioned using the UBC-91 (Thomsen and Wallace, 1995, Thomsen and Wallace, 2004).

Key observations gleaned from the study of Orakcal and Wallace (2006) are bullet-pointed below.

- The effective elastic (linear) stiffness to the yield point is very close to the value commonly used in design, that is $0.5E*I_g$ (Figure 2.12b). The results of the shake table test of a full-scale, 7-storey RC building slice (Panagiotou and Restrepo, 2007) suggested a lower effective stiffness of $0.2E*I_g$ (Maffei, 2007). However, it is important to note that the tension reinforcement ratio in the RC walls of the shake table test was less than one-half of that used by Thomsen and Wallace (2004). Indeed, that was the objective of the shake table test, to demonstrate that adequate lateral load resistance of RC walls can be achieved by using just one-half of the longitudinal reinforcement normally required by codes that were enforced at the time of the testing program (e.g. UBC, 1997, IBC, 2003). The use of significantly lower longitudinal reinforcement is expected to substantially reduce the effective stiffness at yield since the yield curvature is mainly a function of the wall length (Wallace and Moehle, 1992). Therefore, a reduction in the yield moment strength by a factor of two renders the effective stiffness to be reduced almost equally. Given that, the $0.2E*I_g$ reported in the shake table testing program is not inconsistent with the $0.5E*I_g$ value recommended by Orakcal and Wallace (2006). Accordingly, an effective yield stiffness of $0.5E*I_g$ is considered appropriate for RC walls with code-compliant strength and axial stress level up to $0.15A_g*f_c'$. it is worth noting that when fibre-based modelling approach is used, the effective stiffness is automatically calculated based on the adopted material constitutive relations, level of axial stress, and the analysis current state.

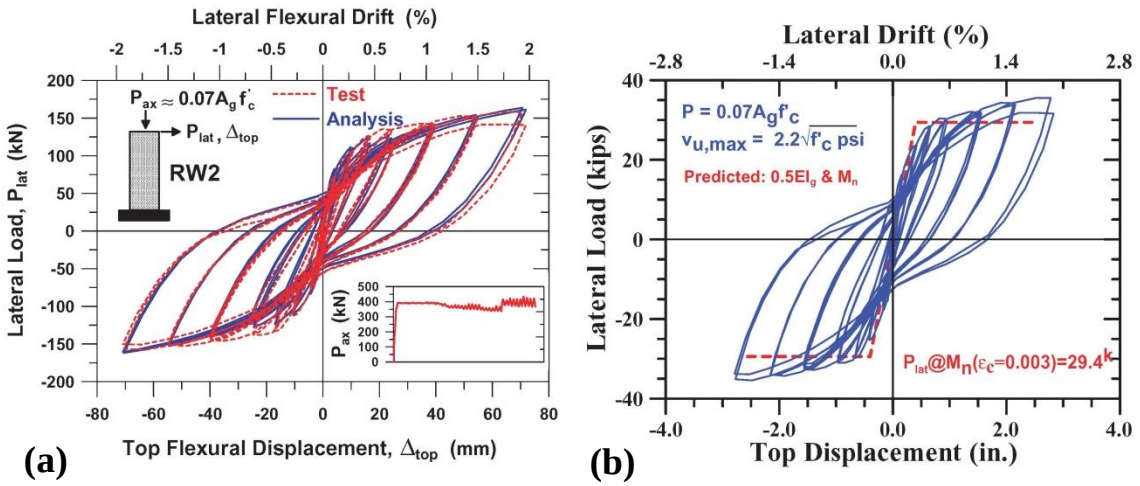

Figure 2.12. Test results for specimen RW2: (a) model results; and (b) bilinear fit for $0.5E*I_g$ and M_n (after Orakcal and Wallace, 2006)

- The study results indicate that when using cyclic material constitutive relations (relations with a strength and stiffness degradation law), the predicted overall load-deformation response is generally consistent with the test results for a wide range of DIs (e.g. roof displacement, plastic hinge rotation, and average strains). Figure 2.13 (after the study of Orakcal and Wallace, 2006) shows a good prediction of the tensile strain by the model. However, it also shows that the model peak compressive strains are substantially underestimated when compared to the values measured from the test. In general, peak measured compressive strains were about double the values predicted by the model for relatively slender walls [$h_w*l_w=M_u/(V_u*l_w)=3$], where h_w is the wall height, l_w is the wall length, M_u is the ultimate moment, and V_u is the ultimate shear force. Preliminary analytical studies have indicated that the interaction occurs between flexure and shear behaviour may be one of the reasons for this discrepancy (Wallace, 2007).

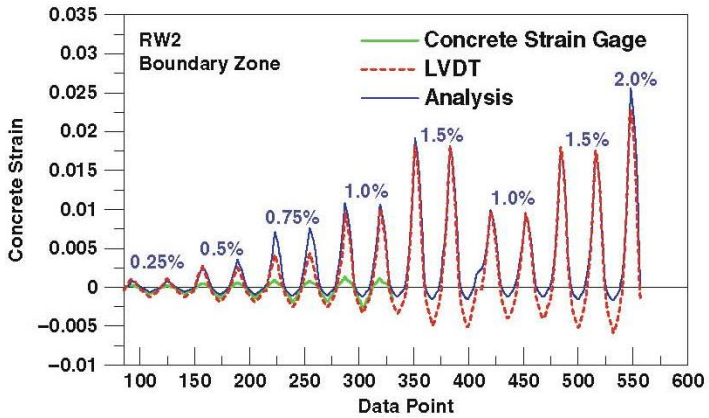

Figure 2.13. RW2-Wall average strain at wall base (after Orakcal and Wallace, 2006)

- Subdividing the wall into elements of appropriate heights and its cross-section into an appropriate number of concrete and steel fibres is an essential step in the structural modelling for NRHA. The studies of Orakcal et al. (2004) and Orakcal and Wallace (2006) revealed that the predicted lateral top displacement is insensitive to the number of elements and number of material fibres (Figure 2.14a). Notwithstanding, the results shown in Figure 2.14b present an important consequence, that is using coarse mesh is likely to underestimate the maximum tension and compression strains for the material fibres (Orakcal et al., 2004). Therefore, acceptance criteria for wall strains should carefully consider the model characteristics in order to establish an appropriate limit for peak strains in concrete and steel at wall critical locations.

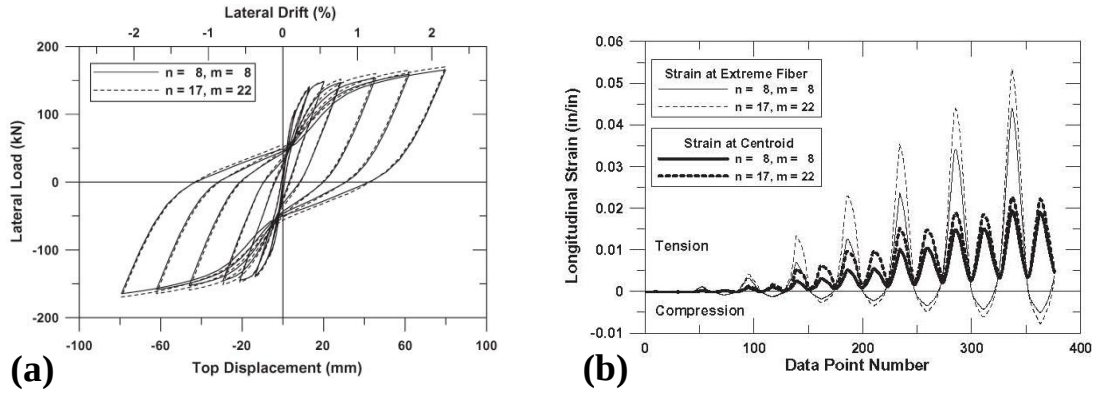

Figure 2.14. Response sensitivity to model parameters: (a) load-top displacement relation; and (b) wall critical strain (after Orakcal and Wallace, 2006)

- The ability of the model to estimate the local deformations can be affected by localisation of inelastic deformations. To avoid this problem, proper selections of the material constitutive relations and model attributes are required. The study of Orakcal and Wallace (2006) concluded that in general, the element height at the wall critical section is to be approximately equal to the plastic hinge length. Orakcal and Wallace (2006) have also concluded that to help avoid the localisation of inelastic deformations, modest reinforcement strain hardening slope in the order of 3% to 5% is to be used. According to the study results, using modest strain hardening in the model contributes to a better prediction of the test measured cyclic loading versus displacement.

- In the study of Orakcal and Wallace (2006), linear shear behaviour was assumed in the presence of nonlinear flexure response. In other words, flexural and shear behaviours were uncoupled. The experimental results, however, showed that inelastic shear deformations initiated at the same applied load level as nonlinear flexure deformations, indicating that shear and flexure response behaviours are

indeed coupled. To account for the shear-flexure interaction, a coupled model can be employed as shown in Figure 2.15 (e.g. Massone, 2006, Orakcal et al., 2006, Kolozvari, 2013, Kolozvari et al., 2014a, Kolozvari et al., 2014b, Massone et al., 2015). However, such coupled models are not yet available in commercially-available computer packages since the development of coupled cyclic material models remains a major research challenge. Given these limitations, a simplified uncoupled modelling approach can be used to reasonably capture the shear-flexure interaction behaviour of slender walls. An example of such modelling approaches is the use of nonlinear shear spring similar to that recommended by ASCE/SEI 41-06 (2007) and ASCE/SEI 41-16 (2017). The shear force-deformation relation required to define the shear spring can be based on test results by Thomsen and Wallace (2004), calibration studies by Gogus (2010), and modification to the post-cracking slope suggested by Massone (2006). More details on this model approach are given in CHAPTER 3 of this thesis.

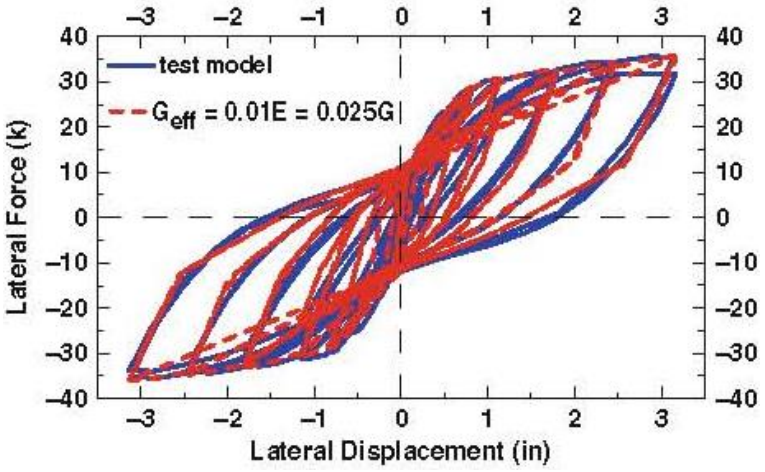

Figure 2.15. Nonlinear wall modelling - Combined flexure and shear behaviour: Load versus lateral displacement (after Orakcal and Wallace, 2006)

2.2.3.1.2 Coupling beams

Reinforced concrete walls are usually coupled with beams to create openings to access elevators, stairwells, and other systems. Those coupling beams are subjected to double curvature and intended to yield under lateral loading. The shear demands resulting in the beams are transferred to the coupled walls as axial tension and compression loads. As the use of NRHA and performance-based design have become more common for high-rise wall buildings, attention to the nonlinear modelling of coupling beams continues to

increase. Modelling parameters of particular interest are the effective flexural stiffness at yield and the allowable inelastic rotation prior to significant lateral strength degradation. Test programs in this field were conducted either on coupling beams as individual elements or on coupled-wall as a complete system. Historically, most of the tests belonged to the former category with only a few large-scale tests dealing with the latter. A detailed review of previous studies related to coupling beam seismic behaviour and design was given by Mohr (2007), while Turgeon (2011) provided a thorough review of experimental test programs of coupled-wall system.

Recent tests have been conducted using eight one-half-scaled RC coupling beams to assess the modelling parameters alongside the detailing and configurations common for both residential and office buildings, including the influence of post-tensioned and reinforced slab flooring systems (Naish et al., 2009, Naish, 2010, Naish and Wallace, 2010, Wallace, 2012). In these tests, 2.4 and 3.33 aspect ratios (beam net length to depth ratio) were adopted for beams representing residential and office buildings, respectively. Tested beams were reinforced diagonally with transverse reinforcement placed either around the bundles of diagonal bars (labelled as CB24D and CB33D in the tests) or around the entire beam cross-section (labelled CB24F and CB33F in the tests) following the provisions of the ACI 318 code used in the design stage.

The main conclusions of the above-mentioned studies are bullet-pointed hereafter.

- The load-deformation relations of the 2.4 aspect ratio-beams with both transverse reinforcement arrangements (CB24D and CB24F) were quite similar over the entire range of applied rotations (Figure 2.16a). Similar results were observed for the 3.33 aspect ratio-beams (Figure 2.16b).

- Tested beams with a 2.4 aspect ratio obtained large rotation in the range of 8% before any significant degradation in lateral load resistance occurred. Furthermore, shear strengths in the range of 1.17 and 1.25 times the ACI 318 nominal strength were achieved by test beams with transverse reinforcement placed around the diagonal bars and around the entire cross-section, respectively.

- Additional beams with a 2.4 aspect ratio were tested to evaluate the slab impact (post-tensioned or RC) on the load-deformation relations. The tests revealed that

the shear strength of the coupling beams increases by the existence of the slab. This strength increase can be accounted for by considering the nominal moment capacity increase in the beams due to the presence of the prestress and the slab. The axial growth in the coupling beams prior to yield is restrained by the presence of a flooring system (RC or PT slab), leading to slightly higher stiffness. However, the secant stiffness for beams with and without slabs following yield was very similar, where significant strength degradation occurred at around the same rotation (8%).

- Tests conducted on 3.33 aspect ratio-beams with longitudinal flexure reinforcement instead of diagonal bars indicated that total rotation greater than 4% could be achieved prior to significant strength degradation. It is also observed that the load-deformation relations for beams with longitudinal reinforcement experience more pinching when compared to the diagonally-reinforced beams, indicating less energy dissipation. Nevertheless, given the less construction complexity, coupling beams with longitudinal reinforcement are still appropriate to use in high-rise buildings when shear stress and rotation demands are modest.

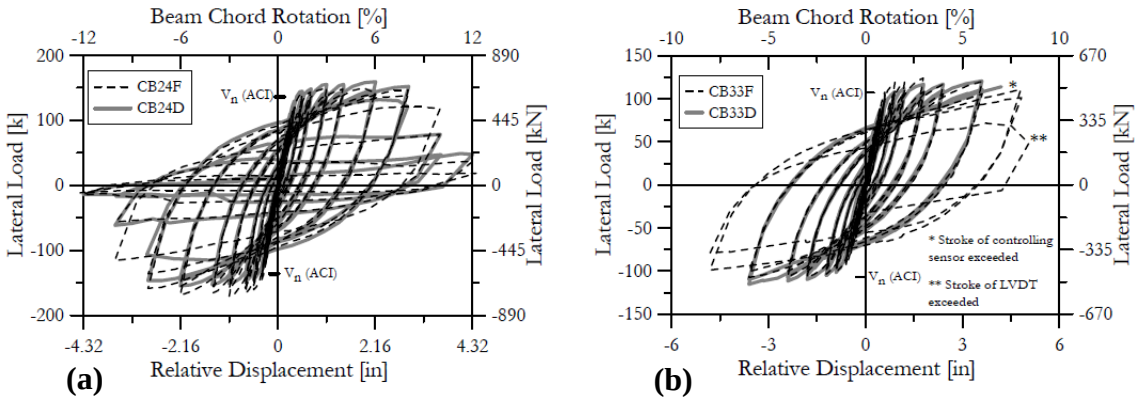

Figure 2.16. Cyclic load-deformation relations: (a) CB24F versus CB24D; and (b) CB33F versus CB33D (Naish et al., 2009)

To model a coupling beam for NRHA, two nonlinear modelling approaches are commonly used: (a) moment-hinge approach, consisting of an elastic cross-section beam with rotational springs at beam ends to account for nonlinear flexure (and slip/extension) deformation; and (b) shear-hinge approach, consisting of an elastic cross-section beam with a nonlinear shear spring at beam mid-span.

Previous studies (e.g. Naish et al., 2009, Naish, 2010, Naish and Wallace, 2010) investigated the two modelling approaches using full-scale-modified linearised backbone relation for normalised shear versus rotation and effective stiffnesses resulted from the testing program. The studies concluded that despite the better representation of the unloading characteristics by the moment-hinge model, both models accurately capture the overall load-rotation response of the member. Since the unloading characteristics of the load-deformation relation have no significant impact on the current work objective, it is decided to use the nonlinear shear-hinge approach in modelling the coupling beams in the case study building. It is worth noting that a number of previous studies dealing with the vulnerability assessment of RC high-rise wall structures have adopted this nonlinear shear-hinge approach in the modelling of coupling beams (e.g. Ghodsi and Ruiz, 2010, Tuna, 2012). More details of the shear-hinge modelling approach and the parameter used to define the force-deformation relation assigned to the coupling beams in the model of the reference structure are given in CHAPTER 4.

2.2.3.1.3 Flooring system

For high-rise wall buildings, the most common flooring system is flat plate slabs, either of reinforced or post-tensioned concrete. This system is a preference to both architects and mechanical engineers as it allows for more floor-to-floor clear height for the former and more flexibility in running the mechanical services for the latter. Three main modelling approaches are available to model flat plate slabs in high-rise wall buildings, namely: (1) omitting the slab from the model and assigning diaphragm constraints to the RC piers and core walls at each floor level; (2) modelling the slab using elastic, equivalent slab-beam or shell elements; and (3) modelling the slab using inelastic fibre-based elements. A brief discussion of each of the three abovementioned modelling approaches is given below.

- ***Modelling approach-1:*** The advantage of this approach obviously lies in the saving of computational effort and time by dropping the slab from the model. Given that slabs typically have high in-plane stiffness, rigid diaphragm constraints are assigned to the wall ends at floor level in each storey for lateral load analysis. In this modelling approach, all constrained nodal joints in the same floor are slaved to one another hence they undertake similar in-plain deformations. Several researches have implemented this approach in their

modelling of high-rise wall buildings (e.g. Ghodsi and Ruiz, 2010, Tuna, 2012).

This approach, however, comes with a major drawback, that is not accounting for the influence of the 3-dimensional interaction between the flooring system and the walls on the overall lateral performance of the building. The shear forces in the slab developed under lateral loading are transferred to the connected walls in the form of axial forces (tension and compression), which intern contribute either positively or negatively to the walls lateral force resistance and ductility. This issue has been confirmed by previous studies (e.g. Panagiotou and Restrepo, 2006).

- ***Modelling approach-2:*** In this approach, the slab is modelled using either an elastic, equivalent slab-beam element or an elastic shell element. An equivalent slab-beam is an elastic flexural element having a rectangular section with its depth and width dimensions representing the total slab thickness and its effective width, respectively (Allen and Darvall, 1977, Grossman, 1997, Hwang and Moehle, 2000, Kang and Wallace, 2005, Kang, 2006, Kang and Wallace, 2006, Elwood et al., 2007, Kang et al., 2009, Waugh and Sritharan, 2010). Elastic shell element is a 4-node element with in-plane (membrane) and out-of-plane (bending) plate elastic stiffnesses. The element is available in several computer packages such as PERFORM-3D (CSI, 2011).
  Using the equivalent slab beam and shell elements will obviously overcome the drawback associated with the modelling approach-1. The shortcoming of using these types of elements, on the other hand, is that they both can only be used to model floor slabs that are expected to remain elastic throughout the earthquake excitation. For slabs that are expected to crack and yield, the inelastic element should be used, where the slab deformation can be accurately calculated along with its impact on the additional axial forces induced in the walls. Furthermore, using elastic element to model slabs that are expected to undergo plastic deformation will hinder the use of these deformations as a damage index in the process of estimating performance state criteria for the building.

- ***Modelling approach-3:*** Using nonlinear fibre-based beam element in modelling floor slabs is considered the most realistic of the three approaches

listed herein since it overcomes the shortcomings in the modelling approach 1 and 2. Using this approach, the total width of the slab panel can be utilised since the cracking and yielding events in the slab are automatically taken into account through the fibre-based model.

In the current work, the third modelling approach (fibre-based beam element) is utilised in modelling the RC flat slabs of the reference structure due to its effectiveness and ability to overcome the shortcomings in other modelling approaches.

2.2.3.1.4 Coupling beam/Slab/Wall connection

In a 4-noded fibre-based shear wall element, the nodes have no in-plane rotational stiffness. Therefore, when connecting an element that represents a coupling beam or a slab to a shear wall, the connection is pinned. To specify moment-resisting connections between a wall and a beam or a slab, an embedded element in the wall is to be added to the model as shown in Figure 2.17. The embedded element must have a very stiff section in bending in the plane of the wall to provide a stiff connection between the wall and the coupling beam or the slab. On the other hand, it should obtain very small axial, torsional, and out-of-plane bending stiffnesses to avoid adding artificial stiffness to the wall elements.

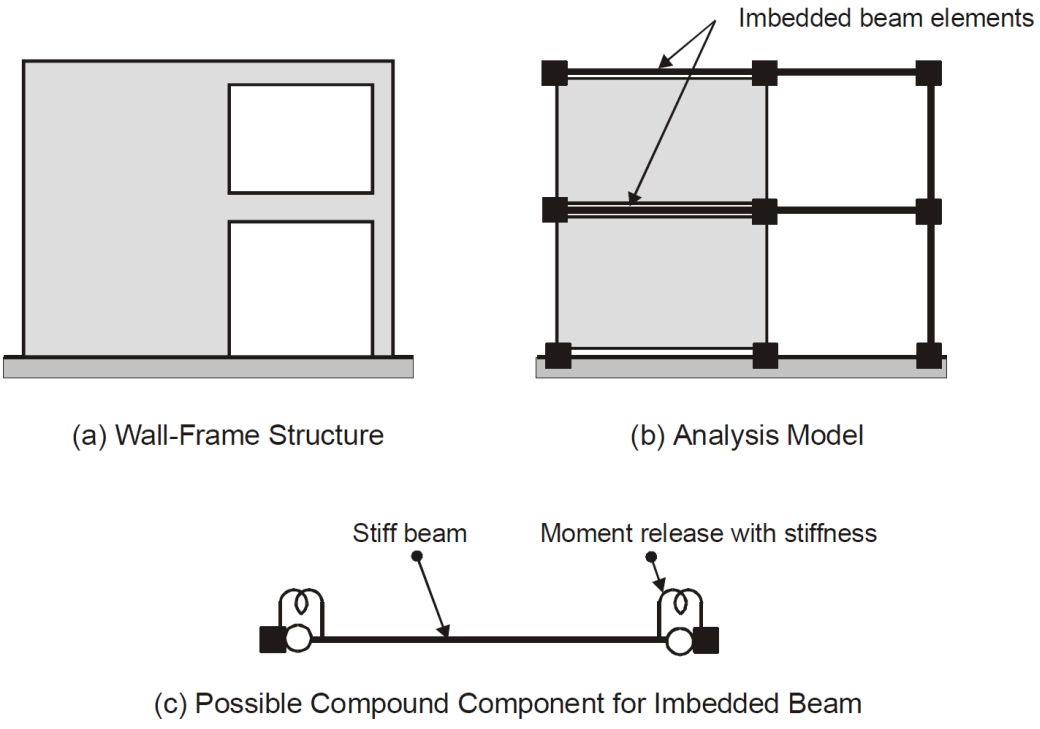

Figure 2.17. Imbedded element for coupling beam/slab-wall connection (*after* CSI, 2011)

In reality, there may be significant local deformation where the coupling beam or the slab connects to the wall. The rotational stiffness of the elastic connection component in the embedded element can be selected to provide an appropriate amount of fixity. It is worth noting that the degree of fixity between the coupling beams or the slabs and the walls may have an impact on the overall elastic stiffness of the structure. However, after the coupling beam or the slab yields, the amount of end fixity is expected to have little effect. As an alternative, inelastic moment connection component rather than elastic release component may be used with the embedded element so that the beam- or slab-to-wall connection is nonlinear.

2.2.3.2 Material constitutive models

Given the Bernoulli beam assumption that plane section remains plane after deformation, uniaxial stress-strain constitutive laws are sufficient to model the steel and concrete materials of RC members with fibre-discretized cross-sections. The main objective of seismic vulnerability assessment studies of high-rise RC buildings is to evaluate the performance of the structure at different seismic hazard levels. This necessitates the use of hysteretic models that incorporate all key properties of steel and concrete materials contributing to demand estimation as the building approaches collapse. Furthermore, NRHA models should be based on expected material properties rather than minimum specified properties. The term “expected” refers to properties that are characterised based on median values from a large population of materials. The definition of a typical hysteretic model comprises three steps:

- A backbone curve, which is a force-deformation relation that sets the bounds within which the hysteretic response of the member (component) is confined,
- A set of rules defining hysteretic behaviour between the bounds defined by the backbone curves, and
- A set of rules defining various modes of degradation with reference to the backbone curve. Degradation rules are based on the hysteretic energy dissipation in the member (component) as it is subjected to cyclic loading.

The initial backbone curve defines the monotonically increasing deformation in the material constitutive relation. Generally, the initial backbone curve is defined by the following parameters: initial (elastic) stiffness, yield strength, post-capping stiffness, strength cap and associated deformation, post-capping stiffness and deformation range,

residual strength, and ultimate deformation. Figure 2.18 illustrates a typical formation of an initial backbone curve. As necessitated, different properties can be assigned to the curve in the positive and negative directions.

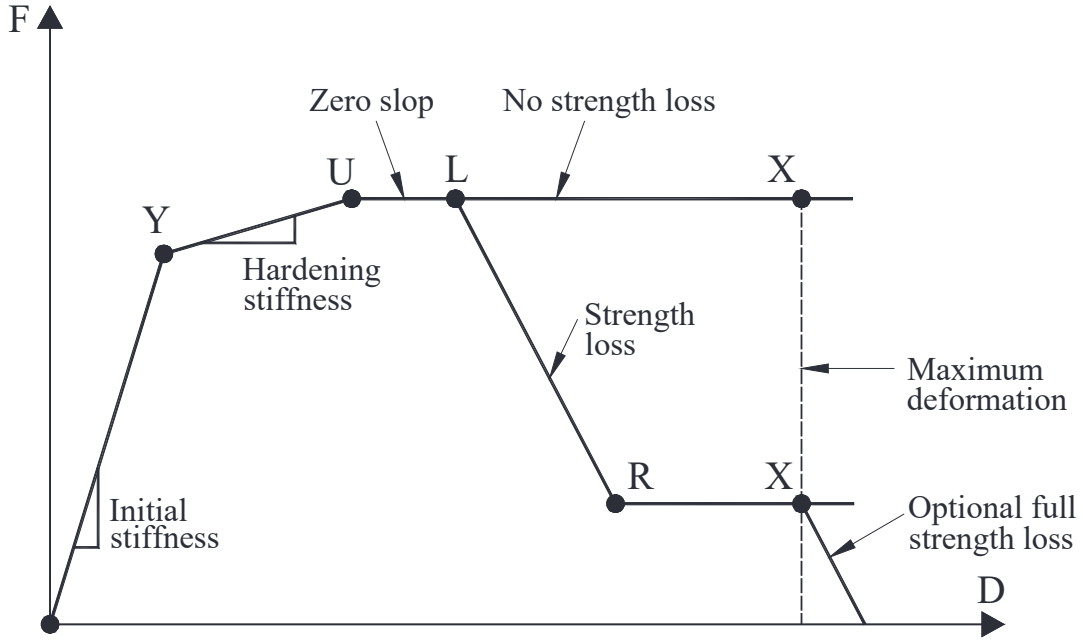

Figure 2.18. Typical formation of an initial backbone curve for a material constitutive relation

Among the well-established hysteresis rules are those of linearised bilinear, peak oriented, and pinched models. This does not preclude the more refined hysteresis models such as multi-linear or curvilinear models (e.g. Bouc, 1967, Baber and Wen, 1981, Foliente, 1995, Carr, 2007) and the hysteresis model presented in PERFORM-3D (CSI, 2011). Figure 2.19 illustrates some of the mentioned hysteresis models.

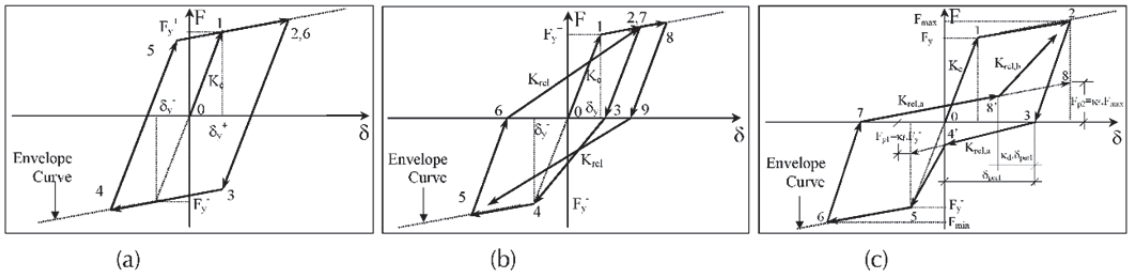

Figure 2.19. Samples of hysteresis characteristics: (a) bilinear; (b) peak oriented; and (c) pinching (after Medina and Krawinkler, 2003, Medina and Krawinkler, 2004)

The extent to which cyclic degradation is modelled will determine the calibration level applied to the backbone curve. Degradation can be categorised into four modes (PEER/ATC, 2010): (i) basic strength degradation; (ii) post-capping strength degradation; (iii) unloading stiffness degradation; and (iv) accelerated reloading

stiffness degradation. In RC structural members, deterioration can be the result of several phenomena, among them is cracking/spalling/crushing of concrete, buckling/fracture of rebars, bond-slip, and reduction in confinement. These four degradation modes are presented in Figure 2.20 for a peak oriented model.

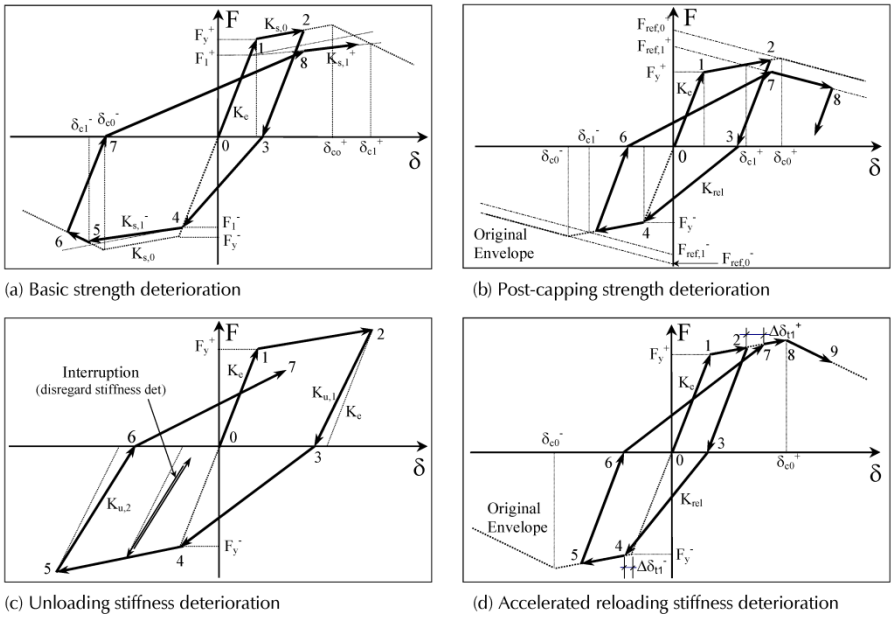

Figure 2.20. Degradation modes illustrated for a peak oriented model (*after* Ibarra and Krawinkler, 2005)

With regard to confined concrete, many constitutive models have been developed over the last fifty years. Some of these models are based on biaxial compression experiments whereas others utilised the results of triaxial compression experiments to extended the database on behaviour of concrete that can be utilised to develop confined concrete models (e.g. Darwin and Pecknold, 1977, Elwi and Murray, 1979, Ottosen, 1979, Smith et al., 1989, Madas and Elnashai, 1992, Xie et al., 1995, Attard and Setunge, 1996, Imran and Pantazopoulou, 1996, Candappa et al., 2001, Lim et al., 2016, Moharrami and Koutromanos, 2016, Xu and Wen, 2016, Jiang et al., 2017, Piscesa et al., 2017).

Other concrete models were developed based on experiments that involved concrete confined with transverse steel reinforcement. Of the widely accepted models under this category, Mander et al. (1988) proposed a constitutive relation for confined concrete that incorporated the confinement effect provided by the transverse reinforcement, assuming a constant confining pressure through the full stress-strain range. Improved cyclic rules are later proposed to the Mander model by Martinez-Rueda and Elnashai (1997). The confined concrete model of Chang and Mander (1994) emphasised on the

transition of the stress-strain relation at the opening and closure of cracks. In this model, the concrete in tension was modelled with cyclic behaviour. The model envelopes for tension and compression have control on the slope at the origin as well as on the shape of both pre-peak and post-peak zones of the stress-strain relation. Other examples of transverse reinforcement-confined concrete are (Sheikh and Uzumeri, 1980, Scott et al., 1982, Sheikh and Uzumeri, 1982).

For high-strength concrete, there are many confinement models proposed by researchers (e.g. Fafitis and Shah, 1985, Yong et al., 1988, Bjerkeli et al., 1990, Nagashima et al., 1992, Cusson and Paultre, 1993, Muguruma, 1993, Sun and Sakino, 1993, Li, 1994, Ibrahim and MacGregor, 1996, Diniz and Frangopol, 1997, Kappos and Konstantinidis, 1999, Konstantinidis et al., 2007, Akiyama et al., 2010). The uniaxial, nonlinear constant confinement constitutive for the high-strength concrete model of Kappos and Konstantinidis (1999) has been embedded in some nonlinear analysis computer packages such as SeismoStruct (SeismoSoft, 2019). In this model, the confinement effect delivered by the transverse reinforcement were accounted for through the modified Sheikh and Uzumeri factor (1982).

For steel reinforcement, among the widely used stress-strain models is the Menegotto-Pinto relation (Menegotto and Pinto, 1973), coupled with isotropic hardening rules introduced by Filippou et al. (1983). This model has been embedded in several research software packages such as OpenSees (Mazzoni et al., 2006, McKenna and Fenves, 2006, McKenna, 2011), ZEUS-NL (Elnashai et al., 2012), and SeismoStruct (SeismoSoft, 2019). Another commonly used model is the one proposed by Dodd and Restrepo (1995). It accounts for the reduction in the unloading modulus with the plastic strain, whereas the ultimate tensile strain reduction is taken exclusively as a function of the maximum compressive strain.

In the present study, the modified Mander model (Martínez-Rueda and Elnashai, 1997) and the Menegotto-Pinto relation (Menegotto and Pinto, 1973), coupled with isotropic hardening rules proposed by Filippou et al. (1983) are utilised to present the stress-strain relations of confined concrete and reinforcing steel, respectively. More details on the used material models are given in CHAPTER 4.

2.2.3.3 Damping

Damping is generally associated with the reduction in dynamic response due to energy dissipation in the building. Depending on the physical contributors to damping, it can be mathematically modelled in a variety of forms, including viscous damping, hysteretic damping, or friction damping. Proper modelling of damping requires an appreciation for its physical sources, and how these sources may vary in their contribution from one building to another based on the building geometry and its dynamic characteristics. This is especially true for tall buildings, where the structural systems, foundations, and non-structural components can be quite different from those in conventional low- to mid-rise construction. Damping in structures due to earthquake-induced motions can generally be attributed to three main sources: (1) structural components; (2) nonstructural components; and (3) the soil-structure interaction.

Viscous damping (also called inherent damping, initial elastic damping, or simply elastic damping) in NRHA is necessary to account for damping prior to the onset of hysteretic response (Priestley and Grant, 2005, Smyrou et al., 2011, Paulay and Priestley, 2013). Some researchers (e.g. Priestley and Grant, 2005, Smyrou et al., 2011) stated that viscous damping is not needed in the post-yield phase except during elastic loading/unloading. Nevertheless, for certain constitutive relations that lead to vanishing effective damping ratios at large amplitudes, some degree of viscous damping is believed necessary to avoid unstable inelastic response computation (Luco and Lanzi, 2017a).

While the effect of damping in the linear stage of response is typically small except at resonance condition, the mathematical modelling and details of viscous damping for the inelastic stage have significant effects on the seismic response of high-rise buildings, particularly, on the estimated damping forces in the equation of motion. Currently, proper modelling and key parameters to represent viscous damping are still a topic of argument between researchers. A number of different mathematical models involving Rayleigh, Caughey, and modal viscous damping matrices based either on initial or effective stiffnesses have been proposed. In the meantime, warnings about the unintended problems that may be encountered from using (or misusing) these options have been risen for the last three decades by a number of researchers (e.g. Chrisp, 1980, Shing and Mahin, 1987, Léger and Dussault, 1992, Bernal, 1994, Carr, 1997, Hall, 1998, Carr, 2005, Hall, 2006, Carr, 2007, Charney, 2008, Ryan and Polanco, 2008,

Zareian and Medina, 2010, Jehel et al., 2014, Hardyniec and Charney, 2015, Chopra and McKenna, 2016a, Chopra and McKenna, 2016b, Hall, 2016). some studies suggested to abandon altogether using conventional viscous damping model and replace it with nonlinear hysteretic mechanism (e.g. Charney, 2008) or by a capped viscous model (e.g. Hall, 1998, Hall, 2006, Hall, 2016). Other studies (e.g. Kausel, 2014) recommended abandoning, when necessary, the classical or orthogonal damping matrix assumption.

In the process of developing a damping model, two conflicting objectives must be considered, these are: (1) arriving at a proper mechanical or physical representation of the damping model while keeping the computational efficiency in mind; and (2) respecting the limitation in experimental data available for damping of buildings at full scale. Viscous damping in high-rise buildings represents a variety of damping sources including internal friction in structural material, hysteresis response in nonstructural elements, external friction between structural and nonstructural members, and radiation into the surrounding soil. Mainly due to the computational convenience, viscous damping models, in which nodal damping forces and nodal velocities are connected together through a damping matrix, are ubiquitous. This is despite the extensive data on material damping (Lazan, 1968) suggesting that linear hysteretic damping models would be adequate for this particular damping component and that friction between structural and nonstructural elements can be best represented by a Coulomb model (Luco and Lanzi, 2017a). Strict obedience to the physical interpretation would necessitate the assembly of the global damping matrix from the damping properties of each of the structural elements in the building in correspondence to the process of assembling the global stiffness matrix based on elastic and inelastic properties of the structural elements. Notwithstanding the availability of damping information for different structural members (e.g. Lazan, 1968), this approach is considered unrealistic, and the damping matrix is conventionally formed on the bases of more global aspects.

The damping matrix is usually assumed orthogonal (classical), although this is not necessary for step-by-step nonlinear analysis. This assumption enables continuity with elastic analysis and taking advantage of experimental data that is usually presented in the form of modal damping ratios. Orthogonal damping matrix is usually presented in the form of Rayleigh damping (originally proposed by John W. Strutt, aka Lord Rayleigh in 1877), Caughey damping (O'Kelly and Caughey, 1965), or modal damping

(Wilson and Penzien, 1972). Again, for firm adherence to physical representation, implying that damping forces at a given structural node should only be contingent on the velocities at the adjacent nodes, limits the formation of classical damping matrix to only a stiffness-proportional matrix and excludes the mass-proportional terms. The choice of stiffness-proportional damping leads to modal damping ratios that increase with frequency. This contradicts some of the experimental results as well as reduced response in nonlinear analysis. Hall (1998, 2006) proposed a remedy to this issue involving capping the nodal damping forces using certain rules. A comprehensive discussion of Hall's approach can be found in the studies of Chopra and McKenna (2016a, 2016b).

Lesser concerns to the physical representation of the terms forming the damping matrix have emerged as a more promising approach. This approach focuses more on the global aspects, such as a more proper frequency-dependency of modal damping ratios and the elimination of unjustifiably large nodal damping forces. The said approach, supported by Carr (2007), requires shifting away from the conventional Rayleigh damping to non-banded damping matrices based on modal or Caughey damping approaches. Variation of modal damping ratios with frequency can be more realistically achieved by the use of either modal damping matrix (Carr, 2007, Chopra and McKenna, 2016a) or Caughey model with optimised coefficients (Lanzi and Luco, 2017, Luco and Lanzi, 2017b). These two mathematical models also allow for the exclusion of the mass-proportional term from the damping matrix, a term which can lead to unrealistic results in high-rise and base-isolated buildings (Hall, 2006, Ryan and Polanco, 2008). Furthermore, moving beyond Rayleigh damping is also epitomised by the need to limit the spurious, large damping forces at massless degrees of freedom identified by Bernal (1994). It was concluded in the latter study that these large spurious damping forces can be eradicated primarily by condensation of the massless nodes, and secondarily by the use of Caughey damping series along with negative powers assigned to the stiffness matrix. It is noted later that the modal damping matrix attains the same results (Carr, 2007, Chopra and McKenna, 2016a). According to the study of Hall (2016), however, these strategies do not eliminate all sources of spurious, large damping forces.

Another source of uncertainty in viscous damping modelling, independently of the mathematical approach used in forming the damping matrix, is the need to decide whether to use initial or tangent (degraded) stiffness in the formation of the damping

matrix. Despite the increase of related experimental data (e.g. Takayanagi and Schnobrich, 1979, Otani, 1980, Celebi, 1996, Satake et al., 2003, Rodriguez et al., 2006, Petrini et al., 2008, Papagiannopoulos and Beskos, 2012), the issue has not been fully settled. One of the reasons is the difficulty in distinguishing between the viscous damping from the hysteretic damping associated with nonlinear response and the contribution of SSI (e.g. Celebi, 1996). Most of the aforementioned experimental studies, however, suggested that tangent stiffness-based damping models seem to fit the experimental data better than those based on initial stiffness. Studies like the one by Carr (2007) indicated that using tangent stiffness in the damping matrix is one of the ways to compensate for the large damping forces resulting from a conventional Rayleigh model. Other studies (e.g. Chopra and McKenna, 2016a), on the other hand, have passionately argued for utilising initial stiffness in the damping matrix. Some research structural analysis packages allow for using tangent stiffness in the formation of the damping matrix while others neither allow nor recommend it (Charney, 2008). It is worth mentioning that the PERFORM-3D (CSI, 2011) commercial nonlinear analysis package gives no allowance for using the tangent stiffness in modelling the viscous damping.

Studies involving damping of higher modes of vibration in high-rise buildings are limited. Yokoo and Akiyama (1972) gathered damping data from a total of 17, 4 to 40-storey steel and RC buildings. It was concluded that damping ratios from higher modes were larger than those associated with the fundamental mode. The results, however, were insufficient to draw the overall frequency-damping ratio trend. Hart and Vasudevan (1975) utilised the accelerograms recorded during the 1971 San Fernando earthquake to study the damping ratio of 12 instrumented buildings using the amplitude of the roof-to-basement transfer function at modal frequencies. No substantial differences were found between the damping ratio of higher modes and those of the first mode. The results of this study were the base of several others that recommended using the same damping ratio for all modes of vibration (e.g. O'Rourke, 1976, Chopra, 2016). Cruz and Miranda (2017) highlighted that the method used in the study of Hart and Vasudevan (1975) produces systematic bias toward damping overestimation, similar to the half-power bandwidth method, therefore not reliable in estimating damping of structures. Specifically, Stagner (1972) concluded that many factors (such as spectral frequency resolution, noise, Fourier amplitude spectrum smoothing, and zero paddings) affect the shape and amplitudes of the peaks in the transform functions thus influencing

the damping computation. The same conclusion was drawn by several other studies (e.g. Jeary, 1986, Anderson et al., 1991, Miranda, 1992), that is the use of the half-power bandwidth or the peak of the transfer function method renders the computed damping ratio systematically overestimated.

In the study of O'Rourke (1976), damping data reported by eight investigations were analysed. Most of the data came from ambient and forced vibrations, with some from the 1971 San Fernando earthquake. The study revealed that in 61% of the cases, the damping ratio associated with the second mode was higher than the one associated with the fundamental mode and that the damping ratio allied to the third mode was higher than the one to the second in 53% of the cases. Kareem (1981) suggested a stiffness-proportional equation to calculate the modal damping using a normalised frequency ratio. The proposed equation was tested by Kareem and Gurley (1996) against new experimental data from Tamura et al. (1994) and other sources. Satake et al. (2003) investigated the damping ratio of 205 buildings in Japan. The study concluded that the damping ratio increases with frequency in different rates according to the material forming the structural system of the building. For RC buildings, the proposed increase rate is $\xi_i = 1.4\xi_{i-1}$, where ξ_i is the damping ratio of the i-th mode. Recently, a similar study was conducted by Cruz and Miranda (2017). This time, a total of 24 buildings in the range of 7 to 54 storeys, located in California, USA, were the studied material, where 119 seismic response recorded during 46 earthquake events are investigated. The proposed equation for the mean damping ratio of higher modes is: $\xi_i = \xi_1 \left[1 + \gamma\left(\frac{f_i}{f_1} - 1\right)\right]$, where ξ_i is the damping ratio for the i-th mode, ξ_1 is the damping ratio at the first mode, f_i is the frequency of the i-th mode, f_1 is the frequency of the first mode, and γ can be taken as 1.2 for RC buildings.

For the viscous damping ratios to be used in NRHA of high-rise RC buildings, scattered values, in the range of 0.75% to 2.5%, have been proposed in different seismic guidelines and previous studies (e.g. CTBUH, 2008, PEER, 2010, Mwafy, 2012a). It is important to keep in mind, as discussed earlier, that the value of the damping ratio to be used is largely affected by the analysis method and the adopted damping matrix properties. Different analysis methods (i.e. elastic response spectrum analysis, elastic response history analysis, and nonlinear response history analysis) necessitate a different range of viscous damping ratios. A key aspect of defining a proper viscous

damping ratio is the stiffness assumed in the model of the structure. The 5%, commonly adopted in code seismic provisions (e.g. ASCE/SEI-7, 2017) when using the elastic analysis corresponds to secant stiffness conditions at yield. The same ratio (5%) was adopted by Priestley (1993, 1999) using the displacement-based design method in which secant stiffness at target (design) displacement was utilised. On the other hand, when NRHA accompanied with fibre-based models are adopted, either initial or tangent (degraded) stiffness is used in the formation of the damping matrix. The initial stiffness-proportional damping, adopted in the current study, assumes initially uncracked concrete and hence the model would only match dynamic test results if very low viscous damping ratio is assumed.

This considerable scattering in the experimental damping data is highlighted by the study of Smith and Willford (2007) which was based on the damping data of tall buildings gathered from the work of different researchers (Figure 2.21). The figure depicts that for RC buildings with 100m height, for instance, an elastic damping ratio of approximately 1% is measured with the damping value decreases as the building height increases.

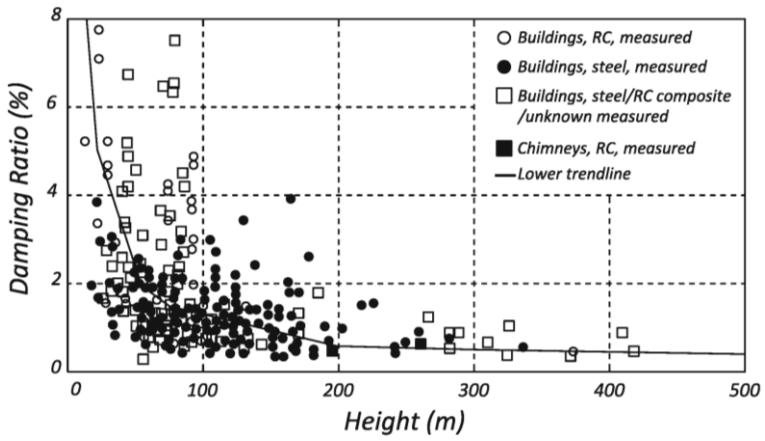

Figure 2.21. Measured damping ratio for a number of high-rise buildings (*after* Smith and Willford, 2007)

The shake table testing program of a full-scale 7-storey RC wall building conducted by Panagiotou et al. (2007a, 2007b, 2010) at the University of California, San Diego stands as a great opportunity to investigate the appropriate viscous damping values to be used in nonlinear simulation of the test structure and accordingly for RC wall buildings. The estimated viscous dumping ratios by those researchers were in the range of 0.3% to 1.0%, using different mathematical damping models and damping matrix properties

(e.g. Panagiotou and Restrepo, 2006, Martinelli and Filippou, 2009, Waugh and Sritharan, 2010).

2.2.3.4 Numerical solution

Nonlinear analysis of earthquake-excited structures requires the use of robust and efficient computational methods to accurately estimate the demands and response. Compared to linear static or linear dynamic problems, the solution of the nonlinear dynamic equation of motion involves numerical difficulties and demands that increase the computational effort. In the second half of the last century, the solution of highly nonlinear problems went through significant progress by developing several robust solution algorithms These algorithms have the capability to trace equilibrium paths of nonlinear problems that involve limit points in the type of snap-through and snap-back. When examining the seismic response of buildings, the equilibrium path usually consists of an upper limit point (snap-through) followed by a post-yield branch of often a negative slope (snap-back). The softening is usually the result of material constitutive relations or other sources such as connection fracture in steel buildings.

Nonlinear response history analysis is considered the most realistic method of analysis and often provides a reference to other analysis methods (linear dynamic, linear static, and nonlinear static). On the other hand, it is the analysis method with the most time-consuming and computational effort. Although Newton-Raphson is still needed in every time step, the computational treatment of nonlinearities using the NRHA method is less problematic considering the favourable effect of the mass term in the stiffness matrix. In the seismic analysis, implicit integration algorithms, such as the Newmark integration (Newmark, 1959) and the Hilber-Hughes-Taylor integration (Hilber et al., 1977), are almost always preferred. These algorithms allow relatively large time step in the inelastic stage, especially when the building response is dominated by the first or few modes of vibration. Given that ground motion accelerograms are classically discretized in time steps of 0.005 or 0.01 seconds, using an explicit integration scheme that demands a very dense time step for stability assurance would be inefficient.

The achievement of a stable, accurate, and solution convergence in NRHA is always a big challenge that requires a great amount of knowledge and judgment. Slow convergence or even divergence of the solution to the equation of motion is commonly encountered for this kind of problems (Bathe and Cimento, 1980). Divergence is

normally taking place when softening/stiffening of the force-deformation relation occurs. One of the solutions to this problem is to restart the analysis from the last converged time step using a smaller time step. Another solution is to use more refined energy-conserving integration algorithms (e.g. Armero, 2006). The solution algorithms, integration schemes, and divergence treatment employed in the present work are detailed in CHAPTER 3.

2.2.3.5 Model verification

For RC high-rise wall buildings, NRHA is the most suitable analysis method for predicting building response at different levels of ground motion intensity. The accuracy of the nonlinear model is assessed by its capability of capturing the significant modes of failure from within the elastic and inelastic building response. Various aspects of nonlinear modelling, such as element discretisation, material constitutive laws, and assumptions on modelling of viscous damping, are essential in defining the level of accuracy a model can have in predicting the seismic response of the structure both at global and local levels.

The high cost and lack of facilities render shake table full or large-scale testing programs of wall structures that can be used for model verification process very limited (e.g. Panagiotou et al., 2007a, Panagiotou et al., 2007b, Nagae et al., 2011). Consequently, most of the conducted testing programs involve isolated wall elements or coupled walls system (e.g. Ji et al., 2007a, Wallace, 2007, Beyer et al., 2008, Wallace and Moehle, 2012, Lehman et al., 2013). Hence, there is still a need for a verified nonlinear modelling approach which is essential for assessing the seismic vulnerability and estimating the seismic risk of such structures (Ji et al., 2007a, Martinelli and Filippou, 2009, PEER/ATC, 2010).

Different nonlinear analysis computer packages offer different modelling approaches in terms of element discretisation, material models, damping, and mass representation. Therefore, it is essential to investigate various modelling approaches in order to understand the consequences of using one analytical tool over. In the present work, a comprehensive MLNMVS is presented in CHAPTER 3.

2.2.4 Soil-Structure Interaction

The structural response of a building to earthquake ground shaking is the result of the interaction between three interrelated systems: the structure, the foundation, and the surrounding/underlying soil (e.g. FEMA, 2015). The collective response of these systems to given free-field ground motion is evaluated using Soil-Foundation-Structure Interaction (SFSI) analysis or simply referred to as SSI analysis. Conventionally, engineering practice ignores the SSI effects when evaluating the seismic response of buildings based on the perception that inclusion of SSI effects will reduce the demands on the structure, therefore, ignoring it will lead to a conservative analysis and design. However, previous studies have shown that this is not always the case (e.g. Givens, 2013). Furthermore, conventional engineering practice is force-based, normally intending to achieve a single performance (life safety). Seismic vulnerability assessment of buildings, on the other hand, is a performance-based approach where the evaluation of the building response under increasing seismic intensities is intended. Therefore, depending on the characteristics of the building, the foundation, and the surrounding/underlying geological media, the consideration of SSI may be important for a reliable seismic vulnerability assessment of buildings.

2.2.4.1 SSI effects on the performance of mid- and high-rise buildings under past earthquakes

The seismic performance of mid- and high-rise buildings (normally pile-supported) under past earthquakes is a good illustration of the SSI effects. A summary of varying studies on past earthquakes-induced damage on pile-supported mid- and high-rise buildings is given by (Meymand, 1998). The main outcomes of this study are briefly presented hereafter.

The 7.3M, 1964 Niigata (Japan) earthquake had caused liquefaction-related damage and failures to a widespread of pile-supported buildings. The damage modes in those buildings include losing of pile bearing capacity, broken piles, and differential settlement of buildings.

The 8.1M, 1985 Mexico City (Mexico) earthquake, triggered over 400 km away from the city centre, caused enormous damage to the mid- and high-rise buildings in the Lake Zone of the city as a result of convergence site response factors. The travelling distance along with the deep soft clay deposits in the Lake Zone had effectively filtered the

seismic waves to a long period motion in the range of approximately 2 seconds. This amplified long period motion came into resonance with many buildings of similar fundamental period, resulting in different modes of failure in these buildings including failure of piles, large settlement, and tilting (Girault, 1986, Mendoza and Romo, 1989).

Another example of SSI effects on mid- and high-rise buildings is the damage observed due to the 7.2M, 1995 Kobe (Japan) earthquake. The ground-shaking duration of this earthquake was 20 seconds, causing over 5500 casualties and more than 200,000 damaged housing units. Studies on damage patterns caused by the Kobe earthquake have recognised different failure modes including separation between piles and pile caps, damage of or near the pile head and at deeper levels of piles, and settlement/tilting of buildings (Mizuno et al., 1996, Tokimatsu et al., 1998, Hayashi and Takahashi, 2004).

The last example presented in this literature review is the 7.6M, 1999 Chi-Chi (Taiwan) earthquake and its subsequent aftershocks, four of them with a magnitude of larger than 6.5. This catastrophic event had induced heavy damage in the centre counties of Nantou, Yunlin, and Taichung. Losses presented in over 2,400 dead, over 10,000 injured, and around 15,000 buildings either completely destroyed or seriously damaged. Many of the mid- and high-rise buildings were settled or even collapsed during the temporary loss in foundation soil strength due to the earthquake-induced widespread liquefaction problems. This was despite the deep raft foundation or raft foundation with large diameter piles commonly found in this class of buildings in Taiwan (Hsieh, 2000).

The aforementioned examples emphasise the significance of the SSI effects when assessing the vulnerability of high-rise buildings in regions prone to liquefaction and other problems associated with soft underlying soil.

2.2.4.2 Overview of SSI

In the definition of SSI analysis, the term free-field refers to a ground motion that is not affected by the vibration of the structure or the waves scattering around and or at the foundation. In the theoretical scenario of a rigid foundation supported on a rigid soil (rigid base condition), SSI effects do not exist. Hence, SSI accounts for the difference between the structure actual response and the theoretical response of the rigid base condition. SSI effects can be classified into three components (e.g. NEHRP, 2012, FEMA, 2015): (1) inertial interaction effects; (ii) kinematic interaction effects; and (iii)

soil-foundation flexibility effects. The first to introduce the terms inertial and kinematic interaction was Robert Whitman in 1975 (Kausel, 2010). Engineering-wise, these three components are related to the following parameters and or actions:

- ***Inertial interaction effects:*** in a vibrating structure, the developed inertia causes moment, torsion, and base shear. These demands produce displacements and rotation at the soil-foundation interface as a consequence of the flexibility in the soil-foundation system. Furthermore, these displacements cause energy dissipation in the form of radiation damping and hysteretic soil damping (material damping). These inertial interaction effects, called so since they are rooted in structural inertia, can significantly affect overall system flexibility and damping.
- ***Kinematic interaction effects:*** A free-field ground motion can vary from a foundation input motion due to: (1) base slab averaging related to foundation geometry, wave scattering, and embedment effects in the absence of the structure inertial response; and (2) relative rotations and displacements between the foundation system and the free-field allied with the foundation and structure inertia.
- ***Foundation deformation effects:*** The structural foundation elements are subjected to axial, flexural, and shear deformations as a result of displacements and forces induced by the superstructure and the surrounding/underlying soil. These demands, of which the foundation elements should be designed, could be important, especially in flexible foundation systems such as piles.

The analysis approaches that can be utilised to evaluate the SSI effects can be classified as ***direct, substructure, and hybrid*** (NEHRP, 2012, Givens, 2013). In the direct approach, the soil and structure are analysed as a complete system by including them in the same model. In the substructure approach, the problem is divided into discrete parts that are eventually combined to form the complete solution. In the hybrid approach, the former two approaches are used in a combination. The concepts behind these three approaches are given hereafter.

2.2.4.3 Literature on the SSI effects in high-rises and wall buildings

The effects of the SSI on high-rises and wall buildings were the subject of several studies in the last half-century or so. A brief presentation of some of these studies is given hereafter.

Ukaji (1975) studied the SSI effects on mid- and high-rise buildings during earthquakes using a two-dimensional coupled model. Studying the response of three buildings (5, 10, and 20-storey), he investigated the effects of soil properties, soil depth, ground motion characteristics, building characteristics, and foundation system properties among other parameters. The study concluded that when the natural period ratio between the underlying soil and the building is unity, the base shear tends to maximum for a given soil damping ratio and that base shear value decreases when soil damping increases. It was also concluded that the best approach for the study of the ground motion effect should be statistical-based since the results of the base shear amplification factor from the three past earthquakes considered in the study were widely scattered without any sort of correlation. As far as flexible structures are concerned (such as most of the high-rise buildings), the study revealed that the response of the foundation system and the soil deposit to the bed-rock motion is almost independent of the building characteristics.

Using the substructure approach, Han and Cathro (1997) analysed a pile-supported, 20-storey building under different scenarios: rigid base, linear soil-foundation system, and nonlinear soil-foundation system. The conclusions of the study were: (1) the seismic behaviour of pile-supported high-rise buildings is different from those with rigid base or shallow foundation; (2) the effects of the SSI on pile-supported high-rises is complex, therefore the substructure approach is a realistic method of analysis; (3) the nonlinear response of a pile foundation system can be approximately considered by a boundary zone model with non-reflective interface; and (4) for the seismic response of high-rise buildings, the group effect and nonlinearity of pile-soil-pile interaction are important factors.

Shiming and Gang (1998) used the substructure analysis approach to present a three-dimensional SSI and corresponding analysis software. The analyses were conducted on a 12-storey building with two types of structural systems (frame and frame-wall) and two types of foundations (raft with and without piles). Some of the conclusions drawn from the study were: (1) the building natural period of each mode with SSI is greater in

varying percentage than that without SSI. The softer the soil and the stiffer the structure, the greater is the increase in the natural period of the system; (2) the increase in natural period is smaller for a pile-supported foundation than that without piles; and (3) the seismic response of high-rise buildings considering the SSI effects depend on the soil stiffness, foundation type, and spectral characteristics of the input motion.

Inaba et al. (2000) investigated the nonlinear response of the NTT Kobe Ekimae building and the surface soil in the site including the SSI during the 1995 Kobe earthquake. The building, built in 1972, is a steel-RC frame structure with a total of 11 storeys (8 above ground and 3 subterranean levels) with a raft foundation. In this study, two-dimensional finite element method was used to model the soil and the building. The base of the building was set as a stiff basement in the model, whereas the boundary surface was modelled as viscous. Among the conclusions of the study are: (1) significant nonlinearity of the soil deposit occurred at the foundation corner for both vertical compressive and shear stress-strain; (2) the maximum displacement due to foundation rocking observed at the top floor of the building was in the range of 15-18% of the total displacement.

Hayashi and Takahashi (2004) studied the raft foundation uplift and the separation between the underground exterior walls and soil through the modelling of a 9-storey building under the 1995 Kobe earthquake using 2-dimensional finite element approach. Linear springs were used to model the building, while equivalent linear and viscous models were adopted to simulate the soil and the boundary surface, respectively. The study revealed that the rotation of the raft foundation significantly increased in the uplift case. Hence, inter-storey drifts in the building reduced with the increases of the foundation rotational angle. The results estimated that the uplifting effect could be the main reason why high-rise buildings in the affected area rarely suffered structural damage during the Kobe earthquake.

In the study of Nghiem (2009), one of the main objectives was to investigate the SSI effect on acceleration, top displacement, and base shear of high-rise buildings under strong ground motions. In this study, SSI3D computer code was developed to investigate the seismic response of two 20-storey hypothetical buildings and one 30-storey actual (existing) building. The first hypothetical structure was a 75.6m tall RC office building with a lateral force-resisting system comprised of RC shear walls and moment frames. The second hypothetical structure was an 82.2m tall office tower with a

perimeter steel moment frame representing the lateral force-resisting system. The existing Y-shaped, 30-storey building (total height was not stated in the study) comprised of RC ductile moment frames with RC shear walls presented in the central core. All three building were supported by deep piles with raft or pile caps. Different site conditions and soil profiles were considered in the analyses of the above-mentioned buildings including reclaimed soil, weathered bed-rock underlying surficial clayey silts and sands, and very stiff-to-hard sandy clays and silty sand. Different modelling approaches were employed to reflect the way SSI effects were included. These are rigid base, flexible base with linear foundation springs, flexible base with linear soil, flexible base with nonlinear foundation springs, and flexible base with nonlinear soil. With numerous analyses conducted on the three reference buildings, the study concluded that the inclusion of the SSI effects increases the building base flexibility and hence increases the building natural period and decreases the base shear.

Tang (2009) assessed the SSI effects on the response of shear wall structures using two- and three-dimensional analyses with pulse motion as input. In this study, the SSI effects on shear wall structures were investigated by conducting probabilistic seismic demand analyses with the nonlinear hysteretic behaviour of the foundations and the shear walls. The study results indicated that although a number of discrete cases exist where SSI increases the structural response, in general, the inclusion of the SSI effects tends to lower the vulnerability of shear walls and hence shear wall structures.

Givens (2013) investigated the SSI effects on a 13-storey RC moment frame building with 2-basement levels and a 10-storey RC wall building with no basements. The foundation system comprised bored piles, grade beams, and pile caps for the former building, whereas the foundation system for the latter building contained spread footing, drilled piles, and raft elements. The substructure approach was utilised to perform the SSI analysis in this study considering different model configurations (three-dimensional baseline model; flexible structure with rigid basement/soil model; flexible structure/basement with rigid soil model; flexible structure/basement/soil model; and bathtub model). In the bathtub approach, vertical and horizontal soil springs are used to support the subterranean floors with these springs fixed at their ends to a rigid bathtub. The bathtub is excited with either a horizontal FIM or a FFM. The conclusion of the study was that the bathtub model provides a good estimation of the superstructure response given the baseline model as a reference. In general, the study suggested that

the substructure approach is practical to incorporate the SSI effects into realistic response history analyses of buildings. Several other studies had similar conclusions to the ones discussed above (e.g. Tang and Zhang, 2011, Balkaya et al., 2012, NEHRP, 2012, Pitilakis et al., 2014).

In the study of Li et al. (2014), the substructure approach is utilised to investigate the influence of the SSI on the seismic resistance of supper tall structures with the Shanghai Tower (632m total height) as a study building. A refined Finite Element model of the superstructure along with a simplified model of the foundation and the surrounding soil are created to collapse process and modes of failure of the tower considering the SSI effect. The study main conclusions were: (i) the SSI effect extends the periods of the lower order modes of vibration, particularly the 1st mode period, while the effect has a minor impact on the translational modal shape vectors; (ii) the SSI effect improves the collapse resistance capacity by increasing the collapse margin ratio; and (iii) under extremely strong earthquakes, the SSI effect has some impact on the failure sequence of the study building but a negligible impact on the final failure modes.

Lu et al. (2016) conducted a parametric study to investigate the seismic performance of multi-storey shear wall buildings (1, 5, 10, 15, and 20-storey) considering SSI. The investigated structures were subjected to 3-sets of synthetic spectrum-compatible earthquakes. Among the investigated parameters were site condition, soil stiffness, design lateral load pattern, fundamental period, structure slenderness ratio, and the number of storeys. The results indicated that, generally, SSI may reduce the strength and ductility demands of mid- and high-rise buildings up to 60%., especially those with low ductility demands.

In the study of Bagheri et al. (2018), Soil-Pile-Structure Interaction (SPSI) effect was investigated on two 15- and 30-story moment-resisting steel frame buildings with total heights of 45 and 90 m, respectively. Numerical analyses were performed to investigate the different factors affecting seismic response, including building configuration, pile length, building height, and input ground motion characteristics. The structural and soil elements were modelled as inelastic and elastic-plastic continuum materials. Among other findings by the study, SPSI was found to have a favourable effect in reducing the amount and trend of shear forces in the superstructure. The reduction level is found to be influenced by the pile diameter, length, and configuration.

Considering the very dense (or stiff) soil and soft rock underlying deposits of Dubai's sites (the case study region in the current work), liquefaction and or other soft underlying soil-associated problems are unlikely to be encountered. When consulting the above-detailed literature, the SSI is likely to have insignificant adverse if not favourable effects on the seismic response of the study case buildings in the present work, namely: (i) extending the fundamental period of the structure (Shiming and Gang, 1998, Nghiem, 2009, Li et al., 2014); (ii) reducing base shear and hence storey shear (Nghiem, 2009, Bagheri et al., 2018); (iii) reducing inter-storey drift due to the foundation system rotation (Hayashi and Takahashi, 2004); and (iv) reducing strength and ductility demands in the lateral force-resisting system hence reducing the vulnerability and improving the collapse resistance capacity of shear walls and shear wall structures (Tang, 2009, Li et al., 2014, Lu et al., 2016). It is worth noting that SSI effect on buildings response is a huge field of ongoing research, normally handled as a main topic in post-graduate researches where the full time of the study is dedicated to the topic. Moreover, investigating the effect of SSI on building response would require the use of special analytical software with features that allow for proper and realistic modelling of all involved components (i.e. superstructure, foundation, and soil). The PERFORM-3D commercial package utilised in the present work, despite its advancement in the nonlinear fibre-based modelling of the superstructure, has very limited capabilities in modelling the stiffness and damping of the surrounding soil. Taking all the above arguments into account, it is decided not to include the SSI effects in the current work. Meantime, it is recommended for future work to investigate these effects on the seismic vulnerability assessment of RC high-rise wall structures located in areas with less favourable site conditions.

2.2.5 Uncertainty modelling

For the development of reliable fragility relations, it is essential to account for the uncertainties in the seismic demands and the system capacity. Some of these uncertainties are inherently random (aleatoric) while others are due to errors arising from lack of knowledge (epistemic), (Wen et al., 2003). Typically, simulation methods such as the Monte Carlo and the Latin Hypercube are used to account for demand and capacity uncertainties. However, for large structures such as high-rise buildings, applying these techniques renders a large number of computationally demanding NRHAs. Hence, it is more efficient to focus on the uncertainty sources that impact the

probabilistic response, while consulting previous studies in estimating the influence of others. Uncertainties in the seismic demands and the system capacity, forming the collapsing chart for the "Uncertainty" component in the IPO model (Figure 2.22), are briefly discussed hereafter.

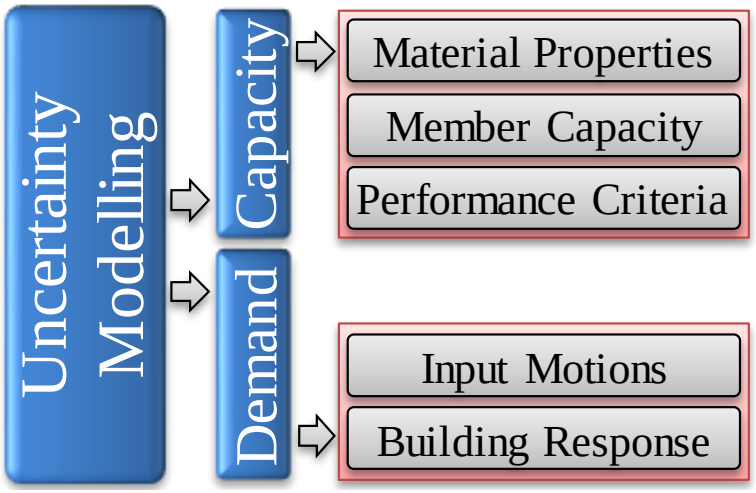

Figure 2.22. Collapsing chart for the "Uncertainty" component in the IPO model

2.2.5.1 Uncertainty in the seismic demand

Two main sources can be identified for the seismic demand uncertainty: (i) input motions; and (ii) building response. These two sources are briefly discussed hereafter.

2.2.5.1.1 Input motions

Among all other demand and capacity uncertainties, the input motion characteristics have the most significant impact on the fragility curves (Elnashai and Izzuddin, 1993b, Wen et al., 2003, Wen et al., 2004, Kwon and Elnashai, 2006, Soltangharaei et al., 2016, Abdelnaby, 2018). A wide range of frequency content and seismic energy levels must be included in the selection of the input motions in order to account for this source of uncertainty in the vulnerability assessment of high-rise buildings. To achieve that, the combination of the following three main parameters is to be considered (e.g. Kwon and Elnashai, 2006, Mwafy et al., 2006, Mwafy, 2012a):

- ***Source mechanisms:*** Frequency content and inherent energy are controlled by random source mechanisms,
- ***Path:*** Different paths of wave propagation lead to different attenuation effects, and

- ***Site condition:*** The seismic response can be amplified or mitigated as a result of the soil interference at the site.

In the present study, the above-mentioned parameters are considered in the selection of a total of 40 seismic scenario-based input ground motions (two sets of 20 records each). More insight on the record selection criteria is given in Section 2.2.2 and CHAPTER 4.

2.2.5.1.2 Building response

Accounting for the uncertainty associated with the building response to seismic excitations is a challenging task, especially in the case of high-rise structures when the response can be highly inelastic. The most effective approach to deal with this source of uncertainty is to use the NRHA method to predict the response. Probabilistic structural demands can be attained using sampling techniques. Alternatively, regression analyses with the best fit power-law expression (Vamvatsikos and Cornell, 2002, Luco and Cornell, 2007) through MRIDAs can be employed to establish functional relations between the adopted IM and DM.

In the present study, the method of analysis and the approach used to estimate the probabilistic structural demands in the reference building are the most effective for deriving fragility relations for high-rise structures, which intern contribute to the reduction of the uncertainty in seismic demands.

2.2.5.2 Uncertainty in the system capacity

Uncertainty in the system capacity can be traced back to three main sources: (i) material properties; (ii) member capacity; and (iii) performance criteria. These sources are briefly discussed hereafter.

2.2.5.2.1 Material properties

The strength of reinforcing steel and concrete is inherently variable. However, when compared to the variability of ground motions, the uncertainty associated to the material properties is proven to have little impact on the structural response with even lesser impact at high ground motion intensities (e.g. Kappos, 1986, Kappos and Penelis, 1986, Wen et al., 2003, Kwon and Elnashai, 2006, Mwafy et al., 2015b). Accordingly, material properties are considered deterministic in the present study, set to their mean (expected) values.

2.2.5.2.2 Member capacity

The capacity of a structural member is the maximum force or deformation that the member can endure before reaching a predefined damage state. The main keys controlling the member capacity are the modelling approach of the member component(s) and the force-deformation relation assigned to the member materials.

In the present study, the uncertainty in the member capacity is accounted for by adopting the fibre-based modelling approach along with force-deformation material relations that incorporate hysteresis rules as well as strength and stiffness degradation. The adopted modelling approach and modelling key parameters are verified against shake table experimental results from a full-scale 7-storey RC wall building (Panagiotou et al., 2007a, Panagiotou et al., 2007b, Panagiotou et al., 2010). More details on the verification process are given in CHAPTER 3.

2.2.5.2.3 Performance criteria

The damage states and the global DM to be used in the definition of the performance limit states for the structure of interest can be considered as one of the sources of uncertainty in assessing the seismic vulnerability. The uncertainty level, therefore, varies according to the attention given to the selection and definition of the local DIs and the global DM.

In the present study, the uncertainty in the performance criteria is accounted for by the definition and selection of seven local DIs for the reference building. These DIs are examined, mapped, and correlated to one another. Additionally, a new global DM is proposed to be used in defining the performance criteria and in the development of the vulnerability relations. More details on this topic are given in CHAPTER 5.

2.2.6 Demands

Given that NRHA is the most suitable method of analysis available for high-rise buildings, MRIDA has been emerged and evolved during the past four decades to become the most preferred method for thoroughly estimating the structural demands (response) of a building under seismic loads. The method involves applying multiple input ground motions to a structural model, each of which is scaled to multiple intensity levels, hence producing multiple response curves, parameterized against a predefined intensity level.

The MRIDA approach has been introduced as early as 1977 by Bertero (1977) and has been implemented in many studies related to the performance-based design and the vulnerability assessment of buildings and bridges (e.g. Kappos, 1990, Nassar, 1992, Bazzurro and Cornell, 1994a, Bazzurro and Cornell, 1994b, Luco and Cornell, 1998, De Matteis et al., 2000, Dubina et al., 2000, Luco and Cornell, 2000, Mehanny and Deierlein, 2000, Psycharis et al., 2000, Kappos, 2001, Mwafy and Elnashai, 2001, Vamvatsikos and Cornell, 2002, Kappos et al., 2004, Vamvatsikos and Cornell, 2004a, Vamvatsikos and Cornell, 2004b, Vamvatsikos and Cornell, 2005b, Kappos et al., 2006, Vamvatsikos and Cornell, 2006, Ji et al., 2007a, Ji et al., 2009, Kappos and Panagopoulos, 2010, Mwafy, 2012a, Mwafy et al., 2015a, Soltangharaei et al., 2016, Khorami et al., 2017, Mwafy and Khalifa, 2017, Stefanidou and Kappos, 2017). The concept has also been implemented in the U.S. Federal Emergency Management Agency (FEMA) and the American Society of Civil Engineers (ASCE) documents as the state-of-the-art method to estimate the global collapse capacity of buildings (e.g. FEMA, 2015, ASCE/SEI-41, 2017).

2.2.6.1 Multi-Record Incremental Dynamic Analysis (MRIDA)

To construct MRIDA curves that can sufficiently and efficiently reflect the variable status of the building response to different earthquake records with increasing intensities, three parameters are to be defined: (i) IM; (ii) DM; and (iii) scaling algorithm. These parameters, forming the collapsing chart for the "Demands" component in the IPO model (Figure 2.23), are briefly discussed hereafter.

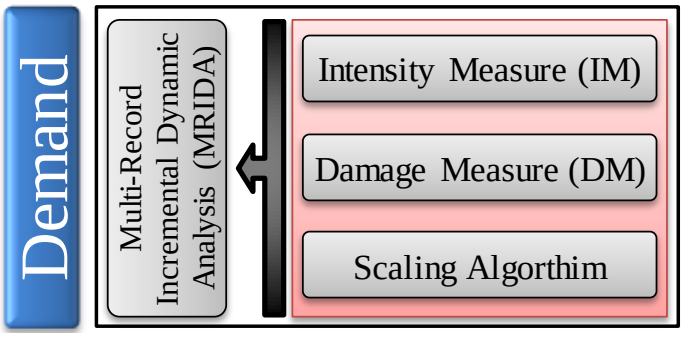

Figure 2.23. Collapsing chart for the "Demands" component in the IPO model

2.2.6.1.1 Intensity Measure (IM)

The IM, as defined in Section 2.1, is a non-negative scalar (or vector) that constitutes a function of the scaled accelerogram. It refers to the unscaled accelerogram and is increasing or decreasing monotonically with a predefined scaling algorithm.

In the past, PGA used to be the most preferred intensity measure. In recent years, however, the elastic spectral acceleration at the fundamental period of the structure, $S_a(T_1)$ or S_a in short, has been found to be more efficient, since it is structure-dependent, and became a frequently used intensity measure for short buildings. However, S_a is shown to be neither efficient nor sufficient to be used with tall buildings (Shome, 1999, Vamvatsikos and Cornell, 2002) and for structures subjected to near-source earthquakes (Luco and Cornell, 2007). Other intensity measures have been proposed in the literature to overcome the major shortcomings of S_a, namely discounting the contribution of the higher modes and fundamental period lengthening of the structure associated with stiffness degradation (Shome, 1999, Carballo and Cornel, 2000, Cordova et al., 2000).

New approaches have led to other kinds of intensity measures such as inelastic spectral value-based scalar intensity measures (e.g. Luco and Cornell, 2007) and vector-valued intensity measures (Bazzurro and Cornell, 2002, Conte et al., 2003, Baker and Cornell, 2005). These approaches, although promising, are not easy to apply since they require probabilistic seismic hazard assessment based on custom-made attenuation laws to obtain the joint hazard curve. In the present study, a new scalar intensity measure termed spectral acceleration at weighted-average period $S_{a(wa)}$, is proposed. More insight about this IM is given in CHAPTER 5.

2.2.6.1.2 Damage Measure (DM)

The DM, as defined in Section 2.1, is a structural state variable represented by a non-negative scalar that signifies the additional response of the structural model as a result of a predefined seismic loading. In other words, a DM is a quantitative parameter that forms a part of the output of the corresponding NRHA.

Different DMs can be selected depending on the application and the assessed structure itself. They can be categorised as: (i) demand-based; (ii) deformation-based; (iii) force-based; (iv) energy-based; and (v) stability-based. For the structural damage of buildings, the deformation-based maximum total peak inter-storey drift is a strong DM candidate.

It is found to well relate to the member rotation and both local and global storey collapse. Hence, this DM is adopted in many loss estimation programs such as HAZUS (FEMA, 2019, Kircher et al., 2006), seismic code provisions (e.g. PEER/ATC, 2010, FEMA, 2015, ASCE/SEI-41, 2017), and previous studies (e.g. Vamvatsikos and Cornell, 2002, 2004a, Mwafy, 2012a, Yamin et al., 2017). For high-rise buildings, however, the maximum net (effective) peak inter-storey drift, accounting for the rigid body motion effects, is argued to be a more reliable DM (e.g. Ji et al., 2009). More insight on this DM is given in CHAPTER 5.

2.2.6.1.3 Scaling algorithm

Performing a MRIDA can be quite intensive in terms of computational efforts and resources. Although an almost continuous representation of the IDA curves is preferred, the high cost associated with each NRHA run for a high-rise building necessitates the employment of a scaling algorithm. As defined in Section 2.1, scaling algorithm is an algorithm intended to select an optimum grid of distinct intensity measure values that will deliver the desired coverage of the building seismic response with the objectives of achieving a minimum number of runs, high demand resolution, and high capacity resolution. In a MRIDA study, a different scaling algorithm can be designed for each record set separately. The results obtained from the first record in the set can be utilised to define the scaling algorithm to be used on the rest of the records in that set. The simplest form of scaling algorithms is the so-called stepping algorithm, where a constant step is adopted to increase the IM from zero to collapse level. The end result is IM-uniformly spaced grid of points where only a pre-defined step value and a run-stopping rule are required. The quality of this type of scaling algorithm is principally dependent on the selected IM step. A version of this form is detailed in Yun et al. (2002) and is used in the FEMA guidelines (e.g. FEMA, 2015).

A more advanced technique that can be adopted is the *hunt and fill* tracing algorithm. This technique was discussed in detail by Vamvatsikos and Cornell (2004b). In this algorithm, the first routine, also called the hunting part, involves increasing the step interval until all damage states associated with the collapse prevention performance level are bracketed with the means of only a few runs. Step interval increasing can be achieved by applying either a constant, resulting in a quadratic series of IMs, or a factor, producing a geometric series. To improve upon capacity resolution of the IDA curve, a step reducing (second routine) is to be added to the algorithm once the first damage

associated with collapse prevention state is detected. The third and final routine in this algorithm is to fill in the gaps created by the enlarged step intervals introduced in the first routine. This will enhance the demand resolution in the IDA curve. The *hunt and fill* tracing algorithm require the definition of an initial step, a run-stopping rule, a step interval increasing function, and capacity and demand resolutions. The *hunt and fill* tracing algorithm are adopted in the present study in which the step interval increasing function and capacity and demand resolutions are selected so that a predefined number of runs (fourteen) is performed on each of the 40 used records.

2.2.7 Damage Indices (DIs)

Earthquakes with varying scenarios are expected to impose different excitation levels to different modes of vibration in high-rise buildings. Furthermore, it may impose different nature of excitation on an individual structural element such as a structural wall or a coupling beam. Therefore, a wide range of DIs is to be considered for a proper vulnerability assessment study of this class of structures. As highlighted in Section 2.2.6.1.2, DIs can be categorised as:

- ***Demand-based:*** Such as peak floor acceleration. This DI is widely used if the damage of non-structural contents or sensitive equipment in a multi-storey building is to be assessed.
- ***Deformation-based:*** Such as strains (tensile and compressive) in reinforcing steel and concrete materials, shear strain in walls, rotations in structural members, peak storey ductilities, total peak roof drift, and maximum total peak inter-storey drift.
- ***Force-based:*** Such as base shears, base overturning moments, and capacities of structural members in shear/axial/bending.
- ***Energy-based:*** Such as the global Park-Ang index (Park and Ang, 1985).
- ***Stability-based:*** Such as the stability index proposed by Mehanny and Deierlein (2000).

For the definition of reliable performance criteria of high-rise buildings, local DIs (such as strains and rotations) and global DIs (such as drifts) are to be selected, mathematically defined in the model, mapped, and linked to one another. Mapping of the local damages resulting from the MRIDA on a building provides insight into the nature of the building response under varying earthquake scenarios. This enables

reliable seismic scenario-based definitions of the performance criteria. On the other hand, interrelating (linking) local to global DIs helps in selecting a proper DM to be used in defining the seismic performance criteria of the building(s) under assessment and to represent the building(s) capacity in the development of the vulnerability relations. Figure 2.24 illustrates the collapsing chart for the DIs component in the IPO model

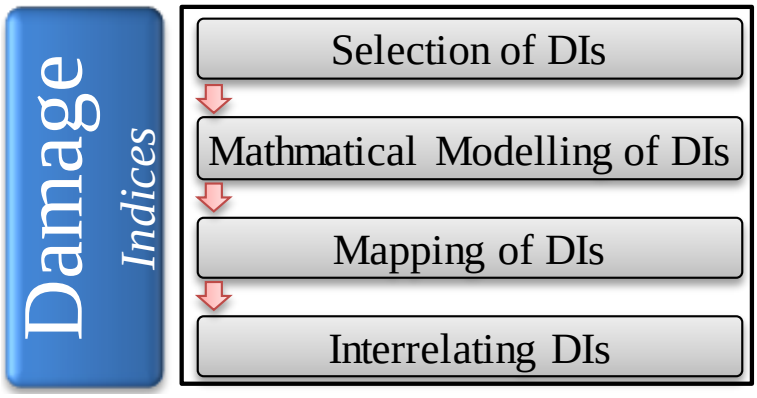

Figure 2.24. Collapsing chart for the DIs component in the IPO model

In the present study, a total of seven local DIs for the reference building are selected, mathematically modelled, mapped, and correlated to one another. More details on this topic are given in CHAPTER 5.

2.2.8 Performance criteria

The definition of accurate and comprehensive seismic scenario-based limit states and hence the identification of performance criteria forms the spine of the seismic vulnerability studies. Such a definition is a challenging task when high-rise wall buildings are of interest as several factors affect failure modes in this class of structures. Among these factors are:

- ***Building height:*** The taller the building, the larger is the expected TISD at specified performance levels due to the increasing influence of the rigid body motion phenomenon. This is not necessarily reflecting higher seismic demands in the structural members of the building.
- ***Axial demands:*** In high-rise wall buildings, especially at lower storeys, the level of the axial compressive force is influenced by the arrangement of the RC shear walls and cores in the building. This arrangement is usually dominated by the gravity loads, particularly for internal shear walls. High compressive loads are

expected to delay the onset of the initial cracking and yielding in vertical elements but can decrease ductility and hence the TISD at which concrete core crushing and rebar buckling occur.

- ***Supplementary regulations and construction trends:*** The supplementary regulations of local authorities, as well as trends adopted by both consultants and contractors, may impact the design and hence the seismic performance of high-rise buildings. For instance, the minimum steel ratio in vertical elements may exceed the value that is stated in the code provisions.

Limit states present propagating points on a continuous scale of damage states of the structure, therefore, described with potential and tolerable losses such as the structural and non-structural damage, the number of casualties, the facility non-operational time, repair cost and others. There are two different approaches for defining the limit states for a building or a building inventory. These are:

I. ***Qualitative approach:*** This approach, where the limit states are defined through the description of the structure's damage state, is the most used in building regulations and seismic codes (e.g. ASCE/SEI-41, 2017, FEMA, 2019). For instance, in a study by Rossetto and Elnashai (2003), this approach is utilised to define seven limit sates based on post-earthquakes observed damage data on buildings.

II. ***Quantitative approach:*** The definition of limit states based on this approach requires mathematical representations of local DIs (such as deformations, forces, and energy) based on designated building performance levels. This necessitates the adoption of a suitable DM to sufficiently correlate local damage events in the building to its global response. Several researchers have adopted this approach in their definitions of limit states (e.g. Kappos, 1991, Kappos and Dimitrakopoulos, 2008, Ji et al., 2009, Kappos et al., 2010, Mwafy, 2012a, Pejovic and Jankovic, 2016)

Due to the lack of sufficient post-earthquake data in the case of RC high-rise wall buildings, the qualitative approach would not be suitable for defining the performance criteria for this building class. Nevertheless, the limit states defined in previous studies and seismic codes using qualitative approaches can serve as references (e.g. Ji et al., 2007b).

Based on the above, a more detailed quantitative approach is adopted in the present study to define seismic scenario-based limit states for the reference building. Figure 2.25 illustrates the collapsing chart for the "Performance Criteria" component in the IPO model. A brief discussion of each of the components in the collapsing chart is given hereafter.

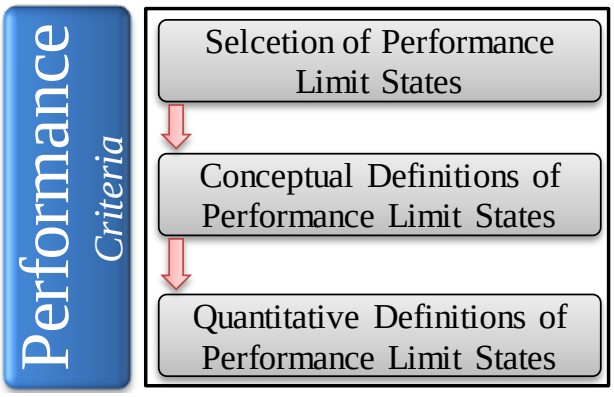

Figure 2.25. Collapsing chart for the "Performance" component in the IPO model

2.2.8.1 Selection of performance limit states

As researches come with varying aims and objectives, varying performance limit states can be assigned to a building or stock of buildings depending on the study desired outcomes. The most commonly used performance levels are IO; LS; and CP (e.g. FEMA, 2015, ASCE/SEI-41, 2017). A building at the point of IO limit state is considered to sustain slight or no damage. A building at the point of LS limit state is considered to sustain moderate damage but still in the zone of high safety against collapse. At the point of CP limit state, a building is considered to sustain large and significant damage and to be at the verge of collapse.

Examples of other limit states that have been adopted in previous studies are no damage, negligible damage, light repairable damage, moderate reparable damage, irreparable damage, severe damage, and collapse state damage (e.g. Shea, 1999, Ghobarah, 2004). In the present study, the three performance levels recommended by the ASCE/SEI 41-17 (2017) are adopted (IO, LS, and CP). More details are given in CHAPTER 5.

2.2.8.2 Conceptual definitions of performance limit states

Each of the predefined limit states for a building needs to be conceptually defined either explicitly or implicitly in relation to a specific damage event or pattern. For that matter,

different approaches have been adopted in seismic codes and previous studies. In the study of Vamvatsikos and Cornell (2004a) on steel moment-resisting frame buildings, the characteristics of the IDA curves were utilised to conceptually define the CP and collapse limit states. The former was linked to the "80% reduction in slope" point on the curve while the latter was associated with reaching the flatness zone (global dynamic instability). In the ASCE/SEI 41-06 standard (2007), specific rotation values in RC walls and coupling beams are associated to each of the three predefined limit states (IO, LS, and CP) for the primary and secondary components controlled by the flexural response. In the study of Ji et al. (2007b) which involved a 54-storey RC high-rise wall building, pushover and time-history analyses were performed to conceptually define the three selected limit states (Serviceability, Damage Control, and CP). The Serviceability limit state was linked to the initiation of minor cracks in main resisting members. The Damage Control limit state was linked to the first yielding in longitudinal reinforcement or to the occurrence of the first plastic hinge (whichever happens first). The CP limit state was linked to the reach of the ultimate capacity in the main resisting members and to the start of the descending zone in the capacity curve.

Another example is the study of Mwafy (2012a) that involved pushover and incremental dynamic analyses on the nonlinear models of six reference RC wall buildings with varying heights (10 to 60 storeys). In this study, the CP limit state was selected based on the recommendation of previous studies. The LS limit state was linked to the global yielding point of the building, which was estimated from the capacity curve using the elastic-perfectly plastic idealization concept. The IO limit state was associated with the most conservative first yielding values obtained from pushover analysis and median IDA results of 20 earthquake records. A more recent study by Mwafy and Khalifa (Mwafy and Khalifa, 2017) on vertically irregular high-rise buildings estimated the limit states from IDA by linking local response to TISD.

In the present study, seven local DIs are used to conceptually define the adopted performance limit states for the reference building. More details are given in CHAPTER 5.

2.2.8.3 Quantitative definitions of performance limit states

Using TISD as a DM, seismic guidelines and previous studies have adopted a wide range of quantitative values to define limit state criteria associated with different

performance levels of RC shear walls and wall structures. The SEAOC blue book (1999) proposed TISDs of 0.4%, 0.9%, 1.4% and 2.1% for RC shear walls at performance levels SP1 (negligible damage), SP2 (minor to moderate reparable damage), SP3 (moderate to major irreparable damage) and SP4 (collapse performance level), respectively. In ASCE/SEI 41-06 (2007), TISDs of 0.5%, 1%, and 2.0% are assigned to the IO, LS and CP performance levels, respectively. In a study involving post-earthquakes observed damage data on RC wall buildings, Rossetto and Elnashai (2003) suggested TISD values of 0.00, 0.026, 0.34, 0.72, 1.54, 2.56, and > 3.31 for the damage states of none, slight, light, moderate, extensive, partial collapse, and collapse, respectively. For ductile RC walls, Ghobarah (2004) recommended TISDs of <0.2%, 0.4%, <0.8%, >0.8%, 1.5% and >2.5% corresponded to damage levels of none, light reparable, moderate reparable, irreparable, severe (or life safe) and collapse, respectively. In contrast, Ji et al. (2007a) suggested conservative TISDs to define three performance limit states obtained from inelastic pushover and time history analyses for a 54-storey RC wall building. The proposed TISDs were 0.2%, 0.52% and 1.1% for serviceability, damage control, and collapse prevention limit states, respectively. In a study of RC wall buildings with a number of storeys ranging between 10 to 60, Mwafy (2012a) suggested a TISD value of 2.5% for CP, while height-dependent TISDs were proposed for IO (0.32% to 0.83%) and LS (0.81% to 1.35%). In the study of Jeong et al. (2012), TISDs of 0.4% to 0.7%, 1.5%, and 2.5% were associated to the limit states of IO, LS, and CP, respectively, for 8-storey wall-frame buildings with different ductility and input ground motion intensity levels. More recently, a study conducted by Pejovic and Jankovic (2016), involving RC high-rise wall buildings (10-, 30-, and 40-storey) located in the southern Euro-Mediterranean zone, suggested TISD values of 0.25%, 0.53%, 0.95%, and 1.64% for the limit states of slight damage, moderate damage, extensive damage, and collapse, respectively.

It is essential to highlight that all the above-mentioned recommendations of TISDs, as quantitative definitions to the performance limit states of RC wall buildings, have not taken into consideration the need for seismic scenario-based limit state definitions. The broad range of frequency content in real strong ground motions, representative of different seismic scenarios (i.e. distant and near-field earthquakes), can impose a different level of excitation on both fundamental and higher modes in the RC high-rise wall structures and consequently different nature of response. Therefore, for an accurate vulnerability and seismic risk assessment studies on this class of buildings, seismic

scenario-based limit state definitions are required. This issue is considered in the present study, more details are given in CHAPTER 5.

2.2.9 Fragility/Vulnerability

In the theorem of total probability that shapes the framework for seismic risk assessment, three fundamental contributors take place: (i) seismology; (ii) structural engineering; and (iii) direct/indirect losses. The second contributor is represented by fragility/vulnerability relations. As defined in Section 2.1, fragility is the conditional probability of a system (a structural member, a storey in a building, a building, or a stock of buildings) reaching a predefined performance limit state (PLS) for a given demand (force, deformation, energy dissipation, or more generally a DM). In general expression, the fragility curve (FC) is a function of the system capacity against a predefined PLS (controls the central location of the FC) along with the uncertainty in the capacity (controls the shape "dispersion" of the FC); (Figure 2.26). Hence, for a deterministic system with no uncertainties, the FC would be a step function. Generally, the FC is strictly a limit state-dependent with no or very little dependency to the site seismic characteristics. In other words, if the demand is force or structural response, identical buildings located in areas with different seismicity will have the same FC. Meanwhile, the FCs will be similar (not exactly the same) for these identical buildings if the IM is spectral acceleration since spectral acceleration for higher modes would be different for different locations (Wen et al., 2004).

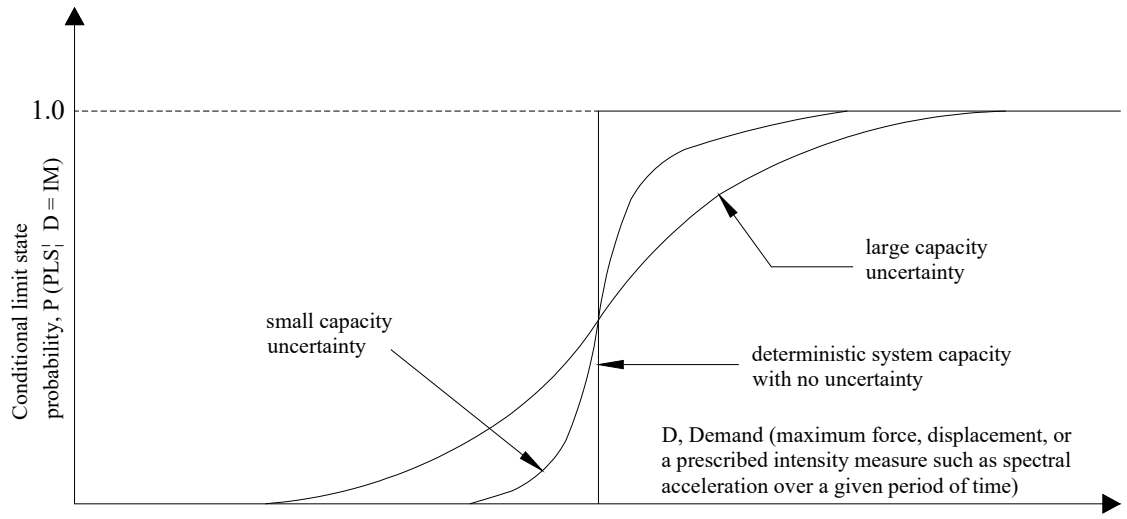

Figure 2.26. Characteristics of a fragility curve, (*after* Wen et al., 2004)

To generate a fragility/vulnerability curve, the following order-wise steps are needed:

1. Defining the PLSs of interest and the IM. In the present study, the defined performance limit states are IO, LS, and CP (more details are given in Section 2.2.8 and CHAPTER 5). The proposed IM is the spectral acceleration at weighted-average period $S_{a(wa)}$ (more details are given in Section 2.2.6.1.1 and CHAPTER 5).

2. Performing regression analysis on the limit states-related building response as a function of the IM (MRIDAs results). Considering the nonlinear nature of the problem and the record-to-record response variation, nonlinear regression analysis in the power-law form is recommended (Vamvatsikos and Cornell, 2002, Luco and Cornell, 2007, Mwafy, 2012a, Mwafy and Elkholy, 2017). Other nonlinear regression analysis may be implemented if found to better fit the LSs-IM relation.

3. Accounting for the uncertainties in the FC development process. These uncertainties can be categorised as (i) demand uncertainty; capacity uncertainty; and modelling uncertainty. Details on the estimation of these uncertainties are given in CHAPTER 6.

4. Generating the FCs using a proper distribution function. Generally, a lognormal cumulative distribution function provides a good fit (Wen et al., 2004) therefore adopted in the present study. More details on the components of the FC function are given in CHAPTER 6.

5. The probabilistic earthquake risk assessment for a building or a building stock may be expressed in terms of a probability distribution function of economic losses (vulnerability curves) by further processing the FCs. An example of such a presentation is shown in Figure 2.27. Several methods have been proposed by previous studies to develop the vulnerability functions (e.g. Scholl, 1980, Kustu et al., 1982, Kustu and Miller, 1984, Singhal and Kiremidjian, 1996, Porter et al., 2001, D'ayala et al., 2014, Yamin et al., 2014a, Yamin et al., 2014b, Yamin et al., 2017). Those methods have been imbedded in earthquake risk assessment platforms such as CAPRA (ERN-CAPRA, 2011), HAZUS (FEMA, 2019, Kircher et al., 2006), Risk-UE (RISK-UE, 2001-2004), and other recently developed platforms (e.g. GEM, 2019). To develop the vulnerability relations,

the main parameters that need to be accounted for are: (i) the type of occupancy of the assessed building(s); (ii) local estimates of the repair cost; and (iii) local estimates of reconstruction cost. Once such data is available, the analyst can calculate the total repair cost, given damage threshold.

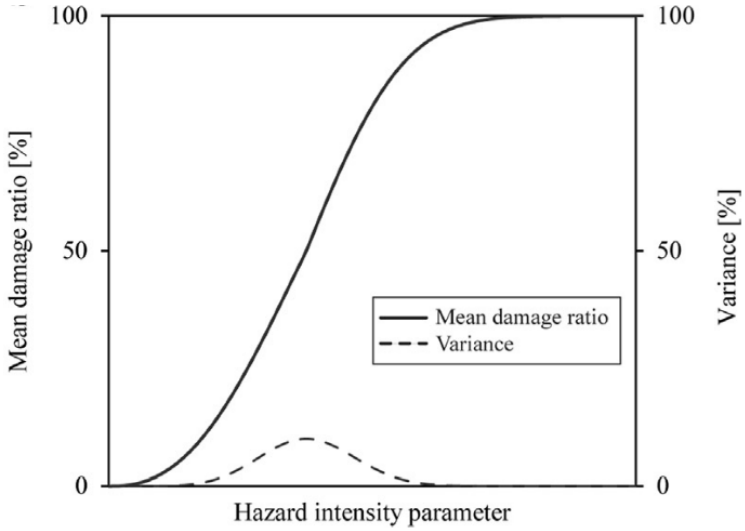

Figure 2.27. A typical presentation of a vulnerability relation (*after* Yamin et al., 2017)

Following the above steps, the collapsing chart for the "Vulnerability" component in the IPO model is given in Figure 2.28. In the present study, the vulnerability assessment of the reference building is presented with the fragility relations only. Further processing of these FCs to develop vulnerability relations can be part of future work. This will extend the proposed framework by including the earthquake risk assessment component.

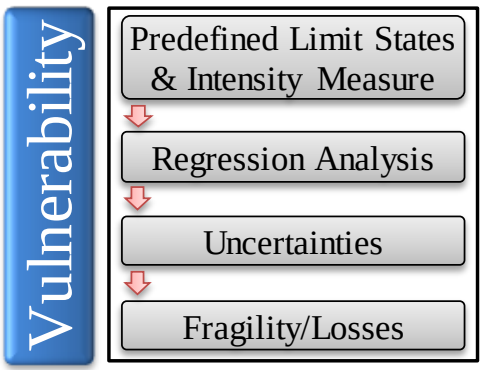

Figure 2.28. Collapsing chart for the "Vulnerability" component in the IPO model

This page is intentionally left in blank

CHAPTER 3. Multi-level nonlinear modelling verification scheme of RC high-rise wall buildings

Earthquake-resistant structures are designed and detailed to respond well beyond the elastic range under the DBE. However, in terms of analysis, RC walls are often treated as linear elements despite their considerable depth ignoring the effect of deformation compatibility. Due to the limited number of comprehensive experimental studies on RC structural wall systems subjected to cyclic loading, few in-depth analytical verification studies have been conducted. Motivated by the increasing need for more accurate seismic risk assessment of high-rise buildings adopting RC shear walls as the lateral force-resisting system, a MLNMVS is developed in this chapter to investigate two different nonlinear modelling techniques for shear walls (i.e. 2- and 4-noded fibre-based elements). The investigated modelling approaches and their key parameters are verified against the results of Phase-I of shake table specimen tests for a seven-storey full-scale

RC shear wall structure. The test structure was subjected to base excitations representing four earthquake records of increasing intensities. The uniaxial shake table tests were performed at the University of California, San Diego (Panagiotou et al., 2007a, Panagiotou et al., 2007b). In the established MLNMVS, three analytical models are developed using two different software (ZEUS-NL and PERFORM-3D). The results obtained from the analytical models are compared with the experimental results both on the global and local response levels (top displacement, inter-storey drift, storey shear force, storey bending moment, period elongation and rebar tensile strain). The study reveals the superior performance of 4-noded fibre-based wall/shell element modelling approach in accounting for the 3D effects of deformation compatibility between lateral and gravity-force-resisting systems. The study also highlights the sensitivity of attained results to the stiffnesses assigned to the rigid links and 3D joints required to connect the shear walls to neighbouring elements when a 2-noded element is used.

3.1 Introduction

With increasing concern for the seismic performance of RC buildings following extensive damage caused by recent strong earthquakes (e.g. Kobe 1995; Kocaeli, 1999; Chi-Chi, 1999; and Tohoku, 2011), the use of RC shear walls in medium- to high-rise buildings is favoured in earthquake-prone regions. Shear walls can be found either as single elements coupled with moment-resisting frames, or in the shape of L, T, U, or tubular cross-sections. Based on modern seismic codes, earthquake-resistant buildings are designed and detailed to respond inelastically under the DBE and MCE. In RC high-rise buildings, well designed and proportioned RC slender shear walls can provide the required strength, stiffness and deformation ductility to ensure the adequate performance of the structure in the “service”, “ultimate”, and “collapse prevention” limit states. Nonetheless, RC shear walls are often modelled as linear elements during the analysis for simplicity despite their considerably large depth (PEER, 2010, PEER/ATC, 2010). This can lead to a considerable underestimation of the deformed shape and compatibility issues between shear and flexural lateral resisting mechanisms, as well as, of local high deformation demand issues. Furthermore, due to high costs and lack of availability of large scale testing facilities, there are few reliable and comprehensive studies on the cyclic behaviour of RC wall buildings that could have been used for verification purposes (Ji et al., 2007a, Wallace, 2007, Beyer et al., 2008, Wallace and Moehle, 2012). Hence, there is still a need for a verified nonlinear

modelling approach which is essential in assessing the seismic vulnerability of wall structures (e.g. Ji et al., 2007a, Martinelli and Filippou, 2009, PEER/ATC, 2010, Sadraddin et al., 2016, Nazari and Saatcioglu, 2017).

NRHA is the most reliable tool currently available for predicting the building response at different levels of ground motion intensity. In NRHA, the accuracy of the nonlinear model is measured by its sufficiency in capturing significant modes of deformation and deterioration in the analysed structure from the onset of damage all the way to collapse. Various aspects of nonlinear modelling, such as element discretisation, material force-deformation relationships, and assumptions on modelling of viscous damping are essential in defining the level of accuracy a model can have in predicting the seismic global and local response of the structure. Very sophisticated wall micro-level models (i.e. continuum FE models) have the ability to provide a refined and detailed definition of the local response with a high level of flexibility and accuracy. However, the time requirement for computer runs, post-processing and interpretation of the analytical results render these models forbiddingly expensive for the seismic vulnerability assessment of high-rise structures especially when MRIDA techniques are adopted. Alternatively, the meso-scale fibre-based element modelling approach is commonly used for RC shear walls (e.g. Wallace, 2007, Wallace, 2012). This approach provides a proper description of wall geometry, detailing of steel reinforcing bars and material behaviour. It accounts for key response features such as (1) relocation (shifting) of the neutral axis along the cross-section of the wall during loading and unloading phases; (ii) interacting with the other components in the structure that connect to the walls (both in- and out-of-plane) such as the gravity frames and the coupling beams; and (iii) considering the impact of variation of axial load on wall flexural strength and stiffness. The experimental data of RC structural wall systems subjected to cyclic loading are limited as most tests conducted are on isolated wall elements. Given that, few in-depth analytical verification attempts have been conducted for such systems. Therefore, there is a pressing need to verify the nonlinear modelling techniques and key parameters to be used with RC wall buildings against full-scale shake-table tested RC wall structures.

The aim of the MLNMVS developed in the present study is to arrive at a verifiable nonlinear modelling approach and key modelling parameters that can be adopted in assessing the seismic performance of RC high-rise wall buildings. This is achieved by simulating the nonlinear dynamic response of a shake table full-scale seven-storey RC

wall building slice. This building was tested under base excitations representing four earthquake records of increasing intensities on the Large high-performance outdoor shake table at the University of California, San Diego (Panagiotou et al., 2007a, Panagiotou et al., 2007b, Panagiotou et al., 2010). To model the shear walls in the tested structure, two fibre-based modelling approaches are investigated: (i) 2-noded beam-column line element (also called wide-column element), where an equivalent column at the wall centroidal axis with wide cross-section is used to model the property of the wall; and (ii) 4-noded wall element, a modelling approach conceptually similar to the Multiple-Vertical-Line-Element model (Wallace, 2007, Wallace, 2010). ZEUS-NL analytical software (Elnashai et al., 2012) is utilised to implement the former modelling approach, while PERFORM-3D (CSI, 2011) is chosen to investigate the latter.

In Section 3.2 of this chapter, key features of the utilised analytical software are presented, including cross-sections, element formulation, material models and numerical strategy. A brief description of the shake table test program and the test structure are given in Sections 3.3. Section 3.4 discusses the four input ground motions used in the tests. The analytical models created in the current study along with the comparison of their results with the experimental data are detailed in Section 3.5. The chapter concludes with a summary of the work, findings, and modelling recommendations (Section 3.6).

3.2 Analytical Tools

There is a wide variety of finite element (FE) structural software available to researchers that are capable of performing fibre element-based nonlinear analysis. Among these packages are DRAIN-3DX (Prakash et al., 1994), OpenSees (Mazzoni et al., 2006, McKenna and Fenves, 2006, McKenna, 2011), ZEUS-NL (Elnashai et al., 2012) and PERFORM-3D (CSI, 2011). Depending on the geometry of the structure, the purpose of the analysis, and the efficiency of the software to perform the required tasks, one tool may be selected over the others. The first three packages are essentially frame element analysis software with mostly comparable elements and capabilities.

In the current study, ZEUS-NL and PERFORM-3D analytical software are utilised in the MLNMVS. The main capabilities of both packages are summarised below:

- Predicting the response of RC, steel and composite structures under static and dynamic loading, taking into account the effects of both material and geometric nonlinearities.

- The applied load can be constant or variable forces, displacements and or accelerations.

- The ability to perform different methods of analysis such as eigenvalue, pushover, and response histories.

- The ability to model different concrete and steel material relations, with the option of including hysteresis loops of strength and stiffness degradation.

- Built-in Library of elements and components that can be used with a wide range of concrete, steel and composite cross-sectional configurations.

A detailed description of the utilised software is beyond the scope of this study. Only the cross-sections, element formulations, material models and numerical strategies that relate to the present work are briefly presented in the succeeding sub-sections. Further information regarding the software is available in the ZEUS-NL user manual (Elnashai et al., 2012) and its counterpart for PERFORM-3D (CSI, 2011).

3.2.1 ZEUS-NL

ZEUS-NL is a fibre-based nonlinear analysis platform developed at Imperial College London, UK and the University of Illinois at Urbana-Champaign, U.S., and has been verified against experimental tests of steel and concrete frame elements and structures in Europe and the U.S. (e.g. Elnashai and Elghazouli, 1993, Elnashai and Izzuddin, 1993a, Elnashai et al., 2012, Izzuddin, 2016). The package is employed in several research projects in Europe, the U.S. and the Middle East (e.g. Elnashai, 2006, Kim and Elnashai, 2008, Ji et al., 2009, Mwafy, 2012a, Mwafy et al., 2015a).

3.2.1.1 Cross-sections

A large number of cross-section configurations is available in ZEUS-NL library. General use sections include solid rectangular; symmetrical hollow-I-T, Asymmetric L-C, and fully/partially-encased composite I. For RC elements, there are specific sections available in the library such as rectangular/circular column section, T-beam section, and

rectangular flexural wall section. Figure 3.1 illustrates some of the above-mentioned cross-sections.

3.2.1.2 Element formulations

ZEUS-NL library contains a set of elements that can be utilised to model the elasto-plastic structural behaviour, the dynamic characteristics of the model, and the boundary conditions. Among the element types used in the current study are cubic elasto-plastic beam-column element, 3D joint element, lumped mass element, and Rayleigh damping element.

For the cubic elasto-plastic element, the classical displacement-based FE formulation is employed (Hellesland and Scordelis, 1981, Mari, 1984). A cubic-shape function is used for calculating transverse displacement v(x). This function is given by Eqn. (3.1), where all the equation symbols are graphically defined in Figure 3.2. The formulation of this element represents the inelastic cyclic response of RC members, accounting for geometrical and material nonlinearities. The axial strain is assumed constant along the element length in this formulation and hence a refined discretisation, typically three or more elements per structural member, is required to achieve a reasonable accuracy in the inelastic modelling. The expected length of the plastic hinge is another factor to be considered when deciding the number of elements in a structural member. This issue is further investigated in the model verification process. Cross-section behaviour is represented using the fibre approach, where element cross-sections are divided into a number of fibres (layers). An appropriate material model is assigned to each fibre where strains and stresses are monitored. The sectional stress-strain state is then obtained through the integration of the nonlinear stress-strain response of the individual fibres. Two controlling (Gauss) sections along each element are used for the numerical integration of the governing equations in the element formulation (Figure 3.3).

$$v(x) = \left(\frac{\theta_1 + \theta_2}{L^2}\right)x^3 - \left(\frac{2\theta_1 + \theta_2}{L}\right)x^2 + \theta_1.x \tag{3.1}$$

In the cubic elasto-plastic element formulation, the cross-section fibres have no ability to deal with shear stress. Hence, the shear deformation is not calculated at the section level and the effect of shear-flexure interaction on the element's ductility is not accounted for. To determine the shear deformation in a member, a displacement-type

shear hinge can be introduced at a certain point in the cubic elasto-plastic element using a 3D joint element with an appropriate force-deformation relationship.

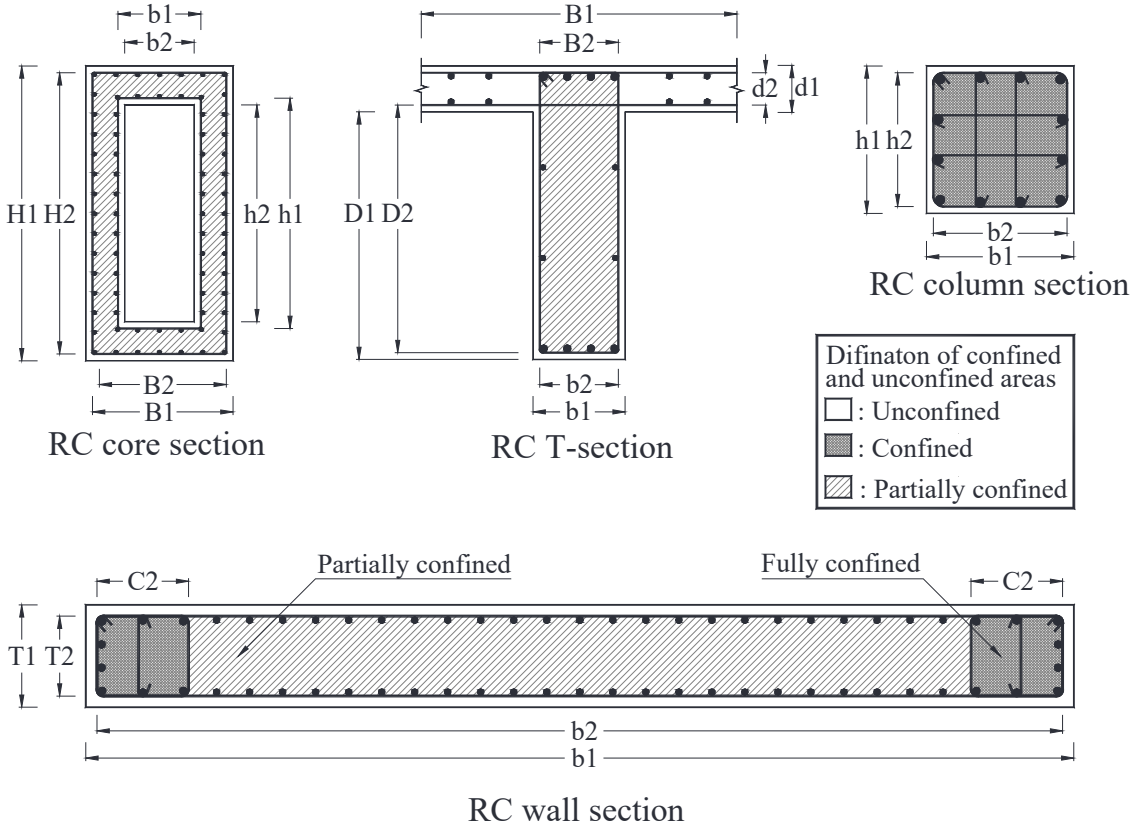

Figure 3.1. Cross-sections from ZEUS-NL library

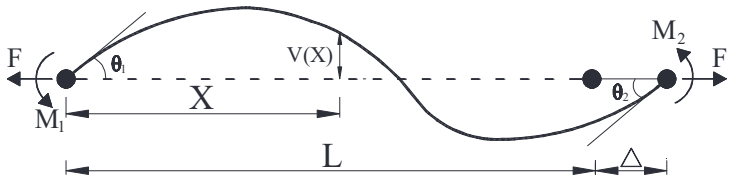

Figure 3.2. ZEUS-NL: Forces and displacements of cubic formulation

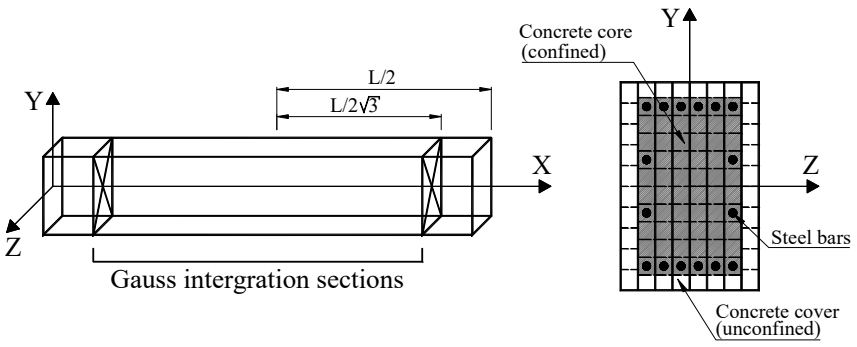

Figure 3.3. ZEUS-NL: Location of the two Gauss sections

The 3D joint element can be used to model pin joints, inclined supports, structural gaps, soil-structure interaction and elasto-plastic joint behaviour. To define a 3D joint element, four nodes are required. Nodes 1 and 2 are the end nodes of the element and must be initially coincident; node 3 defines the x-axis of the joint, while the fourth node defines the x-y plane. Each of nodes 1 and 2 has 6-degrees of freedom with three different types of force-deformation relationships (linear elastic, trilinear symmetric elasto-plastic and trilinear asymmetric elasto-plastic) that can be assigned to each degree of freedom to represent axial, shear and bending cyclic behaviour. Figure 3.4 illustrates the formulation of the 3D joint element, while Figure 3.5 depicts the force-deformation relationships for this element.

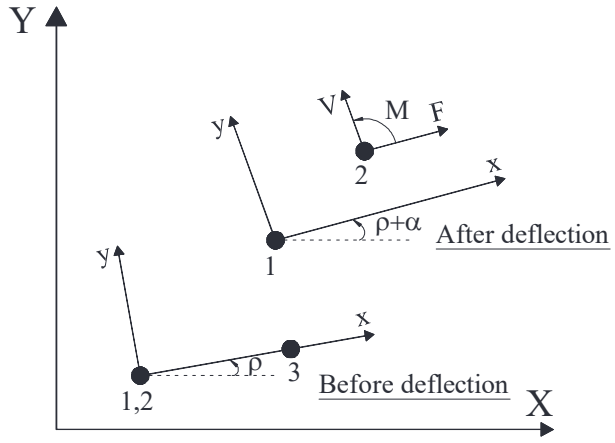

Figure 3.4. ZEUS-NL: Forces and degrees of freedom for the 3D Joint element

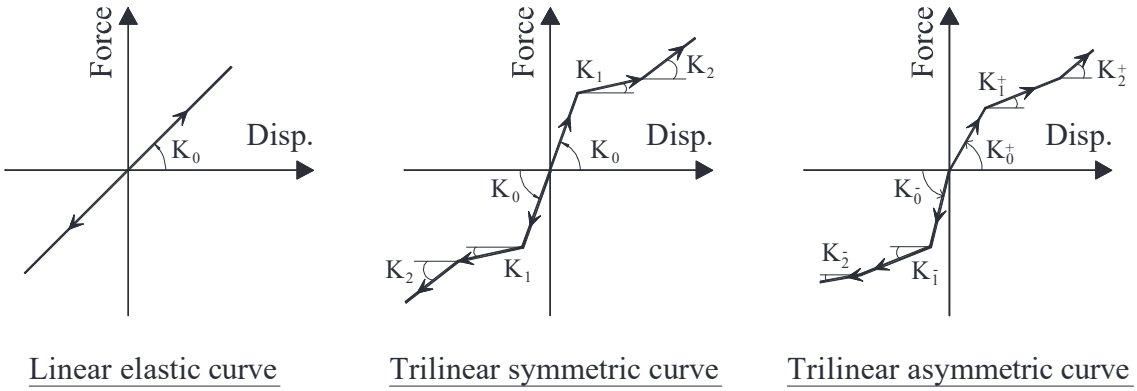

Figure 3.5. ZEUS-NL: Force-Deformation relations for 3D Joint element

Another two elements in ZEUS-NL library which are employed in the current study are the lumped mass element and the Rayleigh damping element. The former is employed to model the inertia masses of the structure, lumped (concentrated) at element end nodes while the latter is utilised in modelling equivalent viscous damping effects in NRHA. Figure 3.6 illustrates the formulation of these two elements.

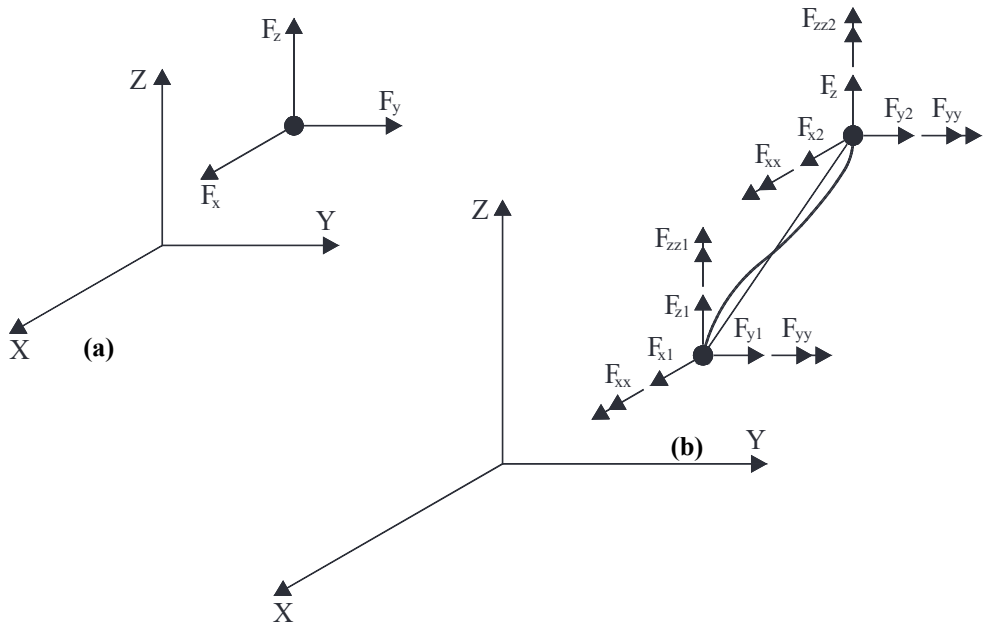

Figure 3.6. ZEUS-NL: Element formulation: (a) lumped mass element; and (b) Rayleigh damping element

3.2.1.3 Material Models

Under the assumption of a Bernoulli beam that plane sections remain plane after deformation, uniaxial stress-strain laws are sufficient for modelling the constituent materials of RC members with fibre-discretized cross-sections. There are several uniaxial concrete models available in ZEUS-NL library. In the present study, the Mander et al. (1988) uniaxial nonlinear constant confinement constitutive model is used along with the improved cyclic rules proposed by Martínez-Rueda and Elnashai (1997). In this model, the confinement pressure provided by the lateral transverse reinforcement is assumed constant throughout the entire stress-strain range. In order to fully describe the concrete mechanical characteristics using this model, four model calibrating parameters need to be defined: (1) ultimate compressive strength of unconfined concrete (f_c); (2) concrete tensile strength (f_t); (3) concrete strain (ε_c) corresponding to the point of unconfined peak compressive stress; and (4) confinement factor (k) which defines the ratio between confined and unconfined compressive stress in the concrete. There are several confinement models available in the literature to compute the confinement factor k (e.g. Park et al., 1982, Scott et al., 1982, Sheikh and Uzumeri, 1982, Mander et al., 1988, Eurocode, 1998, Kappos and Penelis, 2014). For the current work, the Mander et al. confinement model is used (1988) is used. Figure 3.7 shows a typical stress-strain relationship for concrete material responding to cyclic loading. The concrete model employed in the present study follows the backbone curve in the figure in presenting the

response under compressive load histories. When compressive stress is decreased and increased again, the unloading and reloading curves are followed, respectively.

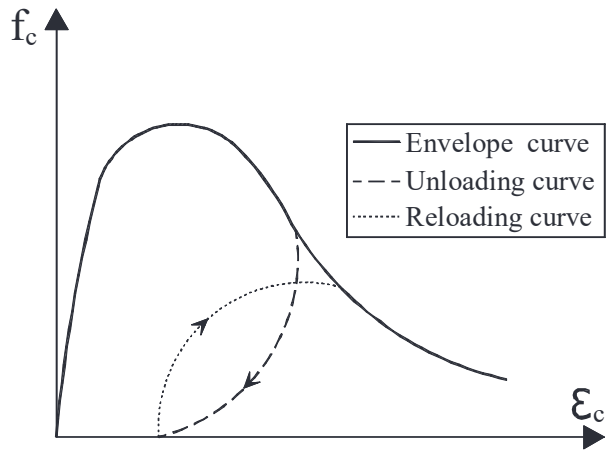

Figure 3.7. Typical stress-strain relation for concrete material under cyclic loading

To model steel material, two uniaxial stress-strain laws are utilised of the four available in ZEUS-NL library: (1) The Menegotto and Pinto uniaxial steel model (1973) coupled with the isotropic hardening rules proposed by (Filippou et al., 1983); and (2) Uniaxial elastic model with symmetric behaviour in tension and compression. The Menegotto-Pinto steel model is a well-known nonlinear relationship in modelling of reinforcing steel in RC structures, particularly those subjected to complex loading histories where significant load reversals might occur. When there is a need to model steel structural members that are expected to remain elastic during the analysis, the elastic model is used. Figure 3.8 shows the stress-strain relationship for the two adopted uniaxial steel models. In Figure 3.8a, E_o is the initial elastic modulus of steel, E_1 is the strain-hardening modulus, R_o is a parameter defining the initial loading curvature, a_1 to a_4 are experimental-based parameters that control the curvature and isotropic strain hardening in subsequent load cycles.

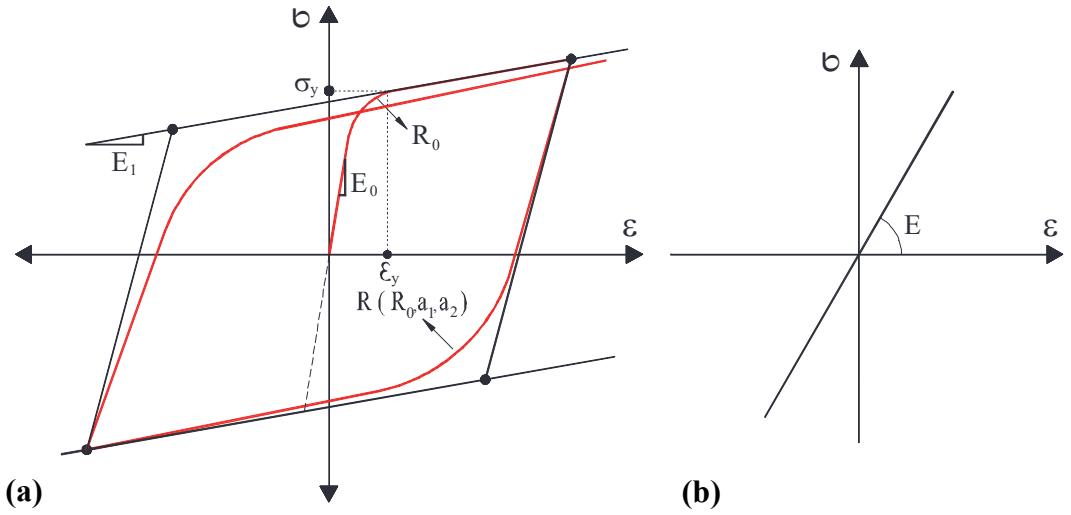

Figure 3.8. ZEUS-NL: Stress-strain laws for steel material: (a) Menegotto-Pinto steel model; and (b) linear elastic steel model

3.2.1.4 Numerical Strategy

In ZEUS-NL package, solving the system of equations of motion in NRHA can be carried out by the means of two different numerical direct integration schemes; (1) the Newmark integration scheme (Newmark, 1959); and (2) the Hilber-Hughes-Taylor integration scheme (Hilber et al., 1977). The solution algorithm allows the employment of either Newton-Raphson or modified Newton-Raphson iterative procedures, where convergence is defined based on either displacement-rotation or force-moment criteria. The efficient Lanczos algorithm (Hughes, 2012) is used by default for the evaluation of structural natural frequencies and mode shapes. However, the Jacobi algorithm with Ritz transformation is also available as another option to the user.

3.2.2 PERFORM-3D

PERFORM-3D (CSI, 2011) is a structural-engineering nonlinear analysis software developed by Dr. Graham H. Powell (Professor Emeritus, University of California at Berkeley) for Computers & Structures, Inc. In recent years, this software has been utilised in many studies and research programs to assess the seismic performance of RC high-rise wall structures and buildings utilising other structural systems (e.g. Ghodsi and Ruiz, 2010, PEER, 2011, Tuna, 2012). The 4-noded fibre-based wall element implemented in PERFORM-3D is conceptually the same as the MVLE model, a model that has previously been validated using experimental results from seismic tests at the component level (e.g. Orakcal and Wallace, 2006, Wallace, 2007, Wallace, 2012).

3.2.2.1 Cross-sections

The cross-sections available in PERFORM-3D library can be divided into two categories: (i) elastic sections to be used with linear analysis such as general, symmetric-I, rectangular and membrane/shell RC and steel sections; and (ii) inelastic (fibre) sections to be assigned to beams, columns and shear walls expected to experience inelastic behaviour. Inelastic fibre section for beams, columns and shear walls can be discretized to a maximum of 12, 60 and 16 fibres, respectively. Beam sections use fibre properties for axial and in-plane bending (with P-M interaction) only and are elastic for out-of-plane bending, while for column sections, fibre properties for bending about both axes are used with biaxial bending and P-M-M interaction. Beam and column fibre sections are both assumed to be elastic in shear. When inelastic shear is to be considered, the shear hinge component is to be added.

The fibres in a shear wall section account for the vertical axial, vertical in-plane bending and their interaction. The section is assumed elastic for the out-of-plane bending as well as for horizontal axial/bending. Shear properties (elastic or inelastic) are not assigned to the cross-section itself, but rather to the shear wall compound component, where uncoupled shear deformation and compressive strain in concrete due to shear can be determined. Figure 3.9 shows the modelling approach of some fibre-based cross-sections in PERFORM-3D.

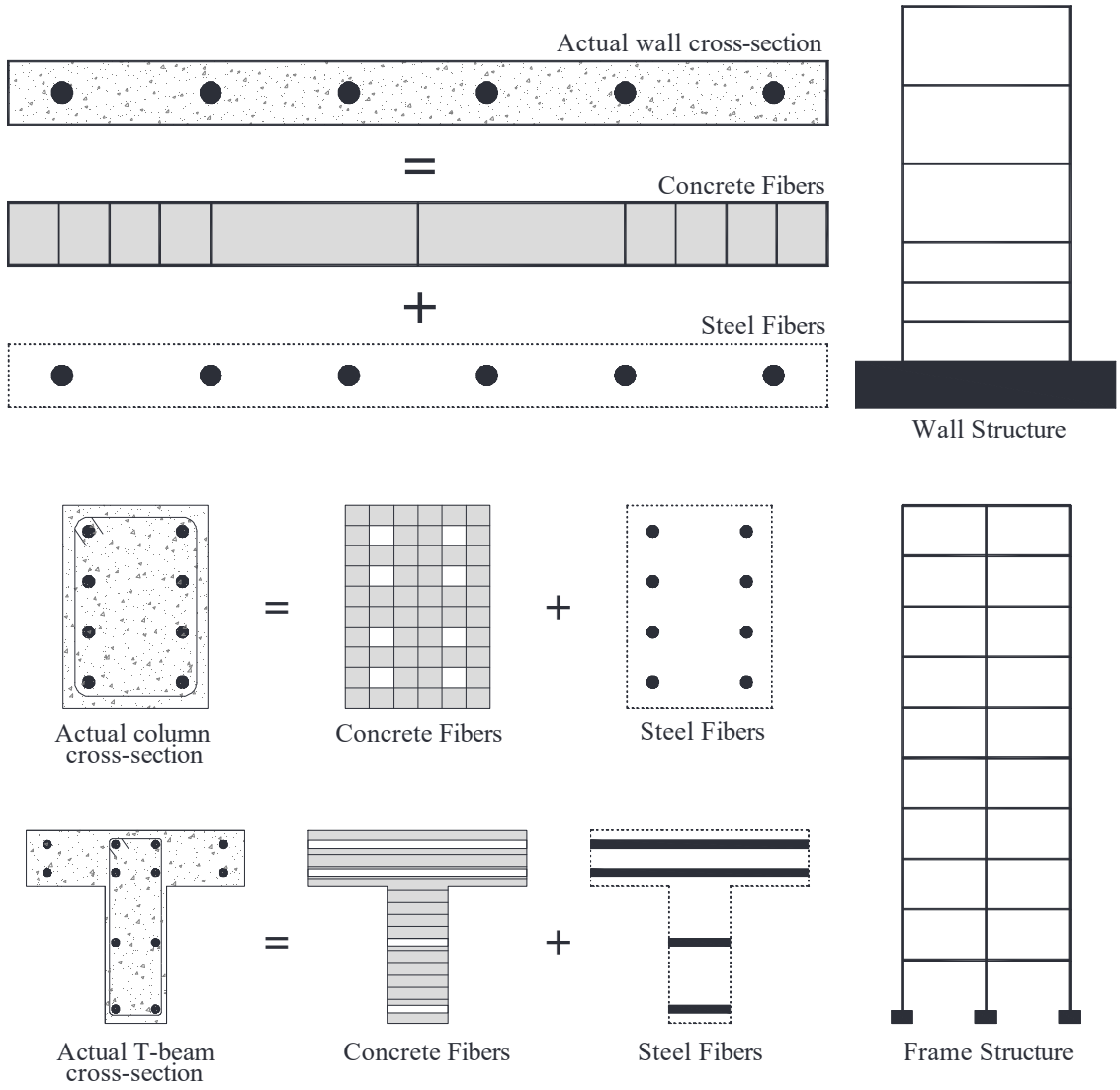

Figure 3.9. PERFORM-3D: Modelling approach of RC cross-sections

3.2.2.2 Element formulations

PERFORM-3D element library includes a wide range of element types. Among the elements utilised in the present work are the frame element, the wall element, the elastic slab/shell element, the bar element and the deformation gauge elements. The frame element is a 2-noded element that can be used in modelling beams, columns and diagonal braces with bending stiffness. It can be either elastic or inelastic. Distributed and/or concentrated gravity loads can be assigned to a frame element along its length. The wall element, on the other hand, can be used to model RC shear walls and cores. The wall element acts essentially as a beam, with bending, axial and shear deformations. It can be either elastic or inelastic for shear and bending.

In modelling, a frame or wall structural member can be discretised into a number of fibre-based elements, each of which is a segment of finite length with a uniform fibre cross-section. PERFORM-3D determines the behaviour of a fibre cross-section by monitoring the stresses in all of its fibres. However, this is done at only one section located at the midpoint of the element length. In other words, PERFORM-3D has one controlling section only in each fibre element compared to two in ZEUS-NL. Consequently, fibre elements should be fairly short, especially in members where bending moments (and hence stresses) varies rapidly over the member length.

The slab/shell element is a 4-noded elastic element with membrane and plate bending stiffnesses. It can be used to model deformable floor slabs (diaphragms) and curved shells. The 2-noded bar element, although considered as the simplest element in PERFORM-3D library, can be utilised in a variety of applications including elastic truss members, elastic braces in braced frames, buckling or yielding truss bars, yielding supports, supports that allow uplift in tension, and strut-and-tie formation. Initial strains can be specified in bar elements which make them also useful for modelling pre-stressed members.

Finally, the deformation gauge elements are provided by PERFORM-3D to calculate axial strain (tension/compression) and shear strain/rotation in all inelastic elements. Deformation gauges can be linked to a single element to calculate actual strains or to a number of elements when the average strain is of concern. Figure 3.10 illustrates possible formulation of a 2-noded strain gauge in shear walls and a 2–noded rotation gauge in frame members. Figure 3.11 shows a 4-noded rotation gauge element that can be used with shear walls, while Figure 3.12 presents a 4-noded shear strain gauge.

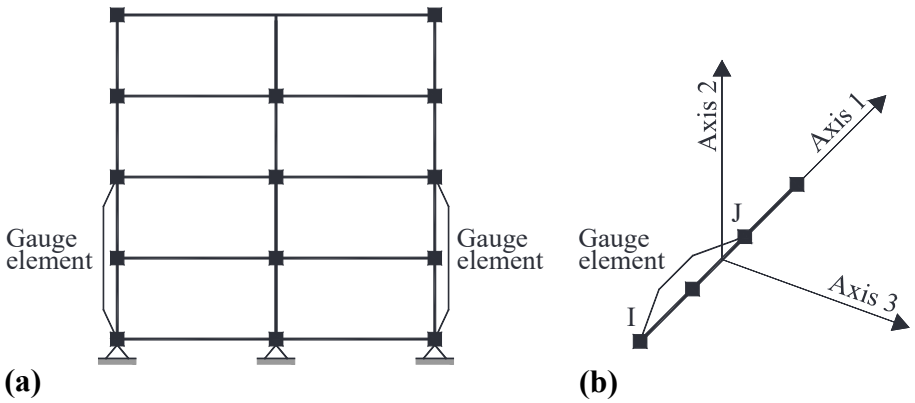

Figure 3.10. PERFORM-3D: Deformation gauge elements: (a) strain gauge over two wall elements; and (b) rotation gauge over two beam elements

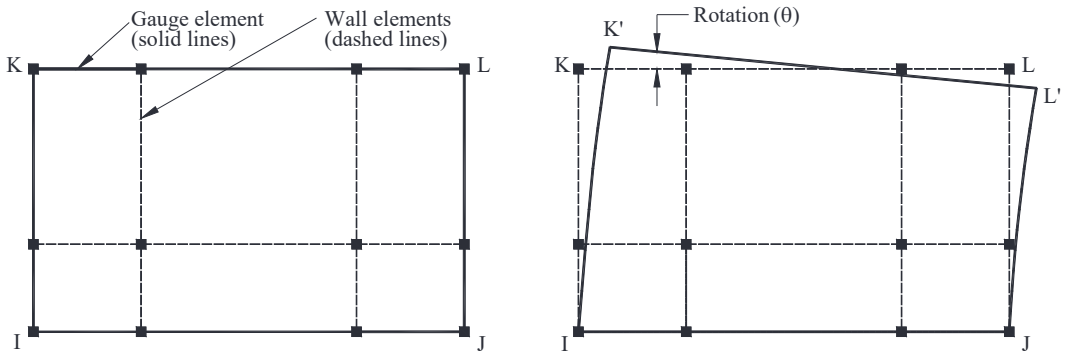

Figure 3.11. PERFORM-3D: 4-noded rotation gauge element

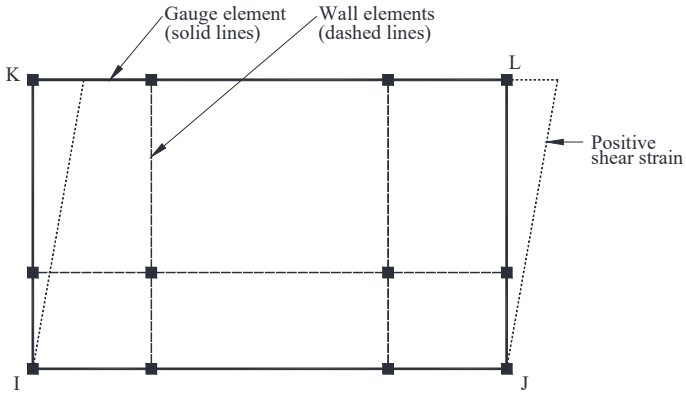

Figure 3.12. PERFORM-3D: 4-noded shear strain gauge element

3.2.2.3 Material Models

In PERFORM-3D, the relations that describe actions (force, moment, stress, etc.) and corresponding deformations (deflection, rotation, strain, etc.) in any material (steel or concrete) are called Force-Deformation (F-D) relation. Linear and nonlinear F-D relations are used to model elastic and inelastic materials, respectively. For inelastic materials, PERFORM-3D offers trilinear and four-linear F-D relations as shown in Figure 3.13. Cyclic degradation and strength loss are optional and can be defined when required. In Figure 3.13, Y is the first yield point, U is the ultimate strength point, L is the ductile limit point where significant strength loss begins, R is the residual strength point and X is a point to specify a deformation value at which the analysis is to be stopped. F-D relation can be unsymmetrical, where positive and negative deformations are different.

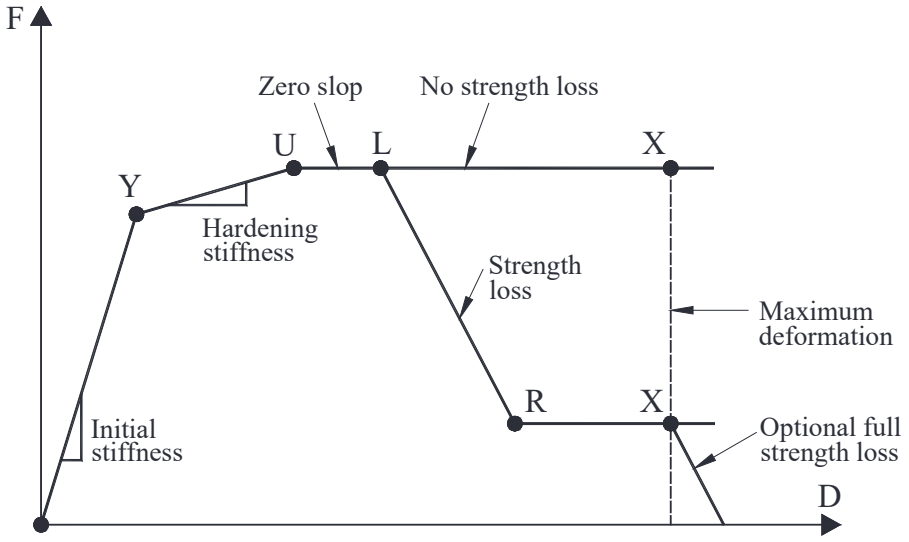

Figure 3.13. PERFORM-3D: Trilinear and four linear F-D relations

3.2.2.4 Numerical Strategy

In PERFORM-3D, NRHA is performed with step-by-step integration in the time domain using the Newmark method (Newmark, 1959) and modified Newton-Raphson iterative procedure. PERFORM-3D uses an event-to-event solution strategy, where the structure stiffness matrix is re-formed each time there is a nonlinear event (a change in stiffness). The program automatically divides each time step that is initially specified by the user into a number of sub-steps with a new sub-step for each nonlinear event. In the eigenvalue analysis, Lanczos algorithm (Hughes, 2012) is implemented.

3.3 Description of the test structure

The test program was performed on the large high-performance outdoor shake table at the University of California, San Diego as part of the George E. Brown Jr. network for earthquake engineering simulation program. The tests were conducted in two phases: Phase I: Rectangular Wall (Panagiotou et al., 2007a); and Phase II: T-Wall (Panagiotou et al., 2007b, Panagiotou et al., 2010). In the current work, test results from Phase I (inter-storey drifts, storey displacements, storey shears, storey moments, period elongation and local strains) are used to verify the analytical results obtained from the MLNMVS.

The test structure consisted of a slice of a 7-storey prototype residential load bearing wall building located in Los Angeles, California. Figure 3.14 shows the floor plans of the prototype building with a perspective view of the test structure.

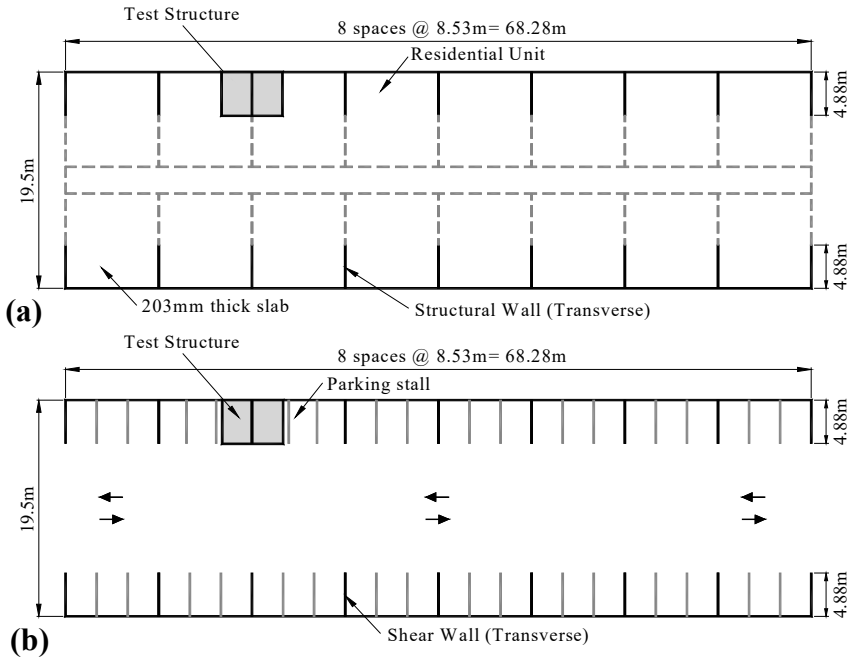

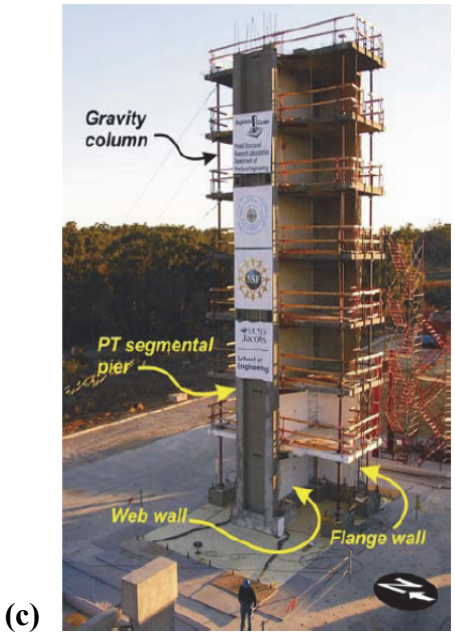

Figure 3.14. Prototype building and test structure used in modelling verification: (a) Residential floor plan; (b) Parking floor plan; and (c) Perspective view of the test structure (Panagiotou et al., 2007a)

In Phase I of the test, resistance to lateral forces was provided by a 3.66m long load-bearing RC rectangular wall, hereafter referred to as "web wall". The web wall was directed East-West (loading direction) and provided support to seven 200mm thick RC slabs spaced at 2.74m. Two transverse walls were built to provide lateral and torsional stability; the East RC wall, hereafter referred to as "flange wall" and the West precast, prestressed segmental wall. The test structure height, starting from the top of the foundation, was 19.20m with total mass (excluding the foundation) of around 210tons.

Web and flange walls were linked with a 610mm wide slab. The link slab had two, 140mm deep by 51mm wide, slots on both ends. These pin-pin connections had the capability of transferring in-plane diaphragm shear, moment, and axial forces but had a reduced capacity to transfer out-of-plane actions during phase I of the test. The North and South ends of the RC floor slabs were supported on four pin-ends gravity columns designed and detailed to carry axial tension and compression only. Concrete with a target 27.6MPa specified compressive strength and Grade-60 steel reinforcement were used in the test structure. The measured average concrete compressive strength at the day of the final test was 37.9MPa, while the average measured reinforcing steel yield strength was 455MPa. The footings under the web and flange walls were longitudinally prestressed and designed to remain elastic during testing. The geometry of the test structure and the reinforcement details for the web wall, flange wall, and slabs are given in Figure 3.15 and Figure 3.16, respectively. More details about the test structure can be found in Panagiotou et al. (2007a, 2010).

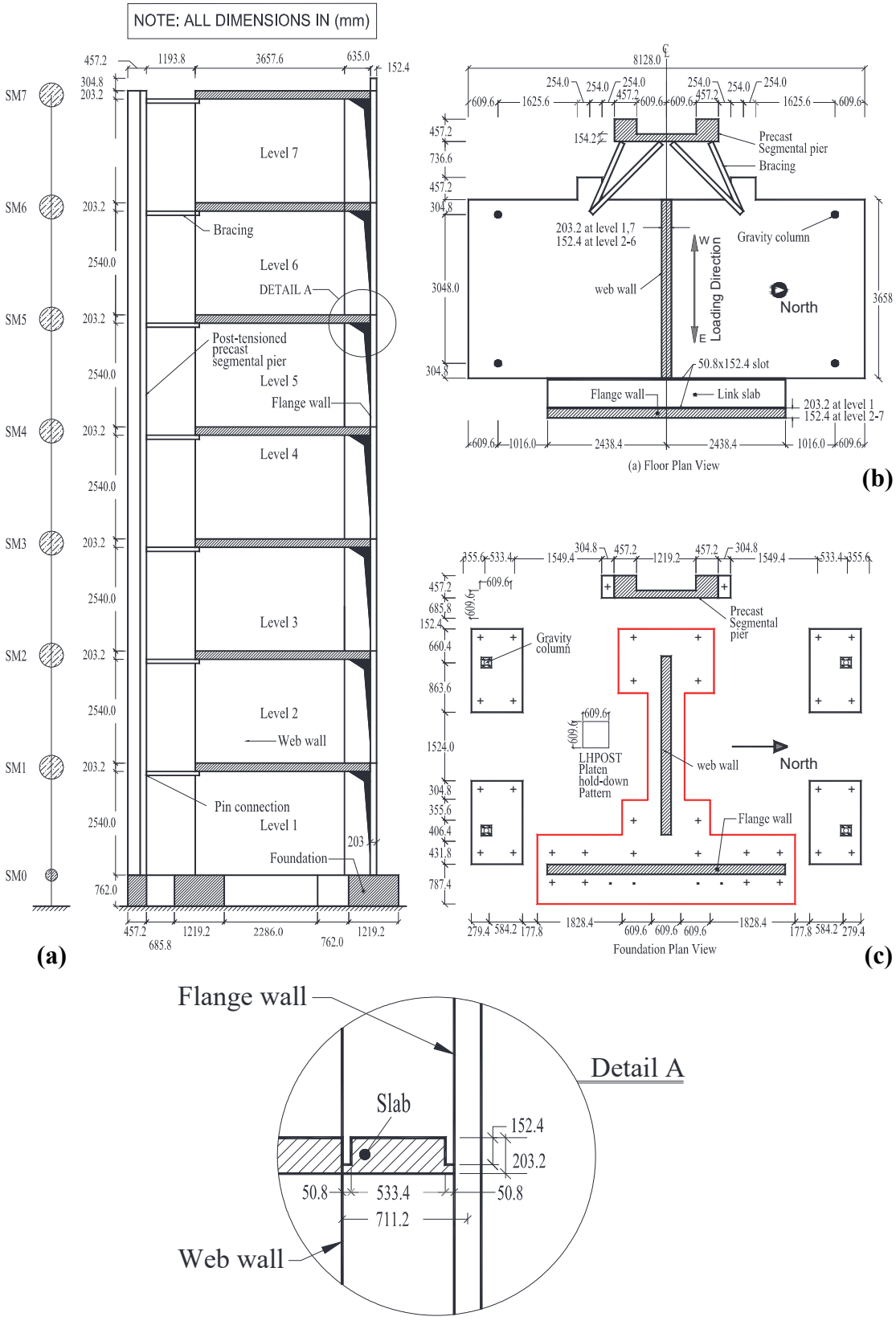

Figure 3.15. Test structure used in modelling verification: (a) Elevation; (b) Floor plan view; and (c) Foundation plan view

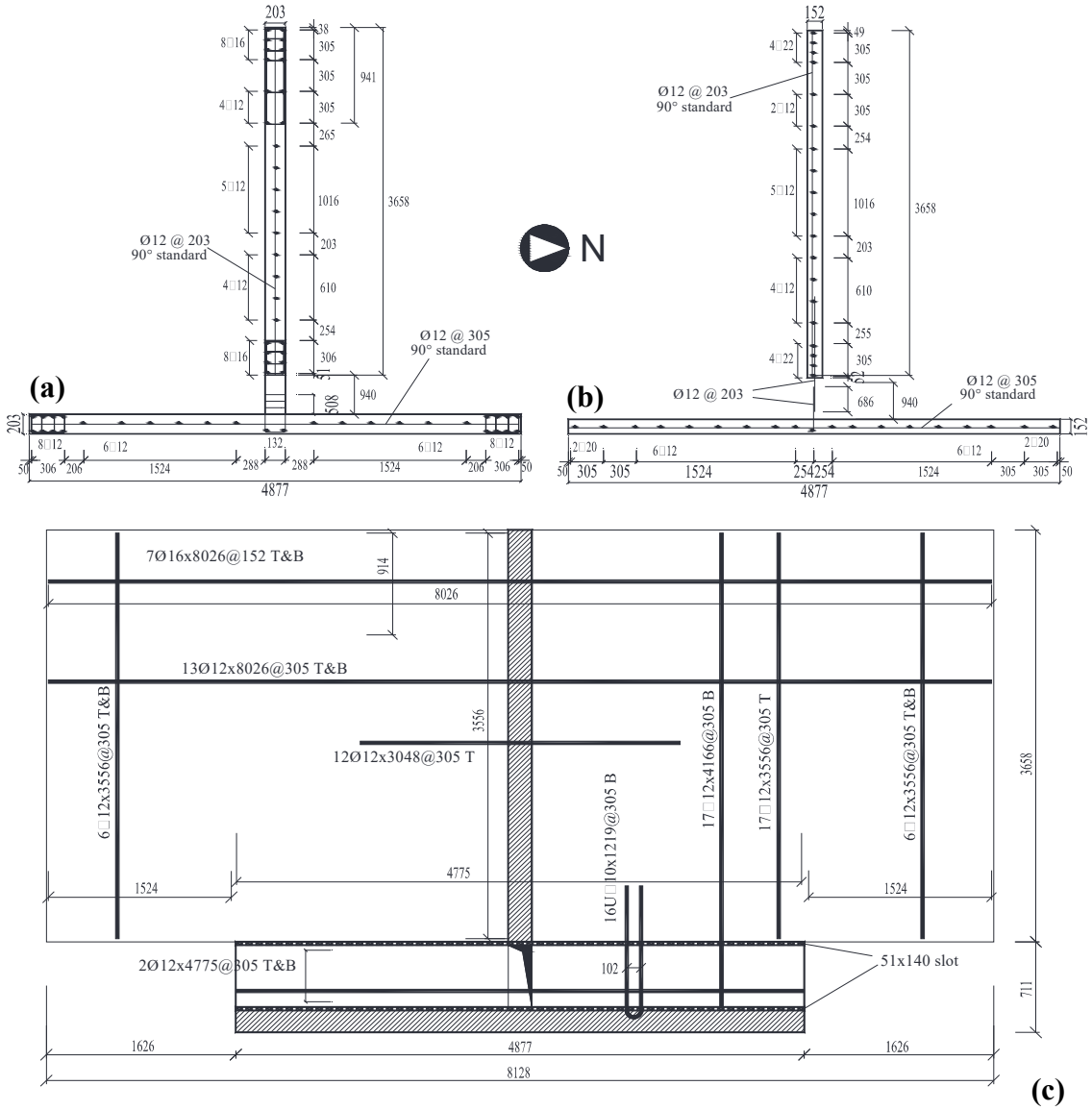

Figure 3.16. Reinforcement details for the test structure: (a) web and flange walls at first level; and (b) web and flange walls at levels 2-6; and (c) floor and link slabs at all levels

3.4 Input ground motions

Phase I of the test program investigated the response of the cantilever web wall to four levels of excitation with increasing intensities (EQ1-EQ4), representing four historical earthquakes recorded in Southern California. Prior to and between the earthquake tests, the structure was subjected to long-duration ambient vibration tests and long-duration low-amplitude white noise tests for system damage identification (Moaveni et al., 2010). The low-intensity input motion EQ1 was the VNUY longitudinal component from the 1971 M_w 6.6 San Fernando earthquake. The two medium intensity input motions EQ2 and EQ3 were the VNUY transverse component record from the 1971 M_w 6.6 San Fernando earthquake and the WHOX longitudinal component from the 1994 M_w 6.7 Northridge earthquake, respectively. The large intensity input motion EQ4 was

the Sylmar Olive View Med 360^{o} component record from the 1994 M_w 6.7 Northridge earthquake. Figure 3.17 shows the acceleration time-histories alongside the acceleration and displacement response spectra of the four input motions while Table 3.1 lists the peak recorded values of selected response parameters for the test structure (Panagiotou et al., 2010).

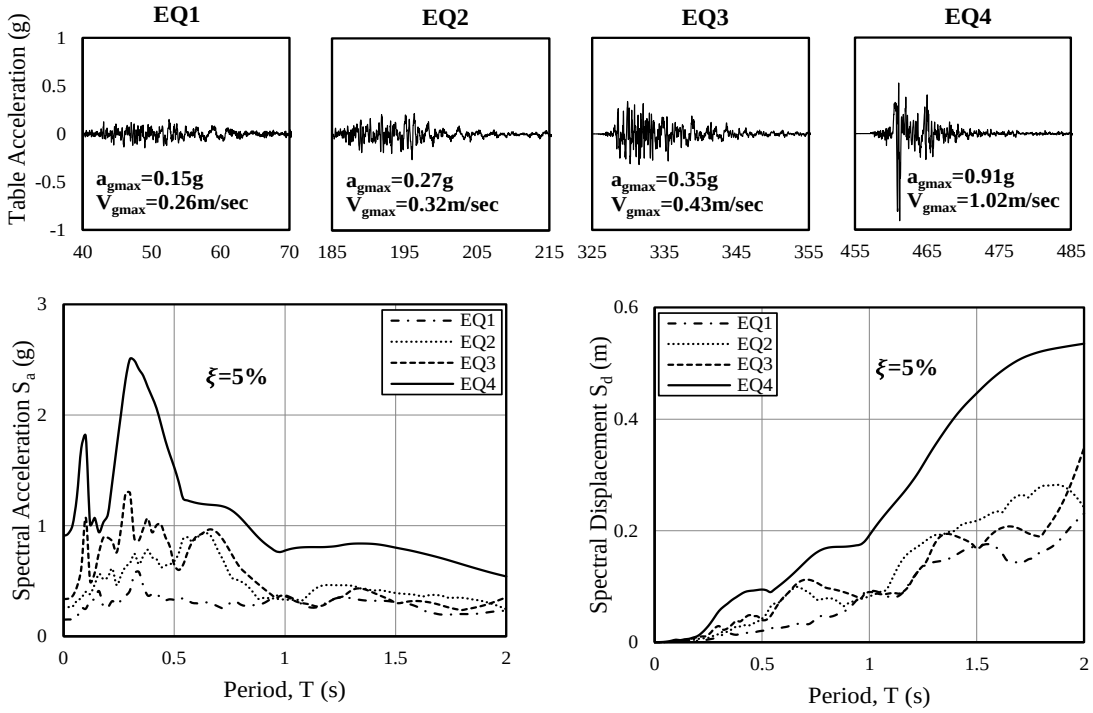

Figure 3.17. Most intense 30s-time histories and response spectra of recorded table ground motions for the test structure used in modelling verification

Table 3.1. Peak recorded values of selected response parameters for the test structure (Panagiotou et al., 2010)

Response Parameter	Before EQ1	After EQ1	After EQ2	After EQ3	After EQ4
Fundamental period (s)	0.51	0.65	0.82	0.88	1.16
Roof relative lateral displacement (m)	-	0.05	0.14	0.16	0.38
Roof drift ratio (%)	-	0.28	0.75	0.83	2.06
Inter-storey drift ratio[A]	-	0.35	0.89	1.03	2.36
Peak table acceleration (g)	-	0.15	0.27	0.35	0.91
System base shear (kN)[B]	-	425	628	704	1185
System base moment (kNm)[B]	-	5606	8093	8490	11839

[A] *Over all storeys*

[B] *Calculated as the product of storey mass with measured horizontal floor acceleration*

3.5 Analytical models and results

Three analytical models are developed for this study. ZEUS-NL (Elnashai et al., 2012) is utilised to develop the first two: "Z-Model" and "IZ-Model"; while PERFORM-3D (CSI, 2011) is used to develop the third: "P-Model". Brief descriptions of the features of each model and the comparison between the predicted and measured results are given in the following sections. Figure 3.18 shows schematic diagrams of the three models.

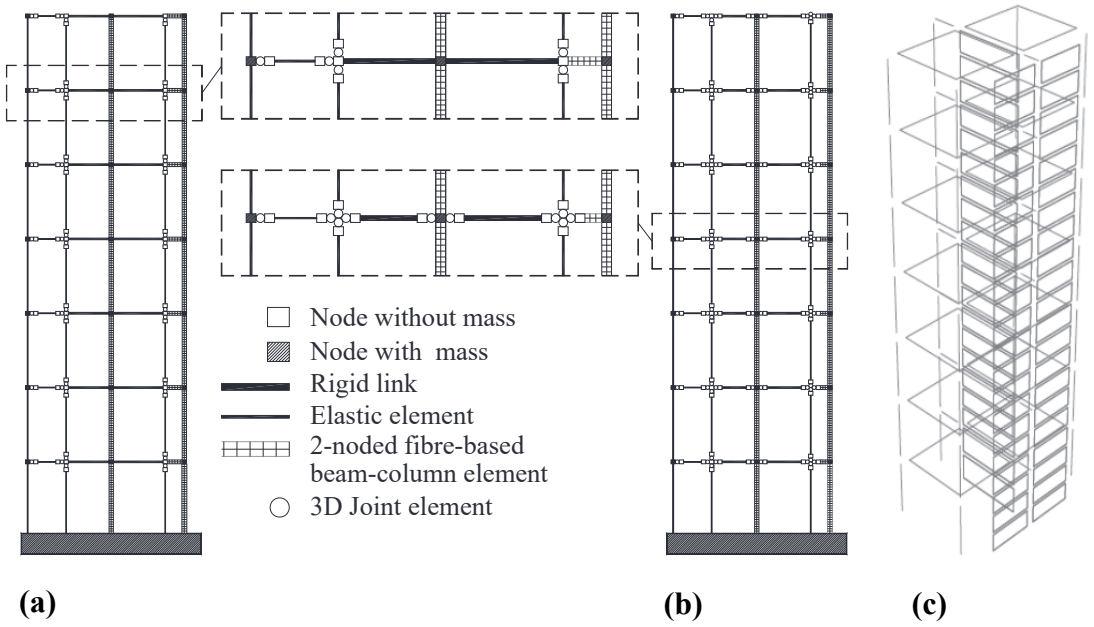

Figure 3.18. Schematic diagrams of developed models for the test structure used in modelling verification: (a) Z-Model; (b) IZ-Model; and (c) P-Model

3.5.1 Analytical model "Z-Model"

The 2D (in the plane of excitations) model for the test structure is developed using ZEUS-NL (Figure 3.18a). The centreline model included the web wall, the flange wall, the gravity columns, the prestressed segmental pier, the link slab, and the braces connecting the segmental pier to the structure. The 2-noded fibre-based cubic elasto-plastic element is used to model the response of the web and the flange walls as well as the slotted slab connecting them. The elastic frame element is used to model the prestressed segmental pier, the gravity columns, and the braces. Rigid links are utilised to connect the web wall centreline to the gravity column elements at both ends of the wall. The 3D joint element, characterised by linear elastic behaviour is used to simulate the pin-pin connection of the gravity columns, the braces and the East-West hinge connection between the segmental prestressed pier and its footing. The seismic mass of

the test structure is lumped at floor levels to simplify the analytical model. The weight of the structure is also applied as nodal loads to account for the gravity and the P-Δ effects during NRHA.

The uniaxial nonlinear constant confinement constitutive model of Mander et al. (1988) with improved cyclic rules proposed by Martínez-Rueda and Elnashai (1997) is used to calculate the properties of the confined concrete and assigned to the corresponding fibres in the web and the flange walls' cross-section at the first storey (Figure 3.7). The concrete in the upper storeys had no confinement reinforcement and thus modelled using unconfined concrete fibres. In both cases, the tensile strength of concrete is neglected. The F-D behaviour of the steel reinforcing bars in the test structure is idealised using the uniaxial steel model of Menegotto and Pinto (1973) coupled with the isotropic hardening rules proposed by Filippou et al. (1983), as shown in Figure 3.8a. In this figure, E_o is the initial elastic modulus of steel, E_1 is the strain-hardening modulus, R_o is a parameter defining the initial loading curvature, and a_1 to a_4 are experimental-based parameters that control the curvature and isotropic strain hardening in the subsequent load cycles, taken as 20, 18.5, 0.15, 0.01 and 7, respectively (Elnashai et al., 2012). Previous studies indicated that shear deformation may have a significant contribution to the lateral displacement of walls especially at lower storeys, even in walls that are categorised as flexure-dominated (e.g. Thomsen and Wallace, 1995). In ZEUS-NL, the fibres in the cubic elasto-plastic element used to model the web wall have zero resistance to transverse forces, and hence shear deformation cannot be determined at the section level. It can be, however, explicitly modelled by introducing shear springs to the wall element. Justified by the fact that the experimental results for the test structure evidenced almost exclusively flexural cracking at the web wall base (Panagiotou et al., 2007a, Martinelli and Filippou, 2009), shear deformation is not considered in this analytical model.

ZEUS-NL includes Rayleigh damping as the only option to account for the effects of the viscous damping during dynamic analysis. The mathematical model of Rayleigh damping in this package is based on the initial stiffness in calculating the damping matrix. When the use of tangent stiffness-proportional damping is not an available option, previous studies recommended lowering the first mode initial stiffness-proportional damping value (e.g. Hall, 2006, Smyrou et al., 2011). The use of the mass-proportional damping term in the damping matrix is discouraged by several researchers.

For an instant, Priestley and Grant (2005) showed that including the mass-proportional term in the damping equation can heavily weight the mass matrix, leading to a nearly constant damping matrix during the post-elastic response of the structure regardless of stiffness degradation. Hall (2006) suggested that the presence of mass-proportional damping will generate extraneous damping forces due to the rigid body motion component involved in the formulation of earthquake analysis that is based on total motion. It is worth noting that rigid body motion phenomena become more significant in the analysis of tall buildings. For the test structure, previous studies have adopted different approaches and values to model viscous damping. For instance, Panagiotou and Restrepo (2006) used a damping ratio of 0.3% for the first longitudinal mode to accurately simulate the response to earthquake input motions; Martinelli and Filippou (2009) used Rayleigh damping with mass and initial stiffness-proportional damping matrix and a 1.0% damping ratio for the first two flexural modes; while Waugh and Sritharan (2010) used tangent stiffness-proportional viscous damping corresponded to 0.5% and 0.8% damping ratios for the first and third uncracked mode periods, respectively. The use of such a low damping ratio in modelling the test structure can be attributed, in addition to the discussion included in Section 2.2.3.3, to the absence of non-structural elements and also to the fact that flexural cracking was largely limited to the lower part of the structure as a consequence of the low ratio of the longitudinal reinforcements led to by the design approach of the building (i.e. displacement-based design). Based on the above, an initial stiffness-proportional viscous damping corresponding to 0.5% damping ratio in the first longitudinal mode is used in the Z-Model, while the mass-proportional damping term is set to zero.

The input motions shown in Figure 3.17 are applied to the base of the Z-Model in the East-West direction parallel to the web wall. Using the Newmark integration scheme, NRHA is conducted at a time step of 1/60s. The four input motions, EQ1 to EQ4, are concatenated to account for the accumulated structural damage on the response of the test structure. Six seconds of zero-base acceleration is added in between the earthquake records to allow the structure to come to rest prior to being subjected to the next record. The applied concatenated base motion record is 523s long in total.

The capability of the Z-Model in predicting the global response of the test structure during the most intense 30s of each of the four earthquake input motions is assessed by comparing the analytical results with measured data for top-floor relative displacement

time histories (Figure 3.19), response envelopes of storey displacement, inter-storey drift (ISD), storey shear force and storey overturning moment (Figure 3.20). Figure 3.19 shows that the model well captures all the significant peak relative displacements recorded during EQ1, EQ2 and EQ4. The relatively poor prediction of the last part of the peak displacement histories in Figure 3.19 can be attributed to the assumptions made in the modelling of viscous damping. The peak displacements on EQ3 are underpredicted by as much as 25%, the discrepancies in the computed response under EQ3 have also been recorded in other studies (e.g. Kelly, 2007, Waugh and Sritharan, 2010). This is mainly attributed to the similarity in the earthquake intensity between EQ2 and EQ3 input motions. As a consequence of these two records having comparable intensities, the unloading and reloading paths of the material models rather than their envelopes have a big influence on the analytical response under EQ3. Accurate representation of the unloading and reloading behaviour of material models becomes more important when the structure does not move into virgin territory, as during aftershocks for example. Figure 3.20a shows very good agreement between predicted and measured displacement envelopes at floor-levels (storey displacement). As expected, the displacements under EQ3 are under predicted. The maximum calculated roof drift ratios are found to be 0.30% under EQ1, 0.75% under EQ2 and 2.05% under EQ4, compared to their corresponding measured values of 0.28%, 0.75% and 2.06%, respectively. While for the response under EQ3, the obtained and measured maximum roof drifts are 0.78% and 0.83%, respectively. ISD is typically considered as a key parameter in defining performance limit states for seismic vulnerability assessment of buildings and hence it is essential to have this parameter accurately predicted. As shown in Figure 3.20(b), the ISD envelopes are well predicted by the analysis under EQ1, EQ2 and EQ4, while under EQ3 it is within 30% of the experimental values for the same reasons discussed above.

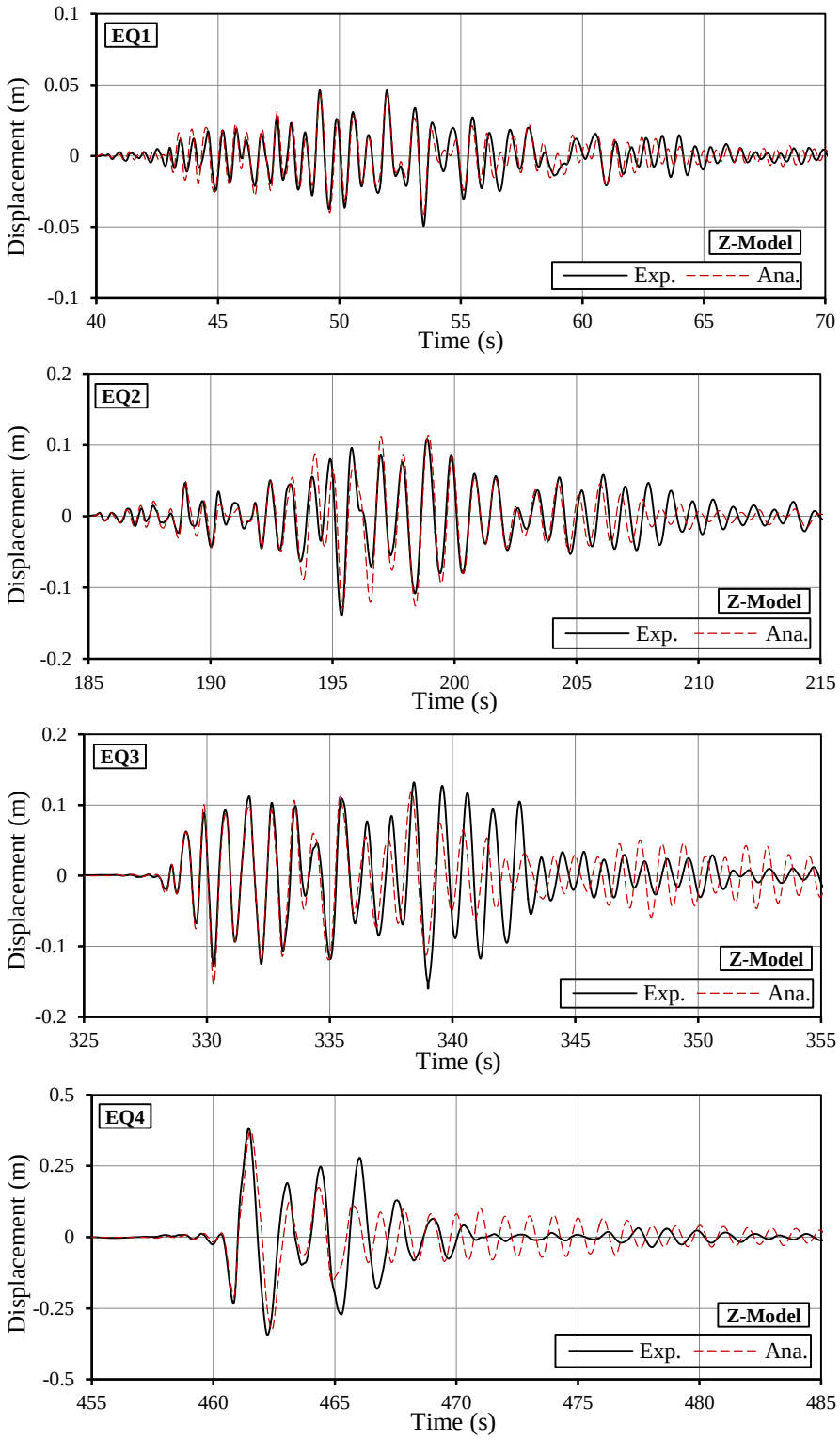

Figure 3.19. Z-Model: measured versus computed top relative displacement under the four Input motions

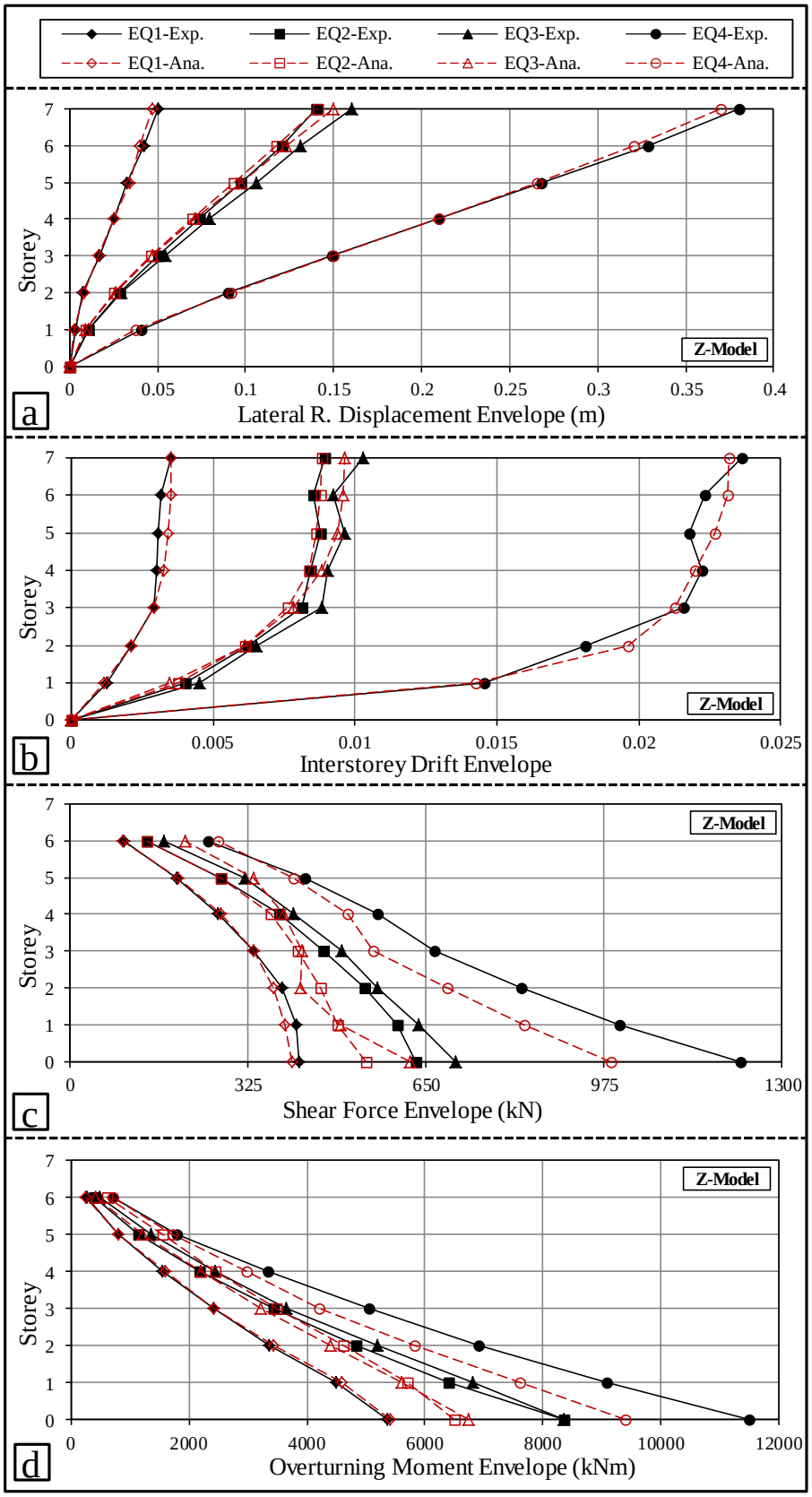

Figure 3.20. Z-Model: measured versus computed envelopes: (a) relative displacement; (b) inter-storey drift; (c) storey shear; and (d) storey overturning moment

Despite the good agreement between predicted and measured response values of top displacement time histories, storey displacement and ISD envelopes discussed above, the Z-Model underestimates the storey shear and consequently storey moment envelopes of the test structure. Especially when the structure behaves inelastically (Figure 3.20c and Figure 3.20d). The discrepancies between the reported and the analytical storey shear and moment values can be attributed to the influence of the 3D interaction between the gravity columns, the floor slabs and the web wall on the overall lateral capacity of the test structure. The significant contribution of this interaction to the lateral force resistance of the test building was confirmed by Panagiotou and Restrepo (2006) using pushover analysis. The main reason for this influence is that, due to their interaction with the floor slab, the gravity columns developed significant axial strains during testing. Consequently, the columns near the tension side of the web wall were experiencing tensile forces and those closer to the compression side were subjected to compression forces. Given the 3.05m span between the columns, the tension and compression forces enabled a large moment to be developed and effectively increased the lateral force resistance of the test structure.

3.5.2 Analytical Model "IZ-Model"

To address the shortcomings of the Z-Model, IZ-Model is developed as an improved 2-noded fibre-based model to introduce the 3D slab-columns-web wall interaction effect. In the IZ-Model, 3D joint elements are introduced at both ends of the rigid link that connects the web wall centreline to the gravity columns at each floor level (Figure 3.18b). A bilinear asymmetric moment-curvature relation is assigned to those elements to simulate the out-of-plane flexural rigidity of the slab. Figure 3.21 shows the storey shear and moment envelopes predicted using the IZ-Model under EQ1 to EQ4, where significant improvement can be seen. This exercise highlights the importance of taking into account the 3D interaction effect of all structural members in the building to accurately predict the seismic response.

To assess the capability of the IZ-Model to capture the damage evolution of the test structure under the four input motions, the frequency spectra of the top relative displacement time-histories using the Fast Fourier Transform (FFT) method and the structure periods of the first two modes are plotted under EQ1 to EQ4 in Figure 3.22. It is worth noting that the measured fundamental frequency of the test structure changed from 1.96Hz before testing to 0.86Hz at the end of EQ4, with corresponding

fundamental periods of 0.51s and 1.16s, respectively. Despite the significant lengthening of the fundamental period of the test structure by more than 127%, the IZ-Model was able to track this damage progression with good accuracy. At the end of EQ4, the observed difference between measured and predicted first mode frequency is 20%. This can be attributed to the high flexural stiffnesses of the rigid links and the 3D joints in the model.

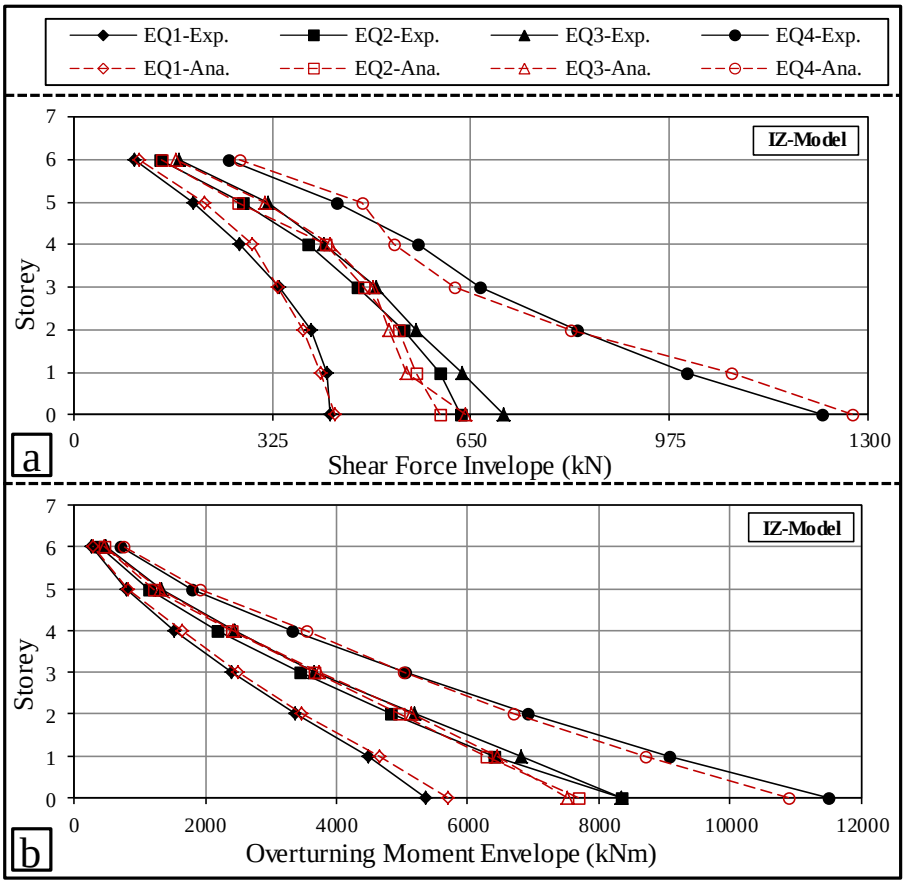

Figure 3.21. IZ-Model: measured versus computed envelopes: (a) storey shear; and (b) storey moment

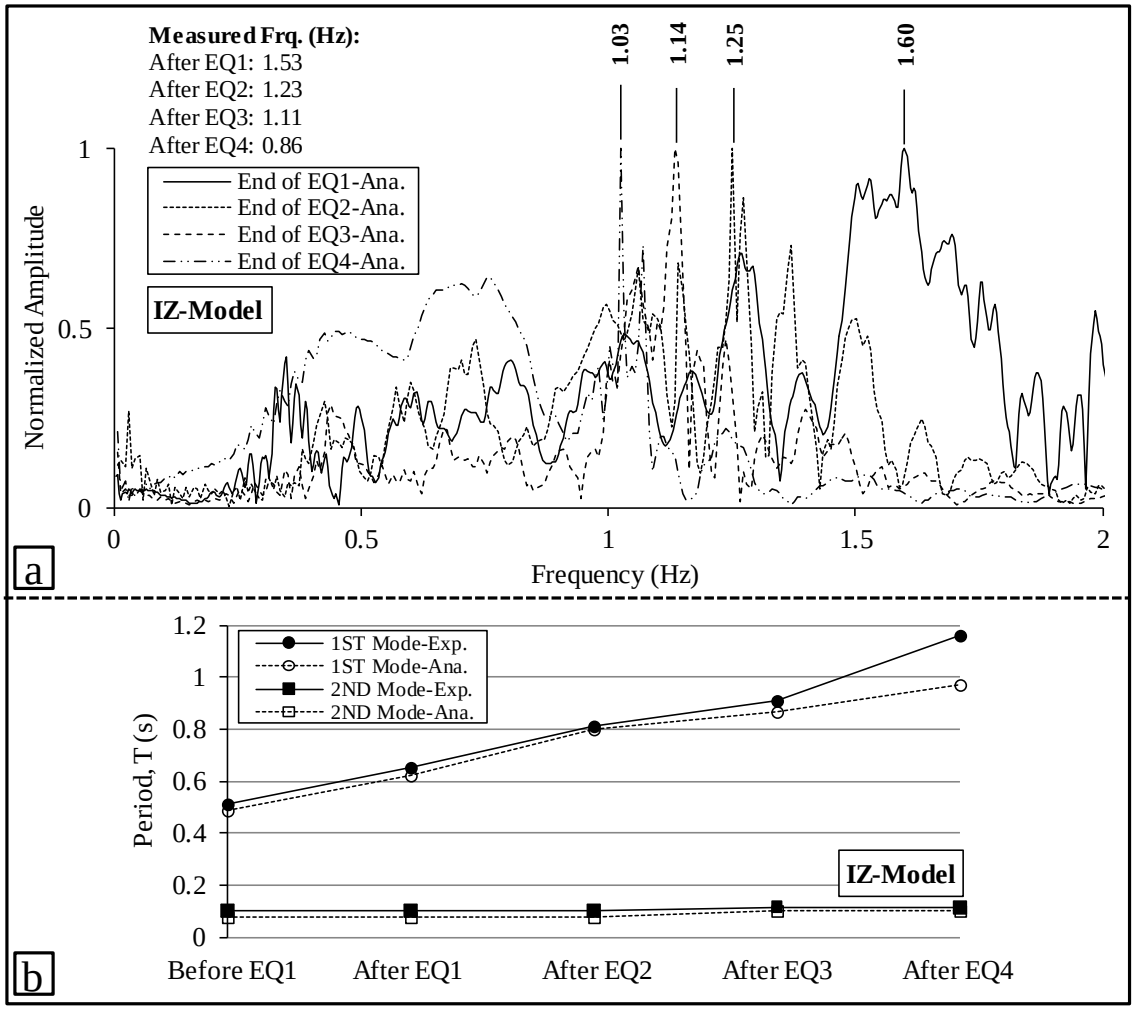

Figure 3.22. IZ-Model: evolution of modal characteristics during the four input motions: (a) frequency spectra; and (b) structure periods

Another measure of the capability of the analytical model is the determination of the local damage. Figure 3.23 depicts the tensile strain envelope of an outer reinforcing bar located in the web wall (marked as ST2 in the tests) over the height of the first level under EQ4 input motion. It should be noted that computed strains can be mesh-sensitive, especially at zones of concentrated plasticity. To investigate the influence of the mesh size on the computed stains, the web wall member in the first level of the building is modelled using four different meshes: One Element-mesh (1E); Two Element-mesh (2E); Three Element-mesh (3E); and Six Element-mesh (6E). The results presented in Figure 3.23 show that the IZ-Model with 2E predicted the tensile strain envelops of ST2 reinforcing bar with good accuracy. It is worth mentioning that the 2E needed an element length of 1321mm, which is close to the expected plastic hinge length at the web wall base (0.5 times the flexural depth of the wall=1830mm) as proposed by ASCE/SEI 41-06 (2007). Hence, mesh size not exceeding the expected

plastic zone length is confirmed as being suitable for fibre-based modelling of RC shear walls.

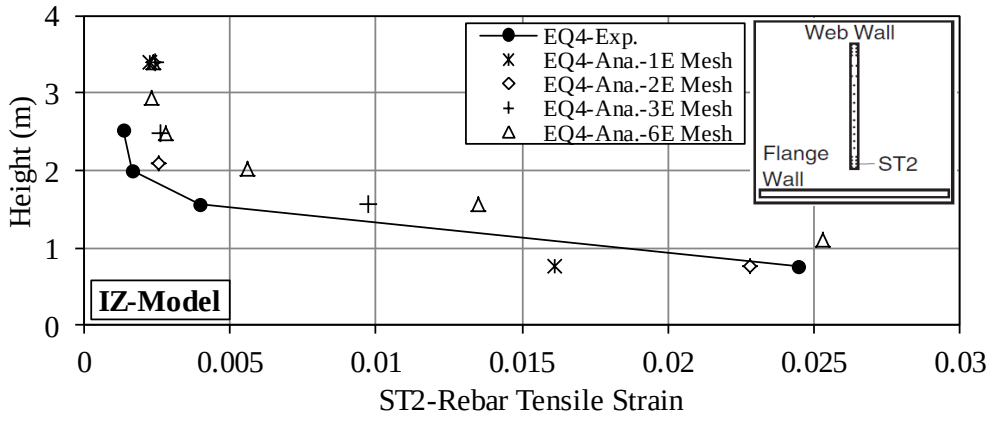

Figure 3.23. IZ-Model: tensile strain of ST2 reinforcing bar over the height of first level under EQ4

3.5.3 Analytical Model "P-Model"

To evaluate the capability of the 4-noded element modelling approach in predicting the response of the test structure, the P-Model is developed using PERFORM-3D (CSI, 2011). To model the web and the flange walls, the 4-noded fibre-based shear wall element is used with nonlinear vertical fibres to represent the behaviour of concrete and reinforcing steel. Based on the outcome of the element mesh sensitivity study conducted on the IZ-Model in Section 3.5.2, the web wall in the first level is represented with two vertical elements "1E Mesh", as shown in Figure 3.18c. The link slab is modelled using the 2-noded fibre-based frame element. An elastic frame element with specified cross-section properties is used to model the prestressed segmental pier, while the elastic bar element is utilised to model the pin-pin end braces and gravity columns. Finally, the elastic 4-noded slab element is used to represent the floor slabs. For the sake of comparison, the same principles used in Z-Model and IZ-Model for modelling the seismic mass of the test structure are followed.

The four-linear segment F-D relation is used to approximate the concrete stress-strain relationship based on the modified Mander model (Figure 3.13). For the reinforcing steel material model, a similar relation is used with the post-yield stiffness and cyclic degradation parameters defined following the adjustments described by Orakcal and Wallace (2006). The linear stress-strain relation is used to model the materials of the prestressed segmental pier, floor slabs, braces and gravity columns. In PERFORM-3D, viscous damping can be modelled using modal damping, a more preferred viscous

damping modelling approach (CSI, 2011). However, for consistency, the same assumptions and procedures used in the ZEUS-NL models for the viscous damping, input motion application, and numerical strategy are adopted in this model.

The shear deformation in the web wall is accounted for in the P-Model by assigning a trilinear relation to the wall element similar to the one recommended by ASCE/SEI 41-06 (2007) and ASCE/SEI 41-16 (ASCE/SEI-41, 2017). to represent the nonlinear shear behaviour of the wall. Test results by Thomsen and Wallace (2004) and the follow-up calibration study by Gogus (2010) are used to define the shear F-D relation. In the used trilinear relation, the uncracked shear modulus is taken as $0.4E_c$ and diagonal (shear) cracking is assumed to start at $0.25\sqrt{fc'} \leq 0.5v_n$, where v_n is the wall nominal shear strength from ACI 318 (2014). The post-cracking slope is reduced to $0.01E_c$ to account for the nonlinear shear deformations due to shear-flexure interaction (Massone, 2006).

Following the same sequence used in the previous section, Figure 3.24 to Figure 3.27 show predicted versus measured top-floor relative displacement time-histories, response envelopes, the evolution of modal characteristics and ST2 steel rebar tensile strain, respectively. Good agreement can be seen for all predicted response except the ones under EQ3, where, for the same reasons discussed earlier, predicted response of the test structure have some discrepancies when compared with measured values.

While the data measured from the shake table test confirmed the accuracy of the investigated modelling approaches and key parameters in predicting global response and local damage induced by the seismic demands on slender wall structures, some limitations became apparent in the 2-noded fibre-based modelling approach (e.g. accounting for 3D compatibility effects). The study reveals the superior ability of the 4-noded fibre-based wall/shell element to account for the 3D effects of deformation compatibility between lateral and gravity-force-resisting systems. The study also addresses the sensitivity of attained results to the stiffnesses assigned to the rigid links and the 3D joints required to connect the shear walls to neighbouring elements when the 2-noded fibre-based element modelling approach is used.

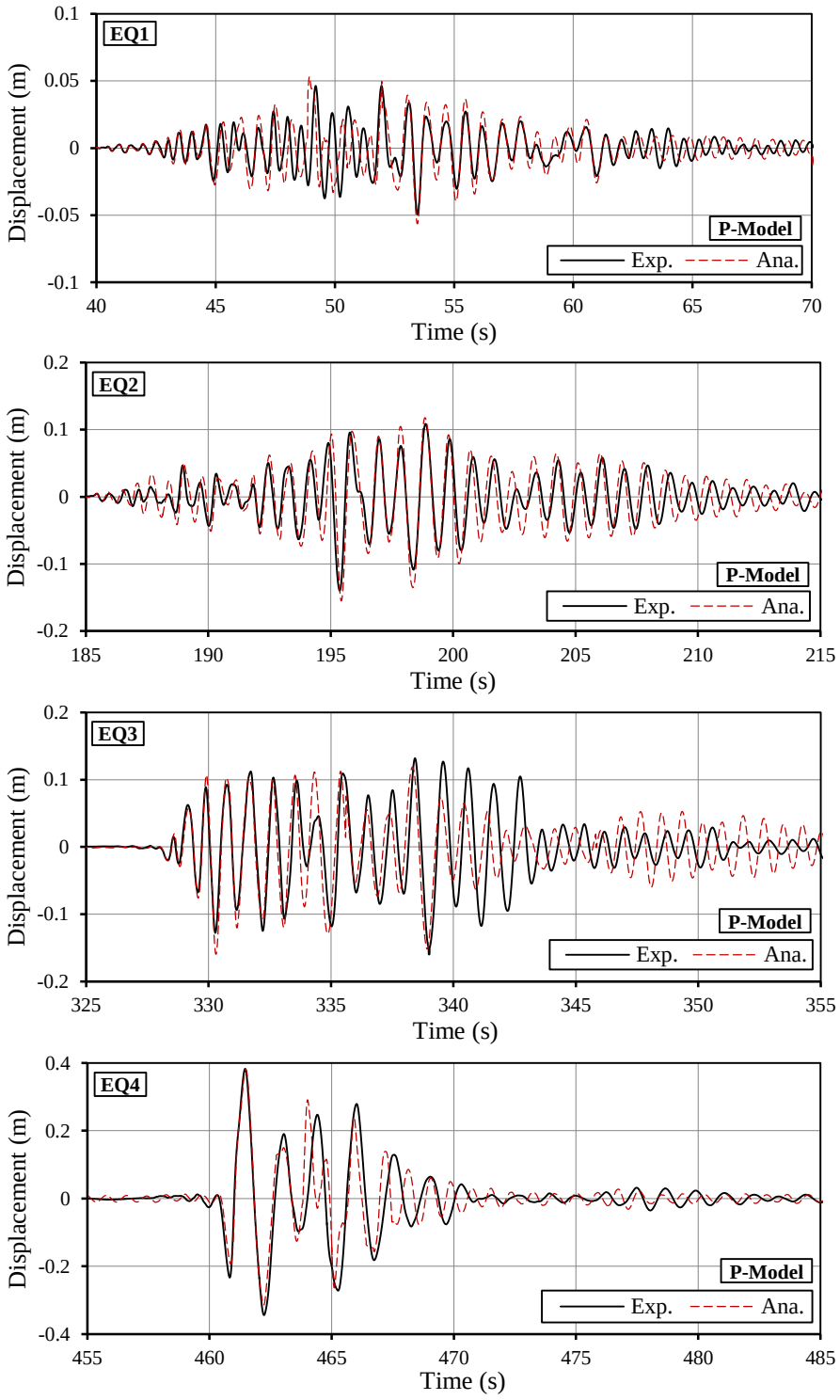

Figure 3.24. P-Model: measured versus computed top relative displacement under the four input motions

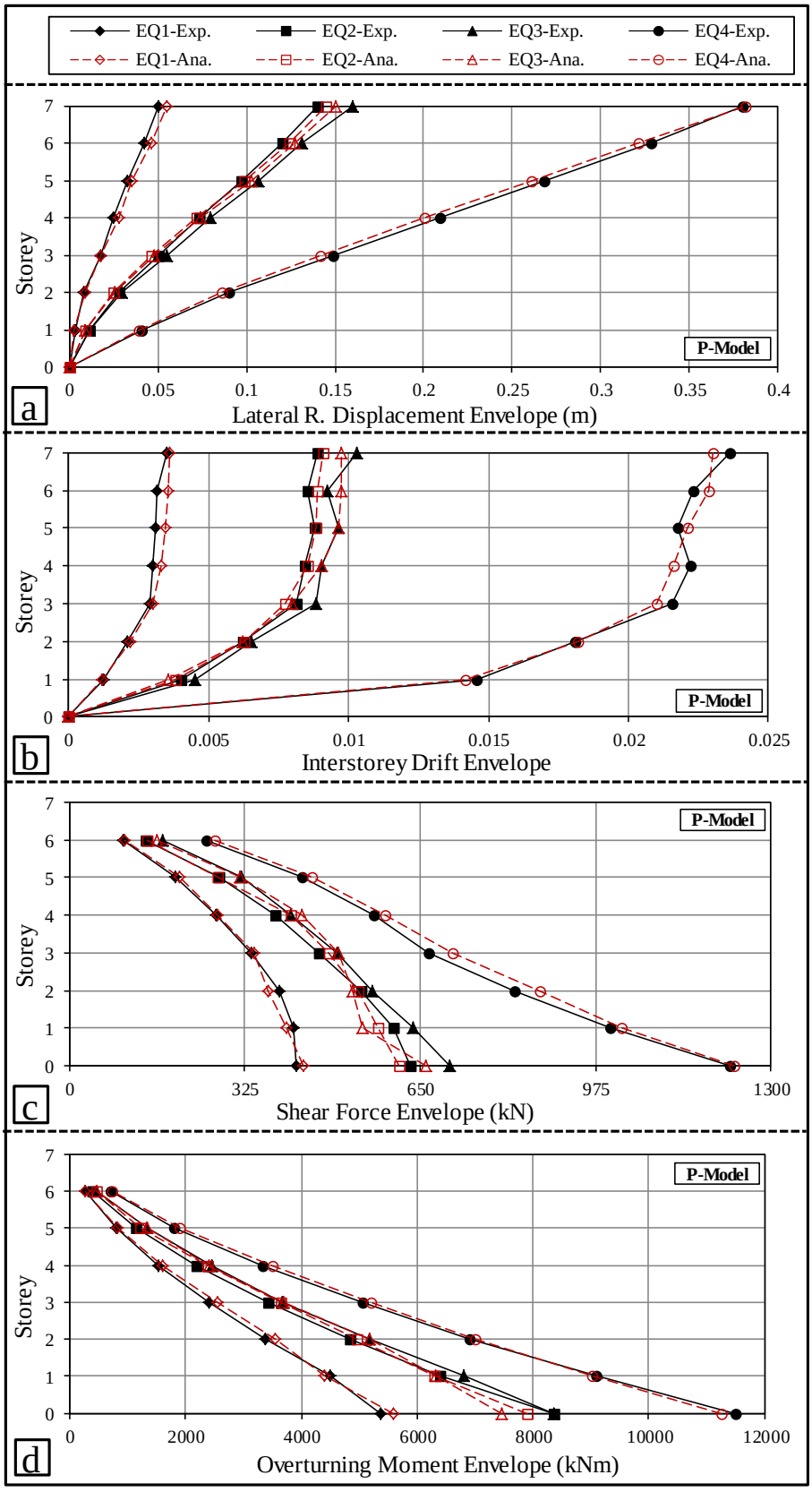

Figure 3.25. P-Model: measured versus computed envelopes: (a) relative displacement; (b) inter-storey drift; (c) shear force; and (d) storey overturning moment

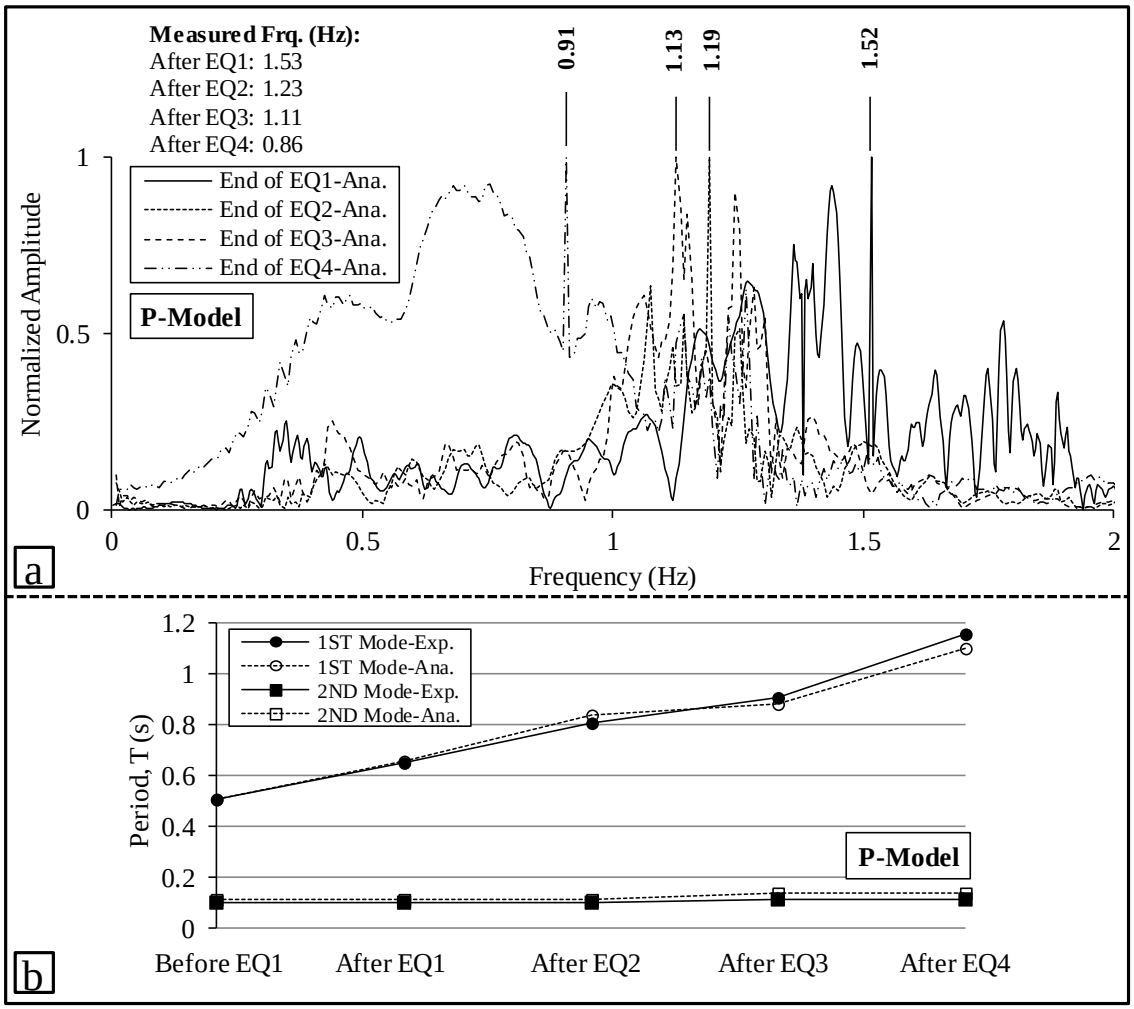

Figure 3.26. P-Model: evolution of modal characteristics during the four input motions: (a) frequency spectra; and (b) structure periods

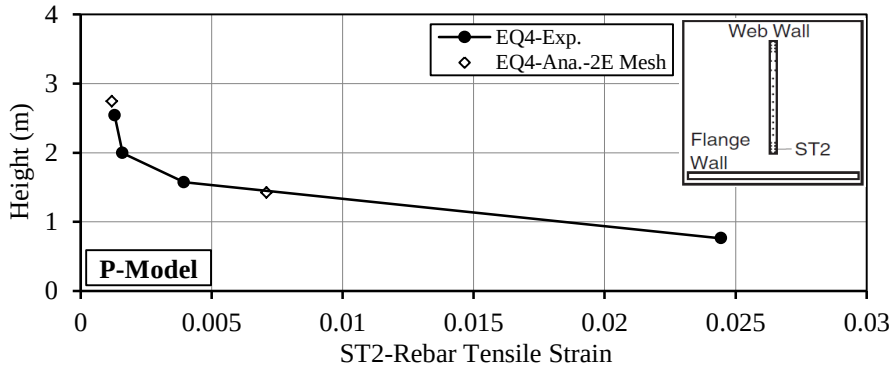

Figure 3.27. P-Model: tensile strain of ST2 reinforcing bar over the height of the first level under EQ4

3.6 Summary and conclusions

In this chapter, the results from Phase I of the shake table tests undertaken at the University of California, San Diego of a full-scale slice of a seven-storey RC wall building are employed to conduct a MLNMVS. The scheme verifies different approaches and key parameters in modelling RC slender shear walls forming the lateral force-resisting system in RC high-rise wall buildings. Three analytical models are created to simulate the nonlinear response of the test structure under four consecutive table excitations. The excitations represent real earthquake motions with increasing maximum acceleration from 0.15g to 0.91g. The 2-noded fibre-based beam-column element approach is adopted to model the web and the flange walls of the test structure in 2D centreline models using ZEUS-NL tool. PERFORM-3D package is utilised to create the third (3D) model using the 4-noded fibre-based wall/shell element. The main conclusions drawn from this study are:

- With appropriate care in the modelling of the geometry, both investigated nonlinear modelling approaches (2- and 4-noded fibre-based elements) are sufficient to predict global deformation response (storey lateral displacement and ISD) of RC wall buildings with relatively good accuracy.

- The study reveals the supremacy of the 4-noded fibre-based wall/shell element in accounting for the 3D effects of deformation compatibility between lateral and gravity-force-resisting systems. The 3D interaction between the gravity columns, the floor slabs, and the web wall significantly contributed to the overall lateral capacity of the test structure.

- When initial stiffness is used in constructing the damping matrix for RC wall buildings with no or well-isolated non-structural elements, low damping ratio (0.5% for the test structure) is suitable for assessing their seismic performance.

- The observed difference between the predicted and the measured response of the test structure under the two consecutive input motions with comparable intensities (EQ2 and EQ3) highlights the importance of accurate representation of the unloading/reloading paths of the material models. This is especially true when assessing the performance of buildings under earthquake motions that do not considerably take the structure into virgin territory.

- No noticeable change is observed in the analytical response of the test structure when shear deformation was accounted for in the P-Model compared to the results obtained from the IZ-Model. This is justified by the test results that demonstrated almost exclusively flexural cracking at the web wall base. However, shear deformation may still make a significant contribution to the lateral displacement of walls, even in walls categorised as slender and or flexure-dominated. Hence, considering the shear deformation either implicitly (coupled model) or explicitly (uncoupled model) is recommended.

This page is intentionally left in blank

CHAPTER 4. Case study

To demonstrate the proposed framework for assessing the seismic vulnerability of RC high-rise wall buildings under different earthquake scenarios, the city of Dubai (UAE) is chosen in the present work as a case study for two main reasons: (i) due to the unprecedented level of growth in property development in recent years. In this growth, high-rise buildings are forming the biggest share of the new construction. This class of buildings represents high levels of financial investment and population density increase which significantly increases exposure; and (ii) the multi-scenario earthquakes under which the region is vulnerable, where high-rise buildings are expected to respond to in different ways.

This chapter consists of four main sections. Section 4.1 presents the seismicity of Dubai city. Hazard studies on the region are critically reviewed and appropriate seismic characteristics are selected for the subsequent seismic vulnerability assessment. The criteria for selecting the input ground motions are discussed in Section 4.2, where forty real records are selected to represent two seismic scenarios. Section 4.3 discusses the

selection, the analysis, and the design of a 30-storey RC building which is utilised as the reference structure in the current study. The building footprint, layout and lateral force-resisting system are commonly adopted in the study region. Finally, Section 4.4 details the nonlinear modelling of the reference building using the modelling approach and key parameters presented in CHAPTER 3.

4.1 Seismicity of the study region

The United Arab Emirates, where the city of Dubai is located, is situated on the Arabian Gulf, southeast of the Arabian Peninsula, bordering Saudi Arabia to the south and Oman to the east. The country also shares sea borders with Iran to the north and Qatar to the west. The Arabian plate is categorised as a stable continental region (Fenton et al., 2006). The regional-scale general tectonic setting is shown in Figure 4.1.

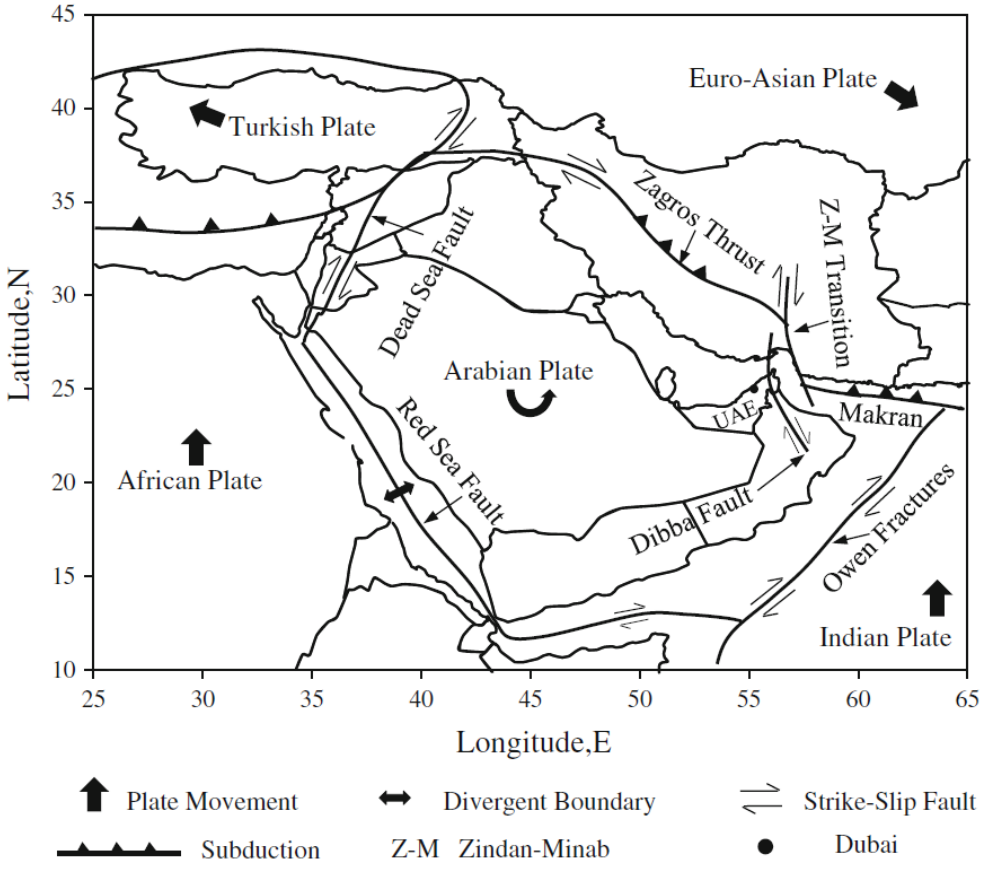

Figure 4.1. General tectonic setting around UAE (*after* Khan et al., 2013)

Over the last three decades, there have been over eleven studies presenting the seismic hazard for Dubai, either specifically (e.g. Sigbjornsson and Elnashai, 2006, Shama, 2011), as part of the UAE (e.g. Abdalla and Al-Homoud, 2004, Musson et al., 2006, Malkawi et al., 2007, Aldama-Bustos et al., 2009, Khan et al., 2013), or on a wider scale

that covers most of the Arabian Peninsula (e.g. Al-Haddad et al., 1994, Grünthal et al., 1999, Peiris et al., 2006, Pasucci et al., 2008). The conclusions drawn by these studies are quite different with regard to the level of seismicity in Dubai and the UAE as a whole, with estimates of the PGA in Dubai ranging from less than 0.05g to 0.32g for a return period of 475 years.

The work of Peiris et al. (2006), Musson et al. (2006), Malkawi et al. (2007), and Pasucci et al. (2008) have less impact as the former two are published in conference proceedings and the latter two as international and technical reports, respectively. It is worth mentioning though that the outcome for Dubai (PGA for a return period of 475 years) in the above-mentioned studies by Peiris et al., Musson et al., and Pasucci et al. (0.06g, 0.06g and 0.05g, respectively) is very close to the result obtained by Aldama-Bustos et al. (2009). On the other hand, the study by Malkawi et al. reported a PGA value greater than 0.2g.

The work of Grünthal et al. (1999) basically aimed to fill in the blank areas left in the global hazard map produced by the Global Seismic Hazard Assessment Project (GSHAP), of which the northeast corner of the Arabian Peninsula was not covered in any of its regional sub-projects. The UAE hazard was mapped by simulating the attenuated effect of the seismic activity in the Dead Sea fault area and in Zagros province of Iran, without performing actual seismic hazard analysis for sites in UAE. Therefore, the estimates of Grünthal et al. are disregarded in the current study.

With the exception of the latter work, the above-mentioned studies have implemented the PSHA methodology, based essentially on Poisson Model framework (Cornell, 1968). In a PSHA framework, there are several key input parameters. These parameters are highlighted below with a critical review on their impact on the concluded results of some of the aforementioned studies.

4.1.1 Earthquake data, faulting structures and seismic source models

To compile an appropriate seismic source model for the use within a PSHA study, it is essential to identify the individual faulting structures both on the local and the regional levels. The faulting structures to be identified are the ones which have the potential to generate earthquakes that could affect Dubai and other sites within the UAE. Based on the tectonic setting of the region, four main seismic sources can be identified: (i) Zagros fold-thrust; (ii) Zendan-Minab-Palami fault system; (iii) Makran subduction zone; and

(iv) local crustal faults including Oman mountains, Dibba line, Wadi Ham, Wadi El-Fay, Wadi Shimal and the controversial West Cost Fault (WCF), (Johnson, 1998). Defining the seismic source zones, in terms of covered area, assigned faults, and seismicity (recurrence parameters) has a major impact on the output of the PSHA.

In the study of Al-Haddad et al. (1994), UAE region has not been included in any of the considered seismic source zones. The closest considered source was the one that combines the western edge of the Makran subduction zone and the southernmost part of Zagros fold-thrust (Figure 4.2a). In this study, international earthquake data bank sources alongside Saudi Arabian Earthquake Data File (SAEDF) were utilised to assemble the earthquake catalogue used with the PSHA. The study was based on instrumented and historic events covering a time span from 2150 BC to 1990 AD and a geographic region bounded by 10^o N to 35^o N and 30^o E to 60^o E.

The first PSHA conducted specifically for the UAE was presented by Abdulla and Al-Homoud (2004). The seismic source zones defined in this study are similar to those of Al-Haddad et al. (1994), with the exception of two additional small zones. The two added zones are effectively linking the stable UAE with the active areas of Makran and Zagros regions (Figure 4.2b). These source zones have contributed to inflating the seismic hazard within the UAE. The earthquake data were based on the catalogue of the International Institute for Earthquake Engineering and Seismology (IIEES, 2019) and the work of Farahbod and Arkhani (2002). The employed time span was between 1008 AD to 2002 AD and the covered area bounded by 20^o N to 30^o N and 50^o E to 60^o E.

Sigbjornsson and Elnashai (2006) conducted a hazard study focusing only on Dubai (Figure 4.2e). The study indicated that the seismic source zonation is based on the work of Tavakoli and Ghafory-Ashtiany (1999), but also included the Dibba and West Coast faults. The earthquake data for the study area of 20^o N to 30^o N and 50^o E to 60^o E and for the period of 734 AD to 1996 AD were extracted from three main sources: (i) Ambraseys and Melville (2005); (ii) Ambraseys and Srbulov (1994); and (iii) GSHAP data (2004). USGS data (2019) were also used to include additional events up to 2004.

The study of Aldama-Bustos et al. (2009) concentrated on the major cities of Abu Dhabi, Dubai, and Ras Al Khaymah in the UAE. Twenty distinct seismic sources were included within the seismic source model, mainly related to the Zagros fold and thrust belts using the work of Berberian (1995) to partition this overall region into sub-sources

(Figure 4.2c). The stable carton consisting most of the Arabian Peninsula was treated as a background source. Earthquake data were gathered from several sources (e.g. Ambraseys and Srbulov, 1994, Ambraseys and Melville, 2005, IIEES, 2019, ISC, 2019, USGS, 2019). The spatial study region spanned 21^o N to 31^o N and 47^o E to 66^o E and covered the period from 3000 BC up to 2003 AD.

In the study of Shama (2011), a PSHA was performed to establish the hazard spectrum for a site located at Dubai Creek on the west coast of the UAE where a new bridge was proposed. A definite number and borders for the seismic source zones were not reported. However, the study provided details of the characteristics of four seismic sources: Zagros fault-thrust region, Zendann-Minab-Palami fault system, Makran subduction zone, and local faults in the UAE (including the WCF). The effect of background seismicity was not included in this study. The covered area spanned 22^o N to 31^o N and 49^o E to 67^o E, and the earthquake catalogue was mainly based on IRIS (2019) and (IIEES, 2019).

One of the most recent studies in this field was conducted by Khan et al. (2013). In this study, seven distinct seismic sources are included (Figure 4.2d), based primarily on the work of Berberian (1995), Engdahl et al. (2006), and Aldama-Bustos et al. (2009). The USGS, the National Geosciences of Iran (NGI), and the National Centre of Meteorology and Seismology of UAE (NCMS-UAE) were used as sources to assemble the earthquake catalogue for the study region with covered area of 18^o N to 32^o N and 45^o E to 70^o E. Events dated between 1900 AD and 2010 AD were used.

4.1.2 Ground motion prediction equations

Ground Motion Prediction Equations (GMPEs) are normally developed using statistical regression on data of the observed ground motion intensities. These models are used to predict the probability distribution of ground motion intensity as a function of variables such as event magnitude, distance, faulting mechanism, site conditions, and directivity effect.

It is always preferable to use ground motion prediction models which are based on strong-motion recordings from the study areas. There were no seismograph networks in UAE until recently when one was set up by the governments of Abu Dhabi and Dubai in 2010 (Khan et al., 2013). Hence, the data available for this region is very limited to drive site-specific equations. For that reason, all above-mentioned studies used GMPEs

developed for other geographical regions, with the choice of such equations in recent studies often based on guidelines proposed by Cotton et al. (2006). Table 4.1 lists the GMPEs used in the aforementioned studies alongside their references.

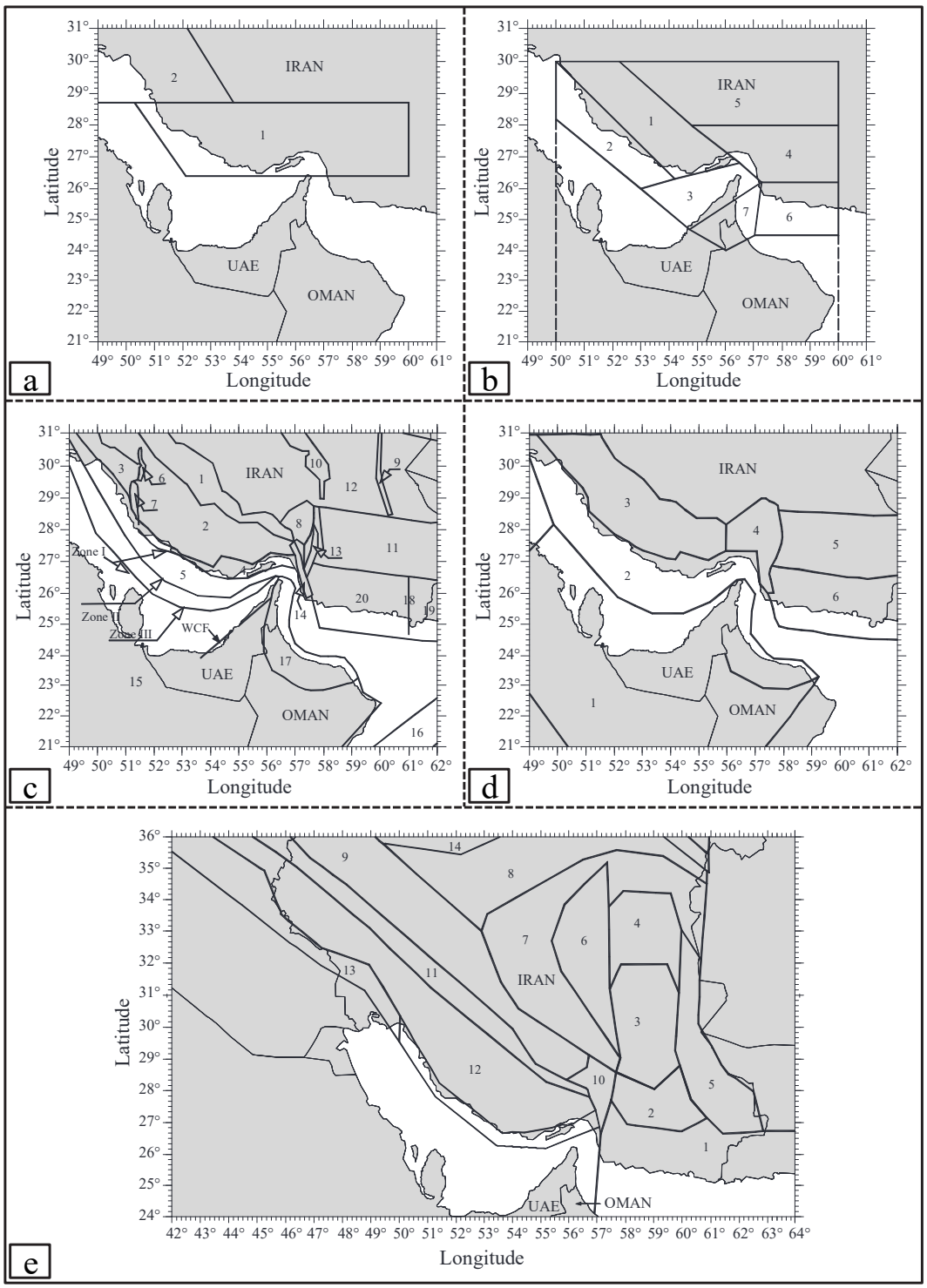

Figure 4.2. Seismic source zones defined for the PSHA studies of the region by (a) Al-Haddad et al. (1994); (b) Abdulla and Al-Homoud (2004); (c) Aldama-Bustos et al. (2009); (d) Khan et al. (Khan et al., 2013); and (e) Sigbjornsson and Elnashai (2006)

Table 4.1. GMPEs for the reviewed studies alongside their references

Reviewed study	GMPE #
Al-Haddad et al. (1994)	1
Abdalla and Al-Homoud (2004)	2
Sigbjornsson and Elnashai (2006)	3, 4
Peiris et al. (2006)	3, 5, 6, 7, 8
Musson et al. (2006)	3, 9
Malkawi et al. (2007)	7
Pasucci et al. (2008)	6, 10, 11, 12, 13
Aldama-Bustos et al. (2009)	10, 11, 13, 14, 15, 16, 17
Shama (2011)	3, 10, 14, 18, 19, 20, 21
Khan et al. (2013)	10, 13, 14, 16, 22, 23, 24

GMPE #	Reference study	GMPE #	Reference study
1	Campbell (Campbell, 1985)	13	Atkinson and Boore (Atkinson and Boore, 2006)
2	Zare (Zare, 2002)	14	Abrahamson and Silva (Abrahamson and Silva, 1997)
3	Ambraseys et al.(Ambraseys et al., 1996)	15	Ambraseys et al. (Ambraseys et al., 2005)
4	Simpson (Simpson, 1996)	16	Atkinson and Boore (Atkinson and Boore, 2003)
5	Sadigh et al. (Sadigh et al., 1997)	17	Boore (Atkinson and Boore, 2007)
6	Spudich et al.(Spudich et al., 1999)	18	Boore et al. (Boore et al., 1997)
7	Atkinson and Boore (Atkinson and Boore, 1997)	19	Gregor et al. (Gregor et al., 2002)
8	(Dahle et al., 1990)	20	Campbell (Campbell, 2003)
9	Dahle et al. (Ambraseys, 1995)	21	Campbell and Bozorgnia (Campbell and Bozorgnia, 2003)
10	Youngs et al. (Youngs et al., 1997)	22	*Boore and Atkinson (Boore and Atkinson, 2008)
11	Akkar and Bommer (Akkar and Bommer, 2007)	23	*Abrahamson and Silva (Abrahamson and Silva, 2008)
12	Campbell and Bozorgnia (Campbell and Bozorgnia, 2007)	24	*Campbell and Bozorgnia (Campbell and Bozorgnia, 2008)

**New Generation Attenuation (NGA) equation*

4.1.3 Results of PSHA studies on the region

The results of Al-Haddad et al. (1994) were presented in a PGA map for a 475 years return period. For the Dubai region, the PGA value is shown to be less than 0.05g. Abdalla and Al-Homoud (2004) presented PGA maps with 10% Probability of Exceedance (POE) in 50, 100 and 200 years (475, 950 and 1900 years return periods, respectively). In this study, the estimated PGA value for Dubai at 475 years return period was 0.15g. Sigbjornsson and Elnashai (2006) presented PGA hazard curves, UHS for return periods of 974 and 2475 years, and synthetic records to be used in dynamic analysis. The study suggested PGA values of 0.16g and 0.22g in Dubai for return periods of 475 and 2475 years, respectively. Aldama-Bustos et al. (2009) presented seismic hazard curves (PGA and $S_{a(1s)}$) and UHS for a wide range of return periods (500, 1000, 2500, 5000, and 10000 years). The PGA for Dubai was estimated as 0.049g and 0.086g for return periods of 475 and 2475 years, respectively. Shama (2011) presented seismic hazard curves (PGA and Spectral accelerations with periods ranging from 0.1s to 10s) and UHS for 475 years and 2475 years return periods. The hazard in Dubai (PGA) based on this study was estimated at 0.17g and 0.33g for return periods of 475 and 2475 years, respectively. Khan et al. (2013) presented the results in terms of PGA and spectral acceleration ($S_{a(0.2s)}$ and $S_{a(1s)}$) contour maps as well as in seismic hazard and UHS curves. The 475 and 2475 years return period PGA reported for Dubai were 0.047g and 0.118g, respectively. Table 4.2 summarises the results of previous studies in terms of PGA for 475 and 2475 years return periods.

Table 4.2. Results for Dubai from reviewed hazard studies in PGA at 475 and 2475 return periods

Reviewed study	PGA (g) for return period of 475 years (10% POE in 50/Y)	PGA (g) for return period of 2475 years (2% POE in 50/Y)
Al-Haddad et al. (1994)	<0.05	-
Abdalla and Al-Homoud (2004)	0.15	0.19
Sigbjornsson and Elnashai (2006)	0.16	0.22
Aldama-Bustos et al. (2009)	0.05	0.09
Shama (2011)	0.17	0.33
Khan et al. (2013)	0.05	0.12

The wide differences in PGA shown in Table 4.2 can be attributed to the fact that different assumptions were made for the key elements of the PSHA framework, such as borders, faulting structures and seismic parameters assigned to each seismic source. An obvious difference is in the treatment of the WCF, a fault that has been reported on the tectonic map of the Arabian Peninsula as a left-lateral strike-slip fault that runs from

Abu Dhabi through Dubai and Sharjah to Ras Al Khaimah, parallel to the west coast of UAE (Brown, 1972, Johnson, 1998). The existence and activity level of this fault has been the focus of ongoing debate, with some of the studies considering it as a major active source (Sigbjornsson and Elnashai, 2006, Shama, 2011) while others (e.g. Aldama-Bustos et al., 2009, Khan et al., 2013) excluding it from their source model. Notwithstanding the currently weak evidence for its existence, if the WCF was shown to exist with a proven degree of activity (using geomorphic indicators and paleo seismological investigation), the implication on the PSHA would be serious (Aldama-Bustos et al., 2009). Other elements like the type and number of GMPEs used with each seismic source and the definition of the horizontal component of motion could also have a considerable effect on the outcome of the PSHA.

Considering the level of detail and assumptions made in the discussed studies, the study of Aldama-Bustos et al. (2009) represents a comprehensive investigation. However, and since the objective of the current work is to assess the seismic vulnerability of RC high-rise wall buildings, it is reasonable to lean towards studies with reasonably conservative outcomes that are in line with the seismic design criteria currently enforced in the UAE. Among these are the peer-reviewed works of Abdalla and Al-Homoud (2004), Sigbjornsson and Elnashai (2006), and Shama (2011). In these three studies, the PGA in Dubai ranges between 0.15g to 0.17g for a return period of 475 years and 0.19g to 0.33g for 2475 years return period. For the spectral acceleration, the values for 0.2s and 1.0s from the 2475 years return period UHS curves are given as 0.8g and 0.28g in (Shama, 2011), 0.72g and 0.58g in (Sigbjornsson and Elnashai, 2006). These spectral acceleration values are taken as 0.85g and 0.26g in the seismic maps included in the Abu Dhabi International Building Code “ADIBC”, (DMA, 2013) based on the study of Abdalla and Al-Homoud (2004). The high spectral accelerations in long periods from Sigbjornsson and Elnashai are hard to justify even by accounting for the possible use of GMPEs that are based on the larger horizontal component (Aldama-Bustos et al., 2009).

In conclusion, the hazard values in terms of PGA at 475 years return period and spectral accelerations for 2475 years return period at 0.2s and 1.0s adopted for Dubai in the current work are 0.16g, 0.80g and 0.24g, respectively. These are consistent with the design values approved by the Dubai Municipality; the legal body responsible for reviewing and approving all civil and structural designs in Dubai. Figure 4.3 and

Figure 4.4 show a comparison of the results obtained by some of the discussed studies in terms of seismic hazard curves (or data) and UHS, respectively.

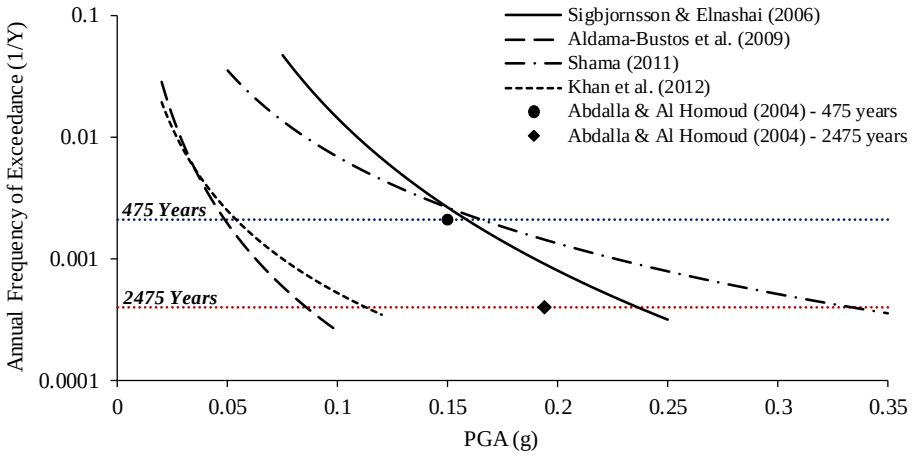

Figure 4.3. Seismic hazard curves (or data) for Dubai from some of the reviewed hazard studies

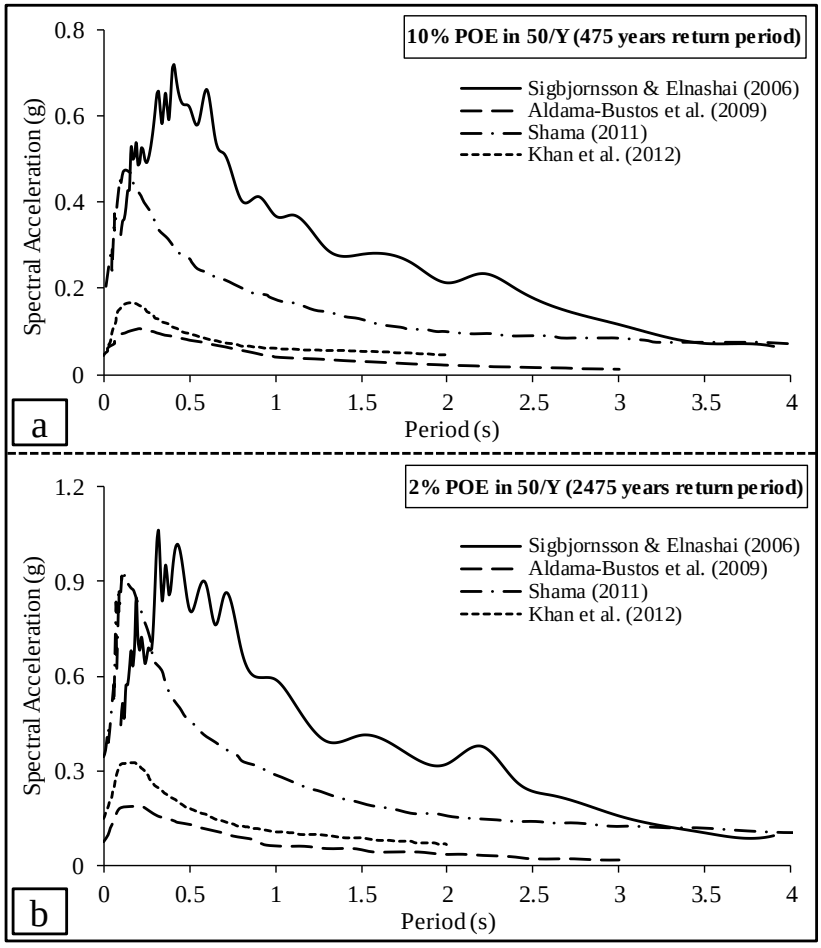

Figure 4.4. UHS for Dubai from some of the reviewed hazard studies: (a) 10% POE in 50/Y; and (b) 2% POE in 50/Y

4.1.4 Site conditions

In all the studies listed in Table 4.1, the site condition used is bedrock except for Sigbjornsson and Elnashai (2006) where the assumed site classification adopted in the attenuation relationships has not been specified explicitly. However, Sigbjornsson and Elnashai compared the results directly with the work of Abdalla and Al-Homoud (2004), suggesting that the site condition considered in their work is also bedrock.

Amplification of site response due to the effect of surface soil deposits of a particular site has been demonstrated in many previous events. Among others, are the Mexico earthquake in 1985 and the Bam earthquake in 2003. The seismic waves at site surface have been amplified by 5-fold the ground motion at bedrock level in the former (Celebi et al., 1987), while the ground surface motion was significantly altered in the latter (Rayhani et al., 2008). The level of response amplification caused by site condition depends on, among other factors, the properties of soil deposits and the characteristics of bedrock motion (e.g. Day, 2002).

Based on the author's personal experience from working as a senior structural designer in Dubai and related studies (e.g. Irfan et al., 2012), the near-surface soil in most of the Dubai region can be classified as "Class C: very dense soil and soft rock" with a small portion classified as "Class D: stiff soil". This classification is based on the average shear wave velocity for the top 30m, following site classification system of ASCE/SEI 7-16 (2017) and FEMA P-1050 (2015). The classification of Dubai soil may considerably amplify ground motions generated by low-to-moderate near-field and strong distant earthquakes, which in turn, impacts the seismic response of RC high-rise buildings with long fundamental periods and short higher mode periods.

For a site condition like the one in Dubai (very dense or stiff soil overlaying bedrock), site response amplification can be estimated either by (a) developing the response spectrum at the ground surface directly from the region hazard study using attenuation equations that are driven specifically for computing stiff soil-site response spectra (instead of bedrock response spectra); (b) using code-provided site coefficients to adjust the response spectrum values for the stiff soil overburden; or (c) region hazard study followed by dynamic site response analysis, (e.g. FEMA, 2015, ASCE/SEI-7, 2017).

Although dynamic nonlinear (or equivalent linear) site response analysis is a more accurate, yet complicated, method to account for the site response amplification,

approach (b) is adopted in the current work for the design of the case study high-rise building. For the vulnerability study, real input ground motions recorded on similar soil classes as those known in Dubai were adopted, as discussed hereafter. Figure 4.5 presents a comparison of 475 years return period code spectra of Dubai for site class B (bedrock), C (very dense soil and soft rock) and D (stiff soil), based on the 0.2s and 1.0s spectral accelerations adopted in the current study and site coefficients of ASCE/SEI 7-16 (2017).

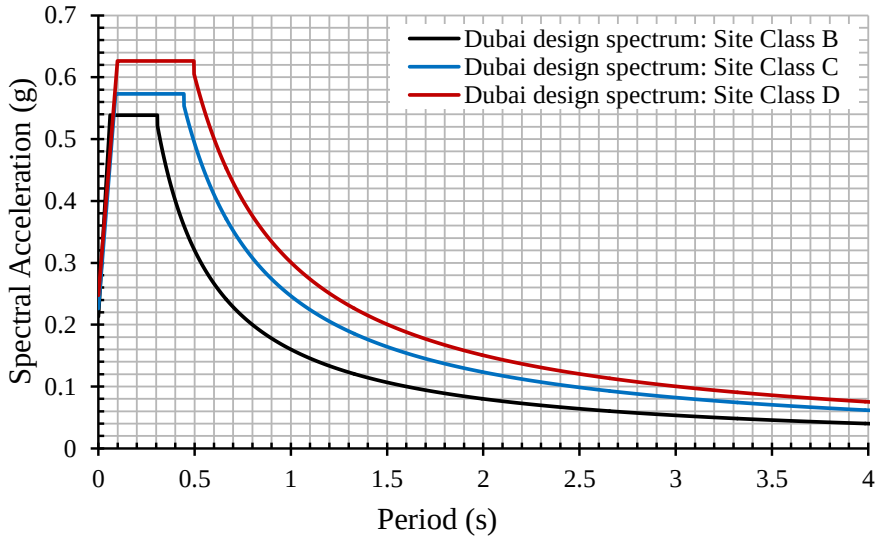

Figure 4.5. Dubai design spectra for site class B, C and D using 0.2s and 1.0s spectral acceleration values adopted in the present study and site coefficient of ASCE/SEI 7-16 (2017)

4.1.5 Earthquake Scenarios

The UHS represent the envelope (aggregation) of the effect of all earthquakes contributing to the study region with different combinations of magnitudes and distances. However, at a given time, a building will normally undergo only one earthquake as far as design is concerned. Hence, disaggregation of the rate of occurrence associated with the level of ground motion corresponding to selected return periods is required in order to identify the magnitude-distance scenarios most significantly contributing to the hazard (Bazzurro and Cornell, 1999)

Mwafy et al. (2006) demonstrated the characteristic difference in response induced by earthquakes due to strong distant and moderate near-field events, especially for high-rise buildings with long fundamental periods. The disaggregation process in the work of Aldama-Bustos et al. (2009) clearly showed that for spectral accelerations at longer response periods, larger magnitude earthquakes located at greater distances are the main contributor to risk. It also illustrated that as one moves towards the north part of the

UAE (from Abu Dhabi to Dubai and Ras Al-Khaimah), the contributions of the Makran and Zagros regions to the hazard at short response periods relatively increases. Similar findings were reported by Mwafy et al. (2006), Shama (2011), and Khan (2013).

Based on the disaggregation process in the above-mentioned studies, two main scenarios can be identified: (i) 5-6 magnitude earthquake at 10-60km epicentral distance generated by local faults (Dibba fault and WCF); and (ii) 7-8 magnitude earthquake at 100-200km epicentral distance that could be triggered at the Makran subduction zone. The selected response spectra of the input ground motions that represent the aforementioned earthquake scenarios are expected to match different parts of the code spectra for the study region (Figure 4.5) according to the earthquake scenario they represent. These records will be used in the nonlinear dynamic analyses of the reference building in CHAPTER 5.

4.2 Input ground motions

Ground excitation induced by different earthquake scenarios is a major source of uncertainty in determining seismic demands. To account for this uncertainty, the two aforementioned earthquake scenarios are represented in the current study by two sets with 20 natural earthquake records in each set (total of 40 records). Record Set#1 contains the input motions representing the severe distant earthquake scenario, while Record Set#2 represents the moderate near-field scenario. The European Strong-motion (Ambraseys et al., 2004) and the Pacific Earthquake Engineering Research Centre (PEER, 2019) databases are used to select the earthquake records due to the insufficient number of recorded events within the study region. Four parameters are considered in the selection criteria of the 40 records; (i) event magnitude (M); (ii) distance to source (R); (iii) site soil condition (S); and (iv) ground motion acceleration to velocity (a/v) ratio.

Earthquakes with larger magnitudes come with significantly longer effective durations and more significant peaks compared to smaller ones. The site-to-source distance generally affects the ground motion at the site through path attenuation and high-frequency filtration. Depending on the characteristics of the site soil strata, the seismic wave is either amplified or dissipated while travelling from the bedrock to the ground level. This modification in the seismic wave impacts the dynamic behaviour of wide frequency-sensitive high-rise buildings. The a/v ratio forms an important measure to

magnitude, frequency content and site-to-source distance of the earthquake event (Tso et al., 1992). High a/v ratios (>1.2g/ms^{-1}) signify events with high dominant frequencies, medium-to-small magnitudes, short site-to-source distances and short duration periods. Low a/v ratios (<0.8g/ms^{-1}), on the other hand, represent earthquakes with low dominant frequencies, high-to-medium magnitudes, long site-to-source distances and long duration periods. The a/v classification is applied to all of the 40 records in the current study.

For the ground motion effective duration, the interval between 0.5% and 95% of each of the acceleration, velocity and displacement integrals are used (Kwon and Elnashai, 2006). This procedure will significantly reduce the computational effort required to perform the MRIDAs for the reference structure, particularly when applying the 20 records that are characterised by long duration (Record Set#1). Figure 4.6 depicts the response spectra with their means for the two record sets alongside the uniform hazard spectra for 10% POE in 50 years (UHS-10% POE in 50Y) and the design spectra of the study region (site class C and D). The figure shows that the selected 40 input ground motions correlate well with the UHS and design spectra of the study region in both short and long period zones. Table 4.3 and Table 4.4 list the accelerograms (base-line corrected) with their characteristics for Record Set#1 and Record Set#2, respectively.

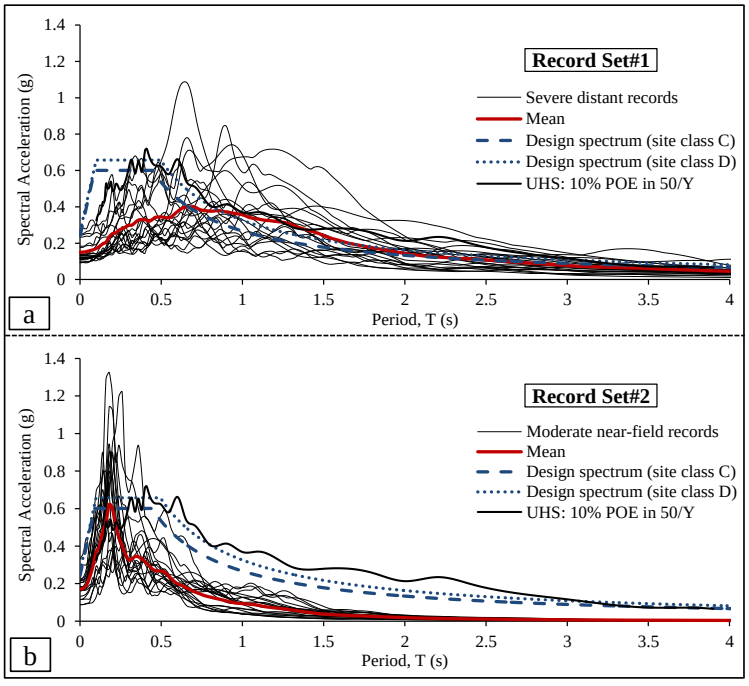

Figure 4.6. Response spectra of the 40 selected records with mean spectra, design spectra and 10% POE in 50Y-UHS for the study region: (a) Record Set#1 and (b) Record Set#2 representing moderate near-field earthquake scenario

Table 4.3. Identification and characteristics for input ground motions in Record Set#1

Record ID	Earthquake	Station	Component	Date	Magnitude (M_w)	Site class	Epicentral Distance (km)	Duration (sec)	Sample Step (s)	PGA (g)	(a/v) g/ms^{-1}	(a/v) Class
R1	Bucharest	Building res. Institute	EW	04-03-1977	7.53	D	161	18	0.005	0.176	0.60	
R2	Chi-Chi	CWB 99999 ILA013	EW	20-09-1999	7.62	C	135	60	0.004	0.139	0.52	
R3	Loma Prieta	Emeryville	260	18-10-1989	6.93	C	96.5	28	0.01	0.250	0.57	
R4	Loma Prieta	Golden Gate Bridge	270	18-10-1989	6.93	C	100	28	0.005	0.233	0.61	
R5	Hector Mine	Indio - Coachella Canal	0	16-10-1999	7.13	D	99	60	0.02	0.092	0.70	
R6	Izmit	Ambarli-Termik	EW	17-08-1999	7.64	D	113	50	0.005	0.183	0.60	
R7	Izmit	Istanbul-Zeytinburnu	NS	17-08-1999	7.64	D	96	96	0.01	0.110	0.77	
R8	Kocaeli	Bursa Tofas	E	17-08-1999	7.51	D	95	70	0.005	0.108	0.49	
R9	Kocaeli	Hava Alani	90	17-08-1999	7.51	C	102	90	0.005	0.094	0.46	
R10	Loma Prieta	Alameda Naval Air Stn Hanger	270	18-10-1989	6.93	D	91	29	0.005	0.244	0.73	LOW
R11	Loma Prieta	Berkeley LBL	90	18-10-1989	6.93	C	98	39	0.005	0.117	0.65	
R12	Loma Prieta	Oakland-Outer Harbor Wharf	0	18-10-1989	6.93	D	94	40	0.02	0.280	0.67	
R13	Manjil	Abhar	N57E	20-06-1990	7.42	D	91	29	0.01	0.133	0.62	
R14	Manjil	Tonekabun	N132	20-06-1990	7.42	C	131	40	0.005	0.124	0.76	
R15	Chi-Chi	TAP005	E	20-09-1999	7.62	D	156	60	0.005	0.137	0.49	
R16	Chi-Chi	TAP010	E	20-09-1999	7.62	D	151	60	0.005	0.121	0.50	
R17	Chi-Chi	TAP021	E	20-09-1999	7.62	D	151	60	0.005	0.117	0.47	
R18	Chi-Chi	TAP032	N	20-09-1999	7.62	C	144	60	0.005	0.115	0.64	
R19	Chi-Chi	TAP090	E	20-09-1999	7.62	D	156	60	0.005	0.130	0.41	
R20	Chi-Chi	TAP095	N	20-09-1999	7.62	D	158	60	0.005	0.098	0.52	

Table 4.4. Identification and characteristics for input ground motions in Record Set#2

Record ID	Earthquake	Station	Component	Date	Magnitude (M_w)	Site class	Epicentral Distance (km)	Duration (sec)	Sample Step (s)	PGA (g)	(a/v) g/ms^{-1}	(a/v) Class
R1	Coalinga-04	Anticline Ridge Free-Field	270	07-09-1983	5.18	C	6.34	15	0.005	0.328	2.048	
R2	Coalinga-04	Anticline Ridge Pad	270	07-09-1983	5.18	C	6.34	14	0.005	0.331	2.350	
R3	Coalinga-05	Burnett Construction	360	07-22-1983	5.77	D	12.38	21	0.005	0.297	1.988	
R4	Coyote Lake	San Juan Bautista, 24 polk St	213	08-06-1979	5.74	C	19.7	26	0.005	0.101	1.424	
R5	Friuli	Breginj-Fabrika IGLI	Y	15-09-1976	6	C	21	9.9	0.01	0.505	2.333	
R6	Hollister-04	City Hall	271	28-11-1974	5.14	C	9.8	20	0.01	0.168	1.480	
R7	Lazio Abr. Y	Cassino-Sant Elia	EW	07-05-1984	5.93	C	16	30	0.005	0.114	1.590	
R8	Livermore-02	Livermore-Morgan Terr Park	355	01-27-1980	5.42	C	14.1	15	0.005	0.228	2.581	
R9	Mammoth L. 06	Mammoth Lakes H. S.	344	05-25-1980	5.69	C	3.49	12	0.005	0.414	1.957	
R10	Mammoth L. 06	Fish & Game (FIS)	0	05-27-1980	5.94	D	12.02	11	0.005	0.406	2.753	HIGH
R11	Montenegro	Petrovac-Hotel Oliva	Y	04-15-1979	5.80	C	24.0	28	0.01	0.089	1.426	
R12	Northridge-06	Panorama City-Roscoe	90	03-20-1994	5.28	D	11.8	7.2	0.01	0.116	1.916	
R13	Umbria Ma.	Castelnuovo-Assisi	NE	26-09-1997	6.04	C	16.0	45	0.005	0.163	1.254	
R14	Whittier N. 01	Brea Dam (L Abut)	130	10-01-1987	5.99	C	24.0	20	0.005	0.132	1.460	
R15	Whittier N. 01	LA-Centry City CC North	90	10-01-1987	5.99	D	29.9	30	0.005	0.087	1.788	
R16	Whittier N. 01	LB-Orange Ave	2280	10-01-1987	5.99	D	24.5	21	0.005	0.215	1.468	
R17	Whittier N. 01	Alhambra - Fremont School	180	10-01-1987	5.99	C	6.77	26	0.005	0.388	1.514	
R18	Whittier N. 01	Garvey Res. - Control Bldg	60	10-01-1987	5.99	C	2.86	38	0.005	0.385	2.432	
R19	Whittier N. 01	LA - 116th St School	360	10-01-1987	5.99	D	21.26	25	0.005	0.341	1.888	
R20	Whittier N. 01	LA - Obregon Park	360	10-01-1987	5.99	D	9.05	30	0.02	0.424	1.748	

4.3 Selection and design of the 30-storey reference building

Following the definition of high-rise buildings as those with a height greater than 48m above ground level (PEER/ATC, 2010, LATBSDC, 2011), a 30-storey, 97.3m in height, RC structure is selected as a reference building for the current work. The footprint, layout and structural system of the building are common in the study region for this range of height (e.g. Mwafy, 2012a, Mwafy et al., 2015a). The structure is fully designed and proportioned for the purpose of the current study taking into consideration modern code provisions, as well as, local authority supplementary regulations and construction practices adopted in UAE.

4.3.1 General properties and loading of the reference building

The building consists of a bearing wall lateral force-resisting system in both orthogonal horizontal directions. Table 4.5 summarises the general building properties. In addition to the self-weight of the structure, Table 4.6 lists the values used for the calculation of live and superimposed dead loads. Figure 4.7 shows a typical floor layout and 3D view of the building design model.

Table 4.5. General building properties

Building usage	Residential
Total building height	97.30m (including basement levels)
Building footprint (L x W)	42.25m x 29.25m
Number of storeys	28 above ground 2 below ground
Storey height	3.20m below ground (storey 1 & 2) 4.50m for ground level (storey 3) 3.2m above ground (storey 4 to 29) 3.2m roof level (storey 30)
Flooring system	260mm thick RC flat slab at all building levels plus 1000mm x 200mm RC periphery beams from storey 4 to 30
Coupling beam depth	1000mm typical
Basement retaining walls	300mm thick, fc' = 50MPa

Table 4.6. Load criteria

Location	Use	Live load (kN/m²)	Superimposed load (kN/m²)
Basement levels (storey 1 & 2)	Parking	3.0 (reducible)	-
Ground level	Retail and public use areas	4.8 (unreducible)	2.0
Building periphery	Cladding	-	0.7
Ground level and above	Corridors and exit areas	4.8 (unreducible)	2.0
Storey 2 to 29	Residential	2.0 (reducible)	3.0 (including partitions)
Roof level	Roof	1.0 (reducible)	3.0
Certain areas at roof level	Mechanical	1.5 (reducible)	4.8
Certain areas at roof level	Water tanks	20.0 (unreducible)	3.0

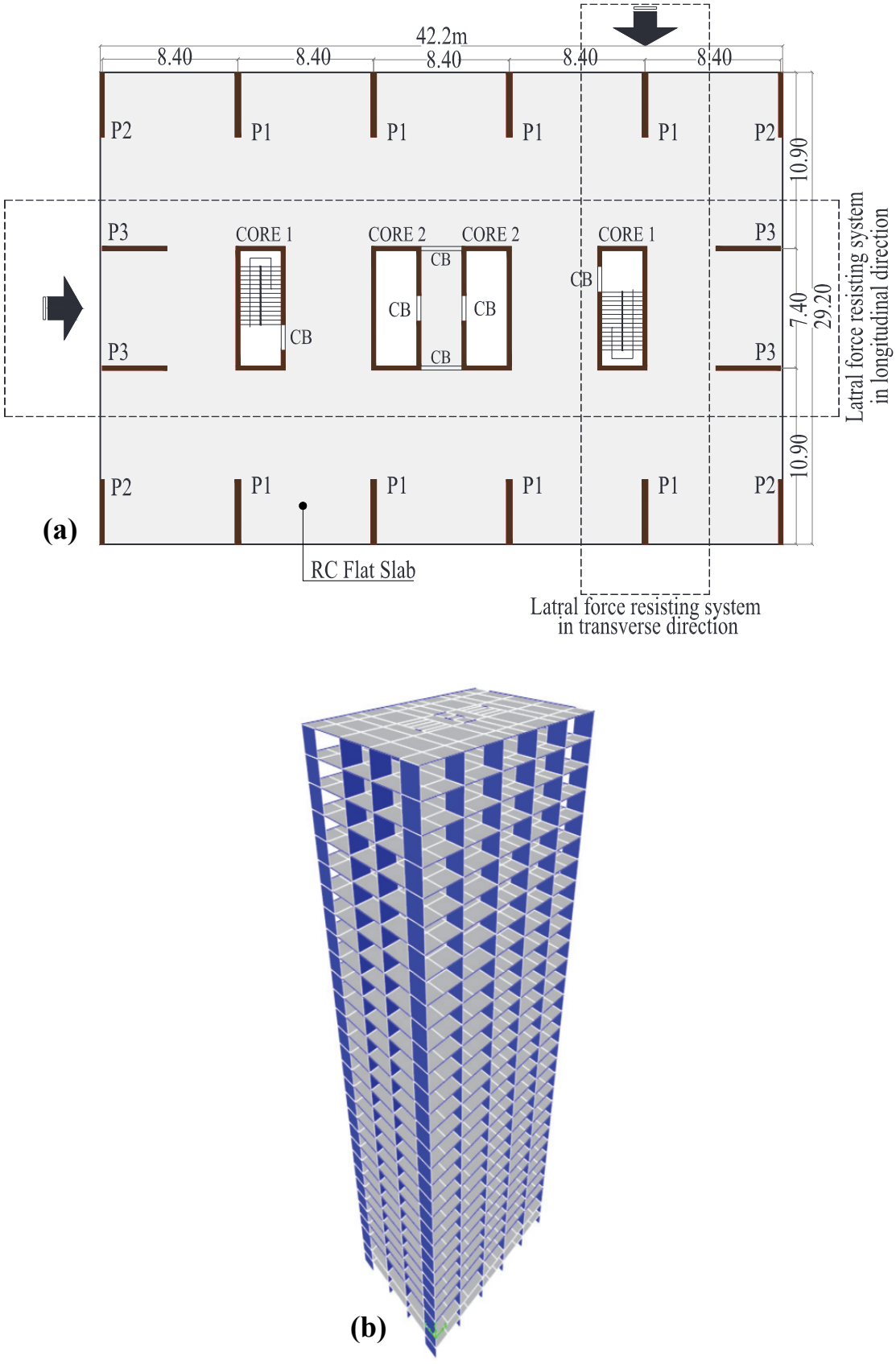

Figure 4.7. Reference building: (a) typical floor layout; and (b) 3D rendering of structure from ETABS model

A basic wind speed of 45m/s with an importance factor of 1.0 and exposure type C are considered in estimating wind loads using the ASCE/SEI 7-05 (2005). Following the discussion in Section 4.1.3, the seismic design loads are calculated using mapped spectral response accelerations of 0.80g and 0.24g at 0.2s and 1.0s, respectively. Site class S_C (very dense soil and soft rock) is considered in the seismic analysis.

4.3.2 Analysis and design of the reference building

ETABS (CSI, 2015), a commercial structural analysis and design software for high-rise buildings, is utilised to model the reference building in 3D. For the analysis and design of the flooring system, The SAFE flooring analysis and design software is used (CSI, 2014). Shell elements are used to model shear walls and floor slabs, while frame elements are adopted in modelling periphery and coupling beams. In the analysis, seismic demand is estimated using both Equivalent Lateral Force Procedure (ELFP) and Modal Response Spectrum Analysis (MRSA). A sufficient number of modes were included in the analysis to obtain combined modal mass participation of at least 90% of the actual mass in each of the orthogonal directions (ASCE/SEI-7, 2017). The combined response of the model base shear from MRSA is scaled up to a minimum of 85% of the base shear calculated from ELFP (ASCE/SEI-7, 2017). Complete Quadratic Combination (CQC) method and Ritz-vector procedure are used for the MRSA. Critical viscous damping of 5% is considered for all modes of vibration. Eccentricity ratios of 5% are considered for the diaphragm centre of rigidity in both orthogonal directions to account for accidental torsional effects on the building. P-Δ effects are also accounted for in the analysis.

The design of the building is performed in general compliance with the IBC (2015), which requires the use of the ASCE/SEI 7-10 (2010) and ACI 318 (2014). ASTM 706 reinforcing steel is used with a specified yielding strength of 460MPa. The specified concrete strengths used in the flooring system, retaining walls at basements, piers, cores and coupling beams range between 40MPa and 50MPa. Cross-sections and corresponding reinforcement of piers and cores vary over the building height. Cast-in-situ RC flat slabs of 0.26m thickness with periphery beams are adopted for the flooring system, also serving as a rigid diaphragm to transfer lateral forces to the vertical structural elements at each floor. The flooring system is subjected to special design requirements, including punching shear, so as to resist the combination of seismic deformations and gravity loads. The stiffness assumptions given in Table 4.7 are used to

determine actions and deformations (Ghodsi and Ruiz, 2010, Tuna, 2012). Associated design spectrum parameters and characteristics of the first-nine vibration modes of the building are provided in Table 4.8 and Table 4.9, respectively.

To comply with the local supplementary regulations and the trends of design and construction practices in the study region, the following assumptions were made during the analysis and design stages: (i) the stiffness modifier for all vertical structural elements is set to 0.7; and (ii) the minimum ratio of vertical steel reinforcement in core wall segments at the lower two-thirds of the building height is set to 1%, and (iii) boundary elements are to be considered for all pies and core wall segments according to the special structural wall provisions for the seismic design category (SDC) "D" through "F" in ACI 318 (2014). The reason for enforcing the consideration of the boundary elements is that the calculated S_{Ds} and S_{D1} values for site class C in the study region (0.576g and 0.249g, respectively, Table 4.8) are very close to the threshold values between SDC-C and SDC-D according to the ADIBC (2013). These threshold values are 0.60g and 0.25g for S_{Ds} and S_{D1}, respectively. Figure 4.8 presents typical cross-section detailing of Core 1, Pier P1, and coupling beams, while Table 4.10 summarises the design detailing of Pier P1 and Core 1.

Table 4.7. Stiffness assumptions (Ghodsi and Ruiz, 2010, Tuna, 2012)

Element	Strength-level design	Serviceability design
Modulus of elasticity	Specified concrete strength	Specified concrete strength
Piers and core wall segments	Flexure: $0.7EI_g$	Flexure: $1.0EI_g$
	Shear:$1.0GA_g$	Shear:$1.0GA_g$
Retaining walls at basements	Flexure: $0.8EI_g$	Flexure: $1.0EI_g$
	Shear: $0.8GA_g$	Shear:$1.0GA_g$
Coupling beams	Flexure: $0.2EI_g$	Flexure: $0.5EI_g$
	Shear:$1.0GA_g$	Shear:$1.0GA_g$
Peripheral beams	Flexure: $0.35EI_g$	Flexure: $0.7EI_g$
	Shear:$1.0GA_g$	Shear:$1.0GA_g$
Flooring slabs	Flexure: $0.25EI_g$	Flexure: $0.5EI_g$
	Shear:$0.5GA_g$	Shear:$0.8GA_g$

Table 4.8. Adopted design parameters[A]

$S_{s(0.2s)}$	0.80g
$S_{1(1.0s)}$	0.24g
Site class	C
F_a	1.08
F_v	1.56
S_{Ms}	0.864g
S_{M1}	0.374g
S_{Ds}	0.576g
S_{D1}	0.249g
SDC (DMA, 2013)	C
Risk category	I
Seismic importance factor	1.0
R	4.0
C_d	4.0
Seismic weight (W)	466696kN (47590t)
Modal combination method	Complete quadratic combination (CQC)
Redundancy factor (ρ)[B]	1.0
Accidental eccentricity	5%
Viscous damping	5%
Modal base shear	11299kN[C]

[A] *Refer to ASCE/SEI 7-10 for the definition of table parameters*

[B] *The redundancy factor = 1, the structure complies with 12.3.4.1 of ASCE/SEI 7-10*

[C] *Per Section 12.9.4 of ASCE/SEI 7-10, for strength design, the modal analyses are scaled to match 0.85V = 11299kN*

Table 4.9. Building vibration mode periods and mass participation summary

Vibration mode #	Uncracked period (s)	Equivalent inelastic period (s)	Mode dominate direction	Mass participation (%)
1	3.44	5.30	Translation mode on X direction (H1)	71
2	3.21	4.46	Translation mode on Y direction (H2)	66
3	3.03	3.96	Torsional mode	72
4	1.03	1.43	Translation mode on X direction (H1)	14
5	0.91	1.09	Torsional mode	13
6	0.82	0.96	Translation mode on Y direction (H2)	18
7	0.52	0.65	Translation mode on X direction (H1)	6
8	0.36	0.40	Torsional mode	5.5
9	0.32	0.39	Translation mode on Y direction (H2)	6.5

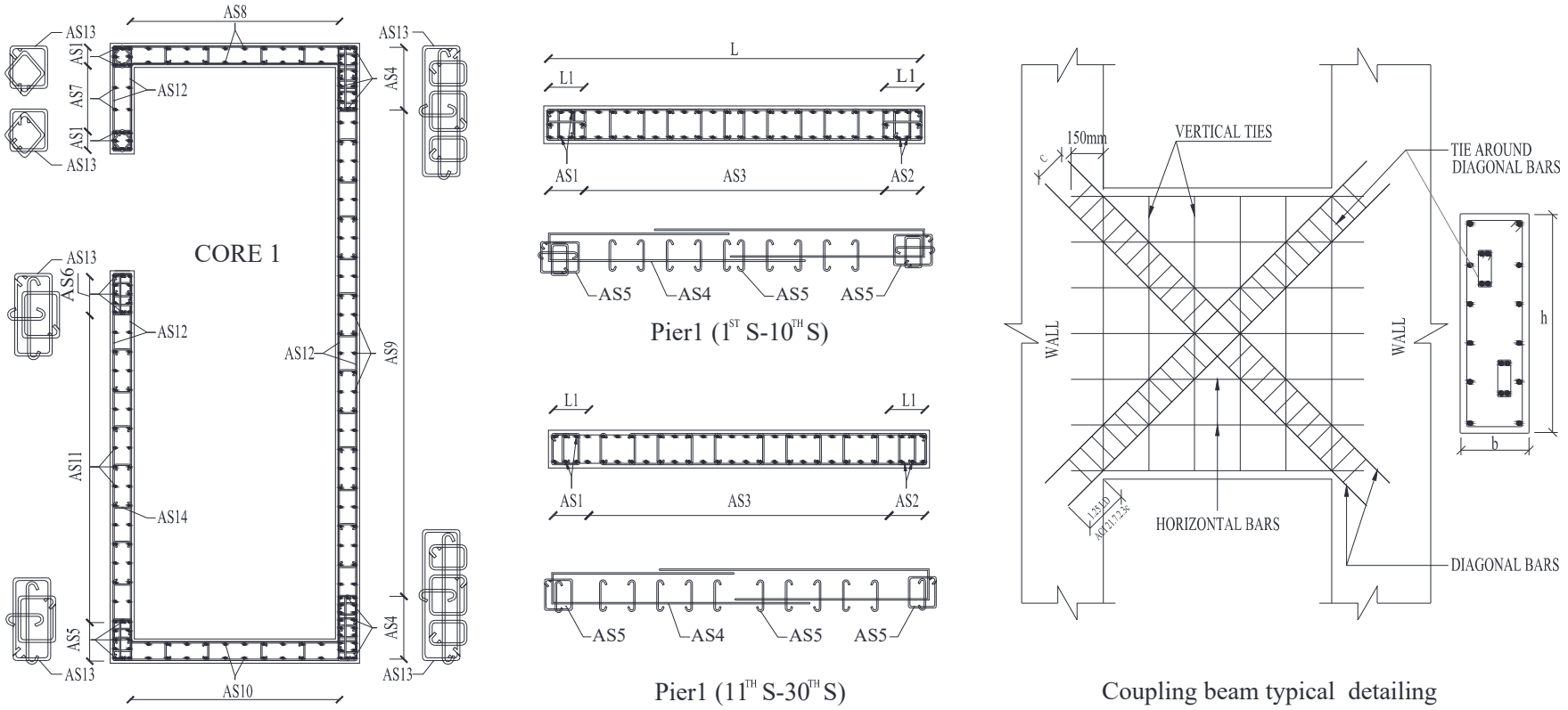

Figure 4.8. Typical cross-section detailing of Core 1, Pier P1, and coupling beams in the reference building

Table 4.10. Design summary for Pier P1 and Core 1 in the reference building

PIER P1								**CORE 1**					
Element position		1-5 S	6-10 S	11-15 S	16-20 S	21-25 S	26-30 S	Element position			1-10 S	11-20 S	21-30 S
Pier cross-section (LxW)		4000x350	4000x325	4000x300	4000x275	4000x250	4000x225	Core thickness			250	200	200
Concrete strength (f_{cu})		50	50	50	50	50	50	Concrete strength (f_{cu})			50	50	50
Concrete strength (f_c')		40	40	40	40	40	40	Concrete strength (f_c')			40	40	40
Provided steel (vertical), (%)		3.45	2.27	0.71	0.34	0.37	0.41	Provided steel (vertical), (%)			1.00	1.00	0.75
Boundary zone length		400	400	400	250	250	250	Boundary zone length			(10% - 15% of segment length)		
Horizontal shear reinforcement (area/ratio), (mm^2/m / %)		875 / 0.25	813 / 0.25	750 / 0.25	688 / 0.25	625 / 0.25	563 / 0.25	Horizontal shear reinforcement (area/ratio), (mm^2/m / %)			658 / 0.26	601 / 0.30	601 / 0.30
Reinforcement	Vertical*	AS1+AS2	20T32	20T25	20T16	12T12	12T12	12T12	Reinforcement	Vertical*	AS1, AS6	80T20	80T16	NA
		AS3	40T32	40T25	40T12	30T10	30T10	30T10			AS7, AS11	198T12	200T12	250T12
	Horizontal*	AS4	T10-100	T10-125	T10-150	T10-150	T10-150	T10-150		Horizontal*	AS12	T10-100	T10-150	T10-150
		AS5	T10-100	T10-125	T10-150	T10-150	T10-150	T10-150			AS13, AS14	T10-100	T10-150	T10-150

**Refer to Figure 4.8*

Concrete strength is in MPa and all dimensions are in mm unless otherwise stated

S: Storey, L: Length, W: Width

4.4 Nonlinear modelling of the reference building

PERFORM-3D analytical tool (CSI, 2011) is utilised to create the nonlinear model of the reference building. The selection of the tool, modelling approach and key modelling parameters are based on the MLNMVS presented in CHAPTER 3 of this thesis

Although PERFORM-3D is an efficient 3D modelling package, it is computationally demanding to execute a large number of NRHAs for a 3D model of an entire high-rise structure, particularly when a wide range of input ground motions is employed. A 3D-slice idealization is therefore adopted to develop the nonlinear model of the reference building. The lateral force-resisting system of the building in the transverse direction is assumed to consist of four framing bays. Each of these, carrying 25% of the total mass of the building, consisted of two external piers (P1) and an internal core, as shown in Figure 4.7a. Conservatively, the two framing bays at the right and left edges of the building are assumed not to form part of the lateral force-resisting system and only carry gravity load. In the longitudinal direction, the lateral forces are resisted by a single framing system which consists of all the internal cores and piers P3. Other piers (P2 and P1) are assumed not to be participating in resisting lateral forces in the longitudinal direction. The results from the free vibration analysis conducted on the entire building using the ETABS 3D model indicate a comparable lateral capacity in the two orthogonal directions with the fundamental mode uncracked periods of 3.44s and 3.21s in the longitudinal and transverse directions (H1 and H2), respectively. Vindicated by this fact, the number of MRIDAs, and thus the computational effort, can be significantly reduced by focusing only on one direction of the building. As a result, the 3D-slice representing the lateral force-resisting system in the transverse direction of the reference building is modelled and employed in the next chapter to define the performance limit states. To confirm the suitability of the 3D-slice model in representing the transverse direction of the reference building, Table 4.11 lists the equivalent inelastic and uncracked periods of the first three modes in the transverse direction of both the reference building and the modelled 3D-slice. As the table depicts, these periods are very close, mostly identical. The maximum difference in the equivalent inelastic periods of modes 1, 2, and 3 between the entire building and the 3D-slice transverse direction is 0.30s (6.7%), 0.00s (0.0%), and 0.00s (0.0%), respectively. These small-to-no differences, are attributed to the minor contribution of the two framing bays at the right and left edges of the building to the overall lateral stiffness in the transverse direction.

Figure 4.9 presents 3D, elevation and plan views from the PERFORM-3D analytical model.

Table 4.11. Comparison of equivalent inelastic and uncracked periods in the transverse direction between the entire reference building and the modelled 3D-slice

Mode in Transverse Direction	Uncracked period				Equivalent inelastic period			
	Entire Building (s)	3D-slice (s)	Difference (s)	Difference (%)	Entire Building (s)	3D-slice (s)	Difference (s)	Difference (%)
1	3.21	3.44	0.23	7.1	4.46	4.76	0.30	6.7
2	0.82	0.86	0.04	4.9	0.96	0.96	0.00	0.0
3	0.32	0.36	0.04	12.5	0.39	0.39	0.00	0.0

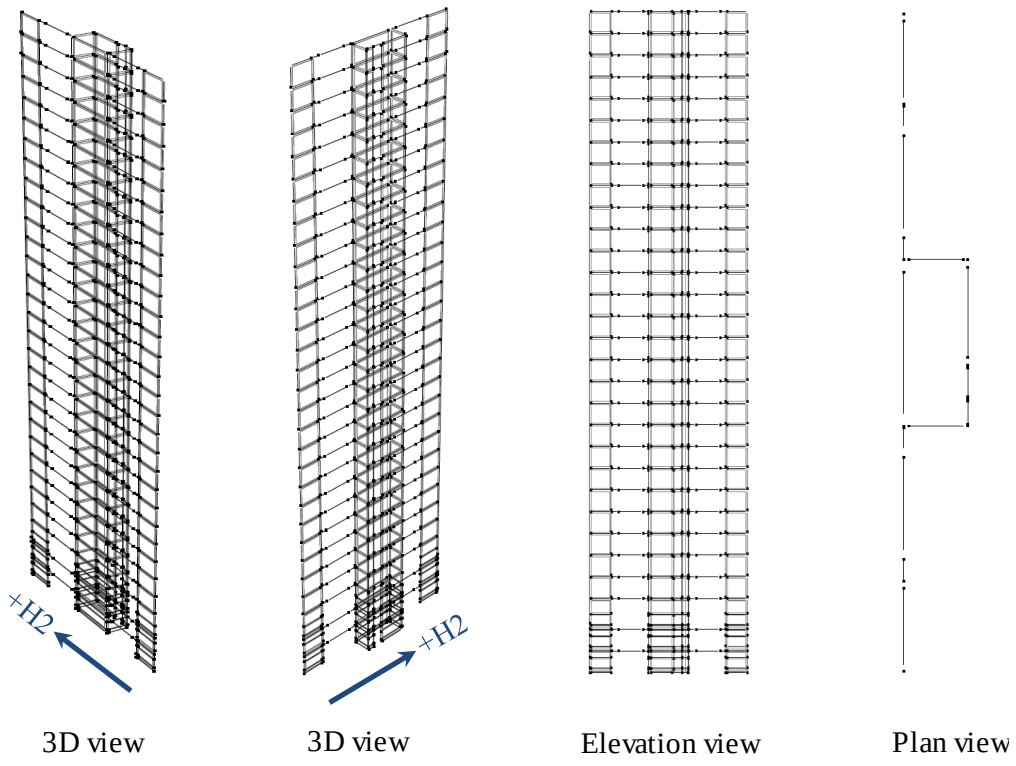

Figure 4.9. Views of the structural model for the reference building in PERFORM-3D

A rigid diaphragm was incorporated into the model by slaving the horizontal translation degrees of freedom in each floor of the building. To account for the P-Delta effect in the model, a dummy large deformation frame element (column) running throughout the entire height of the building is created (Powell, 2007, Powell, 2010). This column has no lateral stiffness and subjected to an axial load of (P=D+0.25L), where P is the axial load, D is the dead load, and L is the live load. The element nodes are slaved at floor levels at each column end. This creates an additional moment at element ends,

proportional to the lateral displacement. The seismic masses are assigned to the nodes at each storey level in terms of dead load. The base of the structure is rigidly modelled using vertical supports at the top-of-foundation level.

4.4.1 Modelling of piers and core wall segments

The 4-noded fibre-based shear wall element is utilised to model the piers and core wall segments. Only confined concrete is modelled, i.e., the unconfined concrete cover is neglected. Expected strengths of $1.3f_c^{'}$ and $1.17f_y$ are used for concrete and reinforcing steel, respectively (LATBSDC, 2011).

The four-linear segment relation (Figure 4.10a) is used to model the concrete stress-strain relation based on the modified Mander model (Martínez-Rueda and Elnashai, 1997). Having the piers and core wall segments modelled using fibre elements; the effective bending stiffness is not assigned explicitly to the concrete material model as it is the product of the assumed stress-strain relations. Therefore, the effective bending stiffness decreases with increasing fibre strains.

For the steel in tension, the post-yield stiffness and cyclic degradation parameters are defined following adjustments described by Orakcal and Wallace (2006). In compression, buckling of steel rebars is modelled based on experimental results and analytical models from previous studies (e.g. Rodriguez et al., 1999, Bae et al., 2005, Cosenza and Prota, 2006, Tuna, 2012). Reinforcing steel stress-strain relation is shown in Figure 4.10b.

As adopted and verified in CHAPTER 3, the inelastic shear deformation in piers and core wall segments is accounted for by assigning a trilinear relation (Figure 4.10c) similar to the one recommended by ASCE/SEI 41-06 (2007) and ASCE/SEI 41-16 (ASCE/SEI-41, 2017). Test results by Thomsen and Wallace (2004) and calibration study by Gogus (2010) are used to define the shear F-D relation. In the used trilinear relation, the uncracked shear modulus is taken as $0.4E_c$ and diagonal (shear) cracking is assumed to start at $0.25\sqrt{fc'} \leq 0.5v_n$, where v_n is the wall nominal shear strength from the ACI 318 (2014) and f_c' is the concrete expected compressive strength in MPa. The post-cracking slope is reduced to $0.01E_c$ to account for the nonlinear shear deformations due to shear-flexure interaction (Massone, 2006).

4.4.2 Modelling of coupling beams

The coupling beams between the core wall segments are modelled as elastic beam elements with nonlinear displacement shear hinge at mid-span (Figure 4.11), based on test results by Naish et al. (Naish and Wallace, 2010). For obtaining the nominal expected shear capacity, the angle of the diagonal reinforcement in the coupling beam (α) is calculated based on 125mm distance from the centre of gravity of the diagonal reinforcement bundle to the face of the coupling beam.

To define the behaviour of the displacement shear hinge in PERFORM-3D, the displacement of the coupling beam is related to its rotation as described in Eqn. (4.1).

$$\delta_\theta = \theta \times L_{cb} \tag{4.1}$$

Where θ is the coupling beam rotation in radians, L_{cb} is the length of the coupling beam and δ_θ is the equivalent displacement at rotation θ. Figure 4.12 illustrates the backbone parameters alongside the cyclic energy dissipation factors (degradation parameters) used to model the shear displacement hinges for the coupling beams in the reference building.

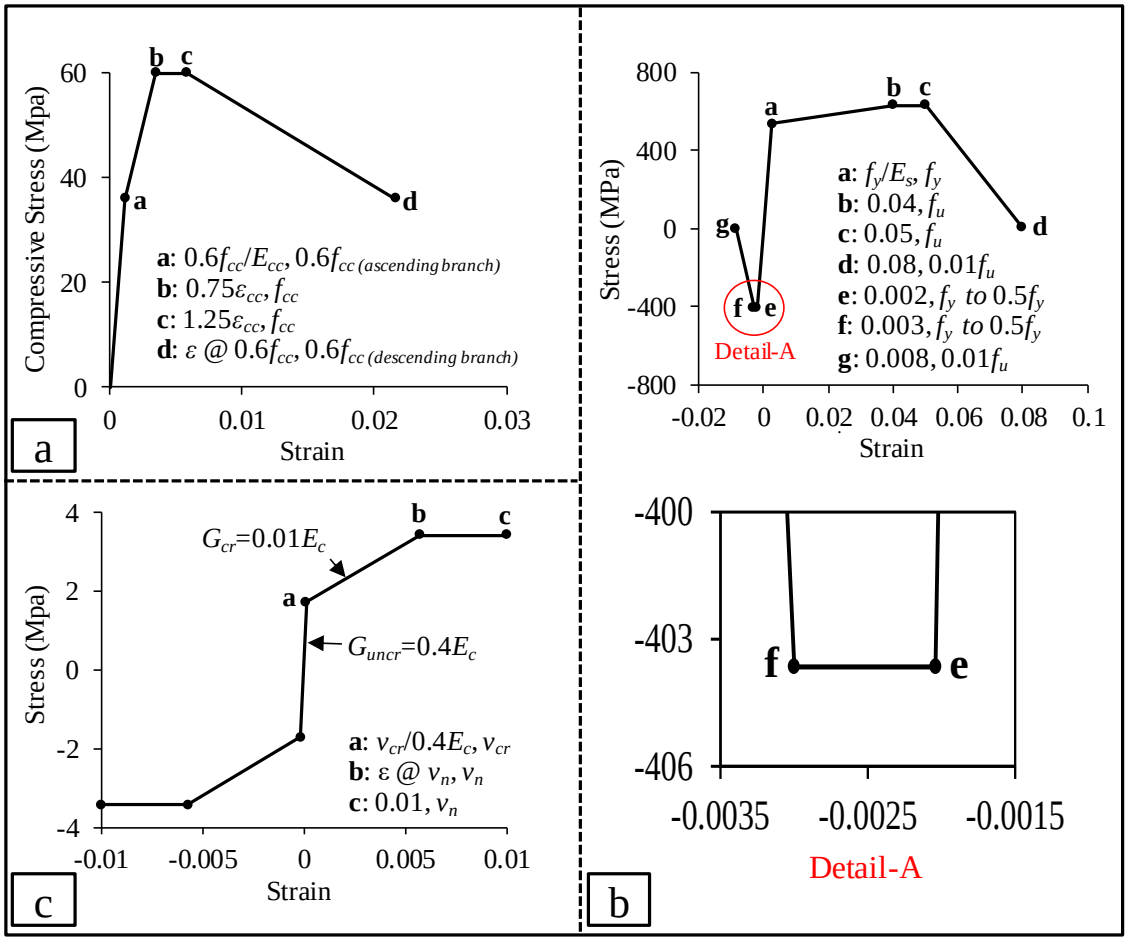

Figure 4.10. General force-deformation relations for the RC walls: (a) confined concrete; (b) reinforcing steel; and (c) wall inelastic shear behaviour

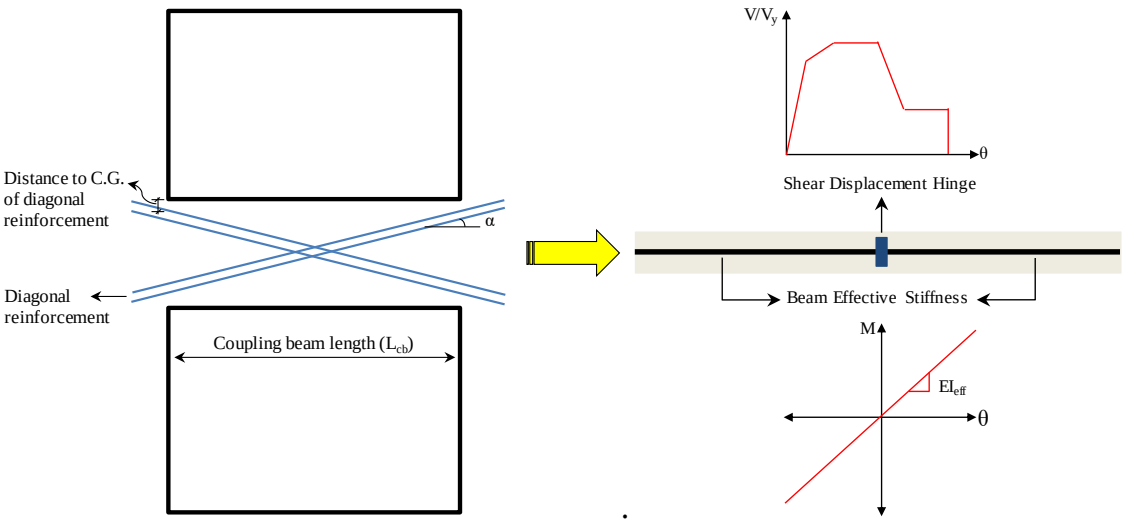

Figure 4.11. Typical coupling beam modelling in PERFORM-3D

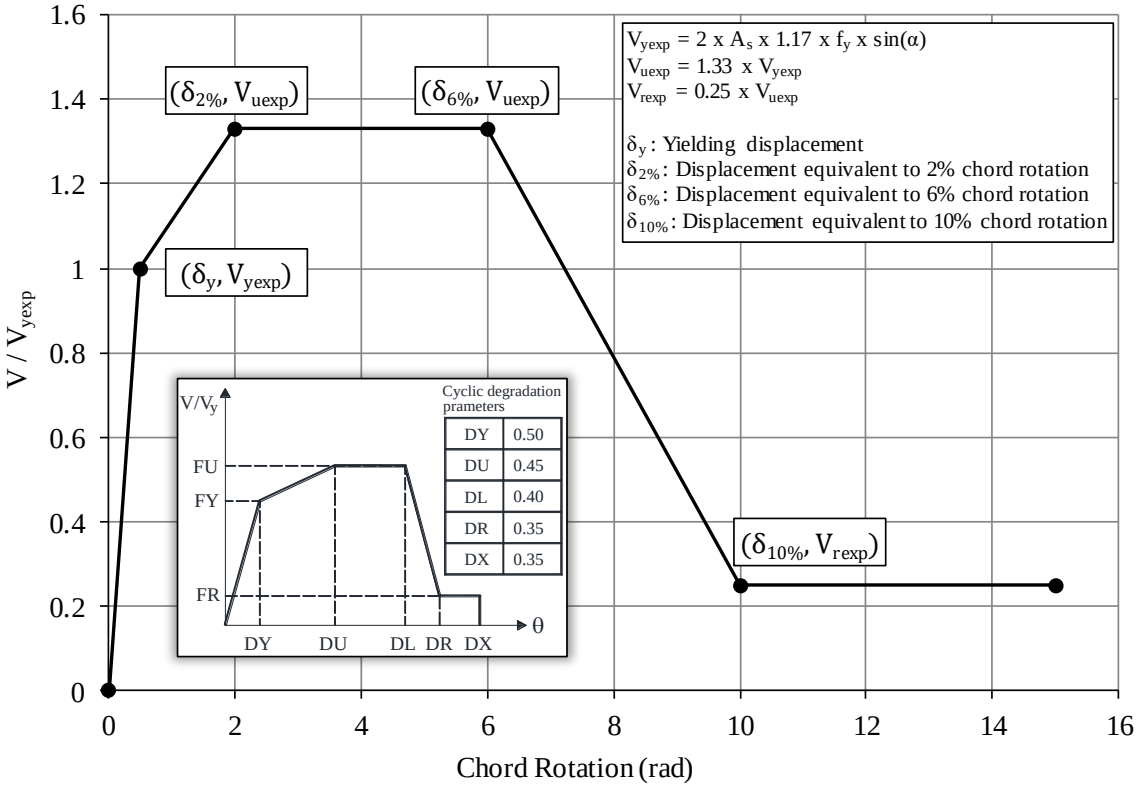

Figure 4.12. Shear displacement hinge backbone curve alongside cyclic degradation parameters

4.4.3 Modelling of floor slabs

The 2-noded fibre-based frame element is used in modelling the floor slabs. The total width of the element cross-section is taken as 8.4m; half the slab span from each side of the piers. To establish a rigid connection between the slabs and the piers/core, additional (embedded) beams are used (CSI, 2011). The embedded beams have a very stiff section for bending in the plane of the wall but very small axial, torsional and out-of-plane bending stiffnesses to avoid artificially stiffening the walls.

4.4.4 Damping

Viscous damping in the first translational mode (fundamental mode) is accounted for by using an initial stiffness-based modal damping with 0.5% damping ratio. For computing higher mode damping, the following relationship is adopted: $\xi_i = 1.4\,\xi_{i-1}$, where ξ_i is the damping ratio of the i-th mode (Satake et al., 2003). Accordingly, the damping ratios for the next five translational modes are set to 0.7%, 1.0%, 1.4%, 1.9% and 2.7%, respectively. In addition, and to stabilize less important (higher frequency) modes, a small amount (0.1%) of Rayleigh damping is added to the model (Powell, 2007, CSI, 2011).

4.5 Concluding remarks

This chapter provided all the input data for the analysis of a case study high-rise RC building in Dubai (UAE), a region that is vulnerable to different earthquake scenarios. The results of the analysis will be used in the subsequent chapters to develop/demonstrate the framework for the seismic vulnerability assessment of RC high-rise wall buildings.

CHAPTER 5. Seismic scenario-structure-based limit state criteria for RC high-rise wall buildings using net inter-storey drift

As a result of population growth and consequent urbanisation, the number of high-rise buildings is rapidly growing worldwide resulting in increased exposure to multiple-scenario earthquakes and associated risk. The wide range in frequency contents of possible strong ground motions can have an impact on the seismic response, vulnerability and limit state criteria definitions of such structures. In this chapter, new, reliable SSSB definitions of limit state criteria for RC high-rise wall buildings are proposed. The 30-storey reference building is utilised to illustrate the methodology for defining the limit state criteria. The building is designed following modern seismic code provisions and then modelled with PERFORM-3D using the nonlinear fibre-based approach as discussed in CHAPTER 3. Uncertainty in ground motions is accounted for by the selection of forty real earthquake records representing the two seismic scenarios

in which the study region is vulnerable to (CHAPTER 4). Seismic scenario-based building local response at increasing earthquake intensities is mapped using MRIDAs with an improved scalar IM. NISD is selected as a global DM based on the outcome of the mapping process and a parametric study involving seven buildings ranging from 20-50 storeys. This DM is used to link local damage events, including shear, in the reference building to global response under different seismic scenarios. While the study concludes by proposing SSSB limit state criteria for the reference building, the proposed limit state criteria are applicable to comparable RC high-rise wall buildings and seismic regions.

5.1 Introduction

With changing socioeconomic conditions, rapid population growth and urbanisation, many cities all over the world have expanded rapidly in recent years. This expansion has led to a massive increase in high-rise buildings and to the spread of cities to multiple-scenario earthquake-prone regions. This increases exposure to seismic risk. A risk which to quantify and mitigate, a better understanding of the hazard and vulnerability is required.

The majority of high-rise buildings in most countries employ RC piers and core walls as the primary lateral force-resisting system due to their effectiveness in providing the strength, stiffness and deformation capacity needed to meet the seismic demand. The trend to increasingly use RC in high-rise buildings is expected to continue due to the development of commercial high-strength concrete and new advances in construction technologies (Ali and Moon, 2007). Quantitative definitions of limit state criteria form the spine to seismic vulnerability assessment and consequently to the seismic risk analysis and mitigation for RC high-rise wall buildings. These definitions require mathematical representations of local DIs, such as deformations, forces or energy, corresponding to designated structural response levels. Therefore, a suitable DM needs to be adopted to sufficiently correlate local damages (events) in the building to its global response.

The broad range of frequency content in real strong ground motions, representative of different seismic scenarios such as distant and near-field earthquakes, can impose different levels of excitation on both fundamental and higher modes in RC high-rise wall structures. This can result in more complex, seismic scenario-based inelastic

response. Another special issue in RC high-rise wall buildings is the definition of limit state criteria corresponding to predefined performance levels since there are several factors affecting the failure modes. Among these factors are building height, axial force levels, supplementary regulations introduced by local authorities, and local trends in design and construction. For buildings with fundamental mode-dominated response, the taller the building, the larger is the expected TISD at specified performance levels. For high-rise wall buildings, especially at lower storeys, axial compressive force levels are influenced by the arrangement of the RC shear walls and cores in the building. This arrangement is usually dominated by gravity loads, particularly for internal shear walls. High compressive loads are expected to delay the onset of initial cracking and yielding in vertical elements but can decrease ductility and hence the TISD at which concrete core crushing and rebar buckling occur. Finally, the supplementary regulations of local authorities, as well as the trends adopted by both consultants and contractors, may impact the design and hence the seismic performance. For instance, the minimum steel ratio in vertical elements may exceed the value that is stated in code provisions.

Adopting the methodology presented in CHAPTER 2, new, reliable SSSB definitions of performance limit state criteria for RC high-rise wall buildings are proposed in this chapter. Following a brief introduction, this chapter presents in detail: (i) a discussion on the main parameters of the conducted MRIDAs including a proposition for an improved scalar IM; (ii) the mapping of seismic scenario-based building local response; (iii) relating local response to the ground motion characteristics; (iv) the selection of a suitable DM to correlate local to global response; (v) the proposal for new SSSB performance limit state criteria for the reference building and RC high-rise wall buildings in similar seismic regions. This chapter ends with a summary of the work and concluding remarks. Figure 5.1 summarises pictorially the flowchart for obtaining the SSSB limit state criteria proposed in the current work.

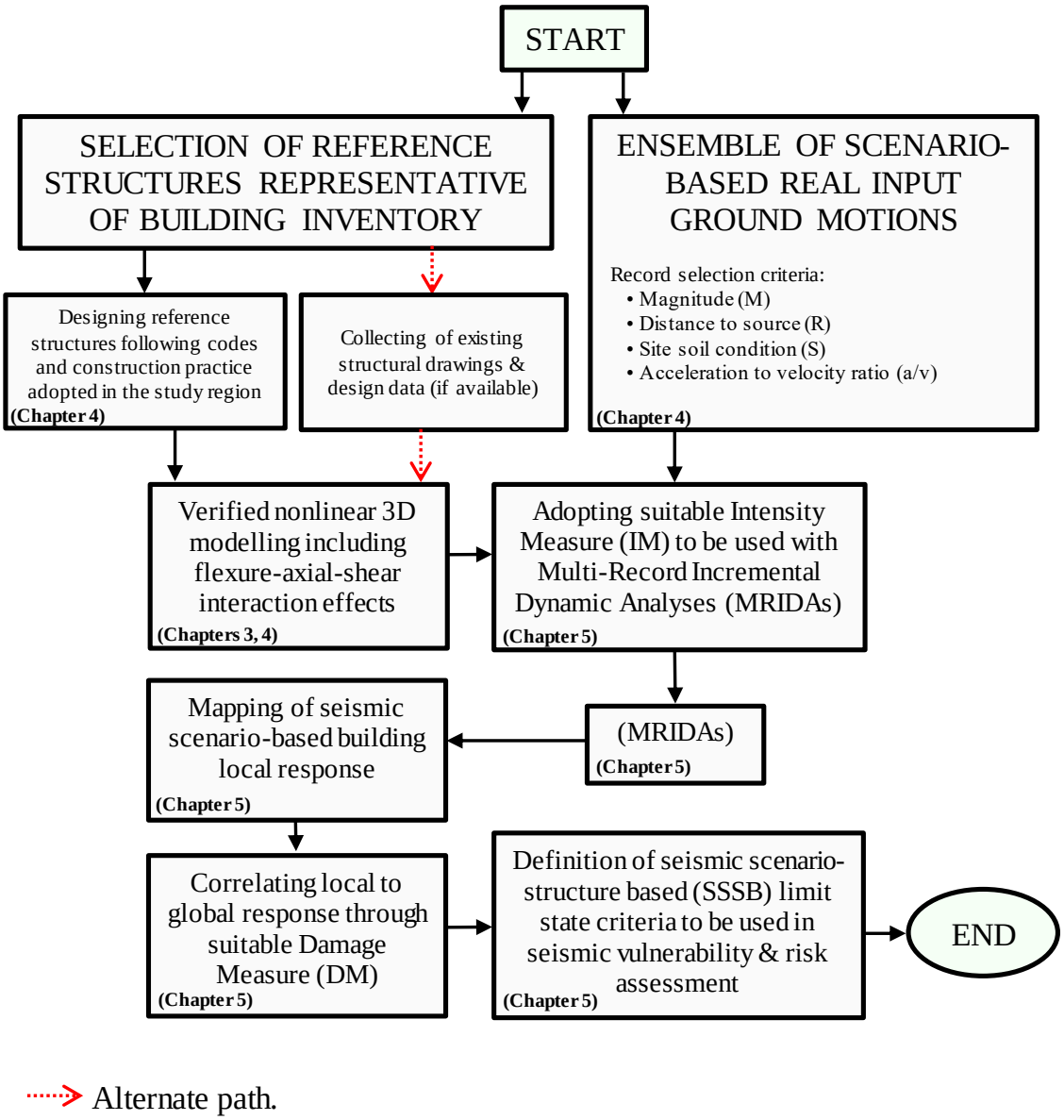

Figure 5.1. Flowchart for obtaining the proposed SSSB limit state criteria for RC high-rise wall buildings

5.2 Multi-record incremental dynamic analysis

For the purpose of defining SSSB performance limit state criteria for the reference building, MRIDAs are performed using the two sets of records assembled in CHAPTER 4. To construct IDA curves that can sufficiently and efficiently represent the variable states of the response of the structure to different earthquake records with increasing intensities, a suitable ground motion intensity measure needs to be defined. PGA was used to be the most accepted intensity measure. The elastic spectral acceleration at the fundamental period of the structure, $S_a(T_1)$, or S_a in short, has been found to be more efficient since it is structure-dependent and become a frequently used intensity measure for low- to mid-rise buildings. However, S_a is neither suited for tall buildings (Shome,

1999, Vamvatsikos and Cornell, 2002) nor for structures subjected to near-source earthquakes (Luco and Cornell, 2007). Other intensity measures have been proposed in the literature in an attempt to overcome the major shortcomings of S_a, namely discounting the contribution of the higher modes and fundamental period lengthening associated with stiffness degradation in the structure (Shome, 1999, Carballo and Cornel, 2000, Cordova et al., 2000). New approaches have led to other kinds of intensity measures such as inelastic spectral value-based scalar intensity measures (e.g. Luco and Cornell, 2007) and vector-valued intensity measures (Bazzurro and Cornell, 2002, Conte et al., 2003, Baker and Cornell, 2005). These approaches, though promising, are not easy to apply since they require probabilistic seismic hazard assessment based on custom-made attenuation laws to obtain the joint hazard curve.

In a comprehensive study by Kappos and Kyriakakis (2000), the problem of reducing scatter in the seismic response calculated using NRHA with natural records was reevaluated. In this study, a total of seven IMs were investigated, namely: PGA, PGV, Arias Intensity, (Root-Mean Square) Acceleration "RMS Acceleration", Spectrum Intensity (i.e. area under the pseudo-velocity spectrum), Root-Mean Square Acceleration "RMSA", and the Fajfar et al. (1990) PGV-duration combined IM "I_v". Two sets of ground motions were used, representing two different seismotectonic environments (Greece and California). The study comprised two parts, the first focused on the scaling effect on both strength and displacement spectra, while the second part addressed the problem in the context of response variability in MDOF systems with a focus on multistorey frames. The first part of the study concluded that in the intermediate and long period ranges, any of the three velocity-related IMs (PGV, SI, and I_v) can be adopted to good effect. In case of systems with ductility factor >1, it is concluded that the use of SI scaling along with entire period range leads to a reasonably low scattering in both strength and displacement spectra, with the coefficient of variation (COV) hardly exceeding 0.5 within any zone of practical interest. In the second part of the study, an alternative scaling method (narrow-band spectrum intensities calculated on the basis of elastic and inelastic pseudo-velocity spectra) was proposed. The study revealed that, from the practical point of view, both proposals based on the narrow-band SI concept lead to COV values between 0.1 and 0.4 in the calculated drifts and member ductilities.

The concept of using average acceleration values over a certain period range as an intensity measure in probabilistic seismic demand assessment was introduced in previous studies. However, different approaches were followed in the averaging process as well as in estimating the period range. To account for the elongation of the structural periods due to the post-yield behaviour (inelasticity) of RC members, the period range used to define the intensity measure is normally bracketed by values corresponding to a fractional and a multiple of the fundamental uncracked period of the structure. In the study of Cordova et al. (2000), a two-parameter scalar IM that accounts for the period lengthening was proposed. The proposed IM was calculated as $S_a(T_1)\left[\frac{S_a(cT_1)}{S_a(T_1)}\right]^{\alpha}$, where c and α are parameters estimated by the response calibration of four, relatively long-period frame structures (Three composite moment frames and one steel space frame) to two sets of eight ground motions. The number of storyes of the used structures was ranging between 6 to 12. The values of c and α resulted from the study were 2 and 0.5, respectively. Vamvatsikos and Cornell (2005a) developed scalar and vector IMs for efficient estimation of limit state capacities through MRIDAs. The study showed that by using the developed IMs on three frame structures (5-, 9-, and 20-storey), significant dispersion reduction was realised. The results revealed the most influential spectral regions/periods for each limit state and building, illustrating the evolution of such periods as the seismic intensity and the structural response increase up to the global collapse. For the 20-storey structure with higher modes having a significant effect on the response, the study revealed that as damage increases (reaching global collapse), the optimal period that produces the least dispersion of the IM capacity values was somewhere in the middle of first and second mode uncracked periods. In the studies of Bianchini (2008) and Bianchini et al. (2009), the geometric mean of spectral acceleration ordinates ($S_{a,avg}$) over a certain range of periods was used as an intensity measure to predict the inelastic structural response of buildings subjected to strong ground motions. $S_{a,avg}$ was calculated using ten points logarithmically-spaced in a period range of (T_1-T_n), where both T_1 and T_n were tied to the uncracked fundamental period of the structure (T). T_1 and T_n were calculated such that $T_1 = k_l T$ and $T_n = k_u T$, where k_l and k_u are constants representing lower and upper bounds, respectively, relative to T. The studies of Bianchini have shown that $S_{a,avg}$ is a better intensity measure than both the elastic spectral acceleration at fundamental period ($S_{a(T)}$) and the peak ground acceleration (PGA), especially for inelastic structural systems with long periods as it takes into account both higher modes effect and period elongation. Several other studies

related to spectral acceleration-based IMs are available in the literature (e.g. Kurama and Farrow, 2003, Baker and Cornell, 2004, Mehanny, 2009, Bojórquez and Iervolino, 2011).

In the present study, an improved scalar intensity measure termed spectral acceleration at weighted-average period $S_{a(wa)}$, is proposed. Using the 10% POE in 50-years UHS for the study region, the weighted-average period (T_{wa}) is the period linked to the spectral acceleration value that represents the average of the spectral acceleration ordinates pinned to the equivalent inelastic period of the first three modes of vibration weighted by their corresponding mass participation ratios (MPR). The procedure of calculating the $S_{a(wa)}$ of the reference building is illustrated in Figure 5.4a. $S_{a(wa)}$ is calculated using Eqn. (5.1) below:

$$S_{a(wa)} = \frac{\sum(S_{ai} * MPR_i)}{\sum MPR_i} \tag{5.1}$$

Where i is the mode of vibration number (i = 1 to 3), S_{ai} is the spectral acceleration ordinate corresponded to the equivalent inelastic period of the i^{th} mode of vibration, and MPR_i is the mass participation ratio corresponding to the i^{th} mode of vibration. The proposed intensity measure follows the average spectral acceleration concept discussed above, yet with a different technique in bracketing the period interval and defining the points within the chosen range of periods. The 1^{st} mode equivalent inelastic period (around 1.40 of the uncracked fundamental period), calculated using the reduced stiffnesses given in Table 4.7, is employed as a bracket to account for the elongation due to the post-yield behaviour (stiffness degradation) of the reference building.

To illustrate the suitability of the 1^{st} mode equivalent inelastic period to account for the period elongation of the structure at the post-yield zone, two examples are given hereunder. The first example (Figure 5.2) shows the 1^{st} mode period propagation of the shake table-tested seven-storey full-scale RC wall structure utilised in the MLNMVS in CHAPTER 3, while the second (Figure 5.3) illustrates the 1^{st} mode period propagation of the 30-stoery reference building. It is worth noting that the detailed mapping of the 30-stoery reference structure is presented in Section 5.3 hereafter. In Figure 5.2, the uncracked fundamental period of the test structure was measured as 0.51s (Table 3.1) and estimated as 0.50s from the PERFORM-3D model (Figure 3.26). The equivalent inelastic 1^{st} mode period of the test structure is calculated as 0.84s using

the reduced stiffnesses presented in Table 4.7, while the 1st mode cracked period at yield, considered to be corresponding to the seismic intensity where the first yield at the tested web wall occurred, is calculated as 0.67s using the Fourier Transformation Analysis (FTA). To arrive at this seismic intensity, EQ3 shake table input motion is down-scaled by a scale factor of 0.65. In the second example (30-storey reference building), the uncracked fundamental period (Period #1 in Figure 5.3) is calculated as 3.21s (Table 4.9). Using FTA, the cracked period at first yield in core walls (Period #2 in Figure 5.3) and the period corresponding to the CP-related 1st steel buckling in core walls (Period #4 in Figure 5.3) are calculated as 4.13s and 4.87s, respectively. The equivalent inelastic period (Period #3 in Figure 5.3) is calculated as 4.46s (Table 4.9) using the reduced stiffnesses in Table 4.7. In both examples, the calculated equivalent inelastic period falls between the cracked period at yield and the CP-related period.

The structural characteristics of the building are not only represented by the equivalent inelastic fundamental period but also with the equivalent inelastic periods of higher modes (2nd and 3rd). Furthermore, the dynamic characteristics of the building are accounted for by weighting the spectral acceleration values that are corresponding to the first three modes' equivalent inelastic periods to their respective mass participation factors. It is noteworthy that the weighted-average period (T_{wa}) estimated in the current work is in-line with what was proposed in previous studies for long-period structures (e.g. Vamvatsikos and Cornell, 2005a).

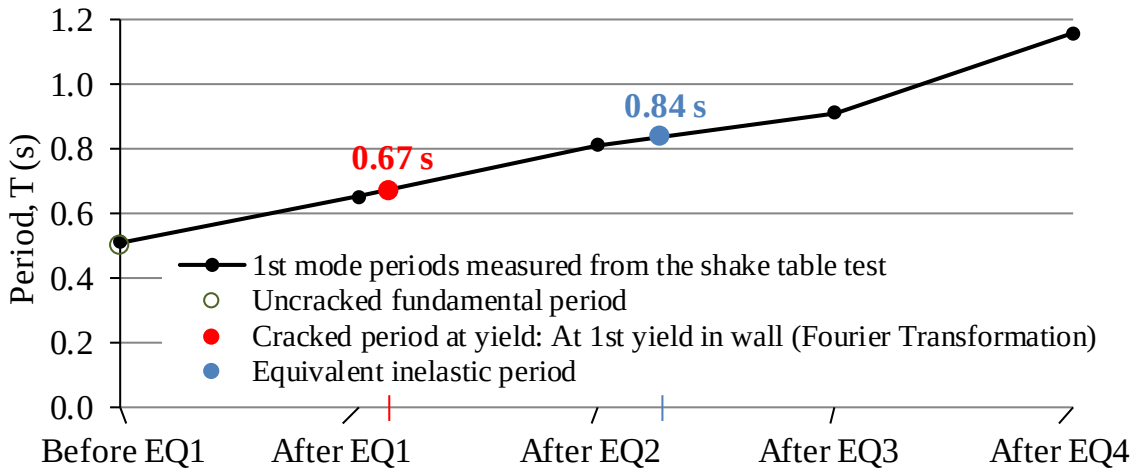

Figure 5.2. Seven-storey test structure: 1st mode period propagation

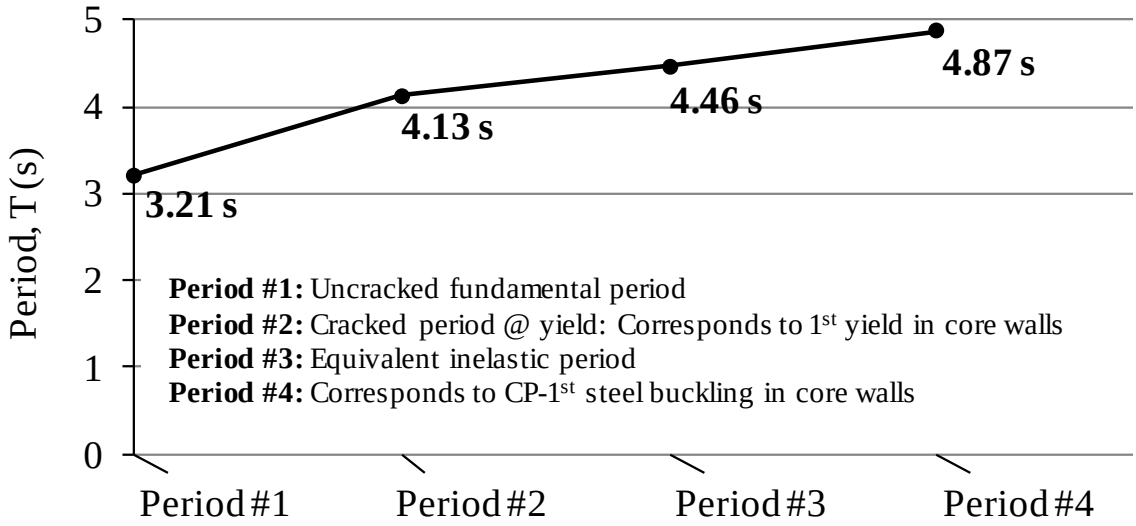

Figure 5.3. 30-storey reference building: 1st mode period propagation under R#5 of Record Set #1

The response spectra of the two sets of records used in the present study are anchored to their mean spectral acceleration at the calculated T_{wa} (2.54s) and their accelerograms are scaled accordingly. The proposed IM has higher efficiency compared to S_a as it takes into account both the impact of higher modes and period elongation. It is also a more efficient IM compared with the approach that relies on approximate upper and lower period bounds rather than using the actual inelastic periods of the structure (e.g. Bianchini, 2008). Figure 5.4b and Figure 5.4c depict the elastic response spectra for the two sets of records when anchored at the T_{wa}. Each of the 40 records associated with the anchored response spectra is then appropriately scaled up.

Although the reference building is assessed with MRIDAs using the 40 selected records, and due to the large number of monitored DIs, one earthquake record is selected from each set of records to map the response of the reference building. These are: (i) The 7.13M Hector Mine Earthquake of 16th October 1999 recorded at the CGS 12026 Indio-Coachella Canal station in California USA (R#5 in Record Set#1); and (ii) The 5.77M Coalinga-05 earthquake of 22nd July 1983 recorded at USGS 1606 Burnett Construction station in California USA (R#3 in Record Set#2). As can be seen in Figure 5.5, the reason for choosing these records is that their IDA curves match reasonably well with the 50% fractile of the IDA curves obtained from each of the two sets of records. Figure 5.6 and Figure 5.7 depict the ground motion time histories (ground acceleration, ground velocity, and ground displacement) for records R#5 from Record Set#1 and R#3 from Record Set#2, respectively.

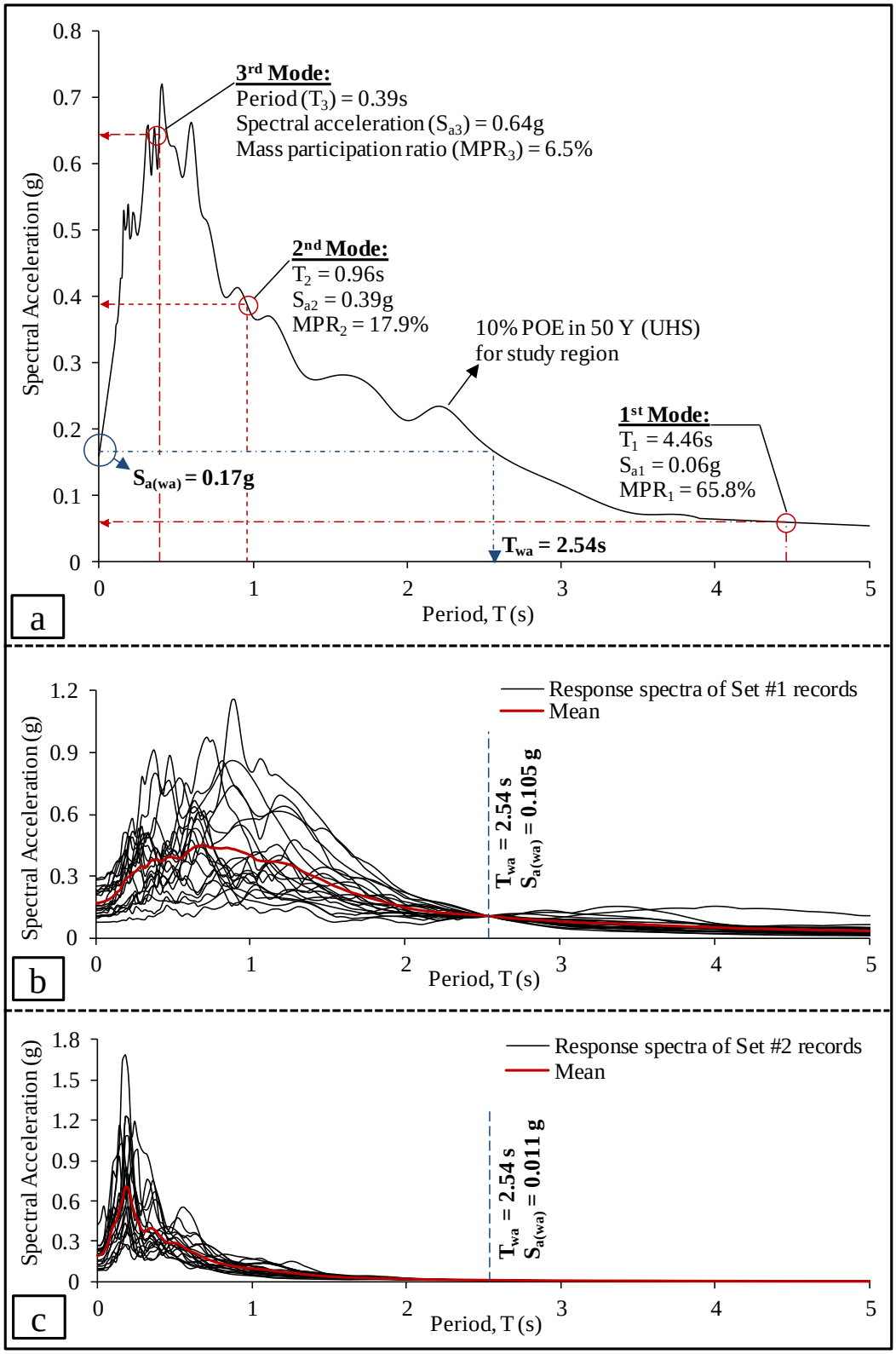

Figure 5.4. Proposed improved scalar IM: (a) calculation of weighted-average period (T_{wa}); (b) response spectra for Record Set#1 anchored to the proposed IM; and (c) response spectra for Record Set#2 anchored to the proposed IM

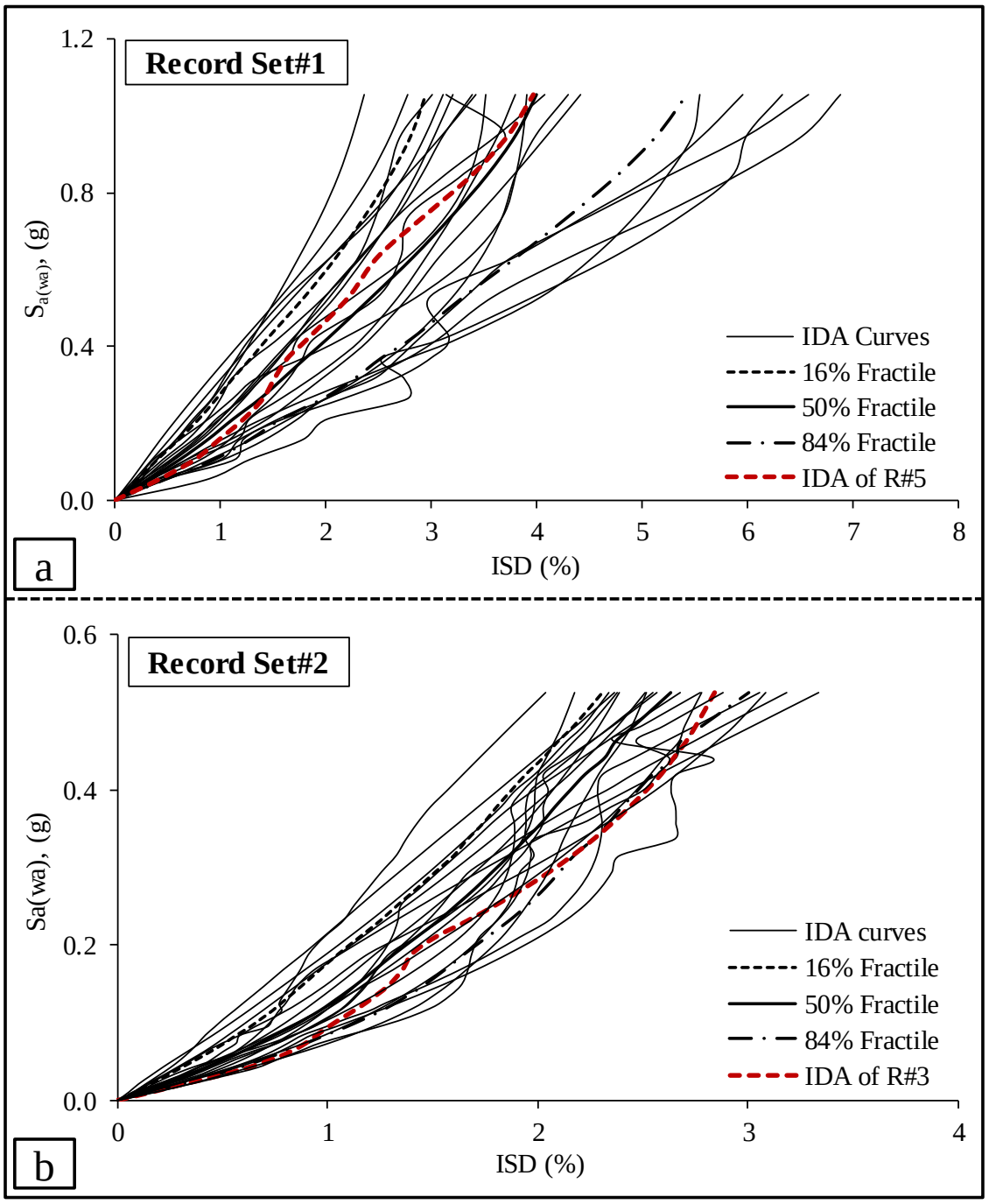

Figure 5.5. IDA curves of the reference building along with their 16%, 50%, 84% fractile curves and selected records to represent the 50% fractile: (a) under Record Set#1; and (b) under Record Set#2

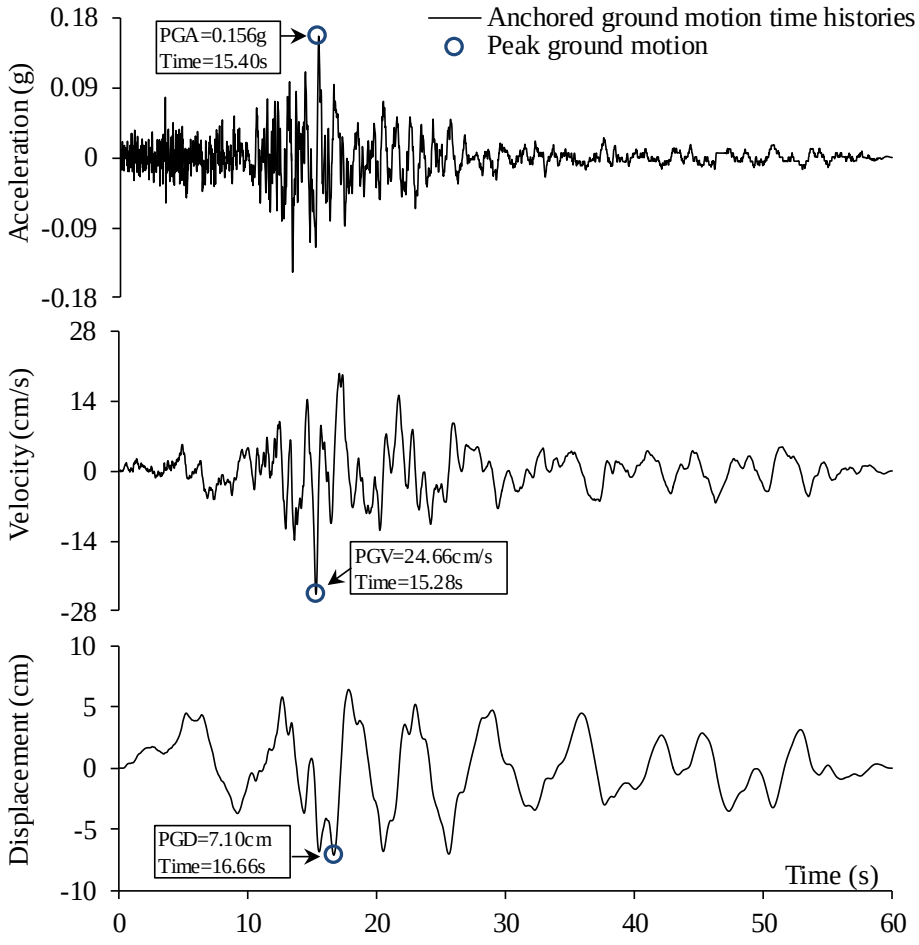

Figure 5.6. R#5 of Record Set#1: Anchored ground acceleration, ground velocity, and ground displacement time histories

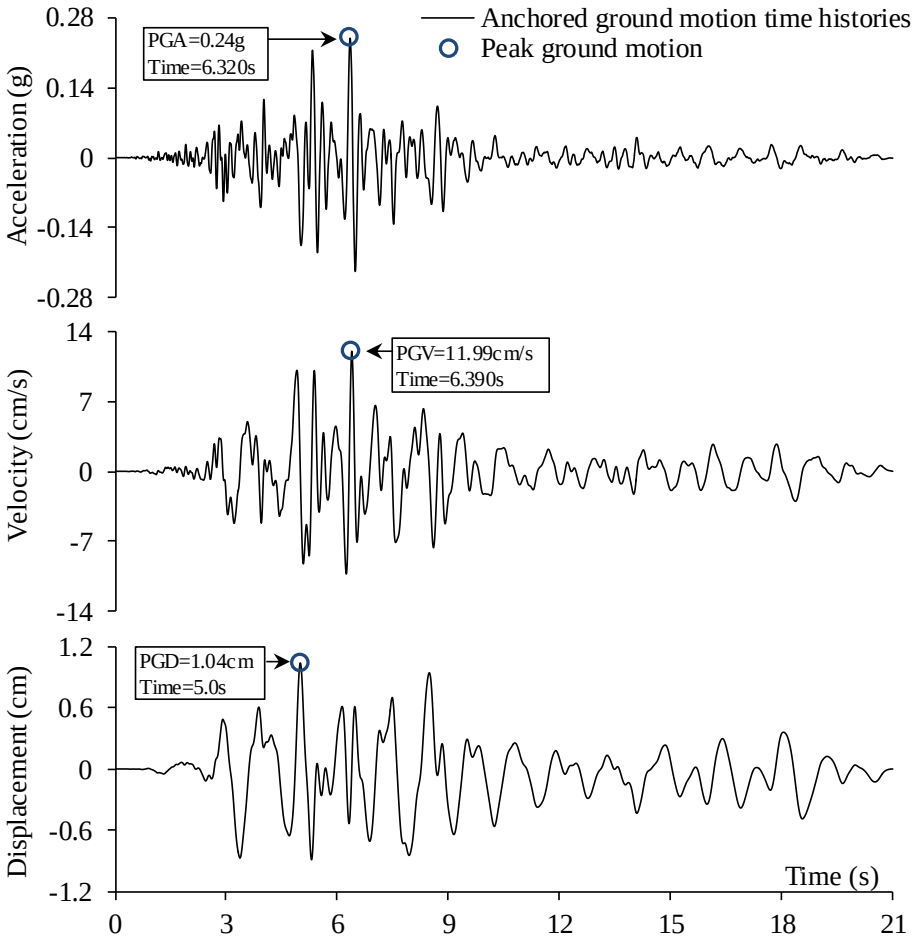

Figure 5.7. R#3 of Record Set#2: Anchored ground acceleration, ground velocity, and ground displacement time histories

5.3 Mapping of seismic scenario-based building local response

To determine the SSSB quantitative performance limit state definitions for the reference building, a total of seven local DIs are mapped during the MRIDAs (Table 5.1). At every time step of the MRIDAs, demand values of deformations and forces corresponding to the mapped DIs are estimated. The estimated demands are used to calculate the capacity over demand (C/D) ratios which are then, as appropriate, used to check whether a predefined limit state is exceeded. The mapped DIs are briefly discussed in the following sub-sections.

Table 5.1. Local DIs adopted in the mapping of the reference building response

Local Damage Index (DI)	Description
1st Rebar Yield-H	First yielding in steel rebars of RC slabs
1st Rebar Yield-V	First yielding in steel rebars of RC walls
Wall Rotation	Exceeding rotation limits for RC walls according to ASCE/SEI 41-06 (Table 6.18)
Coupling Beam Rotation	Exceeding rotation limits for RC coupling beams according to ASCE/SEI 41-06 (Table 6.18)
1st Steel Buckling	First buckling in steel rebars of RC walls
1st Concrete Crushing	First crushing in the confined concrete zone of RC walls
Exceedance of Shear Capacity	Exceeding shear capacity in wall segments

5.3.1 Strains in concrete and reinforcing steel bars

The tensile strain of the reinforcing steel bars in the RC slabs is monitored using two approaches: (i) specifying monitored reinforcing steel fibres at the extreme top and bottom points (where the strains have maximum values) of the slab cross-section in the elements that represent the slab ends; and (ii) average curvature over the plastic zone length in the slab, estimated as 10% of the total slab length running between the pier and the core (ASCE/SEI-41, 2007). The second approach (average curvature) is employed to verify the practicality of the strain values obtained using the first approach (monitored fibres) as the maximum calculated strain (or curvature) may get progressively larger in elements with relatively small length. This is because for inelastic behaviour, the beam theory predicts very large localized curvatures (strains) at the points of maximum bending moments, usually at the beam (slab) ends.

In the RC piers and core wall segments, tensile strain in steel rebars, as well as compressive strains in both steel and concrete, are monitored using monitored fibres (approach "i" above). Strain gauge elements at the wall end (Figure 3.10a) are also used to verify the strain values estimated at the monitored fibres. When using strain gauge elements, strain calculations are based on the wall vertical nodal displacement and mesh geometry. Considering the deformed shape of the wall segment in Figure 5.8, axial strain values at the right and left sides can be obtained as $\varepsilon_{(2-4)} = \frac{(Dis_{V2} - Dis_{V4})}{h_w}$ and $\varepsilon_{(1-3)} = \frac{(Dis_{V1} - Dis_{V3})}{h_w}$, respectively, where Dis_V.is the vertical displacement at the wall segment node and h_w is the wall segment height.

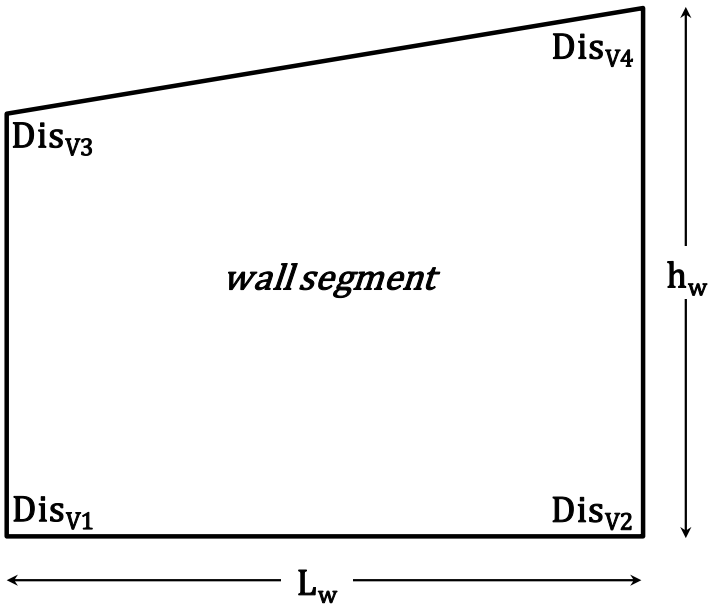

Figure 5.8. Elevation view of the deformed wall segment

Yielding strain capacity of reinforcing steel bars is calculated as 0.00269 based on an expected tensile strength of 538MPa and a steel modulus of elasticity of 200GPa (point "a" in Figure 4.10b), while the rebar fracture strain capacity is set to 0.05 (point "c" in Figure 4.10b), (PEER/ATC, 2010). In compression, the strength degradation in steel rebars is assumed to start at a strain of 0.003, a value corresponding to the spalling of surrounding concrete (point "f" in Figure 4.10b). The maximum compressive strain reached in steel rebars (ε = 0.008), calculated based on the stirrups spacing to longitudinal rebar ratio (e.g. Bae et al., 2005), is considered as the steel rebar buckling threshold (point "g" in Figure 4.10b). Previous studies have used a similar range of steel rebar buckling strain values (between 0.005 and 0.01), depending on the stirrups

spacing to longitudinal rebar ratio (e.g. Ghodsi and Ruiz, 2010, Tuna, 2012). Finally, the crushing strain of confined concrete is taken as the strain value at 60% of the peak confined concrete strength on the descending branch of the Mander stress-strain curve (point "d" in Figure 4.10a).

5.3.2 Rotation in coupling beams and wall segments

Rotation in coupling beams is estimated using the 2-noded rotation gauge element. The rotation demand is calculated as the rotation at End J of the beam element minus the rotation at End I (Figure 3.10b). Like the beam element, the 2-noded rotation gauge has local axes 1, 2 and 3, where the calculated rotation is about axis-3. A positive rotation corresponds to a positive moment about axis-3 in the coupling beam element. In the wall segments, the rotation is calculated using the 4-noded rotation gauge element shown in Figure 3.11. The gauge rotation is the rotation of the side KL minus the rotation of the side IJ, where side rotation is positive clockwise. Hence, positive gauge rotation corresponds to tension on the side IK and compression on the side JL. It is worth noting that all deformation (strain and rotation) gauge elements in PERFORM-3D do not add any stiffness or strength to the structure.

For each predefined performance limit state, the rotation capacity of the coupling beams and wall segments in the reference structure is set following table 6-18 of ASCE/SEI 41-06 (2007). In the wall segments, Table 6-18 of ASCE/SEI 41-06 relates the rotation capacity to the shear and axial force demands in the wall. Since the wall rotation gauge in the adopted version of PERFORM-3D has constant rotation capacities that are unrelated to the axial and shear demands, a post-processor was created for this study to monitor the axial and shear demand levels in each wall segment at every time step of the MRIDAs, where the rotation capacity is adjusted accordingly.

5.3.3 Shear capacity in wall segments

Using the "structural section" feature in PERFORM-3D, the shear capacity in piers and core wall segments of the reference building is assessed throughout the MRIDAs taking into account the shear strength degradation depending on the level of nonlinear flexural deformation (Wallace, 2010, Tuna, 2012). Pairs of normalised shear demand and curvature ductility in wall segments are pinned at each time step and checked against a trilinear trend line and a flat line as predefined envelopes. The trilinear trend line shown in Figure 5.9, representing the median shear strength of structural walls from a previous

test (Tuna, 2012), is anchored at the shear strength of $1.5V_n$ for curvature ductility less than 2 (Orakcal et al., 2009), linearly reduces to $0.75V_n$ at curvature ductility of 8, while it remains constant for larger values of curvature ductility. The flat line, on the other hand, represents the upper shear strength limit of $0.83\sqrt{f'_c}$ given by the ACI 318 (2014).

For curvature ductility calculation, the following procedure is adopted and presented in Figure 5.8 and Eqns (5.2) to (5.4). This procedure is repeated for each wall element.

$$\text{curvature } \varphi = \frac{\varepsilon_{(2-4)} - \varepsilon_{(1-3)}}{L_w} \tag{5.2}$$

$$\text{yield curvature } \varphi_y \approx \frac{0.00269}{L_w} \tag{5.3}$$

$$\text{curvature ductility } = \frac{\varphi}{\varphi_y} \tag{5.4}$$

Where φ is curvature, φ_y is yield curvature, ε is strain, and L_w is the wall length. For the presentation of the reference building response, the storeys are labelled as in Figure 5.10, with the first storey (1st S) assigned to the 2nd basement, second storey (2nd S) assigned to the 1st basement, third storey (3rd S) assigned to the ground floor and so on. The roof of the building is labelled as the thirtieth storey (30th S).

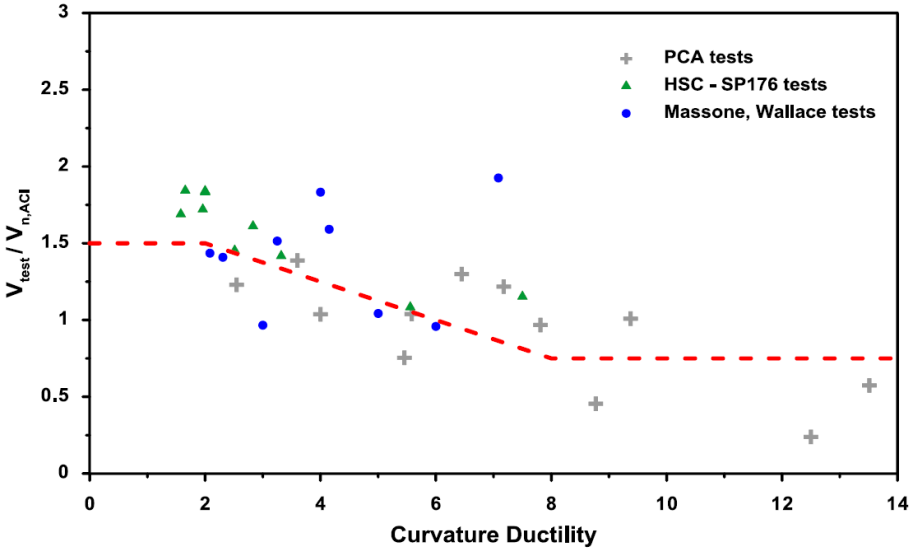

Figure 5.9. Shear failure criterion for structural walls from previous tests (Tuna, 2012)

Figure 5.11 to Figure 5.18 and Figure 5.19 to Figure 5.26 present the response of the reference building to R#5 and R#3, respectively. Figure 5.11 to Figure 5.26 are organised based on performance levels as IO (Figure 5.11, Figure 5.12, Figure 5.19, and Figure 5.20); LS (Figure 5.13 and Figure 5.21); and CP (Figure 5.14 to Figure 5.18 and Figure 5.22 to Figure 5.26).

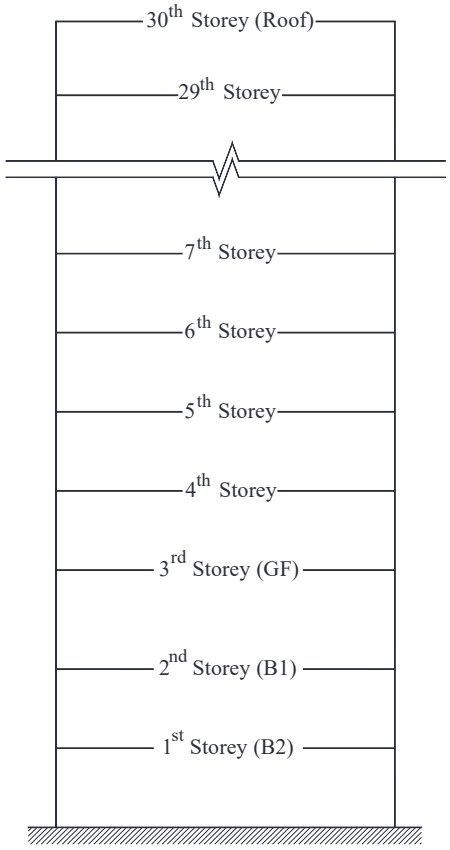

Figure 5.10. Storey labelling for the reference building

The main observations from Figure 5.11 to Figure 5.26 are:

- For both records, first yielding in steel rebars of RC flooring system occurred at the storey where maximum differential vertical displacement developed between slab ends (Figure 5.11c and Figure 5.19c). This is not necessarily the storey associated with maximum ISD, as will be shown later.

- For R#5, the event sequence starts with yielding in the slab at $S_{a(wa)}$=0.13g/PGA=0.20g (Figure 5.11), followed by the following events in the wall: yielding (Figure 5.12), exceedance of LS rotation limit (Figure 5.13), rebar buckling (Figure 5.15), concrete crushing (Figure 5.16), exceedance of CP rotation limit (Figure 5.14), and finally exceedance of shear capacity at

$S_{a(wa)}$=0.84g/PGA=1.25g (Figure 5.17). All events occurred within the lower five storeys of the building except for the slab yielding which occurred at the 24th storey. As above, the event sequence for R#3 starts with yielding in the slab at $S_{a(wa)}$=0.06g/PGA=1.43g (Figure 5.19) followed by yielding in the wall (Figure 5.20). However, the sequence of the other events in the wall conspicuously differs with exceedance of shear capacity next (Figure 5.25), followed by rebar buckling (Figure 5.23), exceedance of LS rotation limit (Figure 5.21), concrete crushing (Figure 5.24), and ends with exceedance of CP rotation limit at $S_{a(wa)}$=0.34g/PGA=7.64g (Figure 5.22). In R#3, the yielding events in slab and wall occurred at higher storeys; 28th storey and 21st storey, respectively, while all other events occurred within the lower five storeys of the building.

- For R#5, the shape of the relative lateral displacement plot at the onset of the sequence of events indicates a first mode-dominated response (Figure 5.11c to Figure 5.16c). However, the second mode appears responsible for the exceedance of the wall shear capacity event (Figure 5.17c). On the contrary, for R#3, the shape of the relative lateral displacement plots indicate that the building response is controlled by the second mode (Figure 5.19c and Figure 5.21c to Figure 5.24c) except for wall yielding and shear capacity exceedance where the response is dominated by the third mode (Figure 5.20c and Figure 5.25c). This is further discussed in Section 5.5.

- By post-processing the time history results, it is observed that the potential failure in wall segments when shear capacity is exceeded under the two records differs in nature. The time history of normalised shear demand and curvature ductility curves for the concerned wall segment at the 1st storey and the storey where the shear capacity is exceeded under R#5 and R#3 are plotted in Figure 5.18 and Figure 5.26, respectively. Under both records, the maximum shear demand has occurred at very low curvature ductility; 0.61/0.41 in 1st storey/2nd storey under R#5, and 0.059/0.055 in 1st storey/3rd storey under R#3. Notwithstanding, the walls in the 1st and 2nd storeys under R#5 developed a considerable amount of curvature ductility (4.64 and 1.80, respectively) prior to the exceedance of shear capacity, while under R#3, the maximum curvature ductility in the walls at the 1st and 3rd storeys was less than 1.0 (0.44 and 0.25,

respectively). This indicates that under R#5, shear failure is preceded by flexural yielding in walls, giving the chance to flexure-related damages (strains and or rotations) to occur first. While under R#3, wall segments in the concerned storeys remain elastic (curvature ductility < 1) over the entire time history of the record at the seismic intensity level corresponding to shear failure. This observation is further analysed in Section 5.5.

- For both seismic scenarios, at the onset of each of the damage events in the walls, seismic demands (strain/rotation/shear) reduce with building height, diminishing at the top five storeys (Figure 5.12(a, b) to Figure 5.17(a, b) and Figure 5.19(a, b) to Figure 5.25(a, b)). This trend is inconsistent with the fact that these top storeys are showing maximum overall TISDs during the damage sequence. This is examined further in the next section.

As one of the considered DIs in the current study, the overall nonlinear rotation of the coupling beams is monitored throughout the entire range of the adopted seismic intensity levels under both R#5 and R#3. Figure 5.27a shows that under R#5, the beam rotation exceeded the ASCE/SEI 41-06 limit for IO limit state (0.006 rad) at higher seismic intensity level (PGA=0.55, $S_{a(wa)}$=0.37g) compared to the ones corresponding to other IO DIs such as first yield in slabs (PGA=0.20g, $S_{a(wa)}$=0.13g) and first yield in walls (PGA=0.31g, $S_{a(wa)}$=0.21g). Under this record, the ASCE/SEI 41-06 rotation limits for LS and CP limit state (0.018rad and 0.03rad, respectively) were not reached even at the highest considered seismic intensity level in the current study (PGA=1.87g, $S_{a(wa)}$=1.27g). Similar results are observed under R#3 (Figure 5.27b), with beam rotation exceeding IO and LS limits at higher intensity levels compared to the intensities marking the exceedance of other related DIs. Under this record, the rotation limit associated with CP has never been reached even at the highest considered seismic intensity level.

The above indicates that, for diagonally-reinforced coupling beams such as the ones used in the reference building, potential damage due to earthquakes is insignificant to have any influence on the definition of limit state criteria. Similar conclusions were also drawn from previous studies (Tuna, 2012). It is noteworthy that in the case study building, the coupling beams only connected core walls. The rotation may be higher for coupling beams connecting shear walls.

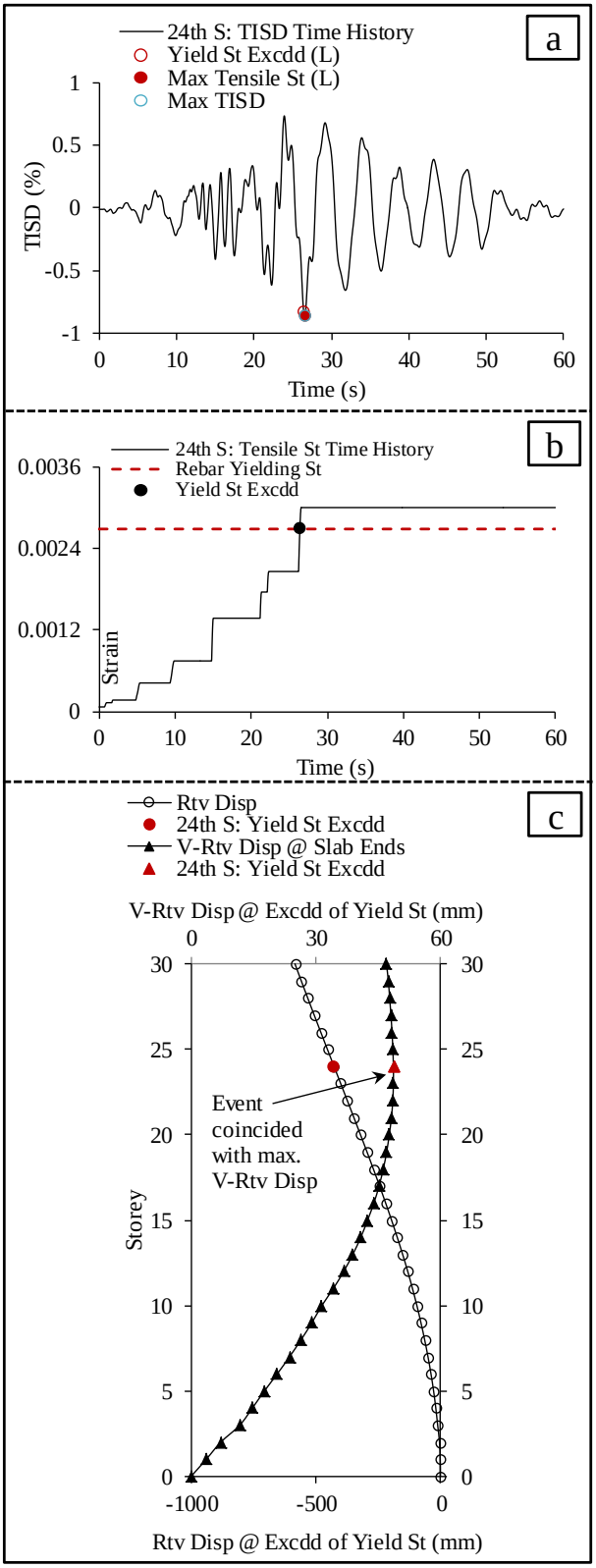

Figure 5.11. Rebar yielding in slabs under R#5 of Record Set#1 (IO): (a) TISD time history at event level; (b) slab rebar tensile strain time history at event level; and (c) relative lateral and vertical displacement envelopes in slab ends over building height at the time of event occurrence

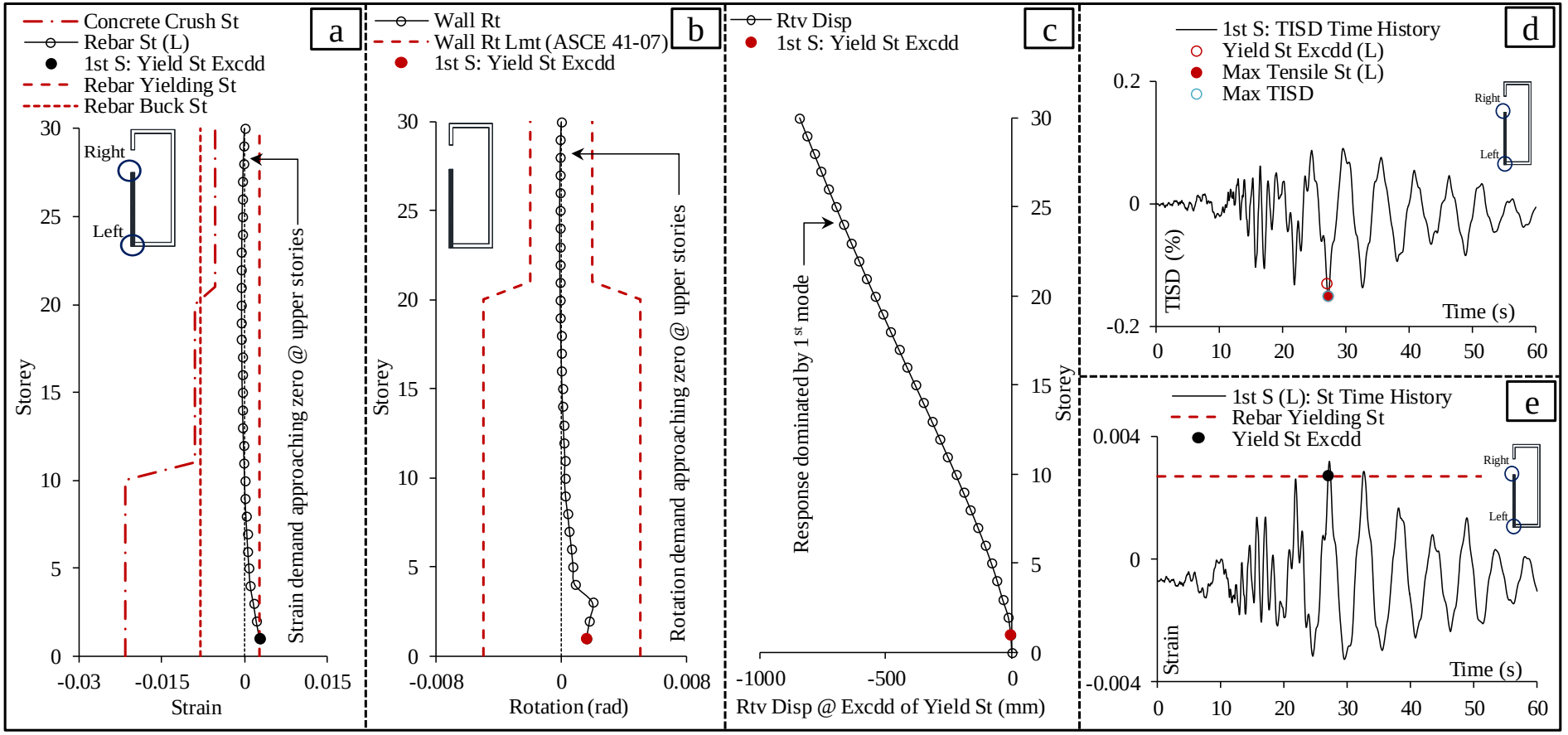

Figure 5.12. Rebar yielding in walls under R#5 of Record Set#1 (IO): (a) rebar strain envelope in the wall segment over building height at the time of event occurrence; (b) rotation envelope in the wall segment over building height at the time of event occurrence; (c) relative lateral displacement envelope in the wall segment over building height at the time of event occurrence; (d) TISD time history in the wall segment at event level; and (e) rebar strain time history in the wall segment at event level

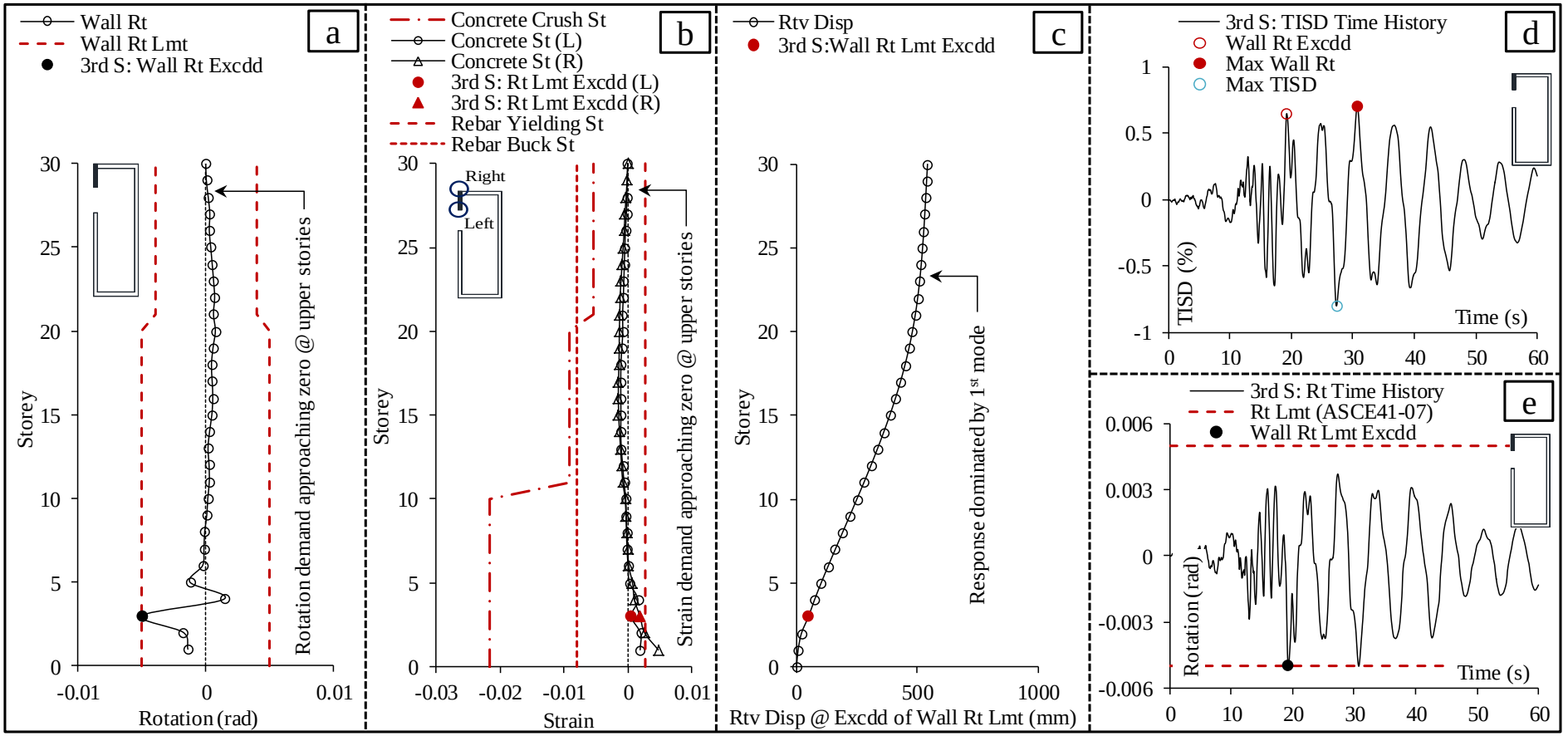

Figure 5.13. Rotation in walls under R#5 of Record Set#1 (LS): (a) rotation envelope in the wall segment over building height at the time of event occurrence; (b) strain envelope in the wall segment over building height at the time of event occurrence; (c) relative lateral displacement envelope in the wall segment over building height at the time of event occurrence; (d) TISD time history in the wall segment at event level; and (e) rotation time history in the wall segment at event level

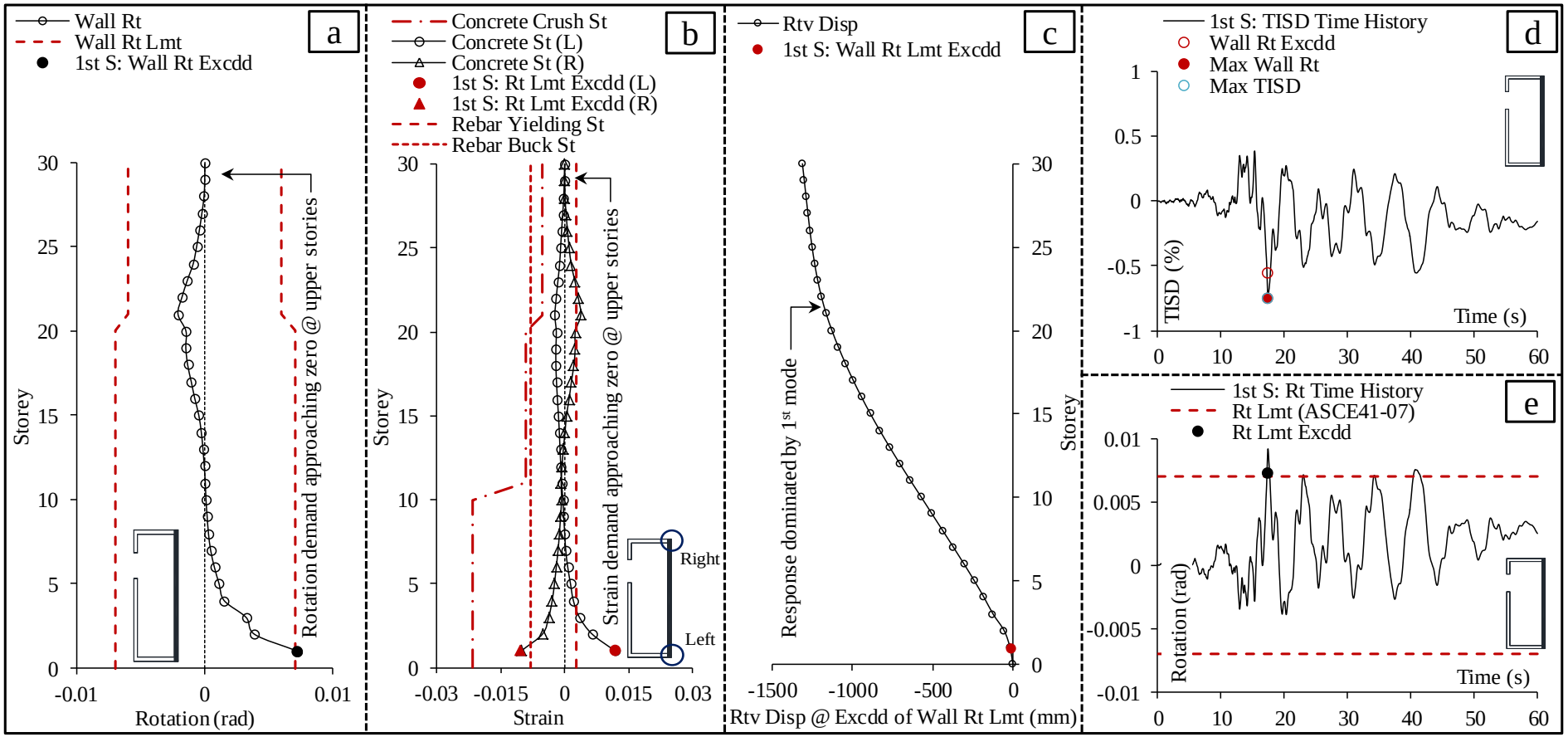

Figure 5.14. Rotation in walls under R#5 of Record Set#1 (CP): (a) rotation envelope in the wall segment over building height at the time of event occurrence; (b) strain envelope in the wall segment over building height at the time of event occurrence; (c) relative lateral displacement envelope in the wall segment over building height at the time of event occurrence; (d) TISD time history in the wall segment at event level; and (e) rotation time history in the wall segment at event level

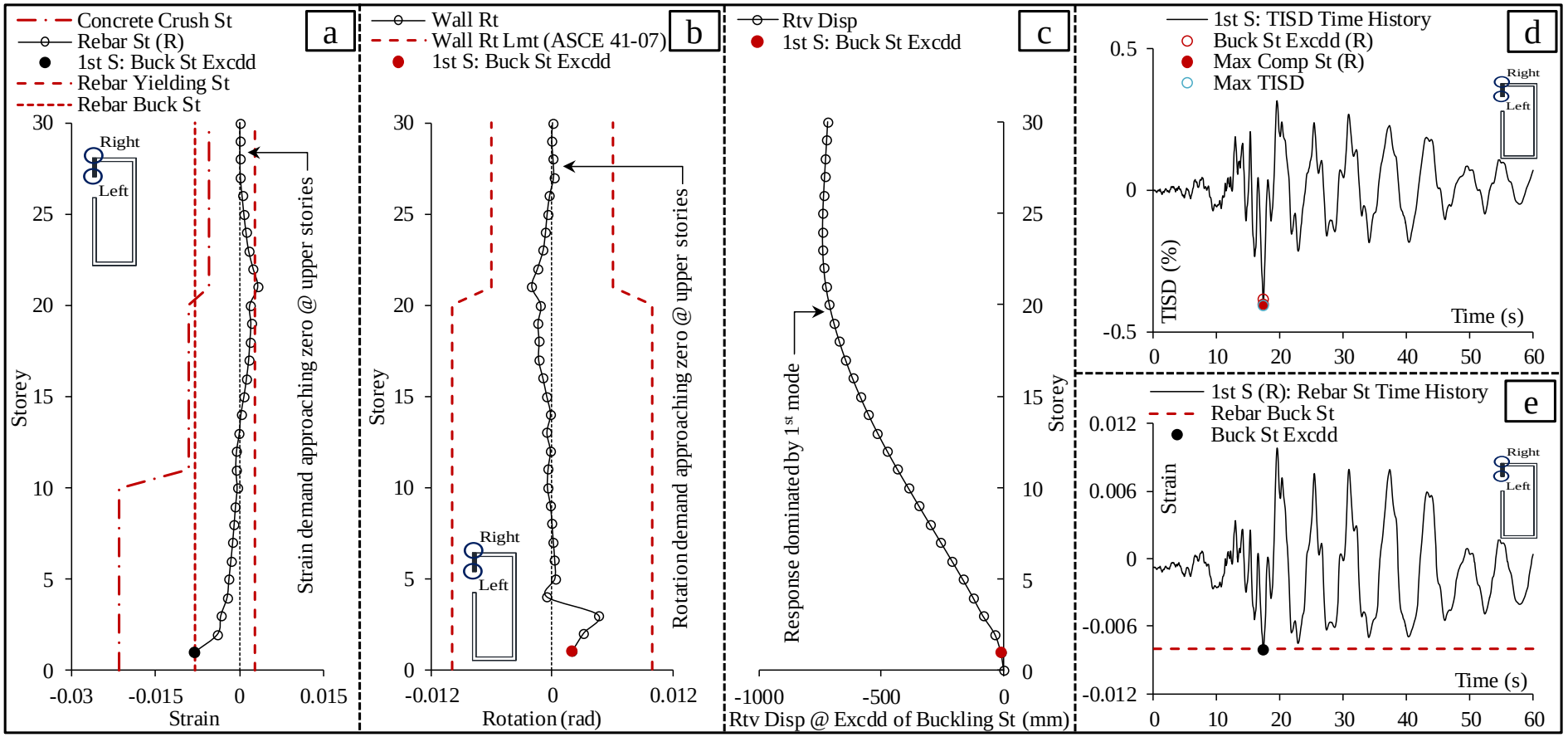

Figure 5.15. Rebar buckling in walls under R#5 of Record Set#1 (CP): (a) rebar strain envelope in the wall segment over building height at the time of event occurrence; (b) rotation envelope in the wall segment over building height at the time of event occurrence; (c) relative lateral displacement envelope in the wall segment over building height at the time of event occurrence; (d) TISD time history in the wall segment at event level; and (e) rebar strain time history in the wall segment at event level

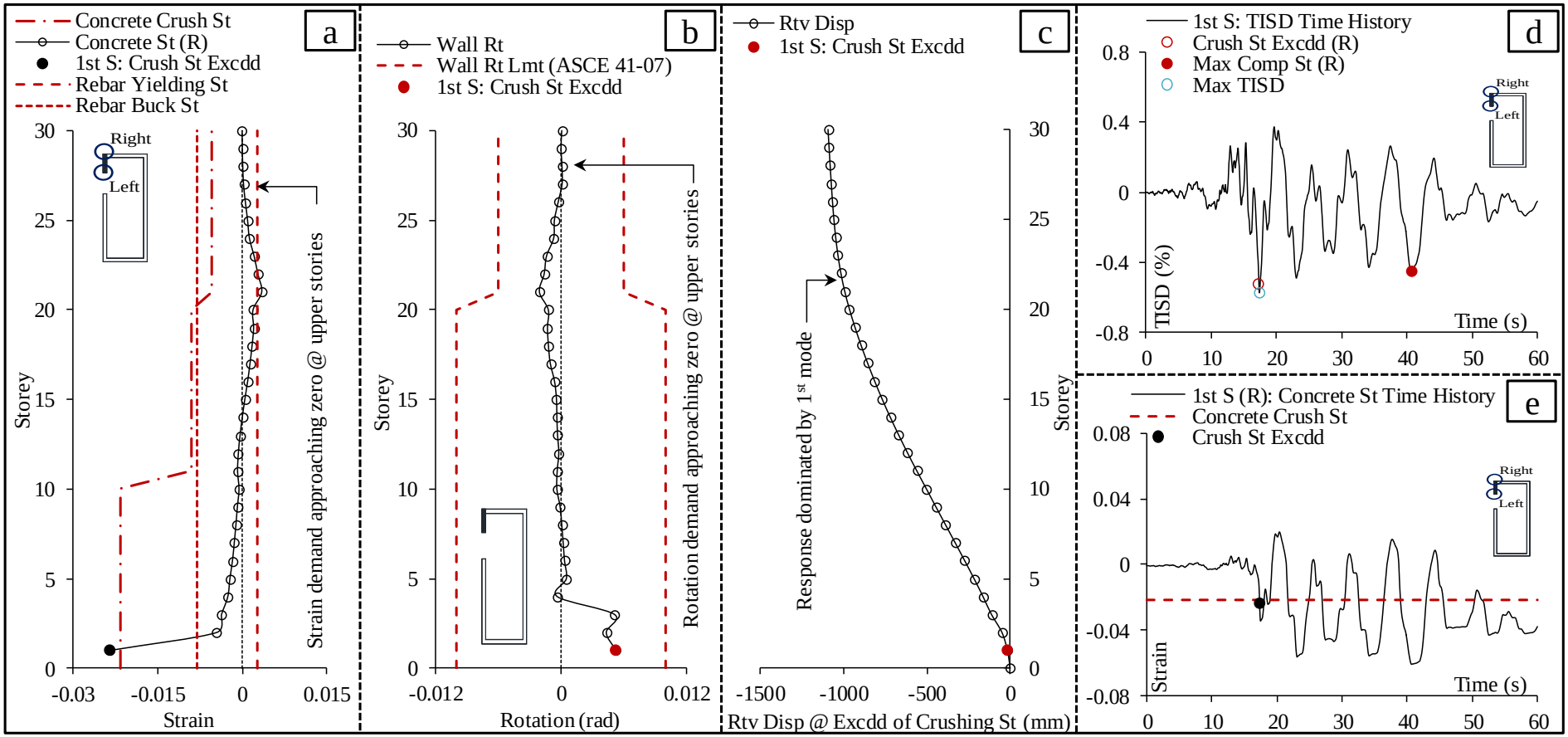

Figure 5.16. Concrete crushing in walls under R#5 of Record Set#1 (CP): (a) concrete strain envelope in the wall segment over building height at the time of event occurrence; (b) rotation envelope in the wall segment over building height at the time of event occurrence; (c) relative lateral displacement envelope in the wall segment over building height at the time of event occurrence; (d) TISD time history in the wall segment at event level; and (e) concrete strain time history in the wall segment at event level

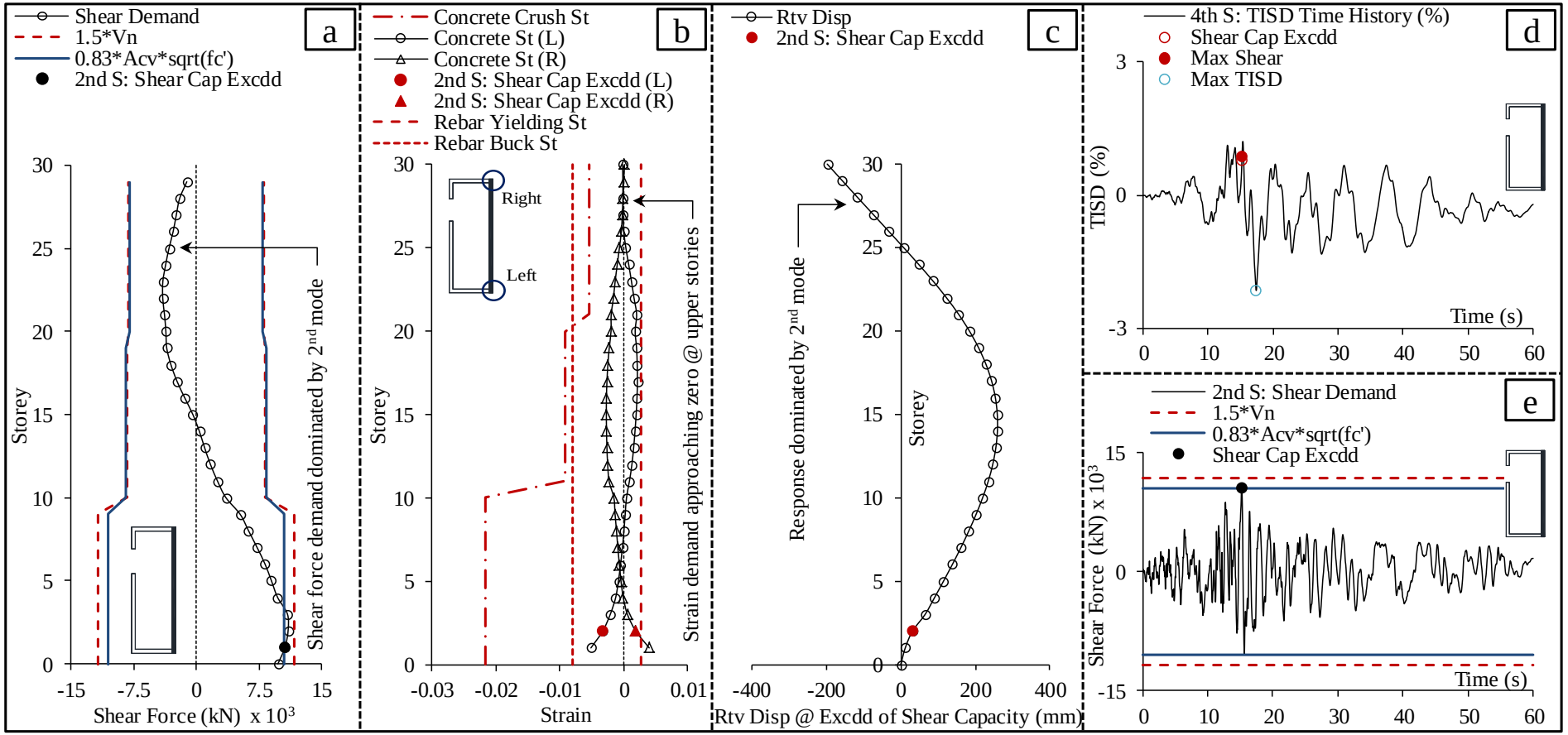

Figure 5.17. Shear capacity exceedance in walls under R#5 of Record Set#1 (CP): (a) shear force envelope in the wall segment over building height at the time of event occurrence; (b) concrete strain envelope in the wall segment over building height at the time of event occurrence; (c) relative lateral displacement envelope in the wall segment over building height at the time of event occurrence; (d) TISD time history in the wall segment at event level; and (e) shear force time history in the wall segment at event level

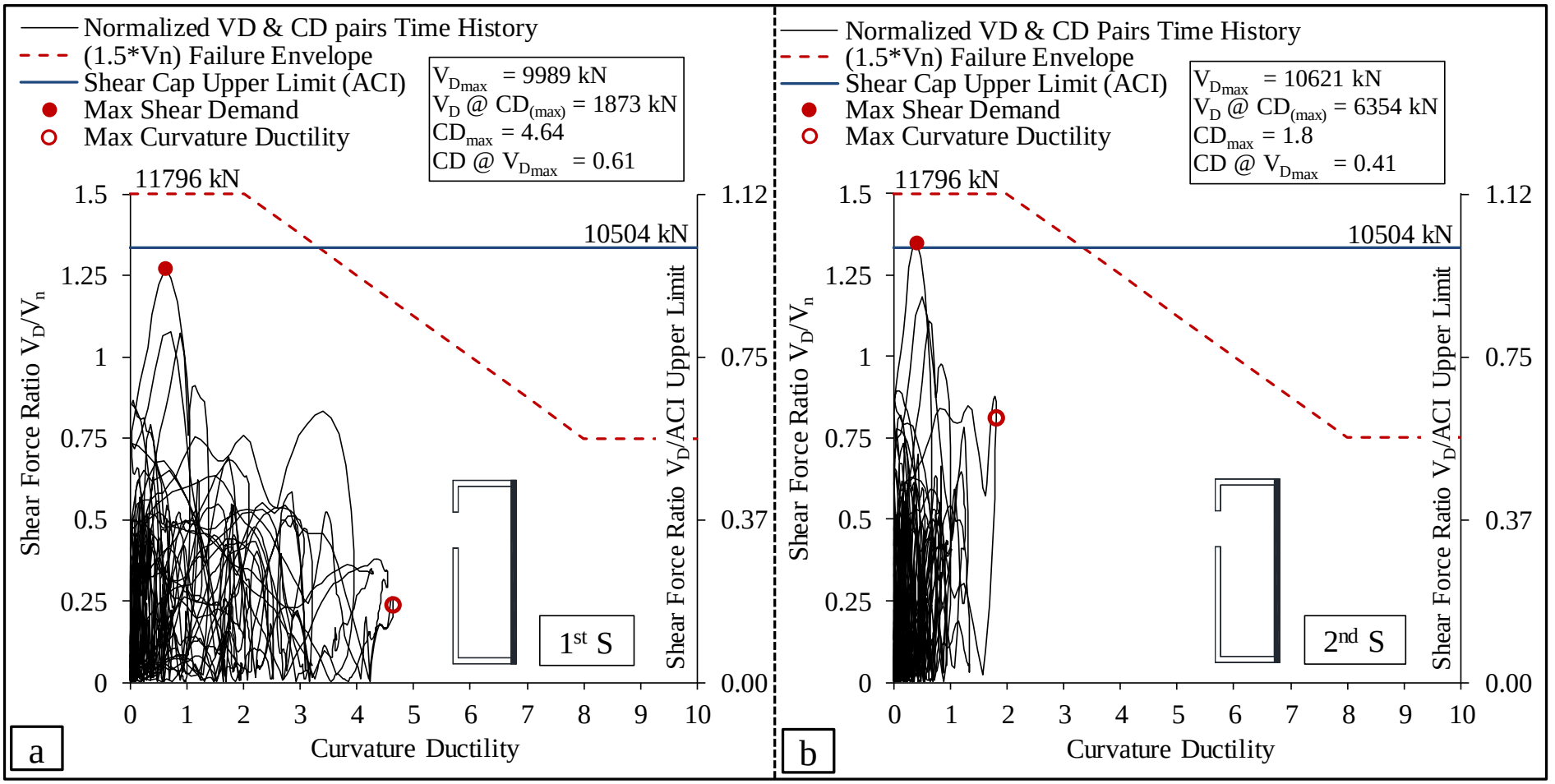

Figure 5.18. Time history of normalised shear force and curvature ductility pairs in walls under R#5 of Record Set#1 (CP): (a) 1st storey; and (b) 2nd storey

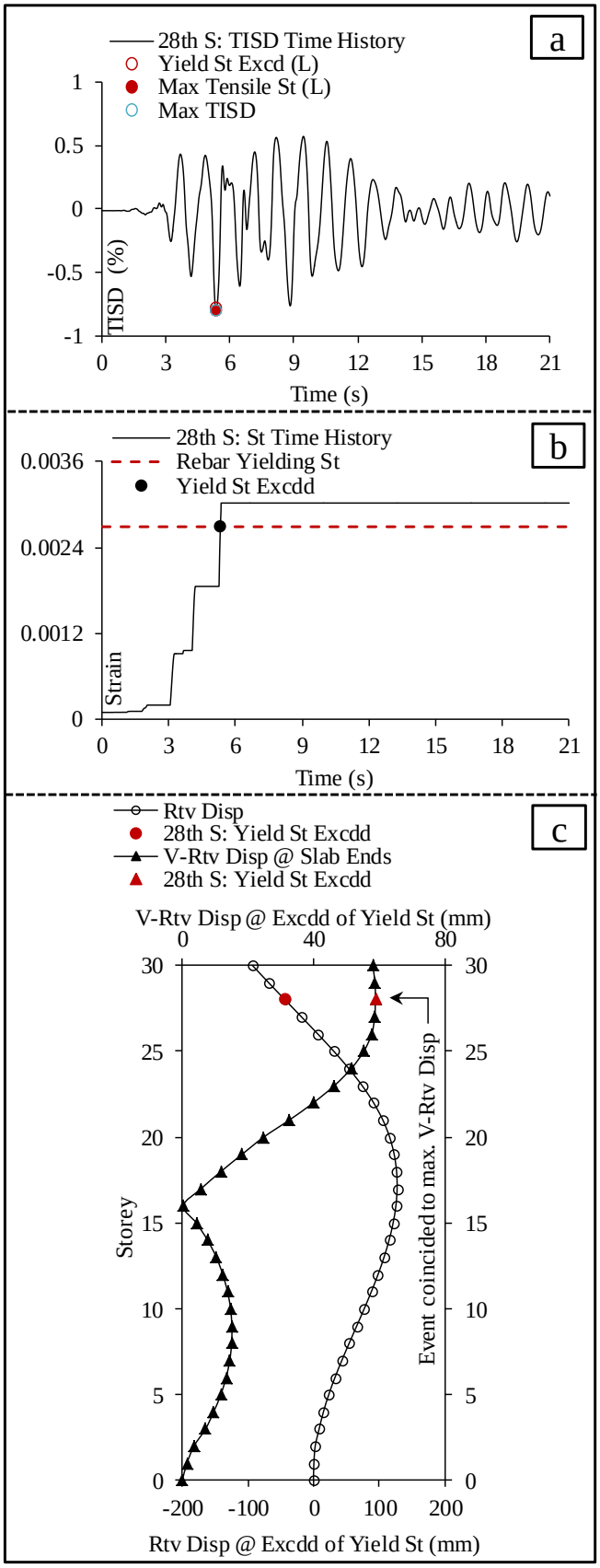

Figure 5.19. Rebar yielding in slabs under R#3 of Record Set#2 (IO): (a) TISD time history at event level; (b) slab rebar tensile strain time history at event level; and (c) relative lateral and vertical displacement envelopes in slab ends over building height at the time of event occurrence

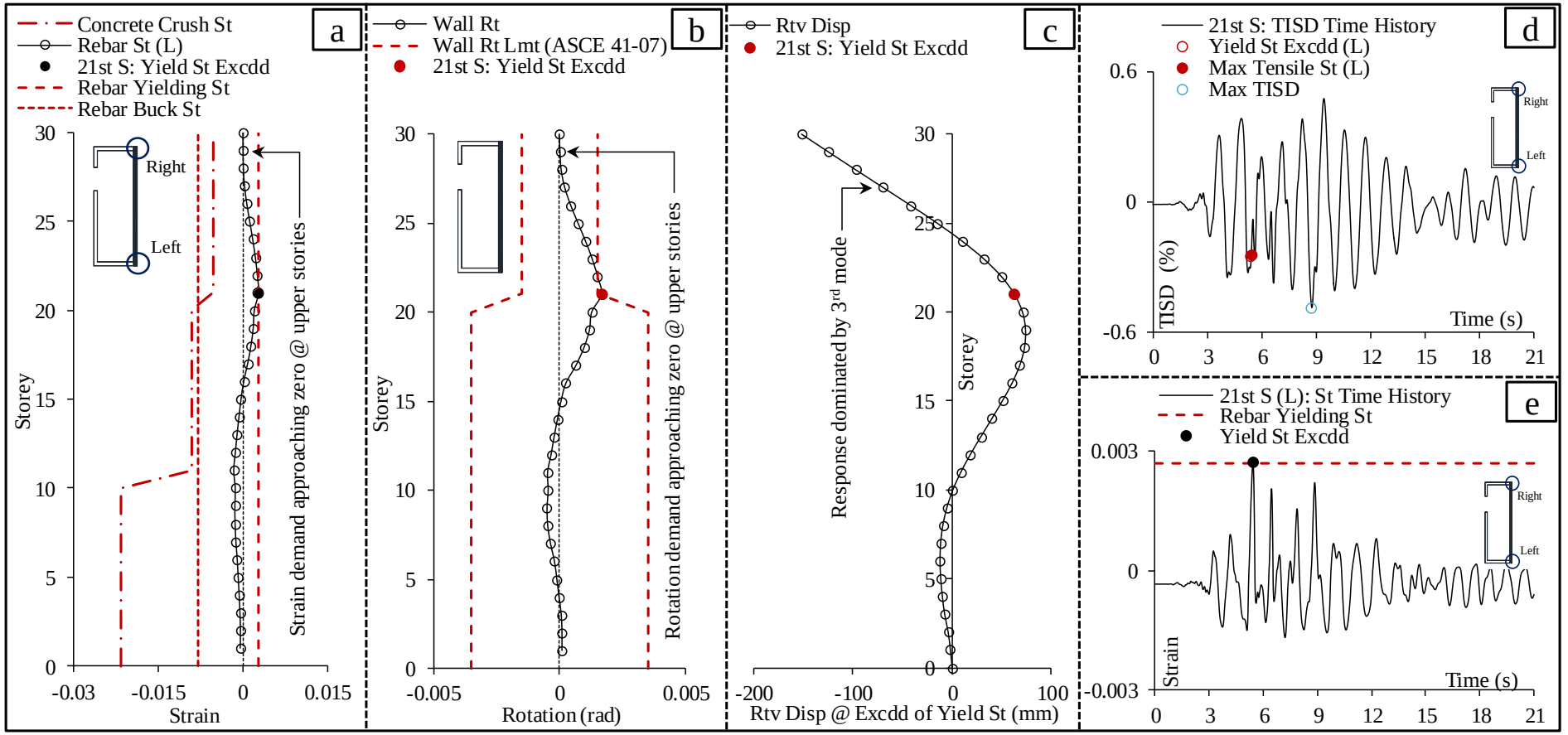

Figure 5.20. Rebar yielding in walls under R#3 of Record Set#2 (IO): (a) rebar strain envelope in the wall segment over building height at the time of event occurrence; (b) rotation envelope in the wall segment over building height at the time of event occurrence; (c) relative lateral displacement envelope in the wall segment over building height at the time of event occurrence; (d) TISD time history in the wall segment at event level; and (e) rebar strain time history in the wall segment at event level

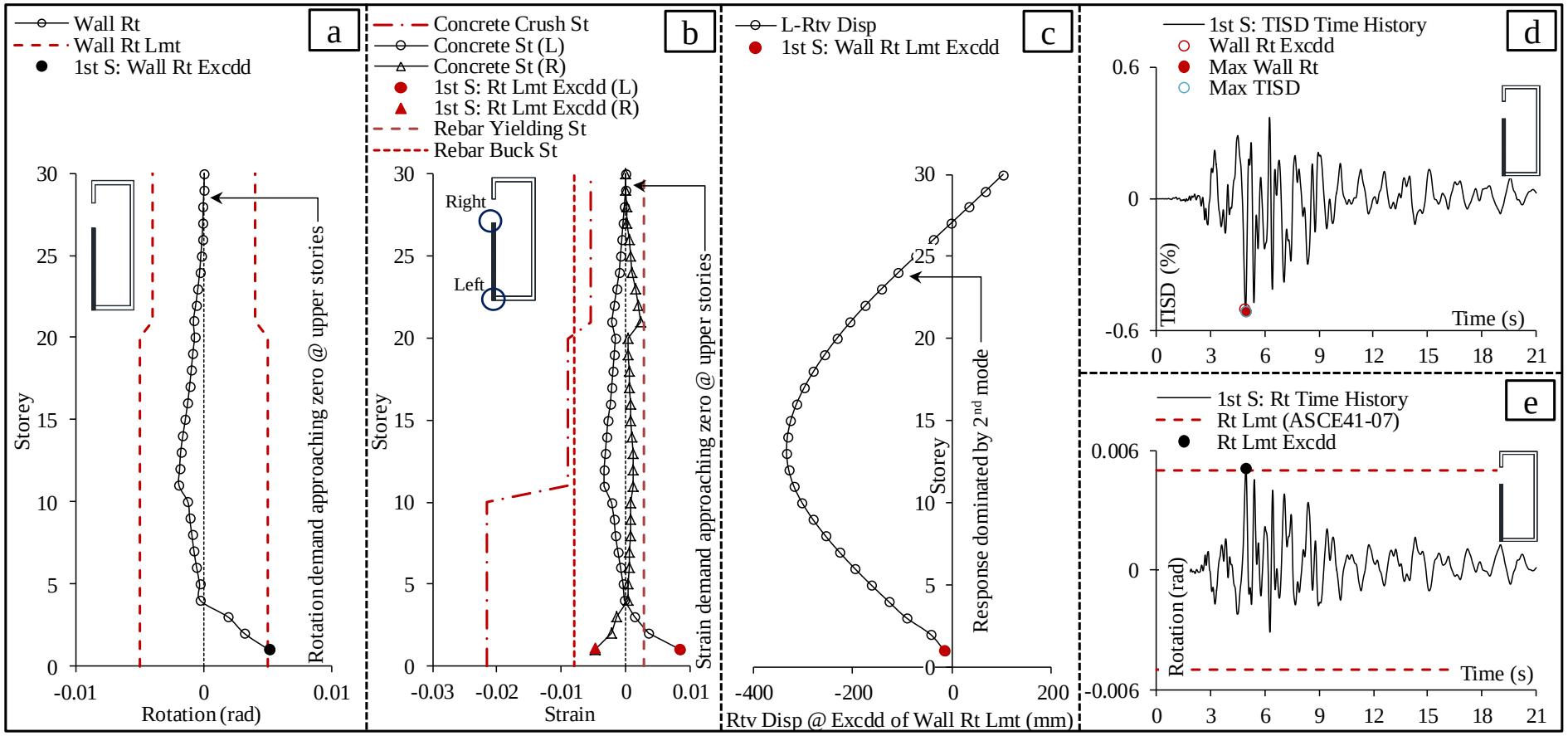

Figure 5.21. Rotation in walls under R#3 of Record Set#2 (LS): (a) rotation envelope in the wall segment over building height at the time of event occurrence; (b) strain envelope in the wall segment over building height at the time of event occurrence; (c) relative lateral displacement envelope in the wall segment over building height at the time of event occurrence; (d) TISD time history in the wall segment at event level; and (e) rotation time history in the wall segment at event level

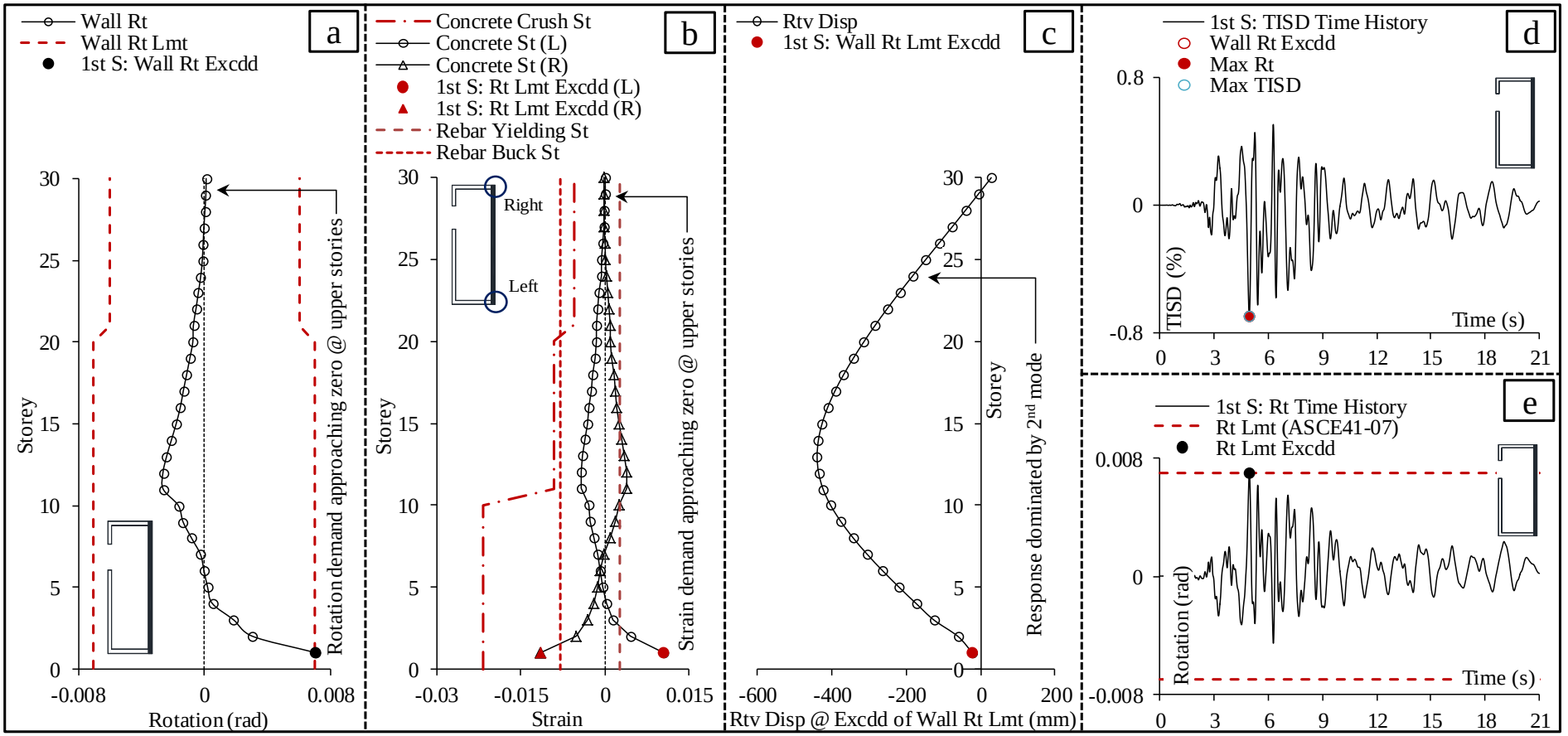

Figure 5.22. Rotation in walls under R#3 of Record Set#2 (CP): (a) rotation envelope in the wall segment over building height at the time of event occurrence; (b) strain envelope in the wall segment over building height at the time of event occurrence; (c) relative lateral displacement envelope in the wall segment over building height at the time of event occurrence; (d) TISD time history in the wall segment at event level; and (e) rotation time history in the wall segment at event level

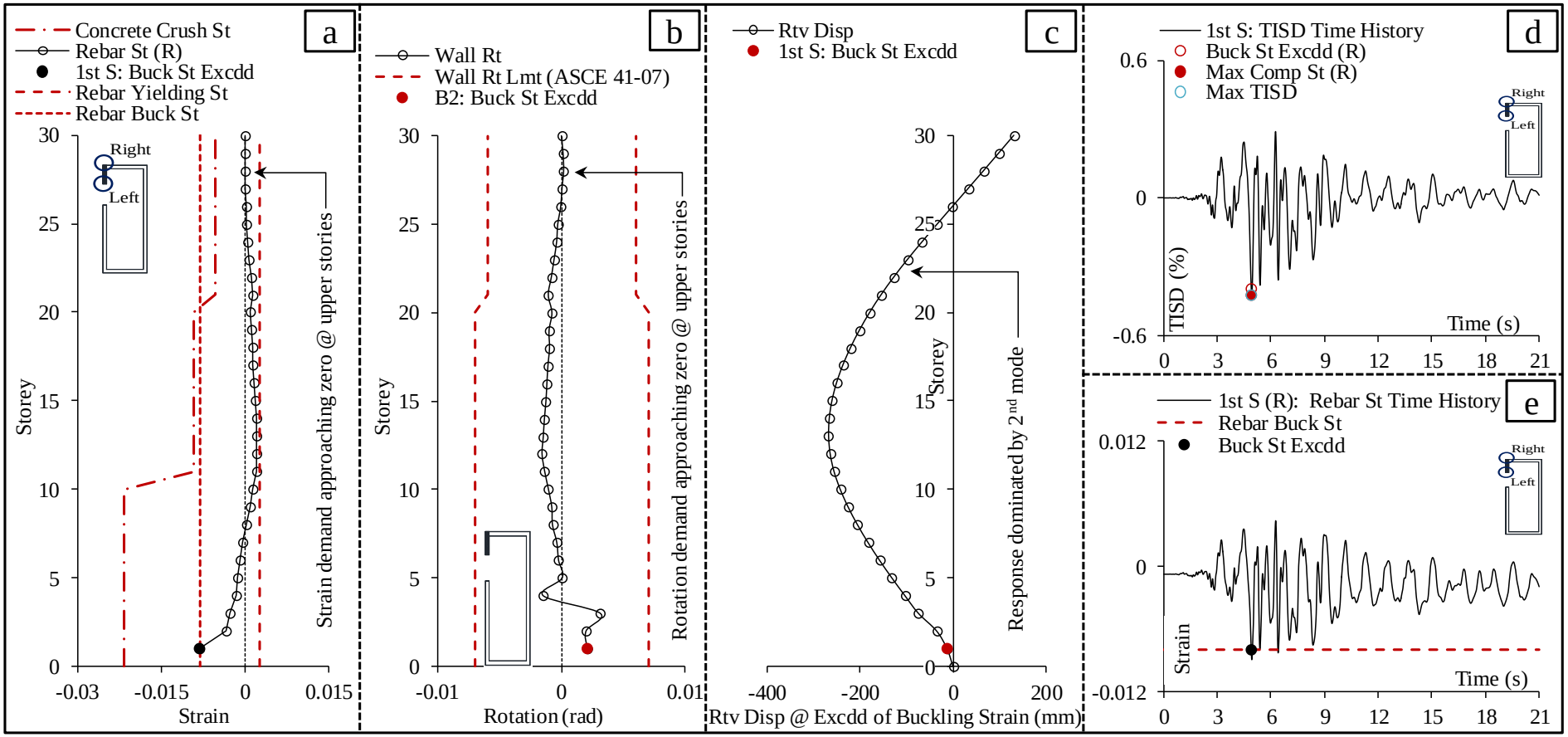

Figure 5.23. Rebar buckling in walls under R#3 of Record Set#2 (CP): (a) rebar strain envelope in the wall segment over building height at the time of event occurrence; (b) rotation envelope in the wall segment over building height at the time of event occurrence; (c) relative lateral displacement envelope in the wall segment over building height at the time of event occurrence; (d) TISD time history in the wall segment at event level; and (e) rebar strain time history in the wall segment at event level

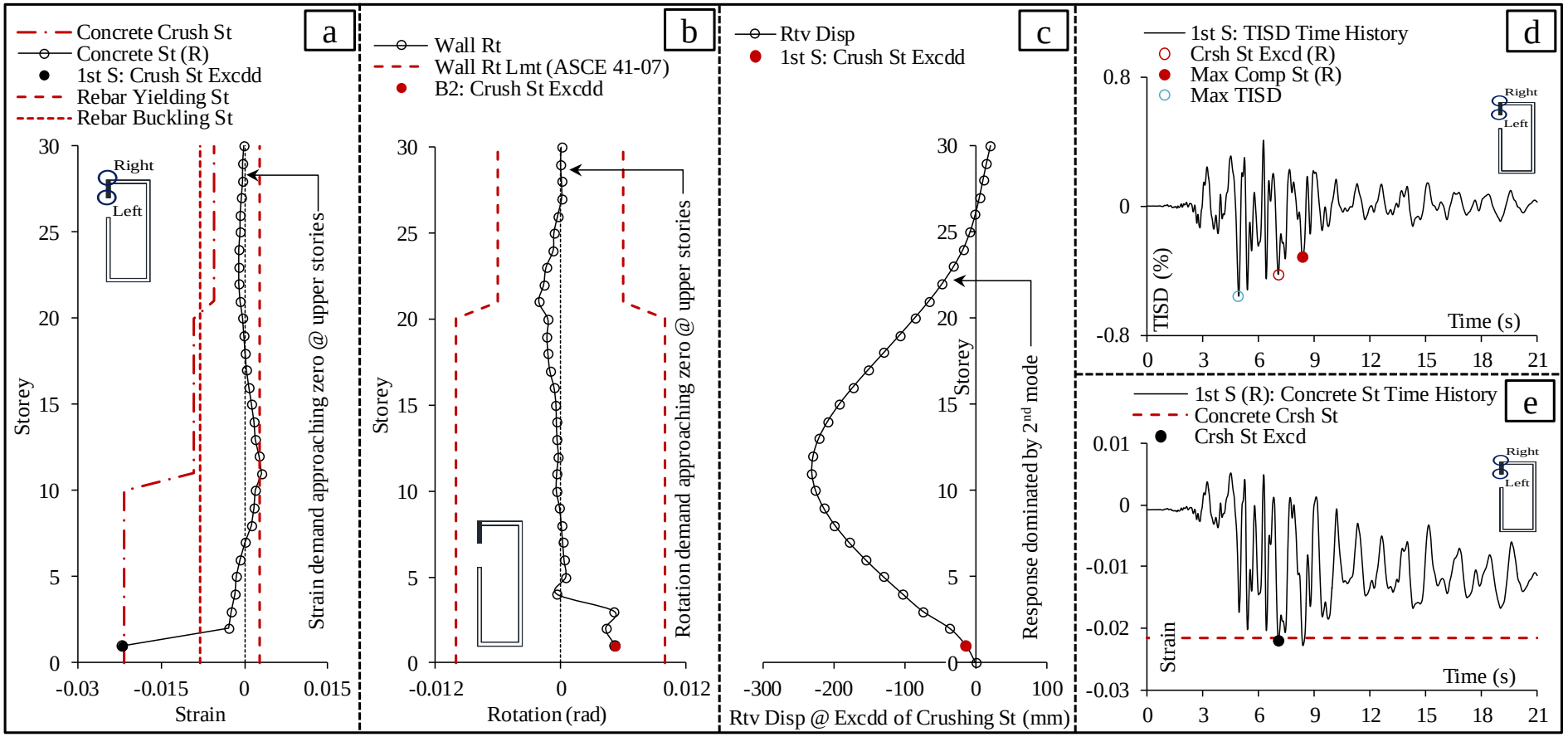

Figure 5.24. Concrete crushing in walls under R#3 of Record Set#2 (CP): (a) concrete strain envelope in the wall segment over building height at the time of event occurrence; (b) rotation envelope in the wall segment over building height at the time of event occurrence; (c) relative lateral displacement envelope in the wall segment over building height at the time of event occurrence; (d) TISD time history in the wall segment at event level; and (e) concrete strain time history in the wall segment at event level

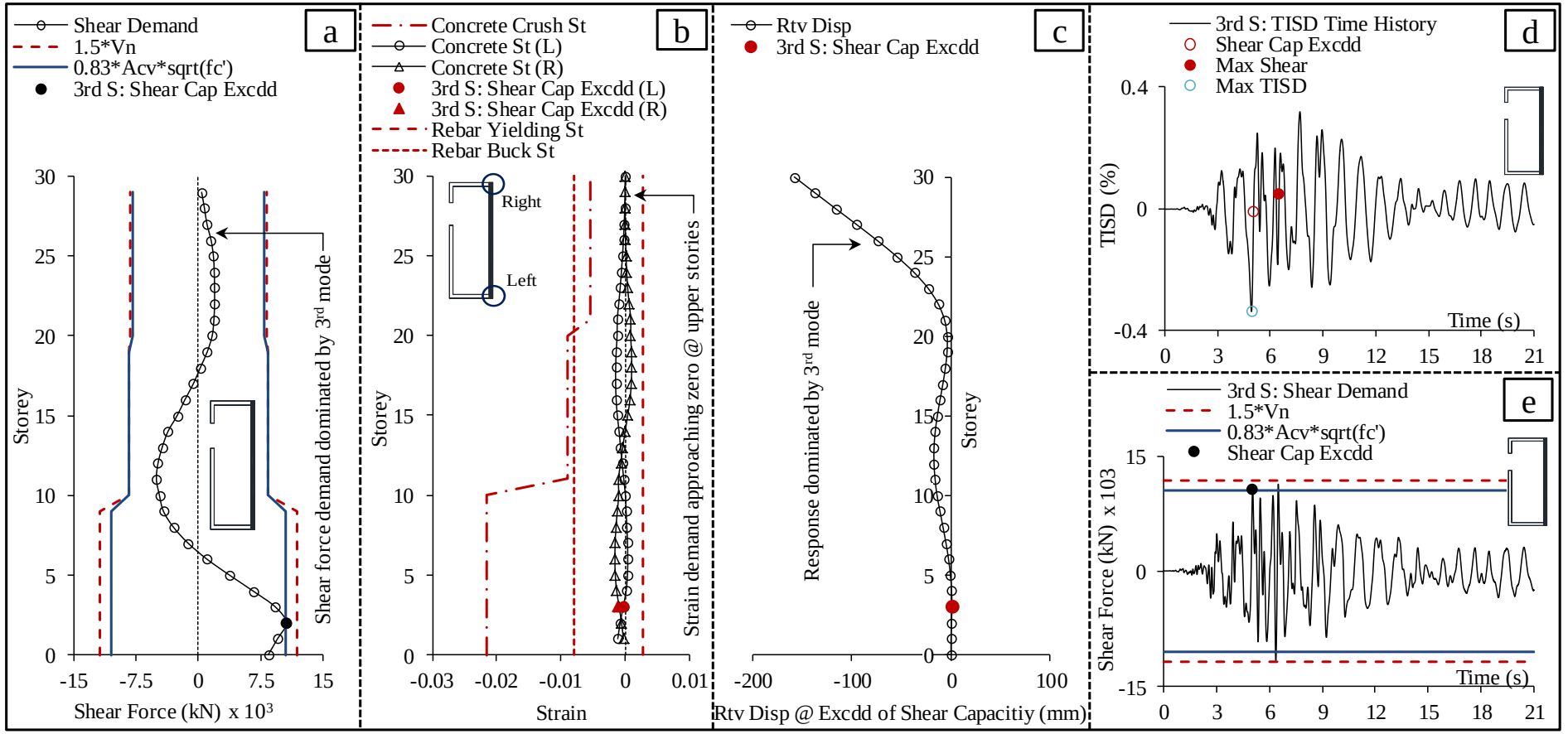

Figure 5.25. Shear capacity exceedance in walls under R#3 of Record Set#2 (CP): (a) shear force envelope in the wall segment over building height at the time of event occurrence; (b) concrete strain envelope in the wall segment over building height at the time of event occurrence; (c) relative lateral displacement envelope in the wall segment over building height at the time of event occurrence; (d) TISD time history in the wall segment at event level; and (e) shear force time history in the wall segment at event level

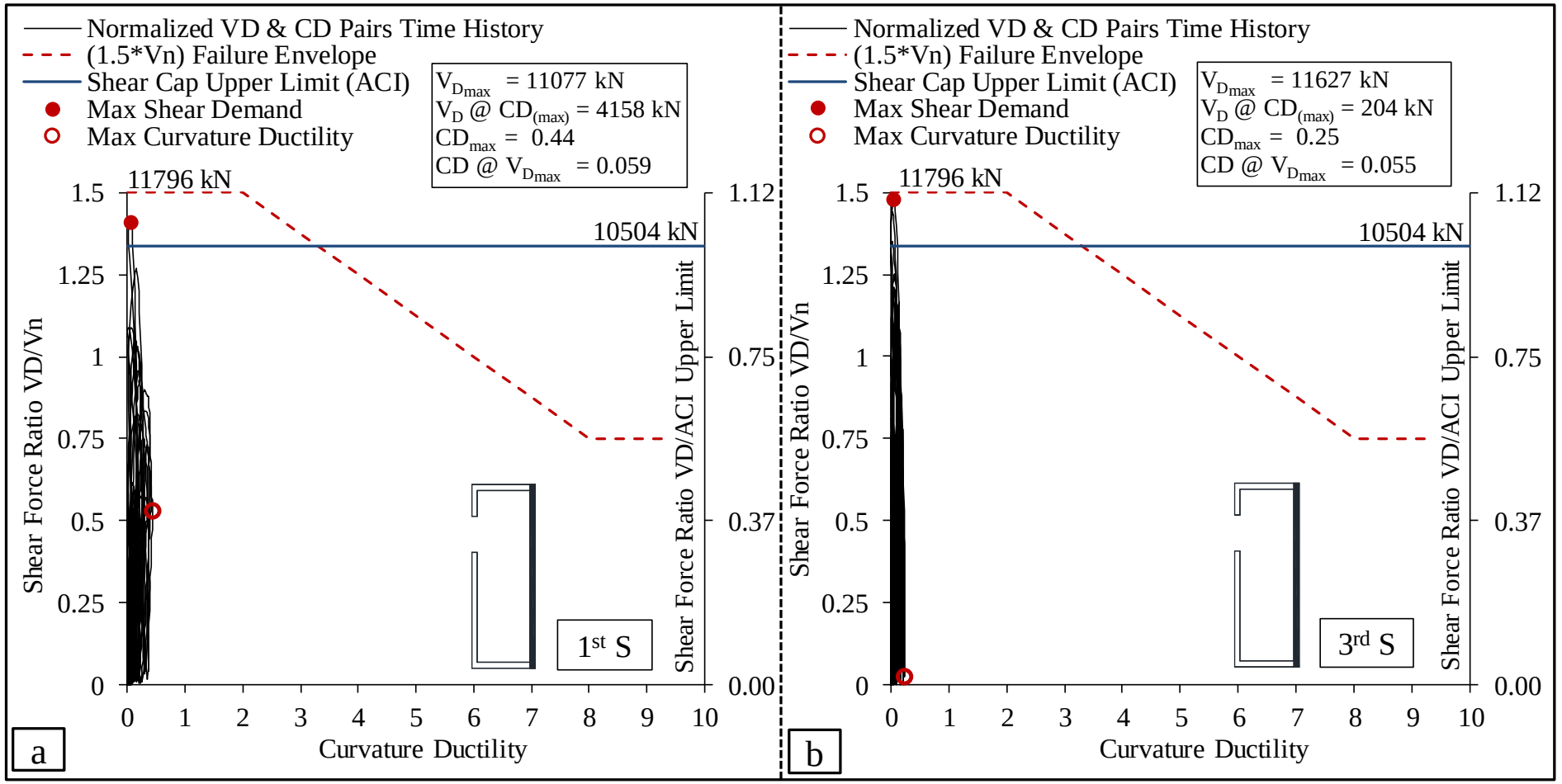

Figure 5.26. Time history of normalised shear force and curvature ductility pairs in walls under R#3 of Record Set#2 (CP): (a) 1st storey; and (b) 3rd storey

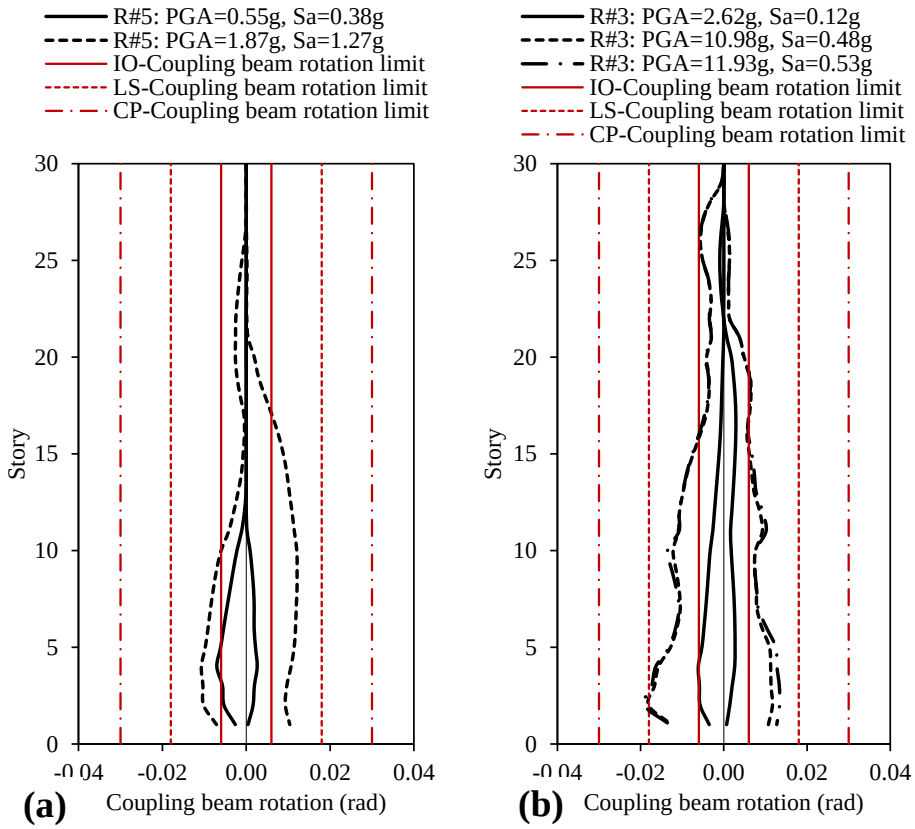

Figure 5.27. Coupling beam rotation envelope at different intensity levels: (a) R#5; and (b) R#3

5.4 Relating seismic scenario-based building local response to ground motion characteristics

To gain more insight on the relation between the reference building local response to the ground motion characteristics under the two investigated seismic scenarios, the local damage events are mapped on the time histories of R#5 and R#3 ground motions. The selected damage events (rebar yielding in slabs and walls, rebar buckling in walls, wall rotation with LS and CP limits, and shear exceedance in walls) are mapped on acceleration, velocity and displacement time histories of R#5 (Figure 5.28 to Figure 5.33) and R#3 (Figure 5.34 to Figure 5.39). Figure 5.40 and Figure 5.41 depict the acceleration, velocity and displacement response spectra of R#5 and R#3, respectively. In these response spectra, the first three translational mode periods in the transverse direction of the reference building along with the zones related to the 1st, 2nd, or 3rd mode period are illustrated.

The following can be concluded from the aforementioned figures:

- Under R#5, the IO and LS deformation-related damage events, which correspond to the 1st mode of vibration, are associated with ground displacement or ground displacement spikes which are close in value to the peak ground displacement. While for the CP deformation-related damage events, they are associated with either ground displacement and velocity peaks or spikes which are close in value to the ground peaks. For the shear exceedance in walls, the event is associated with both peak ground velocity and ground acceleration spike.

- Under R#3, the pattern for the local damage events does not correlate well to the record ground motion time histories as under R#5. The deformation-related damage events are found to be associated with peaks or with spikes close to the peaks of ground displacement, velocity, and or acceleration with more obvious correlation to ground velocity peaks (or spikes). This illustrates the effect of higher mode on building response, having in mind that all deformation-related damage events under R#3 correspond to the 2nd mode of vibration, except for rebar yielding in walls which corresponds to the 3rd mode. For the shear exceedance in walls (which corresponds to the 3rd mode), failure is associated with spikes in all ground motion time histories (displacement, velocity and acceleration). This again illustrates the importance of higher modes.

- Under R#5 (Figure 5.40c), it can be seen that the maximum spectral displacement is found in the region of the 1st mode period. The maximum spectral velocity (Figure 5.40b) and moderate spectral acceleration (Figure 5.40a) correspond to the region of the 2nd mode period.

- Under R#3, the maximum spectral displacement is correlated to the 2nd mode period (Figure 5.41c). While maximum spectral velocity (Figure 5.41b) and maximum spectral acceleration (Figure 5.41a) are correlated to the 3rd mode period.

The abovementioned observations indicate the following:

- To minimise the dispersion of the MRIDAs results, it might be more appropriate to use the displacement and velocity uniform hazard spectra as references when

selecting, scaling and anchoring real ground motions to be used in the NRHAs under strong distant and moderate near-field earthquake scenarios, respectively.

- When the performance-based design is adopted, the building seismic performance may be further optimised by avoiding critical frequency range associated with response spectral amplifications.

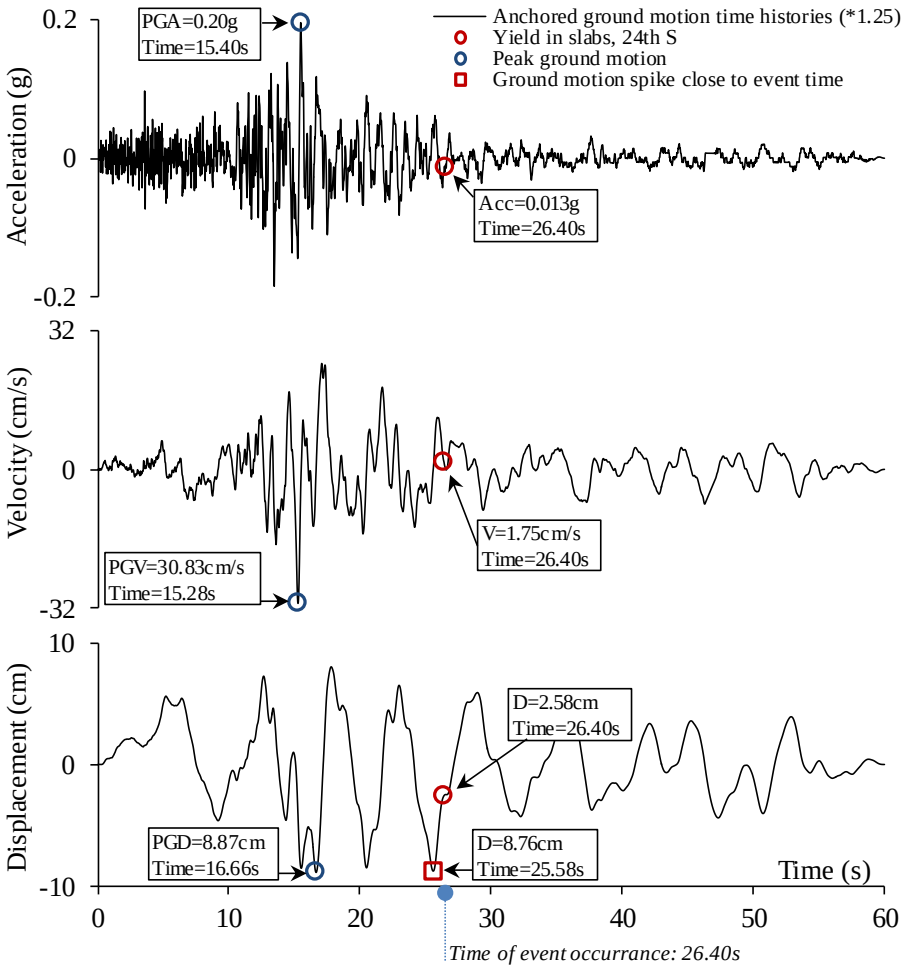

Figure 5.28. R#5 of Record Set#1: Anchored ground motion time histories at the onset of rebar yielding in slabs

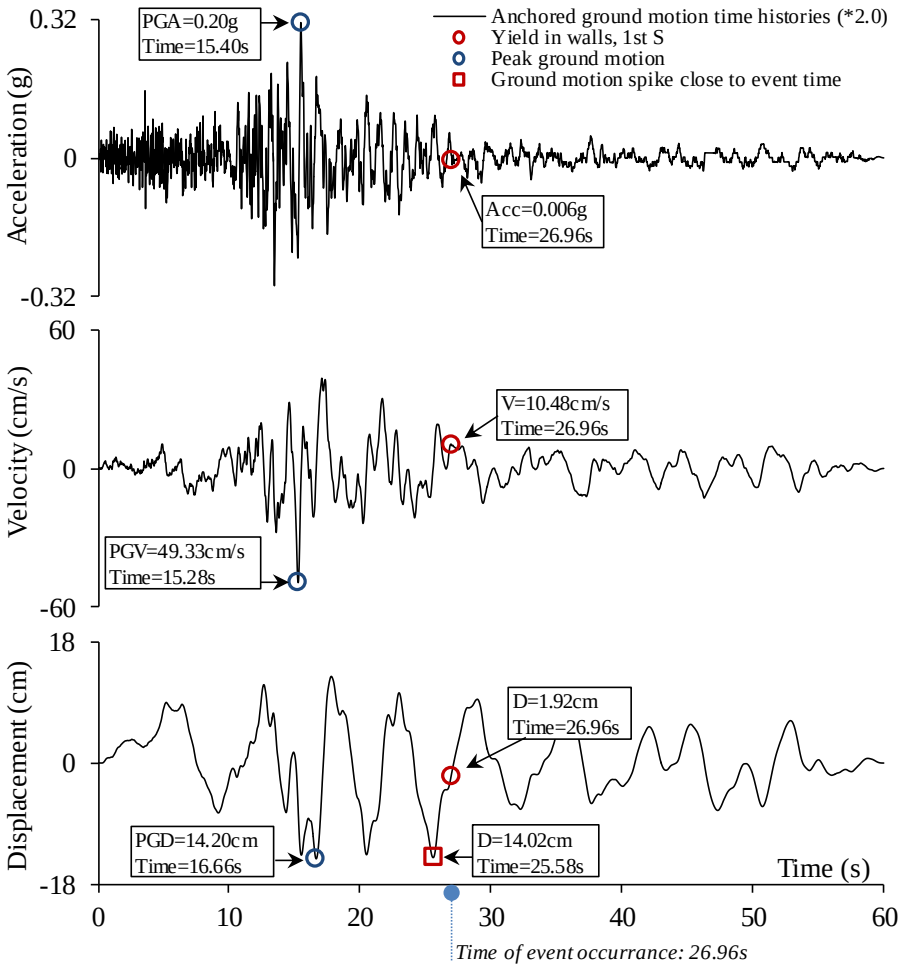

Figure 5.29. R#5 of Record Set#1: Anchored ground motion time histories at the onset of rebar yielding in walls

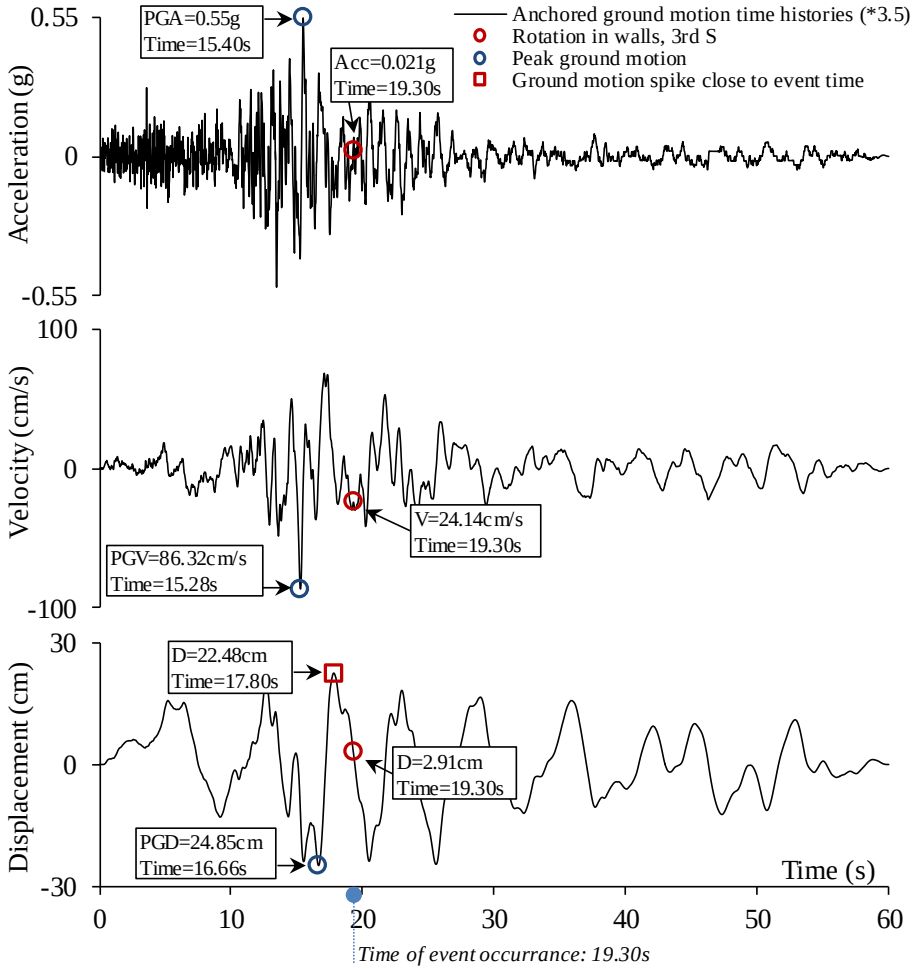

Figure 5.30. R#5 of Record Set#1: Anchored ground motion time histories at the onset of exceeding (LS) rotation limit in walls

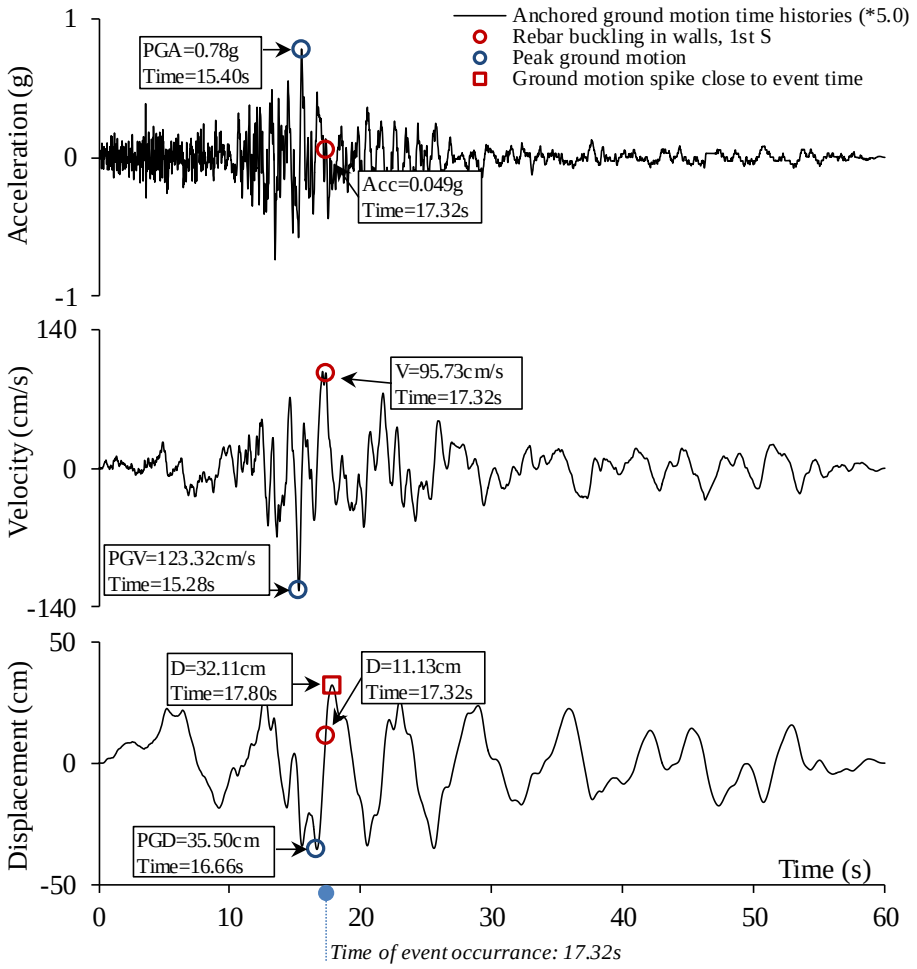

Figure 5.31. R#5 of Record Set#1: Anchored ground motion time histories at the onset of rebar buckling in walls

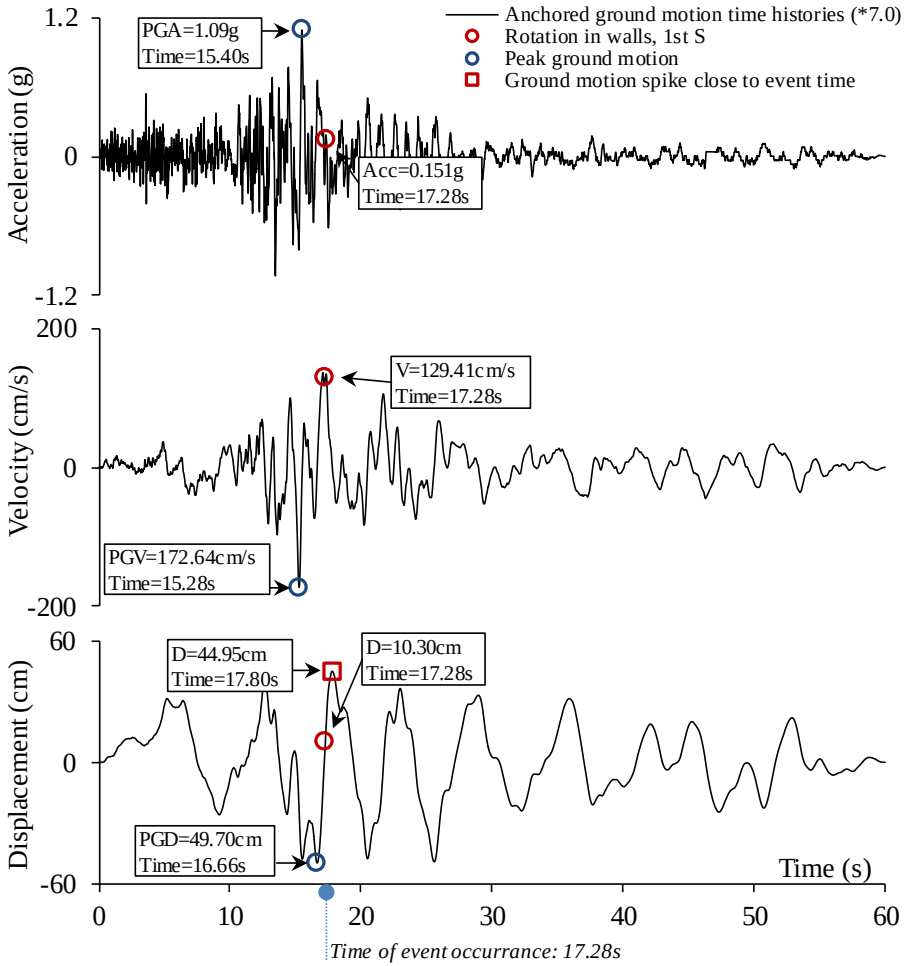

Figure 5.32. R#5 of Record Set#1: Anchored ground motion time histories at the onset of exceeding (CP) rotation limit in walls

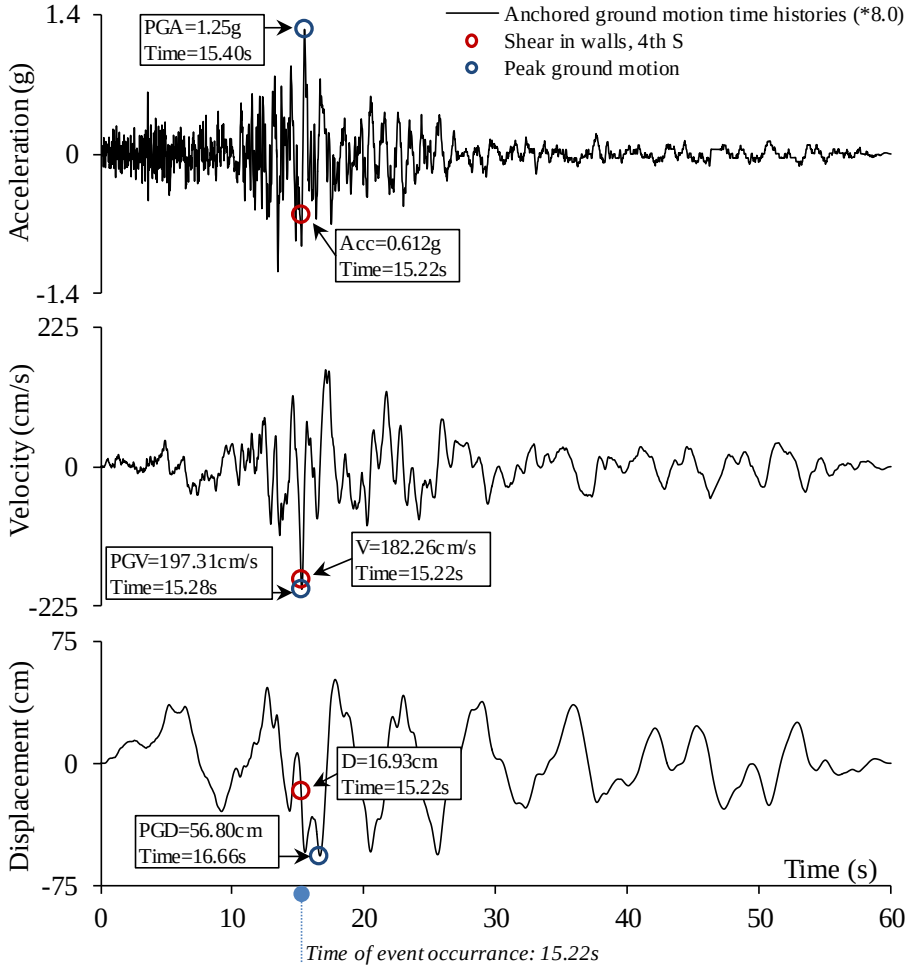

Figure 5.33. R#5 of Record Set#1: Anchored ground motion time histories at the onset of exceeding shear capacity in walls

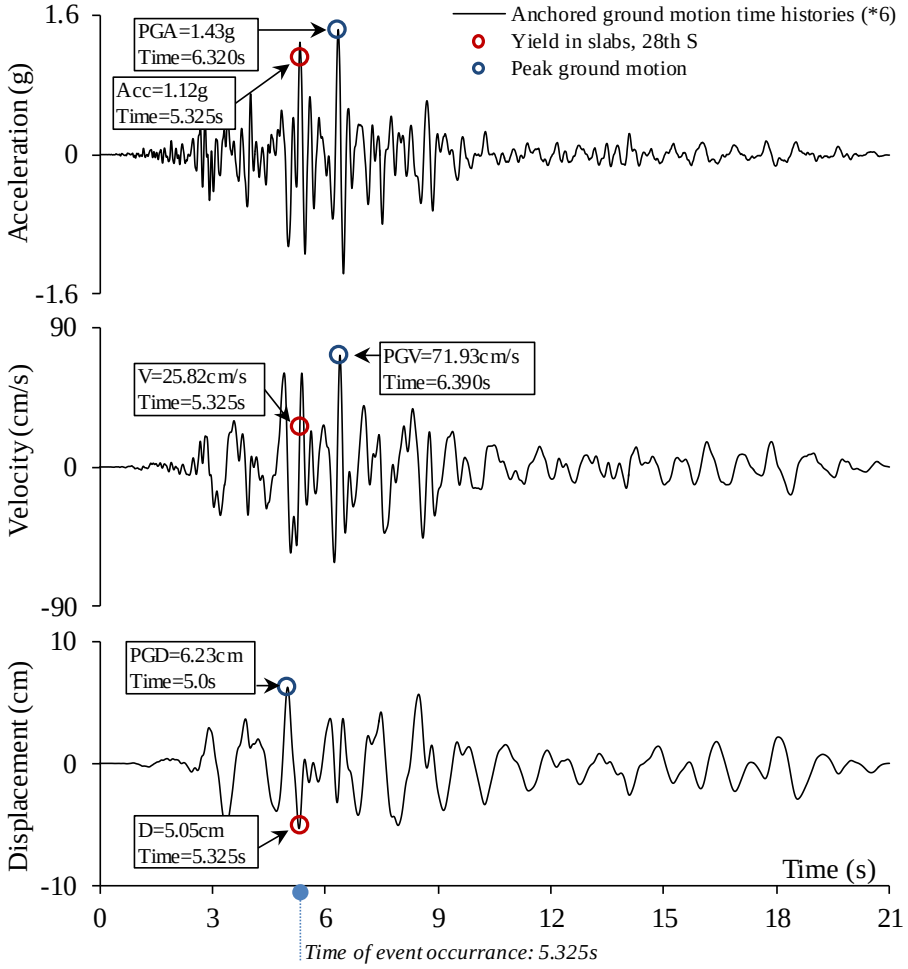

Figure 5.34. R#3 of Record Set#2: Anchored ground motion time histories at the onset of rebar yielding in slabs

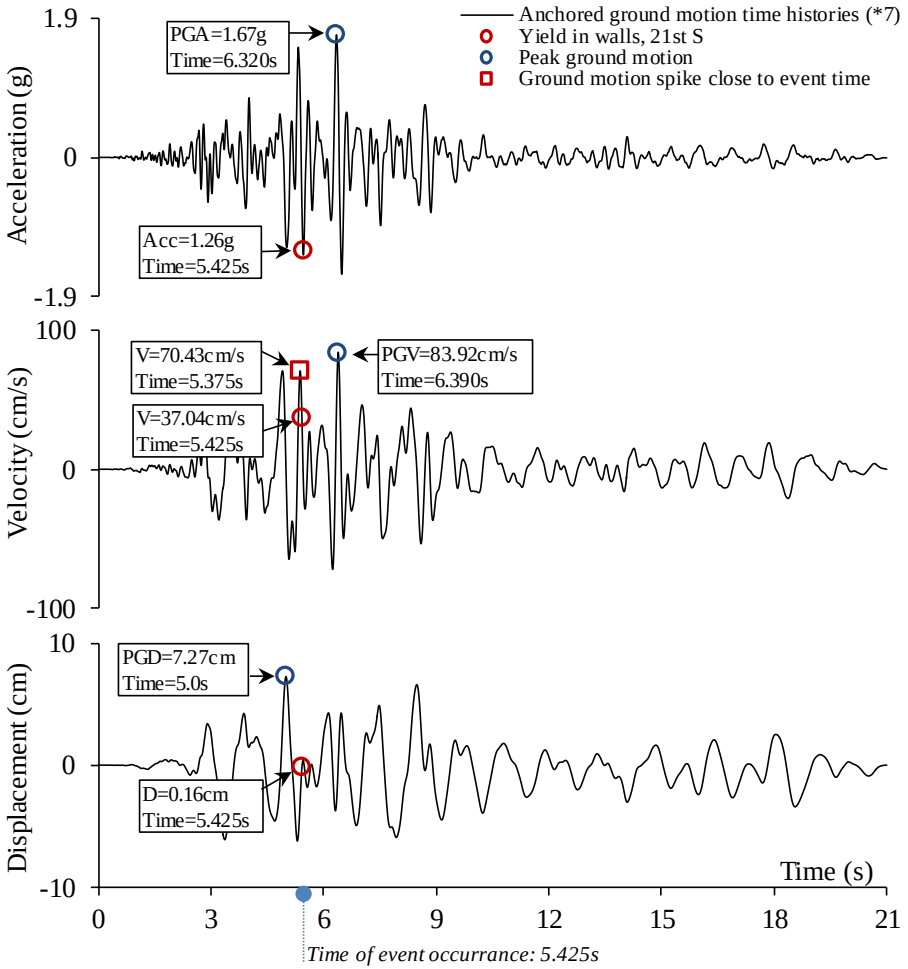

Figure 5.35. R#3 of Record Set#2: Anchored ground motion time histories at the onset of rebar yielding in walls

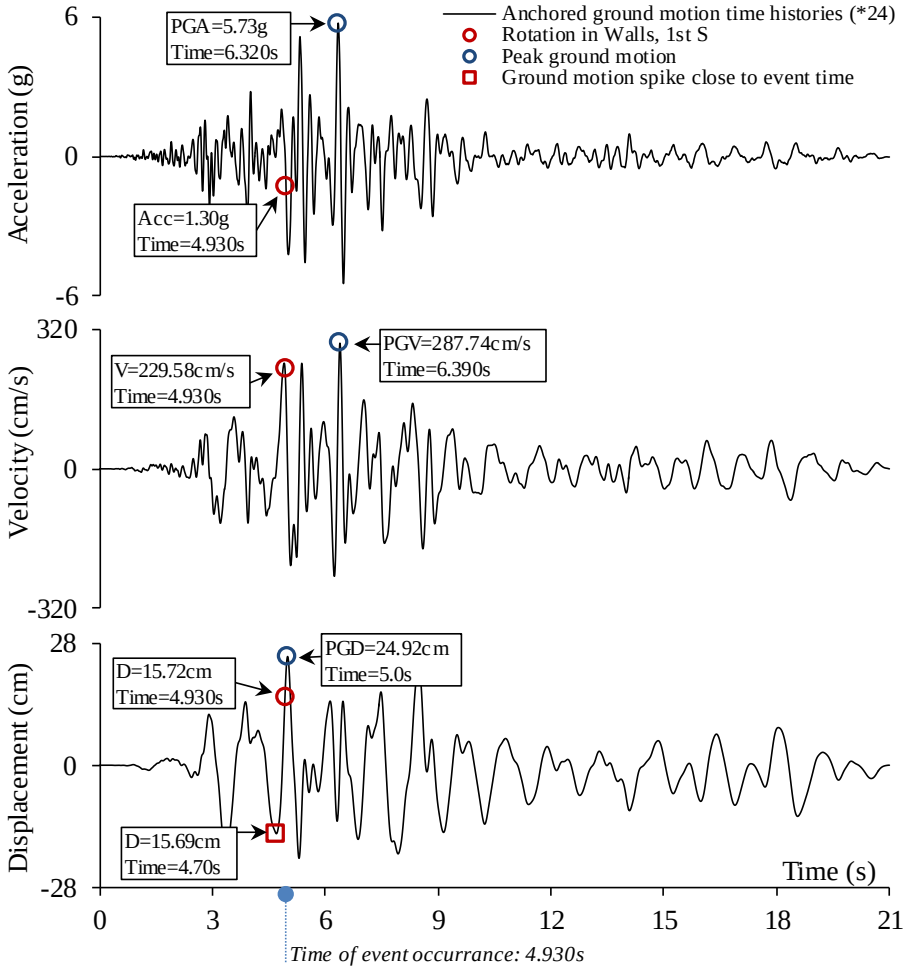

Figure 5.36. R#3 of Record Set#2: Anchored ground motion time histories at the onset of exceeding (LS) rotation limit in walls

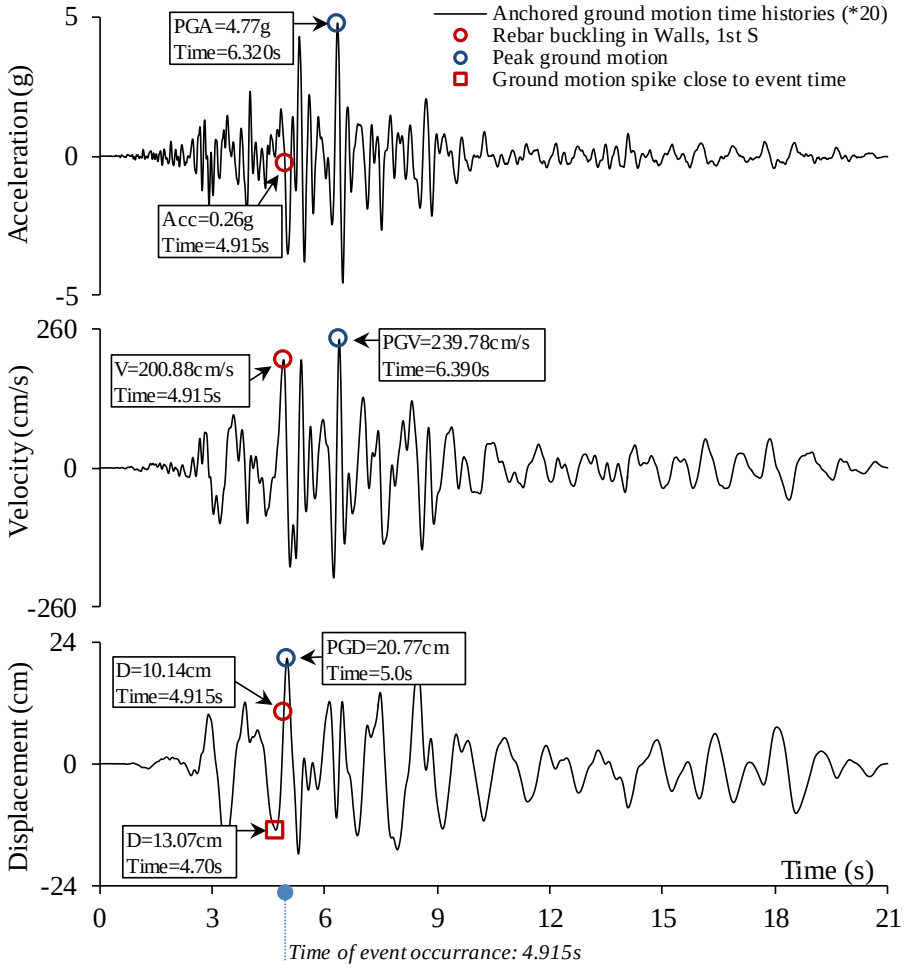

Figure 5.37. R#3 of Record Set#2: Anchored ground motion time histories at the onset of rebar buckling in walls

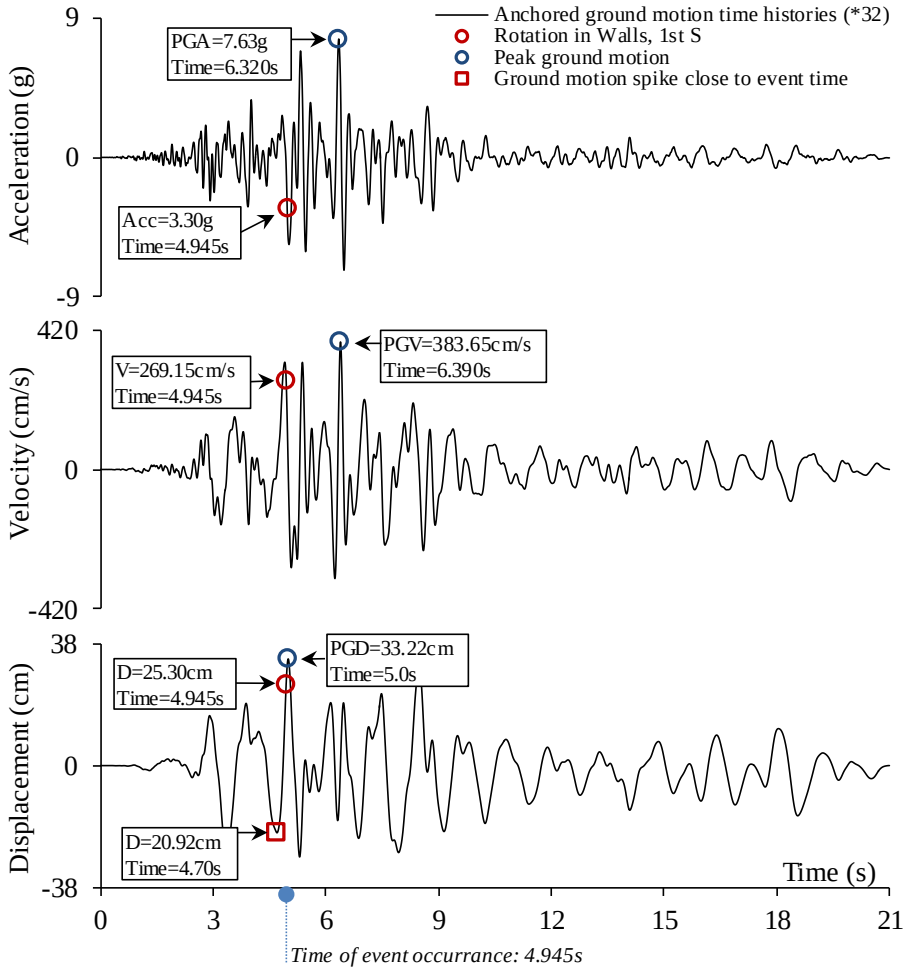

Figure 5.38. R#3 of Record Set#2: Anchored ground motion time histories at the onset of exceeding (CP) rotation limit in walls

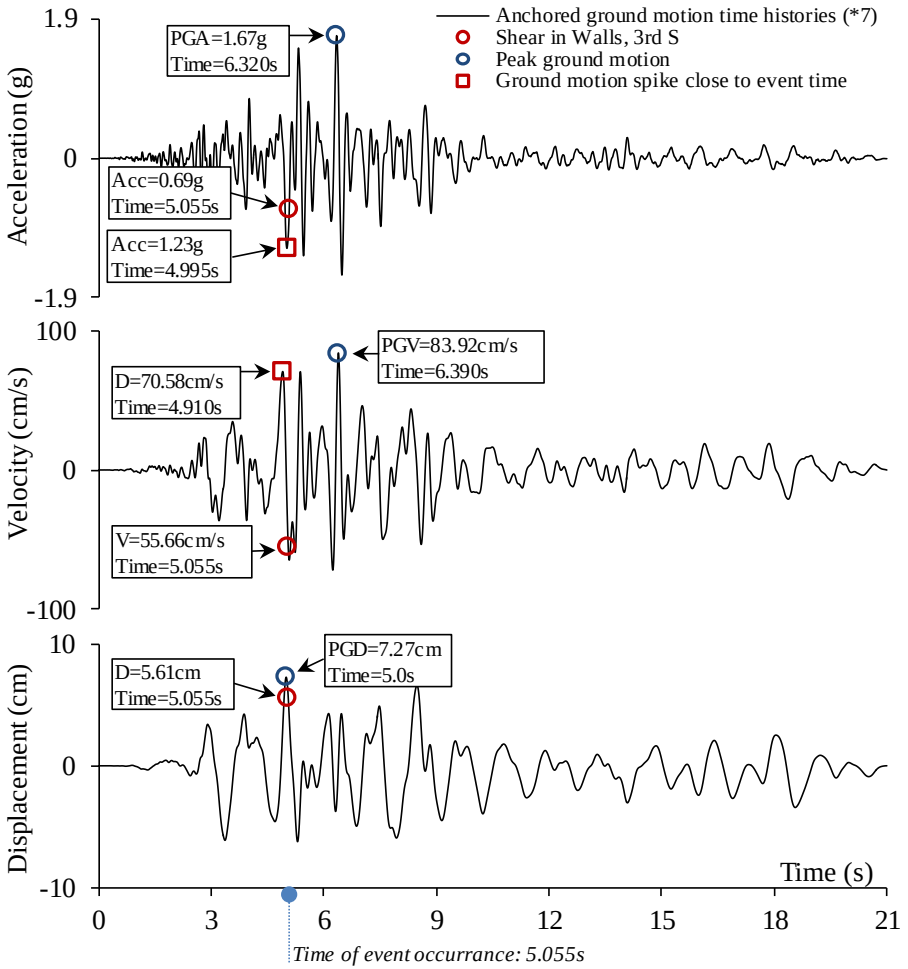

Figure 5.39. R#3 of Record Set#2: Anchored ground motion time histories at the onset of exceeding shear capacity in walls

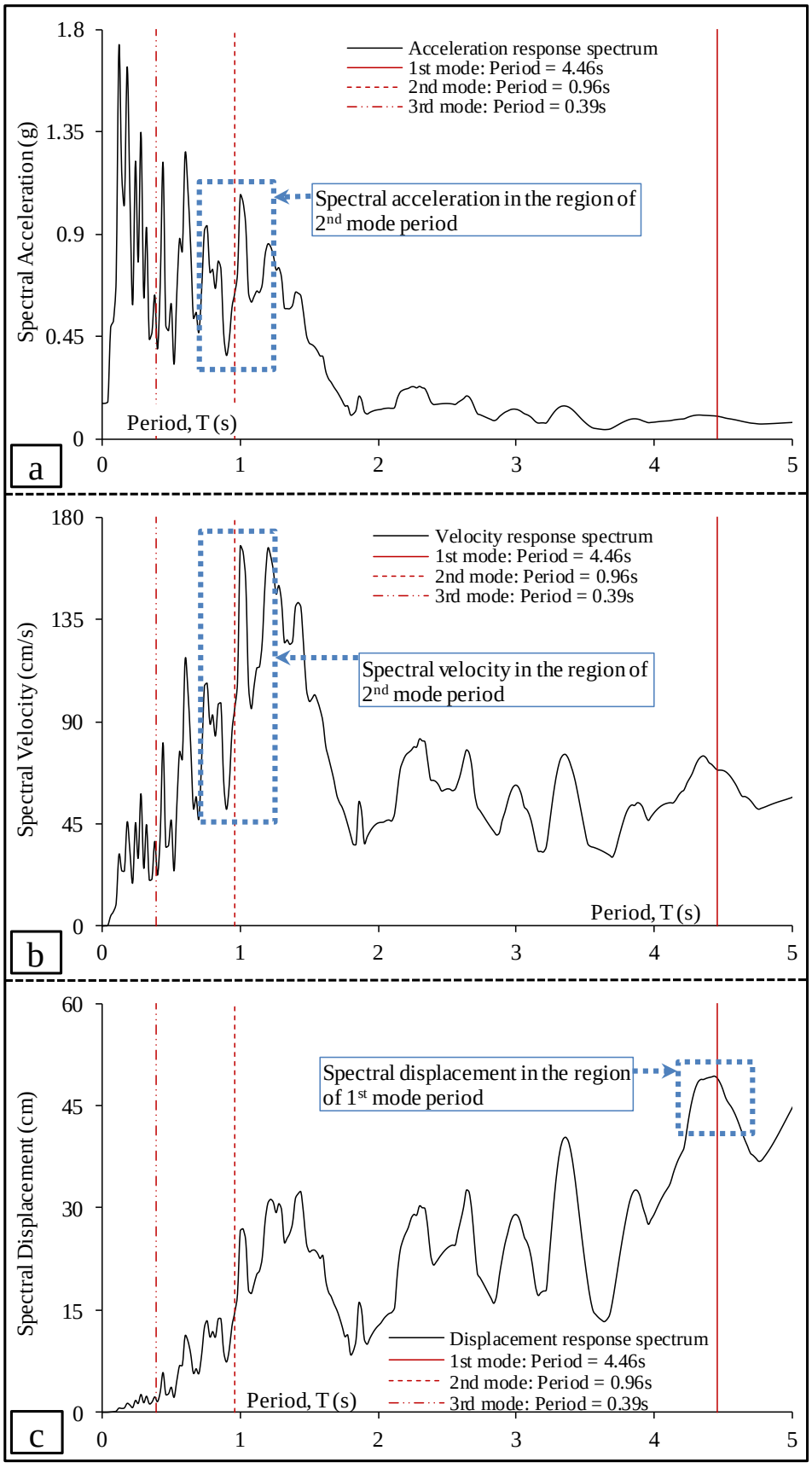

Figure 5.40. Response spectra with regions of the first 3 translational modes of vibration in the transverse direction of the reference building under R#5 of Record Set#1: (a) acceleration response spectrum; (b) velocity response spectrum; and (c) displacement response spectrum

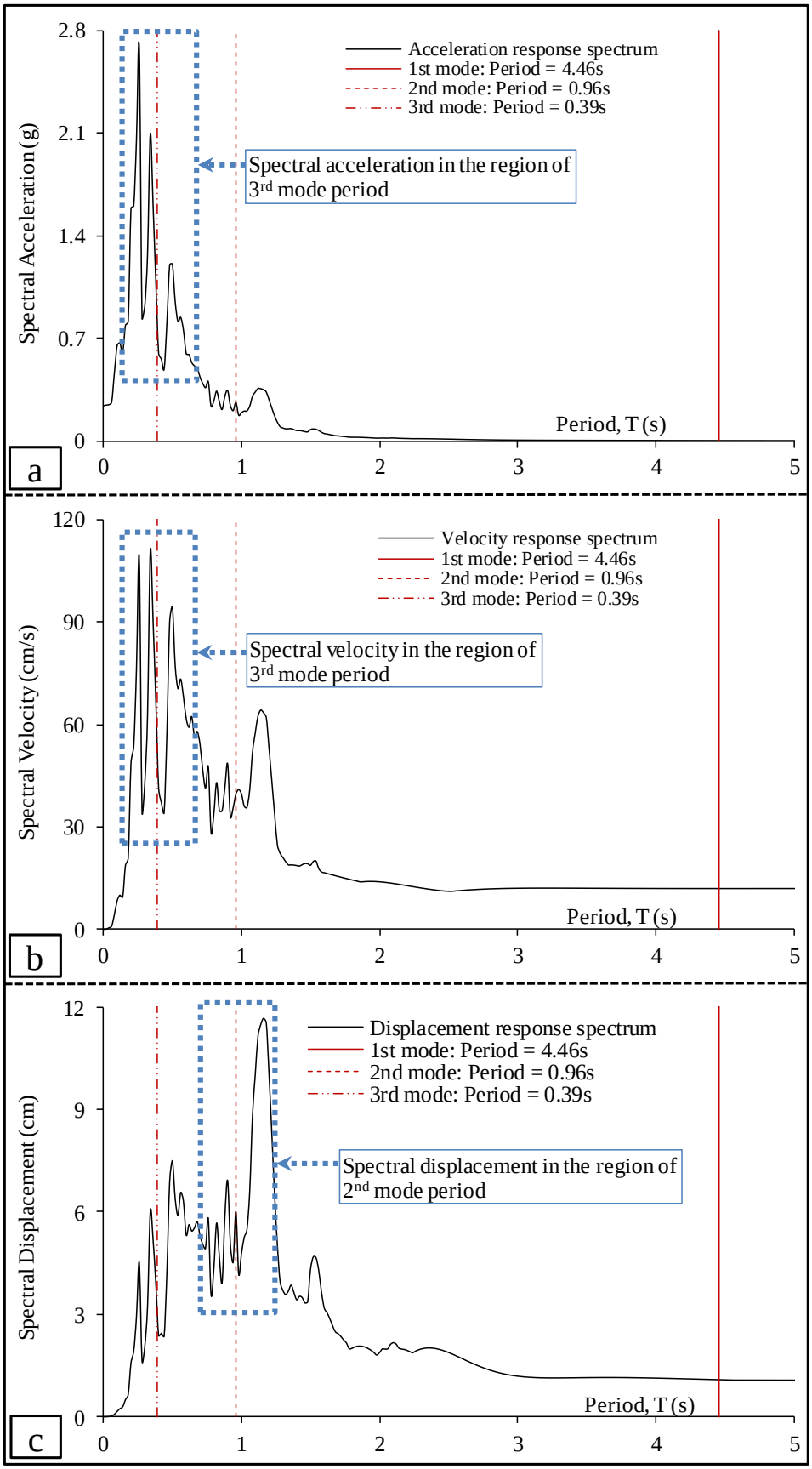

Figure 5.41. Response spectra with regions of the first 3 translational modes of vibration in the transverse direction of the reference building under R#3 of Record Set#2: (a) acceleration response spectrum; (b) velocity response spectrum; and (c) displacement response spectrum

5.5 Linking local to global response

To quantitatively define the performance limit states, DMs need to be adapted to link local-to-global response. The selection of a DM depends primarily on the structural characteristics of the assessed building and its usage. DMs include: (i) deformation-based DMs such as roof drift and TISD; (ii) force-based DMs such as base shear; and (iii) energy-based DMs such as the global Park-Ang index (Park and Ang, 1985). TISD has been frequently used as a global DM in previous studies since it is adopted by most of the seismic design and assessment code provisions and can be easily calibrated against experimental data available in the literature.

Using TISD, seismic guidelines and previous researches have proposed a wide range of limit state criteria associated with different performance levels of RC shear walls and wall structures. In ASCE/SEI 41-06 (2007), TISDs of 0.5%, 1% and 2.0% are assigned to the IO, LS, and CP performance levels, respectively. The SEAOC blue book (1999) proposed TISDs of 0.4%, 0.9%, 1.4% and 2.1% for RC shear walls at performance levels SP1 (negligible damage), SP2 (minor to moderate reparable damage), SP3 (moderate to major irreparable damage), and SP4 (collapse performance level). Seismic codes tend to lean to the conservative side, but less conservative TISDs have been recommended in the literature based on experimental and analytical results. For ductile RC walls, Ghobarah (2004) recommended TISDs of <0.2%, 0.4%, <0.8%, >0.8%, 1.5% and >2.5% corresponded to damage levels of none, light reparable, moderate reparable, irreparable, severe (or life safe), and collapse, respectively. In another study of RC wall buildings with a number of storeys ranging between 10 to 60, Mwafy (2012a) suggested a TISD value of 2.5% for CP, while height-dependent TISDs were proposed for IO (0.32% to 0.83%) and LS (0.81% to 1.35%). In contrast, Ji et al. (2009) suggested conservative TISDs to define three performance limit states obtained from inelastic pushover and time history analyses for a 54-storey RC wall building. The proposed TISDs were 0.2%, 0.52% and 1.1% for serviceability, damage control and collapse prevention limit states, respectively. Bearing the above in mind, reliable definitions of performance limit state criteria for RC high-rise wall structures remain a significant research issue.

TISD at any storey is a combination of two major components: (i) lateral net drift caused by shear and flexure deformation, referred to hereafter as NISD; and (ii) drift from rigid body motion (RBM) caused by the rotation in the lower storey, referred to

hereafter as RBMISD. The former relates storey deformation to the stress and strain demands of members in that storey, while the latter has no contribution to structural demand. The weight of RBM component in the TISD value is influenced by the location of the storey in the building, the total building height and the effect of higher modes on the seismic response. Ji et al. (Ji et al., 2009) illustrated that for high-rise buildings, the traditional DM of TISD is insufficient to be directly related to the structural performance and therefore needs to be disaggregated to its main sources. This argument is further investigated in the present study.

There are several methods available for calculating NISD including secant, improved secant, fixing floor and tangent (e.g. Cai et al., 2014). The latter method is adopted in the current work to calculate the NISD using post-processed element deformation data (mainly from the wall segment) as illustrated in Figure 5.42 and Eqn. (5.5).

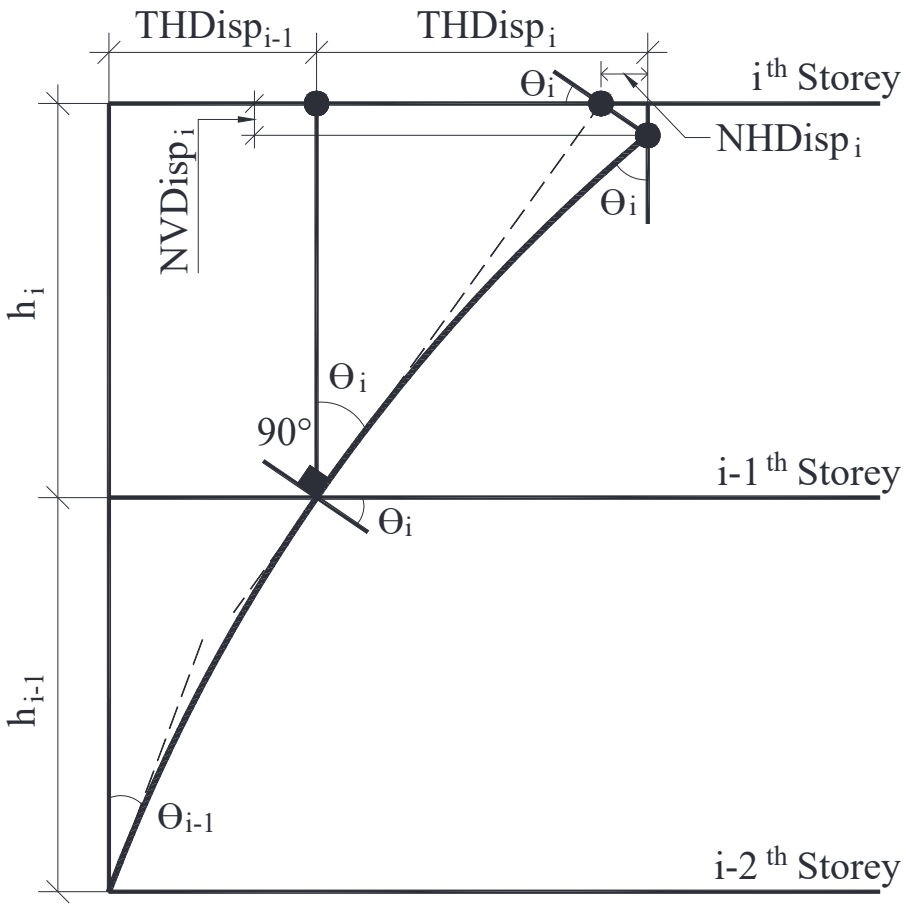

Figure 5.42. Member deformation shape for calculation of NISD

$$NISD_i = \frac{1}{h_i}\left\{\frac{(THDisp_i - h_i \sin\theta_i)}{\cos\theta_i} + [NVDisp_i - h_i\ (1-\cos\theta_i) - (THDisp_i - h_i\ \sin\theta_i)\tan\theta_i]\sin\theta_i\right\} \quad (5.5)$$

Where $NISD_i$ is the NISD of the i^{th} storey, h_i is the height of the i^{th} storey, θ_i is the tangent angle at the bottom end of the i^{th} storey, $THDisp_i$ is the total lateral (horizontal) inter-story displacement of the i^{th} storey, and $NVDisp_i$ is the net vertical inter-story displacement of the i^{th} storey. Figure 5.43a shows TISD vs NISD envelopes for the reference building at selected seismic intensities of R#5 ($S_{a(wa)}$=0.13g, 0.52g, and 0.84g) and R#3 ($S_{a(wa)}$=0.07g, 0.21g, and 0.34g). From both seismic scenarios and at all seismic intensities, it can be seen that the NISD approaches zero at the top storeys. This is consistent with the low seismic demands in the respective RC walls.

The ratios of RBMISD to TISD at the onset of local damage events are plotted in Figure 5.43b for selected seismic intensities. For R#5 and R#3, these ratios rise from 0.0 and 0.0 at the first storey, to an average of 0.91 and 0.70 at the twentieth storey, and 0.99 and 0.98 at the thirtieth storey, respectively. This confirms that at the higher storeys TISD is almost entirely dominated by RMBISD resulting from the rotation of lower storeys; hence there is practically no NISD and no damage at the higher storeys.

The relation between local damage events and ISDs is presented in Figure 5.44 and Figure 5.45 through plots of both TISD and NISD distribution over the building height at the onset of different events for R#5 and R#3, respectively. As expected, all deformation-based damage events (Figure 5.44(b-g) and Figure 5.45(b-g)) in walls occurred at the same level as maximum NISD. The force-based event of exceedance of wall shear capacity (Figure 5.44h and Figure 5.45h) is related to neither NISD nor TISD. The same applies to the rebar yielding in the slab (Figure 5.44a and Figure 5.45a), that is related to the maximum differential vertical displacement between slab ends rather than to lateral drift.

To investigate the effect of building total height on the relationship between local damage events and drifts, a numerical parametric study is conducted. Maintaining the footprint and the geometry of the reference building, six more buildings with a total number of storeys of 20, 25, 35, 40, 45 and 50 (total height of 65.3m, 81.3m, 113.3, 129.3, 145.3, 161.3m, respectively) are designed and nonlinearly modelled as explained in CHAPTER 4. Table 5.2 shows the predominant mode periods and design proportions

of the six additional buildings, while Figure 5.46 and Figure 5.47 depict NISD and TISD at the onset of local damage events against building total height when subjected to R#5 and R#3, respectively. Under R#5, nearly all events, except the exceedance of wall shear capacity occur at a similar NISD for all building heights. The NISD results under R#3 show higher variability and this can be attributed again to the bigger impact of higher modes on the response of such buildings to moderate near-field earthquakes.

TISD can be responsible for non-structural damage in tall buildings and inconvenience to the occupants, hence is important at least when evaluating the performance of high-rise buildings at serviceability level. However, the above discussion confirms the superiority of NISD over TISD as a global DM for the vulnerability assessment of high-rise buildings due to its structural significance, its correlation with local response and its consistency in buildings with varying heights. Thus, it is decided to use the NISD as the global DM in the present study.

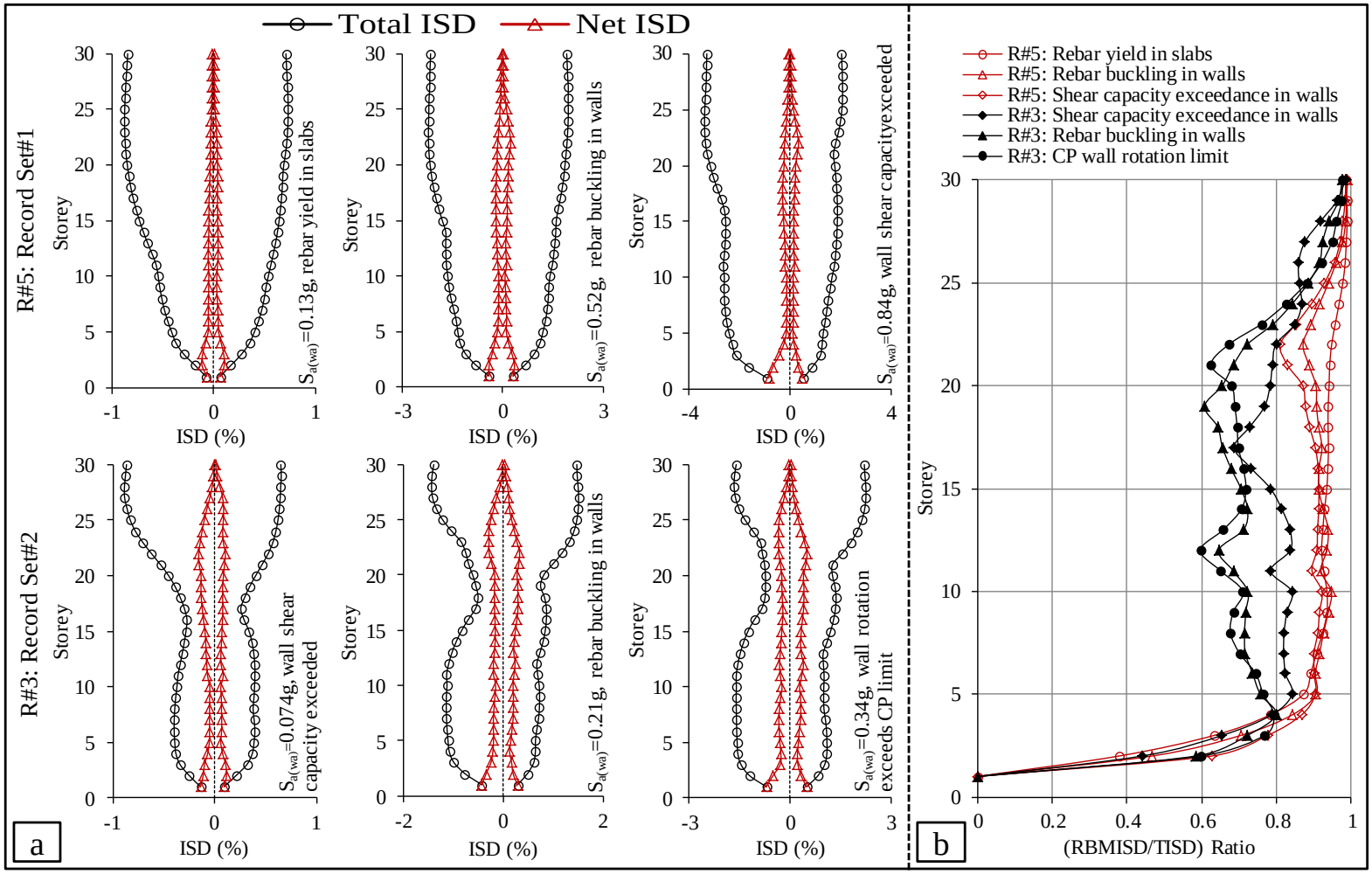

Figure 5.43. Reference building response at selected seismic intensity levels under R#5 and R#3: (a) TISD vs NISD envelopes; and (b) Ratio of RBMISD to TISD envelopes

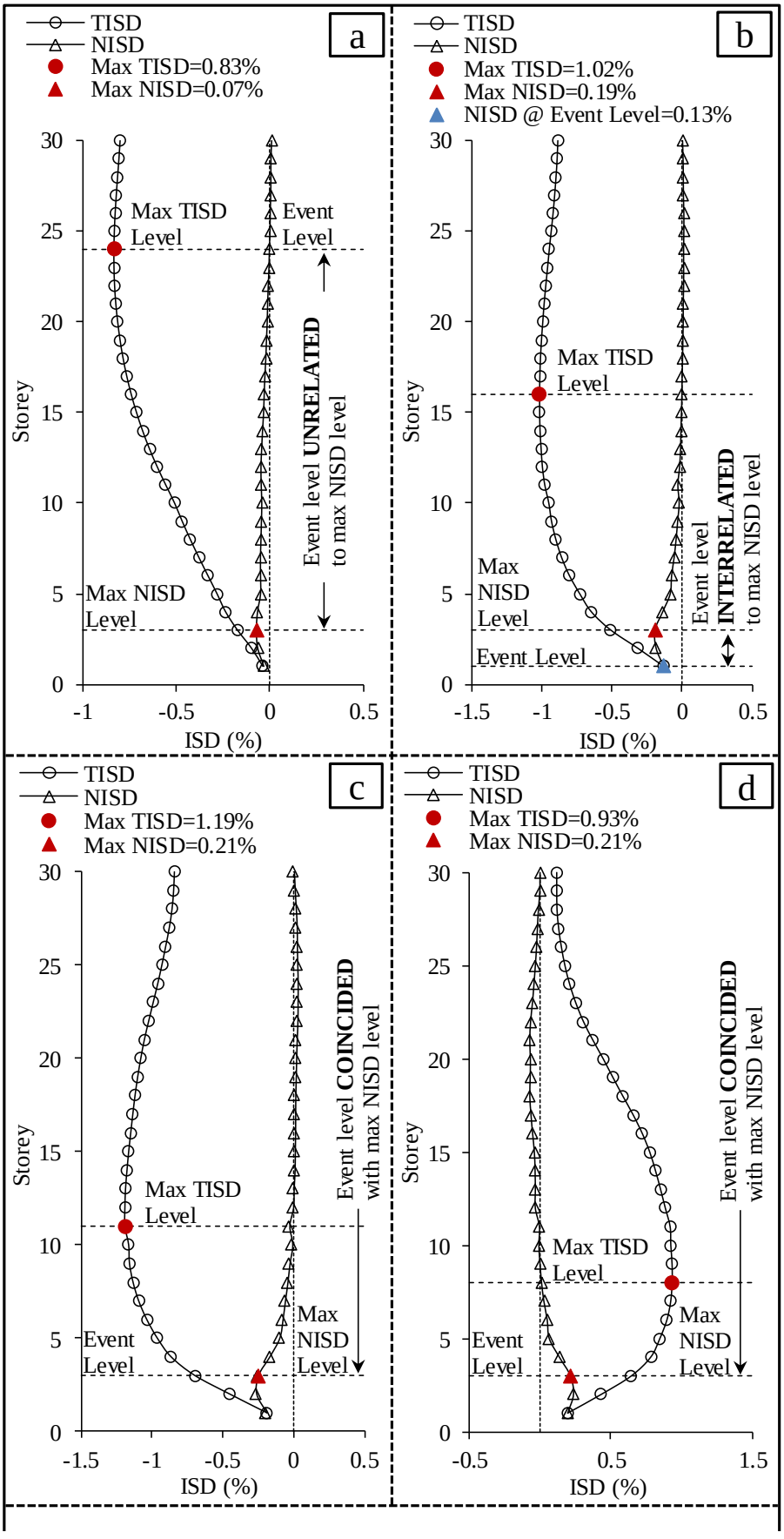

Figure 5.44. R#5 of Record Set#1: TISD vs NISD over height of reference building at the onset of local damage events: (a) rebar yield in slabs; (b) rebar yield in walls; (c) IO wall rotation limit; (d) LS wall rotation limit; ***(figure continues in the next page)***

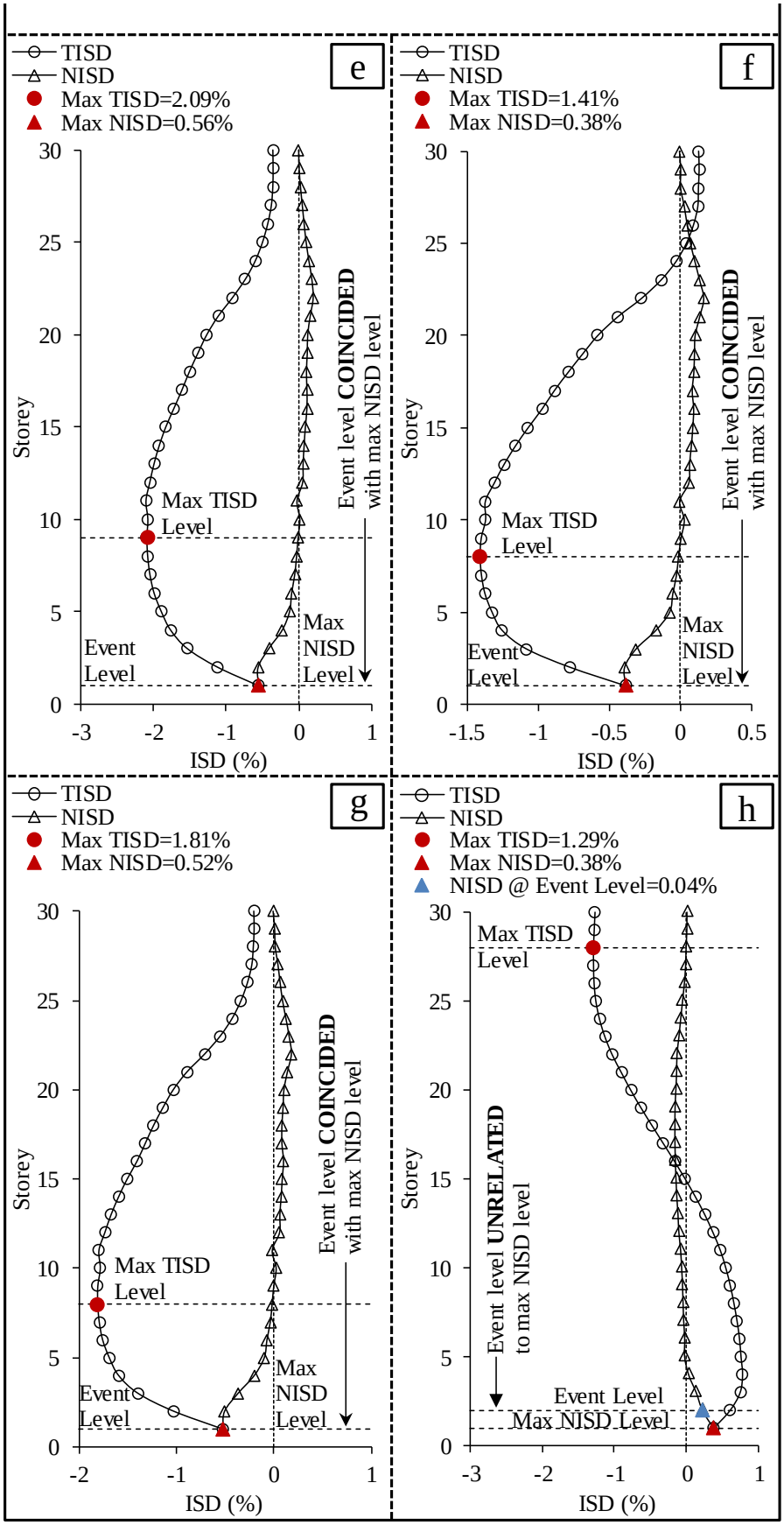

Figure 5.44 (continued). R#5 of Record Set#1: TISD vs NISD over the height of reference building at the onset of local damage events: (e) CP wall rotation limit; (f) rebar buckling in walls; (g) confined concrete crushing in walls; and (h) exceedance of shear capacity in walls

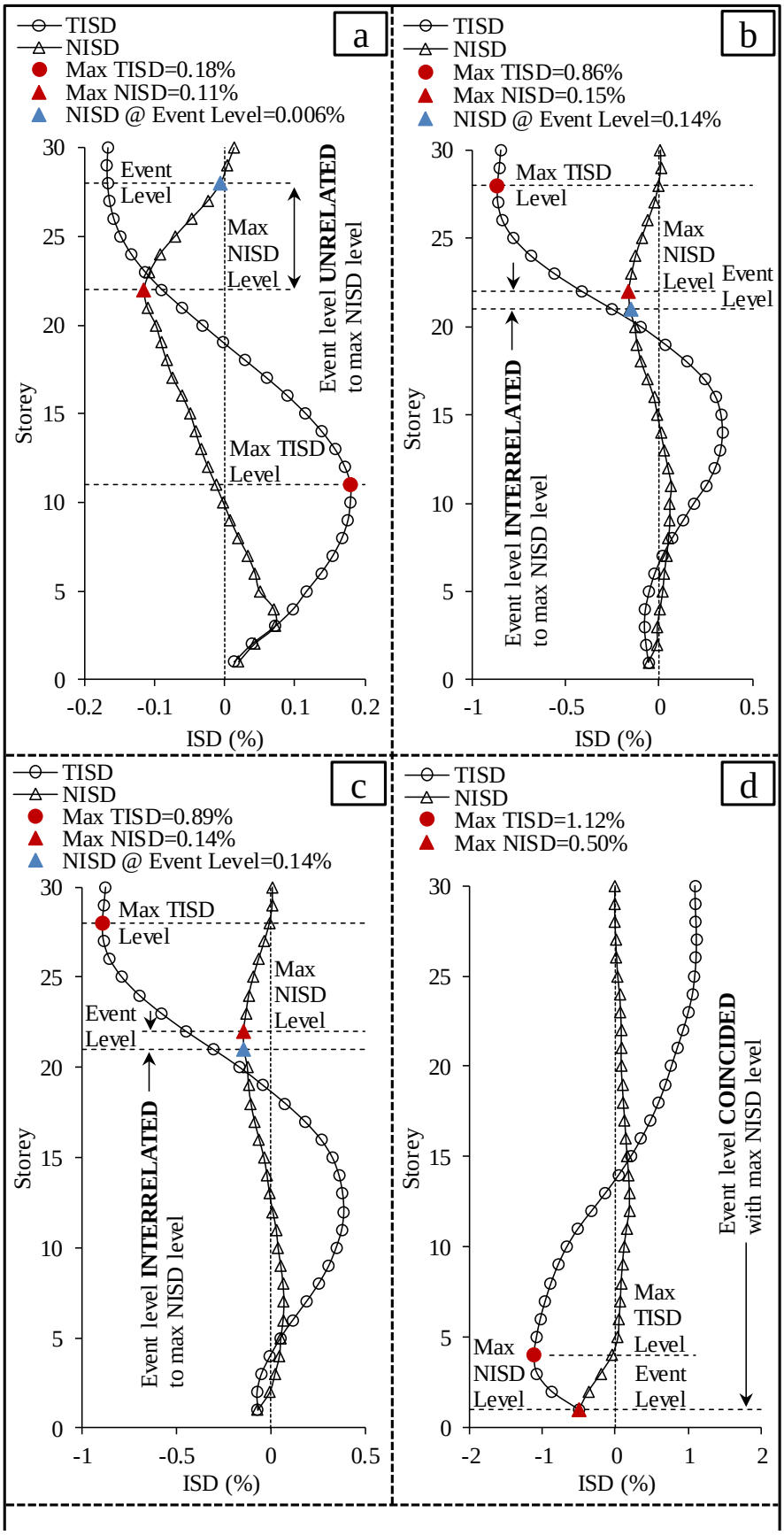

Figure 5.45. R#3 of Record Set#2: TISD vs NISD over height of reference building at the onset of local damage events: (a) rebar yield in slabs; (b) rebar yield in walls; (c) IO wall rotation limit; (d) LS wall rotation limit; ***(figure continues in the next page)***

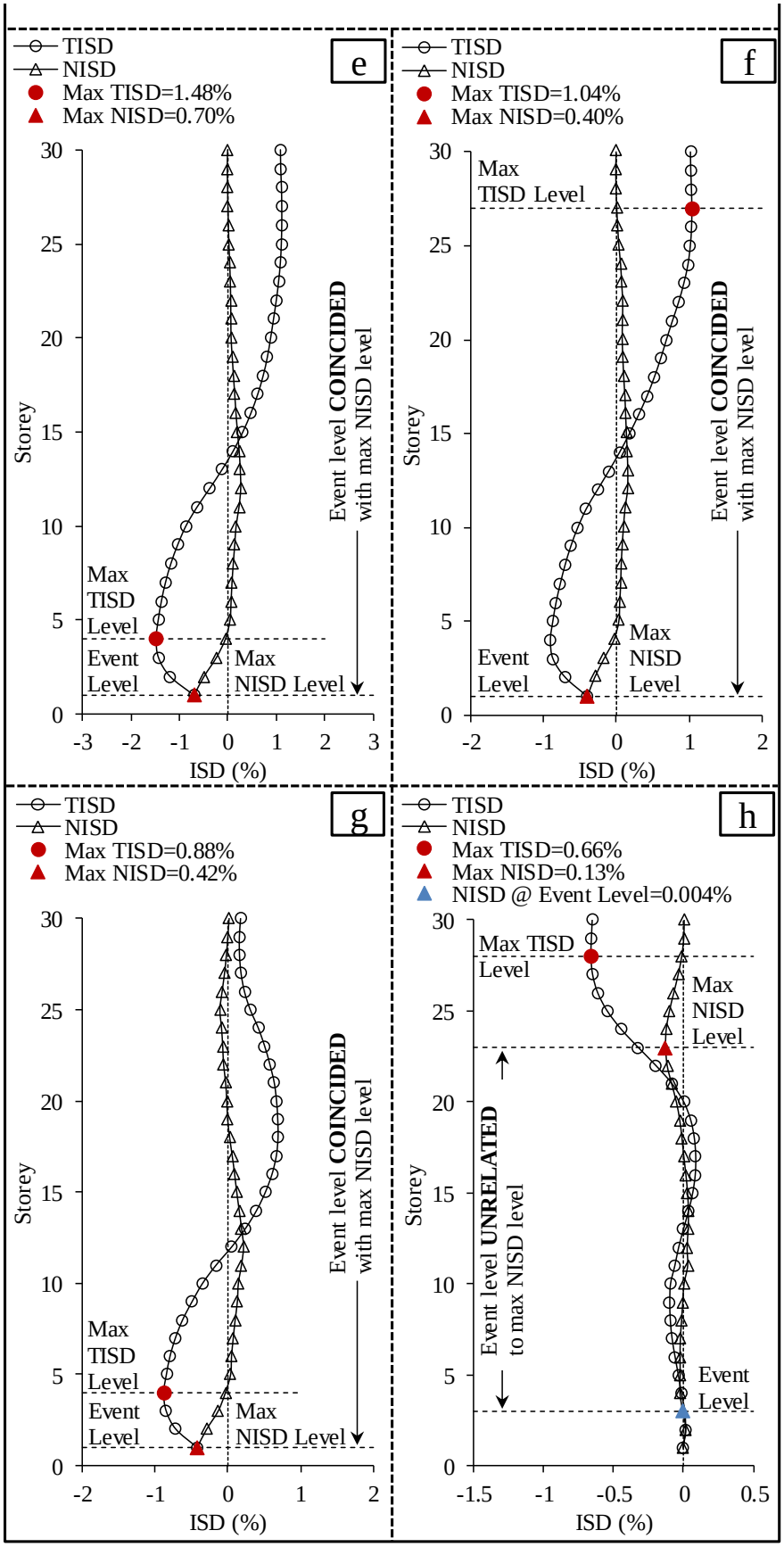

Figure 5.45 (continued). R#3 of Record Set#2: TISD vs NISD over the height of reference building at the onset of local damage events: (e) CP wall rotation limit; (f) rebar buckling in walls; (g) confined concrete crushing in walls; and (h) exceedance of shear capacity in walls

Table 5.2. Predominant mode periods and design proportions of the six additional buildings for the parametric study

Building	Mode periods in the transverse direction (s)				Member	Proportion	Storey									
							1-5	6-10	11-15	16-20	21-25	26-30	31-35	36-40	41-45	46-50
20-Stories	Uncracked		Equivalent inelastic		Core 1	Thickness	225	225	200	200						
						f_c'	40	40	40	40						
	1st	1.83	1st	2.29		V. Reinf.	2.30	1.00	1.00	0.80						
						H. Reinf.	0.80	0.91	0.74	0.61						
	2nd	0.42	2nd	0.47	Pier 1	Thickness	275	250	225	200						
						f_c'	40	40	40	40						
	3rd	0.17	3rd	0.19		V. Reinf.	0.87	0.75	0.90	1.86						
						H. Reinf.	0.25	0.25	0.28	0.25						
25-Stories	Uncracked		Equivalent inelastic		Core 1	Thickness	225	225	200	200	200					
						f_c'	40	40	40	40	40					
	1st	2.45	1st	3.29		V. Reinf.	2.15	1.00	1.00	0.85	0.76					
						H. Reinf.	1.08	0.92	0.82	0.63	0.63					
	2nd	0.60	2nd	0.69	Pier 1	Thickness	300	275	250	225	200					
						f_c'	40	40	40	40	40					
	3rd	0.26	3rd	0.28		V. Reinf.	2.43	0.62	0.89	0.93	2.01					
						H. Reinf.	0.25	0.25	0.25	0.25	0.25					
35-Stories	Uncracked		Equivalent inelastic		Core 1	Thickness	300	300	300	250	250	200	200			
						f_c'	40	40	40	40	40	40	40			
	1st	3.71	1st	5.16		V. Reinf.	4.56	1.24	1.16	1.00	1.00	0.80	0.68			
						H. Reinf.	0.83	0.67	0.54	0.54	0.54	0.61	0.66			
	2nd	0.95	2nd	1.12	Pier 1	Thickness	450	425	400	375	350	325	300			
						f_c'	40	40	40	40	40	40	40			
	3rd	0.37	3rd	0.44		V. Reinf.	5.85	4.31	4.09	2.67	1.54	0.95	1.38			
						H. Reinf.	0.25	0.25	0.25	0.25	0.25	0.25	0.25			

Concrete compressive strength (fc') is in MPa; "Pier1" length is 4000mm, all reinforcement is given in (%); all dimensions are in mm.

Table 5.2 (continued). Predominant mode periods and design proportions of the six additional buildings for the parametric study

Building	Mode periods in the transverse direction (s)				Member	Proportion	Storey									
							1-5	6-10	11-15	16-20	21-25	26-30	31-35	36-40	41-45	46-50
40-Stories	Uncracked		Equivalent inelastic		Core 1	Thickness	375	375	375	325	325	325	275	275		
						f_c'	48	48	48	48	48	48	48	48		
	1st	4.23	1st	5.96		V. Reinf.	5.48	2.31	2.52	1.00	1.00	0.69	0.62	0.49		
						H. Reinf.	0.74	0.58	0.46	0.49	0.49	0.47	0.45	0.50		
	2nd	1.08	2nd	1.29	Pier 1	Thickness	600	575	550	525	500	450	425	400		
						f_c'	48	48	48	48	48	48	48	48		
	3rd	0.42	3rd	0.50		V. Reinf.	6.50	5.18	5.01	3.64	2.65	1.57	0.55	0.83		
						H. Reinf.	0.25	0.25	0.25	0.25	0.25	0.25	0.25	0.25		
45-Stories	Uncracked		Equivalent inelastic		Core 1	Thickness	475	475	475	475	425	425	425	375	375	
						f_c'	48	48	48	48	48	48	48	48	48	
	1st	4.92	1st	6.94		V. Reinf.	5.97	3.06	3.41	2.17	1.49	1.00	0.32	0.41	0.26	
						H. Reinf.	0.63	0.58	0.42	0.40	0.48	0.44	0.35	0.38	0.43	
	2nd	1.19	2nd	1.48	Pier 1	Thickness	700	675	650	625	600	575	550	525	500	
						f_c'	48	48	48	48	48	48	48	48	48	
	3rd	0.47	3rd	0.57		V. Reinf.	7.05	6.12	6.08	4.80	3.78	2.78	0.75	0.73	1.01	
						H. Reinf.	0.25	0.25	0.25	0.25	0.25	0.25	0.25	0.25	0.25	
50-Stories	Uncracked		Equivalent inelastic		Core 1	Thickness	600	600	600	600	525	525	525	525	450	450
						f_c'	48	48	48	48	48	48	48	48	48	48
	1st	5.63	1st	8.00		V. Reinf.	6.89	4.36	4.19	3.06	2.48	1.47	1.00	0.41	0.58	0.25
						H. Reinf.	0.65	0.67	0.45	0.42	0.49	0.48	0.40	0.34	0.35	0.45
	2nd	1.32	2nd	1.70	Pier 1	Thickness	850	825	800	775	750	725	700	650	600	550
						f_c'	48	48	48	48	48	48	48	48	48	48
	3rd	0.54	3rd	0.66		V. Reinf.	7.25	6.52	6.58	5.57	4.54	3.57	0.61	0.45	0.42	1.86
						H. Reinf.	0.25	0.25	0.25	0.25	0.25	0.25	0.25	0.25	0.25	0.25

Concrete compressive strength (fc') is in MPa; "Pier1" length is 4000mm, all reinforcement is given in (%); all dimensions are in mm.

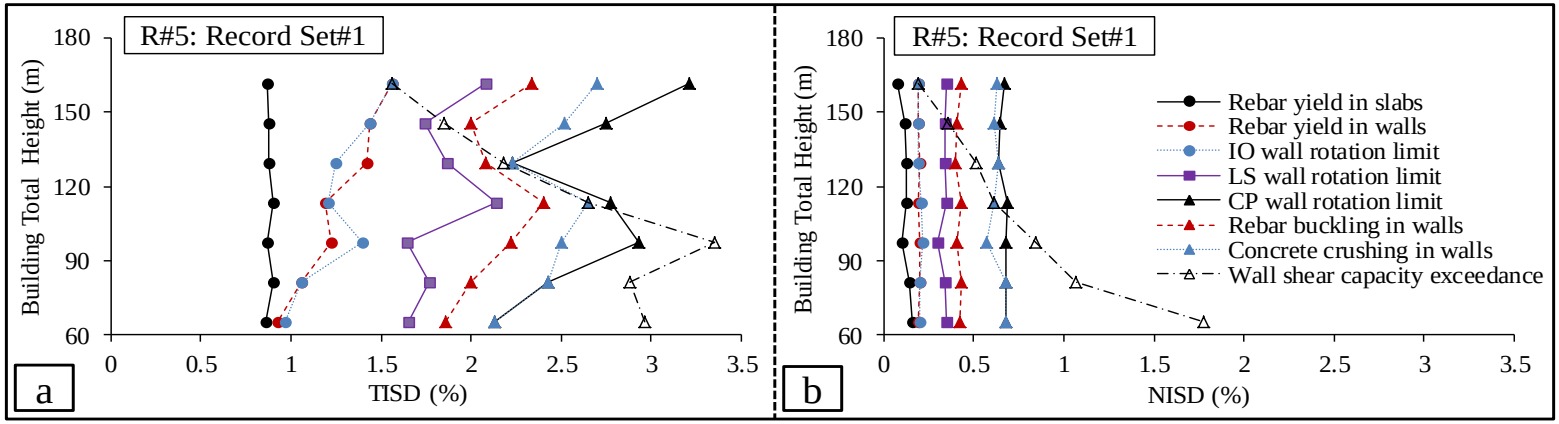

Figure 5.46. R#5 of Record Set#1: Global response of buildings with different heights at seismic intensity levels corresponded to the onset of damage events: (a) TISD; and (b) NISD

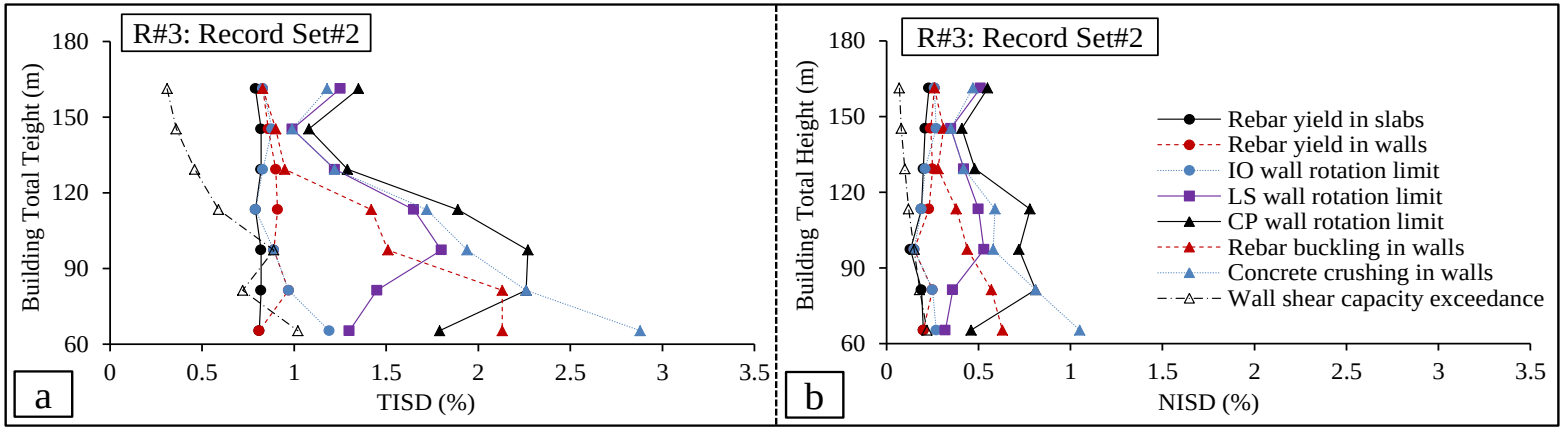

Figure 5.47. R#3 of Record Set#2: Global response of buildings with different heights at seismic intensity levels corresponded to the onset of damage events: (a) TISD; and (b) NISD

5.6 Definition of performance limit state criteria

The three commonly used performance levels (IO, LS, and CP) are adopted in the present study. New SSSB limit state criteria are proposed using the MRIDAs results from the 40 selected records and the mapping/linking of predefined local damage discussed in Sections 5.3 and 5.5 of this chapter. Table 5.3 summarises the conceptual definitions of the proposed limit state criteria, while Figure 5.48 and Figure 5.49 depict the 50% fractile of the NISDs related to selected local damage events (or combination of events) in the reference building under R#5 and R#3, respectively. The proposed limit state criteria associated with the two investigated seismic scenarios are discussed in the succeeding sub-sections.

Table 5.3. Conceptual definitions of adopted limit state criteria for the reference building

Limit State	Wall response	Definition
Immediate Occupancy (IO)	Wall response controlled by flexure	The onset of the first yield of reinforcing steel in all vertical/horizontal elements or the (IO) ASCE/SEI 41-06 rotation limits in shear walls/core system/coupling beams, whichever comes first.
	Wall response controlled by shear	NISD corresponding to values in Table 6-19 (ASCE/SEI 41-06).
Life Safety (LS)	Wall response controlled by flexure	The onset of the (LS) ASCE/SEI 41-06 rotation limits in shear walls/core system/coupling beams or 50% of CP-related NISD from all deformation-based DIs combined, whichever comes first.
	Wall response controlled by shear	NISD corresponding to values in Table 6-19 (ASCE/SEI 41-06).
Collapse Prevention (CP)	Wall response controlled by flexure	The onset of buckling/fracture of reinforcing steel, crushing of concrete core, the (CP) ASCE/SEI 41-06 rotation limits in shear walls/core system/coupling beams or the exceedance of shear capacity in shear walls/core system, whichever comes first.
	Wall response controlled by shear	The onset of exceedance of shear capacity in shear walls/core system or NISD corresponding to values in Table 6-19 (ASCE/SEI 41-06), whichever comes first.

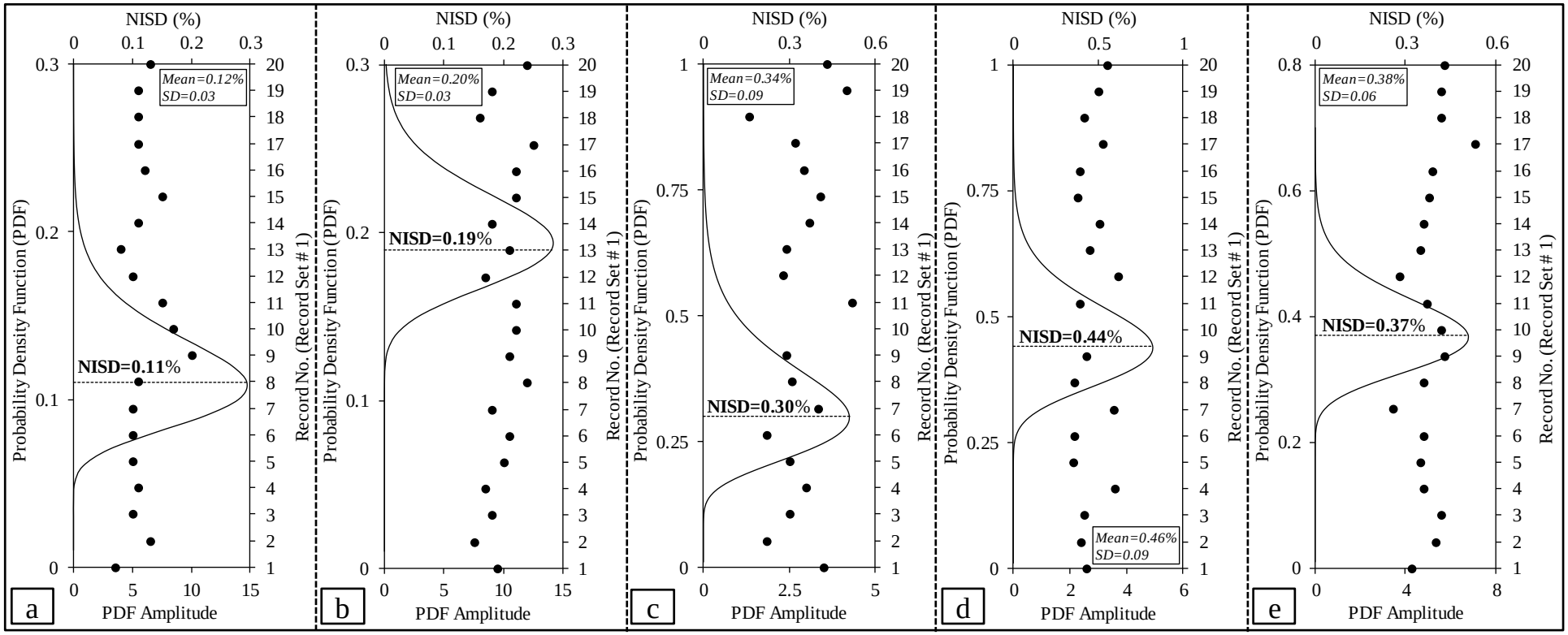

Figure 5.48. 50% fractile of NISDs associated with selected local damage events obtained from MRIDAs of the reference building under Record Set#1: (a) rebar yield in slabs; (b) rebar yield in walls; (c) exceedance of (LS) rotation limit in walls; (d) all CP-related local damage events excluding shear capacity exceedance; and (e) all CP-related local damage events including shear capacity exceedance

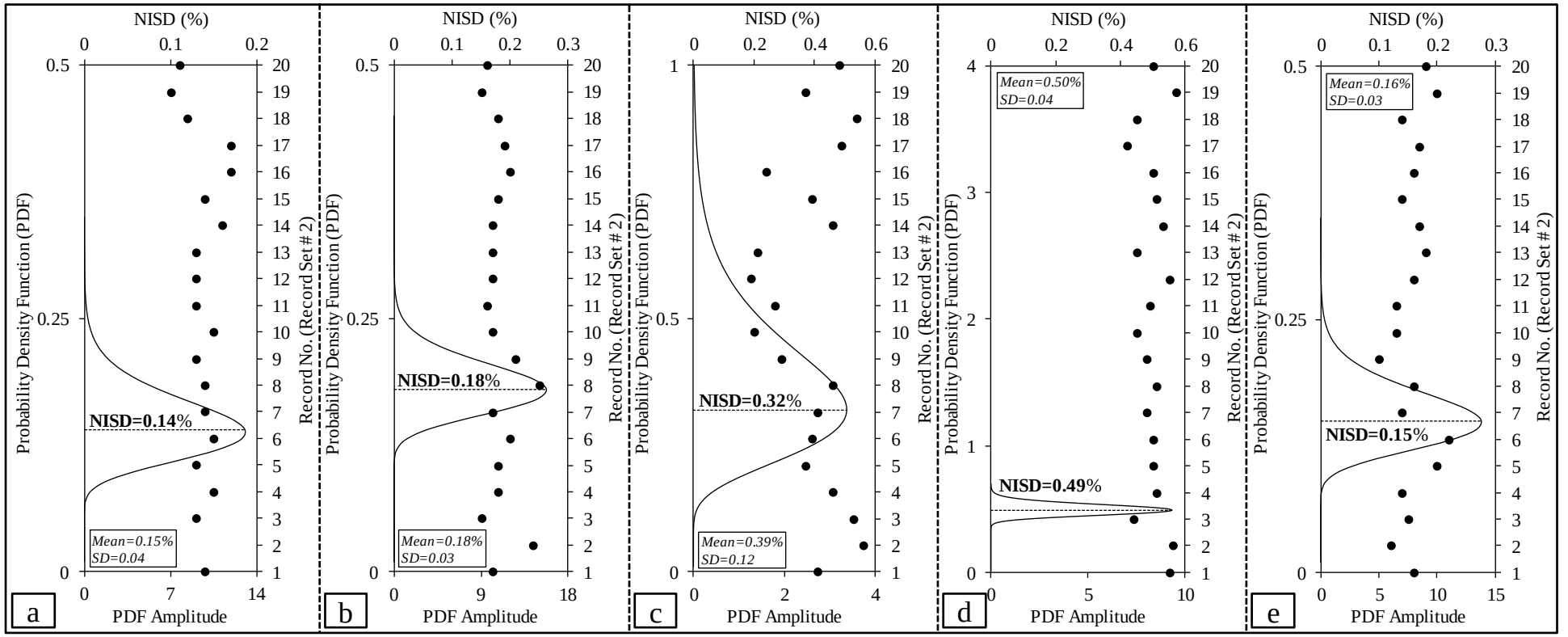

Figure 5.49. 50% fractile of NISDs associated with selected local damage events obtained from MRIDAs of the reference building under Record Set#2: (a) rebar yield in slabs; (b) rebar yield in walls; (c) exceedance of (LS) rotation limit in walls; (d) all CP-related local damage events excluding shear capacity exceedance; and (e) all CP-related local damage events including shear capacity exceedance

5.6.1 Limit states for severe distant earthquake scenario

For this scenario, the 50% fractile of the NISDs associated with the first reinforcing steel yield in the flooring system is 0.11% (Figure 5.48a). This value is selected as the IO limit state in the present study. Although the 50% fractile TISD (0.81%) corresponding to this value is higher than that suggested by ASCE/SEI 41-06 (0.5%), it is justified by the fact that the structural system of the reference building (piers and core walls with flat slabs) has potentially larger deformations when compared with structures employing other flooring systems. For the first yield in walls, the 50% fractile of the NISDs is 0.19% (corresponding to 50% fractile TISD=1.43%), (Figure 5.48b). This relatively high NISD value is attributed to the high compressive load on the lower storeys which delays the onset of initial yielding and cracking of vertical elements.

For the CP limit state, the 50% fractile of the NISDs associated with all monitored CP-related damage events without and with considering shear demand/supply local damage index are 0.44% and 0.37% (corresponding to 50% fractile TISD=2.72% and 2.39%), respectively (Figure 5.48d and e). In 11 out of the 20 input ground motions, wall shear capacity, particularly of core segments at lower storeys, is exceeded prior to the onset of any other CP-related damage events. This is attributed to the increasing influence of higher modes on the structural response at higher input ground motion intensities, as shown in Figure 5.17. Hence, the NISD associated with the CP limit state is taken as 0.37%.

The adopted criteria for reaching the LS limit state are either the wall rotation limit according to ASCE/SEI 41-06 or 50% of the NISD associated with all CP-related deformation-based DIs, whichever comes first. As shown in Figure 5.48c, the 50% fractile of NISD associated with wall rotation is 0.30% (corresponding to 50% fractile TISD=2.09%), while the 50% NISD of the deformation-based DIs corresponding to CP is calculated as 0.22%. Hence, the latter value is selected as the level of NISD that corresponds to the LS limit state.

It is important here to highlight that in the ASCE/SEI 41-17 (2017), some changes have been introduced to the recommended values of acceptable wall and coupling beams rotation for RC shear walls and associated components controlled by flexure (in Table 10.19 ASCE/SEI 41-17) as opposed to the values recommended in Table 6.18 of ASCE/SEI 41-06 (2007). These changes, however, have impact neither on the mapping

results in Section 5.3 nor on the performance limit state criteria adopted for the reference building under the severe distant seismic scenario. The reason for that is explained hereafter.

- For RC shear walls and associated components controlled by flexure (under Record Set #1), the acceptable plastic hinge rotations (radians) for shear walls and diagonally-reinforced coupling beams are actually increased for LS and CP limit states in ASCE/SEI 41-17 (Table 10-19) compared to the values recommended by ASCE/SEI 41-06 (Table 6.18), while the values recommended for the IO limit state were left unchanged.

- In the current study, the plastic hinge rotation threshold for shear walls and coupling beams, even though they were based on smaller values recommended by ASCE/SEI 41-06, never control the definition of the adopted CP performance limit state under the severe distant seismic scenario. The mapping of the local damage events under this seismic scenario (Figure 5.14 to Figure 5.18, Figure 5.27a, and Figure 5.48d,e) show that the CP threshold rotations in the cores, piers, and coupling beams of the reference building have always reached at higher seismic intensities compared to other CP-related deformation-based local damage events (i.e. rebar buckling and concrete crushing) and sometimes even when compared to the shear exceedance damage index.

- For the LS performance limit state definition under severe distant seismic scenario, the NISD of 0.22% adopted to define the LS performance limit state (50% of the NISD associated with all CP-related deformation-based damage indices) is lower than the NISD corresponding to the reach of wall/coupling beam acceptable rotations recommended by ASCE/SEI 41-06 (and consequently the values recommended by ASCE/SEI 41-17 since they are higher) under all records of Record Set #1.

5.6.2 Limit states for moderate near-field earthquake scenario

For this scenario, the response of the reference building differs significantly with higher modes dominating. This is attributed to the fact that the spectrum intensities of Record Sets #1 and #2, representing the two investigated seismic scenarios, are completely different with one is significantly stronger than the other (e.g. Kappos and Kyriakakis, 2000). The spectra of input ground motions with high frequencies, short durations, medium-to-small magnitudes, and short site-to-source distances in Record Set #2 have high amplifications concentrated in the short-period range. On the other hand, the high amplification in the spectra of the records in Record Set #1, representing earthquakes with low dominant frequencies, high-to-medium magnitudes, long site-to-source

distances and long durations, are spread over the intermediate-to-long period range. Detailed investigation on the relation between the response nature of the reference building and the ground motion characteristics under the two studied seismic scenarios is given in Section 5.4.

Figure 5.50 shows relative lateral displacements over height at the onset of selected mapped local damage events under R#5 and R#3. It is shown that building response under R#5 is dominated by the first mode (except in shear capacity exceedance) while under R#3, response to all events is dictated by the second or third mode. This is also depicted in Figure 5.11 to Figure 5.17 and Figure 5.19 to Figure 5.25. In fact, higher modes shift the shear wall response from flexure-controlled under Record Set#1 to shear-controlled under Record Set#2. This is confirmed by the NISD distribution shown in Figure 5.49. The figure shows that shear capacity is exceeded in core segments at lower storeys prior to the detection of the first plastic hinge anywhere in the structure in 8 out of 20 records and before the first plastic hinge is initiated in wall elements in 15 out of 20 records.

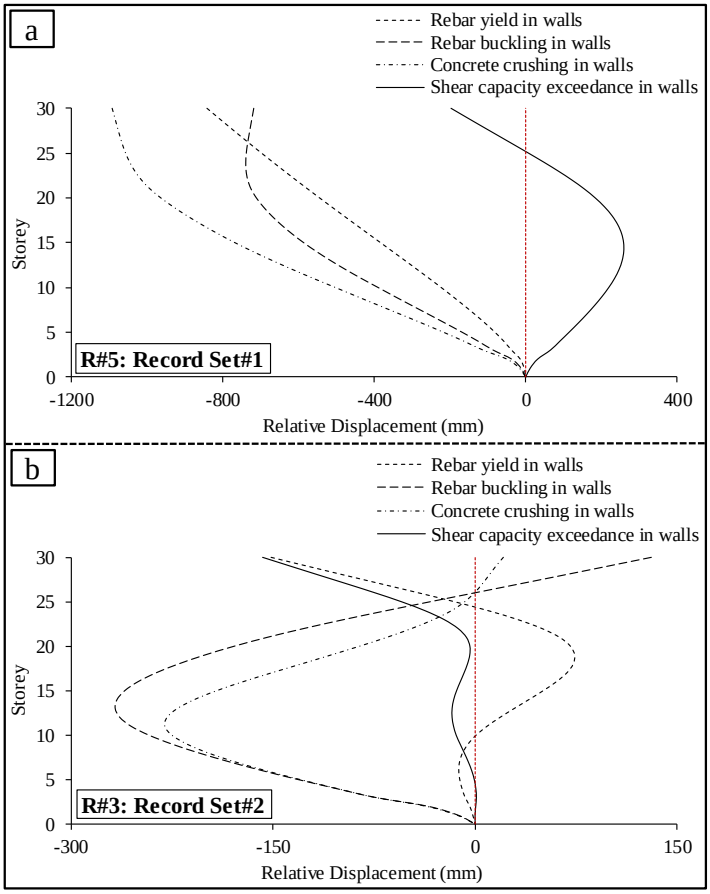

Figure 5.50. Relative lateral displacement over the height of reference building at the onset of selected local damage events: (a) under R#5 of Record Set#1; and (b) under R#3 of Record Set#2

The same can also be concluded from the propagation of local damage events under R#5 and R#3, shown in Figure 5.51. Under R#5, the building responds with rebar yielding in the flooring system, followed by wall rebar yielding, rebar buckling, concrete crushing, and finally with exceedance of shear capacity (Figure 5.51a). Building response to R#3 (Figure 5.51b), on the other hand, differs as the exceedance of shear capacity occurs at the same seismic intensity scale associated with rebar yielding in walls and just after rebar yielding in the flooring system. As shown in Figure 5.49e, the calculated 50% fractile NISD associated with the shear capacity damage index is 0.15%. This value corresponds to 50% fractile TISD=0.79%; a value close to the TISD suggested by ASCE/SEI 41-06 for walls with shear-controlled response at CP (0.75%).

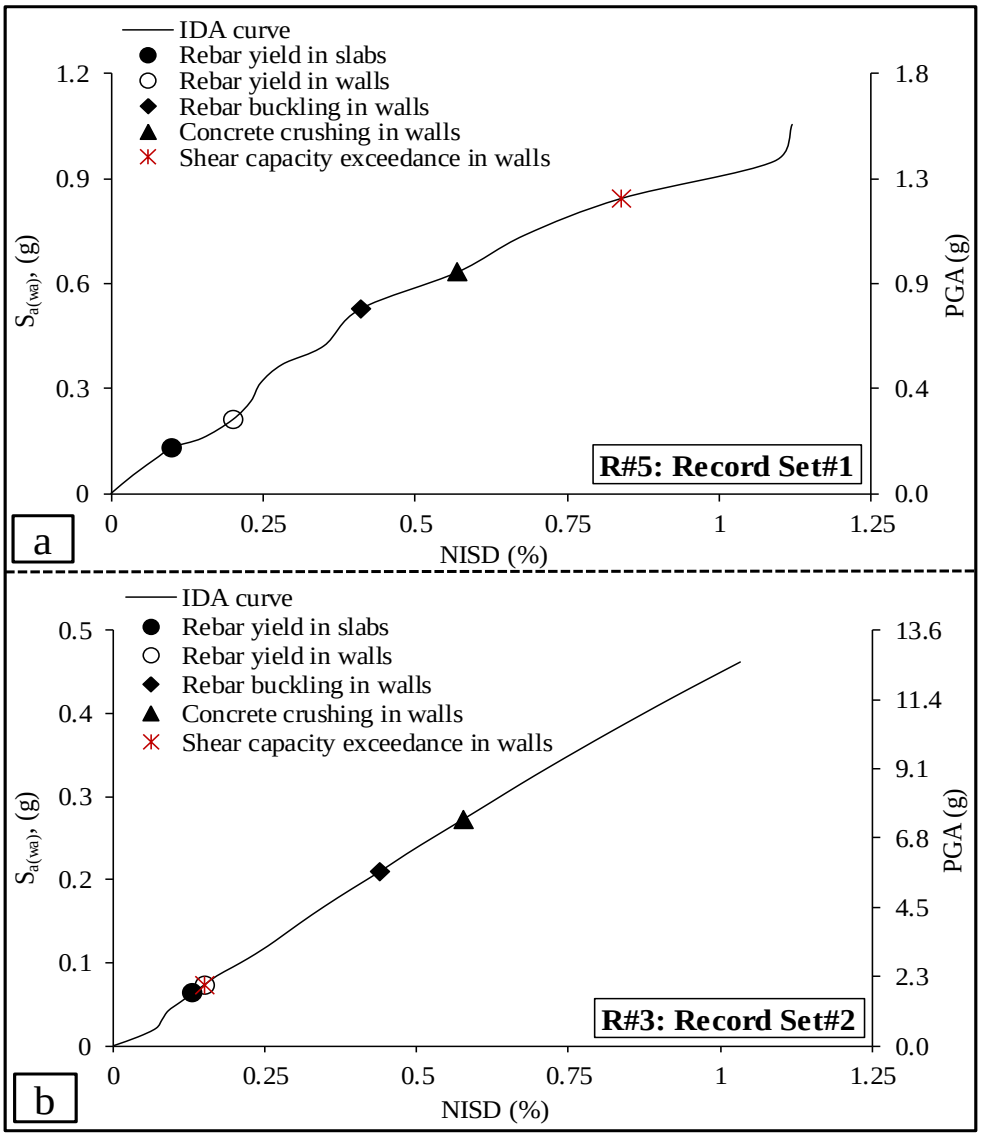

Figure 5.51. Propagation of local damage events in the reference building: (a) under R#5 of Record Set#1; and (b) under R#3 of Record Set#2

To add to the above discussion, the bending moment and shear demand histories in the core wall segments at the time bracketing the onset of exceeding the shear capacity under R#5 and R#3 are plotted in Figure 5.52. Under R#5 (Figure 5.52a), the high bending moment-to-shear ratio (M/V=1.72) corresponds to flexure-controlled behaviour. On the other hand, the low bending moment-to-shear ratio (M/V=0.72) under R#3 (Figure 5.52b) warrants the shear-controlled classification for the response of the reference building.

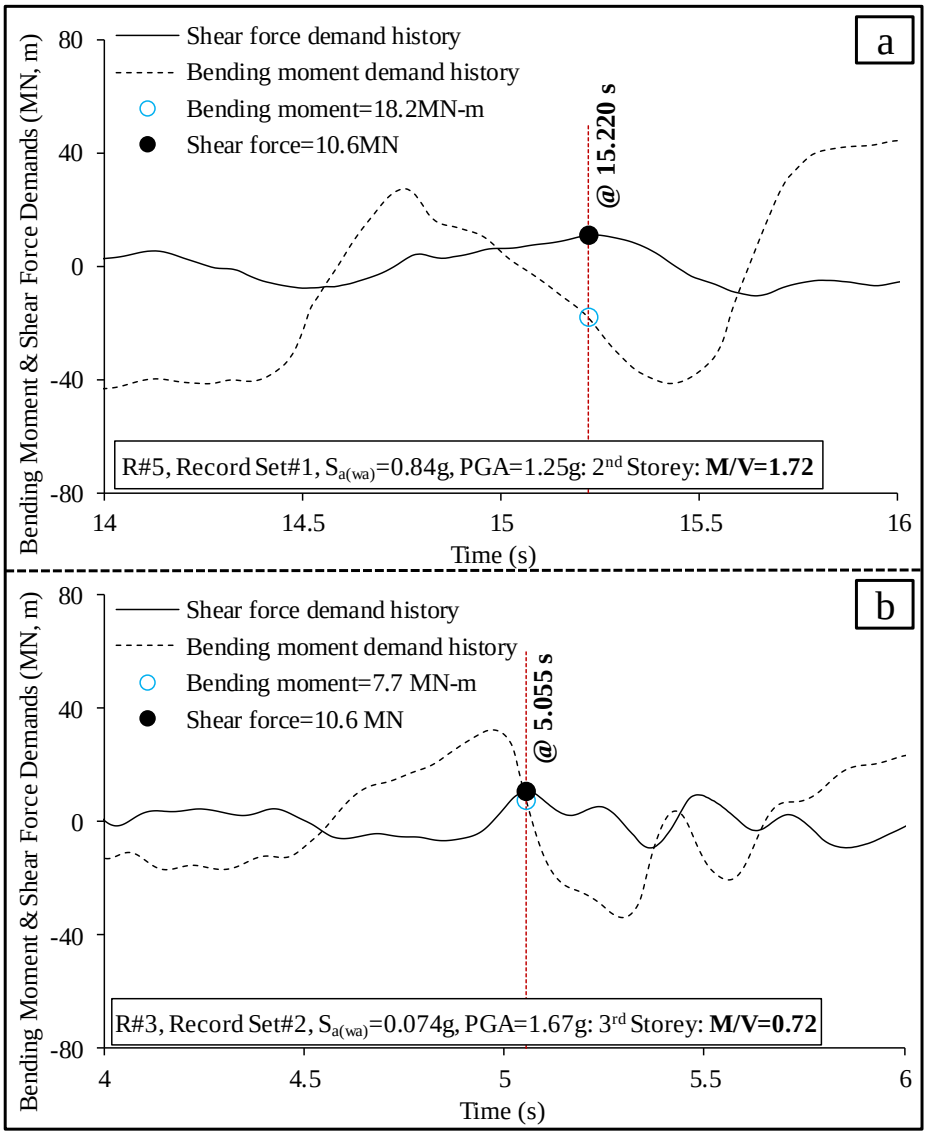

Figure 5.52. Bending moment and shear force demand time histories in the core wall segments of the reference building at the onset of shear capacity exceedance: (a) under R#5 of Record Set#1; and (b) under R#3 of Record Set#2

As another way of analysing the seismic scenario-based shear response of the reference building, the base shear at increasing seismic intensities is plotted in Figure 5.53 and Figure 5.54. In Figure 5.53, the horizontal axes present the ground motion intensity in

terms of PGA and $S_{a(wa)}$. While in Figure 5.54, it presents the overall maximum NISD. As illustrated in Figure 5.53, the base shear values in both earthquake scenarios at the seismic intensity levels corresponded to the shear capacity exceedance in the wall segments (27.5MN under R#5 and 24.5MN under R#3) are related to relatively close PGA values (1.25g under R#5 and 1.67g under R#3) with a difference of only 34%. The figure also shows that base shear-PGA-$S_{a(wa)}$ curves for the two earthquake scenarios have similar trends with base shear values under R#5 30-50% higher than those under R#3 at corresponding PGA-$S_{a(wa)}$ values. Figure 5.54, on the other hand, depicts that these base shear values are pinned to overall maximum NISDs of considerably different values in each of the two earthquake scenarios (0.84% under R#5 and 0.15% under R#3), with a total difference of 460%. The two curves in Figure 5.54 illustrate different trends with base shear values under R#3 dramatically increasing when compared to those under R#5 as maximum NISD increases, with a difference ranging from 200% at NISD=0.12% to as much as 350% at NISD=1.0%. This, again, indicates that the building responds differently under the two investigated seismic scenarios. The very low overall maximum NISD of which the shear failure occurred under R#3 compared to its counterpart under R#5 strengthens the classification of the reference building response under moderate near-field earthquakes as shear-controlled

Based on the above, NISD values of 0.08% and 0.11% are proposed to be associated with IO and LS limit states, respectively. These values correspond to the TISDs (0.4% and 0.6%) recommended in ASCE/SEI 41-06 for walls with response controlled by shear. For CP, NISD of 0.15% is proposed. The mapped and proposed limit state criteria for the building under Record Set#1 and Record Set#2 are listed in Table 5.4.

The ASCE/SEI 41-17 (2017) has introduced some changes to the recommended values of acceptable total drift for RC shear walls and associated components controlled by shear (in Table 10.20 ASCE/SEI 41-17) as opposed to the values recommended in Table 6.19 of ASCE/SEI 41-06 (2007). Again, these changes have impact neither on the mapping results in Section 5.3 nor on the performance limit state criteria adopted for the reference building under the moderate near-field seismic scenario, except for the LS-NISD threshold where a minimal change is introduced compared to the NISD value based on the ASCE/SEI 41-06 recommendations. This conclusion is argued hereafter.

- For RC shear walls and associated components controlled by shear (under Record Set #2), the acceptable total drift (TISD; %) for shear walls are changed

in ASCE/SEI 41-17 (Table 10-20) to 0.75% and 1.00% (under axial force ratio > 0.05) for LS and CP limit states, respectively, compared to the 0.60% and 0.75% values recommended by ASCE/SEI 41-06 (Table 6.19), while the values recommended for the IO limit state were left unchanged (0.40%).

- For the definition of the CP performance limit state criteria in the current study, the drift value recommended by ASCE/SEI 41-06 is not been utilized. The NISD value of 0.15% (corresponding to TISD = 0.79%) adopted in the definition of the CP performance limit state under moderate near-field seismic scenario is based on the mapping of all the adopted CP-related damage indices (Figure 5.22 to Figure 5.26, Figure 5.27b, and Figure 5.49d,e). It is important to emphasize here that, due to the response nature of the reference building under moderate near-field earthquakes, the CP limit state definition is controlled by the shear exceedance damage index for all records in Record Set #2.

- For the definition of the LS performance limit state criteria in the current study, the NISD value of 0.11% adopted in the definition of the LS performance limit state under moderate near-field seismic scenario corresponds to the TISD value of 0.60% recommended by ASCE/SEI 41-06 (Table 6.19). The NISD value corresponding to the new TISD of 0.75% recommended by ASCE/SEI 41-17 (Table 10-20) is 0.117%, that is only 6% higher. It is worth noting that due to the rigid body motion component (RBM), a certain percentage of increase in the TISD value renders a much small percentage of increase in the corresponding NISD.

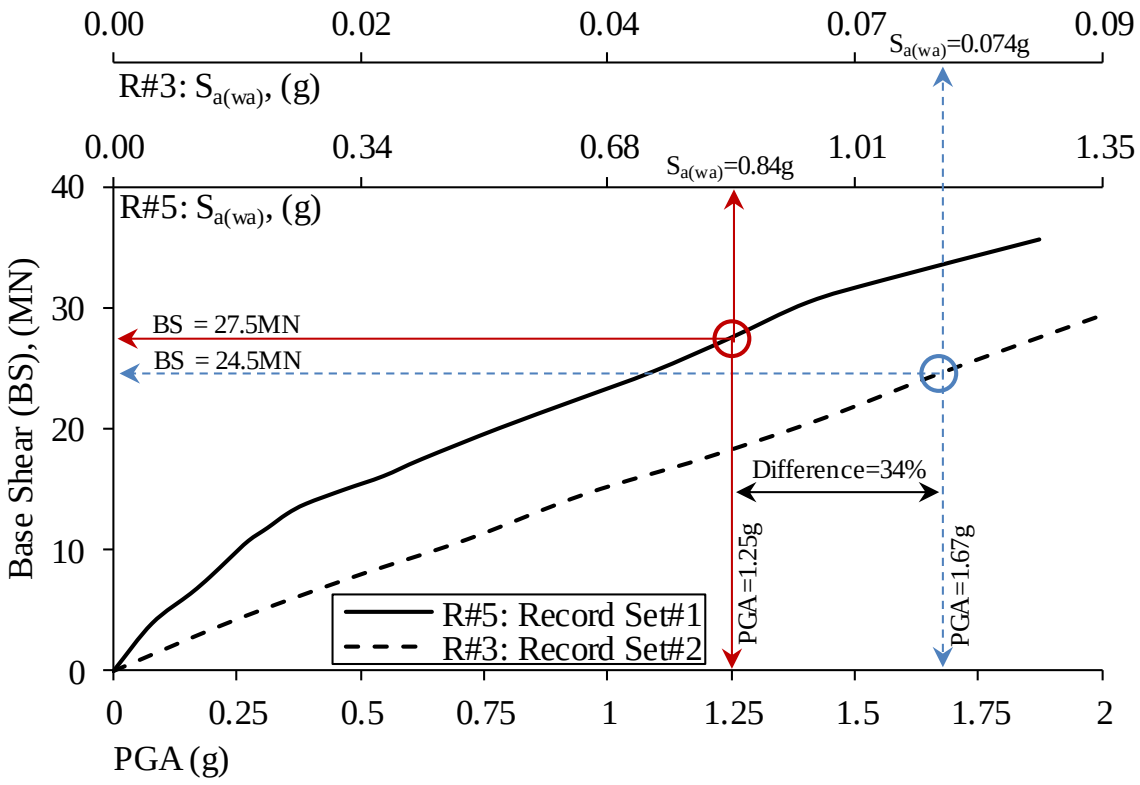

Figure 5.53. Reference building PGA and $S_{a(wa)}$ vs base shear under R#5 of Record Set#1 and R#3 of Record Set#2 at different intensity levels

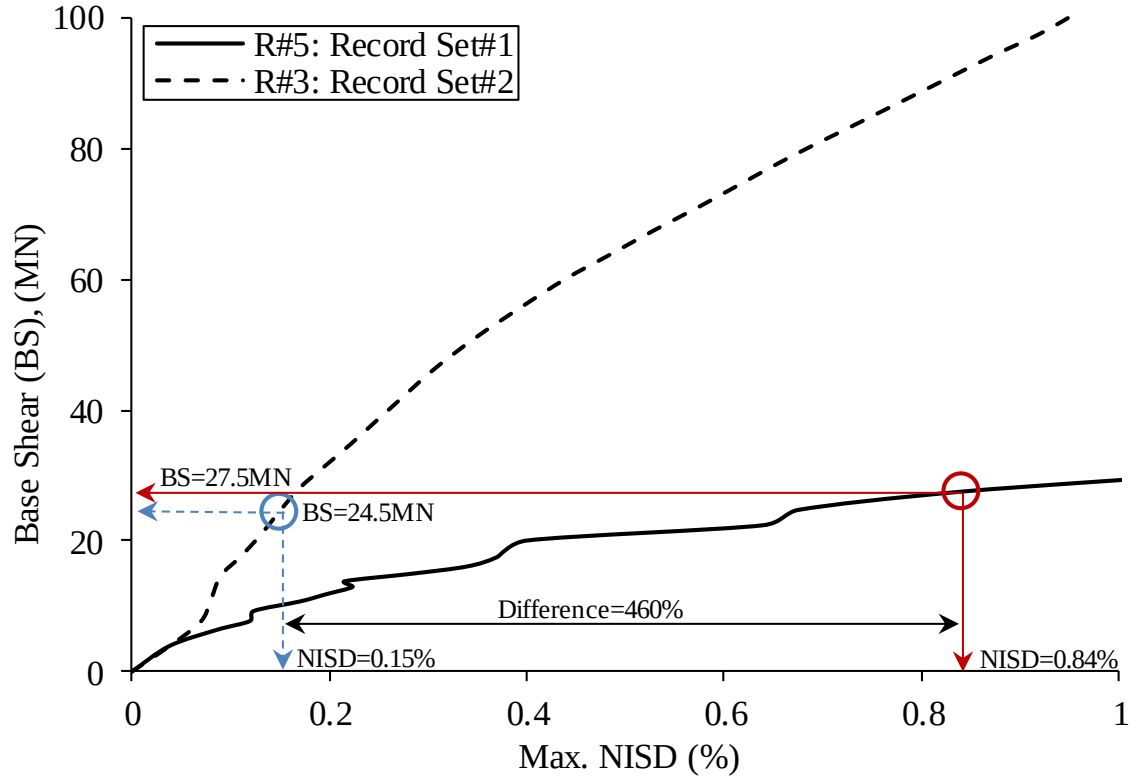

Figure 5.54. Reference building max NISD vs base shear under R#5 of Record Set#1 and R#3 of Record Set#2 at different intensity levels

Table 5.4. Mapped and recommended limit state criteria for the reference building

Limit state	Damage Index (DI)	NISD (%)			
		Record Set#1 (Far-field)		Record Set#2 (Near-field)	
		Mapped	Proposed	Mapped	Proposed
IO	1st rebar yield in slabs	0.11	0.11	0.14	0.08
	1st rebar yield in walls	0.19		0.18	
	Wall rotation limit (ASCE/SEI 41-06)	0.19		0.17	
	All IO-related deformation-based DIs (combined)	0.11		0.14	
	NISD corresponds to value in Table 6-19 of ASCE/SEI 41-06 for RC shear walls controlled by shear	N/A		0.08	
LS	Wall rotation (ASCE/SEI 41-06)	0.30	0.22	0.32	0.11
	50% of NISD from all CP-related deformation-based DIs (combined)	0.22		0.25	
	NISD corresponding to the value in Table 6-19 of ASCE/SEI 41-06 for RC shear walls controlled by shear	N/A		0.11	
CP	1st rebar buckling in walls	0.44	0.37	0.49	0.15
	1st concrete crushing in walls	0.59		0.67	
	Wall rotation (ASCE/SEI 41-06)	0.51		0.71	
	Shear capacity exceedance	0.37		0.15	
	All CP-related deformation-based DIs (combined)	0.44		0.49	
	All CP-related DIs inclusive of shear capacity (combined)	0.37		0.15	
	NISD corresponds to the value in Table 6-19 of ASCE/SEI 41-06 for RC shear walls controlled by shear	N/A		0.14	

5.7 Summary and concluding remarks

In this chapter, the methodology for proposing reliable Seismic Scenario-Structure-Based (SSSB) definitions of performance limit state criteria for high-rise RC wall buildings is illustrated on the 30-storey RC wall reference building located in Dubai (study region). Multi-Record Incremental Dynamic Analyses (MRIDAs) with new intensity measure are conducted to assess building local response to two different seismic scenarios. Seismic scenario-based local damage events, presented with a range of deformation and capacity-based damage indices (DIs), are mapped and linked to building global response. The relation between those local DIs and the input ground motion characteristics are also discussed. Finally, a new set of SSSB limit state criteria is proposed for the reference structure.

A parametric study involving the reference 30-storey structure in addition to six other buildings with different heights shows that, for such buildings, Net Inter-Storey Drift (NISD) is better than Total Inter-Storey Drift (TISD) as a global damage measure (DM) in defining limit state criteria. NISD is better linked with the local response over the height of the building and well correlated to deformation-based local damage events for buildings with varying heights. The study concludes that structural system, arrangement and geometry of vertical elements, and axial force level in the lower storeys influence the seismic intensity and deformation levels that are related to local damage events. It is found that moderate near-field earthquake events can shift the seismic response from flexure-controlled to shear-controlled. This leads to the conclusion that the response of RC high-rise wall buildings and consequently the definition of limit state criteria for designated performance levels are strongly influenced by both the structure and the seismic scenario. As a result, new SSSB limit state criteria are proposed for RC high-rise wall buildings with similar characteristics and subjected to similar seismic scenarios.

This page is intentionally left in blank

CHAPTER 6. Fragility relations: Development, assessment, and simplified methodology

Chapter 6 contains four main sections. Section 6.1 involves the development of the seismic scenario-based fragility relations for the reference building. This represents the concluding step in the proposed framework for the seismic vulnerability assessment of RC high-rise wall buildings (the reader is referred to the IPO model presented in CHAPTER 2). In Section 6.2, the developed fragility relations are examined at selected earthquake intensity levels to assess their accuracy. Furthermore, the characteristics of the developed fragility relations under the two investigated seismic scenarios are analysed and compared. 6.2 is concluded by correlating the developed fragility relations with four states of damage in the reference building, that is unimpaired occupancy, impaired occupancy, structural damage, and structural collapse.

In Section 6.3, a simplified methodology towards developing fragility relations with less computational effort is proposed. Utilising this methodology, the fragility curves of reinforced concrete high-rise buildings can be generated with a much lower number of input ground motions compared to the original number of records adopted in the current study (i.e. twenty records in each set). Using a lower number of records results in a dramatic reduction in time and effort, especially when a big building inventory is under investigation. Accordingly, the fragility curves developed using this simplified methodology are called hereafter Cheaper Fragility Curves (CFC). The chapter is concluded with Section 6.4, where the summary and concluding remarks are presented.

6.1 Development of the fragility relations

In this section, seismic scenario-based fragility relations for the reference building are developed. Furthermore, the efficiency of the proposed damage measure (NISD) is investigated using the confidence interval relative width statistics. The fragility curves are developed using the following equation (Wen et al., 2004):

$$\mathrm{POE}(\mathrm{PLS_i}|\mathrm{IM}) = 1 - \varphi\left(\frac{\alpha_{(\mathrm{DM}|\mathrm{PLS_i})} - \alpha_{(\mathrm{DM}|\mathrm{IM})}}{\sqrt{\beta^2_{(\mathrm{DM}|\mathrm{IM})} + \beta^2_{(\mathrm{DM}|\mathrm{PLS_i})} + \beta^2_{\mathrm{m}}}}\right) \tag{6.1}$$

Where $\mathrm{POE}(\mathrm{PLS_i}|\mathrm{IM})$ is the probability of exceeding a predefined performance limit state ($\mathrm{PLS_i}$) given the IM value, φ is the standard normal cumulative distribution function, $\alpha_{(\mathrm{DM}|\mathrm{PLS_i})}$ = ln (median of the DM capacity for $\mathrm{PLS_i}$), $\alpha_{(\mathrm{DM}|\mathrm{IM})}$ = ln (calculated median demand DM given the IM value from the regression analysis best-fit power-law line), and $\beta_{(\mathrm{DM}|\mathrm{IM})}$, $\beta_{(\mathrm{DM}|\mathrm{PLS_i})}$, and β_{m} are demand, capacity, and modelling uncertainties, respectively, given in the following equations:

$$\beta_{(\mathrm{DM}|\mathrm{IM})} = \sqrt{\ln(1+s^2)}\ , \qquad s^2 = \sum\left(\ln(\mathrm{Y_k}) - \ln(\mathrm{Y_p})\right)^2/(n-2) \tag{6.2}$$

$$\beta_{(\mathrm{DM}|\mathrm{PLS_i})} = \sqrt{\ln(1+\mathrm{cov}^2)} \tag{6.3}$$

$$\beta_{\mathrm{m}} = 0.2 \quad \text{to} \quad 0.4 \tag{6.4}$$

where s^2 is the standard error, Y_k, Y_p are the observed and power-law estimated median DM, respectively, given the IM value, n is the number of sample data demand points, and cov is the coefficient of variation for the MRIDAs. The cov coefficient is taken as 0.3 (Wen et al., 2004) when limit states are defined using pushover analysis or values recommended in the seismic provisions from codes like ASCE/SEI 41-16 (2017) and FEMA P1050 (2015). When NRHA along with MRIDA is adopted, the cov coefficient is automatically calculated within the process. The modelling uncertainty parameter β_m corresponds to the level of accuracy of the seismic response estimates by the numerical modelling compared to the actual response values. It ranges between 0.2 and 0.4 (Wen et al., 2003, Wen et al., 2004), i.e. the response estimates are within 20% to 40% of the actual value with 90% confidence.

It is worth noting that the modelling of the uncertainty in the definition of PLSs has been investigated in previous studies using different approaches (e.g. Monte Carlo sampling, Latin Hypercube sampling, and other statistical techniques) on RC frame structures (e.g. Dymiotis et al., 1999, Sousa et al., 2016, Yu et al., 2016) and shear walls (e.g. Duffey et al., 1994). In the current work, despite using a wide range of deformation- and strength-based DIs to define the threshold of the three adopted PLSs (i.e. rebar yielding in the flooring system, rebar yielding in the piers and cores, wall rotation, coupling beam rotation, rebar buckling, concrete crushing, and section shear capacity) and linking them to a reliable global DM (NISD) in an attempt to reduce the aforementioned uncertainty, the definition of the adopted PLSs, strictly speaking, is deterministic.

The process for developing fragility curves is summarised in Figure 2.28 and schematically presented in Figure 6.1.

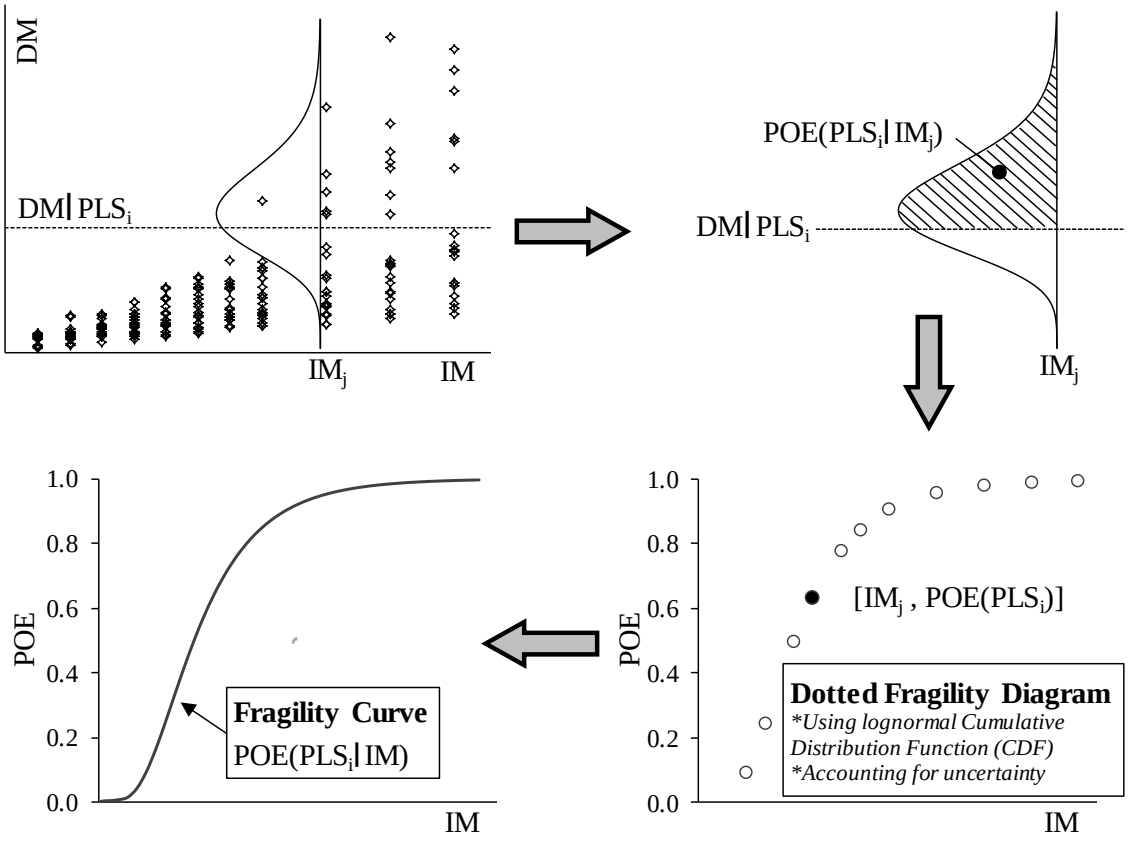

Figure 6.1. Schematic presentation for developing fragility relations

The results of the MRIDAs performed on the reference building (CHAPTER 5) in terms of $S_{a(wa)}$-NISD pair points along with best-fit power-law line and NISD values at limit state threshold for Record Set #1 and #2 are presented in Figure 6.2 and Figure 6.3, respectively. The shown regression lines represent the mean of the random variable ($NISD/S_{a(wa)}$), that is the value at which the random variable has 50% probability of being equal to or less than. In these figures, the high values of the coefficient of determination (R^2 = 0.69 for Record Set #1 and 0.85 for Record Set #2) and the coefficient of correlation ($(R^2)^{0.5}$ = 0.83 for Record Set #1 and 0.92 for Record Set #2) show strong mathematical correlation between the adopted damage and intensity measures. Furthermore, small values of dispersion ($\sigma_{NISD}|S_{a(wa)}$) are obtained (0.33 for Record Set #1 and 0.15 for Record Set #2). Given that NISD values correspond to log-normal distribution, $\sigma_{NISD}|S_{a(wa)}$ is defined as the natural logarithms of the residuals NISD data from the regression line.

The 16%, 50% (mean), and 84% fractile NISD values at the threshold of adopted limit states for the reference building under Record Set #1 and Record Set #2 are listed in Table 6.1 and Table 6.2, respectively. In addition, these tables show the standard

deviation (σ), the confidence intervals (P_{lower}, P_{upper}), and the confidence interval relative width (W) for each limit state. In these tables, the relatively high difference in the 16%, 50%, and 84% fractile NISD values corresponding to a predefined limit state is attributed to the more accurate (hence more sensitive) approach in calculating the DM (NISD) compared to the TISD, resulting from the elimination of the RBM component.

The confidence interval is a statistical value (expressed by the probability) that validates the closeness of the estimated mean value to the population mean value. The plus-minus one-σ confidence interval, corresponds to the probability of 84%, along with its relative width are calculated by the following equations:

$$P_{lower,\ upper} = \eta * e^{\pm\frac{\sigma}{\sqrt{n}}} \tag{6.5}$$

$$W\ (\%) = 100 * \frac{P_{upper} - P_{lower}}{\eta} \tag{6.6}$$

Where P_{lower} and P_{upper} are lower and upper-end points of the confidence interval for the mean of a log-normal distribution, η is the sample mean value for the random variable, $\sigma/\sqrt{n}$ is the standard error of the mean, σ is the standard deviation of the sample mean, and n is the number of sample data demand points.

In analytical practice, the acceptable confidence interval relative width is in the range of 10% (e.g. Pejovic and Jankovic, 2016). For the obtained NISD values at the threshold of the adopted limit states under the two investigated seismic scenarios, the calculated 84% confidence interval relative width is between 1.89 and 2.90 (Table 6.1 and Table 6.2). These small values indicate a high level of accuracy in calculating the random variables which can be attributed to the efficiency of the proposed damage measure (NISD).

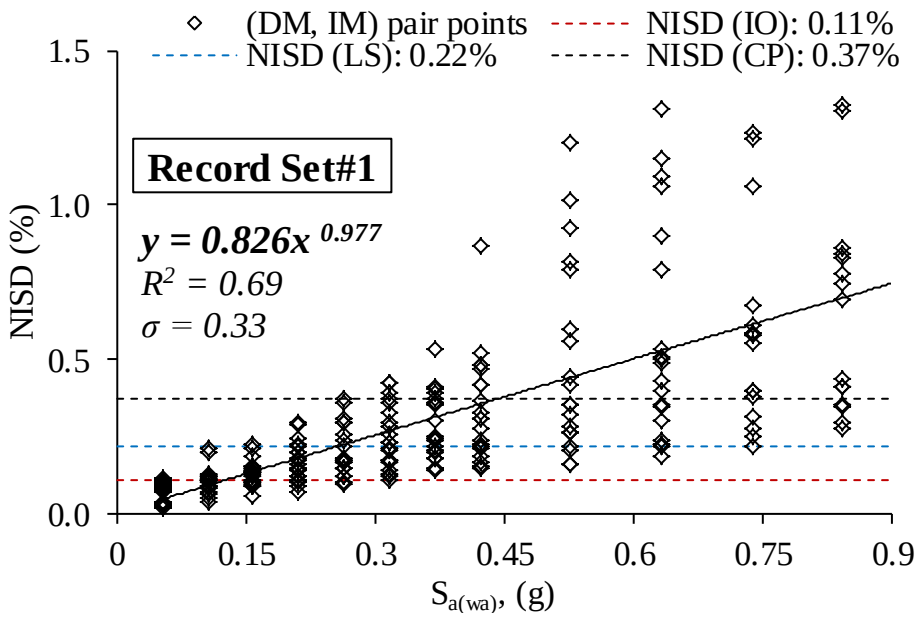

Figure 6.2. Record Set #1: Selected MRIDA results along with best-fit power-law line and NISD values at limit states threshold

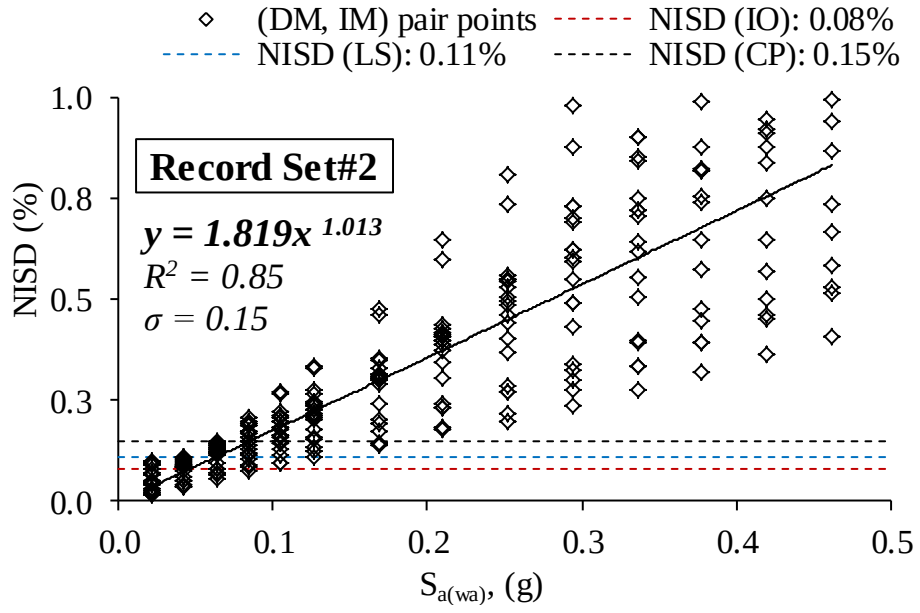

Figure 6.3. Record Set #2: Selected MRIDA results along with best-fit power-law line and NISD values at limit states threshold

Table 6.1. Reference building derived NISD properties at the threshold of performance limit states under Record Set #1

Limit state	NISD at the threshold of performance limit state (DM|PLS$_i$), (%)			Standard deviation (σ)	Lower and upper endpoint of the 84% confidence interval		Relative width of confidence interval (W), (%)
	16% Fractile	50% Fractile	84% Fractile		P_{lower}	P_{upper}	
IO	0.09	0.115	0.146	0.243	0.113	0.116	**2.90**
LS	0.189	0.226	0.271	0.182	0.224	0.229	**2.17**
CP	0.321	0.376	0.441	0.158	0.373	0.379	**1.89**

Table 6.2. Reference building derived NISD properties at the threshold of performance limit states under Record Set #2

Limit state	NISD at the threshold of performance limit state (DM|PLS$_i$), (%)			Standard deviation (σ)	Lower and upper endpoint of the 84% confidence interval		Relative width of confidence interval (W), (%)
	16% Fractile	50% Fractile	84% Fractile		P_{lower}	P_{upper}	
IO	0.059	0.075	0.095	0.237	0.074	0.076	**2.84**
LS	0.093	0.111	0.134	0.182	0.110	0.112	**2.18**
CP	0.128	0.154	0.186	0.187	0.153	0.156	**2.24**

Using the data presented in Figure 6.2 and Figure 6.3, the fragility function parameters for the reference building under the two investigated seismic scenarios are estimated (Table 6.3).

Table 6.3. Function parameters for the fragility curves of the reference building under Record Set #1 and Record Set #2

		Record Set #1			Record Set #2		
Limit states		**IO**	**LS**	**CP**	**IO**	**LS**	**CP**
Function parameters	$\alpha_{(DM\|PLS_i)}$	-2.207	-1.154	-0.994	-2.590	-2.189	-1.897
	$\beta_{(DM\|IM)}$	0.543	0.543	0.543	0.373	0.373	0.373
	$\beta_{(DM\|PLS_i)}$	0.253	0.184	0.154	0.3	0.3	0.188
	β_m	0.2 to 0.4	0.2 to 0.4	0.2 to 0.4	0.2 to 0.4	0.2 to 0.4	0.2 to 0.4

To investigate the effect of the modelling uncertainty parameter β_m, the fragility curves corresponding to the three adopted limit states with three different levels of β_m (0.2, 0.3, and 0.4) are developed under Record Set #1 and #2 and presented in Figure 6.4 and Figure 6.5, respectively. In these figures, comparing the results associated with 20%,

30%, and 40% modelling uncertainty, it can be concluded that the value assigned to β_m has a relatively insignificant effect on the slope for the entire range of the developed fragility functions. On the other hand, Figure 6.4 and Figure 6.5 indicate that beyond the curve central point, the value of $\beta_m = 0.2$ resulting in a slightly higher probability for any of the adopted limit states to be reached or exceeded at any given $S_{a(wa)}$. The upper zone of the fragility curve corresponds to higher seismic intensity levels, therefore, more critical to the vulnerability assessment of a building or a building stock. Giving that, the value of $\beta_m = 0.2$ is adopted for developing all further fragility relations discussed in the present work.

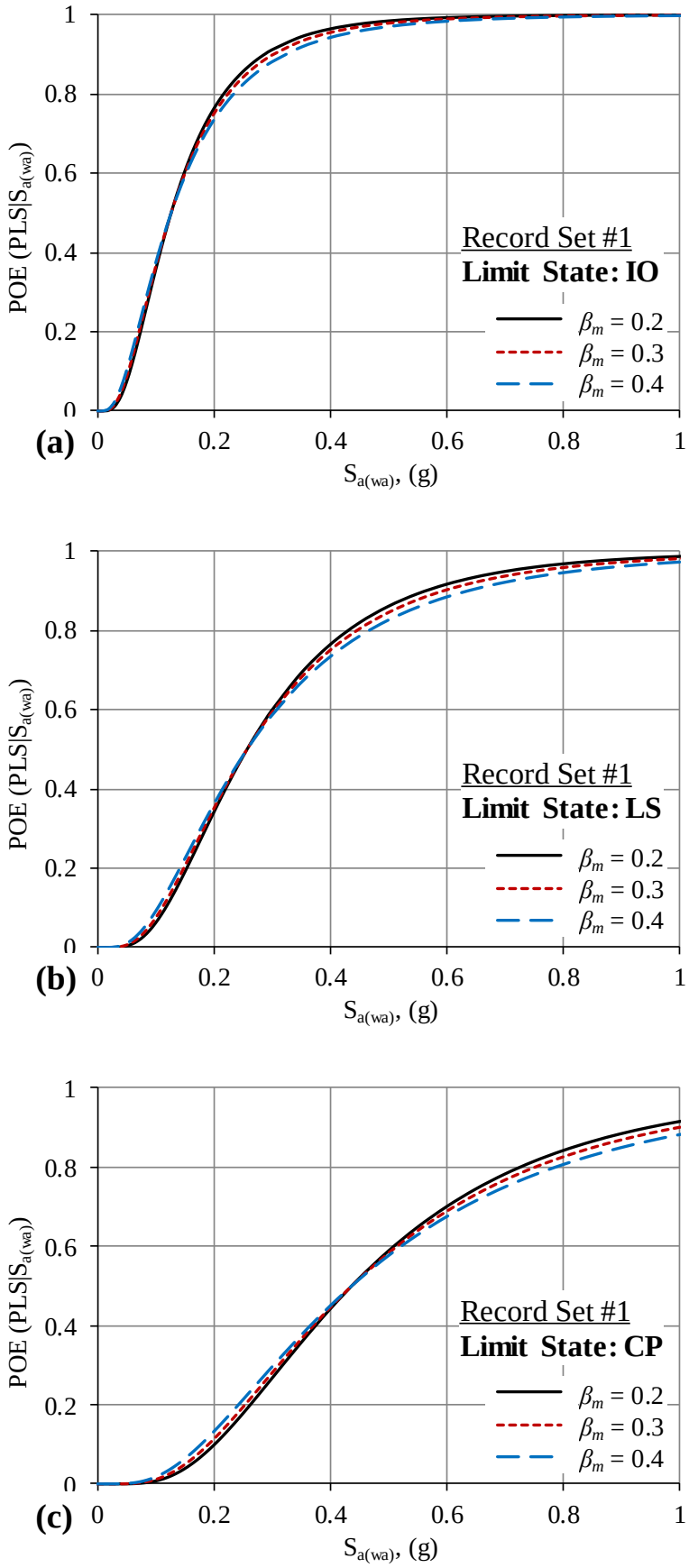

Figure 6.4. Record Set #1 - Reference building fragility curves with different βm values (0.2, 0.3, and 0.4): (a) IO limit state; (b) LS limit state; and (c) CP limit state

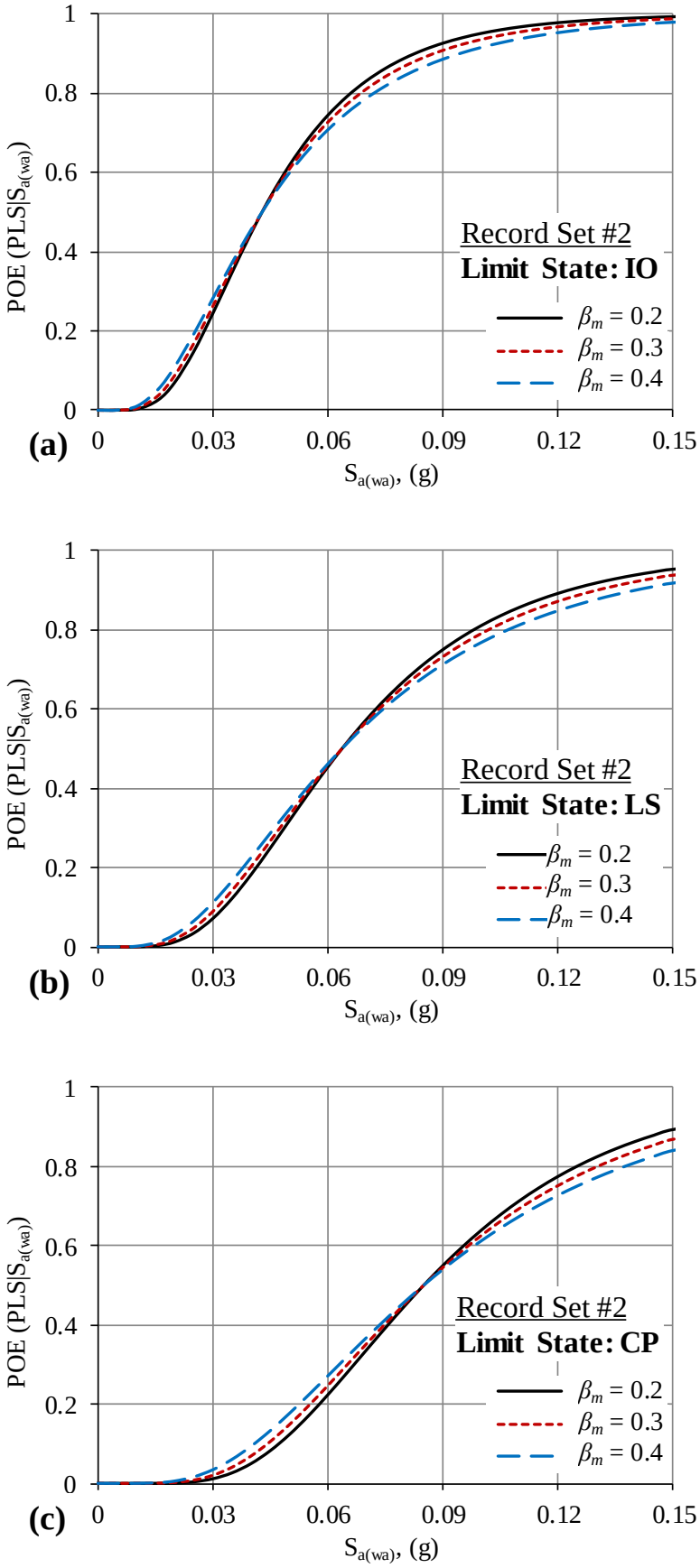

Figure 6.5. Record Set #2 - Reference building fragility curves with different βm values (0.2, 0.3, and 0.4): (a) IO limit state; (b) LS limit state; and (c) CP limit state

6.2 Assessment and comparison of the fragility relations

The developed fragility curves under the two investigated seismic scenarios are assessed and compared in this section to shed more light upon the differences in the vulnerability of RC high-rise wall buildings under multiple earthquake scenarios. Using the intensity measure of $S_{a(wa)}$ and the mean (50% fractile) values of the DM (NISD) used to define the three adopted limit states, the fragility relations of the reference building under Record Set #1 and Record Set #2 are given in Figure 6.6 and Figure 6.7, respectively. In these figures, zoom in to the part of interest of the fragility curves is also shown. These parts of interest cover the $S_{a(wa)}$ values (and their corresponding POE) associated with three selected earthquake intensity levels: (i) Serviceability Level Earthquake (SLE) with 50% POE in 30 years (43-year return period); (ii) DBE with 10% POE in 50 years (475-year return period); and MCE with 2% POE in 50 years (2475-year return period).

The T_{wa} of the reference building (2.54s) falls within the region design spectra zone that envelopes the severe distant seismic scenario. Accordingly, the $S_{a(wa)}$ values associated with the DBE and MCE under this scenario are calculated using the corresponding design spectra of the study region (Figure 4.5). These design spectra are generated using the procedure given in the ASCE/SEI 7-16 (2017) and the IBC (IBC, 2015). These values are 0.105g and 0.158g, respectively. It is worth noting that as per the procedure of the aforementioned codes, the spectral acceleration values associated with the MCE are 1.5 times their DBE counterparts. It can be seen that the calculated $S_{a(wa)}$ value of 0.105g (associated with DBE) is matching with the corresponding $S_{a(wa)}$ value from the mean of the response spectra for Record Set #1 (Figure 4.6a). For the moderate near-field seismic scenario, the $S_{a(wa)}$ value associated with the DBE is estimated from the mean of the response spectra for Record Set #2 as 0.011g (Figure 4.6b). For this seismic scenario, the value associated with the MCE is taken as 0.0165g (1.5 times 0.011 g).

As for estimating the $S_{a(wa)}$ values associated with the SLE under the two investigated seismic scenarios, there are no probabilistic seismic hazard assessment studies available on the study region for this earthquake intensity level. Consulting previous studies (e.g. Ghodsi and Ruiz, 2010, Tuna, 2012), it was decided to take the $S_{a(wa)}$ value associated with the SLE as 0.5 times the DBE-associated value. Accordingly, the $S_{a(wa)}$ values corresponding to the SLE under the severe distant and moderate near-field seismic scenarios are taken as 0.0525g and 0.0053g, respectively.

Again, the 84% confidence interval of the fragility curve for each limit state along with its relative width is calculated under Record Set #1 and Record Set #2 using Eqn (6.5) and (6.6) and listed in Table 6.4 and Table 6.5, respectively. For example, Table 6.4 shows that the mean value of $S_{a(wa)}$ for limit state IO is 0.127g, representing the mean value of IM at which the reference building reaches the threshold of the limit state IO under Record Set #1. In other words, it means that by the probability of 50% for the $S_{a(wa)}$ value of 0.127g, the threshold of the damage state IO under Record Set #1 is reached (i.e. first rebar yield in flooring system). The 16% percentile of $S_{a(wa)}$ value at the threshold of limit state IO under Record Set #1 is 0.067g while the 84% percentile is 0.240g. For the mean value of $S_{a(wa)}$ corresponding to the limit state IO under Record Set #1, the plus-minus one-σ confidence interval is calculated as $[P_{lower}, P_{upper}]$ = [0.122g, 0.132g], returning a relative width value of 7.63. It is important to emphasise that in Table 6.4 and Table 6.5, the presented 16%, 50%, and 84% fractile values are for the $S_{a(wa)}$ at the threshold of different performance limit states, not NISD (response) values. The significant difference in the 16%, 50%, and 84% fractiles of these $S_{a(wa)}$ values corresponding to a specific limit state reflects the variability in the input ground motion characteristics from one record to another in the record set, not to the response (NISD) at different limit states/fractiles. Therefore, for Table 6.4 and Table 6.5, the relative width of confidence interval (W, %) represents a more suitable measure of the accuracy of the developed fragility curves. For the fragility relations of the reference building under the two investigated seismic scenarios, the relative width of confidence interval for all adopted limit states is lower than 10% (between 5.43 and 7.63). This indicates the high accuracy of the obtained fragility curves and the possibility of implementing them for RC high-rise wall buildings with similar structural characteristics and seismicity.

The fragility curves shown in Figure 6.6 and Figure 6.7 are developed using the mean value (50% fractile) of NISDs at the threshold of a given limit state. Given that the seismic vulnerability analysis is probabilistic, the fragility relations based on the 16% and 84% fractiles of the adopted PLSs are developed under Record Set #1 and Record Set #2 and shown in Figure 6.8 and Figure 6.9, respectively. To facilitate the assessment and comparison between the developed fragility relations of the reference building under the two investigated seismic scenarios, Figure 6.10 depicts the compiled fragility relations (50% fractile) under both Record Set #1 and Record Set #2. In this figure, the

POE is given in percentage to better link the data with those in Table 6.6 (will be discussed later).

By analysing the data in Figure 6.10, it can be seen that for the developed fragility relations under the severe distant seismic scenario, the steepness of the curves increases as the limit states shifts from CP to IO. The steep slope of the IO limit state curve is attributed to the high lateral stiffness of the reference building in the elastic range, which significantly decreases the dispersions in the NISD values from different records at the threshold of the limit state. Figure 6.10 also shows that the three fragility curves developed under the moderate near-field earthquake scenario have almost the same steepness. As previously explained, this is due to the fact that, under almost all the records in Record Set #2, the three limit states (IO, LS, and CP) are reached while the structure is still in the elastic zone (Table 5.4).

The latest recommendations in ASCE/SEI 41-17 (2017) for the TISD associated with LS performance limit state (discussed in Section 5.6.2) introduces a minimal change to the LS limit state fragility curves of the reference building under the moderate near-field seismic scenario. Figure 6.11 shows 16%, 50%, and 84% fractile (LS) fragility curves using the drift recommendations of both ASCE/SEI 41-06 and ASCE/SEI 41-17. The difference in the POE ($LS|S_{a(wa)}$) along the entire range of the three curves is limited to 1%-4% only. These results further support the argument on the negligible effect the new recommendations in ASCE/SEI 41-17 have on the framework, methodologies and outcome of the current work.

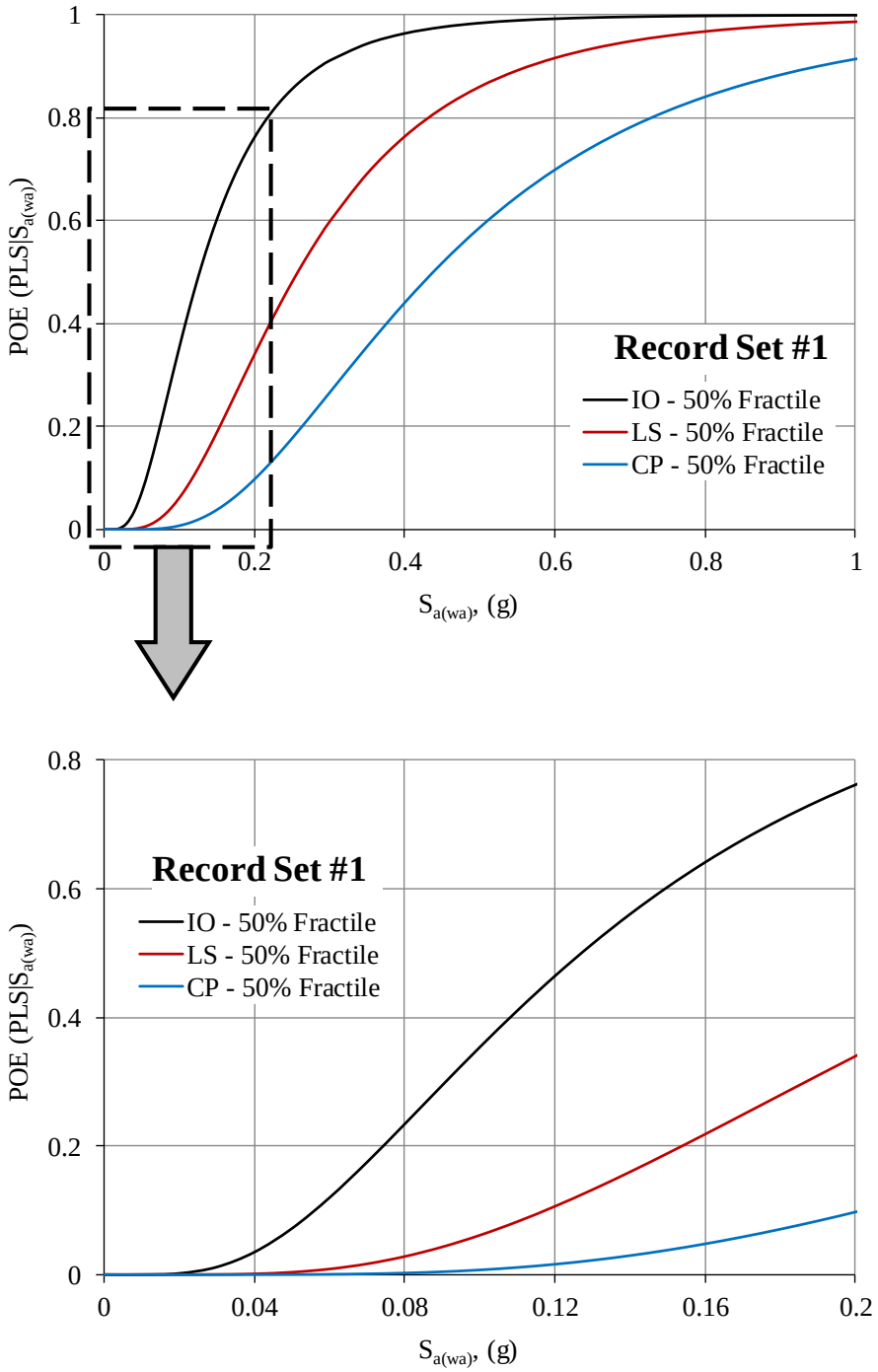

Figure 6.6. Reference building 50% fractile fragility curves for the adopted limit states (IO, LS, and CP) under Record Set #1

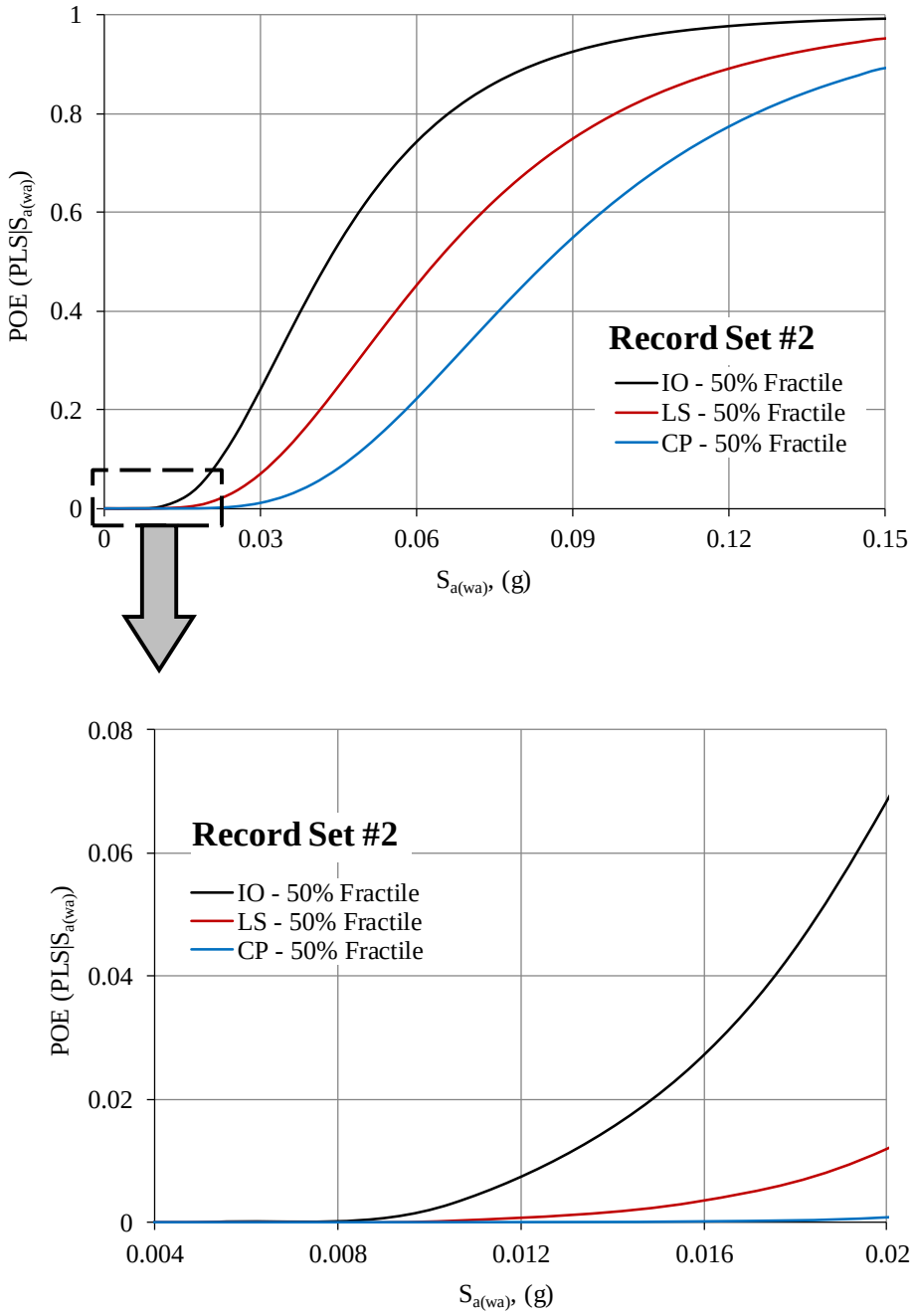

Figure 6.7. Reference building 50% fractile fragility curves for the adopted limit states (IO, LS, and CP) under Record Set #2

Table 6.4. Derived log-normal distribution function properties for the fragility curves of the reference building under Record Set #1

Limit state	$S_{a(wa)}$ at the threshold of performance limit state (IM|PLS_i), (g)			Standard deviation (σ)	Lower and upper endpoint of the 84% confidence interval, (g)		Relative width of confidence interval (W), (%)
	16% Fractile	50% Fractile	84% Fractile		P_{lower}	P_{upper}	
IO	0.067	0.127	0.240	0.638	0.122	0.132	**7.63**
LS	0.140	0.258	0.475	0.611	0.249	0.268	**7.30**
CP	0.240	0.438	0.799	0.601	0.423	0.454	**7.19**

Table 6.5. Derived log-normal distribution function properties for the fragility curves of the reference building under Record Set #2

Limit state	$S_{a(wa)}$ at the threshold of performance limit state (IM|PLS_i), (g)			Standard deviation (σ)	Lower and upper endpoint of the 84% confidence interval, (g)		Relative width of confidence interval (W), (%)
	16% Fractile	50% Fractile	84% Fractile		P_{lower}	P_{upper}	
IO	0.027	0.043	0.072	0.491	0.042	0.044	**5.86**
LS	0.038	0.064	0.106	0.513	0.062	0.066	**6.13**
CP	0.054	0.085	0.134	0.454	0.083	0.087	**5.43**

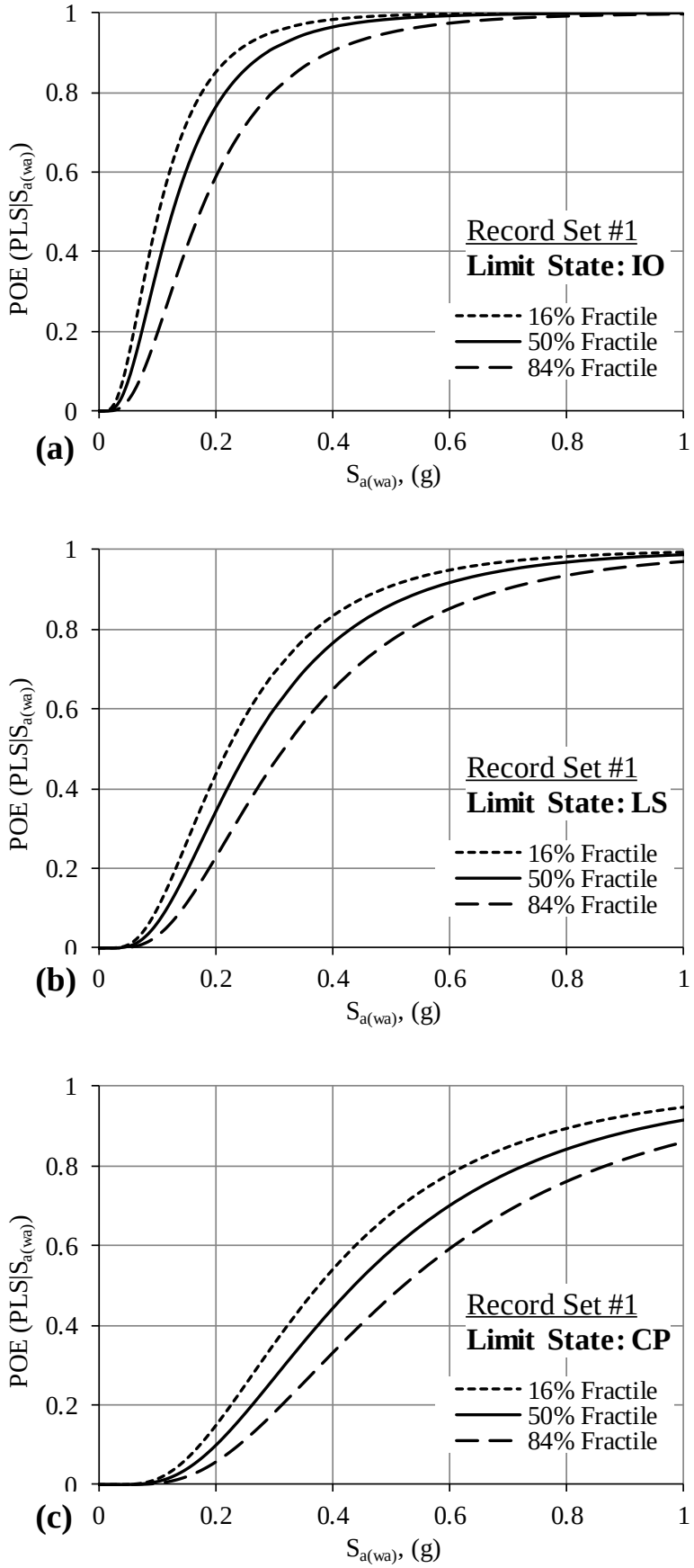

Figure 6.8. Record Set #1 - Reference building fragility curves with 16%, 50%, and 84% fractiles: (a) IO limit state; (b) LS limit state; and (c) CP limit state

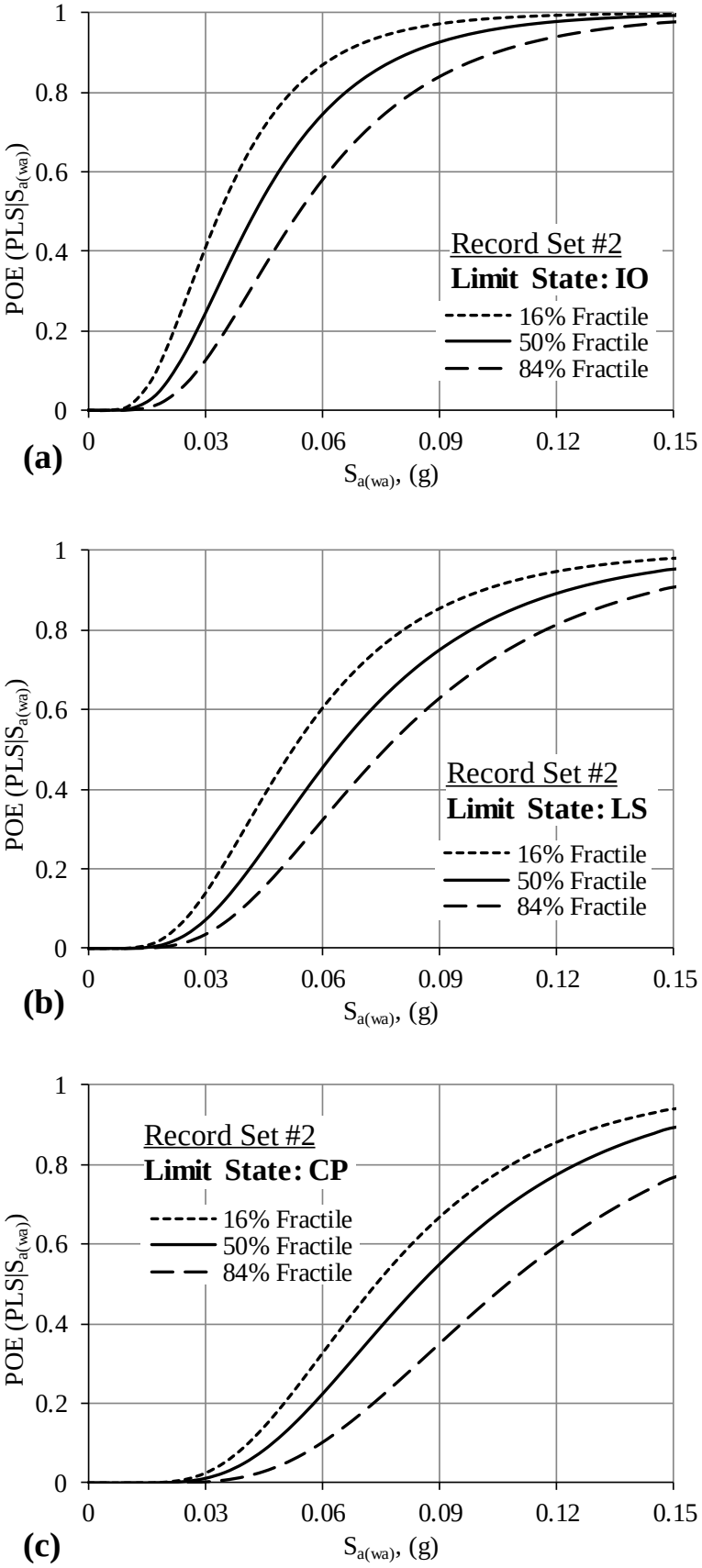

Figure 6.9. Record Set #2 - Reference building fragility curves with 16%, 50%, and 84% fractiles: (a) IO limit state; (b) LS limit state; and (c) CP limit state

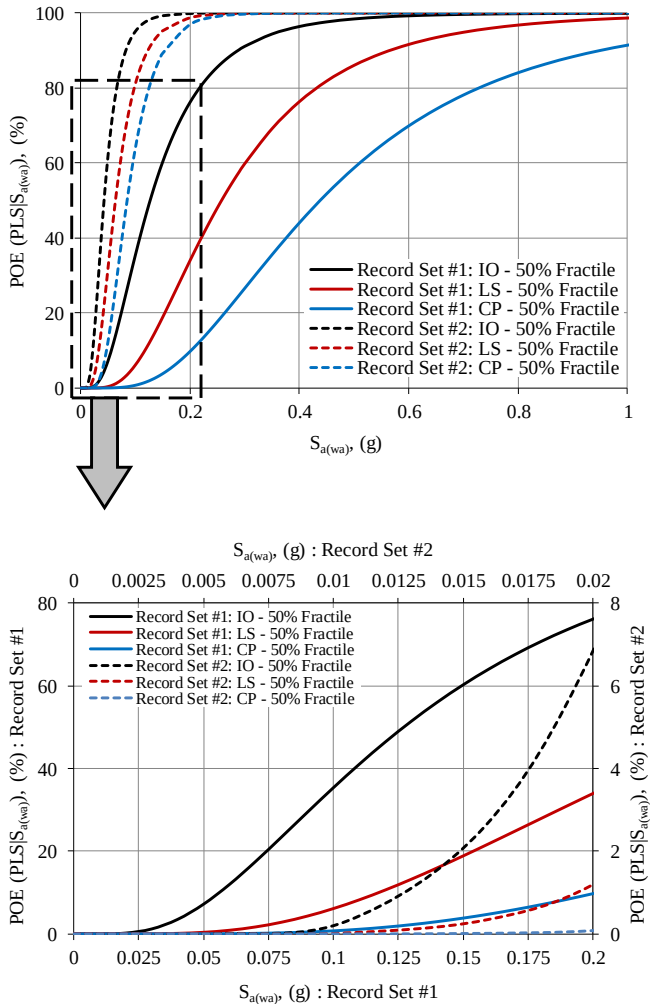

Figure 6.10. Reference building 50% fractile fragility curves for the adopted limit states (IO, LS, and CP) under Record Set #1 and Record Set #2

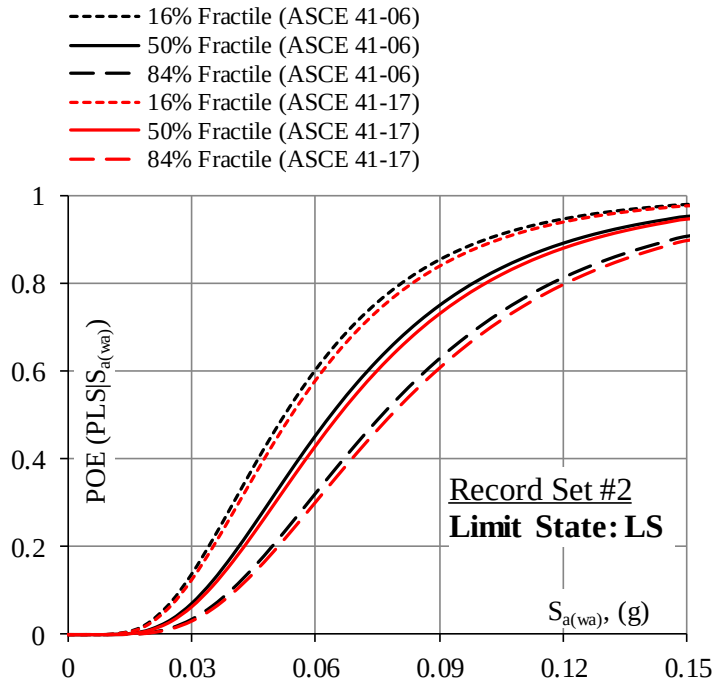

Figure 6.11. Reference building (LS) 16%, 50%, and 84% fractile fragility curves using the drift recommendations of both ASCE/SEI 41-06 and ASCE/SEI 41-17

To correlate the developed fragility relations with the state of damage in the reference building, the three adopted limit states are considered to be the threshold response quantities for the following damage states: (i) unimpaired occupancy (UOC); (ii) impaired occupancy (IOC); (iii) structural damage (SD); and (iv) structural collapse (SC). Damage state is a function of a specified measure of earthquake ground motion intensity but also is required for estimating expected or maximum probable losses. Similar damage state definitions have been adopted for seismic vulnerability assessments in previous studies (e.g. Ellingwood et al., 2007, Celik and Ellingwood, 2010, Jeong et al., 2012). When compared to the damage state definitions adopted in HAZUS (Kircher et al., 2006), the equivalence of UOC, IOC, SD, and SC is "no damage", "slight-to-moderate damage", "extensive damage", and "complete damage", respectively. The damage state probabilities of the reference building are determined by the differences between limit state probabilities. Figure 6.12 schematically illustrates the relationship between the limit states and the damage states, while the calculated damage state probabilities for the three selected earthquake intensity levels (SLE, DBE, and MCE) under the two investigated seismic scenarios are listed in Table 6.6 and graphically illustrated in Figure 6.13 and Figure 6.14.

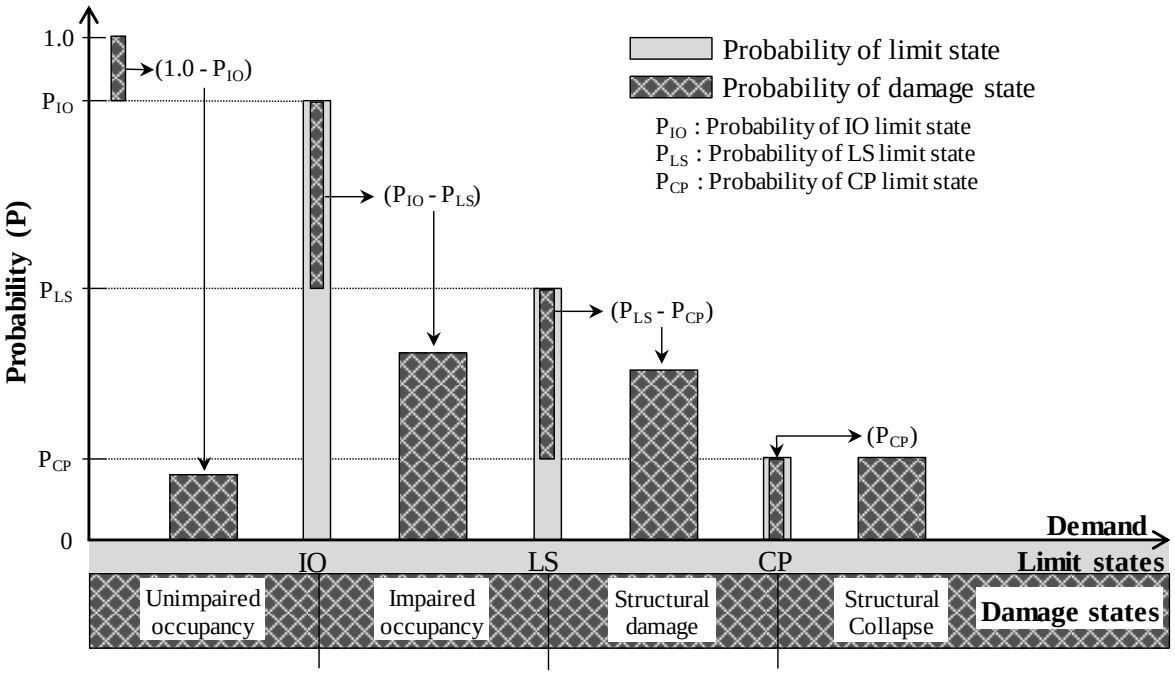

Figure 6.12. Relationship between the probability of limit states and damage states

Under the severe distant earthquake scenario, Table 6.6 and Figure 6.13 show that at $S_{a(wa)}$ corresponding to the DBE, the POE of the IO, LS and CP limit states is 38.2%, 7.1% and 0.9%, respectively. These values return damage state probabilities of 61.8% for unimpaired occupancy, 31.1% for impaired occupancy, 6.2% for structural damage, and 0.9% for structural collapse (Table 6.6 and Figure 6.13). At $S_{a(wa)}$ corresponding to the MCE, these values increase to 63.4%, 21.2% and 4.6% for the IO, LS, and CP limit state probabilities, respectively, returning damage state probabilities of 36.6% for unimpaired occupancy, 42.1% for impaired occupancy, 16.7% for structural damage, and 4.6% for structural collapse.

Under the moderate near-field earthquake scenario, on the other hand, the limit state probabilities corresponding to the DBE are 0.4%, 0.0%, and 0.0% for IO, LS, and CP, respectively (Table 6.6 and Figure 6.14). These values return damage state probabilities of 99.6% for unimpaired occupancy, 0.4% for impaired occupancy, 0.0% for structural damage, and 0.0% for structural collapse (Table 6.6 and Figure 6.14). At $S_{a(wa)}$ corresponding to the MCE, these values are slightly changed to 3.6%, 0.5% and 0.0% for the IO, LS, and CP limit state probabilities, respectively, returning damage state probabilities of 96.4% for unimpaired occupancy, 3.1% for impaired occupancy, 0.5% for structural damage, and 0.0% for structural collapse.

The above emphasises the vulnerability of RC high-rise wall buildings in the study region to severe distant earthquakes. It also indicates that in the study region, this class of buildings is invulnerable to moderate near-field earthquakes even at the MCE level. However, considering the unique response of RC high-rise wall structures under short period records (discussed in CHAPTER 5), this may not be the case for other multiple seismic scenario- prone regions in the world.

Table 6.6. Reference building limit state and damage state probabilities for different earthquake intensity levels under Record Set #1 and Record Set #2

Seismic scenario	Earthquake intensity level	Limit state probability (%)			Damage state probability (%)			
		IO	LS	CP	Unimpaired Occupancy	Impaired Occupancy	Structural damage	Structural collapse
Strong distant earthquakes (Record Set #1)	@ $S_{a(wa)}$ = 0.053 g (SLE)	8.3	0.5	0.0	91.7	7.8	0.4	0.0
	@ $S_{a(wa)}$ = 0.105 g (DBE)	38.2	7.1	0.9	61.8	31.1	6.2	0.9
	@ $S_{a(wa)}$ = 0.158 g (MCE)	63.4	21.2	4.6	36.6	42.1	16.7	4.6
	@ $S_{a(wa)}$ = 0.4 g	96.4	76.4	44.0	3.6	20.0	32.2	44.0
	@ $S_{a(wa)}$ = 0.6 g	99.3	91.6	69.9	0.7	7.6	21.7	69.9
	@ $S_{a(wa)}$ = 0.8 g	99.8	96.8	84.1	0.2	3.0	12.7	84.1
Moderate near-field earthquakes (Record Set #2)	@ $S_{a(wa)}$ = 0.006 g (SLE)	0.0	0.0	0.0	100.0	0.0	0.0	0.0
	@ $S_{a(wa)}$ = 0.011 g (DBE)	0.4	0.0	0.0	99.6	0.4	0.0	0.0
	@ $S_{a(wa)}$ = 0.017 g (MCE)	3.6	0.5	0.0	96.4	3.1	0.5	0.0
	@ $S_{a(wa)}$ = 0.04 g	44.6	18.2	5.0	55.4	26.4	13.2	5.0
	@ $S_{a(wa)}$ = 0.08 g	88.8	67.1	44.4	11.2	21.7	22.4	44.7
	@ $S_{a(wa)}$ = 0.12 g	97.8	89.2	77.4	2.2	8.6	11.7	77.4

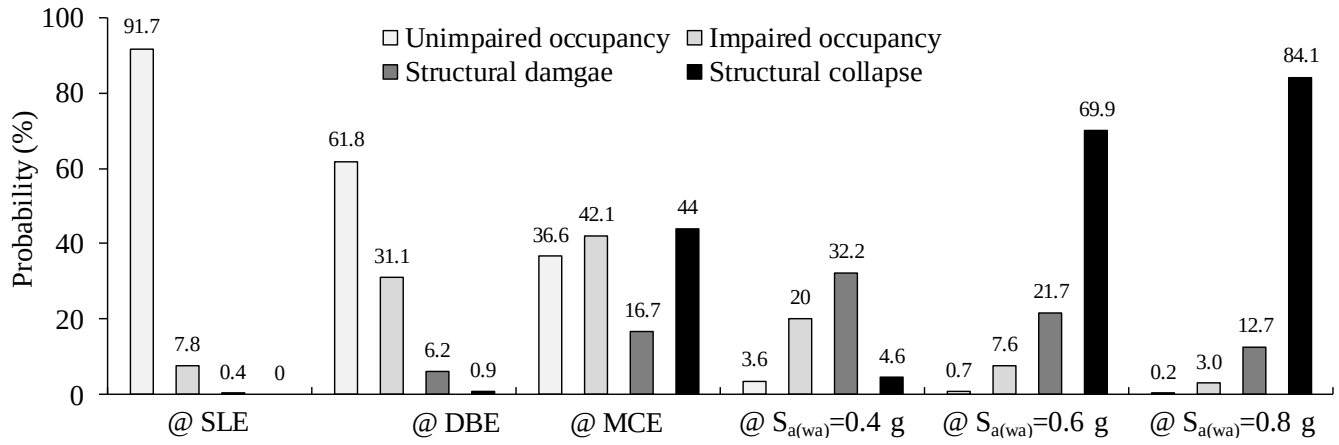

Figure 6.13. Reference building damage state probabilities for different earthquake intensity levels under Record Set #1

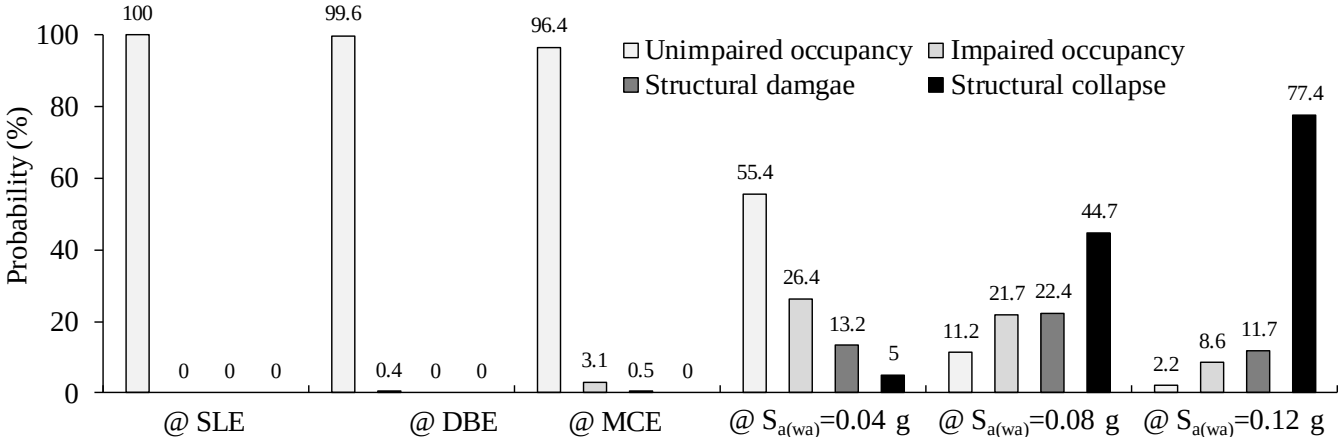

Figure 6.14. Reference building damage state probabilities for different earthquake intensity levels under Record Set #2

6.3 Simplified methodology to develop fragility relations for RC high-rise wall buildings

In this final part of CHAPTER 6, a simplified methodology towards developing fragility relations for high-rise buildings is proposed. The fragility curves generated using the proposed methodology is referred to hereafter as Cheaper Fragility Curves (CFC). The terminology reflects the considerable reduction in time and effort that can be achieved utilising this simplified methodology. The methodology is centred on developing a set of CFCs with a predefined acceptance (tolerance) level for each seismic scenario under investigation using a lower number of earthquake records.

Given that MRIDA is the core and spine of any framework that ends with the development of fragility relations, a number of different methods have previously been proposed either to simplify or to approximate the process of conducting these analyses. Approximate methods for IDAs involved the replacement of dynamic nonlinear analysis by a combination of pushover analysis of a multi-degree-of-freedom (MDOF) model and dynamic nonlinear analysis of single-degree-of-freedom (SDOF) model (e.g. Vamvatsikos and Cornell, 2005b, Han and Chopra, 2006, Vamvatsikos and Cornell, 2006). Other researchers have attempted to simplify the procedure by reducing the dispersion in IDA results (e.g. Shome, 1999, Carballo and Cornel, 2000). Typically, a reduction in dispersion by a factor of two means that four times fewer records are needed to gain the same confidence (Vamvatsikos and Cornell, 2004a).

The selection criteria of real ground motion records for seismic scenario-based MRIDA mainly include magnitude, distance, and site conditions (e.g. Iervolino and Cornell, 2005) without an explicit reflection of structural characteristics of the building(s) under investigation. This way of record selection requires the calculation of seismic response for all ground motion records representative of an earthquake scenario. It would, therefore, be useful to add another criterion to the record selection, such that the selected records are the best representatives for the prediction of the seismic response of the investigated structures. By adding this element to the framework for deriving fragility relations for high-rise buildings, a significant decrease in the number of ground motion records needed for the sufficiently accurate prediction of seismic response and fragility relations at a predefined acceptance level can be achieved.

The acceptance level for the developed CFCs is subjective; therefore, the accepted tolerances can be decided depending on the objectives behind the vulnerability study

and how the outcomes will be utilised. As pictorially illustrated in Figure 2.1, the characteristics of a fragility curve (the output in the IPO model) are mainly determined by the following variables: (i) uncertainties in input ground motions; (ii) building seismic demand (response); and (iii) building seismic performance (capacity).

The building seismic response is characterised by the two main measures that are shaping the MRIDAs, namely the IM and the DM. The scalar IM of $S_{a(wa)}$ proposed in the current study is shown to be efficient for high-rise buildings with varying height range. It takes into account both the impact of higher modes and period elongation and utilises the actual inelastic periods of the structure. As for the damage measure, the numerical parametric study conducted in Section 5.5 revealed the consistency of NISD as a global DM for the vulnerability assessment of high-rise buildings with varying heights.

In multi scenario-seismic-prone regions, the seismic capacity of a building is represented by the seismic scenario-based limit state criteria (CHAPTER 5). The conceptual definitions of the proposed limit state criteria (Table 5.3) is based on the detailed mapping of the seismic scenario-based local response (Section 5.3), utilising the comprehensive list of adopted DIs (Table 5.1). The proposed global DM (NISD) eliminates the RBM-induced artificial component of the TISD, a component that has no contribution to structural demand. The weight of RBM-induced component in the TISD is influenced by the location of the storey in the building, the total building height and the effect of higher modes on the seismic response (e.g. Ji et al., 2009). Accordingly, removing this component (i.e. using NISD rather TISD as a global DM) eliminates the variation in the seismic scenario-based limit state criteria for high-rise buildings with varying heights. As a result, it is fairly acceptable to conclude that adopting the methodology for determining the seismic scenario-based limit state criteria proposed in CHAPTER 5 for RC high-rise buildings with varying structural systems and a wider height range is adequate to return reliable fragility relations.

Based on the above discussion, and to take into account the "uncertainties in input ground motions" variable, a new Record Selection Criterion (RSC) is proposed hereafter as part of the simplified methodology. By adopting the proposed RSC, a considerably lower number of records will be required to develop CFCs for RC high-rise buildings of varying heights.

In Figure 6.15, the methodology to derive refined seismic scenario-based fragility curves (Section 6.1) and the simplified one to derive CFCs proposed in this section are combined in one flowchart that consists of three blocks: (i) default block "A" which includes the pre-steps needed whether refined or cheaper fragility curves are to be developed; (ii) block "B" which includes the steps that need to be added to block "A" to develop refined fragility curves; and (iii) block "C" which includes the steps that need to be added to block "A" to develop CFCs. The steps in blocks "A" and "B" are explained in the related sections of Chapters 3, 4, and 5 along with Section 6.1.

Hereafter, the simplified methodology to develop CFCs (blocks A and C) is described bullet-wise. For easy reference, each bullet is assigned with the same number that is assigned to the related step in the flowchart.

1. Identifying the UHS and seismic scenarios of the study region and selecting the building(s) representative of the building inventory as well as the equivalent inelastic mode periods of the building(s) under investigation. The equivalent inelastic mode periods can be retrieved from the design (linear) model.

2. Designing the reference building(s) in accordance with the relevant seismic provisions of the regional-adopted codes. In case the structural design drawings/data are available, then they can be used.

3. Developing a verified, nonlinear 3D simulation of the reference building(s) and defining the IM and DM to be used in the MRIDAs.

4. Selecting real input ground motions (records) from the earthquake databases following the selection criteria detailed in Section 2.2.2.4.3 of CHAPTER 2 and Section 4.2 of CHAPTER 4. The process starts with the selection of two records only.

5. Examining each of the selected records from step #4 against the set acceptance tolerance value (T_R). If the T_R of each of the selected records is equal or smaller than the set tolerance value, proceed to step #6. Otherwise, the unqualified record(s) is to be discarded and replaced by repeating steps #4 and #5.

6. Conducting MRIDAs for the reference building(s) using the number of records in the current cycle. In the first cycle (n=1), the number of records is 2. The

MRIDAs results are to be mapped, where local building response is correlated to its global response using the adopted global DM (the reader is referred to CHAPTER 5 for more details).

7. Defining seismic scenario-based limit state criteria for the reference building(s) (the reader is referred to CHAPTER 5 for more details).

8. Developing the cheaper fragility curves (CFCs) based on the output of steps #6 and #7.

9. The developed CFCs are to be examined against the set acceptance tolerance value (T_{FC}). If the T_{FC} values of the developed CFCs from two successive cycles (n and n-1) are equal or smaller than the set tolerance value, proceed to step #10. Otherwise, steps #5 to #8 are to be repeated with one more record added to the related set of records.

10. The developed CFCs from the cycle (n-1) is to be adopted for the reference building(s) and used for further seismic hazard assessment and mitigation studies.

In the succeeding sections (6.3.1 and 6.3.2), the simplified methodology is further explained by employing it to the reference building. To verify the simplified methodology outcome, the developed CFCs for the reference building are compared with the refined fragility relations generated in Section 6.1.

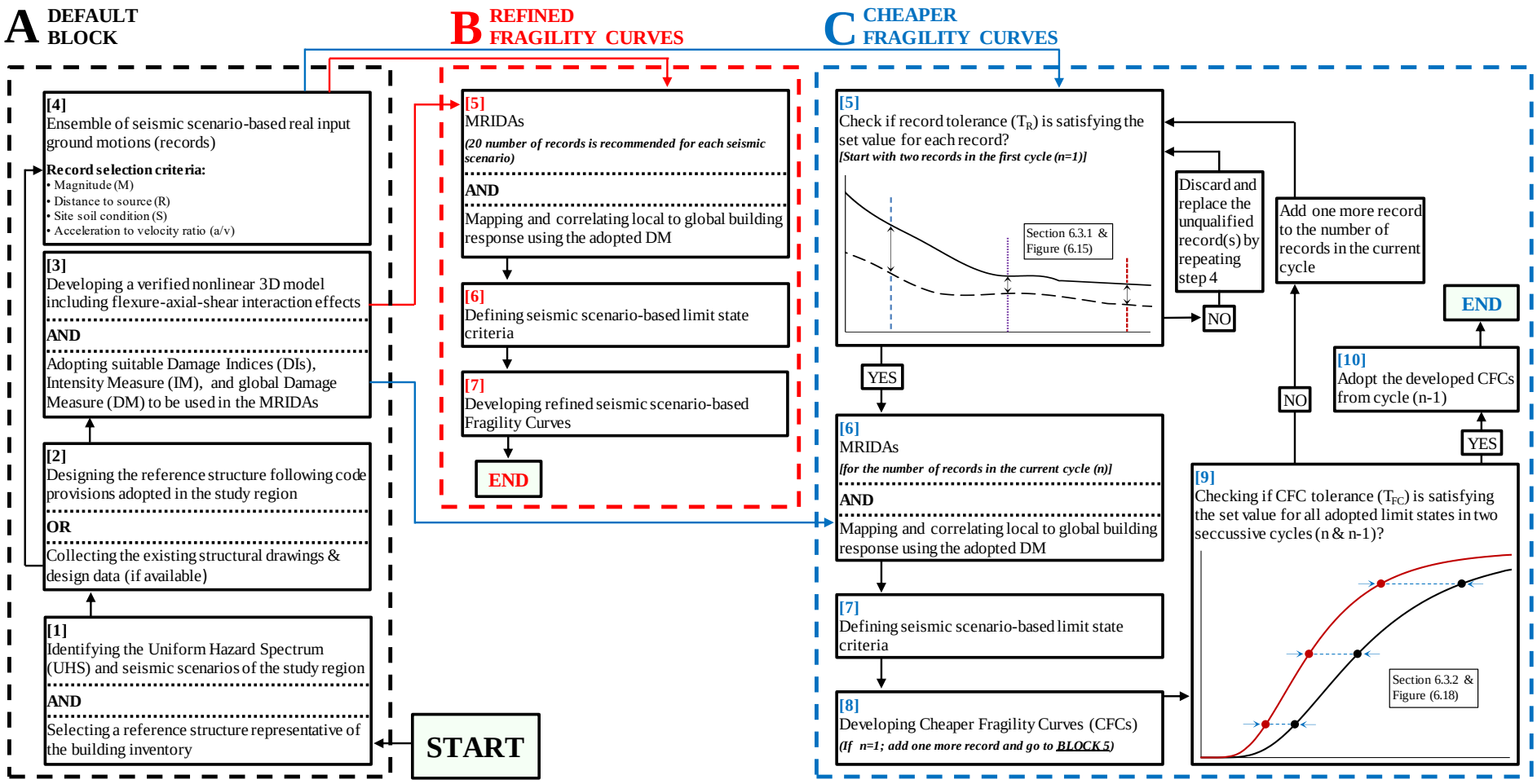

Figure 6.15. Flowchart combining the steps for developing refined and cheaper fragility relations

6.3.1 Record selection criterion (RSC) and record acceptance tolerance (T_R)

To reduce the time and computational effort required to develop the fragility relations with a predefined acceptance level for a building or a building inventory, the total number of earthquake records used in the MRIDAs needs to be lowered to the minimum number of records possible. In Section 5.3 of the current study, the mapping of the seismic scenario-based reference building local response demonstrates that, for RC high-rise wall buildings, the seismic response under severe distant earthquake scenario is dominated by the 1st and 2nd modes of vibration (Figure 5.11 to Figure 5.18). Under moderate near-field earthquakes, on the other hand, the response is dominated by the 2nd and 3rd modes of vibration (Figure 5.19 to Figure 5.26). Utilising these findings, a new RSC is proposed in this section (step #5 of block C in Figure 6.15). When the proposed RSC is added to the seismic scenario-based real records selection criteria detailed in Section 2.2.2.4.3 of CHAPTER 2 and Section 4.2 of CHAPTER 4 (step #4 of block A in Figure 6.15), CFCs with a predefined acceptance level can be developed with a considerably lower number of records. For a building inventory with the same structural system but with different heights, the proposed simplification through reducing the number of records becomes even more substantial when utilising the unified limit state criteria methodology previously proposed in CHAPTER 5.

The proposed RSC is based on selecting the real records that have a close match to the shape of the UHS or the design spectrum at the zone of effective time periods. For the severe distant earthquake scenario, the zone of the effective time periods is set to be bracketing the 1st mode period and the weighted-average of the 1st and 2nd mode periods. Detailed description of the calculation procedure of the weighted-average period can be found in Section 5.2. As for moderate near-field earthquakes, the zone of the effective time periods is set to be bracketing the 3rd mode period and the weighted-average of the 2nd and 3rd mode periods. To measure the closeness of the spectrum zone bracketing by the effective time periods in any selected record to its counterpart in the UHS, a record tolerance factor is proposed (T_R). The calculation of T_R is given in Eqn. (6.7), as follows:

$$T_R = \sigma\left[\left(\frac{S_a^R}{S_a^{UHS}}\right)_{@T_{mi}} ; \left(\frac{S_a^R}{S_a^{UHS}}\right)_{@T_{wa(mi,j)}} ; \left(\frac{S_a^R}{S_a^{UHS}}\right)_{@\text{average }(T_{mi},T_{wa(mi,j)})}\right] \quad (6.7)$$

Where T_R is the record tolerance factor, σ is the standard deviation, S_a^R is the spectral acceleration value of the record at the specified time period, S_a^{UHS} is the spectral acceleration value of the UHS at the specified time period, T_{mi} is the building equivalent inelastic time period of mode i, $T_{wa(mi,j)}$ is the building weighted-average period of modes i and j, and average $(T_{mi}, T_{wa(mi,j)})$ is the arithmetic mean of T_{mi} and $T_{wa(mi,j)}$.

The smaller the T_R value, the closer is the matching of the selected record to the shape of the UHS (or the design spectrum) at the zone of effective mode periods and consequently, the lesser impact the ground motion uncertainties have on the derived fragility relations. In the current study, the acceptance value of T_R is set to 10%. This upper bound will later be shown to be sufficient. Although the proposed methodology requires a minimum of two records for each seismic scenario as a start, seven records are selected hereafter from each of the two sets of records. It is important to state that T_R upper bound can be set to any other value as long as the acceptance level for the CFCs is achieved.

Figure 6.16 shows the schematic for the calculation procedure of T_R, while Figure 6.17 and Figure 6.18 depict the seven records selected for each seismic scenario along with the UHS of the region at the zone of effective time periods. Table 6.7 and Table 6.8 give the parameters for the acceleration response spectra of the selected records at the zone of effective periods from Record Sets #1 and #2, respectively.

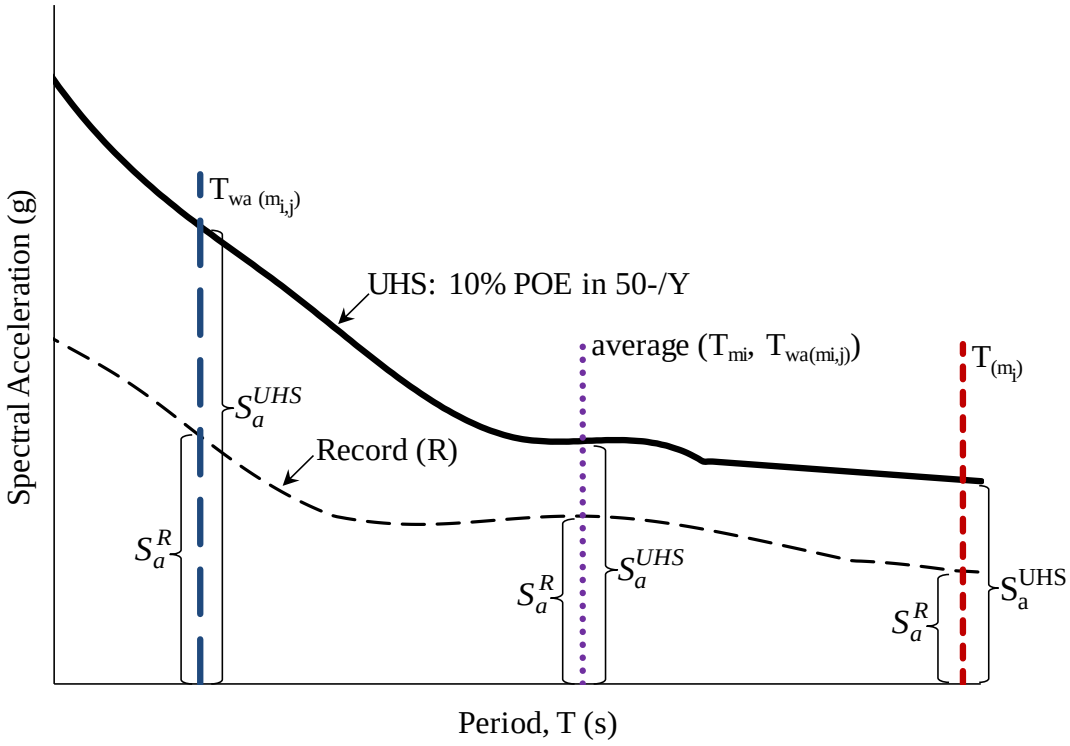

Figure 6.16. Schematic for the record tolerance (T_R) calculation procedure

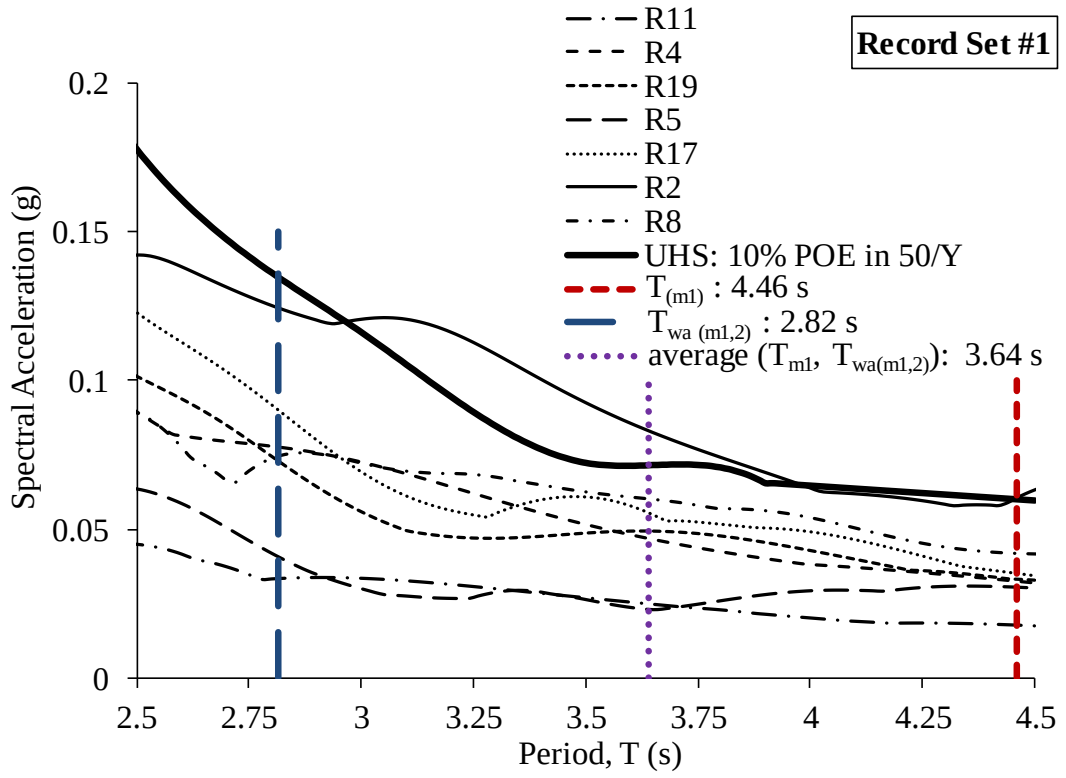

Figure 6.17. Record Set #1: Acceleration response spectra of records #11, #4, #19, #5, #17, #2, and #8 along with 10% POE in 50-years UHS of the study region at zone of effective periods

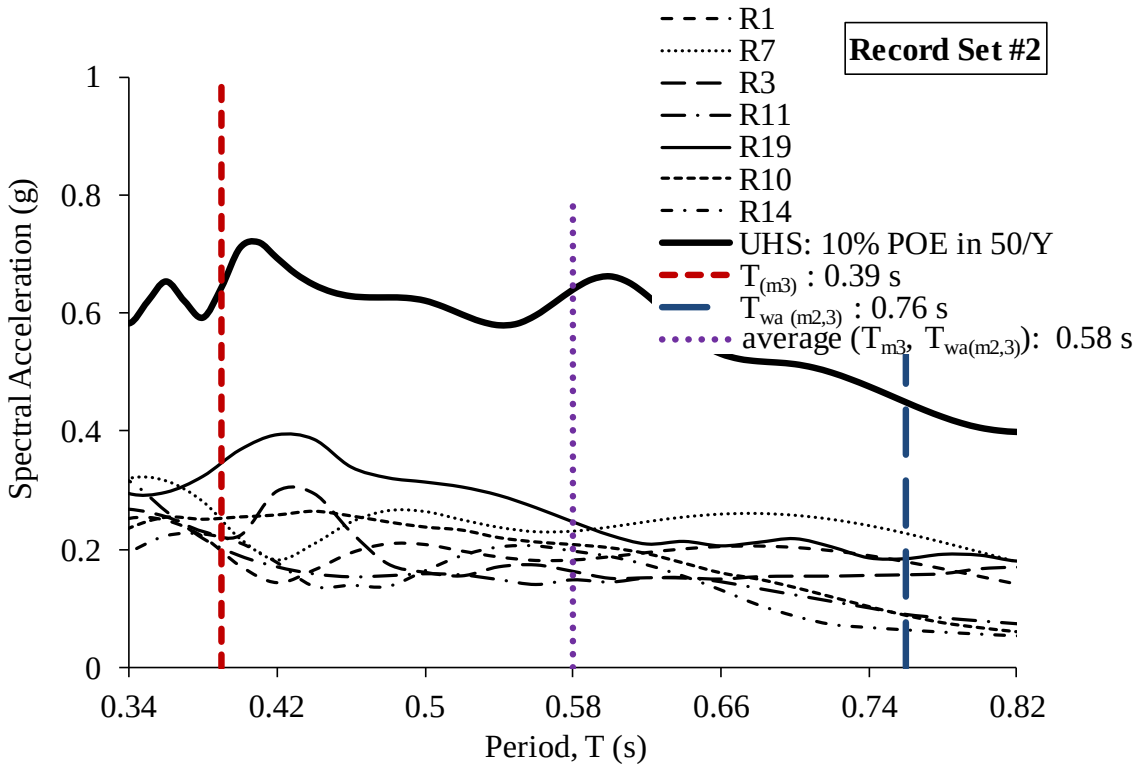

Figure 6.18. Record Set #2: Acceleration response spectra of records #1, #7, #3, #11, #19, #10, and #14 along with 10% POE in 50-years UHS of the study region at zone of effective periods

Table 6.7. Record Set #1: Parameters for the acceleration response spectra of the seven selected records at the zone of effective periods

Record #	@ $T_{(m1)}$ $S_a^{UHS} = 0.060$ g, T = 4.46 s		@ $T_{wa(m1,2)}$ $S_a^{UHS} = 0.135$ g, T = 2.82 s		@ $T_{average\ (m1,T_{wa(m1,2)})}$ $S_a^{UHS} = 0.079$ g, T = 3.64 s		T_R σ[a,b,c] (%)
	S_a^R (g)	$\frac{S_a^R}{S_a^{UHS}}$ [a]	S_a^R (g)	$\frac{S_a^R}{S_a^{UHS}}$ [b]	S_a^R (g)	$\frac{S_a^R}{S_a^{UHS}}$ [c]	
11	0.018	0.271	0.033	0.247	0.025	0.315	3.0
4	0.032	0.497	0.078	0.575	0.047	0.593	5.0
19	0.033	0.507	0.073	0.540	0.049	0.625	6.0
5	0.061	0.925	0.124	0.921	0.083	1.051	7.0
17	0.035	0.537	0.090	0.667	0.055	0.702	9.0
2	0.030	0.466	0.041	0.302	0.023	0.291	10.0
8	0.042	0.640	0.074	0.552	0.060	0.762	10.0

Table 6.8. Record Set #2: Parameters for the acceleration response spectra of the seven selected records at the zone of effective periods

Record #	@ $T_{(m3)}$ $S_a^{UHS} = 0.643$ g, T = 0.39 s		@ $T_{wa(m2,3)}$ $S_a^{UHS} = 0.499$ g, T = 0.76 s		@ $T_{average\ (m3,T_{wa(m2,3)})}$ $S_a^{UHS} = 0.639$ g, T = 0.58 s		T_R σ[a,b,c] (%)
	S_a^R (g)	$\frac{S_a^R}{S_a^{UHS}}$ [a]	S_a^R (g)	$\frac{S_a^R}{S_a^{UHS}}$ [b]	S_a^R (g)	$\frac{S_a^R}{S_a^{UHS}}$ [c]	
1	0.202	0.314	0.182	0.364	0.182	0.285	4.0
7	0.256	0.398	0.230	0.462	0.231	0.361	5.0
3	0.228	0.354	0.157	0.314	0.163	0.255	5.0
11	0.207	0.321	0.093	0.186	0.148	0.232	7.0
19	0.342	0.531	0.185	0.370	0.247	0.386	9.0
10	0.253	0.393	0.092	0.184	0.208	0.326	9.0
14	0.220	0.342	0.065	0.130	0.197	0.309	10.0

6.3.2 Development of CFCs and calculation of fragility curve tolerance (T_{FC})

Using the proposed simplified methodology, the first set of CFCs can be developed using two records only for each seismic scenario. The number of records used to develop the fragility curve is referred to as NOR. The records are selected according to the procedure described in Section 6.3.1. To decide whether the accuracy level for the developed CFCs is acceptable, a tolerance factor denoted T_{FC} is proposed. the calculation of T_{FC} is given in below set of equations:

$$T_{FC} = \left[0.25x\sigma_{NOR}^{NOR+1} + 0.75x(S_a)_{NOR}^{NOR+1}\right] \quad (6.8)$$

$$\sigma^{NOR+1} = \sigma\left[\left(S_a^{NOR+1}@16\%POE\right);\ \left(S_a^{NOR+1}@50\%POE\right);\ \left(S_a^{NOR+1}@84\%POE\right)\right] \quad (6.9)$$

$$\sigma_{NOR} = \sigma[(S_a^{NOR}@16\%POE);\ (S_a^{NOR}@50\%POE);\ (S_a^{NOR}@84\%POE)] \quad (6.10)$$

$$\sigma_{NOR}^{NOR+1} = ABS\left(\frac{\sigma^{NOR+1} - \sigma_{NOR}}{\sigma_{NOR}}\right) \quad (6.11)$$

$$(S_a)_{NOR}^{NOR+1} = ABS\left[\frac{(S_a^{NOR+1}@50\%POE)-(S_a^{NOR}@50\%POE)}{(S_a^{NOR}@50\%POE)}\right] \quad (6.12)$$

Where T_{FC} is the fragility curve tolerance factor, σ^{NOR+1} is the standard deviation of the $S_{a(wa)}$ values at the (NOR+1) fragility curve corresponding to POE levels of 16%, 50%, and 84%, σ_{NOR} is the standard deviation of the $S_{a(wa)}$ values at the (NOR) fragility curve corresponding to POE levels of 16%, 50%, and 84%, σ_{NOR}^{NOR+1} is the absolute of the difference ratio between σ^{NOR+1} and σ_{NOR}, and $(S_a)_{NOR}^{NOR+1}$ is the absolute of the difference ratio between $S_a^{NOR+1}@50\%POE$ and $S_a^{NOR}@50\%POE$. The calculation of T_{FC} is pictorially illustrated in Figure 6.19.

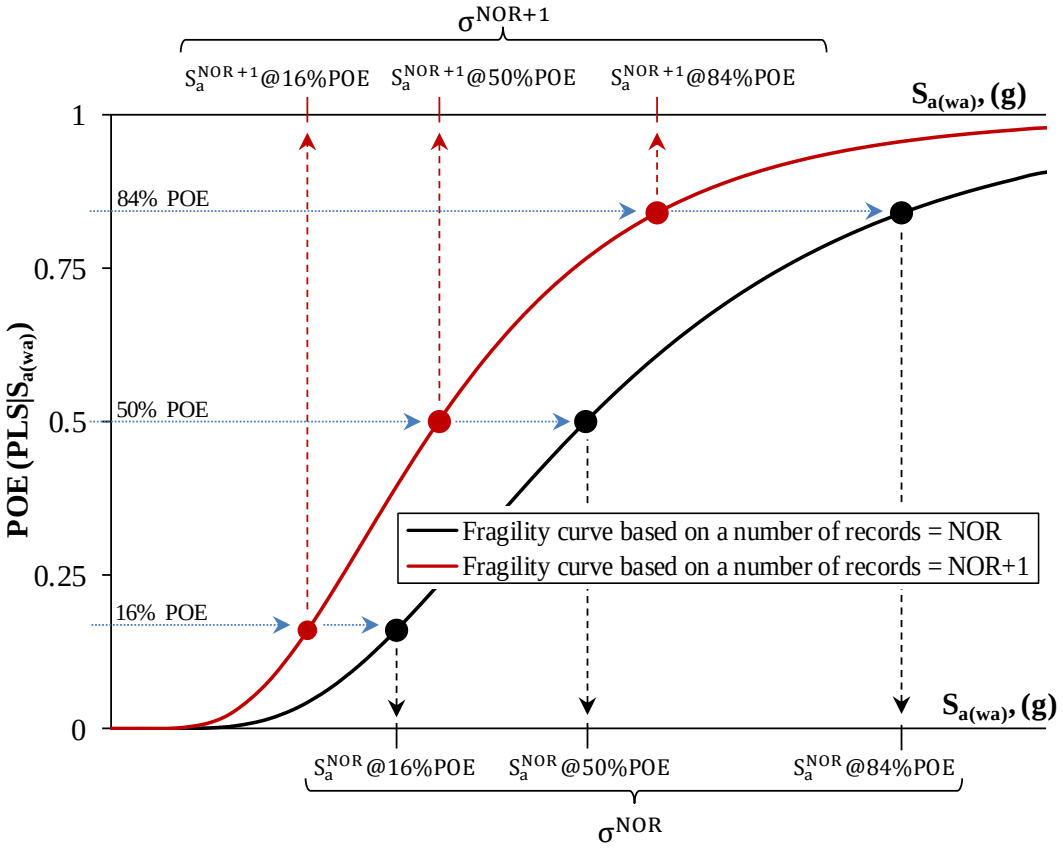

Figure 6.19. Schematic for the calculation procedure of acceptance tolerance T_{FC}

In the T_{FC} equation, the values of $\sigma^{NOR+1}$and σ^{NOR} define the slope of the fragility curves developed NOR+1 and NOR, respectively. Accordingly, the resulting σ_{NOR}^{NOR+1} is a measure of the congruence in the slope of the two fragility curves. The $(S_a)_{NOR}^{NOR+1}$, on the other hand, measures how close the two fragility curves are in terms of the $S_{a(wa)}$ value corresponding to the 50% POE. The two aforementioned measures are weighed

(giving 75% weight to $(S_a)_{NOR}^{NOR+1}$ and 25% to σ_{NOR}^{NOR+1}) and combined to calculate T_{FC}. More weight is assigned to $(S_a)_{NOR}^{NOR+1}$ since, within the zones of interest at a fragility curve, the (IM-POE) corresponding values are more important when compared to the slope of the curve. The CFC tolerance acceptance value is set to 10% in the current study. Again, the upper bound of T_{FC} is subjective, a different value can be set depending on the accuracy level needed for the resultant CFCs and the variability of the input ground motions used in the MRIDAs.

To demonstrate the proposed simplified methodology and verify the acceptance values of T_R and T_{FC} recommended in the current study, the methodology is applied to the reference building. CFCs are developed for each of the three adopted performance criteria (IO, LS, and CP). Out of the seven records from each of Record Set #1 and #2 presented in Table 6.7 and Table 6.8, respectively, six records are needed to satisfy the set value of T_{FC} under severe distance earthquake scenario while all seven records are needed under moderate near-field earthquake scenario. Accordingly, the resulting CFCs are taken as the sets developed using 5-records under the former earthquake scenario and 6-records under the latter. Table 6.9 and Table 6.10 give the calculated values of T_{FC} for one increment-increased number of applied records under severe distance and moderate near-field scenarios, respectively. Meantime, Figure 6.20 and Figure 6.21 show the CFCs corresponding to a different number of applied records and limit states under the severe distant and moderate near-field earthquake scenarios, respectively.

Under the severe distant earthquake scenario, the 10% upper bound set for T_{FC} is satisfied at the two successive cycles using 5 and 6 number of records. Setting the values from the preceding cycle as a reference, the calculated T_{FC} values corresponding to the IO, LS, and CP limit states are (5.0%, 4.0% and 8.0%) and (7.0%, 5.0% and 4.0%) at the 5-records and 6-records cycles, respectively (Table 6.9). These values indicate high similarity in the developed CFCs under severe distant earthquake scenario with the total number of applied records in the range of 5 to 6. This similarity is obvious in Figure 6.20.

The results under moderate near-field earthquake scenario (Table 6.10 and Figure 6.21) revealed that the satisfaction of the 10% upper bound set for T_{FC} occurred at the two

successive cycles using 6 and 7 number of records. The calculated T_{FC} values corresponding to the IO, LS, and CP limit states are (7.0%, 5.0% and 6.0%) and (2.0%, 5.0% and 3.0%) at the 6-records and 7-records cycles, respectively. Again, these values indicate high similarity in the developed CFCs under moderate near-field earthquake scenario with the total number of applied records in the range of 6 to 7. This similarity is clearly illustrated in Figure 6.21.

Table 6.9. Calculated values of T_{FC} for different number of applied records under severe distant earthquake scenario

No. of records (NOR)	Limit state (PLS_i)	$S_{a(wa)}$ at 16%, 50%, and 84% POE of performance limit state ($IM|PLS_i$), (g)			Standard deviation (σ)	σ_{NOR}^{NOR+1}	$(S_a)_{NOR}^{NOR+1}$	T_{FC} (%)
		@ 16%	@ 50%	@ 84%				
2	IO	0.076	0.092	0.134	0.289	0	0	0
	LS	0.132	0.184	0.257	0.333	0	0	0
	CP	0.234	0.290	0.361	0.217	0	0	0
3	IO	0.073	0.103	0.145	0.343	0.19	0.12	14.0
	LS	0.140	0.198	0.239	0.271	0.19	0.08	10.0
	CP	0.281	0.324	0.438	0.227	0.05	0.12	10.0
4	IO	0.072	0.110	0.168	0.424	0.23	0.07	11.0
	LS	0.140	0.219	0.343	0.448	0.65	0.11	24.0
	CP	0.246	0.369	0.550	0.402	0.78	0.14	30.0
5	IO	0.073	0.103	0.145	0.343	0.02	0.05	5.0
	LS	0.145	0.228	0.361	0.456	0.02	0.04	4.0
	CP	0.253	0.405	0.571	0.409	0.02	0.1	8.0
6	IO	0.76	0.109	0.168	0.397	0.08	0.06	7.0
	LS	0.149	0.215	0.375	0.465	0.02	0.06	5.0
	CP	0.244	0.415	0.580	0.437	0.07	0.02	4.0

Table 6.10. Calculated values of T_{FC} for different number of applied records under moderate near-field earthquake scenario

No. of records (NOR)	Limit state (PLS_i)	$S_{a(wa)}$ at 16%, 50%, and 84% POE of performance limit state ($IM|PLS_i$), (g)			Standard deviation (σ)	σ_{NOR}^{NOR+1}	$(S_a)_{NOR}^{NOR+1}$	T_{FC} (%)
		@ 16%	@ 50%	@ 84%				
2	IO	0.028	0.041	0.058	0.364	0	0	0
	LS	0.038	0.054	0.077	0.353	0	0	0
	CP	0.056	0.072	0.090	0.237	0	0	0
3	IO	0.027	0.028	0.041	0.059	0.02	0.00	1.0
	LS	0.037	0.038	0.055	0.078	0.02	0.02	2.0
	CP	0.054	0.056	0.073	0.093	0.07	0.01	3.0
4	IO	0.025	0.045	0.062	0.461	0.24	0.10	13.0
	LS	0.035	0.053	0.078	0.401	0.11	0.04	6.0
	CP	0.052	0.078	0.096	0.312	0.23	0.07	11.0
5	IO	0.027	0.043	0.068	0.462	0.10	0.10	10.0
	LS	0.037	0.059	0.093	0.461	0.15	0.11	12.0
	CP	0.054	0.079	0.116	0.382	0.25	0.11	15.0
6	IO	0.030	0.046	0.070	0.424	0.08	0.07	7.0
	LS	0.04	0.061	0.110	0.508	0.10	0.03	5.0
	CP	0.050	0.083	0.115	0.420	0.10	0.05	6.0
7	IO	0.026	0.047	0.061	0.437	0.03	0.02	2.0
	LS	0.042	0.060	0.100	0.436	0.14	0.02	5.0
	CP	0.048	0.080	0.110	0.418	0.00	0.04	3.0

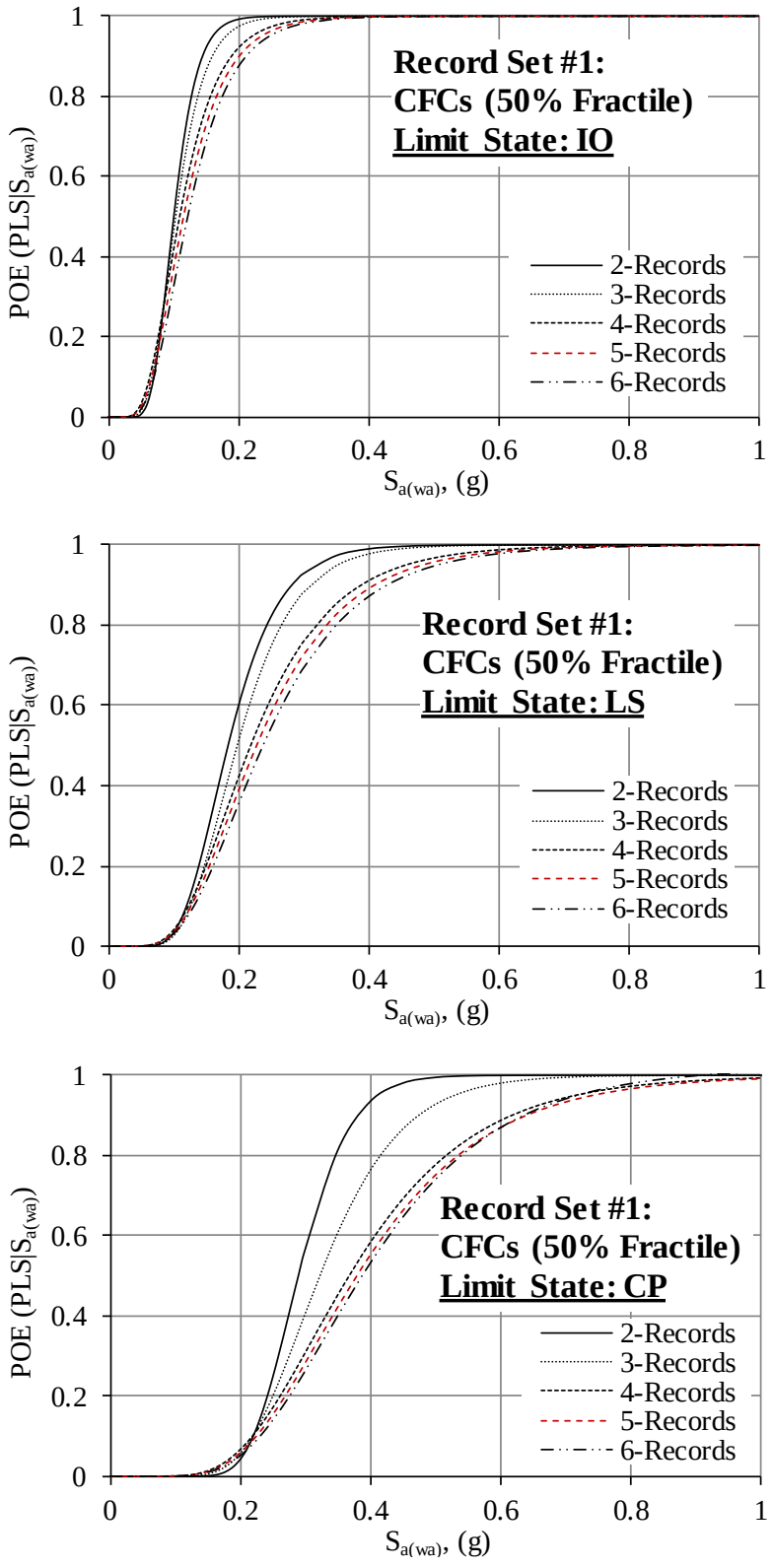

Figure 6.20. CFCs correspond to different number of applied records under severe distant earthquake scenario: (a) @ IO limit state; (b) @ LS limit state; and (c) CP limit state

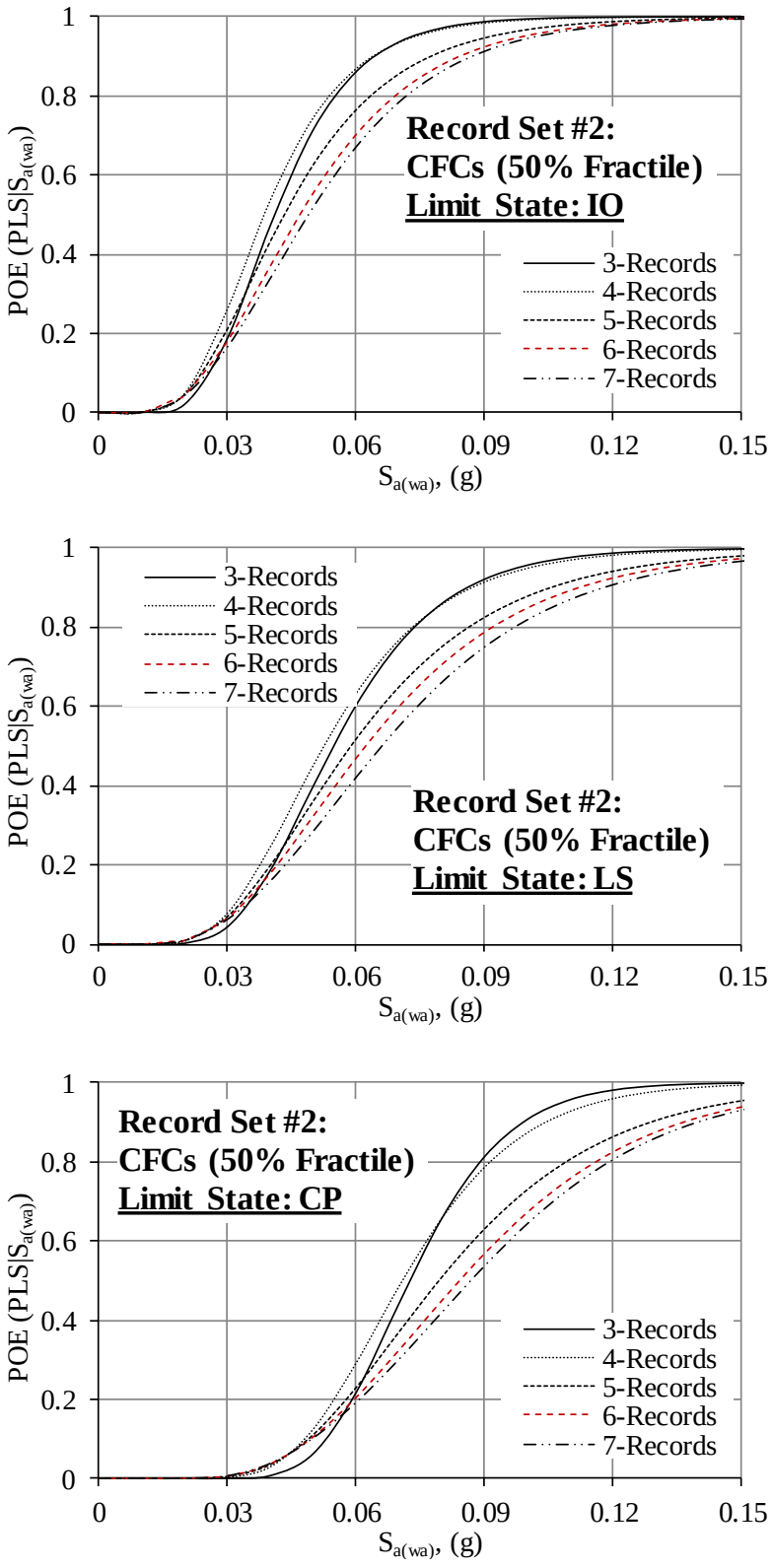

Figure 6.21. CFCs correspond to different number of applied records under moderate near-field earthquake scenario: (a) @ IO limit state; (b) @ LS limit state; and (c) CP limit state

To verify the recommended upper bound value for T_{FC}, the CFCs developed for the reference building at a different number of applied records are plotted against their refined counterparts that were developed in Section 6.1. Figure 6.22 to Figure 6.24 show the CFCs correspond to the IO, LS, and CP limit states under severe distant earthquake scenario, while Figure 6.25 to Figure 6.27 show the same under the moderate near-field scenario. In Figure 6.28, satisfactory CFCs at IO, LS, and CP limit states are plotted against the refined fragility curves of the reference building under both investigated seismic scenarios.

The results presented in Figure 6.22 to Figure 6.28 show that the CFCs developed for the reference building are closer to the refined fragility curves under moderate near-field scenario compared to the ones under severe distant scenario. Under severe distant seismic scenario, the maximum POE difference between the satisfactory CFCs and the refined ones is (4.8% @ IO, 2.7% @ LS, and 1.0% @ CP) at DBE, (13.4% @ IO, 0.1% @ LS, and 3.1% @ CP) at MCE, and (13.0% @ IO, 13.0% @ LS, and 17.0% @ CP) at any intensity level within the range of Figure 6.28a. Under moderate near-field seismic scenario, the maximum POE difference between the satisfactory CFCs and the refined ones is (0.2% @ IO, 0.2% @ LS, and 0.0% @ CP) at DBE, (0.4% @ IO, 0.3% @ LS, and 0.0% @ CP) at MCE, and (7.0% @ IO, 4.0% @ LS, and 6.0% @ CP) at any intensity level within the range of Figure 6.28b.

The higher differences in POEs under severe distant seismic scenario can be attributed to the high nonlinearity that shapes high-rise buildings' complex response subjected to long-period records. The characteristics of long-period records may vary considerably from one record to another and at different period spans in the same record in terms of record intensity, number of peaks, and peak amplitudes, causing higher uncertainties in the input ground motions. As a result, different applied records may trigger different local damage indices, causing the building to respond differently. This issue does not present in the building response under moderate near-field earthquake scenario (Table 6.10), considering the almost elastic, shear-controlled nature of response of the building under this seismic scenario as discussed in details in CHAPTER 5.

Despite the differences between the CFCs and the refined set of fragility curves subjected to severe distant earthquake scenario compared with the ones under the moderate near-field scenario, the relatively small differences from both scenarios reflect the soundness of the

proposed simplified methodology to develop reliable sets of fragility curves with considerably less time and computational effort.

As another form of comparison, which is more convenient for the seismic hazard assessment and mitigation studies, the probabilities of the damage states referred to in Section 6.2 (UOC, IOC, SD, and SC) are calculated and compared at different earthquake intensity levels using the satisfactory CFCs and the refined ones for the reference building under both investigated seismic scenarios. The procedure to calculate the difference between these values at a given earthquake intensity level (T_{DP}) is schematically presented in Figure 6.29. The results are presented in a tabulated format (Table 6.11 and Table 6.12) as well as in bar charts (Figure 6.30 and Figure 6.31). The results show that between the satisfactory CFCs and the refined ones, the maximum difference in the damage state probability at any seismic intensity level is 7% @ UOC, 7% @ IOC, 4% @ SD, and 5% @ SC under moderate near-field seismic scenario (Table 6.12 and Figure 6.31). Under severe distant scenario, the values are 14% @ UOC, 13% @ IOC, 10% @ SD, and 17% @ SC (Table 6.11 and Figure 6.30). Again, these differences are smaller at the DBE and MCE intensity levels for both seismic scenarios.

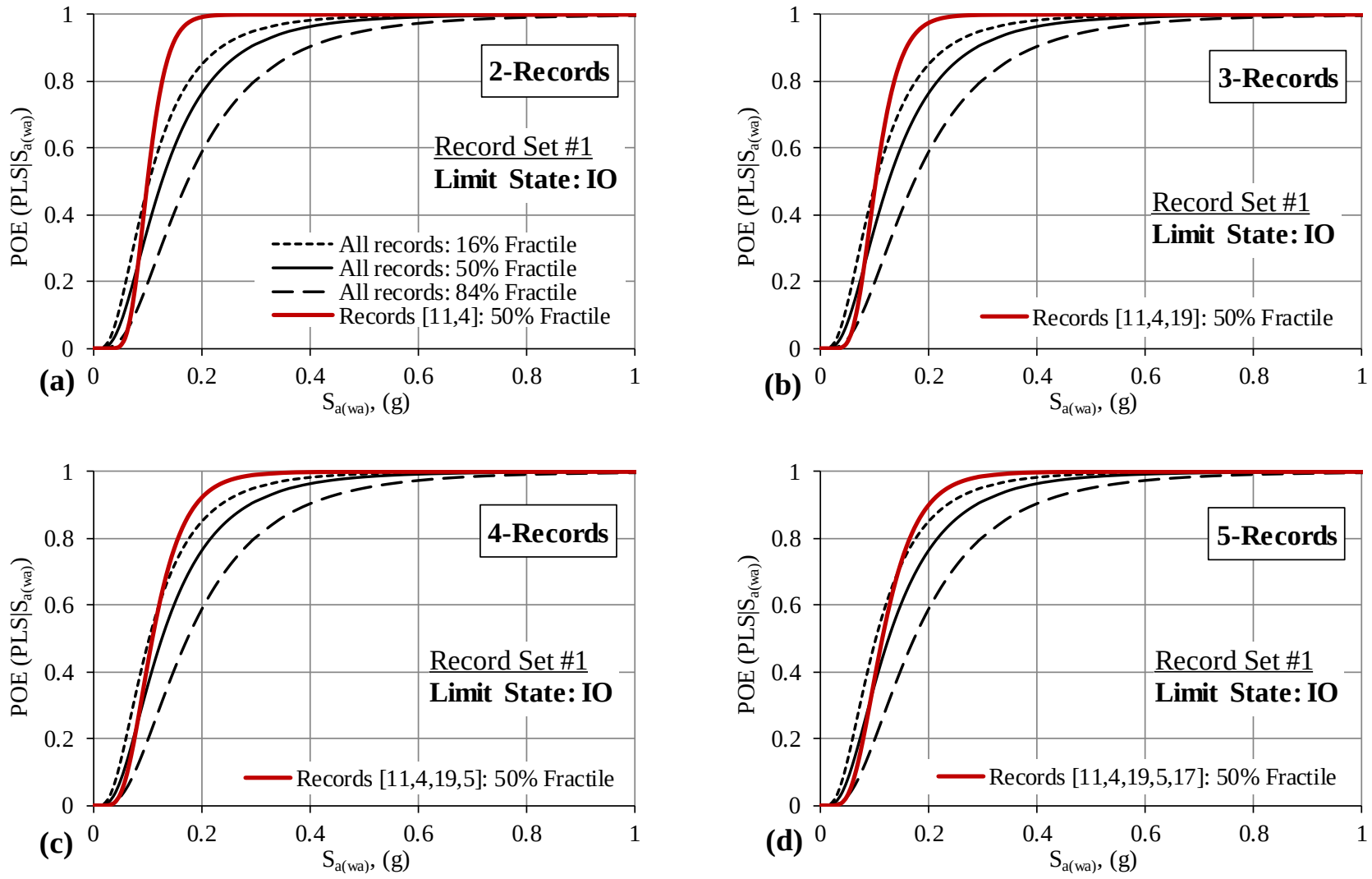

Figure 6.22. IO Limit State: CFCs developed using different number of records combined with the refined, 20 records-based fragility curves for the reference building under severe distant earthquake scenario: (a) 2 records; (b) 3 records; (c) 4 records; and (d) 5 records.

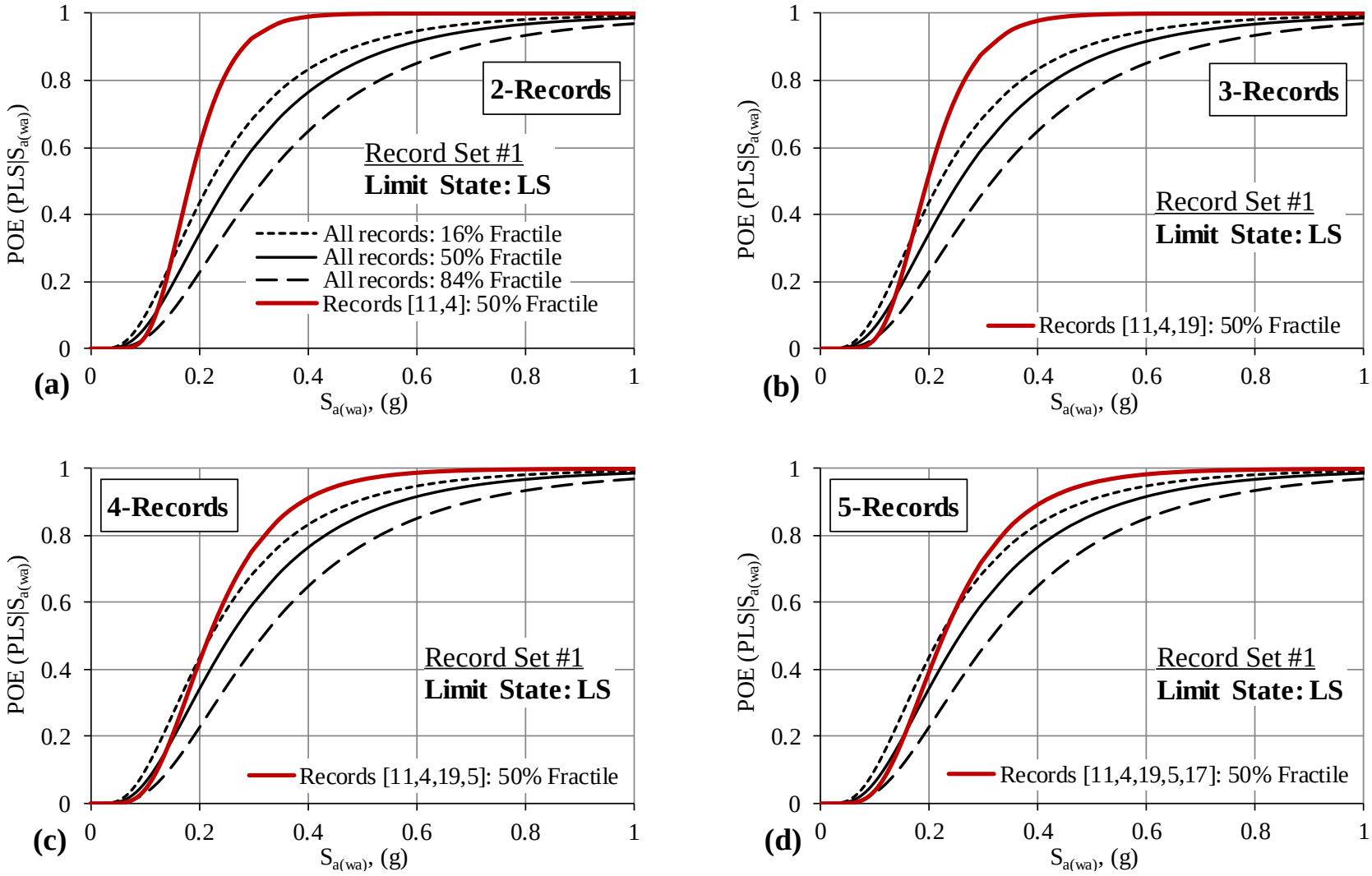

Figure 6.23. LS Limit State: CFCs developed using different number of records combined with the refined, 20 records-based fragility curves for the reference building under severe distant earthquake scenario: (a) 2 records; (b) 3 records; (c) 4 records; and (d) 5 records.

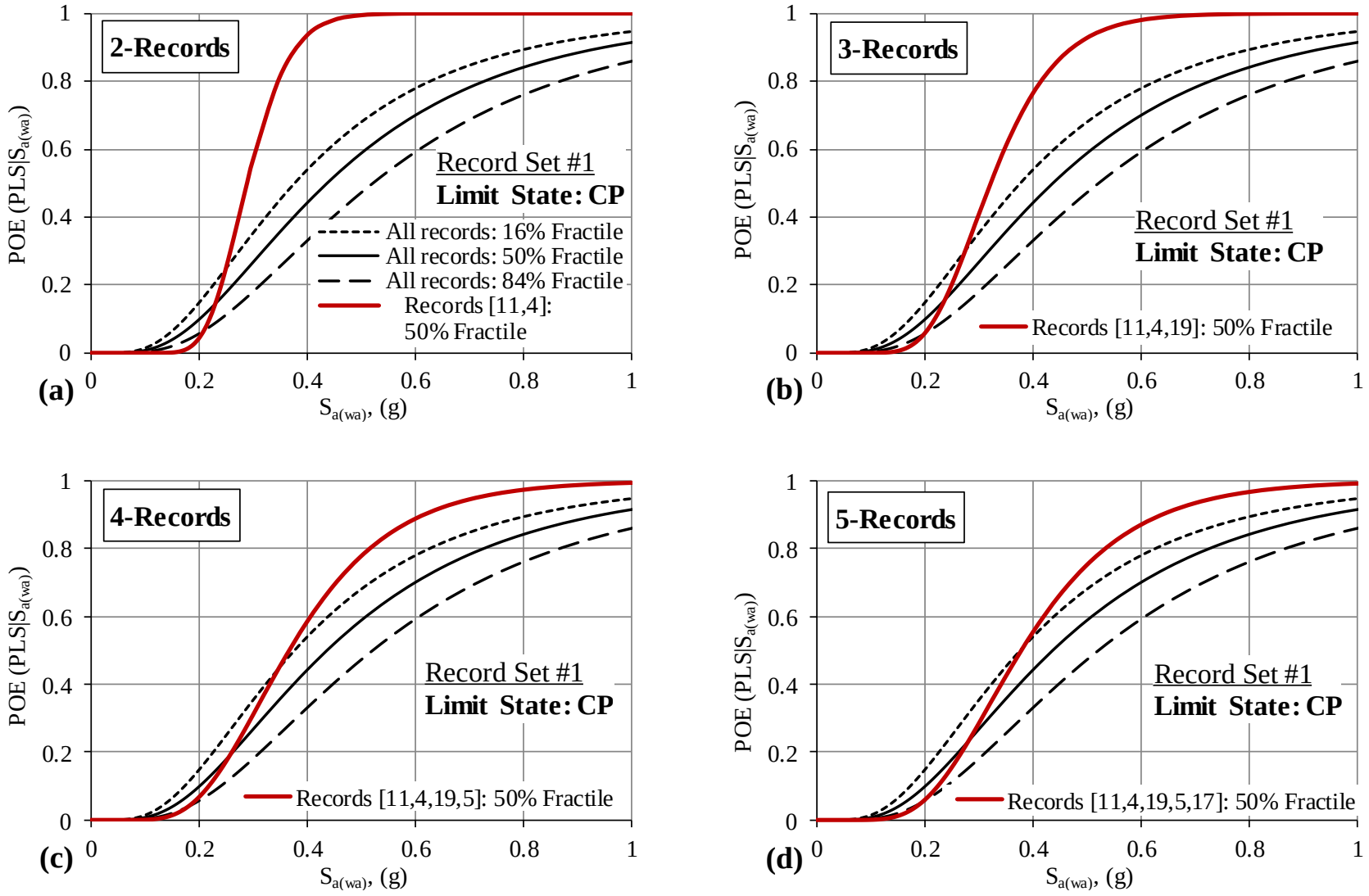

Figure 6.24. CP Limit State: CFCs developed using different number of records combined with the refined, 20 records-based fragility curves for the reference building under severe distant earthquake scenario: (a) 2 records; (b) 3 records; (c) 4 records; and (d) 5 records.

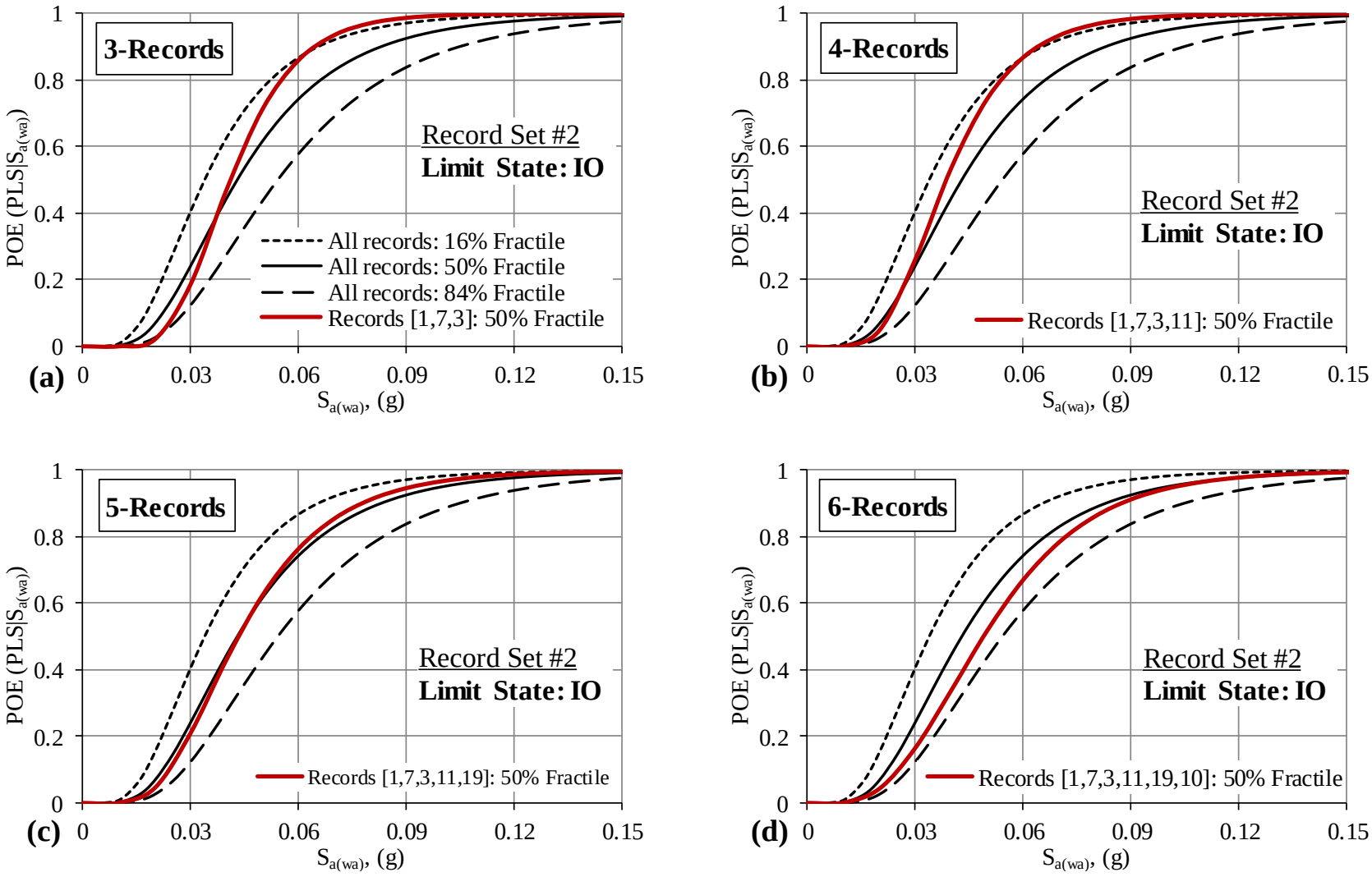

Figure 6.25. IO Limit State: CFCs developed using different number of records combined with the refined, 20 records-based fragility curves for the reference building under moderate near-field earthquake scenario: (a) 3 records; (b) 4 records; (c) 5 records; and (d) 6 records.

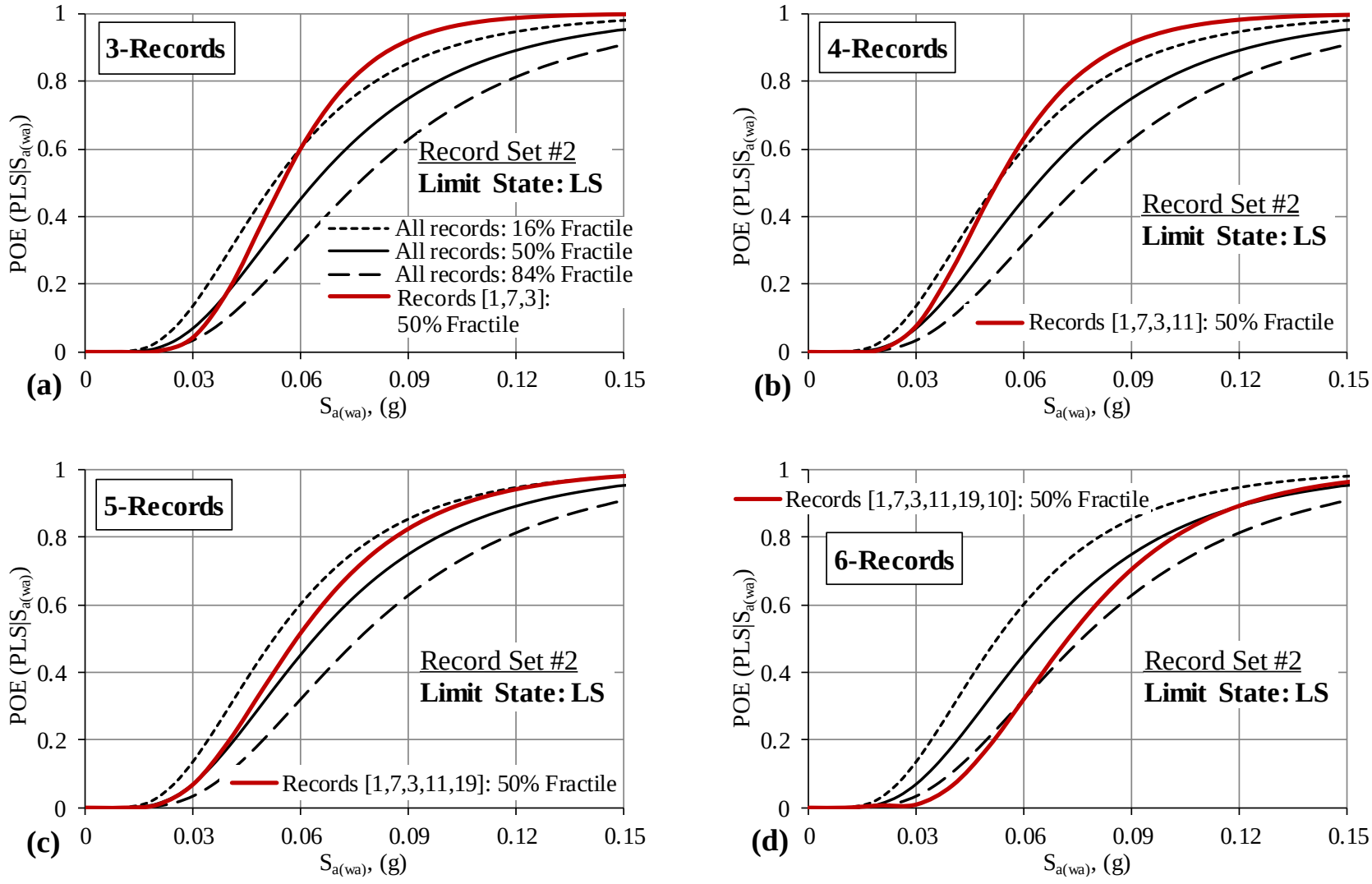

Figure 6.26. LS Limit State: CFCs developed using different number of records combined with the refined, 20 records-based fragility curves for the reference building under moderate near-field earthquake scenario: (a) 3 records; (b) 4 records; (c) 5 records; and (d) 6 records.

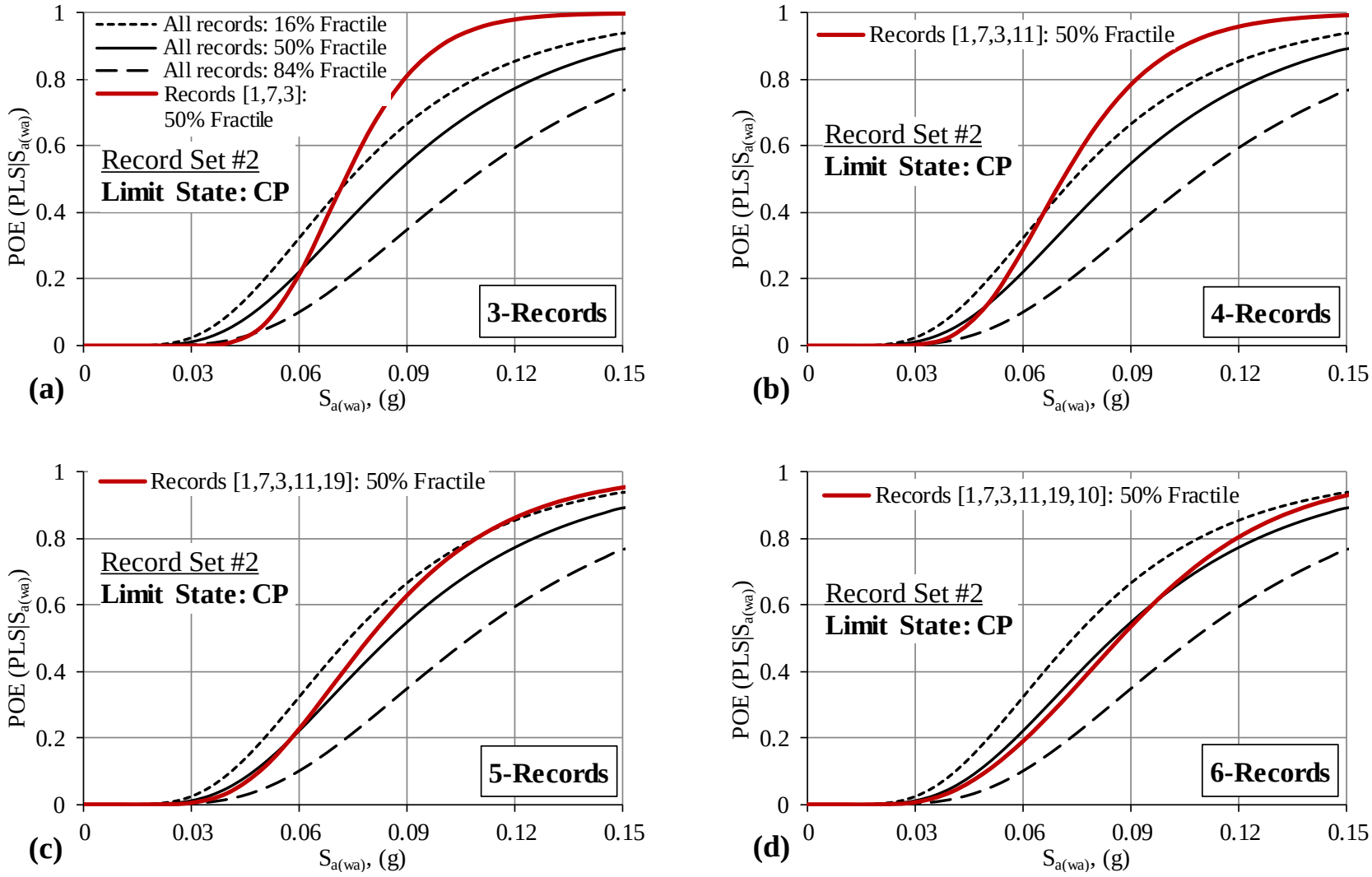

Figure 6.27. CP Limit State: CFCs developed using different number of records combined with the refined, 20 records-based fragility curves for the reference building under moderate near-field earthquake scenario: (a) 3 records; (b) 4 records; (c) 5 records; and (d) 6 records.

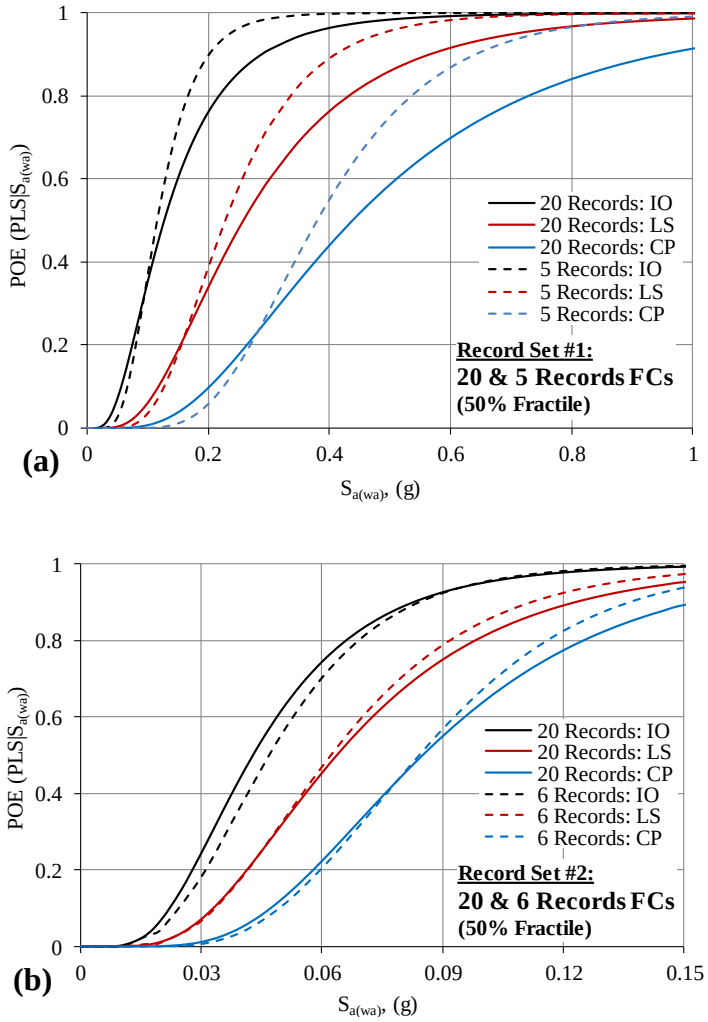

Figure 6.28. Satisfactory CFCs at IO, LS, and CP limit states plotted against the refined fragility curves of the reference building: (a) severe distant earthquake scenario; and (b) moderate near-field earthquake scenario

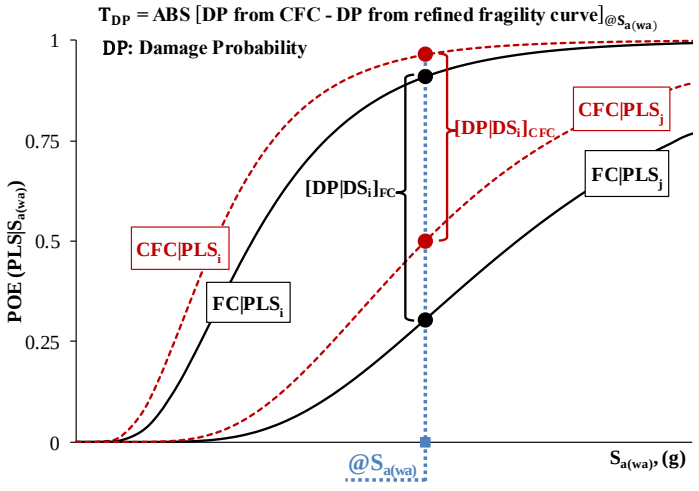

Figure 6.29. Schematic for the calculation procedure of the difference in the damage probability (T_{DP})

Table 6.11. Comparison between satisfactory CFCs and the refined FCs of the reference building in terms of damage state probability at different intensity levels under severe distant earthquake scenario

Earthquake intensity level	No. of records	Damage state probability							
		Unimpaired Occupancy	$^{+}T_{DP}$ (%)	Impaired Occupancy	$^{+}T_{DP}$ (%)	Structural damage	$^{+}T_{DP}$ (%)	Structural collapse	$^{+}T_{DP}$ (%)
@ $S_{a(wa)}$ = 0.053 g (SLE)	**20**	0.92	**5.0**	0.08	**5.0**	0.00	**0.0**	0.00	**0.0**
	5	0.97		0.03		0.00		0.00	
@ $S_{a(wa)}$ = 0.105 g (DBE)	**20**	0.62	**3.0**	0.31	**6.0**	0.06	**2.0**	0.01	**1.0**
	5	0.59		0.37		0.04		0.00	
@ $S_{a(wa)}$ = 0.158 g (MCE)	**20**	0.37	**14.0**	0.42	**13.0**	0.17	**3.0**	0.04	**2.0**
	5	0.23		0.55		0.20		0.02	
@ $S_{a(wa)}$ = 0.4 g	**20**	0.04	**4.0**	0.20	**9.0**	0.32	**2.0**	0.44	**11.0**
	5	0.00		0.11		0.34		0.55	
@ $S_{a(wa)}$ = 0.6 g	**20**	0.01	**1.0**	0.08	**6.0**	0.22	**10.0**	0.70	**17.0**
	5	0.00		0.02		0.11		0.87	
@ $S_{a(wa)}$ = 0.8 g	**20**	0.00	**0.0**	0.03	**3.0**	0.13	**10.0**	0.84	**13.0**
	5	0.00		0.00		0.03		0.97	

$^{+}T_{DP}$: Difference in the Damage Probability = ABS [(5 records damage state probability – 20 records damage state probability], (%)

Table 6.12. Comparison between satisfactory CFCs and the refined FCs of the reference building in terms of damage state probability at different intensity levels under moderate near-field earthquake scenario

Earthquake intensity level	No. of records	Damage state probability							
		Unimpaired Occupancy	$^{+}T_{DP}$ (%)	Impaired Occupancy	$^{+}T_{DP}$ (%)	Structural damage	$^{+}T_{DP}$ (%)	Structural collapse	$^{+}T_{DP}$ (%)
@ $S_{a(wa)}$ = 0.006 g (SLE)	**20**	1.00	**0.0**	0.00	**0.0**	0.00	**0.0**	0.00	**0.0**
	6	1.00		0.00		0.00		0.00	
@ $S_{a(wa)}$ = 0.011g (DBE)	**20**	1.00	**0.0**	0.00	**0.0**	0.00	**0.0**	0.00	**0.0**
	6	1.00		0.00		0.00		0.00	
@ $S_{a(wa)}$ = 0.017 g (MCE)	**20**	0.97	**0.0**	0.03	**1.0**	0.00	**1.0**	0.00	**0.0**
	6	0.97		0.02		0.01		0.00	
@ $S_{a(wa)}$ = 0.04 g	**20**	0.56	**7.0**	0.26	**7.0**	0.13	**1.0**	0.05	**1.0**
	6	0.63		0.19		0.14		0.04	
@ $S_{a(wa)}$ = 0.08 g	**20**	0.11	**1.0**	0.22	**5.0**	0.22	**4.0**	0.45	**0.0**
	6	0.12		0.17		0.26		0.45	
@ $S_{a(wa)}$ = 0.12 g	**20**	0.02	**0.0**	0.09	**3.0**	0.12	**2.0**	0.77	**5.0**
	6	0.02		0.06		0.10		0.82	

$^{+}T_{DP}$: Difference in the Damage Probability = ABS [(6 records damage state probability – 20 records damage state probability], (%)

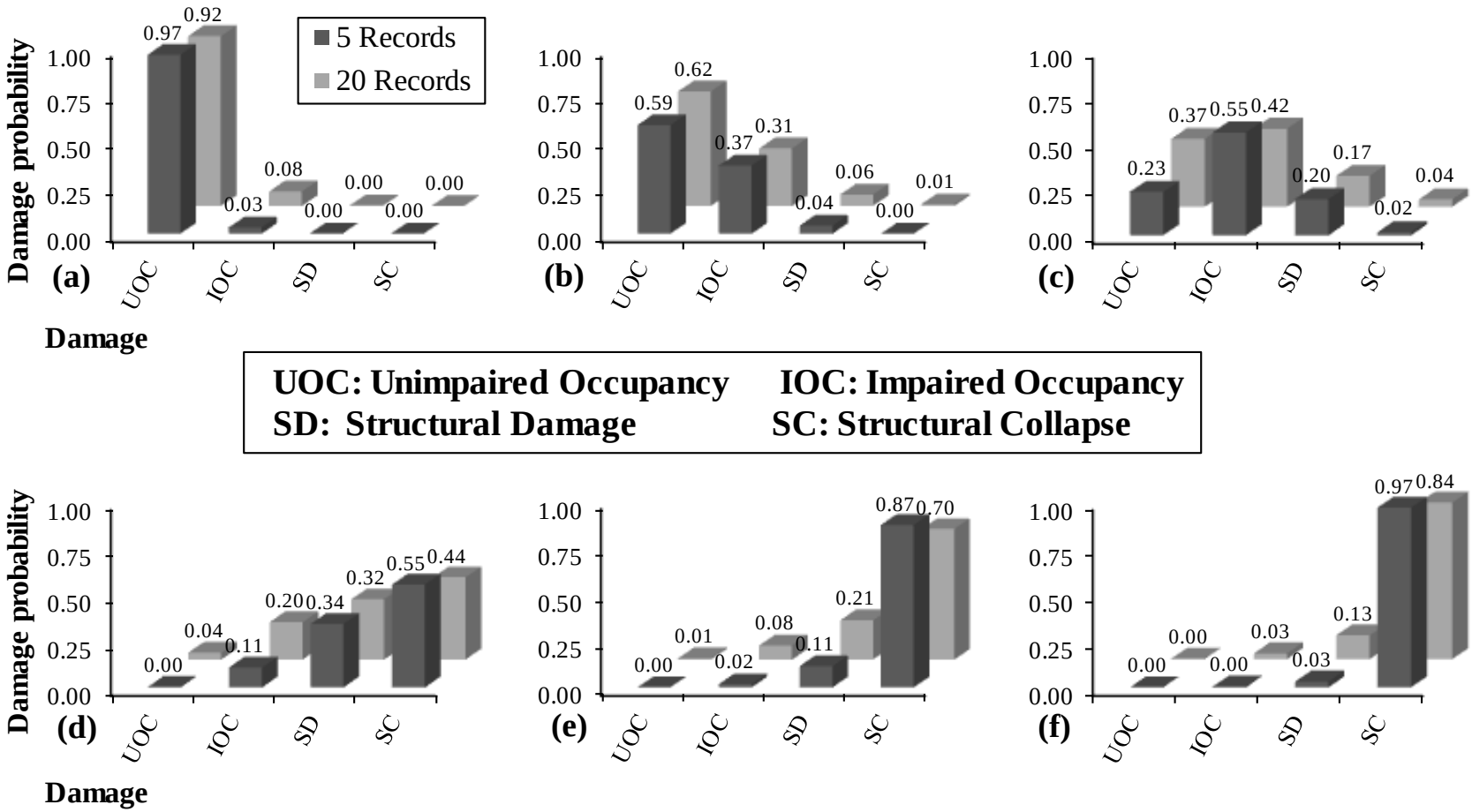

Figure 6.30. Comparison between satisfactory CFCs and the refined FCs of the reference building in terms of damage state probability at different intensity levels under severe distant earthquake scenario: (a) @ SLE; (b) @ DBE; (c) @ MCE; (d) @ $S_{a(wa)}$ = 0.4 g; (e) @ $S_{a(wa)}$ = 0.6 g; and (f) @ $S_{a(wa)}$ = 0.8 g

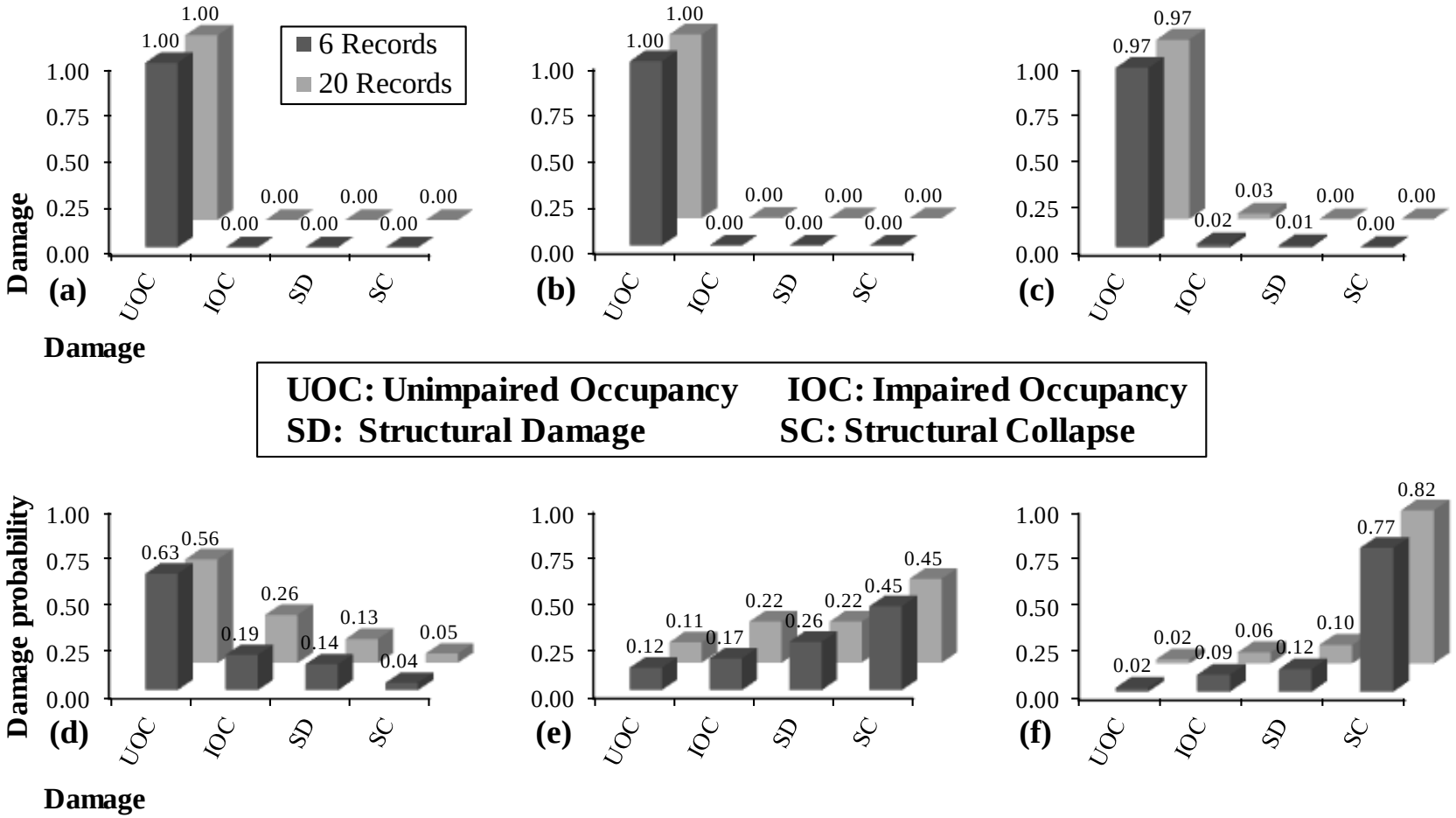

Figure 6.31. Comparison between satisfactory CFCs and the refined FCs of the reference building in terms of damage state probability at different intensity levels under moderate near-field earthquake scenario: (a) @ SLE; (b) @ DBE; (c) @ MCE; (d) @ $S_{a(wa)}$ = 0.04 g; (e) @ $S_{a(wa)}$ = 0.08 g; and (f) @ $S_{a(wa)}$ = 0.12 g

6.4 Consistency of developed fragility curves for buildings with varying height

In Section 5.5, a parametric study, employing six additional buildings, is conducted to investigate the effect of building total height (number of storeys) on the consistency of the adopted global DM (NISD) corresponding to the mapped DIs. The predominant mode periods (uncracked and equivalent inelastic) along with the design proportions of these additional buildings are given in Table 5.2. To take the parametric study one step further, CFCs for three out of the six additional buildings are developed in this section. The three selected buildings are 20-storeys (20S), 40-storeys (40S), and 50-storeys (50S). the same input ground motions from Section 6.3 (5-Records "5R" representing the severe distant seismic scenario and 6-Records "6R" representing the moderate near-field seismic scenario) are utilized to develop CFCs for the aforementioned buildings. Following the methodology presented in CHAPTER 5, performance limit state criteria, with NISD as DM, under both seismic scenarios are specified for each of the three selected buildings (along with the 30S reference building) using the 5R and 6R, respectively. Table 6.13 lists the "specified" PLS criteria for the 20S, 30S, 40S, and 50S based on the 5R and 6R (referred to hereafter as SPLSC) along the adopted "reference" PLS criteria for the 30S building using the twenty records (20R) in each set of records (referred to hereafter as RPLSC).

Table 6.13. Performance limit state criteria for 20S, 30S, 40S, and 50S using 5R and 6R along with limit state criteria for 30S reference building based on 20R

Record Set	Limit State	NISD associated to limit state (%)				
		Building				
		20S	30S	40S	50S	30S (20R)
#1 (5R)	IO	0.15	0.12	0.11	0.06	0.11
	LS	0.25	0.23	0.23	0.12	0.22
	CP	0.46	0.40	0.38	0.19	0.37
#2 (6R)	IO	0.11	0.08	0.08	0.06	0.08
	LS	0.14	0.10	0.10	0.09	0.11
	CP	0.18	0.14	0.12	0.11	0.15

Using the SPLSC listed in Table 6.13, the CFCs for the 20S, 30S, 40S, and 50S buildings along with the RPLSC-based rigorous FCs of the 30S reference building (developed in 6.1) under severe distant and moderate near-field seismic scenarios are presented in Figure 6.32 and Figure 6.33, respectively. The results in these figures are utilised to evaluate the capability of the presented framework and methodologies of

developing one set of fragility curves that can represent RC high-rise buildings with varying total height. To make it more convenient and easier to compare, the results in Figure 6.32 and Figure 6.33 are presented in the form of damage state probabilities in Table 6.14 and Table 6.15, respectively. These tables summarise the probabilities of UO, IO, SD, and SC damage states for the 20S, 40S, and 50S buildings at different earthquake intensity levels under the two investigated seismic scenarios. Furthermore, the tables are listing the difference in damage state probabilities for these three buildings with reference to the rigorous FC-based values calculated for the 30S reference building. Table 6.16 summarises the maximum values of the CFC-based damage state probability difference of all studied buildings (20S, 30S, 40S, and 50S) in reference to the rigorous FC-based damage state probabilities of the 3S reference building.

By analysing the aforementioned figures and tables, the following remarks can be withdrawn.

1. Under the severe distant seismic scenario, Figure 6.32 shows that as the building goes taller (from 20S up to 50S), it becomes less vulnerable. This is attributed to the fact that for the investigated buildings, the lateral stiffness of the piers and cores at lower floors (in the direction of the seismic excitation) increases as the building goes taller. This renders taller buildings needing a higher seismic intensity to reach a predefined NISD value (limit state criteria). This observation is consistent for all PLSs under severe distant seismic scenario except for the IO-CFC of the 20S building and the CP-CFC of the 50S building.

2. The IO-CFC of the 20S building under severe distant seismic scenario indicates a slightly lower vulnerability at $S_{a(wa)} > 0.15g$ when compared to the next building in terms of total height (30S). This may be attributed to the increasing contribution of the first mode of vibration to the IO-related building response at higher seismic intensities as the building total height becomes lower, approaching the height of first mode-dominated structures. For the 50S building under the severe distant seismic scenario, on the other hand, the CP-CFC is close to the 40S CP-CFC at seismic intensities between 0.60g and 0.80g. This is attributed to the shear-controlled CP limit state definition of the 50S building at these high seismic intensities as opposed to the deformation-based definition at lower intensities.

3. The observation discussed in the above points is not applicable to the fragility curves presented in Figure 6.33 (under moderate near-field seismic scenario). This is obviously due to the shear-controlled response of all investigated buildings under this seismic scenario. A lengthy discussion on the characteristics of such a response nature is given in CHAPTER 5.

4. The developed CFCs for the investigated buildings under moderate near-field seismic scenario (Figure 6.33) showing lesser dispersion (curves are closer to each other) compared to the CFCs under sever distant seismic scenario (Figure 6.32). Again, this is attributed to elastic nature of the shear-controlled response of the lateral force-resisting system (piers and cores) in the investigated buildings under Record Set #2 as opposed to the high nonlinearity accompanies the flexure-controlled response of these buildings under Record Set #1.

5. Comparing any CFC-based damage state probability (UOC, IOC, SD, or SC) calculated for the investigated buildings to the rigorous FC-based values for the 30S reference building, the minimum and maximum differences (T_{DP}) under severe distant seismic scenario are 9.0% (40S & 50S: SC) and 32% (50S: UOC), respectively (Table 6.16). Under the moderate near-field seismic scenario, the minimum and maximum differences are 2.0% (50S: IOC) and 17% (40S: UOC), respectively (Table 6.16). Depending on the study purpose and the intended use for the final product (fragility set), the dispersion in the T_{DP} under severe distant seismic scenario can be reduced by tightening the acceptance values of T_R and T_{FC} (i.e. increasing the number of records to be used in developing the CFCs).

In conclusion, the T_{DP} differences reported in point #6 above may still be a reasonable compromise considering the massive saving in effort and computational time when only one set of seismic scenario-based PLS criteria and CFCs are used for an inventory of high-rise buildings with a wide range of total building height. This is especially true for vulnerability assessment studies on the regional or global scale, where the end product is intended for clients such as insurance companies and hazard mitigation/planning governmental and non-governmental bodies.

It is important to emphasise here that these T_{DP} calculated differences are the sum of two components, the first is related to the use of CFC methodology rather than the refined (rigorous) approach in developing the SPLSC-based fragility curves for the 20S,

40S, and 50S buildings in this parametric study, while the second component is related to the variation in the building total height. Considering the T_{DP} related to the 30S reference building (comprises of the first component only), the maximum difference in T_{DP} for the other investigated buildings is expected to drop by more than 50% when eliminating the first component (assuming that the fragility curves for all the investigated buildings were developed using the rigorous approach). This further supports the supremacy of the adopted NISD as DM, $S_{a(wa)}$ as IM, along with all other components and methodologies of the framework proposed in the current work in terms of the ability to develop one set of seismic scenario-based fragility relations that suits a group of RC high-rise buildings with varying height.

To close, it is emphasised that, notwithstanding the number of records employed for the derivation of the refined fragility relations, the rigour of the nonlinear modelling of the reference building and the additional six buildings used in the parametric study, the comprehensive methodology to quantitatively estimate the adopted performance limit state criteria, and the thorough verification of the methodology to derive the CFCs, the conclusions of the parametric study are, strictly speaking, applicable to the buildings' configuration and the seismic scenarios investigated. However, considering the level of detail put in the framework for developing both rigorous and CFCs, some generality to the applicability of the parametric study results for RC high-rise buildings with different configurations and seismicity may fairly be claimed.

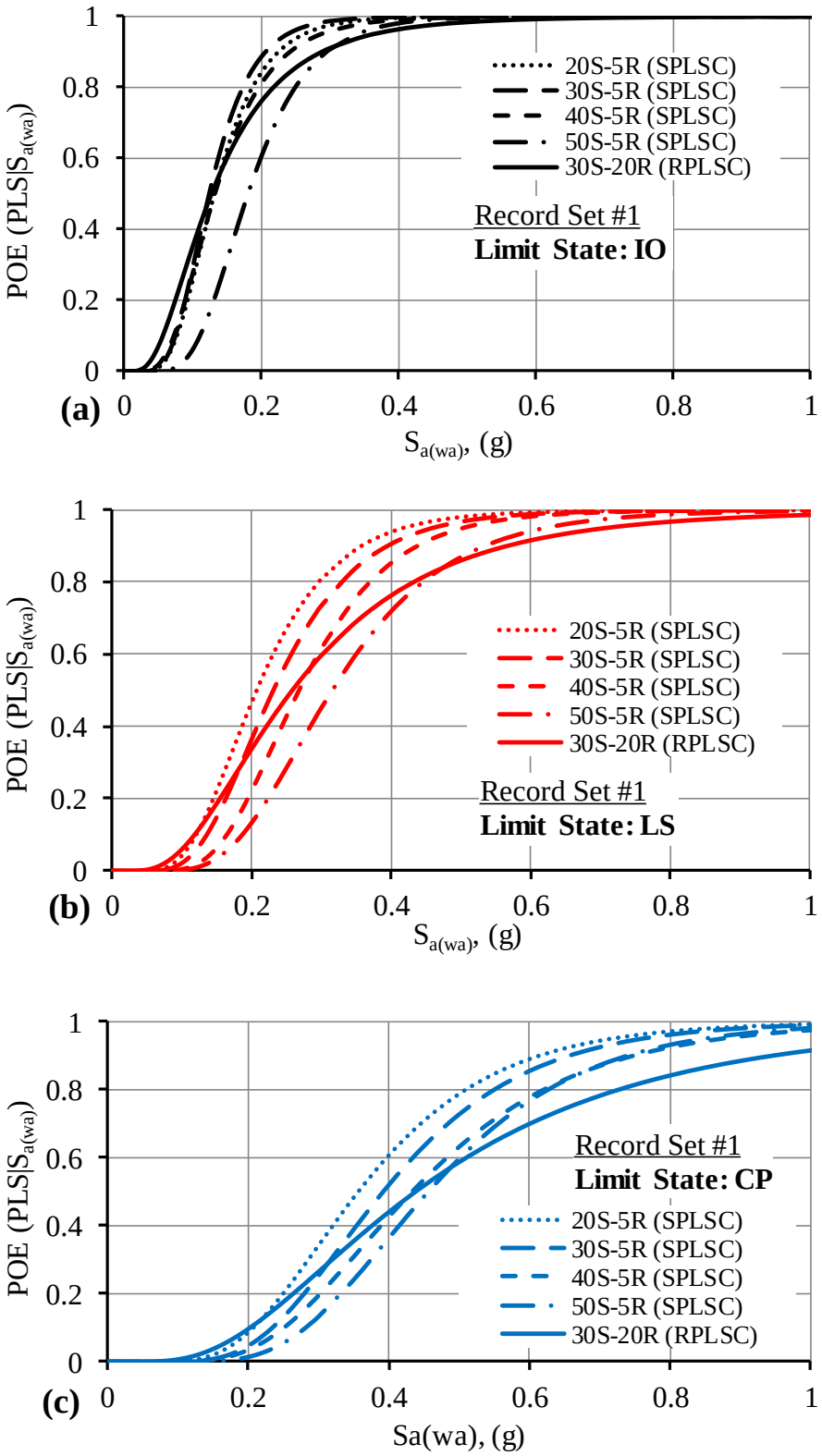

Figure 6.32. Record Set #1-CFCs of 20S, 30S, 40S, and 50S buildings along with the rigorous 20R-based FCs of the 30S reference building: (a) IO; (b) LS; and (c) CP

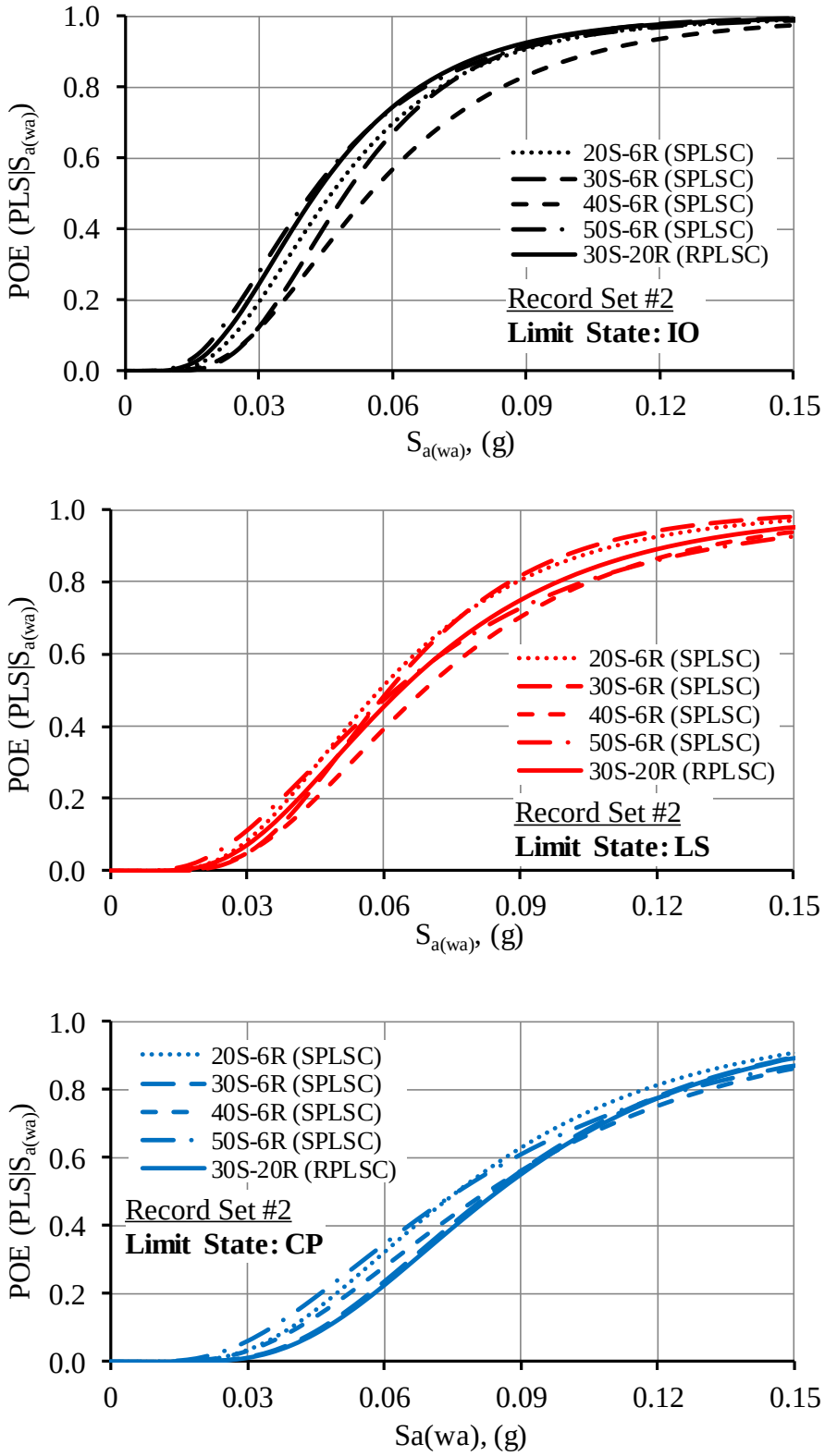

Figure 6.33. Record Set #2-CFCs of 20S, 30S, 40S, and 50S buildings along with the rigorous 20R-based FCs of the 30S reference building: (a) IO; (b) LS; and (c) CP

Table 6.14. 5R-based damage state probabilities of 20S, 40S, and 50S buildings and their differences with reference to the 20R-based damage state probabilities of the reference building under severe distant earthquake scenario

Earthquake intensity level	Building	Damage state probability							
		Unimpaired Occupancy	$^{+}T_{DP}$ (%)	Impaired Occupancy	$^{+}T_{DP}$ (%)	Structural damage	$^{+}T_{DP}$ (%)	Structural collapse	$^{+}T_{DP}$ (%)
@ $S_{a(wa)}$ = 0.053 g (SLE)	20S	0.99	7.0	0.01	7.0	0.00	0.0	0.00	0.0
	40S	0.98	6.0	0.02	6.0	0.00	0.0	0.00	0.0
	50S	1.00	8.0	0.00	8.0	0.00	0.0	0.00	0.0
@ $S_{a(wa)}$ = 0.105 g (DBE)	20S	0.74	12.0	0.22	9.0	0.04	2.0	0.00	1.0
	40S	0.72	10.0	0.27	4.0	0.01	5.0	0.00	1.0
	50S	0.94	32.0	0.06	25.0	0.00	6.0	0.00	1.0
@ $S_{a(wa)}$ = 0.158 g (MCE)	20S	0.32	5.0	0.41	1.0	0.24	7.0	0.03	1.0
	40S	0.34	3.0	0.57	15.0	0.08	9.0	0.01	3.0
	50S	0.62	25.0	0.33	9.0	0.05	12.0	0.00	4.0

$^{+}T_{DP}$: Difference in the Damage Probability = ABS [(5R damage probability of concerned building – 20R damage probability of 30S reference Building], (%)

Table 6.14 (continued). 5R-based damage state probabilities of 20S, 40S, and 50S buildings and their differences with reference to the 20R-based damage state probabilities of the reference building under severe distant earthquake scenario

Earthquake intensity level	Building	Damage state probability							
		Unimpaired Occupancy	$^{+}T_{DP}$ (%)	Impaired Occupancy	$^{+}T_{DP}$ (%)	Structural damage	$^{+}T_{DP}$ (%)	Structural collapse	$^{+}T_{DP}$ (%)
@ $S_{a(wa)}$ = 0.4 g	20S	0.00	4.0	0.06	14.0	0.33	1.0	0.61	17.0
	40S	0.01	3.0	0.14	6.0	0.43	11.0	0.42	2.0
	50S	0.02	2.0	0.26	6.0	0.36	4.0	0.36	8.0
@ $S_{a(wa)}$ = 0.6 g	20S	0.00	1.0	0.01	7.0	0.10	12.0	0.89	19.0
	40S	0.00	1.0	0.02	6.0	0.20	2.0	0.78	8.0
	50S	0.00	1.0	0.06	2.0	0.17	5.0	0.77	7.0
@ $S_{a(wa)}$ = 0.8 g	20S	0.00	0.0	0.00	3.0	0.03	10.0	0.97	13.0
	40S	0.00	0.0	0.00	3.0	0.07	6.0	0.93	9.0
	50S	0.00	0.0	0.01	2.0	0.06	7.0	0.93	9.0

$^{+}T_{DP}$: Difference in the Damage Probability = ABS [(5R damage probability of concerned building – 20R damage probability of 30S reference Building], (%)

Table 6.15. 6R-based damage state probabilities of 20S, 40S, and 50S buildings and their differences with reference to the 20R-based damage state probabilities of the reference building under moderate near-field earthquake scenario

Earthquake intensity level	Building	Damage state probability							
		Unimpaired Occupancy	$^{+}T_{DP}$ (%)	Impaired Occupancy	$^{+}T_{DP}$ (%)	Structural damage	$^{+}T_{DP}$ (%)	Structural collapse	$^{+}T_{DP}$ (%)
@ $S_{a(wa)}$ = 0.006 g (SLE)	20S	1.00	**0.0**	0.00	**0.0**	0.00	**0.0**	0.00	**0.0**
	40S	1.00	**0.0**	0.00	**0.0**	0.00	**0.0**	0.00	**0.0**
	50S	1.00	**0.0**	0.00	**0.0**	0.00	**0.0**	0.00	**0.0**
@ $S_{a(wa)}$ = 0.011 g (DBE)	20S	1.00	**0.0**	0.00	**0.0**	0.00	**0.0**	0.00	**0.0**
	40S	1.00	**0.0**	0.00	**0.0**	0.00	**0.0**	0.00	**0.0**
	50S	0.99	**1.0**	0.01	**1.0**	0.00	**0.0**	0.00	**0.0**
@ $S_{a(wa)}$ = 0.017 g (MCE)	20S	0.98	**1.0**	0.02	**1.0**	0.00	**0.0**	0.00	**0.0**
	40S	0.99	**2.0**	0.01	**2.0**	0.00	**0.0**	0.00	**0.0**
	50S	0.96	**1.0**	0.03	**0.0**	0.01	**1.0**	0.00	**0.0**

$^{+}T_{DP}$: Difference in the Damage Probability = ABS [(6R damage probability of concerned building – 20R damage probability of 30S reference Building], (%)

Table 6.15 (continued). 6R-based damage state probabilities of 20S, 40S, and 50S buildings and their differences with reference to the 20R-based damage state probabilities of the reference building under moderate near-field earthquake scenario

Earthquake intensity level	Building	Damage state probability							
		Unimpaired Occupancy	$^{+}T_{DP}$ (%)	Impaired Occupancy	$^{+}T_{DP}$ (%)	Structural damage	$^{+}T_{DP}$ (%)	Structural collapse	$^{+}T_{DP}$ (%)
@ $S_{a(wa)}$ = 0.04 g	20S	0.62	6.0	0.17	9.0	0.11	2.0	0.10	5.0
	40S	0.73	17.0	0.13	13.0	0.05	8.0	0.09	4.0
	50S	0.53	3.0	0.24	2.0	0.09	4.0	0.14	9.0
@ $S_{a(wa)}$ = 0.08 g	20S	0.14	3.0	0.13	9.0	0.19	3.0	0.54	9.0
	40S	0.23	12.0	0.15	7.0	0.14	8.0	0.48	3.0
	50S	0.012	1.0	0.22	0.0	0.13	9.0	0.53	8.0
@ $S_{a(wa)}$ = 0.12 g	20S	0.03	1.0	0.05	4.0	0.11	1.0	0.81	4.0
	40S	0.06	4.0	0.07	2.0	0.11	1.0	0.76	1.0
	50S	0.03	1.0	0.11	2.0	0.09	3.0	0.77	0.0

$^{+}T_{DP}$: Difference in the Damage Probability = ABS [(6R damage probability of concerned building – 20R damage probability of 30S reference Building], (%)

Table 6.16. Maximum difference summary of the 5R-based damage state probabilities of 20S, 30S, 40S, and 50S buildings with reference to the 20R-based damage state probabilities of the reference building under severe distant and moderate near-field earthquake scenarios

Seismic scenario	Building	Damage state	Max. T_{DP}, (%)	@ $S_{a(wa)}$, (g)
Severe distant earthquakes	20S	Unimpaired Occupancy	12	0.105
		Impaired Occupancy	14	0.40
		Structural damage	12	0.60
		Structural collapse	19	0.60
	30S	Unimpaired Occupancy	14	0.158
		Impaired Occupancy	13	0.158
		Structural damage	10	0.60; 0.80
		Structural collapse	17	0.60
	40S	Unimpaired Occupancy	10	0.105
		Impaired Occupancy	15	0.158
		Structural damage	11	0.40
		Structural collapse	9.0	0.80
	50S	Unimpaired Occupancy	32	0.105
		Impaired Occupancy	25	0.105
		Structural damage	12	0.158
		Structural collapse	9.0	0.80
Moderate near-field earthquakes	20S	Unimpaired Occupancy	6.0	0.04
		Impaired Occupancy	9.0	0.04; 0.08
		Structural damage	3.0	0.08
		Structural collapse	9	0.08
	30S	Unimpaired Occupancy	7.0	0.04
		Impaired Occupancy	7.0	0.04
		Structural damage	4.0	0.08
		Structural collapse	5.0	0.12
	40S	Unimpaired Occupancy	17	0.04
		Impaired Occupancy	13	0.04
		Structural damage	8.0	0.04; 0.08
		Structural collapse	4.0	0.04
	50S	Unimpaired Occupancy	3.0	0.04
		Impaired Occupancy	2.0	0.04; 0.12
		Structural damage	9.0	0.08
		Structural collapse	9.0	0.04

6.5 Summary and concluding remarks

CHAPTER 6 is divided into four main parts. Besides this fourth part (Section 6.4), the first part (Section 6.1) comprises the procedure for developing seismic scenario-based fragility relations for RC high-rise buildings with an application on the reference building. This represents the concluding step in the proposed framework for the seismic vulnerability assessment of RC high-rise buildings. The second part of the chapter (Section 6.2) deals with examining the developed fragility relations at selected earthquake intensity levels to assess their accuracy, study their characteristics, and compare them at different levels. This part of the chapter is concluded with correlating the developed fragility relations with four states of damage in the reference building, that is unimpaired occupancy, impaired occupancy, structural damage, and structural collapse.

In the third part of the chapter (Section 6.3), a simplified methodology is proposed to develop Cheaper Fragility Curves (CFCs), with lesser number of input ground motions compared to the number of records needed for developing the refined fragility curves. Utilising this methodology, the fragility curves of RC high-rise buildings under a specific seismic scenario can be developed with a substantial reduction in time and computational effort, especially when a big building inventory is under investigation. In the proposed methodology, a new Record Selection Criterion (RCS) is proposed with a recommendation for the selected records' acceptance tolerance (T_R). Additionally, a procedure to verify the developed CFCs against a recommended acceptance level (T_{FC}) is proposed. Finally, the developed CFCs are compared with the refined fragility curves from Section 6.1 to verify the proposed simplified methodology.

In Section 6.4, CFCs are developed for three out of the six additional buildings which were employed in the parametric study presented in Section 5.5. The three selected buildings are 20-storeys (20S), 40-storeys (40S), and 50-storeys (50S). The same number of records used in Section 6.3 are utilized to develop CFCs for the aforementioned buildings. The developed CFCs are analysed to confirm the suitability of the refined framework proposed in the current study for developing one set of seismic scenario-based fragility relations that suits an inventory of RC high-rise buildings with varying height.

The main conclusions drawn in this chapter are bullet-pointed below:

- For the reference building under severe distant earthquakes, the steepness of the fragility curves increases as the limit state shifts from CP to IO. This is attributed to the fact that the building is moving from the inelastic to the elastic zone as the limit state shifts towards IO. When the building responds elastically, the dispersions in the NISD values from different records at the threshold of the limit state significantly decreases. On the contrary, the fragility curves developed under the moderate near-field earthquake scenario have almost the same; steep slopes. This is attributed to the shear-controlled response nature of RC high-rise wall buildings under this seismic scenario, where all three limit states (IO, LS, and CP) may be reached while the structure is still in the elastic zone.

- The developed fragility relations in Section 6.1 emphasises the vulnerability of RC high-rise wall buildings in the study region to severe distant earthquakes. It also reveals the invulnerability of this class of buildings to moderate near-field earthquakes even at the MCE level. This may not necessarily be the case for other multiple seismic scenario-prone regions in the world considering the unique response of RC high-rise wall structures under short period records.

- It is concluded that when utilising the simplified methodology proposed in this chapter, fairly reliable seismic scenario-based fragility curves can be developed for RC high-rise buildings with a total number of input ground motions ranging between 5 and 6.

- Depending on the purpose of the study and the way the resultant fragility curves are employed, the acceptance values for the record selection tolerance (T_R) and the fragility curve tolerance (T_{FC}) can be adjusted. Another factor that influences the decided acceptance values for T_R and T_{FC} is the variability of the input ground motions used in the MRIDAs. This is clear in the resultant CFCs for the reference building under the severe distant seismic scenario, where

adopting a smaller value of T_R, T_{FC}, or both may render CFCs that have better matching with the refined set of fragility curves.

- The methodology to derive refined seismic scenario-based fragility curves (Section 6.1) and the simplified one to derive CFCs proposed in this section are combined in one flowchart in Figure 6.15.

- The parametric study results presented in Section 6.4 further supports the supremacy of the adopted NISD as DM, $S_{a(wa)}$ as IM, along with all other components and methodologies of the framework proposed in the current work in terms of the capability for developing only one set of seismic scenario-based PLS criteria and fragility relations which can suit RC high-rise buildings with a wide range of total building height.

- The latest recommendations of ASCE/SEI 41-17 (2017) for the TISD associated with LS performance limit state introduce a minimal change to the LS limit state fragility curves of the reference building under moderate near-field seismic scenario when compared to their counterpart results based on the recommendations of ASCE/SEI 41-06 (2007). The difference in the POE ($LS|S_{a(wa)}$) along the entire range of the 16%, 50%, and 84% curves is limited to 1%-4% only. These results further support the argument on the negligible effect the latest recommendations of ASCE/SEI 41-17 have on the framework, methodologies and outcome of the current work.

This page is intentionally left in blank

CHAPTER 7. Summary, conclusions, and recommendations for future work

7.1 Summary

The aim of this study was to establish a refined framework to assess the seismic vulnerability of RC high-rise wall buildings in multiple-scenario earthquake-prone regions. The framework's output comprises analytically-driven sets of seismic scenario-structure-based (SSSB) fragility relations that can be developed using either a refined or a simplified methodology.

The brief introduction provided in CHAPTER 1 was followed by the problem definition in CHAPTER 2. This Chapter included a list of some of the main terms that are used throughout this thesis along with their definition. Furthermore, an Input-Process-Output (IPO) model is presented as a general framework for assessing the seismic vulnerability of a building or building inventory, with a critical review of the relevant literature on the key parameters and variables shaping the problem.

CHAPTER 3 summarised a detailed study conducted to investigate different nonlinear modelling approaches, software, and key parameters contributing to the nonlinear analytical models. Three numerical models were created using two different software (ZEUS-NL and PERFORM-3D). The investigated nonlinear modelling techniques and their key parameters were verified against the results of Phase I of the uniaxial shaking table specimen tests (performed at the University of California, San Diego) on a seven-storey full-scale RC shear wall structure. The test structure was subjected to base excitations representing four earthquake records of increasing intensities. The results obtained from the numerical models, along with their comparison to the experimental data both on the global and local response, were employed in a Multi-Level Nonlinear Modelling Verification Scheme (MLNMVS). The conducted MLNMVS aims to verify different approaches and key parameters in the modelling of RC slender shear walls that are forming the lateral-force-resisting system in RC high-rise wall buildings. The chapter was concluded with recommendations for the nonlinear modelling approach, software and key parameters to be employed in the current work.

CHAPTER 4 presented a case study that was designed to be used in the current work. To demonstrate the refined framework for seismic vulnerability assessment of RC high-rise wall buildings under multiple earthquake scenarios, the city of Dubai (UAE) was chosen for the case study for two main reasons. The first is due to the unprecedented level of growth in property development in recent years, with high-rise buildings forming the biggest share of new construction, and consequently, representing high levels of financial investment and population density increase which significantly increase exposure. The second reason is the multi earthquake scenarios that the region is vulnerable to, where high-rise structures are expected to return different seismic response. The seismicity of the study region was presented through critical reviewing of the related seismic hazard studies and the selection of appropriate seismic characteristics for use with the proposed refined framework. The criteria for the selection of input ground motions were proposed and discussed. Forty real records were selected to represent the two seismic scenarios which the study region is vulnerable to (severe distant and moderate near-field earthquakes). Furthermore, a 30-storey, 97.3m in height, RC wall structure was selected as a reference building for the current work. The footprint, layout and structural system of the building are common in the study region for this range of height. The reference building was fully designed and proportioned for the purpose of this study taking into consideration modern code

provisions. Finally, PERFORM-3D analytical software was utilised to create the nonlinear model of the reference building. The selection of the software, modelling approach and key modelling parameters were based on the MLNMVS presented in CHAPTER 3.

In CHAPTER 5, a methodology was proposed to obtain reliable SSSB definitions of limit state criteria for RC high-rise wall buildings. The reference 30-storey building was utilised to illustrate the proposed methodology along with its nonlinear model and the seismic scenario-based sets of real records presented in CHAPTER 4. The Building local response at increasing earthquake intensities was mapped to better understand the response nature of this class of structures under different seismic scenarios. In this mapping, a total of seven local Damage Indices (DIs) were employed. Multi-Record Incremental Dynamic Analyses (MRIDAs) were conducted on the reference building using a total of 40 records (20 records for each of the two investigated seismic scenarios). New scalar intensity measure (spectral acceleration at weighted-average period) and global damage measure (net inter-storey drift) were proposed and used with the MRIDAs. Finally, a numerical parametric study was conducted to investigate the effect of building total height on the relation between local damage events and drifts. Maintaining the footprint and the geometry of the reference building, six more buildings with a total number of storeys of 20, 25, 35, 40, 45 and 50 were designed and nonlinearly modelled for the purpose of the parametric study. The chapter was concluded with proposing two sets of SSSB limit state criteria for shear wall high-rise buildings with a similar structural system to that adopted for the reference building. The proposed limit state criteria correspond to the three adopted performance levels: Immediate Occupancy (IO), Life Safety (LS), and Collapse Prevention (CP).

In CHAPTER 6, the current study was concluded with presenting the final layout of the proposed refined framework to assess the seismic vulnerability of RC high-rise wall buildings under multiple earthquake scenarios. A methodology to develop refined fragility relations was presented with an application on the reference building. The refined fragility relations were analysed at selected earthquake intensity levels to correlate them to the mapped response of the reference building. The characteristics of the refined fragility relations under the two investigated seismic scenarios were analysed, compared, and correlated to the four states of damage adopted in the current work, namely unimpaired occupancy, impaired occupancy, structural damage, and

structural collapse. Furthermore, a simplified methodology towards developing fragility relations with less computational effort was proposed. The developed fragility curves using this approach were termed Cheaper Fragility Curves (CFC). Utilising this methodology with the proposed approach for selecting limit states, CFCs for RC high-rise buildings related to a specific seismic scenario can be generated with a considerably lower number of input ground motions compared to those needed to derive the refined fragility curves. As a tool to arrive at the proposed simplified methodology, a new selection criterion for the input ground motions was proposed. The CFCs developed for the reference building were compared with the refined sets to verify the proposed simplified methodology and the recommended acceptance values for the tolerance factors. Finally, CFCs are developed for three out of the six additional buildings which were employed in the parametric study presented in Section 5.5. The three selected buildings are 20-storeys (20S), 40-storeys (40S), and 50-storeys (50S). The developed CFCs are analysed to confirm the suitability of the refined framework proposed in the current study for developing one set of seismic scenario-based fragility relations that suits an inventory of RC high-rise buildings with varying height.

7.2 Conclusions

The primary conclusions drawn from the current study are categorised into three main topics that form the core of the presented refined framework. These topics are (i) nonlinear modelling; (ii) MRIDAs, seismic response mapping, and the definition of seismic scenario-based limit state criteria; and (iii) development of refined and cheaper fragility relations. These conclusions are presented below.

7.2.1 Nonlinear modelling

1. With appropriate care in the modelling of the geometry, both investigated nonlinear modelling approaches (2- and 4-noded fibre-based elements) are sufficient to predict global deformation response (storey lateral displacement and interstorey drift) of RC wall buildings with relatively good accuracy.

2. The 4-noded fibre-based wall/shell element best accounted for the 3D effects of deformation compatibility between the lateral and the gravity load-resisting systems. In high-rise wall buildings, the 3D interaction between the gravity columns, floor slabs, and shear walls/cores significantly contributes to the overall lateral capacity.

3. When the 2-noded fibre-based element modelling approach is used, the study revealed the sensitivity of the results to the stiffnesses assigned to the rigid links and 3D joints required to connect the shear walls to the neighbouring elements.

4. When initial stiffness is employed in constructing the damping matrix for RC wall buildings with no or well-isolated non-structural elements, low modal damping ratio (in the range of 0.5%) assigned to the fundamental mode of vibration is suitable for assessing the seismic performance of such buildings. For the next few higher modes, this value should be increased. In addition, and to stabilize less important (higher frequency) modes, a small amount (in the range of 0.1%) of Rayleigh damping is recommended to be added to the model (Powell, 2007, CSI, 2011).

5. The observed difference between predicted and measured response of the test structure in CHAPTER 3 under the two consecutive input motions with comparable intensities (EQ2 and EQ3) highlights the importance of accurate representation of the unloading/reloading paths of the material models. This is particularly true when assessing the performance of buildings under earthquake motions that do not move the structure into a virgin territory (i.e. past previous deformations).

6. No noticeable change is observed in the numerical response of the test structure (CHAPTER 3) when shear deformation is accounted for in the nonlinear model. This is justified by the test results that demonstrated almost exclusively flexural cracking at the web wall base. However, shear deformation may still contribute to the lateral displacement of walls in tall buildings, even in walls categorised as slender and/or flexure-dominated. Hence, considering the shear deformation either implicitly (coupled model) or explicitly (uncoupled model) is recommended.

7.2.2 MRIDAs, seismic response mapping, and the definition of seismic scenario-based limit state criteria

1. For high-rise buildings, the introduction of an intensity measure that can take into account both the impact of higher modes and period elongation is essential. Accordingly, a new scalar intensity measure termed spectral acceleration at the weighted-average period ($S_{a(wa)}$) was proposed in the present study.

2. The study shows that structural system, arrangement and geometry of vertical structural elements, and axial force level in the lower storeys influence the seismic intensity and deformation levels that correspond to the local damage events. This leads to the conclusion that the response of RC high-rise wall buildings and consequently the definition of limit state criteria for designated performance levels are strongly influenced by both the structure and the seismic scenario.

3. Under both investigated seismic scenarios, almost all damage events that occurred in the walls/cores of the reference building (i.e. rebar yielding and buckling, concrete crushing, wall rotation, and shear strength exceedance) took place in the lower five storeys or one-sixth of the height. Notwithstanding, the event propagation and sequence substantially differ under the two scenarios. This highlights the different nature of the response of RC high-rise wall buildings under different earthquake scenarios.

4. The mapping of the reference building response shows that under both investigated seismic scenarios, coupling beam rotation has not reached the code limits throughout the entire range of intensity levels. This shows that, for diagonally-reinforced coupling beams, potential damage due to earthquakes is too minor to have any influence in the definition of the limit state criteria. It is noteworthy that in the case study building, the coupling beams only connected core walls. The rotation may be higher for coupling beams connecting shear walls.

5. Under the moderate near-field seismic scenario, the high frequencies and short durations of the input ground motions render higher modes dominate the high-rise buildings response. The response mapping results presented in CHAPTER 5 showed that, in RC high-rise wall buildings, higher modes shift the shear wall response from flexure-controlled under severe distant earthquake scenario to shear-controlled under the moderate near-field scenario.

6. The mapping of the building local and global response showed that when comparing between two events occurring at different seismic intensity levels, the event corresponding to the higher intensity level does not necessarily associate with the maximum overall lateral displacement (and consequently maximum

overall TISD). It is also shown that, at the onset of an event, the storey at which maximum overall lateral displacement (global response) is observed is generally not associated with the one where the event (local response) has taken place. This confirms that TISD is not an appropriate damage measure for high-rise buildings.

7. TISD can be responsible for non-structural damage in tall buildings and inconvenience to the occupants, hence is important at least when evaluating the performance of high-rise buildings at serviceability level. However, the current study confirmed the superiority of NISD over TISD as a global DM for the vulnerability assessment of high-rise buildings. NISD is better linked with the local response over the height of the building and well correlated to deformation-based local damage events for buildings with varying heights. Accordingly, when NISD is adopted as the global DM, one set of seismic-scenario-based limit state criteria need to be defined for high-rise buildings with varying height but with the similar structural system.

7.2.3 Development of refined and cheaper fragility relations

1. When RC high-rise wall buildings respond within the elastic range, the dispersion in the NISD values from different records at the threshold of the IO and, with less extent, LS limit states significantly decrease. Consequently, the steepness of the fragility curves increases as the limit state shifts from CP to IO under severe distant earthquakes. On the contrary, the shear-controlled response nature of RC high-rise wall buildings renders the fragility curves associated with the moderate near-field earthquake scenario have almost the same; steep slopes. This is because all three limit states (IO, LS, and CP) may be reached under this seismic scenario while the structure is still in the elastic zone.

2. The developed refined fragility relations emphasised the vulnerability of RC high-rise wall buildings in the study region to severe distant earthquakes. It also revealed the invulnerability of this class of buildings to moderate near-field earthquakes even at the MCE level. This may not necessarily be the case for other multiple-scenario earthquake-prone regions in the world considering the unique response of RC high-rise wall structures under short period records.

3. The ASCE/SEI 41-17 (2017) latest recommendations for the LS performance limit state-associated TISD introduce a minimal change to the LS limit state fragility curves of the reference building under moderate near-field seismic scenario compared to their corresponding results based on the recommendations of ASCE/SEI 41-06 (2007). The difference in the POE ($LS|S_{a(wa)}$) along the entire range of the 16%, 50%, and 84% curves is limited to 1%-4% only. These results emphasise the negligible effect the ASCE/SEI 41-17 latest recommendations have on the framework, methodologies and outcome of the current work.

4. It is concluded that when utilising the simplified methodology proposed in CHAPTER 6, fairly reliable seismic scenario-based fragility curves can be developed for RC high-rise buildings with a considerably lower number of input ground motions ranging between 5 to 6.

5. Depending on the study purpose and the way the resultant fragility curves are employed, the acceptance values for the proposed record selection tolerance factor (T_R) and the fragility curve tolerance factor (T_{FC}) can be adjusted. Another factor that influences the decided acceptance values for T_R and T_{FC} is the variability of the input ground motions used in the MRIDAs. This was shown in the resultant CFCs for the reference building under the severe distant seismic scenario, where adopting a smaller acceptance value of T_R, T_{FC}, or both may yield CFCs that have a better match with the refined set of fragility curves. In the present work, 10% is the recommended acceptance value for both T_R and T_{FC}.

6. The methodology to derive refined seismic scenario-based fragility curves and the simplified one to derive CFCs proposed in the current study were depicted in a combined flowchart in Figure 6.15.

7. The parametric study results presented in Section 6.4 further supports the supremacy of the adopted NISD as DM, $S_{a(wa)}$ as IM, along with all other components and methodologies of the framework proposed in the current work in terms of the capability for developing only one set of seismic scenario-based PLS criteria and fragility relations which can suit RC high-rise buildings with a wide range of total building height. It is worth noting that the conclusions of the

conducted parametric study are, strictly speaking, applicable to the buildings' configuration and the seismic scenarios investigated. However, considering the level of detail put in the framework for developing both rigorous and CFCs, some generality to the applicability of the parametric study results for RC high-rise buildings with different configurations and seismicity may fairly be claimed.

7.3 Recommendations for future work

- The present study utilised a 30-storey RC wall building as a case study. Further research is needed to apply the proposed framework on RC high-rise buildings with different structural systems and total height range.

- In future research, parametric studies may be conducted to verify the efficiency of the new scalar intensity measure proposed in this study $S_{a(wa)}$. Future studies may investigate the impact of this intensity measure on reducing the dispersion in the incremental dynamic analysis curves and on the number of input ground motions required in the proposed simplified methodology to derive fragility relations.

- In this study, only the horizontal components of the input ground motions were used. Further research is required to evaluate the effects of the vertical component of input ground motions on the fragility relations of RC high-rise wall buildings, particularly under near-field earthquake scenario.

- Future research is needed to investigate the effects of plan and vertical irregularities in buildings on the consistency of the proposed global damage measure (NISD) and consequently the definition of the limit state criteria.

- Encouraged by the observations and conclusions drawn from the mapping of the reference building response using NISD, future research is required to back the proposition of adopting this DM in seismic code provisions related to the design and analysis of high-rise buildings.

- The Soil-Structure Interaction (SSI) was not included in the present study. Future research may investigate the impact of this component for different case studies on the proposed framework.

- In the present work, the acceleration uniform hazard spectrum is adopted as a reference when selecting, scaling and anchoring real ground motions. In future studies, the possibilities of using the displacement and velocity uniform hazard spectra as references to minimise the dispersion of the MRIDAs results may be investigated.

- Future research is required to study the effects of considering the local authorities' supplementary regulations and the local construction practices on the seismic response of existing RC high-rise wall buildings.

- Future research is needed to study the possibilities of extending the developed framework to assess the earthquake risk of high-rise buildings in the case study region and embedding the framework in the seismic risk assessment platforms.

REFERENCES

A

ABDALLA, J. A. & AL-HOMOUD, A. S., 2004. "Seismic hazard assessment of United Arab Emirates and its surroundings". *Journal of Earthquake Engineering,* 8 (6)**,** pp. 817-837.

ABDELNABY, A. E., 2018. "Fragility curves for RC frames subjected to Tohoku mainshock-aftershocks sequences". *Journal of Earthquake Engineering,* 22 (5)**,** pp. 902-920.

ABRAHAMSON, N. A. & SILVA, W. J., 1997. "Empirical response spectral attenuation relations for shallow crustal earthquakes". *Seismological Research Letters,* 68 (1)**,** pp. 94-127.

ABRAHAMSON, N. A. & SILVA, W. J., 2008. "Summary of the Abrahamson & Silva NGA ground-motion relations". *Earthquake Spectra,* 24 (1)**,** pp. 67-97.

ACI, 2014. "Building code requirements for structural concrete (ACI 318-14) and Commentary". Farmington Hills, MI: American Concrete Institute Committee 318.

AKIYAMA, M., SUZUKI, M. & FRANGOPOL, D. M., 2010. "Stress-averaged strain model for confined high-strength concrete". *ACI Structural Journal,* 107 (2)**,** pp. 179-188.

AKKAR, S. & BOMMER, J. J., 2007. "Prediction of elastic displacement response spectra in Europe and the Middle East". *Earthquake engineering & structural dynamics,* 36 (10)**,** pp. 1275-1301.

AL-HADDAD, M., SIDDIQI, G. H., AL-ZAID, R., ARAFAH, A., NECIOGLU, A. & TURKELLI, N., 1994. "A basis for evaluation of seismic hazard and design criteria for Saudi Arabia". *Earthquake Spectra,* 10 (2)**,** pp. 231-258.

ALDAMA-BUSTOS, G., BOMMER, J. J., FENTON, C. H. & STAFFORD, P. J., 2009. "Probabilistic seismic hazard analysis for rock sites in the cities of Abu Dhabi, Dubai and Ra's Al Khaymah, United Arab Emirates". *Georisk,* 3 (1)**,** pp. 1-29.

ALI, M. M. & MOON, K. S., 2007. "Structural developments in tall buildings: current trends and future prospects". *Architectural Science Review,* 50 (3)**,** pp. 205-223.

ALLEN, F. & DARVALL, P., 1977. "Lateral load equivalent frame". ACI Journal Proceedings.

AMBRASEYS, N. N., 1995. "The prediction of earthquake peak ground acceleration in Europe". *Earthquake Engineering & Structural Dynamics,* 24 (4)**,** pp. 467-490.

AMBRASEYS, N. N., DOUGLAS, J., SARMA, S. K. & SMIT, P. M., 2005. "Equations for the estimation of strong ground motions from shallow crustal earthquakes using data from Europe and the Middle East: Horizontal peak ground acceleration and spectral acceleration". *Bulletin of Earthquake Engineering,* 3 (1)**,** pp. 1-53.

AMBRASEYS, N. N., DOUGLAS, J., SIGBJÖRNSSON, R., BERGE-THIERRY, C., SUHADOLC, P., COSTA, G. & SMIT, M. P., 2004. "Dissemination of European strong-motion data, Volume 2, using strong-motion dataspace navigator, CD ROM collection". Engineering and Physical Sciences Research Council, UK.

AMBRASEYS, N. N. & MELVILLE, C. P., 2005. "A history of Persian earthquakes", Cambridge, UK.

AMBRASEYS, N. N., SIMPSON, K. U. & BOMMER, J. J., 1996. "Prediction of horizontal response spectra in Europe". *Earthquake Engineering & Structural Dynamics,* 25 (4)**,** pp. 371-400.

AMBRASEYS, N. N. & SRBULOV, M., 1994. "Attenuation of earthquake-induced ground displacements". *Earthquake Engineering & Structural Dynamics,* 23 (5)**,** pp. 467-487.

ANDERSON, J. C., MIRANDA, E. & BERTERO, V. V., 1991. "Evaluation of the seismic performance of a thirty-story RC building", University of California, Berkeley, CA, Earthquake Engineering Research Center.

ARMERO, F., 2006. "Energy-dissipative momentum-conserving time-stepping algorithms for finite strain multiplicative plasticity". *Computer Methods in Applied Mechanics and Engineering,* 195 (37)**,** pp. 4862-4889.

ASCE/SEI-7, 2005. "Minimum design loads for buildings and other structures, ASCE Standard ASCE/SEI 7-05 ". Reston, VA: American Society of Civil Engineers.

ASCE/SEI-7, 2010. "Minimum design loads for buildings and other structures, ASCE Standard ASCE/SEI 7-10". Reston, VA: American Society of Civil Engineers.

ASCE/SEI-7, 2017. "Minimum design loads for buildings and other structures, ASCE Standard ASCE/SEI 7-16", Reston, VA, American Society of Civil Engineers.

ASCE/SEI-41, 2007. "Seismic rehabilitation of existing buildings, ASCE Standard ASCE/SEI 41-06", Reston, VA, American Society of Civil Engineers.

ASCE/SEI-41, 2017. "Seismic evaluation and retrofit of existing buildings, ASCE Standard ASCE/SEI 41-17". Reston, VA: American Society of Civil Engineers.

ASHRI, A. & MWAFY, A., 2014. "3D vulnerability functions for contemporary buildings with varying structural systems and heights". Second European Conference on Earthquake Engineering and Seismology (2ECEES). Istanbul, Turkey.

ATKINSON, G. M. & BOORE, D. M., 1997. "Some comparisons between recent ground-motion relations". *Seismological Research Letters,* 68 (1)**,** pp. 24-40.

ATKINSON, G. M. & BOORE, D. M., 2003. "Empirical ground-motion relations for subduction-zone earthquakes and their application to Cascadia and other regions". *Bulletin of the Seismological Society of America,* 93 (4)**,** pp. 1703-1729.

ATKINSON, G. M. & BOORE, D. M., 2006. "Earthquake ground-motion prediction equations for eastern North America". *Bulletin of the Seismological Society of America,* 96 (6)**,** pp. 2181-2205.

ATKINSON, G. M. & BOORE, D. M., 2007. "Boore-Atkinson NGA ground motion relations for the geometric mean horizontal component of peak and spectral ground motion parameters". Pacific Earthquake Engineering Research Center (PEER).

ATTARD, M. M. & SETUNGE, S., 1996. "Stress-strain relationship of confined and unconfined concrete". *Materials Journal,* 93 (5)**,** pp. 432-442.

B

BABER, T. T. & WEN, Y. K., 1981. "Random vibration hysteretic, degrading systems". *Journal of the Engineering Mechanics Division,* 107 (6)**,** pp. 1069-1087.

BAE, S., MIESES, A. M. & BAYRAK, O., 2005. "Inelastic buckling of reinforcing bars". *Journal of Structural Engineering,* 131 (2)**,** pp. 314-321.

BAGHERI, M., JAMKHANEH, M. E. & SAMALI, B., 2018. "Effect of Seismic Soil–Pile–Structure Interaction on Mid-and High-Rise Steel Buildings Resting on a Group of Pile Foundations". *International Journal of Geomechanics,* 18 (9)**,** pp. 04018103: 1-27.

BAKER, J. W., 2013. An introduction to probabilistic seismic hazard analysis. White Paper Version 2.0, 79 pp.

BAKER, J. W. & CORNELL, C. A.: Choice of a vector of ground motion intensity measures for seismic demand hazard analysis". *13th World Conference on Earthquake Engineering*, 2004.

BAKER, J. W. & CORNELL, C. A., 2005. "A vector-valued ground motion intensity measure consisting of spectral acceleration and epsilon". *Earthquake Engineering & Structural Dynamics,* 34 (10)**,** pp. 1193-1217.

BAKER, J. W. & LEE, C., 2018. "An improved algorithm for selecting ground motions to match a conditional spectrum". *Journal of Earthquake Engineering,* 22 (4)**,** pp. 708-723.

BAKER, W. F., 2017. "Building the world's tallest skyscraper, the Burj Khalifa". In: ATLAS, N. (ed.).

BALKAYA, C., YUKSEL, S. B. & DERINOZ, O., 2012. "Soil-structure interaction effects on the fundamental periods of the shear-wall dominant buildings". *The Structural Design of Tall and Special Buildings,* 21 (6)**,** pp. 416-430.

BANI-HANI, K. A. & MALKAWI, A. I., 2017. "A Multi-step approach to generate response-spectrum-compatible artificial earthquake accelerograms". *Soil Dynamics and Earthquake Engineering,* 97 117-132.

BARANI, S. & SPALLAROSSA, D., 2017. "Soil amplification in probabilistic ground motion hazard analysis". *Bulletin of Earthquake Engineering,* 15 (6)**,** pp. 2525-2545.

BARBOSA, A. R., RIBEIRO, F. L. A. & NEVES, L. A. C., 2017. "Influence of earthquake ground-motion duration on damage estimation: application to steel moment resisting frames". *Earthquake Engineering & Structural Dynamics,* 46 (1)**,** pp. 27-49.

BATHE, K. J. & CIMENTO, A. P., 1980. "Some practical procedures for the solution of nonlinear finite element equations". *Computer Methods in Applied Mechanics and Engineering,* 22 (1)**,** pp. 59-85.

BAZZURRO, P. & CORNELL, C. A., 1994a. "Seismic hazard analysis of nonlinear structures. I: Methodology". *Journal of Structural Engineering,* 120 (11)**,** pp. 3320-3344.

BAZZURRO, P. & CORNELL, C. A., 1994b. "Seismic hazard analysis of nonlinear structures. II: Applications". *Journal of Structural Engineering,* 120 (11)**,** pp. 3345-3365.

BAZZURRO, P. & CORNELL, C. A., 1999. "Disaggregation of seismic hazard". *Bulletin of the Seismological Society of America,* 89 (2)**,** pp. 501-520.

BAZZURRO, P. & CORNELL, C. A., 2002. "Vector-valued probabilistic seismic hazard analysis (VPSHA)". 7th US National Conference on Earthquake Engineering. Boston, MA.

BERBERIAN, M., 1995. "Master “blind” thrust faults hidden under the Zagros folds: Active basement tectonics and surface morphotectonics". *Tectonophysics,* 241 (3)**,** pp. 193-224.

BERNAL, D., 1994. "Viscous damping in inelastic structural response". *Journal of structural engineering,* 120 (4)**,** pp. 1240-1254.

BERTERO, V. V., 1977. "Strength and deformation capacities of buildings under extreme environments". *Structural Engineering and Structural Mechanics,* 53 (1)**,** pp. 29-79.

BEYER, K., DAZIO, A. & PRIESTLEY, M. J. N., 2008. "Quasi-static cyclic tests of two U-shaped reinforced concrete walls". *Journal of Earthquake Engineering,* 12 (7)**,** pp. 1023-1053.

BIANCHINI, M., 2008. "Improved ground motion intensity measures for reliability-based demand analysis of structures". Doctoral dissertation, University of Bologna.

BIANCHINI, M., DIOTALLEVI, P. & BAKER, J.: Prediction of inelastic structural response using an average of spectral accelerations". *Proc. of the 10th International Conference on Structural Safety and Reliability (ICOSSAR09), Osaka, Japan*, 2009. 13-17.

BIRELY, A., LEHMAN, D., LOWES, L., KUCHMA, D., HART, C. & MARLEY, K., 2008. "Investigation of the seismic behavior and analysis of reinforced concrete structural walls". 14th World Conference on Earthquake Engineering (WCEE14). Beijing, China.

BIRELY, A., LEHMAN, D., LOWES, L., KUCHMA, D., HART, C. & MARLEY, K., 2010. "Investigation of the Seismic Response of Planer Concrete Walls". 9th U.S. National Conference and 10th Canadian Conference on Earthquake Engineering. Ontario, Canada.

BJERKELI, L., TOMASZEWICZ, A. & JENSEN, J. J., 1990. "Deformation properties and ductility of high-strength concrete". 2nd International Conference on Utilization of High Strength Concrete. Berkeley, CA.

BOJÓRQUEZ, E. & IERVOLINO, I., 2011. "Spectral shape proxies and nonlinear structural response". *Soil Dynamics and Earthquake Engineering,* 31 (7)**,** pp. 996-1008.

BOMMER, J. J. & ACEVEDO, A. B., 2004. "The use of real earthquake accelerograms as input to dynamic analysis". *Journal of Earthquake Engineering,* 8 (1)**,** pp. 43-91.

BOMMER, J. J. & SCOTT, S. G., 2000. The feasibility of using real accelerograms for seismic design. Implications of recent earthquakes on seismic risk.

BOMMER, J. J., SPENCE, R., ERDIK, M., TABUCHI, S., AYDINOGLU, N., BOOTH, E., DEL RE, D. & PETERKEN, O., 2002. "Development of an earthquake loss model for Turkish catastrophe insurance". *Journal of Seismology,* 6 (3)**,** pp. 431-446.

BOORE, D. M., 2003. "Simulation of ground motion using the stochastic method". *Pure and Applied Geophysics,* 160 (3-4)**,** pp. 635-676.

BOORE, D. M. & ATKINSON, G. M., 2008. "Ground-motion prediction equations for the average horizontal component of PGA, PGV, and 5%-damped PSA at spectral periods between 0.01 s and 10.0 s". *Earthquake Spectra,* 24 (1)**,** pp. 99-138.

BOORE, D. M., JOYNER, W. B. & FUMAL, T. E., 1997. "Equations for estimating horizontal response spectra and peak acceleration from western North American earthquakes: A summary of recent work". *Seismological Research Letters,* 68 (1)**,** pp. 128-153.

BOUC, R., 1967. "Forced vibration of mechanical systems with hysteresis". 4th Conference on Nonlinear Oscillations. Prague.

BROWN, G. G. 1972. *Tectonic Map of the Arabian Peninsula. Saudi Arabian Dir. Gen. Miner. Res. Geol. Map AP-2, at, 1(4,000,000).*

BRUEGGEN, B. L., 2009. "Performance of T-shaped reinforced concrete structural walls under multi-directional loading". Doctoral dissertation, Department of Civil Engineering, University of Minnesota.

BRUEGGEN, B. L. & FRENCH, C. W., 2010. "Simplified modeling of non-rectangular RC structural walls". 9th U.S. National Conference and 10th Canadian Conference on Earthquake Engineering, including Papers from the 4th International Tsunami Symposium. Ontario, Canada.

C

CAI, J., BU, G., YANG, C., CHEN, Q. & ZUO, Z., 2014. "Calculation methods for inter-story drifts of building structures". *Advances in Structural Engineering,* 17 (5)**,** pp. 735-745.

CAMPBELL, K. W., 1985. "Strong motion attenuation relations: A ten-year perspective". *Earthquake Spectra,* 1 (4)**,** pp. 759-804.

CAMPBELL, K. W., 2003. "Prediction of strong ground motion using the hybrid empirical method and its use in the development of ground-motion (attenuation) relations in eastern North America". *Bulletin of the Seismological Society of America,* 93 (3)**,** pp. 1012-1033.

CAMPBELL, K. W. & BOZORGNIA, Y., 2003. "Updated near-source ground-motion (attenuation) relations for the horizontal and vertical components of peak ground acceleration and acceleration response spectra". *Bulletin of the Seismological Society of America,* 93 (1)**,** pp. 314-331.

CAMPBELL, K. W. & BOZORGNIA, Y., 2007. "Campbell-Bozorgnia NGA ground motion relations for the geometric mean horizontal component of peak and spectral ground motion parameters". Pacific Earthquake Engineering Research Center Report (PEER).

CAMPBELL, K. W. & BOZORGNIA, Y., 2008. "NGA ground motion model for the geometric mean horizontal component of PGA, PGV, PGD and 5% damped linear elastic response spectra for periods ranging from 0.01 to 10 s". *Earthquake Spectra,* 24 (1)**,** pp. 139-171.

CANDAPPA, D. C., SANJAYAN, J. G. & SETUNGE, S., 2001. "Complete triaxial stress-strain curves of high-strength concrete". *Journal of Materials in Civil Engineering,* 13 (3)**,** pp. 209-215.

CARBALLO, J. E. & CORNEL, C. A., 2000. "Probabilistic seismic demand analysis: spectrum matching and design". Reliability of Marine Structures Program. Stanford, CA: Department of Civil and Environmental Engineering, Stanford University.

CARLTON, B. & TOKIMATSU, K., 2016. "Comparison of equivalent linear and nonlinear site response analysis results and model to estimate maximum shear strain". *Earthquake Spectra,* 32 (3)**,** pp. 1867-1887.

CARR, A. J., 1997. "Damping models for inelastic structures". Asia-Pacific Vibration Conference. Kyongiu, South Korea.

CARR, A. J., 2005. "Damping models for time-history structural analyses". Asia-Pacific Vibration Conference. Langkawi, Malaysia.

CARR, A. J., 2007. "RUAUMOKO Manual (Volume 1: Theory)". University of Canterbury, Chirstchurch, New Zealand.

CELEBI, M., 1996. "Comparison of damping in buildings under low-amplitude and strong motions". *Journal of Wind Engineering and Industrial Aerodynamics,* 59 (2-3)**,** pp. 309-323.

CELEBI, M., DIETEL, C., PRINCE, J., ONATE, M. & CHAVEZ, G., 1987. "Site amplification in Mexico City (determined from 19 September 1985 strong-motion records and from recordings of weak motions)". *In Developments in Geotechnical Engineering* 44 141-151.

CELIK, O. C. & ELLINGWOOD, B. R., 2010. "Seismic fragilities for non-ductile reinforced concrete frames–Role of aleatoric and epistemic uncertainties". *Structural Safety,* 32 (1)**,** pp. 1-12.

CHANDRAMOHAN, R., BAKER, J. W. & DEIERLEIN, G. G., 2016a. "Impact of hazard-consistent ground motion duration in structural collapse risk assessment". *Earthquake Engineering & Structural Dynamics,* 45 (8)**,** pp. 1357-1379.

CHANDRAMOHAN, R., BAKER, J. W. & DEIERLEIN, G. G., 2016b. "Quantifying the influence of ground motion duration on structural collapse capacity using spectrally equivalent records". *Earthquake Spectra,* 32 (2)**,** pp. 927-950.

CHANG, G. A. & MANDER, J. B., 1994. "Seismic energy based fatigue damage analysis of bridge columns: Part 1-Evaluation of seismic capacity". NCEER Technical (Report No. NCEER-94-0006): State University of New York, Buffalo, NY.

CHARNEY, F. A., 2008. "Unintended consequences of modeling damping in structures". *Journal of Structural Engineering,* 134 (4)**,** pp. 581-592.

CHOPRA, A. K., 2016. "Dynamics of structures: Theory and applications to earthquake engineering", Prentice-hall International Series I Civil Engineering and Engineering Mechanics.

CHOPRA, A. K. & MCKENNA, F., 2016a. "Modeling viscous damping in nonlinear response history analysis of buildings for earthquake excitation". *Earthquake Engineering & Structural Dynamics,* 45 (2)**,** pp. 193-211.

CHOPRA, A. K. & MCKENNA, F., 2016b. "Response to John Hall's Discussion (EQE-16-0008) to Chopra and McKenna's paper,'Modeling viscous damping in nonlinear response history analysis of buildings for earthquake excitation'". *Earthquake Engineering & Structural Dynamics,* 45 (13)**,** pp. 2235-2238.

CHRISP, D., 1980. "Damping models for inelastic structures". Ph.D., University of Canterbury, Christchurch, New Zealand.

COBURN, A. W. & SPENCE, R. J., 2003. "Earthquake protection", John Wiley & Sons.

COBURN, A. W., SPENCE, R. J. & POMONIS, A., 1992. "Factors determining human casualty levels in earthquakes: Mortality prediction in building collapse". First International Forum on Earthquake related Casualties. Madrid, Spain.

COMERIO, M., ELWOOD, K., BERKOWITZ, R., BRUNEAU, M., DISMUKE, J., GAVIN, H., GOULD, K. J. & T., K., 2011. "The M 6.3 Christchurch, New Zealand, Earthquake of February 22, 2011. EERI special earthquake report". Oakland, New Zealand: Earthquake Engineering Research Institute (EERI).

CONTE, J. P., PANDIT, H., STEWART, J. P. & WALLACE, J. W., 2003. "Ground motion intensity measures for performance-based earthquake engineering". In Applications of Statistics and Probability in Civil Engineering: 9th International Conference. San Francisco, CA.

CORDOVA, P. P., DEIERLEIN, G. G., MEHANNY, S. S. & CORNELL, C. A., 2000. "Development of a two-parameter seismic intensity measure and probabilistic assessment procedure". The Second US-Japan Workshop on Performance-Based Earthquake Engineering Methodology for Reinforced Concrete Building Structures. Sapporo, Hokkaido, Japan.

CORNELL, C. A., 1968. "Engineering seismic risk analysis". *Bulletin of the Seismological Society of America*, 58 (5)**,** pp. 1583-1606.

COSENZA, E. & PROTA, A., 2006. "Experimental behaviour and numerical modelling of smooth steel bars under compression". *Journal of Earthquake Engineering*, 10 (3)**,** pp. 313-329.

COTTON, F., SCHERBAUM, F., BOMMER, J. J. & BUNGUM, H., 2006. "Criteria for selecting and adjusting ground-motion models for specific target regions: Application to Central Europe and rock sites". *Journal of Seismology*, 10 (2)**,** pp. 137-156.

CRUZ, C. & MIRANDA, E., 2017. "Evaluation of the Rayleigh damping model for buildings". *Engineering Structures*, 138 324-336.

CSI, 2011. "PERFORM-3D V5: Nonlinear analysis and performance assessment for 3D structures: User Manual", Berkeley, CA, Computer and Structures, Inc. (CSI).

CSI, 2014. "SAFE: Slab analysis by finite element method", Berkeley, CA, Computer and Structures, Inc. (CSI).

CSI, 2015. "ETABS: Extended 3D Analysis of Building Systems", Berkeley, CA, Computer and Structures, Inc. (CSI).

CTBUH, 2008. "Recommendations for the Seismic Design of High-rise Buildings". Chicago, Illinois.: Consensus Document. Report for the Working Group on the Seismic Design of Tall Buildings, for the Council on Tall Buildings and Urban Habitat (CTBUH).

CTBUH, 2019. "The Council on Tall Buildings and Urban Habitat " [Online]. Available: http://www.ctbuh.org [Accessed April 2014].

CUSSON, D. & PAULTRE, P., 1993. "Confinement model for high-strength concrete tied columns". Report No. SMS-9302. Department of Civil Engineering, University of Sherbrooke, Quebec, Canada.

D

D'AYALA, D., MESLEM, A., VAMVATSIKOS, D., PORTER, K., ROSSETTO, T., CROWLEY, H. & SILVA, V., 2014. "Guidelines for analytical vulnerability assessment of low/mid-rise Buildings-Methodology". Report produced in the context of the Vulnerability Global Component Project. GEM Foundation.

DAHLE, A., BUNGUM, H. & KVAMME, L. B., 1990. "Attenuation models inferred from intraplate earthquake recordings". *Earthquake Engineering & Structural Dynamics*, 19 (8)**,** pp. 1125-1141.

DARWIN, D. & PECKNOLD, D. A., 1977. "Nonlinear biaxial stress-strain law for concrete". *Journal of Engineering Mechanics Devision*, 103 (2)**,** pp. 229-241.

DAY, R. W., 2002. "Geotechnical earthquake engineering handbook", New York, NY, McGraw-Hill Professional.

DE MATTEIS, G., LANDOLFO, R., DUBINA, D. & STRATAN, A., 2000. Influence of the structural typology on the seismic performance of steel framed buildings. Moment resistant connections of steel frames in seismic areas: Design and reliability. CRC Press.

DINIZ, S. M. & FRANGOPOL, D. M., 1997. "Strength and ductility simulation of high-strength concrete columns". *Journal of Structural Engineering,* 123 (10)**,** pp. 1365-1374.

DMA, 2013. "Abu Dhabi International Building Code". Department of Municipal Affairs, Abu Dhabi, UAE.

DODD, L. L. & RESTREPO-POSADA, J. I., 1995. "Model for predicting cyclic behavior of reinforcing steel". *Journal of Structural Engineering,* 121 (3)**,** pp. 433-445.

DUBINA, D., CIUTINA, A., STRATAN, A. & DINU, F., 2000. Ductility demand for semi-rigid joint frames. Moment resistant connections of steel frames in seismic areas. CRC Press.

DUFFEY, T. A., FARRAR, C. R. & GOLDMAN, A., 1994. "Low-rise shear wall ultimate drift limits". *Earthquake Spectra,* 10 (4)**,** pp. 655-674.

DYMIOTIS, C., KAPPOS, A. J. & CHRYSSANTHOPOULOS, M. K., 1999. "Seismic reliability of RC frames with uncertain drift and member capacity". *Journal of Structural Engineering,* 125 (9)**,** pp. 1038-1047.

E

EERI, 2011. "Christchurch Clearinghouse" [Online]. Available: http://www.eqclearinghouse.org/2011-02-22/christchurch/ [Accessed May 2015].

EGUCHI, R. T., GOLTZ, J. D., SELIGSON, H. A., FLORES, P. J., BLAIS, N. C., HEATON, T. H. & BORTUGNO, E., 1997. "Real-time loss estimation as an emergency response decision support system: the early post-earthquake damage assessment tool (EPEDAT)". *Earthquake Spectra,* 13 (4)**,** pp. 815-833.

ELLINGWOOD, B. R., CELIK, O. C. & KINALI, K., 2007. "Fragility assessment of building structural systems in Mid-America". *Earthquake Engineering & Structural Dynamics,* 36 (13)**,** pp. 1935-1952.

ELNASHAI, A. S., 2006. "Assessment of seismic vulnerability of structures". *Journal of Constructional Steel Research,* 62 (11)**,** pp. 1134-1147.

ELNASHAI, A. S. & ELGHAZOULI, A. Y., 1993. "Performance of composite steel/concrete members under earthquake loading. Part I: Analytical model". *Earthquake Engineering & Structural Dynamics,* 22 (4)**,** pp. 315-345.

ELNASHAI, A. S. & IZZUDDIN, B. A., 1993a. "Modelling of material nonlinearities in steel structures subjected to transient dynamic loading". *Earthquake Engineering & Structural Dynamics,* 22 (6)**,** pp. 509-532.

ELNASHAI, A. S. & IZZUDDIN, B. A., 1993b. "Sources of uncertainty and future research requirements in seismic analysis of structures". *Nuclear Energy,* 32 (4)**,** pp. 213-220.

ELNASHAI, A. S., PAPANIKOLAOU, V. K. & LEE, D., 2012. "Zeus-NL: A system for inelastic analysis of structures-User Manual ", Mid-America Earthquake Center, University of Illinois at Urbana-Champaign, Urbana, IL.

ELWI, A. A. & MURRAY, D. W., 1979. "A 3D hypoelastic concrete constitutive relationship". *Journal of the Engineering Mechanics Division,* 105 (4)**,** pp. 623-641.

ELWOOD, K. J., MATAMOROS, A. B., WALLACE, J. W., LEHMAN, D. E., HEINTZ, J. A., MITCHELL, A. D., MOORE, M. A., VALLEY, M. T., LOWES, L. N. & COMARTIN, C. D., 2007. "Update to ASCE/SEI 41 concrete provisions". *Earthquake Spectra,* 23 (3)**,** pp. 493-523.

ENGDAHL, E. R., JACKSON, J. A., MYERS, S. C., BERGMAN, E. A. & PRIESTLEY, K., 2006. "Relocation and assessment of seismicity in the Iran region". *Geophysical Journal International,* 167 (2)**,** pp. 761-778.

ERDIK, M. & AYDINOGLU, N., 2002. "Earthquake performance and vulnerability of buildings in Turkey". Disaster Management Facility. Washington, DC: The World Bank Group

ERDIK, M., AYDINOGLU, N., FAHJAN, Y., SESETYAN, K., DEMIRCIOGLU, M., SIYAHI, B., DURUKAL, E., OZBEY, C., BIRO, Y., AKMAN, H. & YUZUGULLU, O., 2003. "Earthquake risk assessment for Istanbul metropolitan area". *Earthquake Engineering and Engineering Vibration,* 2 (1)**,** pp. 1-23.

ERDIK, M. & FAHJAN, Y., 2006. "Damage scenarios and damage evaluation, assessing and managing earthquake risk heo-scientific and engineering knowledge for earthquake risk mitigation: Developments, tools, techniques".

ERN-CAPRA, 2011. "Metodología de modelación probabilista de riesgos naturales ERN-CAPRA-T1". Consorcio Evaluación de Riesgos Naturales-América.

EUROCODE, 1998. "EN1998-Eurocode 8: Design of structures for earthquake resistance". Part 1: General rules, seismic actions and rules for buildings. Bruxelles, Belgium Comité Européen de Normalisation.

F

FAFITIS, A. & SHAH, S. P., 1985. "Lateral reinforcement for high-strength concrete columns". ACI Special Publication. Detroit, MI.

FAHJAN, Y. M., KARA, F. İ. & MERT, A., 2017. Selection and Scaling Time History Records for Performance-Based Design. Performance-Based Seismic Design of Concrete Structures and Infrastructures. IGI Global.

FAJFAR, P., VIDIC, T. & FISCHINGER, M., 1990. "A measure of earthquake motion capacity to damage medium-period structures". *Soil Dynamics and Earthquake Engineering,* 9 (5)**,** pp. 236-242.

FARAHBOD, A. M. & ARKHANI, M., 2002. "Seismicity Catalog of Iran (1900–2000) for moderate and strong earthquakes: An overview and revision". International Institute of Earthquake Engineering and Seismology.

FEMA, 2015. "NEHRP recommended seismic provisions for new buildings and other structures, FEMA P-1050, Part 1: Provisions and Part 2: Commentary". Federal Emergency Management Agency, Washington, D.C.

FEMA, 2019. "HAZUS-MH 4.2.2 User Release Notes. ". Federal Emergency Management Agency, Washington, D.C.

FENTON, C. H., ADAMS, J. & HALCHUK, S., 2006. "Seismic hazards assessment for radioactive waste disposal sites in regions of low seismic activity". *Geotechnical & Geological Engineering,* 24 (3)**,** pp. 579-592.

FILIPPOU, F. C., BERTERO, V. V. & POPOV, E. P., 1983. "Effects of bond deterioration on hysteretic behavior of reinforced concrete joints". Berkeley, CA: University of California.

FOLIENTE, G. C., 1995. "Hysteresis modeling of wood joints and structural systems". *Journal of Structural Engineering,* 121 (6)**,** pp. 1013-1022.

FOX, M. J., STAFFORD, P. J. & SULLIVAN, T. J., 2016. "Seismic hazard disaggregation in performance-based earthquake engineering: occurrence or exceedance?". *Earthquake Engineering & Structural Dynamics,* 45 (5)**,** pp. 835-842.

FRENCH, S. P. & MUTHUKUMAR, S., 2006. "Advanced technologies for earthquake risk inventories". *Journal of Earthquake Engineering,* 10 (2)**,** pp. 207-236.

G

GASCOT, R. L. & MONTEJO, L. A., 2016. "Spectrum-compatible earthquake records and their influence on the seismic response of reinforced concrete structures". *Earthquake Spectra,* 32 (1)**,** pp. 101-123.

GEM, 2019. "Global Earthquake Model Foundation" [Online]. Available: https://www.globalquakemodel.org/ [Accessed March 2018].

GHOBARAH, A., 2004. "On drift limits associated with different damage levels". Performance-Based Seismic Design Concepts and Implementation: Proceedings of the International Workshop. Bled, Slovenia.

GHODSI, T. & RUIZ, J. A. F., 2010. "Pacific earthquake engineering research/seismic safety commission tall building design case study 2". *The Structural Design of Tall and Special Buildings,* 19 (1-2)**,** pp. 197-256.

GHORBANIRENANI, I., TREMBLAY, R., LÉGER, P. & LECLERC, M., 2011. "Shake table testing of slender RC shear walls subjected to eastern North America seismic ground motions". *Journal of Structural Engineering,* 138 (12)**,** pp. 1515-1529.

GHOSH, S. & CHAKRABORTY, S., 2017. "Probabilistic seismic hazard analysis and synthetic ground motion generation for seismic risk assessment of structures in the Northeast India". *International Journal of Geotechnical Earthquake Engineering (IJGEE),* 8 (2)**,** pp. 39-59.

GIRAULT, P. D., 1986. "Analysis of foundation failures ". International Conference on the Mexico Earthquake-1985: Factors Involved and Lessons Learned. American Society of Civil Engineers (ASCE), New York, NY.

GIVENS, M. J., 2013. "Dynamic soil-structure interaction of instrumented buildings and test structures". Doctoral dissertation, University of California, Los Angeles, CA.

GOGUS, A., 2010. "Structural wall systems-nonlinear modeling and collapse assessment of shear walls and slab-column frames". Doctoral dissertation, University of California, Los Angeles, CA.

GREGOR, N. J., SILVA, W. J., WONG, I. G. & YOUNGS, R. R., 2002. "Ground-motion attenuation relationships for Cascadia subduction zone megathrust earthquakes based on a stochastic finite-fault model". *Bulletin of the Seismological Society of America,* 92 (5)**,** pp. 1923-1932.

GROSSMAN, J. S., 1997. "Verification of proposed design methodologies for effective width of slabs in slab-column frames". *Structural Journal,* 94 (2)**,** pp. 181-196.

GRÜNTHAL, G., BOSSE, C., SELLAMI, S., MAYER-ROSA, D. & GIARDINI, D., 1999. "Compilation of the GSHAP regional seismic hazard for Europe, Africa and the Middle East". *Annali di Geofisica,* 42 (6)**,** pp. 1215-1223.

GSHAP, 2004. "Global Seismic Hazard Assessment Program " [Online]. Available: http://www.seismo.ethz.ch/GSHAP/index.html [Accessed January 2015].

H

HA, S. J. & HAN, S. W., 2016. "An efficient method for selecting and scaling ground motions matching target response spectrum mean and variance". *Earthquake Engineering & Structural Dynamics,* 45 (8)**,** pp.

HAJIRASOULIHA, I. & PILAKOUTAS, K., 2012. "General seismic load distribution for optimum performance-based design of shear-buildings". *Journal of Earthquake Engineering,* 16 (4)**,** pp. 443-462.

HALL, J. F., 1998. "Seismic response of steel frame buildings to near-source ground motions". *Earthquake Engineering and Structural Dynamics,* 27 (12)**,** pp. 1445-1464.

HALL, J. F., 2006. "Problems encountered from the use (or misuse) of Rayleigh damping". *Earthquake Engineering & Structural Dynamics,* 35 (5)**,** pp. 525-545.

HALL, J. F., 2016. "Discussion of 'Modelling viscous damping in nonlinear response history analysis of buildings for earthquake excitation' by Anil K. Chopra and Frank McKenna". *Earthquake Engineering & Structural Dynamics,* 45 (13)**,** pp. 2229-2233.

HAN, S. W. & CHOPRA, A. K., 2006. "Approximate incremental dynamic analysis using the modal pushover analysis procedure". *Earthquake Engineering & Structural Dynamics,* 35 (15)**,** pp. 1853-1873.

HAN, Y. & CATHRO, D., 1997. "Seismic behavior of tall buildings supported on pile foundations". Seismic Analysis and Design for Soil-Pile-Structure Interactions Geotechnical Special Publication No. 70, American Society of Civil Engineers.

HANCOCK, J. & BOMMER, J. J., 2006. "A state-of-knowledge review of the influence of strong-motion duration on structural damage". *Earthquake Spectra,* 22 (3)**,** pp. 827-845.

HARDYNIEC, A. & CHARNEY, F. A., 2015. "An investigation into the effects of damping and nonlinear geometry models in earthquake engineering analysis". *Earthquake Engineering & Structural Dynamics,* 44 (15)**,** pp. 2695-2715.

HART, G. C. & VASUDEVAN, R., 1975. "Earthquake design of buildings: Damping". *Journal of the Structural Division,* 101 (1)**,** pp. 11-30.

HAYASHI, Y. & TAKAHASHI, I., 2004. "Soil-structure interaction effects on building response in recent earthquakes". Third UJNR Workshop on Soil-Structure Interaction. Vallombrosa Center, Menlo Park, CA.

HAYS, W. W., 1994. "Assessment and management of earthquake risk in urban areas". First Cairo Earthquake Engineering Symposium on Seismic Risk Assessment, Cairo 1994.

HELLESLAND, J. & SCORDELIS, A., 1981. "Analysis of RC bridge columns under imposed deformations". IABSE colloquium. Delft, the Netherlands.

HILBER, H. M., HUGHES, T. J. & TAYLOR, R. L., 1977. "Improved numerical dissipation for time integration algorithms in structural dynamics". *Earthquake Engineering & Structural Dynamics,* 5 (3)**,** pp. 283-292.

HSIEH, H. S., 2000. "Building Foundation Types in Taiwan". International Training Programs for Seismic Design of Building Structures. Hosted by National Center for Research on Earthquake Engineering. Sponsored by Department of International Program, National Science Council.

HUGHES, T. J., 2012. "The finite element method: Linear static and dynamic finite element analysis", Dover Publications, Kindle edition

HWANG, S. J. & MOEHLE, J. P., 2000. "Models for laterally loaded slab-column frames". *Structural Journal,* 97 (2)**,** pp. 345-352.

I

IBARRA, L. F. & KRAWINKLER, H., 2005. "Global collapse of frame structures under seismic excitations". Johm Blume Earthquake Engineering Center, Department of Civil Engineering, Stanford University, Stanford, CA.

IBC, 2003. "International building code (IBC-2003)". International Code Council (ICC). Washington, DC.

IBC, 2015. "Inernational Building Code (IBC-2015)". Washington, DC: International Code Council (ICC).

IBRAHIM, H. H. & MACGREGOR, J. G., 1996. "Flexural behavior of laterally reinforced high-strength concrete sections". *Structural Journal,* 93 (6)**,** pp. 674-684.

IERVOLINO, I. & CORNELL, C. A., 2005. "Record selection for nonlinear seismic analysis of structures". *Earthquake Spectra,* 21 (3)**,** pp. 685-713.

IERVOLINO, I., MANFREDI, G. & COSENZA, E., 2006. "Ground motion duration effects on nonlinear seismic response". *Earthquake Engineering & Structural Dynamics,* 35 (1)**,** pp. 21-38.

IIEES, 2019. "Earthquake data bank" [Online]. Tahran, Iran.: International Institute for Earthquake Engineering and Seismology (IIEES). Available: http://www.iiees.ac.ir [Accessed January 2012].

ILYAS, A., AZEEM, M. A. & MOHIUDDIN, H., 2018. "Seismic Response of Reinforced Concrete Buildings under Mainshock-Aftershock Earthquake Sequence". *International Journal of Civil Engineering and Technology,* 9 (4)**,** pp. 647-659.

IMRAN, I. & PANTAZOPOULOU, S. J., 1996. "Experimental study of plain concrete under triaxial stress". *ACI Materials Journal-American Concrete Institute,* 93 (6)**,** pp. 589-601.

INABA, T., DOHI, H., OKUTA, K., SATO, T. & AKAGI, H., 2000. "Nonlinear response of surface soil and NTT building due to soil–structure interaction during the 1995 Hyogo-ken Nanbu (Kobe) earthquake". *Soil Dynamics and Earthquake Engineering,* 20 (5-8)**,** pp. 289-300.

INEL, M., SENEL, S. M., TOPRAK, S. & MANAV, Y., 2008. "Seismic risk assessment of buildings in urban areas: A case study for Denizli, Turkey". *Natural Hazards,* 46 (3)**,** pp. 265-285.

IRFAN, M., EL-EMAM, M., KHAN, Z. & ABDALLA, J., 2012. "Local Site Effects on Seismic Ground Response of Dubai-Sharjah Metropolitan Area". GeoCongress 2012. Oakland, CA: Geo-Institute of ASCE.

IRIS, 2019. "IRIS Earthquake Browser (IEB)" [Online]. Washington, DC: Incorporated Research Institution for Seismology (IRIS). Available: http://www.iris.edu [Accessed January 2012].

ISC, 2019. "ISC Online Bulletin" [Online]. Thatcham, UK: International Seismology Centre. Available: http://www.isc.ac.uk [Accessed January 2012].

IZZUDDIN, B. A., 2016. "ADAPTIC User Manual ", Department of Civil and Environmental Engineering, Imperial College, UK.

J

JALAYER, F., 2003. "Direct probabilistic seismic analysis: Implementing non-linear dynamic assessments". Doctoral dissertation, Stanford University, CA.

JEARY, A. P., 1986. "Damping in tall buildings-a mechanism and a predictor". *Earthquake Engineering & Structural Dynamics,* 14 (5)**,** pp. 733-750.

JEHEL, P., LÉGER, P. & IBRAHIMBEGOVIC, A., 2014. "Initial versus tangent stiffness-based Rayleigh damping in inelastic time history seismic analyses". *Earthquake Engineering & Structural Dynamics,* 43 (3)**,** pp. 467-484.

JEONG, S.-H., MWAFY, A. & ELNASHAI, A., 2012. "Probabilistic seismic performance assessment of code-compliant multi-story RC buildings". *Engineering Structures,* 34 527-537.

JI, J., ELNASHAI, A. S. & KUCHMA, D. A., 2007a. "An analytical framework for seismic fragility analysis of RC high-rise buildings". *Engineering Structures,* 29 (12)**,** pp. 3197-3209.

JI, J., ELNASHAI, A. S. & KUCHMA, D. A., 2007b. "Seismic fragility assessment for reinforced concrete high-rise buildings". Mid-America Earthquake Center (MAE). Universty of Illinois at Urbana-Champaign, IL.

JI, J., ELNASHAI, A. S. & KUCHMA, D. A., 2009. "Seismic fragility relationships of reinforced concrete high-rise buildings". *The Structural Design of Tall and Special Buildings,* 18 (3)**,** pp. 259-277.

JIANG, J., XIAO, P. & LI, B., 2017. "True-triaxial compressive behaviour of concrete under passive confinement". *Construction and Building Materials,* 156 584-598.

JOHNSON, P. R., 1998. "Tectonic map of Saudi Arabia and adjacent areas". Technical Report USGS-TR-98-3. Deputy Ministry for Mineral Resources.

K

KANG, T. H., 2006. "Dynamic tests and modeling of RC and PT slab-column connections". 8th US National Conference on Earthquake Engineering. San Francisco, CA.

KANG, T. H. & WALLACE, J. W., 2005. "Dynamic responses of flat plate systems with shear reinforcement". *ACI Structural Journal,* 102 (5)**,** pp. 763.

KANG, T. H. & WALLACE, J. W., 2006. "Punching of reinforced and post-tensioned concrete slab-column connections". *Structural Journal,* 103 (4)**,** pp. 531-540.

KANG, T. H., WALLACE, J. W. & ELWOOD, K. J., 2009. "Nonlinear modeling of flat-plate systems". *Journal of structural engineering,* 135 (2)**,** pp. 147-158.

KAPPOS, A. J.: Input parameters for inelastic seismic analysis of R/C frame structures". *Proceedings of 8th European Conference on Earthquake Engineering, LNEC, Lisbon, Portugal*, 1986. 33-40.

KAPPOS, A. J.: Problems in using inelastic dynamic analysis to estimate seismic response modification factors of R/C buildings". *9th Eur Conf Earthq Eng*, 1990. 20-29.

KAPPOS, A. J., 1991. "Analytical prediction of the collapse earthquake for R/C buildings: Suggested methodology". *Earthquake Engineering & Structural Dynamics,* 20 (2)**,** pp. 167-176.

KAPPOS, A. J., 2001. "Seismic vulnerability assessment of existing buildings in Southern Europe". Keynote lecture, Convegno Nazionale 'L'Ingegneria Sismica in Italia' (Potenza/Matera, Italy), CD ROM Proceedings.

KAPPOS, A. J., 2014. "Dynamic loading and design of structures", CRC Press.

KAPPOS, A. J. & DIMITRAKOPOULOS, E. G., 2008. "Feasibility of pre-earthquake strengthening of buildings based on cost-benefit and life-cycle cost analysis, with the aid of fragility curves". *Natural Hazards,* 45 (1)**,** pp. 33-54.

KAPPOS, A. J. & KONSTANTINIDIS, D., 1999. "Statistical analysis of confined high strength concrete". *Materials and Structures,* 32 (10)**,** pp. 734-748.

KAPPOS, A. J. & KYRIAKAKIS, P., 2000. "A re-evaluation of scaling techniques for natural records". *Soil Dynamics and Earthquake Engineering,* 20 (1-4)**,** pp. 111-123.

KAPPOS, A. J., PANAGIOTOPOULOS, C. & PANAGOPOULOS, G.: Derivation of fragility curves using inelastic time-history analysis and damage statistics". *Proceedings, ICCE '04, Madeira, Portugal,* 2004. 665-672.

KAPPOS, A. J. & PANAGOPOULOS, G., 2010. "Fragility curves for reinforced concrete buildings in Greece". *Structure and Infrastructure Engineering,* 6 (1-2)**,** pp. 39-53.

KAPPOS, A. J., PANAGOPOULOS, G., PANAGIOTOPOULOS, C. & PENELIS, G. G., 2006. "A hybrid method for the vulnerability assessment of R/C and URM buildings". *Bulletin of Earthquake Engineering,* 4 (4)**,** pp. 391-413.

KAPPOS, A. J., PANAGOPOULOS, G., SEXTOS, A., PAPANIKOLAOU, V. K. & STYLIANIDIS, K. C., 2010. "Development of comprehensive earthquake loss scenarios for a Greek and a Turkish city-Structural aspects". *Earthquakes and Structures,* 1 (2)**,** pp. 197-214.

KAPPOS, A. J. & PENELIS, G. G., 1986. "Influence of concrete and steel properties on calculated inelastic seismic response of reinforced-concrete frames". *Journal of the American Concrete Institute* 83 (1)**,** pp. 167-169.

KAPPOS, A. J. & PENELIS, G. G., 2014. "Earthquake resistant concrete structures", CRC Press.

KAREEM, A., 1981. "Wind-excited response of buildings in higher modes". *Journal of the Structural Division,* 107 (4)**,** pp. 701-706.

KAREEM, A. & GURLEY, K., 1996. "Damping in structures: Its evaluation and treatment of uncertainty". *Journal of Wind Engineering and Industrial Aerodynamics,* 59 (2-3)**,** pp. 131-157.

KAUSEL, E., 2010. "Early history of soil-structure interaction". *Soil Dynamics and Earthquake Engineering,* 30 (9)**,** pp. 822-832.

KAUSEL, E., 2014. "Damping matrices revisited". *Journal of Engineering Mechanics,* 140 (8)**,** pp. 04014055 (1-4).

KELLY, T., 2007. "A blind prediction test of nonlinear analysis procedures for reinforced concrete shear walls". *Bulletin of the New Zealand Society for Earthquake Engineering,* 40 (3)**,** pp. 142-159.

KHAN, F. R., 1967. "John Hancock Center". *Civil Engineering,* 37 (10)**,** pp. 38.

KHAN, F. R., 1969. "Recent structural systems in steel for high-rise buildings". British Constructional Steelwork Association Conference on Steel in Architecture London, UK.

KHAN, F. R., 1972. "Influence of design criteria on selection of structural systems for tall buildings". Canadian Structural Engineering Conference. Montreal, Canada.

KHAN, F. R., 1973. "Evolution of structural systems for high-rise buildings in steel and concrete". 10th Regional Conference on Tall Buildings Bratislava, Czech Republic.

KHAN, F. R. & RANKINE, J., 1980. "Structural Systems and concepts". Tall Building Systems and Concepts Council on Tall Buildings and Urban Habitat (CTBUH) & American Society of Civil Engineers (ASCE).

KHAN, F. R. & SBAROUNIS, J. A., 1964. "Interaction of shear walls and frames ". *Journal of the Structural Division,* 90 (3)**,** pp. 285-338.

KHAN, Z., EL-EMAM, M., IRFAN, M. & ABDALLA, J., 2013. "Probabilistic seismic hazard analysis and spectral accelerations for United Arab Emirates". *Natural Hazards,* 67 (2)**,** pp. 569-589.

KHORAMI, M., ALVANSAZYAZDI, M., SHARIATI, M., ZANDI, Y., JALALI, A. & TAHIR, M., 2017. "Seismic performance evaluation of buckling restrained braced frames (BRBF) using incremental nonlinear dynamic analysis method (IDA)". *Earthquakes and Structures,* 13 (6)**,** pp.

KIM, S. J. & ELNASHAI, A. S., 2008. "Seismic assessment of RC structures considering vertical ground motion". University of Ellinios at Urbana Champaign, IL: Mid-America Earthquake Center, Depaertment of Civil and Environmental Engineering.

KIRCHER, C. A., WHITMAN, R. V. & HOLMES, W. T., 2006. "HAZUS earthquake loss estimation methods ". *Natural Hazards Review,* 7 (2)**,** pp. 45-59.

KOHRANGI, M., BAZZURRO, P., VAMVATSIKOS, D. & SPILLATURA, A., 2017. "Conditional spectrum-based ground motion record selection using average spectral acceleration". *Earthquake Engineering & Structural Dynamics,* 46 (10)**,** pp. 1667-1685.

KOLOZVARI, K., 2013. "Analytical modeling of cyclic shear-flexure interaction in reinforced concrete structural walls". Doctoral dissertation, UCLA, Los Angeles, CA.

KOLOZVARI, K., ORAKCAL, K. & WALLACE, J. W., 2014a. "Modeling of cyclic shear-flexure interaction in reinforced concrete structural walls. I: Theory". *Journal of Structural Engineering,* 141 (5)**,** pp. 04014135 (1-10).

KOLOZVARI, K., TRAN, T. A., ORAKCAL, K. & WALLACE, J. W., 2014b. "Modeling of cyclic shear-flexure interaction in reinforced concrete structural walls. II: experimental validation". *Journal of Structural Engineering,* 141 (5)**,** pp. 04014136 (1-12).

KONSTANTINIDIS, D. K., KAPPOS, A. J. & IZZUDDIN, B. A., 2007. "Analytical stress–strain model for high-strength concrete members under cyclic loading". *Journal of Structural Engineering,* 133 (4)**,** pp. 484-494.

KOWSARI, M., GHASEMI, S., FARAJPOUR, Z. & ZARE, M., 2019. "Capturing epistemic uncertainty in the Iranian strong-motion data on the basis of backbone ground motion models". *Journal of Seismology,* 1-13.

KURAMA, Y. C. & FARROW, K. T., 2003. "Ground motion scaling methods for different site conditions and structure characteristics". *Earthquake Engineering & Structural Dynamics,* 32 (15)**,** pp. 2425-2450.

KUSTU, O. & MILLER, D. D., 1984. "A rational methodology for predicting earthquake losses in urban areas". 8th World Conference on Earthquake Engineering (8WCEE). San Francisco, CA.

KUSTU, O., MILLER, D. D. & BROKKEN, S. T., 1982. "Development of damage functions for high-rise building components". San Francisco, CA: URS/John A. Blume and Associates.

KWON, O. S. & ELNASHAI, A. S., 2006. "The effect of material and ground motion uncertainty on the seismic vulnerability curves of RC structure". *Engineering Structures,* 28 (2)**,** pp. 289-303.

L

LANZI, A. & LUCO, J. E., 2017. "Caughey damping series in terms of products of the flexibility matrix". *Journal of Engineering Mechanics,* 143 (9)**,** pp. 04017089 (1-9).

LATBSDC, 2011. "An alternative procedure for seismic analysis and design of tall buildings located in the Los Angeles region". Los Angeles, CA: Los Angeles Tall Buildings Structural Design Council.

LAZAN, B. J., 1968. "Damping of materials and members in structural mechanics", Oxford, UK, Pergamon Press

LÉGER, P. & DUSSAULT, S., 1992. "Seismic-energy dissipation in MDOF structures". *Journal of Structural Engineering,* 118 (5)**,** pp. 1251-1269.

LEHMAN, D. E., TURGEON, J. A., BIRELY, A. C., HART, C. R., MARLEY, K. P., KUCHMA, D. A. & LOWES, L. N., 2013. "Seismic behavior of a modern concrete coupled wall". *Journal of Structural Engineering,* 139 (8)**,** pp. 1371-1381.

LI, B., 1994. "Strength and ductility of reinforced concrete members and frames constructed using high strength concrete". Doctoral dissertation, Department of Civil Engineering, University of Canterbury, Christchurch, New Zealand.

LI, M., LU, X., LU, X. & YE, L., 2014. "Influence of soil-structure interaction on seismic collapse resistance of super-tall buildings". *Journal of Rock Mechanics and Geotechnical Engineering,* 6 (5)**,** pp. 477-485.

LIM, J. C., OZBAKKALOGLU, T., GHOLAMPOUR, A., BENNETT, T. & SADEGHI, R., 2016. "Finite-element modeling of actively confined normal-strength and high-strength concrete under uniaxial, biaxial, and triaxial compression". *Journal of Structural Engineering,* 142 (11)**,** pp. 04016113.

LU, Y., HAJIRASOULIHA, I. & MARSHALL, A. M., 2016. "Performance-based seismic design of flexible-base multi-storey buildings considering soil-structure interaction". *Engineering Structures,* 108 90-103.

LUCO, J. E. & LANZI, A., 2017a. "A new inherent damping model for inelastic time-history analyses". *Earthquake Engineering & Structural Dynamics,* 46 (12)**,** pp. 1919-1939.

LUCO, J. E. & LANZI, A., 2017b. "Optimal Caughey series representation of classical damping matrices". *Soil Dynamics and Earthquake Engineering,* 92 253-265.

LUCO, N. & CORNELL, C. A., 1998. "Effects of Random Connection Fractures on the Demands and Reliability for 3-Story Pre-Northridge SMRF Structure". 6th USA National Conference on Earthquake Engineering. Seattle, WA.

LUCO, N. & CORNELL, C. A., 2000. "Effects of connection fractures on SMRF seismic drift demands". *Journal of Structural Engineering,* 126 (1)**,** pp. 127-136.

LUCO, N. & CORNELL, C. A., 2007. "Structure-specific scalar intensity measures for near-source and ordinary earthquake ground motions". *Earthquake Spectra,* 23 (2)**,** pp. 357-392.

LUCO, N., MAI, P. M., CORNELL, C. A. & BEROZA, G. C., 2002. "Probabilistic seismic demand analysis, SMRF connection fractures, and near-source effects". 7th U.S. National Conference on Earthquake Engineering. Boston, MA.

M

MACEDO, L. & CASTRO, J. M., 2017. "SelEQ: an advanced ground motion record selection and scaling framework". *Advances in Engineering Software,* 114 32-47.

MADAS, P. & ELNASHAI, A. S., 1992. "A new passive confinement model for the analysis of concrete structures subjected to cyclic and transient dynamic loading". *Earthquake Engineering & Structural Dynamics,* 21 (5)**,** pp. 409-431.

MAFFEI, J., 2007. "UCSD building slice test". PEER Tall Buildings Workshop, Task 7 (presentation) San Francisco, CA.

MALKAWI, A. I. H., BARAKAT, S., SHANABLEH, A., AL BDOUR, W., OMAR, M. & ALTOUBAT, S., 2007. "Seismic hazard assessment and mitigation of earthquake risk in United Arab Emirates". Sharjah, UAE: Published jointly by Jordan University of Science and Technology, Aman, Jordan and the Deanship of Research and Higher Studies, University of Sharjah, UAE.

MANDER, J. B., PRIESTLEY, M. J. & PARK, R., 1988. "Theoretical stress-strain model for confined concrete". *Journal of Structural Engineering,* 114 (8)**,** pp. 1804-1826.

MANGALATHU, S., SOLEIMANI, F., JIANG, J., DESROCHES, R. & PADGETT, J. E.: Sensitivity of fragility curves to parameter uncertainty using Lasso regression". *Proceedings of the 16th world conference on earthquake engineering, Santiago de Chile, Chile, Paper*, 2017.

MANOLIS, G. D., 2002. "Stochastic soil dynamics". *Soil Dynamics and Earthquake Engineering,* 22 (1)**,** pp. 3-15.

MARI, A. R., 1984. "Nonlinear geometric material and time dependent analysis of three dimensional reinforced and prestressed concrete frames". Berkeley, CA: Department of Civil Engineering, University of California.

MARTINELLI, P. & FILIPPOU, F. C., 2009. "Simulation of the shaking table test of a seven-story shear wall building". *Earthquake Engineering & Structural Dynamics,* 38 (5)**,** pp. 587-607.

MARTÍNEZ-RUEDA, J. E. & ELNASHAI, A. S., 1997. "Confined concrete model under cyclic load". *Materials and Structures,* 30 (3)**,** pp. 139-147.

MASSONE, L. M., 2006. "RC wall shear–flexure interaction: Analytical and experimental responses". Doctoral dissertation, University of California.

MASSONE, L. M., ORAKCAL, K. & WALLACE, J. W., 2015. Modeling flexural/shear interaction in RC walls. ACI-SP-236: Deformation Capacity and Shear Strength of Reinforced Concrete Members under Cyclic Loadings. Farmington Hills, MI: American Concrete Institute (ACI).

MAZZONI, S., MCKENNA, F., SCOTT, M. H. & FENVES, G. L., 2006. "OpenSees command language manual". Pacific Earthquake Engineering Research (PEER) Center.

MCGUIRE, R. K., 1995. "Probabilistic seismic hazard analysis and design earthquakes: Closing the loop". *Bulletin of the Seismological Society of America,* 85 (5)**,** pp. 1275-1284.

MCKENNA, F., 2011. "OpenSees: A framework for earthquake engineering simulation". *Computing in Science & Engineering,* 13 (4)**,** pp. 58-66.

MCKENNA, F. & FENVES, G. L., 2006. "OpenSees: Open system for earthquake engineering simulation", Berkeley, CA, Pacific Earthquake Engineering Research Center (PEER)

MEDINA, R. & KRAWINKLER, H., 2003. "Seismic demands for nondeteriorating frame structures and their dependence on ground motions". Report No. TR144, John Blume Earthquake Engineering Center, Department of Civil Engineering, Stanford University, Stanford, California, and PEER Report 2003/15, Pacific Earthquake Engineering Research Center, University of California, Berkeley, California.

MEDINA, R. A. & KRAWINKLER, H., 2004. "Seismic demands for nondeteriorating frame structures and their dependence on ground motions". PEER Project 3011999: Seismic demands for performance-based design. Stanford, CA: The John A. Blume Earthquake Engineering Center, Department of Civil and Environmental Engineering, Stanford University.

MEHANNY, S. S., 2009. "A broad-range power-law form scalar-based seismic intensity measure". *Engineering Structures,* 31 (7)**,** pp. 1354-1368.

MEHANNY, S. S. F. & DEIERLEIN, G. G., 2000. "Modeling and assessment of seismic performance of composite frames with reinforced concrete columns and steel beams". Stanford, Stanford, CA: The John A. Blume Earthquake Engineering Center, Department of Civil and Environmental Engineering, , Stanford University.

MENDOZA, M. & ROMO, M., 1989. "Behavior of building foundations in Mexico City during the 1985 Earthquake: Second stage". U.S.-Mexico Workshop on 1985 Mexico Earthquake Research in Lessons Learned from the 1985 Mexico Earthquake. Mexico City, Mexico: Earthquake Engineering Research Institute (EERI).

MENEGOTTO, M. & PINTO, P., 1973. "Method of analysis for cyclically loaded reinforced concrete plane frames including changes in geometry and non-elastic behavior of elements under combined normal force and bending". IABSE Symposium on the resistance and ultimate deformability of structures acted on by well-defined repeated loads. Lisbon, Portugal.

MEYMAND, P. J., 1998. "Shaking table scale model tests of nonlinear soil-pile-superstructure interaction in soft clay". Doctoral Dissertation, Civil Engineering Graduate Division, University of California.

MIRANDA, E., 1992. "Seismic evaluation and upgrading of existing buildings". Doctoral Dissertation, Civil Engineering Graduate Division, University of California.

MIZUNO, H., IIBA, M. & HIRADE, T., 1996. "Pile damage during the 1995 Hyogoken-Nanbu earthquake in Japan". 11th World Conference on Earthquake Engineering (11WCEE). Acapulco, Mexico.

MOAVENI, B., HE, X., CONTE, J. P. & RESTREPO, J. I., 2010. "Damage identification study of a seven-story full-scale building slice tested on the UCSD-NEES shake table". *Structural Safety,* 32 (5)**,** pp. 347-356.

MOEHLE, J. P., 2007. "The tall buildings initiative for alternative seismic design". *The Structural Design of Tall and Special Buildings,* 16 (5)**,** pp. 559-567.

MOHARRAMI, M. & KOUTROMANOS, I., 2016. "Triaxial constitutive model for concrete under cyclic loading". *Journal of Structural Engineering,* 142 (7)**,** pp. 04016039.

MOHR, D. S., 2007. "Nonlinear analysis and performance based design methods for reinforced concrete coupled shear walls". Doctoral Dissertation, University of Washington.

MOON, K. S., 2005. "Dynamic interrelationship between technology and architecture in tall buildings". Doctoral Dissertation, Massachusetts Institute of Technology (MIT).

MOYA, L., MAS, E., ADRIANO, B., KOSHIMURA, S., YAMAZAKI, F. & LIU, W., 2018. "An integrated method to extract collapsed buildings from satellite imagery, hazard distribution and fragility curves". *International journal of disaster risk reduction,* 31 1374-1384.

MUGURUMA, H., 1993. "Stress-strain curve model for concrete with a wide-range of compressive strength". 3rd International conference on utilization of high-strength concrete. Lillehammer, Norway.

MUSSON, R. M., NORTHMORE, K., SARGEANT, S., PHILLIPS, E., BOON, D., LONG, D., MCCUE, K. & AMBRASEYS, N. N., 2006. "The geology and geophysics of the United Arab Emirates. Vol. 4: Geological hazards". *British Geological Survey, Keyworth*.

MWAFY, A., 2012a. "Analytically derived fragility relationships for the modern high-rise buildings in the UAE". *The Structural Design of Tall and Special Buildings,* 21 (11)**,** pp. 824-843.

MWAFY, A., 2012b. "Classification and idealization of the building stock in the UAE for earthquake loss estimation". 15th world conference on earthquake engineering. Lisbon, Portugal

MWAFY, A. & ELKHOLY, S., 2017. "Performance assessment and prioritization of mitigation approaches for pre-seismic code structures". *Advances in Structural Engineering,* 20 (6)**,** pp. 917-939.

MWAFY, A. & ELNASHAI, A. S., 2001. "Static pushover versus dynamic collapse analysis of RC buildings". *Engineering Structures,* 23 (5)**,** pp. 407-424.

MWAFY, A., ELNASHAI, A. S., SIGBJÖRNSSON, R. & SALAMA, A., 2006. "Significance of severe distant and moderate close earthquakes on design and behavior of tall buildings". *The Structural Design of Tall and Special Buildings,* 15 (4)**,** pp. 391-416.

MWAFY, A., HUSSAIN, N. & EL-SAWY, K., 2015a. "Assessment of material strength implications on seismic design of tall buildings through collapse analysis". *Advances in Structural Engineering,* 18 (12)**,** pp. 2017-2033.

MWAFY, A., HUSSAIN, N. & EL-SAWY, K., 2015b. "Seismic performance and cost-effectiveness of high-rise buildings with increasing concrete strength". *The Structural Design of Tall and Special Buildings,* 24 (4)**,** pp. 257-279.

MWAFY, A. & KHALIFA, S., 2017. "Effect of vertical structural irregularity on seismic design of tall buildings ". *The Structural Design of Tall and Special Buildings,* 26 (18)**,** pp. e1399 (1-22).

N

NADIMPALLI, K., CORNISH, L. & KAZEMI, S., 2002. "National Exposure Information System (NEXIS) ". Geoscience Australia.

NAEIM, F. & LEW, M., 1995. "On the use of design spectrum compatible time histories". *Earthquake Spectra,* 11 (1)**,** pp. 111-127.

NAGAE, T., TAHARA, K., MATSUMORI, T., SHIOHARA, H., KABEYASAWA, T., KONO, S., NISHIYAMA, M., WALLACE, J. W., GHANNOUM, W., MOEHLE, J. P., SAUSE, R., KELLER, W. & TUNA, Z., 2011. "Design and instrumentation of the 2010 E-Defense four-story reinforced concrete and post-tensioned concrete buildings". Department of Civil and Environmental Engineering, University of California, Berkeley, CA: Pacific Earthquake Engineering Research Center (PEER).

NAGASHIMA, T., SUGANO, S., KIMURA, H. & ICHIKAWA, A., 1992. "Monotonic axial compression test on ultra-high-strength concrete tied columns". 10th World conference on earthquake engineering (10WCEE). Madrid, Spain.

NAISH, D. A. B., 2010. "Testing and modeling of reinforced concrete coupling beams". Doctoral Dissertation, University of California.

NAISH, D. A. B., FRY, J. A., KLEMENCIC, R. & WALLACE, J. W., 2009. "Experimental evaluation and analytical modeling of ACI 318-05/08 reinforced concrete coupling beams subjected to reversed cyclic loading". Report No. UCLA-SGEL 6, 2009. University of California, Los Angeles, CA.

NAISH, D. A. B. & WALLACE, J. W., 2010. "Testing and modeling of diagonally-reinforced reinforced concrete coupling beams". 9th US National Conference on Earthquake Engineering. Toronto, Canada.

NASSAR, A., 1992. "Seismic demands for SDOF and MDOF systems". Stanford, CA: John A. Blume Earthquake Engineering Center, Department of Civil Engineering, Stanford University.

NAZARI, Y. R. & SAATCIOGLU, M., 2017. "Seismic vulnerability assessment of concrete shear wall buildings through fragility analysis". *Journal of Building Engineering,* 12 202-209.

NCH-433, 1996. "Official Chilean Code 433-96 : Seismic Design of Buildings ". Santiago, Chile: Nacional de Normalizacion.

NEHRP, 2012. "Soil-Structure Interaction for Building Structures". Redwood, CA: NEHRP Consultants Joint Venture (a partnership of the Applied Technology Council and the Consortium of Universities for Research in Earthquake Engineering).

NEWMARK, N. M., 1959. "A method of computation for structural dynamics". *Journal of the Engineering Mechanics Division,* 85 (3)**,** pp. 67-94.

NGHIEM, H. M., 2009. "Soil-pile-structure interaction effects on high rises under seismic shaking". Doctoral Dissertation, University of Colorado, Department of Civil Engineering, Denver.

NZRC, 2012. "Canterbury Earthquake Royal Commission - Final Report". Wellington, New Zealand.

O

O'KELLY, M. E. J. & CAUGHEY, T. K., 1965. "Classical normal modes in damped linear dynamic systems". *Journal of Applied Mechanics,* 32 (3)**,** pp. 583-588.

O'ROURKE, M. J., 1976. "Discussion of response to stochastic wind of N-degree tall buildings by William E. Saul, Alain H. Peyrot and P. Jayachandran". *Journal of the Structural Division,* 102 (12)**,** pp. 2401-2403.

ORAKCAL, K., MASSONE, L. M. & WALLACE, J. W., 2006. "Analytical modeling of reinforced concrete walls for predicting flexural and coupled-shear-flexural responses". Berkeley, CA: Pacific Earthquake Engineering Research (PEER) Center, College of Engineering, University of California.

ORAKCAL, K., MASSONE, L. M. & WALLACE, J. W., 2009. "Shear strength of lightly reinforced wall piers and spandrels". *ACI Structural Journal,* 106 (4)**,** pp. 455-465.

ORAKCAL, K. & WALLACE, J. W., 2006. "Flexural Modeling of Reinforced Concrete Walls-Experimental Verification". *ACI Structural Journal,* 103 (2)**,** pp. 196-206.

ORAKCAL, K., WALLACE, J. W. & CONTE, J. P., 2004. "Flexural modeling of reinforced concrete walls-model attributes". *ACI Structural Journal,* 101 (5)**,** pp. 688-698.

OTANI, S., 1980. "Nonlinear dynamic analysis of reinforced concrete building structures". *Canadian Journal of Civil Engineering,* 7 (2)**,** pp. 333-344.

OTTOSEN, N. S., 1979. "Constitutive model for short-time loading of concrete". *Journal of the Engineering Mechanics Division ASCE,* 105 (2)**,** pp. 127-141.

P

PADGETT, J. E. & DESROCHES, R., 2007. "Sensitivity of seismic response and fragility to parameter uncertainty". *Journal of Structural Engineering,* 133 (12)**,** pp. 1710-1718.

PANAGIOTOU, M. & RESTREPO, J. I., 2006. "Model calibration for the UCSD 7-story building slice". NEES-UCSD Workshop on the Analytical Model of Reinforced Concrete Walls for Earthquake Resistance. San Diego, CA.

PANAGIOTOU, M. & RESTREPO, J. I., 2007. "Practical lessons learned from the full-scale 7-story building shake table test at UC San Diego". 2007 SEAOC Convention. Squaw Creek, CA.

PANAGIOTOU, M., RESTREPO, J. I. & CONTE, J. P., 2007a. "Shake table test of a 7 story full scale reinforced concrete structural wall building slice phase I: Rectangular wall section". San Diego, CA: Department of Structural Engineering, University of California.

PANAGIOTOU, M., RESTREPO, J. I. & CONTE, J. P., 2007b. "Shake table test of a 7 story full scale reinforced concrete structural wall building slice phase II: T-Wall section". San Diego, CA: Department of Structural Engineering, University of California.

PANAGIOTOU, M., RESTREPO, J. I. & CONTE, J. P., 2010. "Shake-table test of a full-scale 7-story building slice. Phase I: Rectangular wall". *Journal of Structural Engineering,* 137 (6)**,** pp. 691-704.

PANDEY, B., JAKKA, R. S. & KUMAR, A., 2016. "Influence of local site conditions on strong ground motion characteristics at Tarai region of Uttarakhand, India". *Natural Hazards,* 81 (2)**,** pp. 1073-1089.

PAPAGEORGIOU, A. S. & AKI, K., 1983. "A specific barrier model for the quantitative description of inhomogeneous faulting and the prediction of strong ground motion. I: Description of the model". *Bulletin of the Seismological Society of America,* 73 (3)**,** pp. 693-722.

PAPAGIANNOPOULOS, G. & BESKOS, D., 2012. "Damping identification for building structures subjected to earthquakes: A Review". *Journal of the Serbian Society for Computational Mechanics,* 6 (1)**,** pp. 129-147.

PARK, R., PRIESTLEY, M. & GILL, W. D., 1982. "Ductility of square-confined concrete columns". *Journal of the Structural Division,* 108 (4)**,** pp. 929-950.

PARK, Y. J. & ANG, A. H. S., 1985. "Mechanistic seismic damage model for reinforced concrete". *Journal of Structural Engineering,* 111 (4)**,** pp. 722-739.

PARRA-MONTESINOS, G. J., WIGHT, J. K., LEQUESNE, R. D. & SETKIT, M., 2012. A summary of ten years of research on HPFRC coupling beams. High Performance Fiber Reinforced Cement Composites 6. RILEM State of the Art Reports Springer, Dordrecht.

PASUCCI, V., FREE, M. W. & LUBKOWSKI, Z. A., 2008. "Seismic hazard and seismic design requirements for the Arabian Peninsula region". 14th World Conference on Earthquake Engineering (14WCEE). Beijing, China.

PAULAY, T. & PRIESTLEY, M. J. N., 2013. "Seismic design of reinforced concrete and masonry buildings", John Wiley and Sons Inc.

PEER, 2010. "Guidelines for performance-based seismic design of tall buildings". College of Engineering, University of California, Berkeley, CA: Pacific Earthquake Engineering Research (PEER) Center.

PEER, 2011. "Case studies of the seismic performance of tall buildings designed by alternative means: Task 12 report for the Tall Buildings Initiative (TBI)". College of Engineering, University of California, Berkeley, CA: Pacific Earthquake Engineering Research (PEER) Center.

PEER, 2019. "Ground motion Database" [Online]. Berkeley, CA: Pacific Earthquake Engineering Research (PEER) Center. Available: http://peer.berkeley.edu/ [Accessed January 01 2019].

PEER/ATC, 2010. "Modeling and acceptance criteria for seismic design and analysis of tall buildings". Redwood City, CA: By Applied Technology Council (ATC) for the Pacific Earthquake Engineering Research (PEER) Center.

PEIRIS, N., FREE, M. W., LUBKOWSKI, Z. A. & HUSSEIN, A. T., 2006. "Seismic hazard and seismic design requirements for the Arabian Gulf region". First European Conference on Earthquake Engineering and Seismology (1ECEES). Geneva, Switzerland.

PEJOVIC, J. & JANKOVIC, S., 2016. "Seismic fragility assessment for reinforced concrete high-rise buildings in Southern Euro-Mediterranean zone". *Bulletin of Earthquake Engineering,* 14 (1)**,** pp. 185-212.

PETRINI, L., MAGGI, C., PRIESTLEY, M. J. N. & CALVI, G. M., 2008. "Experimental verification of viscous damping modeling for inelastic time history analyzes". *Journal of Earthquake Engineering,* 12 (S1)**,** pp. 125-145.

PETROVSKI, J., 1983. Engineering measures for earthquake risk reduction in the Arab countries. Cidlinsky, K., and Rouhban, B.M. eds.: Assessment and mitigation of earthquake risk in the Arab region: Prepared by UNESCO for the Arab Fund for Economic and Social Development.

PILAKOUTAS, K., 1990. "Earthquake resistant design of reinforced concrete walls". Doctoral Dissertation, Imperial College of Science Technology and Medicine.

PISCESA, B., ATTARD, M. M., SAMANI, A. K. & TANGARAMVONG, S., 2017. "Plasticity Constitutive Model for Stress-Strain Relationship of Confined Concrete". *ACI Structural Journal,* 114 (2)**,** pp.

PITILAKIS, K. D., KARAPETROU, S. T. & FOTOPOULOU, S. D., 2014. "Consideration of ageing and SSI effects on seismic vulnerability assessment of RC buildings". *Bulletin of Earthquake Engineering,* 12 (4)**,** pp. 1755-1776.

PORTER, K. A., KIREMIDJIAN, A. S. & LEGRUE, J. S., 2001. "Assembly-based vulnerability of buildings and its use in performance evaluation". *Earthquake Spectra,* 17 (2)**,** pp. 291-312.

POWELL, G. H., 2007. "Detailed example of a tall shear wall building using CSI's Perform 3D nonlinear dynamic analysis", University Avenue, Berkeley, CA, Computers & Structures Educational Services.

POWELL, G. H., 2010. "Modeling for structural analysis: Behavior and basics", University Avenue, Berkeley, CA, Computers & Structures Educational Services.

PRAKASH, V., POWELL, G. H. & CAMPBELL, S., 1994. "Drain-3DX: Base program description and user guide: Version 1.10", Berkeley, CA, Department of Civil Engineering, University of California.

PRIESTLEY, M. J. N., 1993. "Myths and fallacies in earthquake engineering-conflicts between design and reality". *Bulletin of the New Zealand National Society for Earthquake Engineering,* 26 (3)**,** pp. 329-341.

PRIESTLEY, M. J. N.: Displacement-based approaches to rational limit states design of new structures". *Proc. 11th Eur. Conf. Earthquake Eng.: Invited Lectures*, 1999. 317-335.

PRIESTLEY, M. J. N. & GRANT, D. N., 2005. "Viscous damping in seismic design and analysis". *Journal of Earthquake Engineering,* 9 (2)**,** pp. 229-255.

PSYCHARIS, I. N., PAPASTAMATIOU, D. Y. & ALEXANDRIS, A. P., 2000. "Parametric investigation of the stability of classical columns under harmonic and earthquake excitations". *Earthquake Engineering and Structural Dynamics,* 29 (8)**,** pp. 1093-1109.

R

RAFI, M. M., LODI, S. H., AHMED, M., KUMAR, A. & VERJEE, F., 2016. "Development of building inventory for northern Pakistan for seismic risk reduction". *International Journal of Disaster Resilience in the Built Environment,* 7 (5)**,** pp. 501-520.

RAYHANI, M. H. T., EL NAGGAR, M. H. & TABATABAEI, S. H., 2008. "Nonlinear analysis of local site effects on seismic ground response in the Bam earthquake". *Geotechnical and Geological Engineering,* 26 (1)**,** pp. 91-100.

RISK-UE, 2001-2004. "An advanced approach to earthquake risk scenarios, with applications to different European cities. Projet Europen Risk-UE".

ROBINSON, D., FULFORD, G. & DHU, T., 2006. "EQRM: Geoscience Australia's Earthquake Risk Model: Technical Manual Version 3.0", Geoscience Australia.

RODRIGUEZ, M. E., BOTERO, J. C. & VILLA, J., 1999. "Cyclic stress-strain behavior of reinforcing steel including effect of buckling". *Journal of Structural Engineering,* 125 (6)**,** pp. 605-612.

RODRIGUEZ, M. E., RESTREPO, J. I. & BLANDÓN, J. J., 2006. "Shaking table tests of a four-story miniature steel building-model validation". *Earthquake Spectra,* 22 (3)**,** pp. 755-780.

ROJAHN, C. & SHARPE, R. L., 1985a. "Earthquake damage evaluation data for California", Applied technology council.

ROJAHN, C. & SHARPE, R. L., 1985b. "Earthquake damage evaluation data for California". Redwood City, CA: Applied Technology Council (ATC).

ROSSETTO, T. & ELNASHAI, A. S., 2003. "Derivation of vulnerability functions for European-type RC structures based on observational data". *Engineering Structures,* 25 (10)**,** pp. 1241-1263.

RYAN, K. L. & POLANCO, J., 2008. "Problems with Rayleigh damping in base-isolated buildings". *Journal of Structural Engineering,* 134 (11)**,** pp. 1780-1784.

S

SADIGH, K., CHANG, C. Y., EGAN, J. A., MAKDISI, F. & YOUNGS, R. R., 1997. "Attenuation relationships for shallow crustal earthquakes based on California strong motion data". *Seismological Research Letters,* 68 (1)**,** pp. 180-189.

SADRADDIN, H. L., SHAO, X. & HU, Y., 2016. "Fragility assessment of high-rise reinforced concrete buildings considering the effects of shear wall contributions". *The Structural Design of Tall and Special Buildings,* 25 (18)**,** pp. 1089-1102.

SAMANTA, A. & PANDEY, P., 2018. "Effects of ground motion modification methods and ground motion duration on seismic performance of a 15-storied building". *Journal of Building Engineering,* 15 14-25.

SATAKE, N., SUDA, K. I., ARAKAWA, T., SASAKI, A. & TAMURA, Y., 2003. "Damping evaluation using full-scale data of buildings in Japan". *Journal of Structural Engineering,* 129 (4)**,** pp. 470-477.

SCHOLL, R. E., 1980. "Seismic damage assessment for high-rise buildings: Annual technical report". California, CA: URS/John A. Blume & Associates, Engineers.

SCOTT, B. D., PARK, R. & PRIESTLEY, M. J. N., 1982. "Stress-strain behavior of concrete confined by overlapping hoops at low and high strain rates". *Journal Proceedings,* 79 (1)**,** pp. 13-27.

SEIFRIED, A. E. & BAKER, J. W., 2016. "Spectral variability and its relationship to structural response estimated from scaled and spectrum-matched ground motions". *Earthquake Spectra,* 32 (4)**,** pp. 2191-2205.

SEISMOSOFT, 2019. "SeismoStruct: A computer program for static and dynamic nonlinear analysis of framed structures".

ŞEŞETYAN, K., DANCIU, L., TÜMSA, M. B. D., GIARDINI, D., ERDIK, M., AKKAR, S., GÜLEN, L., ZARE, M., ADAMIA, S. & ANSARI, A., 2018. "The 2014 seismic hazard model of the Middle East: overview and results". *Bulletin of Earthquake Engineering,* 16 (8)**,** pp. 3535-3566.

SHAKHRAMANIAN, M. A., LARIONOV, V. I., NIGMETOV, G. M. & SUTSCHEV, S. P., 2000. "Assessment of the seismic risk and forecasting consequences of earthquakes while solving problems on population rescue (theory and practice)". Russian Civil Defense and Disaster Management Research Institute.

SHAMA, A. A., 2011. "Site specific probabilistic seismic hazard analysis at Dubai Creek on the west coast of UAE". *Earthquake Engineering and Engineering Vibration,* 10 (1)**,** pp. 143-152.

SHEA, G. H., 1999. "Recommended Lateral Force Requirements and Commentary", Sacramento, CA, Seismology Committee, Structural Engineers Association of California (SEAOC).

SHEIKH, S. A. & UZUMERI, S. M., 1980. "Strength and ductility of tied concrete columns". *Journal of the Structures Division,* 106 (5)**,** pp. 1079-1112.

SHEIKH, S. A. & UZUMERI, S. M., 1982. "Analytical model for concrete confinement in tied columns". *Journal of the Structural Division,* 108 (12)**,** pp. 2703-2722.

SHIMING, W. & GANG, G., 1998. Dynamic soil-structure interaction for high-rise buildings. Developments in Geotechnical Engineering.

SHING, P. S. B. & MAHIN, S. A., 1987. "Elimination of spurious higher-mode response in pseudodynamic tests". *Earthquake Engineering & Structural Dynamics,* 15 (4)**,** pp. 425-445.

SHOME, N., 1999. "Probabilistic seismic demand analysis of nonlinear structures". Doctoral Dissertation, Stanford University.

SHOME, N. & CORNELL, C. A., 1998. "Normalization and scaling accelerograms for nonlinear structural analysis". 6th US National Conference on Earthquake Engineering. Seattle, WA.

SHOME, N., CORNELL, C. A., BAZZURRO, P. & CARBALLO, J. E., 1998. "Earthquakes, records, and nonlinear responses". *Earthquake Spectra,* 14 (3)**,** pp. 469-500.

SIGBJORNSSON, R. & ELNASHAI, A. S., 2006. "Hazard assessment of Dubai, United Arab Emirates, for close and distant earthquakes". *Journal of Earthquake Engineering,* 10 (5)**,** pp. 749-773.

SIMPSON, K. A., 1996. "Attenuation of strong ground-motion incorporating near-surface foundation conditions". Doctoral Dissertation, Imperial College London (University of London).

SINGHAL, A. & KIREMIDJIAN, A. S., 1996. "Method for probabilistic evaluation of seismic structural damage". *Journal of Structural Engineering,* 122 (12)**,** pp. 1459-1467.

SMITH, R. J. & WILLFORD, M. R., 2007. "The damped outrigger concept for tall buildings". *The Structural Design of Tall and Special Buildings,* 16 (4)**,** pp. 501-517.

SMITH, S. S., WILLAM, K. J., GERSTLE, K. H. & STURE, S., 1989. "Concrete over the top-or, is there life after peak?". *ACI Materials Journal,* 86 (5)**,** pp. 491-497.

SMYROU, E., PRIESTLEY, M. J. N. & CARR, A. J., 2011. "Modelling of elastic damping in nonlinear time-history analyses of cantilever RC walls". *Bulletin of Earthquake Engineering,* 9 (5)**,** pp. 1559-1578.

SOLTANGHARAEI, V., RAZI, M. & VAHDANI, R., 2016. "Seismic fragility of lateral force resisting systems under near and far-fault ground motions". *International Journal of Structural Engineering,* 7 (3)**,** pp. 291-303.

SOUSA, L., MARQUES, M., SILVA, V. & VARUM, H., 2017. "Hazard disaggregation and record selection for fragility analysis and earthquake loss estimation". *Earthquake Spectra,* 33 (2)**,** pp. 529-549.

SOUSA, L., SILVA, V., MARQUES, M. & CROWLEY, H., 2016. "On the treatment of uncertainties in the development of fragility functions for earthquake loss estimation of building portfolios". *Earthquake Engineering & Structural Dynamics,* 45 (12)**,** pp. 1955-1976.

SPUDICH, P., JOYNER, W. B., LINDH, A. G., BOORE, D. M., MARGARIS, B. U. & FLETCHER, J. B., 1999. "SEA99: a revised ground motion prediction relation for use in extensional tectonic regimes". *Bulletin of the Seismological Society of America,* 89 (5)**,** pp. 1156-1170.

SRIRAM, A. & SRITHARAN, S., 2010. "Nonlinear Fiber-Based Analysis of Rectangular Concrete Walls Designed with Different Anchorage Details". 9th U.S. National Conference and 10th Canadian Conference on Earthquake Engineering. Ontario, Canada.

STAGNER, J. R., 1972. "Damping estimation and digital filtering applied to structural motions". Doctoral Dissertation, University of California.

STEFANIDOU, S., SEXTOS, A. G., KOTSOGLOU, A. N., LESGIDIS, N. & KAPPOS, A. J., 2017. "Soil-structure interaction effects in analysis of seismic fragility of bridges using an intensity-based ground motion selection procedure". *Engineering Structures,* 151 366-380.

STEFANIDOU, S. P. & KAPPOS, A. J., 2017. "Methodology for the development of bridge-specific fragility curves". *Earthquake Engineering & Structural Dynamics,* 46 (1)**,** pp. 73-93.

STEWART, J. P., CHIOU, S. J., BRAY, J. D., GRAVES, R. W., SOMERVILLE, P. G. & ABRAHAMSON, N. A., 2002. "Ground motion evaluation procedures for performance-based design". *Soil Dynamics and Earthquake Engineering,* 22 (9-12)**,** pp. 765-772.

SUCUOGLU, H. & YAZGAN, U., 2003. Simple survey procedures for seismic risk assessment in urban building stocks. Seismic assessment and rehabilitation of existing buildings. Dordrecht: Springer.

SUCUOGLU, H., YAZGAN, U. & YAKUT, A., 2007. "A screening procedure for seismic risk assessment in urban building stocks". *Earthquake Spectra,* 23 (2)**,** pp. 441-458.

SUN, Y. P. & SAKINO, K., 1993. "Ductility improvement of reinforced concrete columns with high strength materials". *Transactions of the Japan Concrete Institute (JCI),* 15 455-462.

T

TAKAYANAGI, T. & SCHNOBRICH, W. C., 1979. "Non-linear analysis of coupled wall systems". *Earthquake Engineering & Structural Dynamics,* 7 (1)**,** pp. 1-22.

TAMURA, Y., YAMADA, M. & YOKOTA, H., 1994. "Estimation of structural damping of buildings". Structures Congress XII. Atlanta, USA: ASCE.

TANG, Y., 2009. "Soil-structure interaction and its roles in performance-based seismic analysis of shear wall structures". Doctoral Dissertation, University of California.

TANG, Y., LAM, N., LUMANTARNA, E. & TSANG, H. H.: Generation of synthetic earthquake accelerograms based on up-to-date seismological ground motion models". *The Australian Earthquake Engineering Society 2016 Conference*, 2016.

TANG, Y. & ZHANG, J., 2011. "Probabilistic seismic demand analysis of a slender RC shear wall considering soil-structure interaction effects". *Engineering Structures,* 33 (1)**,** pp. 218-229.

TARANATH, B. S., 2004. "Wind and earthquake resistant buildings: Structural analysis and design", CRC press.

TARANATH, B. S., 2009. "Reinforced concrete design of tall buildings", CRC Press.

TARANATH, B. S., 2016. "Tall building design: Steel, concrete, and composite systems", CRC Press.

TAVAKOLI, B. & GHAFORY-ASHTIANY, M., 1999. "Seismic hazard assessment of Iran". *Annals of Geophysics,* 42 (6)**,** pp. 1013-1021.

THOMSEN, J. H. & WALLACE, J. W., 1995. "Displacement based design of reinforced concrete structural walls: An experimental investigation of walls with rectangular and t-shaped cross-sections: A dissertation". Doctoral Dissertation, Clarkson University.

THOMSEN, J. H. & WALLACE, J. W., 2004. "Displacement-based design of slender reinforced concrete structural walls-experimental verification". *Journal of Structural Engineering,* 130 (4)**,** pp. 618-630.

TOKIMATSU, K., OH-OKA, H., SATAKE, K., SHAMOTO, Y. & ASAKA, Y., 1998. "Effects of lateral ground movements on failure patterns of piles in the 1995 Hyogoken-Nambu earthquake". Proceeding of a Speciality Conference, Geotechnical Earthquake Engineering and Soil Dynamics III. Seattle, WA: ASCE.

TRIFUNAC, M. D., 2016. "Site conditions and earthquake ground motion–A review". *Soil dynamics and earthquake engineering,* 90 88-100.

TSO, W. K., ZHU, T. J. & HEIDEBRECHT, A. C., 1992. "Engineering implication of ground motion A/V ratio". *Soil Dynamics and Earthquake Engineering,* 11 (3)**,** pp. 133-144.

TUNA, Z., 2012. "Seismic performance, modeling, and failure assessment of RC shear wall buildings". Doctoral Dissertation, University of California.

TURGEON, J. A., 2011. "The seismic performance of coupled reinforced concrete walls". Master of Science, University of Washington.

U

UBC, 1997. "UBC-97 Uniform Building Code v. 2: Structural Engineering Design Provisions". Whittier, CA: International Conference of Building Officials.

UKAJI, K., 1975. "Analysis of soil-foundation-structure interaction during earthquakes". Doctoral Dissertation, Stanford University.

USGS, 2019. "United State Geological Survey-National Earthquake Information Centre (NEIC)". U.S.

V

VAMVATSIKOS, D. & CORNELL, C. A., 2002. "Incremental dynamic analysis". *Earthquake Engineering & Structural Dynamics,* 31 (3)**,** pp. 491-514.

VAMVATSIKOS, D. & CORNELL, C. A., 2004a. "Applied incremental dynamic analysis". *Earthquake Spectra,* 20 (2)**,** pp. 523-553.

VAMVATSIKOS, D. & CORNELL, C. A., 2004b. "Tracing and post-processing of IDA curves: Theory and software implementation". Stanford, CA: RMS Program, Stanford University.

VAMVATSIKOS, D. & CORNELL, C. A., 2005a. "Developing efficient scalar and vector intensity measures for IDA capacity estimation by incorporating elastic spectral shape information". *Earthquake engineering & structural dynamics,* 34 (13)**,** pp. 1573-1600.

VAMVATSIKOS, D. & CORNELL, C. A., 2005b. "Direct estimation of seismic demand and capacity of multidegree-of-freedom systems through incremental dynamic analysis of single-degree-of-freedom approximation". *Journal of Structural Engineering,* 131 (4)**,** pp. 589-599.

VAMVATSIKOS, D. & CORNELL, C. A., 2006. "Direct estimation of the seismic demand and capacity of oscillators with multi-linear static pushovers through IDA". *Earthquake Engineering & Structural Dynamics,* 35 (9)**,** pp. 1097-1117.

VLACHOS, C., PAPAKONSTANTINOU, K. G. & DEODATIS, G., 2018. "Predictive model for site specific simulation of ground motions based on earthquake scenarios". *Earthquake Engineering & Structural Dynamics,* 47 (1)**,** pp. 195-218.

W

WALLACE, J. W., 2007. "Modelling issues for tall reinforced concrete core wall buildings". *The Structural Design of Tall and Special Buildings,* 16 (5)**,** pp. 615-632.

WALLACE, J. W., 2010. Performance-based design of tall reinforced concrete core wall buildings. Earthquake Engineering in Europe. Netherlands: Springer.

WALLACE, J. W., 2012. "Behavior, design, and modeling of structural walls and coupling beams-Lessons from recent laboratory tests and earthquakes". *International Journal of Concrete Structures and Materials,* 6 (1)**,** pp. 3-18.

WALLACE, J. W. & MOEHLE, J. P., 1992. "Ductility and detailing requirements of bearing wall buildings". *Journal of Structural Engineering,* 118 (6)**,** pp. 1625-1644.

WALLACE, J. W. & MOEHLE, J. P., 2012. "Behavior and design of structural walls–lessons from recent laboratory tests & earthquakes". International Symposium on Engineering Lessons Learned from the 2011 Great East Japan Earthquake. Tokyo, Japan.

WANG, G., YOUNGS, R. R., POWER, M. & LI, Z., 2015. "Design ground motion library: an interactive tool for selecting earthquake ground motions". *Earthquake Spectra,* 31 (2)**,** pp. 617-635.

WAUGH, J. D., 2009. "Nonlinear analysis of T-shaped concrete walls subjected to multi-directional loading". Doctoral Dissertation, Iowa State University.

WAUGH, J. D., AALETI, S., SRITHARAN, S. & ZHAO, J., 2008. "Nonlinear analysis of rectangular and T-shaped concrete walls". Ames, IA: Department of Civil, Construction and Environmental Engineering, Iowa State University.

WAUGH, J. D. & SRITHARAN, S., 2010. "Lessons learned from seismic analysis of a seven-story concrete test building". *Journal of Earthquake Engineering,* 14 (3)**,** pp. 448-469.

WEN, Y. K., ELLINGWOOD, B. R. & BRACCI, J. M., 2004. "Vulnerability function framework for consequence-based engineering". MAE Center Project. Champaign, IL: University of Illinois at Urbana-Champaign.

WEN, Y. K., ELLINGWOOD, B. R., VENEZIANO, D. & BRACCI, J. M., 2003. "Uncertainty modeling in earthquake engineering". MAE Center Project. Champaign, IL: University of Illinois at Urbana-Champaign.

WILSON, E. & PENZIEN, J. O., 1972. "Evaluation of orthogonal damping matrices". *International Journal for Numerical Methods in Engineering,* 4 (1)**,** pp. 5-10.

X

XIE, J., ELWI, A. E. & MACGREGOR, J. G., 1995. "Mechanical properties of three high-strength concretes containing silica fume". *Materials Journal,* 92 (2)**,** pp. 135-145.

XU, H. & WEN, H. M., 2016. "A computational constitutive model for concrete subjected to dynamic loadings". *International Journal of Impact Engineering,* 91 116-125.

Y

YAMIN, L. E., HURTADO, A. I., BARBAT, A. H. & CARDONA, O. D., 2014a. "Seismic and wind vulnerability assessment for the GAR-13 global risk assessment". *International Journal of Disaster Risk Reduction,* 10 452-460.

YAMIN, L. E., HURTADO, A. I., RINCON, R., BARBAT, A. H. & REYES, J. C., 2014b. "Use of non-linear dynamic analysis in the assessment of seismic vulnerability of buildings". Second European Conference on Earthquake Engineering and Seismology (2ECEES). Istanbul, Turkey.

YAMIN, L. E., HURTADO, A. I., RINCON, R., DORADO, J. F. & REYES, J. C., 2017. "Probabilistic seismic vulnerability assessment of buildings in terms of economic losses". *Engineering Structures,* 138 308-323.

YEPES-ESTRADA, C., SILVA, V., VALCÁRCEL, J., ACEVEDO, A. B., TARQUE, N., HUBE, M. A., CORONEL, G. & MARÍA, H., 2017. "Modeling the residential building inventory in South America for seismic risk assessment". *Earthquake Spectra,* 33 (1)**,** pp. 299-322.

YOKOO, Y. & AKIYAMA, H., 1972. "Lateral vibration and damping due to wind and earthquake effects". The International Conference on Planning and Design of Tall Buildings. NY, U.S.

YONG, Y. K., NOUR, M. G. & NAWY, E. G., 1988. "Behavior of laterally confined high-strength concrete under axial loads". *Journal of Structural Engineering,* 114 (2)**,** pp. 332-351.

YOUNGS, R. R., CHIOU, S. J., SILVA, W. J. & HUMPHREY, J. R., 1997. "Strong ground motion attenuation relationships for subduction zone earthquakes". *Seismological Research Letters,* 68 (1)**,** pp. 58-73.

YOUNGS, R. R., POWER, M. & CHIN, C., 2006. "Design ground motion library". 8th National Conference on Earthquake Engineering. San Francisco, CA.

YU, X., LU, D. & LI, B., 2016. "Estimating uncertainty in limit state capacities for reinforced concrete frame structures through pushover analysis". *Earthquakes and Structures,* 10 (1)**,** pp. 141-161.

YUN, S. Y., HAMBURGER, R. O., CORNELL, C. A. & FOUTCH, D. A., 2002. "Seismic performance evaluation for steel moment frames". *Journal of Structural Engineering,* 128 (4)**,** pp. 534-545.

Z

ZARE, M., 2002. "Attenuation relation and coefficients of movement in Iran". Iran: International Institute of Earthquake Engineering and Seismology.

ZAREIAN, F. & MEDINA, R. A., 2010. "A practical method for proper modeling of structural damping in inelastic plane structural systems". *Computers & Structures,* 88 (1-2)**,** pp. 45-53.

Appendix A. Structural systems in RC high-rise buildings

Based on the distribution of the primary components of the lateral load-resisting system in the building, structural systems in RC high-rise buildings can be classified under three broad categories: interior systems, exterior systems, and hybrid system (e.g Taranath, 2004, Ali and Moon, 2007, Taranath, 2009, Taranath, 2016, CTBUH, 2019). Table A1 summarises the system types under each category, while a brief definition of each category and the structural systems falling under it is given hereafter.

A.1 Interior structural systems

In this structural system, the major part of the lateral load-resisting system is located within the interior zone of the building. Among the well-established structural forms under this category are the rigid frame, shear walls and/or cores, shear wall-rigid frame, and core-supported outrigger.

A.1.1 Moment-resisting frame system

It is a system that comprises of vertical (column) and horizontal (beam) members connected together in a planar grid form by rigid (moment-resisting) joints. The formed planar rigid frames resist lateral loads principally through the flexural stiffness of their members. Frame stiffness resisting the lateral sway of the building is the factor controlling the size of beams. The size of the columns, on the other hand, is largely controlled by gravity loads, leading to progressively larger column sizes towards the base of the structure. In low-to-medium seismic regions, the frame action may be used for lateral resistance of RC buildings up to 15- to 20-storeys except when the building is very slender. An example of a rigid frame system in RC buildings is the 12-storey, 45m Warqaa Residential in Dubai, UAE.

A.1.2 Shear wall system

This system comprises either of RC planar/coupled shear walls, RC core walls, or a combination of the two, have been on the most prevalent lateral load-resisting system in high-rise buildings. In a simplified form, the system is a resemblance of vertical cantilever fixed to the base of the building. When two or more shear walls in the same

planar grid are linked by horizontal members such as slabs or beams, the formed system is called coupled shear walls. The overall lateral stiffness of this system far exceeds the sum of the stiffnesses of the walls forming it. The reason is that the flooring system renders the shear walls acting as coupled. In many tall buildings, the sold single or multiple RC cores located around the building main utility shafts, stairwells, and elevators can alone be sufficient to stabilize the structure against lateral forces. The RC Wave tower in Dubai, UAE with its 28-storeys and 101m of total height stands as a good example of using a combination of planar and coupled shear walls along with core walls.

A.1.3 Shear wall-Frame system

This structural system resulted from the interaction of rigid frame system and shear/core walls system when combined together. Above a certain building height, rigid frame system alone becomes insufficient because of the excessive building sway. Similarly, the shear/core walls system has its limitation in providing lateral resistance to buildings above a certain number of storeys depending on the system height-to-width ratio. In the shear wall-rigid frame system, the horizontal deflection compatibility generates interaction between the two sub-systems. When combining the linear shear-type sway profile of the rigid frame with the parabolic bending-type sway mode of the shear wall, the lateral rigidity of the building enhances. This is so because the shear wall is restrained by the rigid frame at the upper levels while it restrains the frame at the lower levels of the building. This system is applicable for buildings in the range of 50 to 80 storeys. There are, however, examples of this system in buildings of over 100 storeys. The 60-storey, 220m Stella Maris tower located in Dubai, UAE is an example of buildings utilising the shear wall-rigid frame system.

A.1.4 Core-supported outrigger system

This system is a modification of the shear wall-rigid frame system, consisting of an RC core and 1- to 2-storey-high horizontal outriggers in the form of steel trusses or RC walls that connect the core to the perimeter columns. Normally, the core is centrally located with outriggers spreading on both sides of the buildings. In some cases, however, the core may be located at one side of the building with outriggers extending to the perimeter columns on the other side. The outriggers effectively act as stiff caps tending to reverse the bending curvature of the RC core by inducing tension-compression couple in perimeter columns. Furthermore, the system often includes

exterior belt girders (or trusses) that interconnect the perimeter columns. The function of the belt girders is to efficiently distribute the compressive and tensile forces between the perimeter columns, which in turn, help to minimise the differential shortening and elongation of those columns. To reduce the obstruction to the view and occupiable space that outriggers create, they often positioned at mechanical and power equipment floors. Core-supported outrigger systems enable the construction of buildings with great height potential up to 150 storeys and more (Taranath, 2016). An excellent example of buildings utilising the system is the 101-storey, 509m famous Taipei 101 tower in Taipei, Taiwan.

A.2 Exterior structural systems

In this structural system, the major part of the lateral load-resisting system is located at the building perimeter. Among the main structural systems falling under this category are the tubular, with its different forms, and the exoskeleton.

A.2.1 Tubular system

The tubular system is one of the most typical exterior structural systems with the earliest application attributed to Fazlur Khan in the design of the 43-storey DeEitt-Chestnut building in Chicago USA (Ali and Moon, 2007). It is a three-dimensional system utilising the entire depth of the building to resist lateral loads. According to the building height and their structural efficiency, there are several types of the tubular system.

- ✓ **Framed tube:** Is the basic of tubular forms, consisting of closed spaced columns rigidly connected to deep spandrel beams throughout the exterior perimeter of the building. In this system, the axial forces resisted by the corner columns are much greater compared to those carried by the middle columns for both the flange frame (frame perpendicular to the direction of lateral load) and the web frame (frame parallel to the direction of lateral load). This is known as the *shear lag* phenomenon whose effect, for an optimal framed tube design, is to be limited to the lowest and substituted with more of cantilever-type behaviour.

- ✓ **Braced tube:** The concept of this system is to replace the closely spaced perimeter columns with widely spaced columns stiffened by diagonal braces to attain a wall-

like structural characteristics. An early example of this system is the John Hanckok Centre of Chicago, USA (Taranath, 2016)

- ✓ framed tube system becomes increasingly inefficient as the web frame starts to act similar to a conventional rigid frame. Consequently, the size of the columns and beams become larger since their designs are then controlled by bending. The braced tube system overcomes this issue as the perimeter frames are braced in their own planes with diagonals that are connected to the columns at each joint. This arrangement effectively eliminates shear lag effects. As a result, the columns can be spaced more widely and, along with the spandrel beams, have smaller sizes than in the framed tube system (Khan, 1967).

- ✓ **Tube-in-tube:** In this tubular form, the core in the building is utilised as an inner tube alongside the exterior framed tube to enhance the overall lateral stiffness. The lateral load is transferred to both tubes through the floor diaphragm connecting the core to the perimeter columns/spandrels system. An example of this tubular system is the 64-storey Al-Hekma Tower located in Dubai, UAE. Depending on the building height and complexity, the tube-in-tube system may have more than one inner tube connected to the perimeter framed tube.

- ✓ **Diagrid tube:** The diagrid tube -as a portmanteau of diagonal grid tube- is another tubular form of which almost all vertical columns in the conventional perimeter braced frame system are eliminated. The diagrid system consists of perimeter diagonals arranged in a triangulated configuration, carrying lateral forces as well as gravity loads in a distributive manner. Compared to the framed tube system, this tubular form is greatly more effective in minimising shear deformation as it carries shear by axial action of the diagonal members rather than by bending of the spandrel beams and vertical columns forming the exterior framed tube (Moon, 2005). Good examples of RC high-rise buildings built using the diagrid tube system are the O-14 building in Dubai, UAE (23-storey above ground, 102 m) and the COR building in Miami, USA (25-storey above ground, 116 m).

- ✓ **Modular tube:** Also known as *"Bundled Tube"*, is a system of which the underlying principle is to connect two or more widely spaced columns-individual tubes in a vertical modular form with the main objective being to decrease the shear lag effect. The cluster of tubes is interconnected with common interior panels to

generate a multicellular tube. The supremacy of the modular tube system over the single framed/braced tube becomes evident when building dimensions increase in both width and height. The best example of this system in action is the Burj Khalifa tower in Dubai, UAE, standing as the tallest RC building in the world with 828 m of total architectural height and 165 above-ground storeys. It is noteworthy that this structural system of Burj Khalifa is combined with another system termed buttressed core, in which each of the building wings is buttressed down to provide more stiffness (Baker, 2017).

A.2.2 Exoskeleton system

In this structural form, the lateral load-resisting system is positioned outside the building boundary lines of the building away from its façades. The system normally acts as the primary building identifier due to its compositional characteristics. Although fireproofing of the exoskeleton system is not a challenging issue, its thermal expansion-contraction and systematic thermal bridges should be carefully looked into during the design stage. An example of the system is the 44-storey, 154 m Hotel De Artes in Barcelona, Spain.

A.3 Hybrid structural systems

The hybrid system is a complex yet efficient system often formed by the combination of exterior and interior structural forms thereby referred to as “hybrid”. With this type of structural systems, mega tall structures can be achieved. A good example is the structural systems of the 93-storey, 452m Petronas Twin Towers in Kuala Lumpur, Malaysia. The building utilised RC core walls, a framed tube with high strength ring beams, and a composite deck flooring for faster construction.

Table A1. Building examples, gains, and drawbacks of different structural systems in high-rise buildings (Ali and Moon, 2007, Taranath, 2016, CTBUH, 2019)

Broad Category	Structural System	Sub-Category	Common Height Range (m)	Gains	drawbacks	Building example
Interior	Rigid Frames	-	40-70	• Flexibility in interior space planning	• Drop beams affecting floor-to-floor clear height and MEP services • Slow construction	Warqaa Residential, Dubai, UAE (12-storey, 45m)
	Shear Walls and/or Core Walls	-	70-150	• Shear walls and cores effectively resist lateral loads • Fast construction	• The existence of shear walls and cores limits interior space planning	Wave Tower, Dubai, UAE (28-storey, 101m)
	Shear wall-Rigid Frame	-	150-250	• The shear wall-rigid frame interacting system effectively resist lateral loads	• The existence of shear walls and cores limits interior space planning	Stella Maris Tower, Dubai, UAE (60-storey, 220m)
	Core-supported Outrigger	-	> 300	• Minimise lateral deformation of the interior core • Exterior columns connected to the interior core through extended outriggers effectively resists bending	• The 1- to 2-storey depth of outriggers obstruct the use of the storeys of which they are positioned	Taipei 101, Taipei, Taiwan (101-storey, 509m)

Table A1 *(continued)*. Building examples, gains, and drawbacks of different structural systems in high-rise buildings

Broad Category	Structural System	Sub-Category	Common Height Range (m)	Gains	drawbacks	Building example
Exterior	Tube	Framed Tube	175-250	• Efficient resistance to lateral load • Interior floor plan relatively free	• Closely spaced perimeter columns hinder the view • Optimum tubular behaviour hindered by shear lag	Water Tower Place, Chicago, USA (78-storey, 262m)
		Braced Tube	250-350	• Diagonal members effectively carry lateral shear forces through axial tension/compression • Wider spacing between perimeter columns compared with framed tube system	• View obstruction by bracings	Onterie Center Chicago, USA (60-storey, 170m)
		Tube-in-Tube	200-300	• The interior core tube-exterior framed tube interaction system efficiently resisting lateral loads	• The existence of shear core limits interior space planning	Hekma Tower, Dubai, UAE (64-storey, 282m)
		Diagrid Tube	250-350	• Diagonal members effectively carry lateral shear forces through axial tension/compression	• Complicated formwork • Expensive construction • View obstruction by diagonal members	O-14, Dubai, UAE (23-storey, 102m)
		Modular Tube	>400	• Reducing lateral shear lag effects	• Bundled tube configuration may limit interior space planning	Burj Khalifa, Dubai, UAE (165-storey, 828m)
	Exo-skeleton	-	250-350	• Column-free interior	• Thermal bridging • Thermal expansion/contraction of the system	Hotel De Artes, Barcelona, Spain (44-storey, 154m)
Hybrid	Combination of Exterior/ Interior Systems	-	> 400	• Applicable for supertall buildings	• Building form depends greatly on the implemented structural systems	Petronas Towers, Kuala Lumpur, Malaysia (93-storey, 452m)